

KOMPASS-II

Compaction of Crushed Salt for Safe Containment – Phase 2

Supported by:



Federal Ministry
for the Environment, Nature Conservation,
Nuclear Safety and Consumer Protection

based on a decision of
the German Bundestag



U.S. DEPARTMENT OF
ENERGY

KOMPASS-II

Compaction of Crushed Salt for Safe Containment – Phase 2

Larissa Friedenberg (GRS)
Jeroen Bartol (COVRA)
James Bean (Sandia)
Steffen Beese (BGR)
Hans de Bresser (UU)
Jibril B. Coulibaly (Sandia)
Oliver Czaikowski (GRS)
Uwe Düsterloh (TUC)
Ralf Eickemeier (BGR)
Ann-Kathrin Gartzke (BGR)
Suzanne Hangx (UU)
Kyra Jantschik (GRS)
Ben Laurich (BGR)
Christian Lerch (BGE-TEC)
Svetlana Lerche (TUC)
Wenting Liu (BGR)
Christoph Lüdeling (IfG)
Melissa M. Mills (Sandia)
Nina Müller-Hoeppe (BGE-TEC)
Bart van Oosterhout (UU)
Till Popp (IfG)
Ole Rabbel (IfG)
Michael Rahmig (BGE-TEC)
Benjamin Reedlunn (Sandia)
Abram Rogalski (GRS)
Christopher Rölke (IfG)
Nachinzorig Saruulbayar (TUC)
Christopher J. Spiers (UU)
Kristoff Svensson (BGR)
Jan Thiedau (BGR)
Kornelia Zemke (BGR)

January 2024

Remark:

This report refers to the research projects 02E11951A, 02E11951B, 02E11951C and 02E11951D which has been funded by the German Federal Ministry for Environment, Nature Conversation, Nuclear Safety and Consumer Protection (BMUV).

The work was conducted by BGE Technology (BGE-TEC), Bundesanstalt für Geowissenschaften und Rohstoffe (BGR), COVRA, Institut für Gebirgsmechanik (IfG), Sandia National Laboratories, Technische Universität Clausthal (TUC), Utrecht University (UU) and Gesellschaft für Anlagen- und Reaktorsicherheit (GRS).

The authors are responsible for the content of the report.

GRS - 751

ISBN 978-3-910548-42-8

Keywords

Crushed Salt Compaction, Salt Repository, THM-coupled Processes

Abstract

Long-term stable sealing elements are a basic component in the safety concept for a possible repository for heat-emitting radioactive waste in rock salt. The sealing elements will be part of the closure concept for drifts and shafts. They will be made from a well-defined crushed salt in employ a specific manufacturing process. The use of crushed salt as geotechnical barrier as required by the German Site Selection Act from 2017 /STA 17/ represents a paradigm change in the safety function of crushed salt, since this material was formerly only considered as stabilizing backfill for the host rock. The demonstration of the long-term stability and impermeability of crushed salt is crucial for its use as a geotechnical barrier.

The KOMPASS-II project, is a follow-up of the KOMPASS-I project and continues the work with focus on improving the understanding of the thermal-hydraulic-mechanical (THM) coupled processes in crushed salt compaction with the objective to enhance the scientific competence for using crushed salt for the long-term isolation of high-level nuclear waste within rock salt repositories. The project strives for an adequate characterization of the compaction process and the essential influencing parameters, as well as a robust and reliable long-term prognosis using validated constitutive models.

For this purpose, experimental studies on long-term compaction tests are combined with microstructural investigations and numerical modeling. The long-term compaction tests in this project focused on the effect of mean stress, deviatoric stress and temperature on the compaction behavior of crushed salt. A laboratory benchmark was performed identifying a variability in compaction behavior. Microstructural investigations were executed with the objective to characterize the influence of pre-compaction procedure, humidity content and grain size/grain size distribution on the overall compaction process of crushed salt with respect to the deformation mechanisms. The created database was used for benchmark calculations aiming for improvement and optimization of a large number of constitutive models available for crushed salt. The models were calibrated, and the improvement process was made visible applying the virtual demonstrator.

Zusammenfassung

Langzeitwirksame Dichtelemente sind essentiell in dem Sicherheitskonzept für ein mögliches Endlager für wärmeentwickelnde, hochradioaktive Abfälle im Wirtsgestein Steinsalz. Die Dichtelemente sind Teil eines Verschlussystems für Strecken und Schächte. Sie werden aus einem gut bestimmbareren Salzgrus in einem qualifizierten Herstellungsprozess errichtet. Die Funktion von Salzgrus als geotechnische Barriere stellt einen Paradigmenwechsel in der Sicherheitsfunktion von Salzgrus dar, der im Standortauswahlgesetz von 2017 dokumentiert ist /STA 17/. Während der Vergangenheit wurde Salzgrus vorrangig bezüglich seiner Eignung als Versatzmaterial mit Stützfunktion für das umgebende Wirtsgestein betrachtet. Für die nun vorgesehene Verwendung von Salzgrus als geotechnische Barriere ist der Nachweis der langzeitigen Funktionsfähigkeit essentiell.

Das KOMPASS-II Projekt, als Nachfolgevorhaben zum KOMPASS-I Projekt, beschäftigte sich mit der Untersuchung des Kompaktionsverhaltens von Salzgrus mit dem Ziel das Verständnis für die thermisch-hydraulisch-mechanisch (THM) gekoppelten Prozesse zu verbessern und somit die wissenschaftliche Grundlage zur Verwendung von Salzgrus für die langzeitliche Isolation von wärmeentwickelnden, hochradioaktiven Abfällen in Steinsalz zu stärken. Es wurde eine adäquate Beschreibung des Kompaktionsprozesses, sowie der Einflussparameter angestrebt, genauso wie eine robuste und zuverlässige Prognose mit validierten Stoffmodellen für die Langzeitsicherheit.

Für diesen Zweck wurden experimentelle Studien auf Basis von Langzeitkompaktionsexperimenten mit mikrostrukturellen Untersuchungen, sowie numerischen Modellierungen verbunden. Die Untersuchungen des Langzeitkompaktionsverhaltens fokussierten sich auf den Einfluss der mittleren Spannung, der deviatorischen Spannung und der Temperatur auf das Kompaktionsverhalten von Salzgrus. Die Mikrostrukturuntersuchungen beschäftigten sich mit den Einflüssen der Vorkompaktionsmethode, des Feuchtegehalts und der Korngrößen/-verteilung auf die mikrostrukturellen Deformationsmechanismen und deren Beitrag zur übergeordneten Kompaktion von Salzgrus. Die gewonnene Datenbasis wurde im Rahmen von Benchmarkrechnungen zur Verbesserung und Optimierung einer großen Anzahl an verfügbaren Stoffmodellen verwendet. Die Modelle wurden anhand der experimentellen Daten kalibriert, wobei dieser Prozess anhand des virtuellen Demonstrators nachvollziehbar wurde.

Acknowledgements

The authors of BGE TECHNOLOGY (FKZ 02E11951B), Gesellschaft für Anlagen- und Reaktorsicherheit gGmbH (FKZ 02E11951A), Institut für Gebirgsmechanik Leipzig (FKZ 02E11951C) and Clausthal University of Technology (FKZ 02E11951D) gratefully acknowledge the funding received by the Federal Ministry for Environment, Nature Conservation, Nuclear Safety and Consumer Protection (BMUV), represented by the Project Management Agency Karlsruhe (PTKA).

The Sandia National Laboratory authors gratefully acknowledge funding from the U.S. Department of Energy (DOE). Sandia National Laboratories is a multimission laboratory managed and operated by National Technology & Engineering Solutions of Sandia, LLC, a wholly owned subsidiary of Honeywell International Inc., for the U.S. Department of Energy's National Nuclear Security Administration under contract DE-NA0003525, SAND2024-00570R.

This research is funded by the U.S. Department of Energy's Office of Nuclear Energy (DOE-NE) Office of Spent Fuel & Waste Science and Technology.



The project coordinator GRS is sincerely thankful for the great progress achieved within the project due to the excellent collaboration and fruitful discussions along the project lifetime with all project partners.

Table of Contents

	Abstract	I
	Zusammenfassung	II
	Acknowledgements	III
1	Introduction	1
2	Progress in crushed salt investigations	3
2.1	Introduction.....	3
2.2	Main achievements of the KOMPASS-I project.....	3
2.3	Development of a long-term strategy	4
2.4	Collaboration with the SAVER project.....	13
3	Laboratory investigations	17
3.1	Introduction.....	17
3.2	Pre-compaction tests	18
3.2.1	Oedometric pre-compaction (BGR).....	19
3.2.2	Pre-compaction in the “Big oedometer cell” (IfG)	28
3.2.3	Plain-strain pre-compaction (TUC).....	52
3.3	Long-term compaction tests.....	61
3.3.1	Oedometric compaction tests (BGR).....	62
3.3.2	Triaxial compaction tests (BGR)	76
3.3.3	Triaxial compaction tests addressing pre-compaction and mean stress (GRS)	88
3.3.4	Long-term compaction test in the „New IfG crushed salt compaction cell“	100
3.3.5	Long-term triaxial compaction tests addressing the dependency of compaction rate on porosity, mean stress, deviatoric stress and temperature (TUC).....	104
3.3.6	Results of the Laboratory Benchmark	113
3.4	Indexed permeability tests (TUC).....	118

4	Microstructural Investigations.....	123
4.1	Introduction.....	123
4.2	Comparison of pre-compacted samples (BGR).....	123
4.2.1	Method	124
4.2.2	Results	129
4.2.3	Discussion	149
4.2.4	Summary and Outlook.....	152
4.3	The impact of moisture content, compaction speed and compaction stress on microstructure (Sandia)	154
4.3.1	Method	154
4.3.2	Microstructure results	157
4.3.3	Summary	171
4.4	Effect of grain size and its distribution on backfill compaction (UU).....	171
4.4.1	Introduction.....	172
4.4.2	Method	173
4.4.3	Results	174
4.4.4	Discussion	178
4.4.5	Conclusion.....	181
5	Numerical Modelling.....	183
5.1	Introduction.....	183
5.1.1	Deformation mechanism.....	184
5.1.2	Influence of Geometry	188
5.2	Constitutive Models for Crushed salt.....	190
5.2.1	BGR-CRUSHED SALT3 model (BGR).....	190
5.2.2	Callahan model (Sandia)	195
5.2.3	CODE_BRIGTH model (GRS)	203
5.2.4	EXPO-COM (TUC)	207
5.2.5	Hein-Korthaus (BGE-TEC).....	221
5.2.6	CWIPP model (modified by IfG).....	230
5.3	Benchmarking of TUC-V2.....	232
5.3.1	Introduction.....	232

5.3.2	Modelling approaches.....	235
5.3.3	BGR-CRUSHED SALT3 (BGR)	235
5.3.4	Callahan model (Sandia)	237
5.3.5	CODE_BRIGHT model (GRS)	249
5.3.6	EXPO-COM (TUC)	254
5.3.7	Hein-Korthaus (BGE-TEC).....	262
5.3.8	Modified CWIPP (IfG)	272
5.3.9	Summary and Outlook	278
5.4	Virtual Demonstrator	284
5.4.1	Introduction.....	284
5.4.2	Modelling approaches.....	289
5.4.3	Demonstrator results with TK-031 parameters – “Status quo”	295
5.4.4	Demonstrator results with TUC-V2 parameters – Improvements of KOMPASS-II models	299
6	Conclusion and Outlook	309
6.1	Summary	309
6.2	Further recommendations.....	313
	References	315
	List of Figures.....	329
	List of Tables.....	347
A	Compaction test executed by BGR	351
A.1	Oedometer.....	351
A.2	Triaxial tests	363
B	CT Scans of pre-compacted samples	379
B.1	BGR.....	380
B.2	IfG	379
B.3	TUC.....	381

1 Introduction

For the disposal of high-level nuclear waste (HLW) the internationally favored option is the storage in deep geological formations. In several countries like Germany, the Netherlands and the United States rock salt is available as possible host rock formation for a HLW repository.

The safety concept for a HLW repository in rock salt is based on a multi-barrier system including the geological barrier rock salt, geotechnical seals, and the waste canisters. For backfilling of open cavities, drifts and shafts crushed salt may be used due to its favorable properties as mined-off material and its lithological properties which guarantees a maximum compatibility with the host rock. The crushed salt backfill becomes gradually compacted with time by the convergence of the openings which is driven by the creep ability of the rock salt. Crushed salts initially high porosity of 30 – 40 % will be reduced to values which are expected to be comparable with the porosity of undisturbed rock salt (< 1 %).

A comprehensive understanding of the crushed salt compaction process is crucial for the long-term safety assessment. Crushed salt compaction involves several thermal-hydro-mechanical (THM) coupled processes and is influenced by internal properties (e.g., mineralogy, grain size and grain size distribution), as well as external conditions (stress state, strain rate, temperature). Due to the German paradigm change in the long-term safety assessment first with the “New Safety Requirements” in 2010 /BMU 10/ and later with the new “Site Selection Act” in 2017 /STA 17/ the requirements changed from a limited release of radionuclides to a safe containment. The research work now focused especially on the low porosity area and therefore, on the expectations of low permeability. There are some important gaps in the current process understanding, especially in the low porosity range, both in terms of experimental characterization and numerical modelling.

The KOMPASS-II project is a follow-up project of the KOMPASS-I project /KOM 20/. Both projects strived to improve the scientific database behind using crushed salt for the long-term isolation of high-level nuclear waste within rock salt repositories. Section 2 gives a retrospect of the achievements in the KOMPASS-I project which builds the basis for the work summarized in this report. Based on the experiences in KOMPASS-I, a long-term strategy for a systematic investigation of crushed salt compaction processes was developed in KOMPASS-II.

In both projects, three main approaches are followed: laboratory studies, microstructural investigations, and numerical modelling. The laboratory studies presented in Section 3 include pre-compaction tests to produce samples in short-term and under in-situ loading conditions

with a final porosity between 15 – 20 %. The pre-compaction tests comprise not only the production of samples, but also investigations on the reproducibility and homogeneity, as well as dependencies on different factors (e.g., stress, time). The pre-compacted samples are then used in the long-term compaction tests (Section 3.3). The triaxial tests are elaborated following a systematical laboratory program developed in KOMPASS-I /KOM 20/ and address various influencing factors like pre-compaction method, various mean stress levels, various deviatoric stress levels and humidity. For estimating the influence of the laboratory infrastructure an experimental benchmark of the triaxial compaction test TUC-V2 was performed.

Microstructural investigations on crushed salt help to understand the deformation mechanisms occurring during the compaction process. Several microscale deformation mechanisms can be related to compaction conditions and therefore enhance the process understanding and improve constitutive model formulations. In this work, the focuses in the microstructural studies were to investigate the influence of the various pre-compaction methods, humidity, and grain size/grain size distribution on the microscale deformations (Section 4).

Numerical simulations are needed for the prediction of the backfill behavior in long-term. Suitable constitutive models must be applied for a reliable prognosis of long-term safety purposes. The models must be able to describe the thermal-hydro-mechanical (THM) coupled crushed salt property changes over a wide range of influencing parameters. A large number constitutive models was applied in this project for benchmark calculations of triaxial long-term compaction tests (Section 5.3) and comparison in a virtual demonstrator (Section 5.4).

The KOMPASS-II project made a significant progress in the understanding of the crushed salt compaction process. The outcomes and conclusions of the project are summarized in Section 6. Next to the achievements also some important shortcomings were identified which are addressed in Section 6.2.

2 Progress in crushed salt investigations

2.1 Introduction

With the change in the safety requirements for a repository for high-level nuclear waste due to the “New Site Selection Act” /STA 17/, the requirements and objective of research work changed. Referring to this, the “Deutsche Arbeitsgemeinschaft Endlagerforschung” (DAEF) which is a collaboration of German institutions with their research focus on the disposal of nuclear waste, elaborated a state-of-the-art report about the knowledge in crushed salt reconsolidation including the achievements of previous research and needs for further research and development work /DAE 17/.

The KOMPASS-I project (09/2018 – 08/2020) was initiated based on the open questions and research needs discussed by the DAEF state-of-the-art report. The aim of the KOMPASS-I project was to develop methods and strategies for the reduction of deficits in the prediction of crushed salt compaction processes. The main achievements of the KOMPASS-I project are summarized in the next Section. The work was followed-up in a second phase of the project (07/2021 – 06/2023) which results are presented in this report. Within the projects, a long-term strategy for a systematically investigation of the crushed salt compaction process was developed which exceed the project lifetimes of KOMPASS-I and KOMPASS-II. This strategy is presented in Section 2.3.

2.2 Main achievements of the KOMPASS-I project

The key results of the KOMPASS-I project are listed below. More detailed information can be found in the KOMPASS-I final report /KOM 20/.

- Selection of an easily available and permanent reproducible synthetic crushed mixture, acting as reference material for generic investigations (KOMPASS reference material);
- Development and proof of different techniques for producing pre-compacted samples in short-term and under in-situ loading conditions for the use in long-term compaction experiments;
- Execution of long-term compaction experiments, e.g., long-term creep tests which delivered reliable information about time and stress dependent compaction behavior;

- Development of a complex experimental investigation strategy to derive necessary model parameters considering individual functional dependencies. Its technical feasibility was successful verified (Fig. 2.1);
- Establishment of a tool of microstructure investigation methods to relate microstructure effects and deformation mechanism;
- Benchmark calculations with various existing numerical models using data sets from three different triaxial long-term tests. The result was not entirely satisfactory; however, the number of influencing factors is small and further validation work has to be done.

**Proposal for extended systematic laboratory program
for crushed salt compaction**

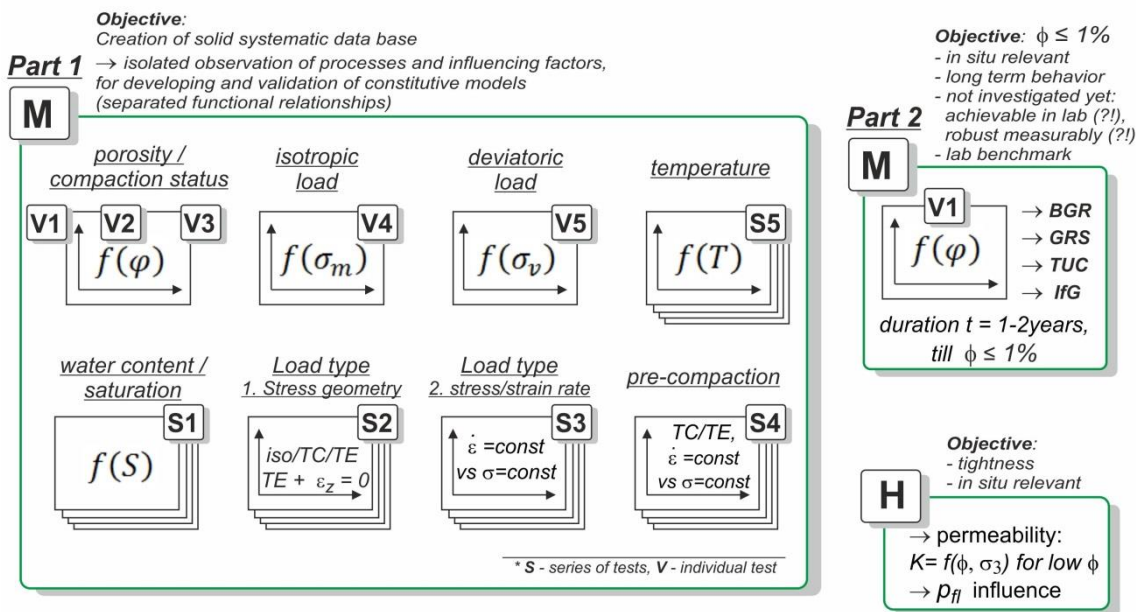


Fig. 2.1 Extended systematic laboratory program as developed in the KOMPASS-I project

2.3 Development of a long-term strategy

In the context of prognostic long-term safety analysis of repositories, suitable numerical equipment is required. Within the scope of investigations to build up and develop a suitable numerical equipment, the following main objectives must be considered (Fig. 2.2):

- the numerical modeling equipment should be checked, demonstrated and characterized regarding an increase of **stability, practicability, plausibility and functionality** and **transferability** (in regard to the in-situ situation);

- prognostic statements based on the usage of the numerical equipment should be characterized by **robustness** and **realism**;
- to quantify and reduce the spread and inaccuracy of the numerical results an increase of the **reliability** of the prognostic statements is demanded;
- suitable numerical equipment should enable us to devise **recommendations** for **optimized backfilling** (location, material, conditions).

The opportunity for development as well as the achievable quality of the numerical equipment are based and strictly depend on a suitable experimental database. Suitable experimental investigations (in microscale, laboratory scale and macroscale) provide the possibility to deepen the understanding of processes in the context of the compaction behavior of the crushed salt. A proper, extensive, and systematized laboratory database gives the possibility for a clear-cut analysis and for the development and validation of constitutive models. Once suitable constitutive models have been evaluated, in the next step these constitutive models must be implemented in numerical software packages.

Against this background, an extensive multi-layered task list results with several interrelated areas and intermediate goals as well as milestones that must be achieved if the development of a suitable numerical equipment is demanded. The development of a suitable numerical equipment requires (Fig. 2.2):

- **continuity** of research (extensive, complex laboratory program containing multiple long-term tests, each lasting from months to years, building altogether a systematic database);
- **multidisciplinary** research work characterized by numerous **interactions** (demands joint project with several partners and different research focuses – e.g., experimental investigation, microstructural investigation, constitutive model development, numerical simulations);
- the definition of **milestones** in **appropriate sequence**, due to time offset between different work areas, since they successively build on each other;
- an **iterative** development **process**, reaching a higher level of quality of milestones in each iteration.

long term strategy for investigations

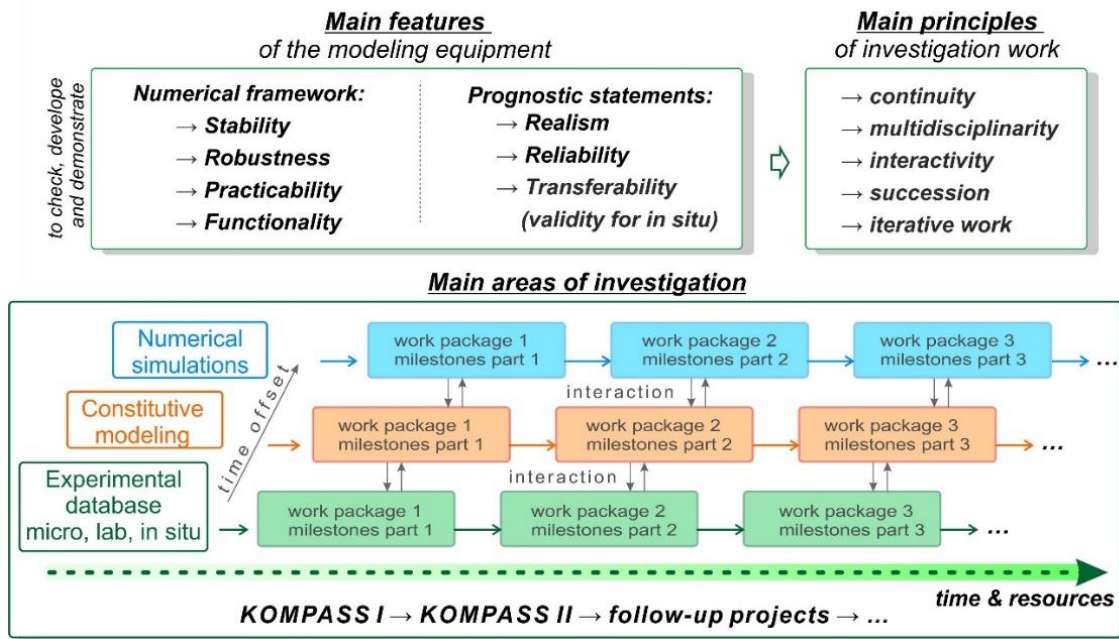


Fig. 2.2 Main aspects of a long-term strategy for investigations to ensure reliable statements in the prognostic analysis of the compaction behavior of crushed salt as a backfilling and sealing material in repositories in rock salt

As show in Fig. 2.2, the main areas of investigation consist of experimental investigations, constitutive modeling, and numerical simulations. They are carried out slightly offset in time, since they build on each other.

Fig. 2.3 gives more detailed information to the aims for the main areas of investigation. Achieving each of these aims successively reduces **inaccuracies** and improves the **quality** and the **reliability** of numerical predictions.

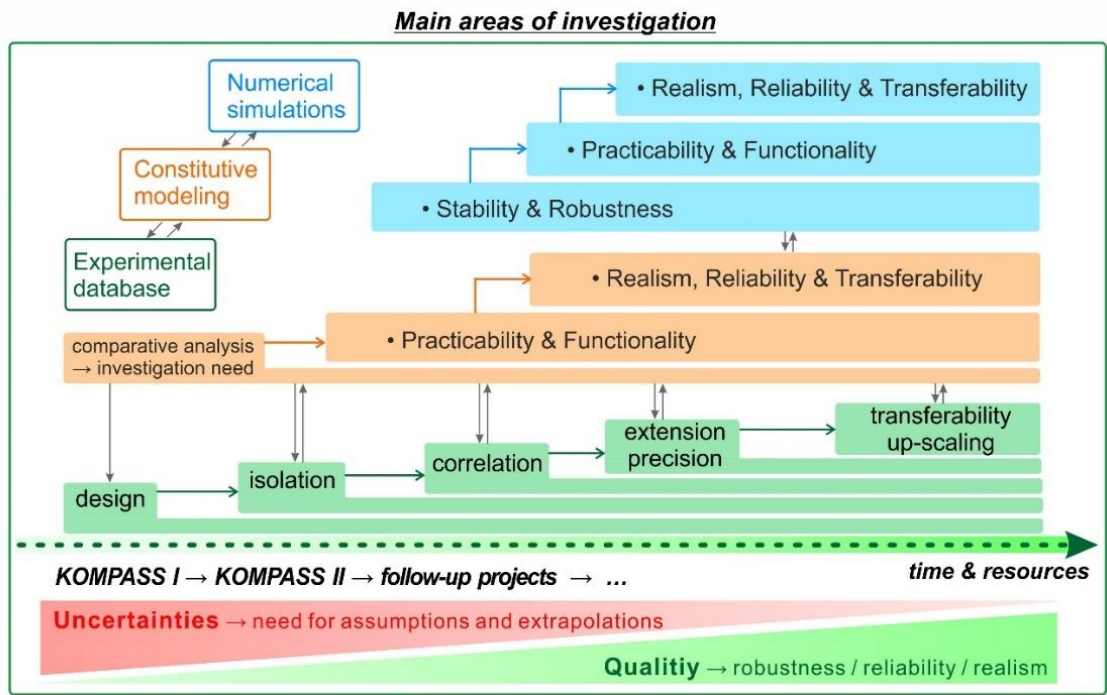


Fig. 2.3 Long-term strategy for investigations – itemization of aims and milestones

Furthermore, Fig. 2.5 to Fig. 2.7 visualize the work packages for **experimental investigations** in further detail.

The individual work packages listed in Fig. 2.3 to Fig. 2.7 must be understood with the following meaning:

- **Design:** Elaboration of an extended systemized laboratory program for isolated/independent observation of all relevant influencing factors for crushed salt compaction behavior (for the time being merely from the phenomenological point of view).
- **Isolation:** Precise planning of suitable loading conditions for individual tests within a laboratory program as well as the performance of individual tests. Testing conditions must be chosen in such a way that the effect of each influencing factor can be observed as independently as possible from other effects. This ensures the possibility of a clear-cut analysis for the development and validation of constitutive models.
- **Correlation:** Factors that are expected to have a correlating effect, must be tested in different combinations, e.g., the response of the material to temperature changes might be different in the low range of stress or porosity as opposed in the high range. Assumptions regarding correlating effects are rooted in expectations for the conditions and state variables that favor different dominating microstructural deformation mechanisms. This means that some of the planned tests from the aforementioned work package 'Isolation'

must be repeated here for additional (or widened) ranges of the assumed correlating factors.

- **Extension and precision:** The investigated ranges of conditions for the influencing factors and the relevant state variables describing the material reaction are chosen in the previous points as pertinent but not covering the entire relevant ranges for in-situ applications. This is to save time and get initial database required for the constitutive modeling as quick as possible. With the help of additional tests, the areas investigated so far will be extended. Furthermore, repeating some experiments with important or unexpected results to confirm or to disprove these results, serves to increase precision, reliability, robustness and completeness or integrity of the generated database.
- **Transferability and up-scaling:** Suitable pilot-plant tests as well as in-situ experiments with appropriate measurements must be performed to produce a database, thereby to examine and to improve the features of the constitutive models and of the numerical equipment. The final goal for a suitable numerical equipment is to be able to reproduce satisfactory results of experimental investigation on all dimensions and scales (observations from microstructural, macrostructural, pilot plant tests and in situ tests). An important requirement or precondition for this goal lies in improved knowledge regarding the microstructural mechanisms and the ranges of conditions and state variables in which they dominate backfill behavior.

Fig. 2.5 and Fig. 2.6 show the progress and milestones achieved in the experimental investigations in the framework of the forerunner project KOMPASS-I and in the current project KOMPASS-II. Finally, Fig. 2.7 gives the targeted objectives and milestones in a proposed follow-up project. In addition, the relatively long unavoidable duration of the long-term tests (several months to a few years in each test) should also be mentioned: the time is necessary to allow realistic loading conditions (stress levels, strain rates), to separate different deformation processes for clear-cut analysis, and to allow technical measurability of the deformations in the laboratory even at low deformation levels.

Thus, despite the progress already achieved in the framework of KOMPASS-I and KOMPASS-II, there are still various extensive investigations to be carried out, as it can be taken from the pictures.

Fig. 2.8 to Fig. 2.10 show, in a similar fashion, the achieved or targeted objectives and milestones in the investigation areas of **constitutive modeling** and **numerical simulations** for the projects KOMPASS-I, KOMPASS-II and following projects, since they are closely coupled with and dependent on the progress of the experimental investigations

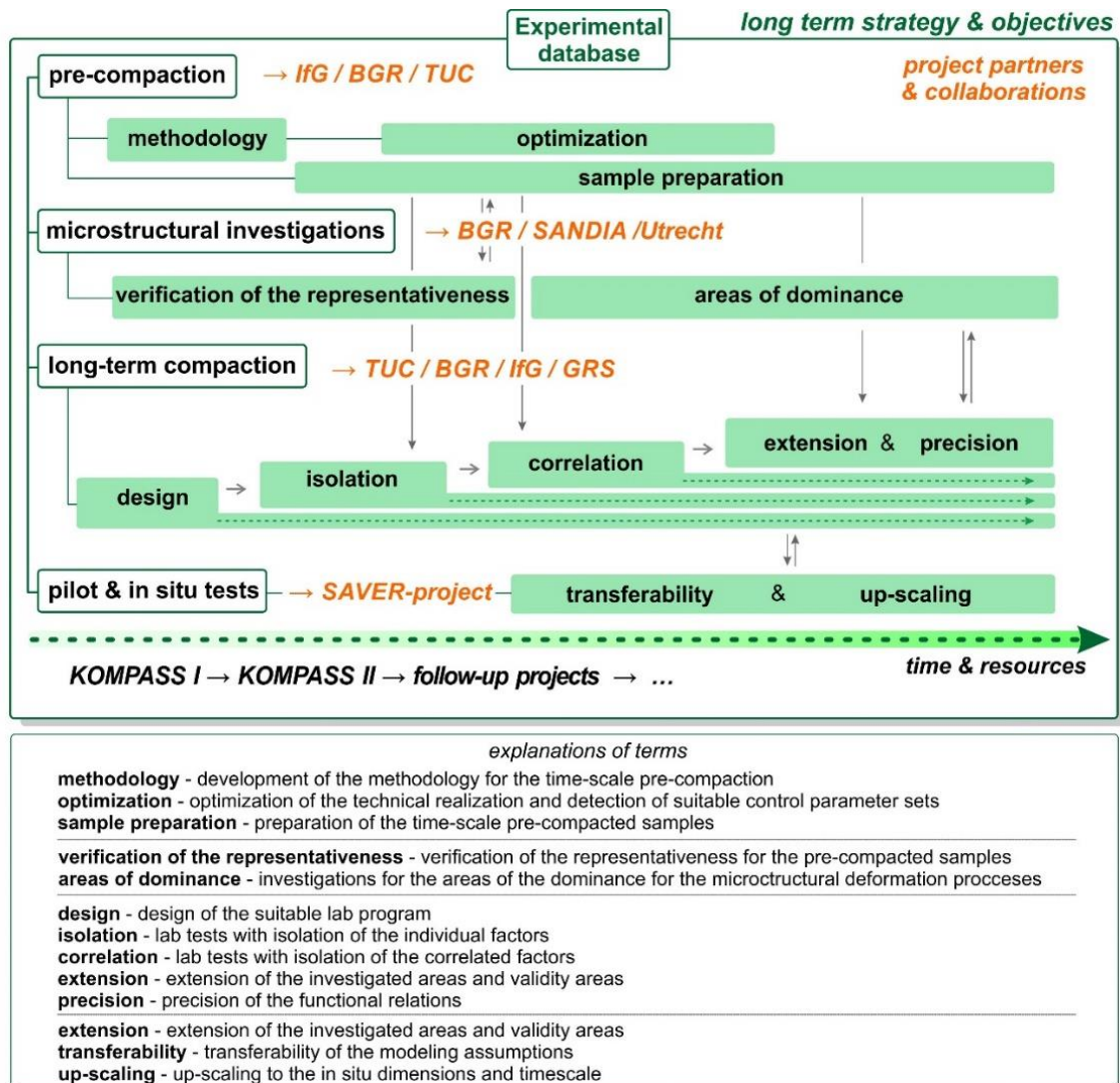


Fig. 2.4 Long-term strategy for experimental investigations - work packages and project partners involved

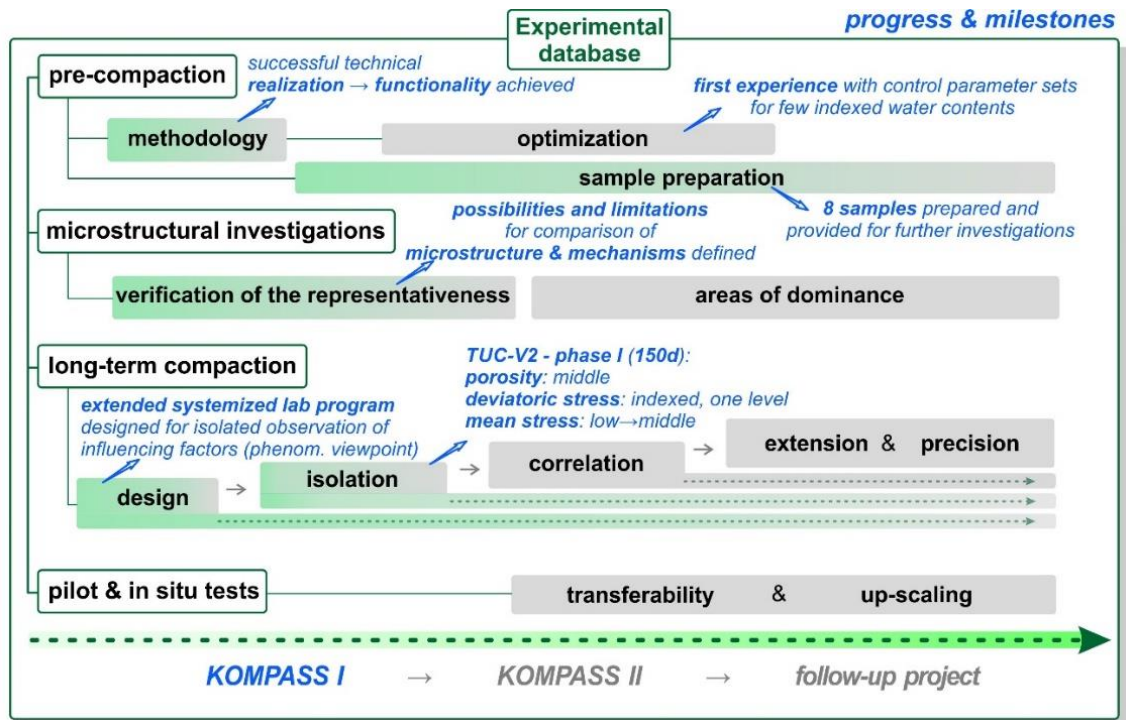


Fig. 2.5 Long-term strategy for investigations – details of the work packages and achieved milestones for experimental investigations for lifetime of the forerunner project KOMPASS-I

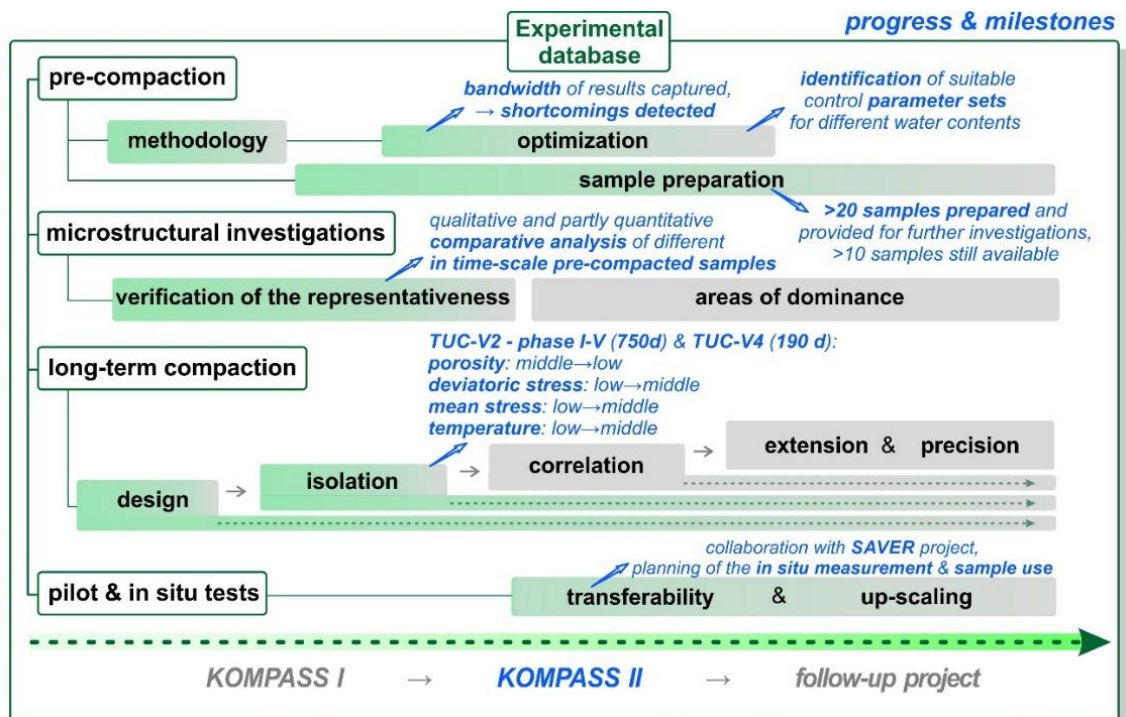


Fig. 2.6 Long-term strategy for investigations – details of work packages and achieved milestones for experimental investigations for lifetime of the current project KOMPASS-II

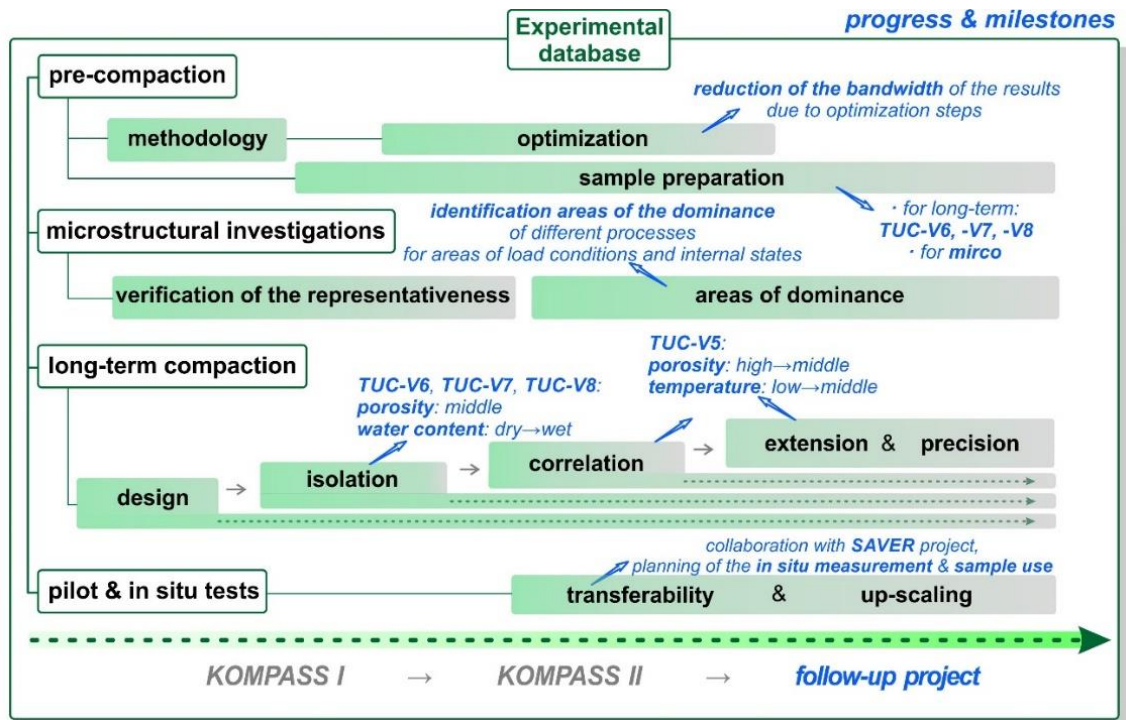


Fig. 2.7 Long-term strategy for investigations – details of work packages and milestones to be reached for experimental investigations for lifetime of the follow-up project

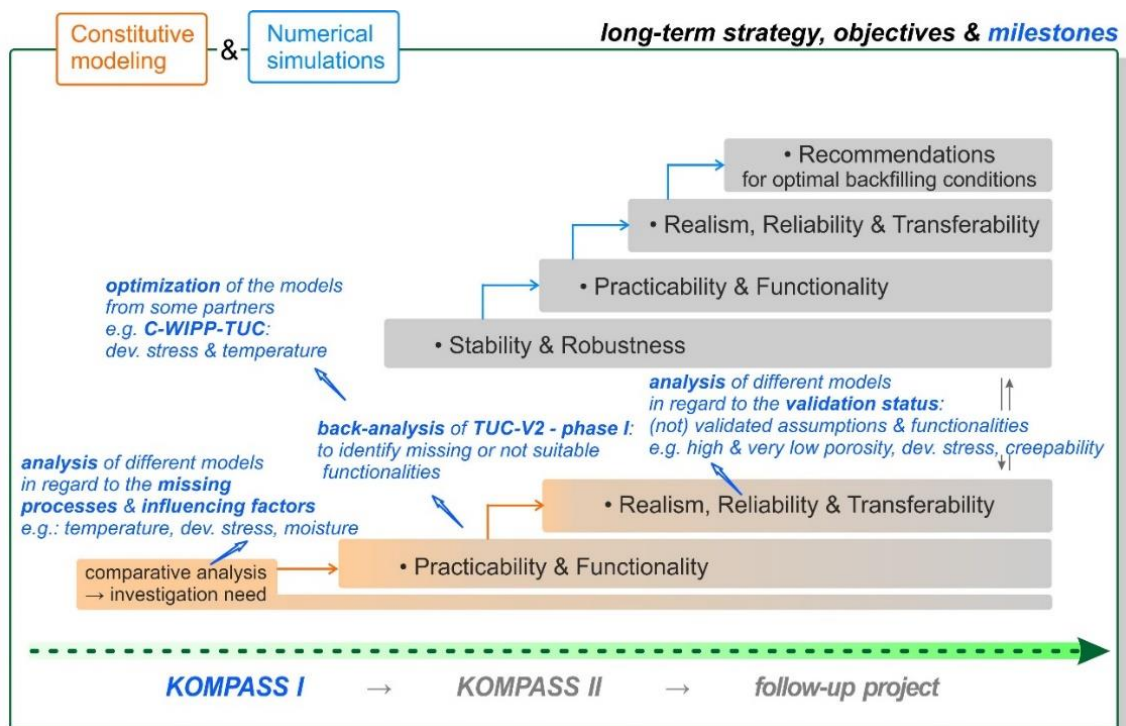


Fig. 2.8 Long-term strategy for investigations – details of objectives & achieved milestones for constitutive modeling and numerical simulations for the lifetime of the forerunner project KOMPASS-I

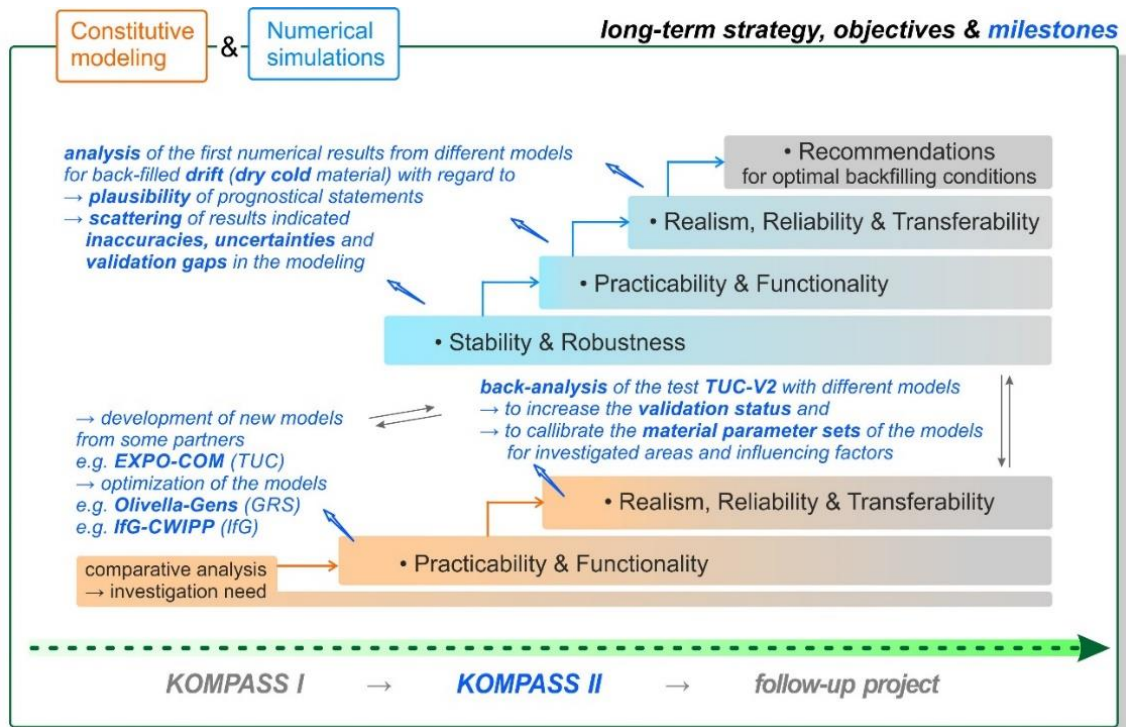


Fig. 2.9 Long-term strategy for investigations – details of objectives & achieved milestones for constitutive modeling and numerical simulations for the lifetime of the current project KOMPASS-II

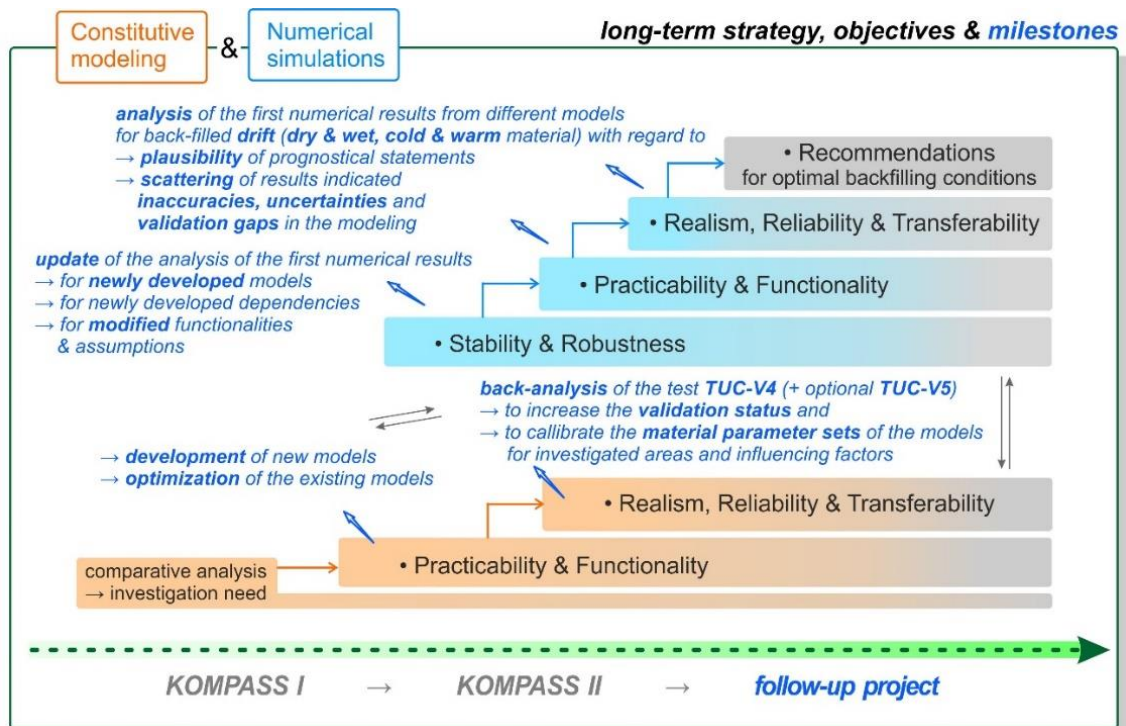


Fig. 2.10 Long-term strategy for investigations – details of objectives & milestones to be reached for constitutive modeling and numerical simulations for the lifetime of the planned follow-up project

2.4 Collaboration with the SAVER project

With the second phase of the KOMPASS project, the collaboration with colleagues from the Technische Universität Bergakademie Freiberg (TU BAF) started. The research project „SAVER“ deals with the comparison and investigation on in-situ material behavior of matrix-stabilized crushed salt backfill and conventional backfill. Within their project they build two fully monitored backfill bodies in the Sondershausen mine (Germany), one of these made of the KOMPASS reference material. The collaboration offers the possibility to investigate the performance of the KOMPASS reference material under in-situ conditions (e.g., settlement due to own weight, compaction process). In short-term it gives the opportunity to gain initial properties of the backfill body which can be used as initial parameter in numerical simulations (e.g., initial porosity).

Fig. 2.11 shows a sketch of the backfill body in the KOMPASS drift. The setup follows the disposal concept for repositories in rock salt. A dummy of a POLLUX waste canister is emplaced in the drift and backfilled with dry crushed salt, since it should be avoided to intrude humidity in the area of the waste canister for corrosion reasons. The rest of the drift is backfilled with the KOMPASS reference material with a moisture content of 1 w.-%. For the monitoring of the KOMPASS backfill body a settlement sensor, a pressure plate and moisture and temperature sensors are installed (Fig. 2.12).

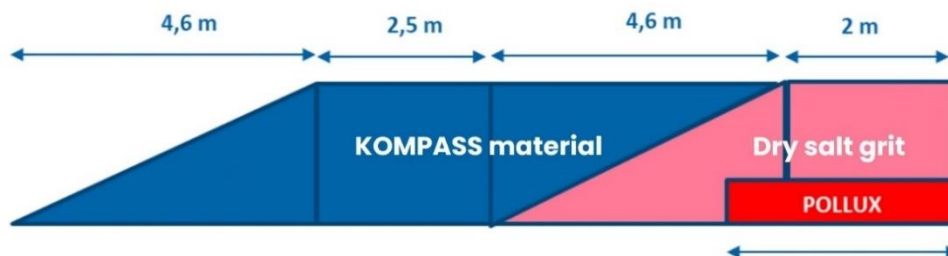


Fig. 2.11 Sketch of the combined backfill body in the KOMPASS drift /SCH 23/

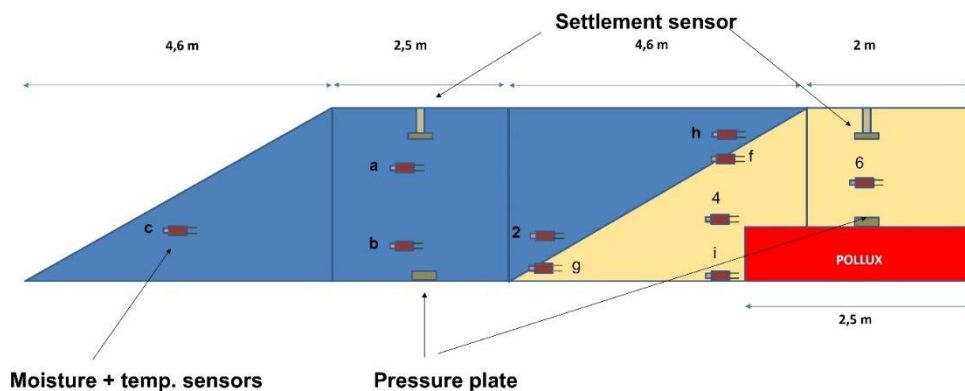


Fig. 2.12 Test site setup for the KOMPASS backfill body /SCH 23/

The construction process of the KOMPASS backfill body is shown in Fig. 2.13. First, the waste canister dummy is emplaced and backfilled with the dry crushed salt with the slinger-backfill method. Afterwards, the KOMPASS reference material is emplaced with a combination of slinger-vibration method.



Fig. 2.13 Construction process of the KOMPASS backfill body. a) Wetting of the KOMPASS material. b) Emplacement of the dry crushed salt backfill. c) KOMPASS backfill body before densification. d) Densification process of the KOMPASS backfill body /SCH 23/

First results for the KOMPASS backfill body and the matrix-stabilized backfill body (GESAV) are shown in Fig. 2.14. The KOMPASS backfill is constructed about 21 days prior to the GESAV body. The KOMPASS body shows large settlements within the first time after construction which results from its own weight. Over time the settlement becomes less but is still ongoing. In correlation with the settlement measurements, the gap between the top of the KOMPASS backfill body and the roof of the drift is measured by hand. Fig. 2.15 shows the gap.

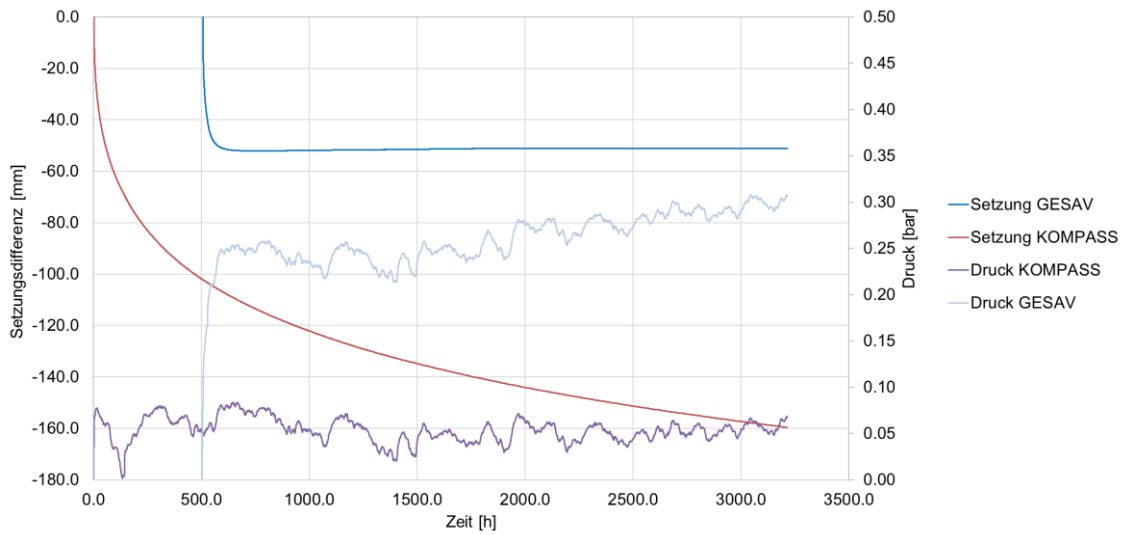


Fig. 2.14 Measurements for the settlement and pressure development of the KOMPASS backfill body and the matrix-stabilized backfill body (GESAV) /SCH 23/



Fig. 2.15 Measurement of gap between the KOMPASS backfill body and the roof of the drift /SCH 23/

The monitoring of the KOMPASS backfill body just started and will be followed-up beyond the KOMPASS-II project.

3 Laboratory investigations

3.1 Introduction

The strategic approach outlined in Section 2.3 and the associated procedure for the development of a suitable numerical equipment for the representation of the load bearing behavior of crushed salt in space and time was initiated by means of selected experiments executed within the framework of the KOMPASS-II research projects. Fig. 3.1 shows the experiments TUC-V2 and TUC-V4 (duration 750 and 190 days respectively) and their integration into the overall experimental program plan. From Fig. 3.1 it is clearly recognizable which variables and stress conditions already have been analyzed for their influence on the load bearing behavior of crushed salt. It is also clear which influencing variables i) have not yet been sufficiently qualified in the sense of strategic planning for a systematic and consecutive analysis of the material behavior, or ii) have been insufficiently characterized in terms of their effects and which are consequently the objective of the research work in the proposed follow-up project. Fig. 3.2 documents the laboratory tests planned in the future. More information on the performed tests can be found in the subsequent sections, which describes in detail the aim of the tests, the loading history, the observed measurements results, and the belonging development of constitutive laws.

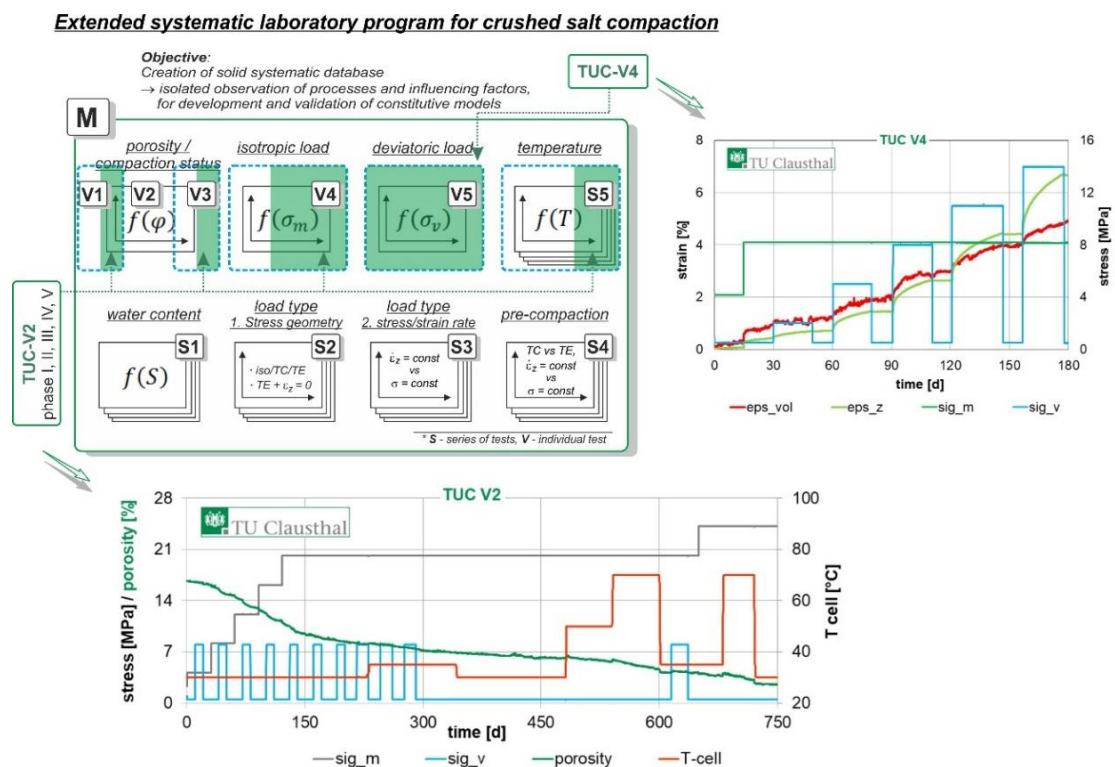


Fig. 3.1 Lab tests TUC-V2 (750 d) and TUC-V4 (190 d) performed in the framework of the current project KOMPASS-II

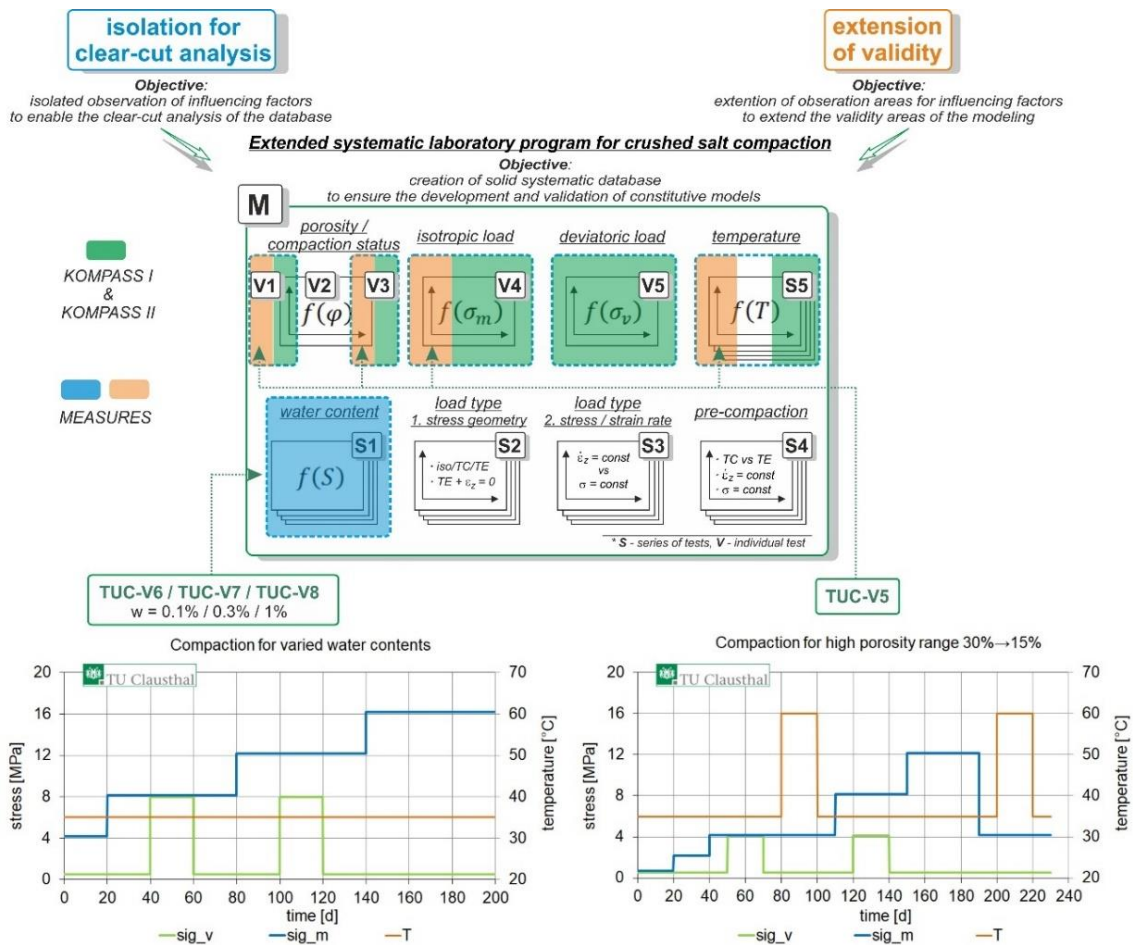


Fig. 3.2 Lab tests TUC-V5 to TUC-V8 (each in duration of 200 – 240 d) planned to perform in the framework of the follow-up project

3.2 Pre-compaction tests

During the KOMPASS-I project, methods for the pre-compaction of crushed salt samples were successfully developed /KOM 20/. These methods allow to produce samples with porosities of 15 – 20 % under in-situ loading conditions and in reasonable time frames. The samples are then used in the long-term compaction tests for the investigation of the THM-coupled compaction behavior of crushed salt characterized by very small porosities (1 – 5 %). In the following, the three pre-compaction factors methods are presented.

3.2.1 Oedometric pre-compaction (BGR)

3.2.1.1 Method

The aim of pre-compaction at BGR is to produce cylindrical crushed salt test specimens with a natural grain structure corresponding to the in-situ compacted material as starting material for triaxial experiments to investigate the THM behavior of crushed salt. Target size are samples with 100 mm in diameter, 200 mm in height and a porosity of around 16.7 %. Porosity is determined from the cylindrical geometry of the pre-compaction cell, the materials' solid matter density and the moisture content.

The materials' humidity was measured by oven drying at 105 °C for at least 5 days until approximate weight constancy for every experiment. Oven drying also reduced grain adhesion (clumping) to ensure accurate subsequent sieving. Therein, the used mesh sizes ranged from 8 to 0.063 mm, with a total of 9 meshes. Crushed salt from all sieving fractions was subsequent mixed to create the designed grain size distribution material Son1 (Section 4.2.1), as a more precise refinement of the KOMPASS material mix for smaller quantities. This artificial more accurate distribution considers the smaller sample size and enables better comparison to previous tests.

For experiments with synthetically humidified crushed salt, the calculated amount of saturated brine was added to the dried crushed salt by spraying and subsequent mechanical mixing immediately before filling. In order to minimize uncontrolled dissolving effects, the brine was prepared from the existing granular salt (450 g) and hot distilled water (1000 g) and the solution was filled without the insoluble set after cooling to 22 °C.

For a homogeneous sample, the crushed salt was filled stepwise into the cylinder in five equal layers (defined material weights of 580 g) using a funnel and tube. Each layer was lightly compacted without destroying the grain structure to get a flat surface. Without measurement and only roughly estimated, a contact pressure of up to 0.1 MPa is assumed. The resulting porosity is approximately 30 – 35 % depending on moisture and scatters strongly due to the statistical distribution of the grains in the relatively small sample (see Tab. 3.1).

The pre-compaction operates by a servo-controlled uniaxial loading in a steel cylinder consisting of four quarter sleeves, which can be easily removed after the experiment /KOM 20/. The confining strain is fixed, and compaction is controlled by axial load or axial strain rate. Three independent linear variable displacement transducers recorded changes in the samples' height

to update its bulk volume and thus its bulk density. The uniaxial stress is servo-controlled by the LVDT-signal (Linear Variable Differential Transformer) to match a user-defined compaction speed. Uniaxial loading implied an increasing frictional resistance between the sample material and the cell inner surfaces. This unwanted effect could not be eliminated and likely lead to an inhomogeneous distribution of stress and compaction within the sample.

During the project we adapted the procedure for pre-compaction from strain to stress controlled and used a new designed cell. The evolution of the development is shown in Tab. 3.1 and comparative results can be found in Section 3.2.1.2.

Tab. 3.1 Evolution of test procedure

Test procedure	Controlled by		Sig _{max}	remarks/future use
Procedure 1	Strain controlled with decreasing rate	0.136 – 0.029 mm/h < 9 E-10 1/s	>20 MPa	Load from one site Interruption of load phase for reversing
Procedure 2	Strain controlled with decreasing rate	0.136 – 0,029 mm/h < 9 E-10 1/s	<16 MPa	New pre-compaction cell - load from both sites
Procedure 3	Stress controlled	Constant axial load rate 5 – 6 kN/d	< 16 MPa	New pre-compaction cell
	Stress controlled	Constant axial load 8 / 16 MPa		New pre-compaction cell

The pre-compaction procedure typically last about two to four weeks. After removal, the compacted specimens were measured with a calliper-gauge to derive its volume, its weight and hence its initial porosity. When not directly used for subsequent triaxial testing or microstructure analysis, it is stored in a vacuum-tight plastic foil. Influence of load level and humidity and the homogeneity of the sample are investigated. Tab. 3.2 gives all pre-compaction experiments with purpose and experimental conditions.

Tab. 3.2 Test parameters for all pre-compaction tests

Name	Material	Controlled by	Sig _{max} [MPa]	Duration [d]	Moisture content [wt.-%]	Porosity range [%]	Application/ further use
VK 20	Asse	strain	29	19	0.07	34 – 17	TK-031
VK 22		strain	31	33	0.15	34 – 17	TK-033
VK 26		strain	25	19	0.15	33 – 17	TK-037
VK 28	Sondershausen Son1	strain	25	18	0.1	31 – 17	TK-038
VK 32		strain	13	22	0.35	33 – 17	TK-041
VK 33		strain	25	29	0.35	32 – 16	distance spacer
VK 34		stress	14	21	0.35	32 – 16	TK-042
VK 35		strain	16	11	0.35	33 – 12	creep
VK 36		strain	19	28	0.35	33 – 17	no distance spacer
VK 37		stress	8	9	0.35	33 – 19	creep
VK 38		strain	21	18	0.1	33 – 20	distance spacer
VK 39		stress	16	13	0.1	31 – 18	creep
VK 40		strain	23	25	0.1	33 – 18	no distance spacer
VK 41		stress	8	27	0.1	31 – 22	creep
VK 43		stress	14	15	0.35	33 – 17	Microstructure
VK 45		stress	14	19	0.5	35 – 17	TK-044
VK 46		stress	15	27	0.1	30 – 19	creep
VK 47		stress	15	22	0.5	34 – 15	TK-045
VK 48		stress	20	37	0.07	34 – 17	GRS
VK 49		stress	15	33	0.07	35 – 19	
VK 50	stress	16	16	2	36 – 9	creep	

3.2.1.2 Pre-compaction tests – Conversion from strain to stress control

The past procedure (like for the TK-031 and TK-033) was executed strain controlled (speed of load piston). The compaction speed was stepwise reduced to get a nearly linear time-stress relation below the possible in-situ stress. The sample becomes compacted from both sides by reversing the cylinder after 50 % of targeted compaction implicating an interruption of the loading phase (procedure 1) /STÜ 13/, /KOM 20/. BGR recently used a second pre-compaction cell, where the axial loading was applied on both, top and bottom of the sample. The maximum axial stress was reduced to 16 MPa – with a smaller corresponding average stress (procedure 2). For the following experiments BGR used a constant stress rate (procedure 3), which corresponds to the stress rate resulting in speed-controlled test (~ 1MPa/d) (see Fig. 3.3). The pre-compaction procedure typically last about two to four weeks. A load level below the in-situ conditions is respected.

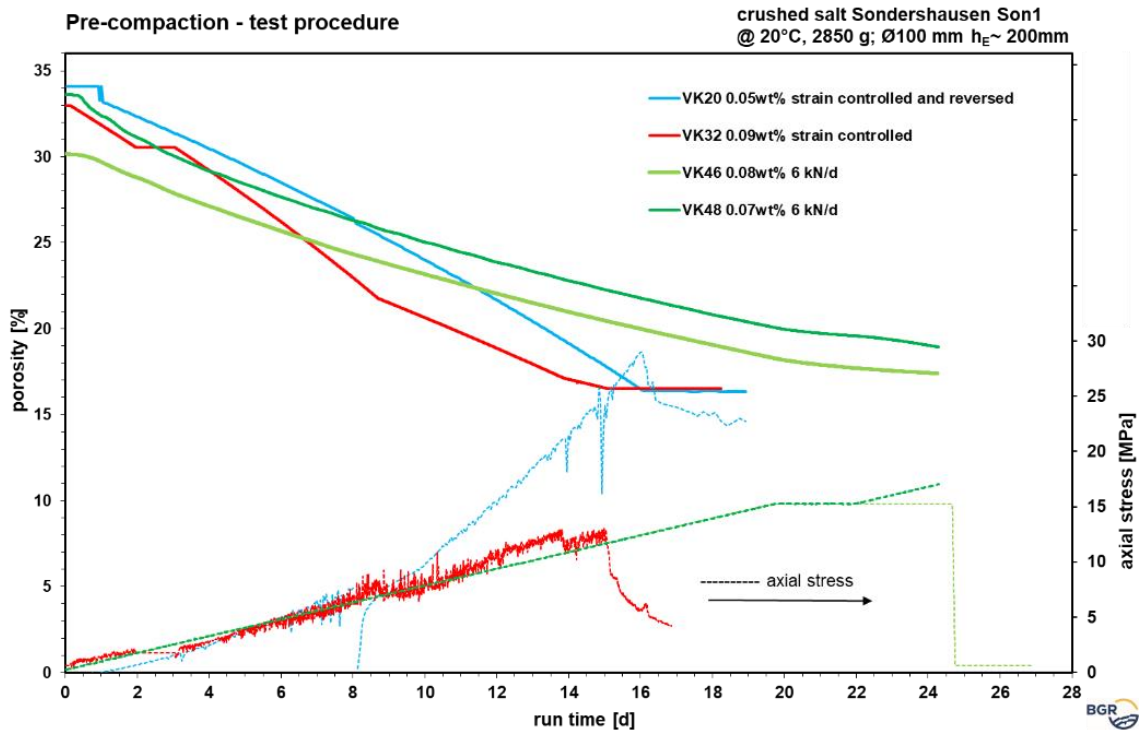


Fig. 3.3 Test procedure for pre-compaction at dry material. Procedure 1: VK-20 – controlled by different customized compaction speed, sample reversed; procedure 2: VK-32 – controlled by different compaction speed; procedure 3: VK-46 and VK-48 – constant loading rate of 6 kN/d and individual creep phase

The adapted procedure 3 with a constant stress rate, two limits for stress and a defined final sample height is better manageable. No human intervention is necessary to adjust the speed. Pre-compacted samples of procedure 3 are of higher quality, because (1) the maximum axial stress does not exceed 16 MPa (previously up to 31 MPa) and (2) the axial loading on both, top and bottom of the sample creates a homogeneous stress distribution without an interrupting unloading phase. The test procedure can be carried out independently of the sample response and is therefore consistent, repeatable, and comparable.

3.2.1.3 Pre-compaction tests – depending on load level and humidity

To optimize the sample preparation, the influence of the load level on compaction duration and the influence of humidity on the compaction process was investigated. The following five pre-compaction experiments ran as creep tests for two weeks at two axial loading pressures: two pre-compaction tests had an initial moisture content of 0.35 wt.-% and were considered as wet samples. Two further pre-compaction tests had an initial moisture content of 0.1 wt.-% and were considered as dry samples. Finally, one additional pre-compaction test with a high moisture content of 2 wt.-% was performed (Fig. 3.4).

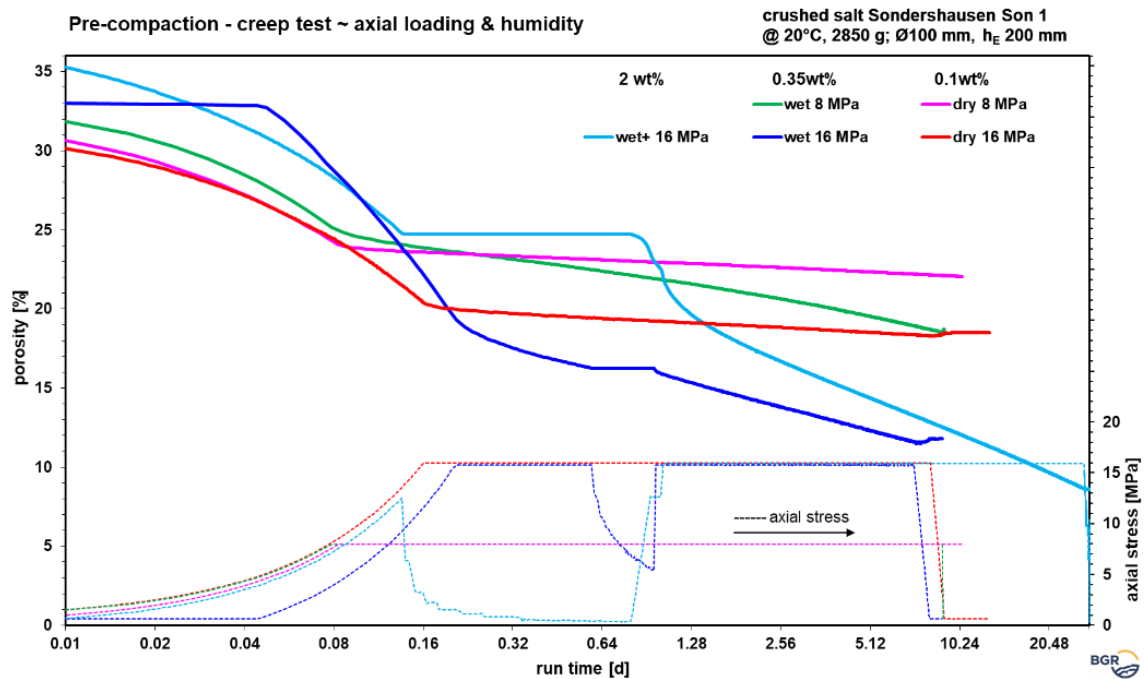


Fig. 3.4 Creep-test for pre-compaction at dry and wet crushed salt from Sondershausen

The findings of this experimental series are in good accordance with the results from the plain-strain pre-compaction method used by Clausthal University of Technology (Section 3.2.3). There, the material was compacted in radial direction by a defined confining pressure and prevented axial elongation. In both series, the porosity decreases with increasing load level and increasing moisture content. The combination of results provides information about the course of the compaction.

Fig. 3.5 shows the extrapolated trend in compaction for one year and the expected final porosity. For the same experiments, Fig. 3.6 shows the trend of the strain rate and Fig. 3.7 the relation between strain and porosity. Especially the dry sample extrapolations show no further compaction.

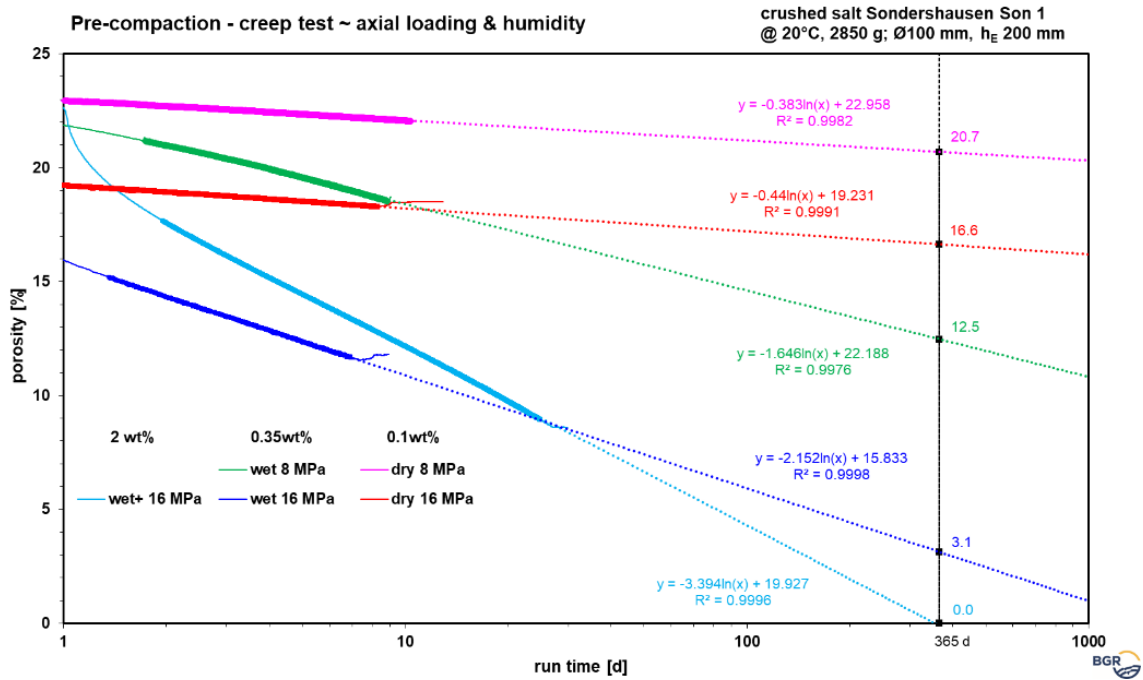


Fig. 3.5 Creep-test for pre-compaction at dry (0.1 wt.-%, magenta and red) and wet (0.35 wt.-%, blue and green) crushed salt. Dotted lines show the logarithmic trend (extrapolated) for porosity

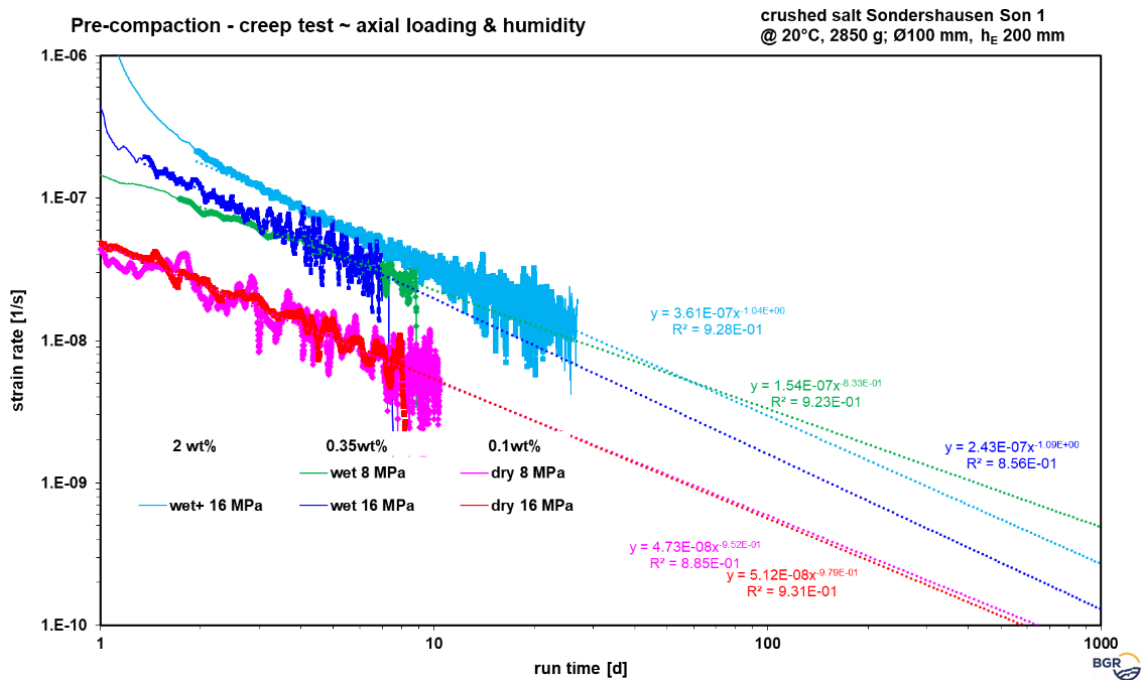


Fig. 3.6 Creep-tests at dry (0.1 wt.-%, magenta and red) and wet (0.35 wt.-%, blue and green) crushed salt. The extrapolated trend of the strain rate is marked in the dotted lines

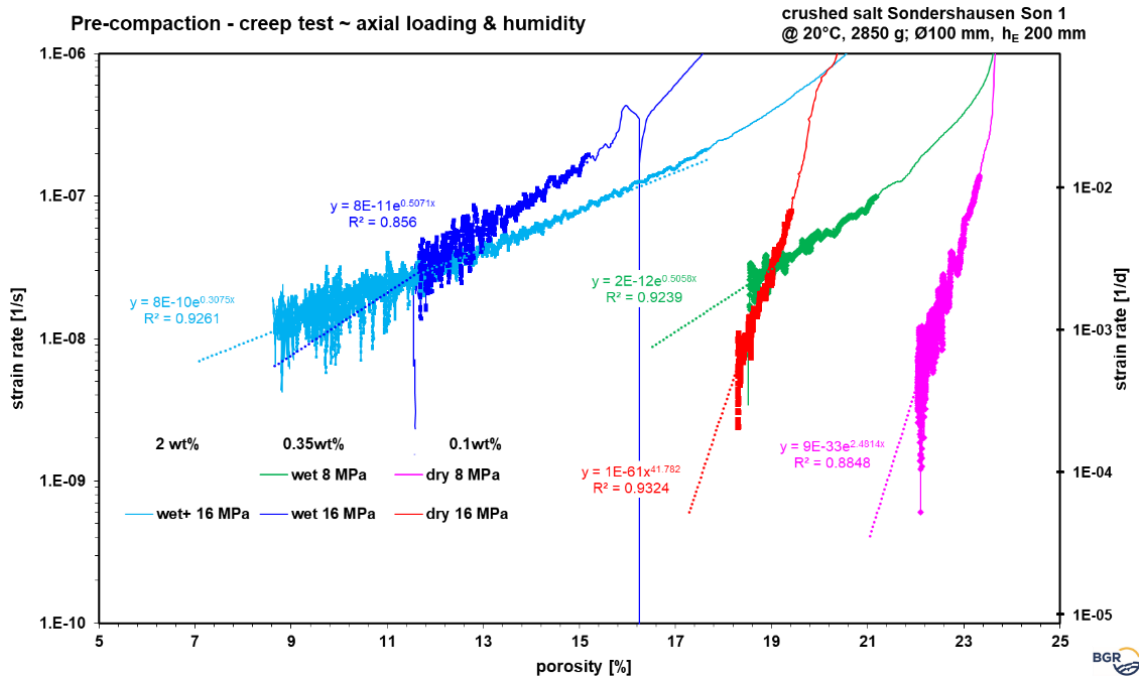


Fig. 3.7 Creep-tests at dry (0.1 wt.-%, magenta and red) and wet (0.35 wt.-%, blue and green) crushed salt. Strain rate vs. porosity – the extrapolated trend is marked by the dotted lines

All experiments confirm the previous attempts:

- Starting porosity, e.g., the filling level in the cell is different for wet and dry material. Wet material has a higher variation in the starting porosity. This is likely because of the inhomogeneity in distribution of grains and moisture.
- The compaction behavior corresponds to the reached load level for similar loading rates that means load level and also loading rate determine the compaction behavior.
- Dry material (0.1 wt.-%) shows a smaller compaction rate with similar extrapolated behaviors for both load levels (8 MPa and 16 MPa).
- At the same conditions, wet material (0.35 wt.-%) reaches lower porosities than dry material (0.1 wt.-%).
- Extrapolating the data to the future, only wet material (0.35 wt.-%) with an axial load of 16 MPa reaches a porosity below 5 % after one year.

The pre-compaction experiments (Tab. 3.2) showed the strong influence of wall friction. It seems, that an increased wall friction is a limiting factor in an oedometric pre-compaction with constant axial loading, if stress kept below the in-situ relevant stresses (for a sample geometry height:diameter of 2:1).

However, it was not possible to quantify the correlations between porosity, confining pressure, compaction time and water content from the test results available up to date.

3.2.1.4 Pre-compaction tests – Homogeneity

Checking the homogeneity of the compacted crushed salt is essential for further experiments and modelling. Due the ratio between height and diameter (2:1) of the pre-compaction cell, friction effects at the wall may result in different compaction grades along the sample height, diameter and, in addition, in anisotropy effects.

In order to investigate the development of the uniaxial compaction within the specimen and the homogeneity of the compaction process, two sets of experiments were performed. Each set consisted of two experiments, dry (0.1 wt.-%) and wet (0.35 wt.-%). In the first set, distance pieces were placed between each of the five salt layers (Fig. 3.8). In the second set, a colored marker spray was used between the five layers. The experiments ran strain-controlled following procedure 1 (Fig. 3.3, Tab. 3.2). The compaction speed was decreased from a maximum strain rate of $\sim 10^{-6} \text{ s}^{-1}$ to a minimum strain rate of $\sim 10^{-9} \text{ s}^{-1}$ (Fig. 3.9).



Fig. 3.8 Pre-compaction experiment with distance pieces. Crushed salt was filled in five equal layers with defined material weights, lightly compacted to get a flat surface

The final porosity was calculated from mass volume and grain density for the whole samples in the second set of experiments and for the five individual specimen sections in the first set of experiments (Fig. 3.10). A correlation between porosity and p-wave velocity was introduced by /POP 98/. The p-wave velocity for each disc of the first set of experiments was measured in three directions. From the p-wave velocity, the porosity was calculated /POP 98/. At the BGR a Krautkramer/Branson device (USN60 with probes K 1.05-C for P-wave) was used for the transit time measurement in conjunction with the p-wave transducer and receiver with a frequency of 1 MHz and a delay of 2.46 μs for the p-wave. The travel time measurements are indicated with an apparent accuracy of 0.01 s. Because of the difficulties in coupling to the test

specimens, the accuracy of the travel time measurement is approx. 0.1 s and thus the accuracy of the velocity is approx. 50 m/s.

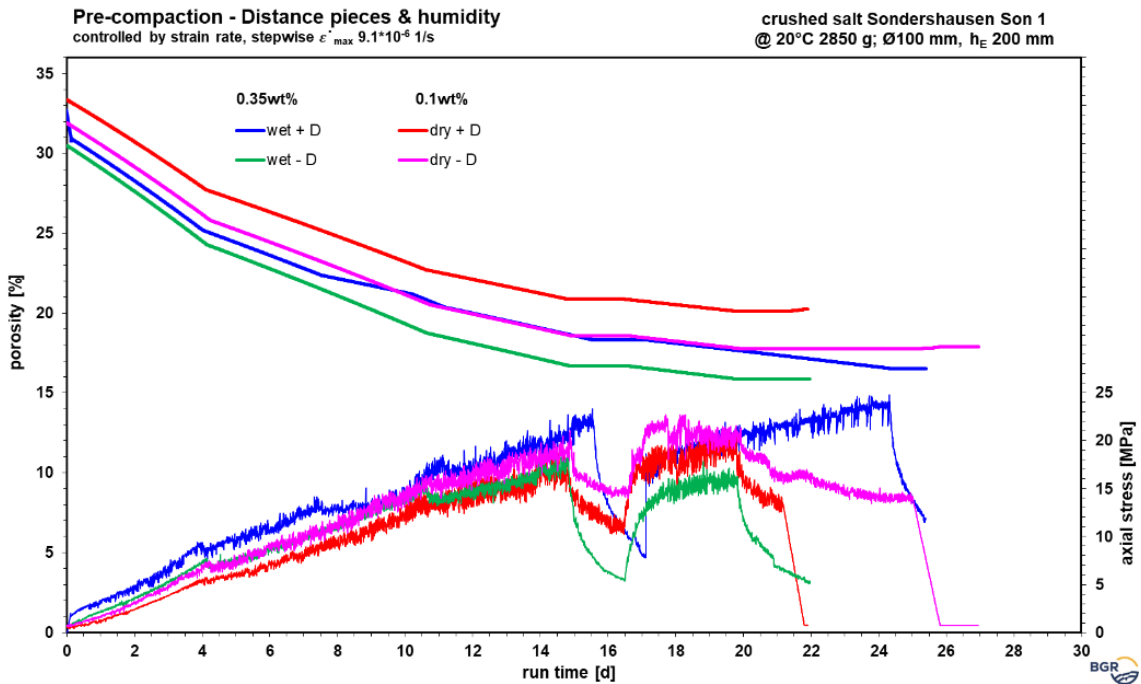


Fig. 3.9 Pre-compaction – dry/wet crushed salt. +D experiments with distance pieces. -D experiments with a color marker spray between the layers

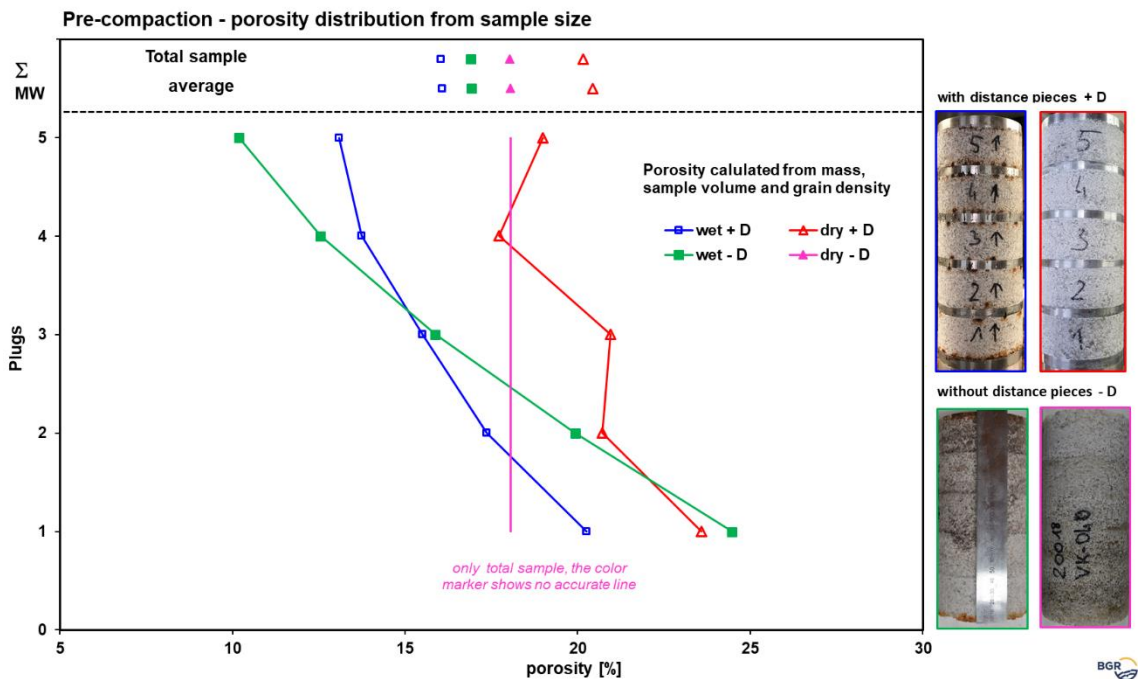


Fig. 3.10 Pre-compaction - dry/wet crushed salt. Porosity distribution for plugs. +D experiments with distance pieces. -D experiments with a color marker spray between the layers

From dry discs of the first set of experiments, small cuboids were cut. Those cuboids were measured in height, width, and depth, from which the volume on the outside was calculated. The solid volume of the cuboids was measured in a Helium-pycnometer. The difference between the outside volume and the solid volume gives an estimation with high uncertainties for the accessible porosity of the sample.

However, the results of the three techniques to estimate the porosity lie in a good agreement (Fig. 3.11). The porosity calculated from axial measured p-wave velocity about the disc height in the sample center is higher than the measured p-wave velocity measured radial. This reflects the increasing sample density from the rim to the center of the sample and is presumably an indicator for the influence of the stress geometry on the compaction behavior and the directional dependence of the material behavior of compacted crushed salt.

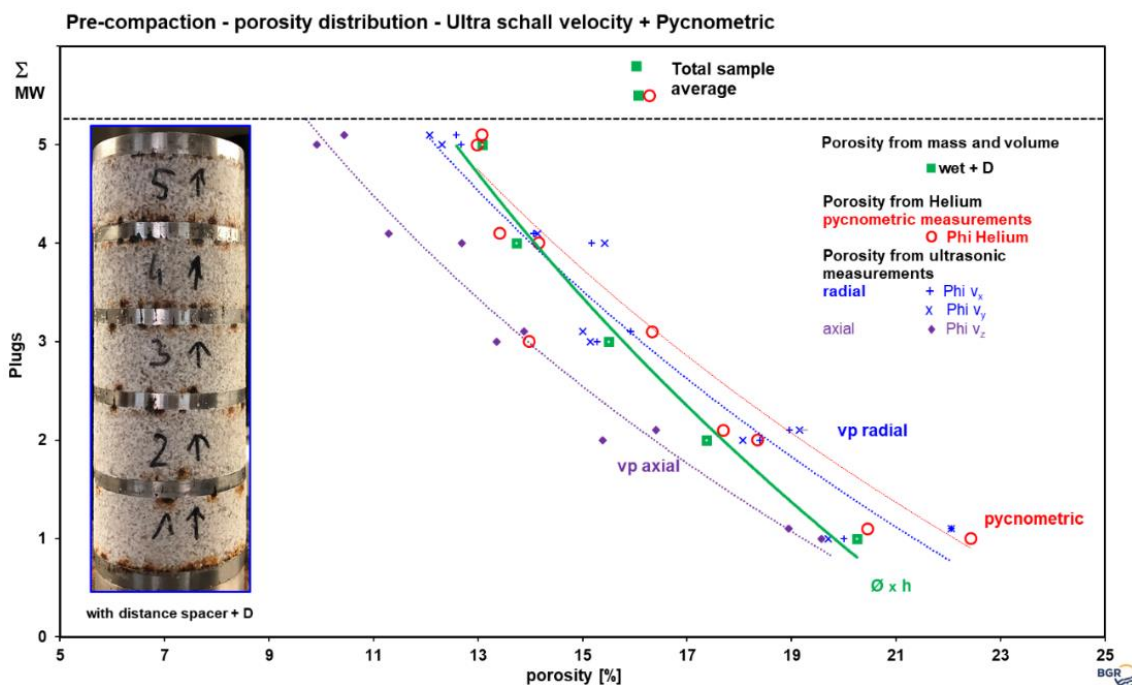


Fig. 3.11 Pre-compaction - wet crushed salt with distance pieces. Porosity distribution for plugs (porosity calculated from mass, volume and grain density, calculated from ultrasonic velocity and by measurements with He-pycnometer)

3.2.2 Pre-compaction in the “Big oedometer cell” (IfG)

To conduct the planned KOMAPSS-II experiments, approximately 2 tons of synthetic crushed salt mixture, formulated as mOBSM (without “Überkorn”) by TU BAF in the ELSA project, were procured from GSES Sondershausen (4 x 0.5 t BigBags, see Fig. 3.13b). The material from the Sondershausen mine represents flat-bedded Staßfurt rock salt with a moisture content of approximately 0.15 wt.-%. It consists of three particle size fractions (14.2 wt.-% fine salt:

0.03 – 0.3 mm, 20.2 wt.-% Band 8: 0.1 – 1 mm, and 65.6 wt.-% Band 6: 0.4 – 4 mm), which have been mixed.

Similar material is also used by the partners TU Clausthal and BGR, but they additionally sieve it to ensure an (absolutely) reproducible particle size distribution and remix it accordingly. However, due to the large quantities required for our experiments (160 L per test), this sieving process is not feasible at IfG. Nevertheless, some variation in material properties can be expected during in-situ conditions.

3.2.2.1 Pre-compaction method

An essential requirement for producing "definitely pre-consolidated sample series" is reproducible installation conditions and reliable knowledge regarding the representativeness of the "small samples" produced from the large samples. This aspect was specifically investigated in this study.

Please note that due to a technical issue in the isostatic compaction tests by IfG (Section 3.2.2.1), some of the tests that were initially planned as pure pre-compaction experiments were extended to oedometric long-term compaction tests to provide data on crushed salt compaction in the low-porosity range ($< 10\%$). Since these long-term tests were performed in the same cell as the "true" pre-compactions tests, we present all of these results in this section.

For the (pre-)compaction experiments, the so-called "large IfG oedometer cell" (measuring 0.78 m in height and 0.51 m in diameter, resulting in ca. 160 L volume) is available at IfG (see Fig. 3.12). Three strain gauges are installed to calculate average backfill stress values as the average of the axial stress and horizontal stress from the active strain gauges (upper and middle will lie above the crushed salt with increasing compaction). To minimize friction effects, the cell wall is lubricated with grease before filling, and an additional plastic film is applied. For installation, the crushed salt is first homogenized in a bucket forced mixer and then moistened with a water amount corresponding to approximately 1 wt.-% H_2O using a handheld sprayer. Subsequently, the salt gravel material is gradually introduced in approximately 10 cm thick layers and pre-compacted to a defined density using tampers (nominal target density $\approx 1.4 \text{ g/cm}^3$). The cell and filling procedure is displayed in Fig. 3.14.

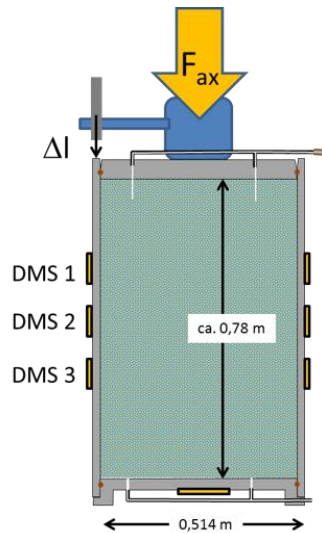


Fig. 3.12 Schematic drawing of the large oedometric cell test setup including three strain gauges (“DMS” for German: “Dehnungsmessstreifen”). With increasing compaction, the first and second strain gauges will be passed by the piston and stop delivering measurements

Components / Grain fractions	Synthetic mixture: (in M%)	Grain sizes (mm)
Band 6 (B6)	65.6 M%	0.4 - 4
Band 8 (B8)	20.2 M%	0.1 - 1
Feinsalz (FS)	14.2 M%	0.03 – 0.3
Sum	100.0 M%	
Humidity content: 0.1 -0.2 %		

(source: TU BAF Freiberg ELSA II)



a)

b)

Fig. 3.13 KOMPASS-II crushed salt for laboratory tests: a) Specification of the optimized crushed salt from the ELSA II project. b) Crushed salt in Big-Bag as delivered by GSES Sondershausen



Fig. 3.14 Preparation of the „large IfG oedometer cell“: Salzgrus (initial state as delivered, pre-treatment (homogenization) and stepwise filling and weight control of the cell

Due to a machine failure in the final phase of the KOMPASS-I project (clamping of the 5000 kN pressure cylinder), after re-working the cylinder it was decided to replace the entire machine control system for the servo-hydraulic testing machine with a new digital control system. The modernization of the machine was carried out by WPM Leipzig (Kögel Werkstoff- und Materialprüfsysteme GmbH) and was completed in spring 2021. The new system allows the automated execution of complex test procedures.

Because homogeneity of the sample may affect the consolidation process of crushed salt the step-by-step filling process has been carefully documented as shown in Fig. 3.14. The analysis of the installation protocols reveals that while the installation values may vary layer by layer (occasionally, too low densities occur likely due to factors such as inadequate manual compaction), the overall target value of 1.405 g/cm^3 was achieved (see example in Fig. 3.15).

In discussions with the project partners, the potential issue of friction was addressed in detail due to the diameter/height ratio of nearly 1:2. It was expected that the bulk sample would be progressively less compacted from the cell top towards the baseplate due to wall friction effects (known as the “silo effect”).

To examine this effect, the cylindrical sample from experiment GV 4 (wet 3) was systematically divided into sample segments using a chainsaw (after halving the sample and creating $\frac{1}{4}$ cake-like segments). From these segments, 6 overlapping cylindrical samples ($d = 40\text{mm} \times l = 80\text{mm}$) were prepared, with three samples taken from the center and three from the outer surface (Fig. 3.16 a, b).

a) Layer-wise preparation parameters (example)

Step no.	Crushed salt mass (kg)	H ₂ O-mass (g)	Σ-ges (g)	Level (cm)	Volume layer (cm ³)	Density (layer) (g/cm ³)	Density (integral) (g/cm ³)
1	12,01	120	12130	4,50	9374	1,294	1,294
2	15,00	150	27280	9,50	10415	1,455	1,379
3	15,00	150	42430	14,50	10415	1,455	1,405
4	15,00	150	57580	19,50	10415	1,455	1,418
5	15,00	150	72730	26,00	13540	1,119	1,343
6	15,00	150	87880	31,00	10415	1,455	1,361
7	15,00	150	103030	36,00	10415	1,455	1,374
8	15,00	150	118180	41,00	10415	1,455	1,384
9	15,00	150	133330	46,00	10415	1,455	1,391
10	15,00	150	148480	51,00	10415	1,455	1,398
11	15,00	150	163630	56,00	10415	1,455	1,403
12	15,00	150	178780	61,00	10415	1,455	1,407
13	15,00	150	193930	66,50	11457	1,322	1,400
14	17,00	170	211100	72,50	12498	1,374	1,398
15	23,00	230	234330	80,07	15769	1,473	1,405

b) Layer-wise and cumulative density as graph

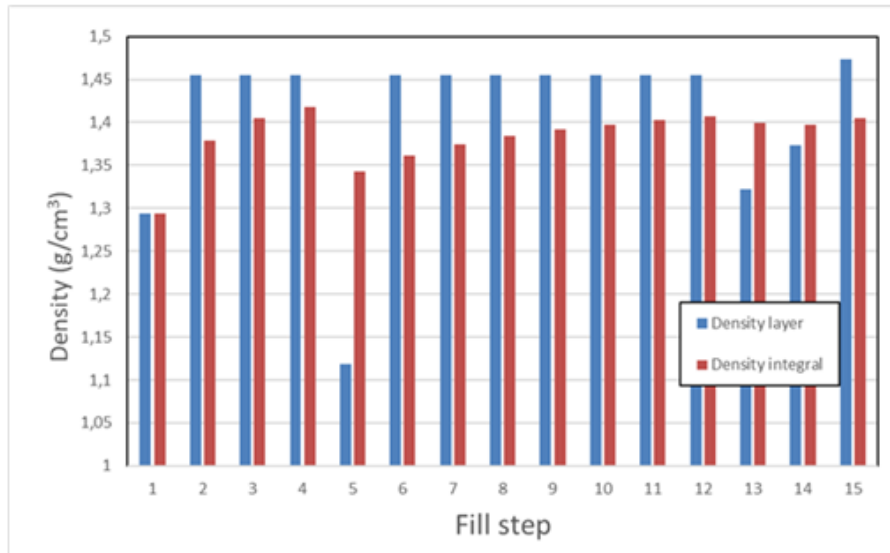


Fig. 3.15 Example of examination of homogeneity during filling: a) Infill parameters per layer until maximum height of ca. 80.07 cm. b) Density of each layer alongside cumulative density for the entire specimen (aim was to reach 1.40 g/cm³ – final measured density was 1.405 g/cm³). This scheme is presented for all KOMPASS-II experiments of IfG

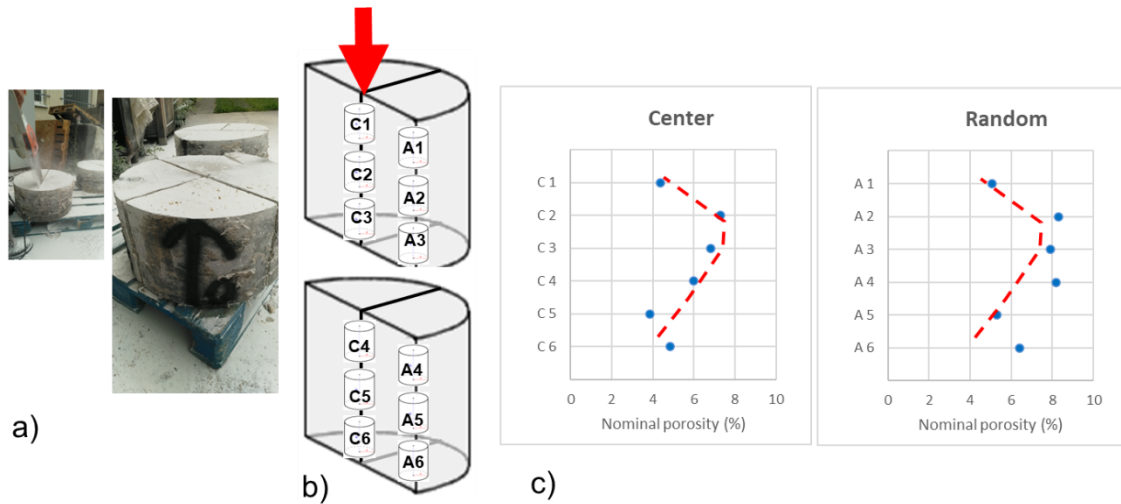


Fig. 3.16 Examination of the porosity distribution in the center and outer sides of the large sample from Experiment GV 4 (wet 3) – initial height approximately 56 cm: (a) The sample was segmented using a chainsaw, first into two halves and then into quarter sections (b) Localization of the samples with respect to the application of force and the cell. (c) Nominal porosity along the sample height (calculated based on grain density; the red curve represents the average porosity profile in the center, serving as a reference)

After measuring the density of the cylindrical samples and estimating the achieved porosity (based on the nominal grain density of 2.1655 g/cm^3), it is evident that the silo effect plays a relatively minor role. Instead, the dominant factors are the pressure shadows below the upper pressure plate and above the cell base, along with frictional effects on the outer wall (Fig. 3.16c, d). Interestingly, the large sample appears to be more compacted in the lower part, despite the assumption of a silo effect in granular materials making this outcome unlikely. One possible explanation is that as compaction increases in the upper part, solution is squeezed downwards, resulting in enhanced volumetric deformation in that region. However, further investigation is required to examine this effect in detail, particularly concerning the inhomogeneous distribution of moisture within the large sample.

Qualitatively, the lithological sample heterogeneity appears to be relatively low, although further investigations are planned for quantification. This also applies to the determination of moisture distribution in the large sample. Regardless, for subsequent analyses, it is necessary to consider the specific sample density or porosity of the test specimens.

3.2.2.2 Investigations

Pre-compaction experiments in the “large oedometer cell”

Crushed salt is a complex material that, if moistened, consists of three phases: (1) Solid phase composed of crushed salt/halite grains, (2) gas/air phase and (3) liquid fluid phase (Fig. 3.17). During compaction, it transitions from a loose granular material to a mechanically compacted and cemented porous solid to a dense solid with very low porosity. With the new wetted (pre) compaction experiments in the large oedometer cell, IfG aimed to investigate several questions of crushed salt compaction at the mesoscale (initial sample height and diameter on the decimeter scale, > 200 kg sample weight), i.e., exceeding the typical laboratory scale.

- How much water is required to initiate fluid-assisted compaction creep?
→ Addition of 1 wt.-% water in the new tests
- It is worth to note that the fluid content in natural salt rocks is in the order lower than 0.5 w.-%, that means fluids can be expelled during crushed salt consolidation.
- How much of the added water is stored in the compacted crushed salt?
→ Drained test with measurements of solution outflow
- What is the stress state in the backfill?
→ placement of pressure cushions in the backfill body

Since the cell was newly build in the beginning of the project, a large component of the outcome was also insight into and improvement of the experimental procedures.

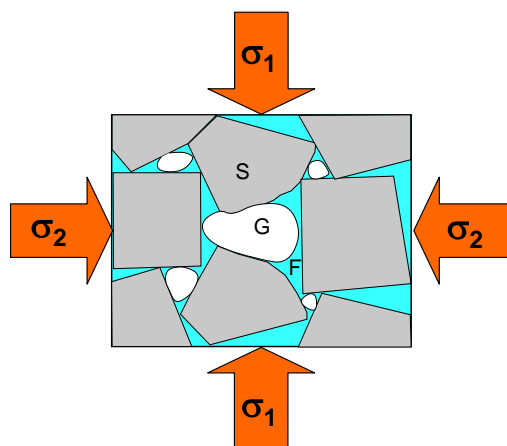


Fig. 3.17 Crushed salt as a complex multi-phase system with rock salt grains (S), air/gas phase (G), and fluid phase (F)

Currently, results from four large-scale experiments are available as listed in Tab. 3.3 one dry (as received) and four moistened (with the addition of 1 wt.-% water). These experiments were conducted as multi-stage tests with axial load levels of approximately 1 MPa, 5 MPa, 10 MPa, and 20 MPa (1-week creep time per load stage).

Here, we will first describe each test individually regarding its initial state, load history, and the results for porosity and compaction rates during each experiment. As GV5 is still ongoing (current status at 27th of July 2023: 133 days running time), the results for this test are not yet conclusive.

Tab. 3.3 Experimental data of samples in the initial and final compaction state, respectively.

Note: the moisture/solution of 1 wt.-% H₂O partially saturates the measured porosity. Porosity values include two values: strain (ϵ_{ax}) derived (continuous measurements) and calculated from final sample density. Note that final values (except current strain-derived porosity) are not yet available for the still ongoing GV5 (wet 4) experiment and given GV5 values are interim results

		Total mass	H ₂ O-mass (added)	Height of crushed salt fill	Volume of saturated NaCl-solution	Dry density	Nominal porosity (dry) from ϵ_{ax} / density
		(kg)	(kg)	(cm)	(cm ³)	(g/cm ³)	(%)
Initial state							
(GV1) dry 1	S	238.00	0.00	79.5	0	1.437	- / 33.6
(GV2) wet 1	S	234.33	2.32	80.7	2569	1.411	- / 35.5
(GV3) wet 2	S	231.68	2.29	79.5	2539	1.416	- / 35.3
(GV4) wet 3	S	234.97	2.47	80.5	2729	1.419	- / 35.2
(GV5) wet 4	S	232.54	2.30	81.0	2547	1.394	- / 36.3
After compaction				Final sample height			
(GV1) dry 1	S	238.00	0.00	64.31	0	1.777	15.6 / 15.6
(GV2) wet 1	S	234.33	2.32	61.86	2569	1.849	16.5 / 16.7
(GV3) wet 2	S	231.68	2.29	55.80	2539	2.031	7.8 / 7.4
(GV4) wet 3	S	234.97	2.47	54.4	2729	2.073	4.1 / 4.2
(GV5) wet 4	S	n/a	n/a	n/a	n/a	n/a	8.8 / 8.4* *(estimated)

Experiment GV3 (wet 2)

The GV3 (wet 2) compaction test was initially prepared by layer-by-layer compaction, following the procedure explained in Section 3.2.2.1. The layer parameters are summarized in Tab. 3.4 and the cumulative and layer densities are visualized in Fig. 3.18. Cumulative dry density was

1.399 g/cm³, and layer densities varied between 1.32 – 1.46 g/cm³. Accordingly, the nominal starting porosity was 35.3 %.

GV3 was planned to follow the identical load path as the GV1 and GV2 compaction tests conducted during the KOMPASS-I project /KOM 20/. However, due to an error in the machine control, each of the four load stages was unintentionally shortened, as visible in Fig. 3.19. We therefore limit our presentation of this experiment to the basic compaction results, as the results cannot be compared to previous experiments. In addition, a short phase (< 1 d) with axial stress of 0.1 MPa is visible in the data, which is not part of the “official” load stages, which still results in a notable compaction and porosity decrease of ca. 2.5 %.

Tab. 3.4 Layer and bulk sample preparation parameters for of experiment GV3

	Crushed salt mass	H ₂ O-mass	Total mass	Layer	Fill height - total	Fill height - Layer	Total Volume	Layer Volume	Layer density	Total density
no.	(kg)	(g)	(kg)	Nr.	(cm)	(cm)	(cm ³)	(cm ³)	(g/cm ³)	(g/cm ³)
1	14.01	140	14.15							
2	14.58	145	28.88	1	10.0	10.0	20831	20831	1.386	1.386
3	15.00	150	44.03							
4	15.00	150	59.18	2	21.0	11.0	43745	22914	1.322	1.353
5	15.00	150	74.33							
6	15.00	150	89.48	3	31.0	10.0	64575	20831	1.455	1.386
7	15.00	150	104.63							
8	15.00	150	119.78	4	42.0	11.0	87489	22914	1.322	1.369
9	15.00	150	134.93							
10	15.00	150	150.08	5	52.0	10.0	108320	20831	1.455	1.385
11	15.00	150	165.23							
12	15.00	150	180.38	6	62.0	10.0	129150	20831	1.455	1.397
13	15.00	150	195.53							
14	15.00	150	210.68	7	72.0	10.0	149981	20831	1.455	1.405
15	15.00	150	225.83							
16	5.80	58	231.68	8	79.5	7.5	165604	15623	1.345	1.399

All load stages show a qualitatively similar behavior with an initially strong transient compaction at high rates ($4 \cdot 10^{-3}$ to 10^{-4} d⁻¹), followed by a steady decrease in compaction rate from 10^{-4} d⁻¹ down to around $3 \cdot 10^{-5}$ d⁻¹. In the first stage (1 MPa), the porosity decreased from around 32 % to 26 %. The shortened stages at 5 MPa and 10 MPa vertical stress led to a combined porosity reduction to ca. 20 %. Qualitatively, none of the two shortened phases fully transitioned into a stable compaction creep phase. They were followed by the final stage at 20 MPa with a calculated final porosity of 7.8 % after an additional 7 days (total 14 days).

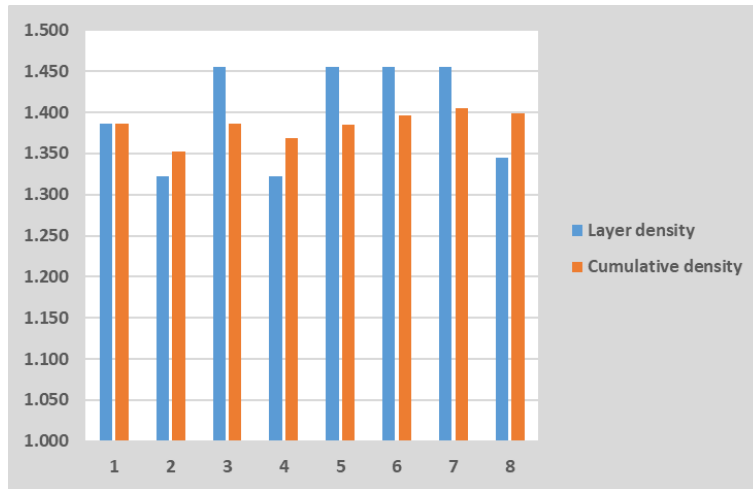


Fig. 3.18 Diagram of layer and cumulative density distribution in experiment GV3 (wet 2)

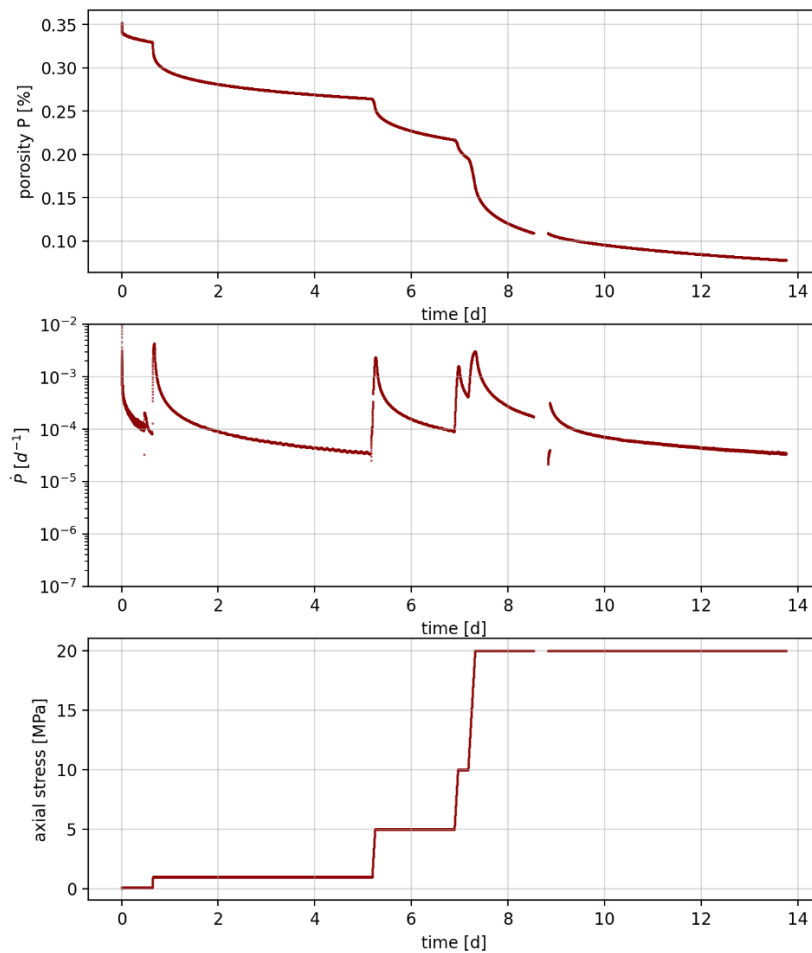


Fig. 3.19 Porosity (top), compaction rate, i.e., porosity reduction rate (middle), and axial stress (bottom) of experiment GV3 (wet 2)

Note that the stages at 5 MPa and 10 MPa were unintentionally shortened due to an error in the machine control. Also note the initial stage of 0.25 MPa, which is not part of the “official” load stage design, but clearly has an initial compaction effect

Experiment GV4 (wet 3)

The GV4 (wet 3) compaction test was prepared in layers, following the procedure explained in Section 3.2.2.1. The layer parameters are summarized in Tab. 3.5 and the cumulative and layer densities are visualized in Fig. 3.20. Cumulative dry density was 1.401 g/cm^3 , and layer densities varied between $1.25 - 1.62 \text{ g/cm}^3$. Accordingly, the nominal starting porosity was 35.2 %. GV4 (wet 3) was conducted according to the correct duration of all load stages and was therefore the first complete and successful compaction experiment in the new large oedometric cell of IfG.

Tab. 3.5 Layer and bulk sample preparation parameters for of experiment GV4 (wet 3)

	Crushed salt mass	H ₂ O-mass	Total mass	Layer	Fill height - total	Fill height - Layer	Total Volume	Layer Volume	Layer density	Total density
no.	(kg)	(g)	(kg)	Nr.	(cm)	(cm)	(cm ³)	(cm ³)	(g/cm ³)	(g/cm ³)
1	14.00	140	14.14							
2	14.00	280	28.42	1	10.0	10.0	20831	20831	1.364	1.364
3	15.00	150	43.57							
4	15.00	150	58.72	2	20.0	10.0	41661	20831	1.455	1.409
5	15.00	150	73.87							
6	15.00	150	89.02	3	30.0	10.0	62492	20831	1.455	1.424
7	15.00	150	104.17							
8	15.00	150	119.32	4	41.0	11.0	85406	22914	1.322	1.397
9	15.00	150	134.47							
10	15.00	150	149.62	5	50.0	9.0	104154	18748	1.616	1.437
11	15.00	150	164.77							
12	15.00	150	179.92	6	61.0	11.0	127067	22914	1.322	1.416
13	15.00	150	195.07							
14	15.00	150	210.22	7	71.0	10.0	147898	20831	1.455	1.421
15	15.00	150	225.37							
16	9.50	95	234.97	8	80.5	9.5	167687	19789	1.250	1.401

Fig. 3.21 and Fig. 3.22 show the experimental data (porosity, compaction rate, stress evolution) for the GV4 (wet 3) test. Again, a short “unofficial” period of compaction at a low axial stress of 0.19 MPa is visible at the start of the experiment, leading to a porosity loss of ca. 3 %. The compaction during all four following load stages followed very similar paths despite different porosity and stress levels. The porosity at the end of the stages at 1 MPa, 5 MPa and 10 MPa are 24 %, 15.5 % and 10 %, respectively. The final measured porosity at the end of the last load stage of 20 MPa was 4.2 %. In all phases, initial compaction rates are on the order of 10^{-3} d^{-1} and decrease to remarkably similar values of ca. $4 \cdot 10^{-5} \text{ d}^{-1}$ within 6 – 7 days of each load stage.

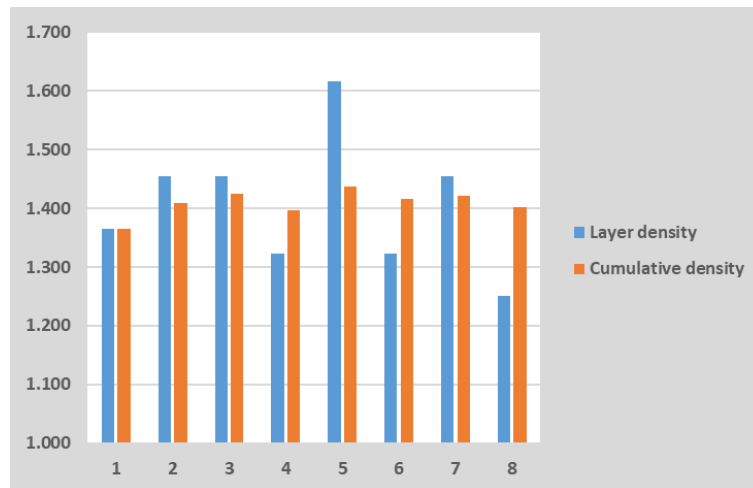


Fig. 3.20 Diagram of layer and cumulative density distribution in experiment GV4 (wet 3)

The strain gauges provide values for the horizontal stresses but show significant scattering and should therefore be treated with caution. Nevertheless, they are the only available values to obtain mean backfill stresses. Note, that first the upper and later also the middle strain gauge does not provide meaningful values once the top of the compacting crushed salt is below the strain gauge. Mean backfill stress is therefore calculated from the axial stress and values of the lower strain gauge (Fig. 3.23), which provides values of ca. 0.6 times the axial stress. Using the values of the strain gauges, horizontal to vertical stress ratios of ca. 0.4 are obtained. During the last creep stage at 20 MPa axial stress, a steady increase in horizontal and therefore mean stress, of 0.4 MPa in 7 days can be observed.

Remarkably, within a test duration of approximately 4 weeks and with the four constant load stages (creep stages), a final compaction resulting in 4.2 % residual porosity was achieved, and the onset of outflow of a few milliliters of NaCl brine from the drainage was observed. For comparison, the porosity analysis based on small cores from the final state of this experiment showed values of 4 – 8 % (Fig. 3.16). The reason for this discrepancy is not yet clear but could be related to damage (disturbing the specimen, consisting of highly compressed salt grains) during sample creation. Note that the topic of reliable porosity measurements will be discussed in the overall summary of the IfG experiments below.

Despite the remaining uncertainty of the real values for final porosity, the separate analysis of the creep phases in Experiment 4 (wet 3) for the various load levels indicates that nominal final porosities close to zero can be achieved in relatively short time periods (Fig. 3.22). Assuming that the power law relationship is a good approximation also at very low porosity, an extrapolation was made and IfG decided to run the next test (GV5, wet 4) such that the final load stage would be held, if possible, until complete compaction. Depending on the applied load, the

extrapolation indicated that the corresponding time spans range from several hundred days to a few weeks (Fig. 3.22). GV5 was thus also designed to test this extrapolation.

As stated before and shown in Fig. 3.24, several cylindrical samples were prepared from the huge compacted body and used for further investigations (e.g. homogeneity analyses and porosity estimation).

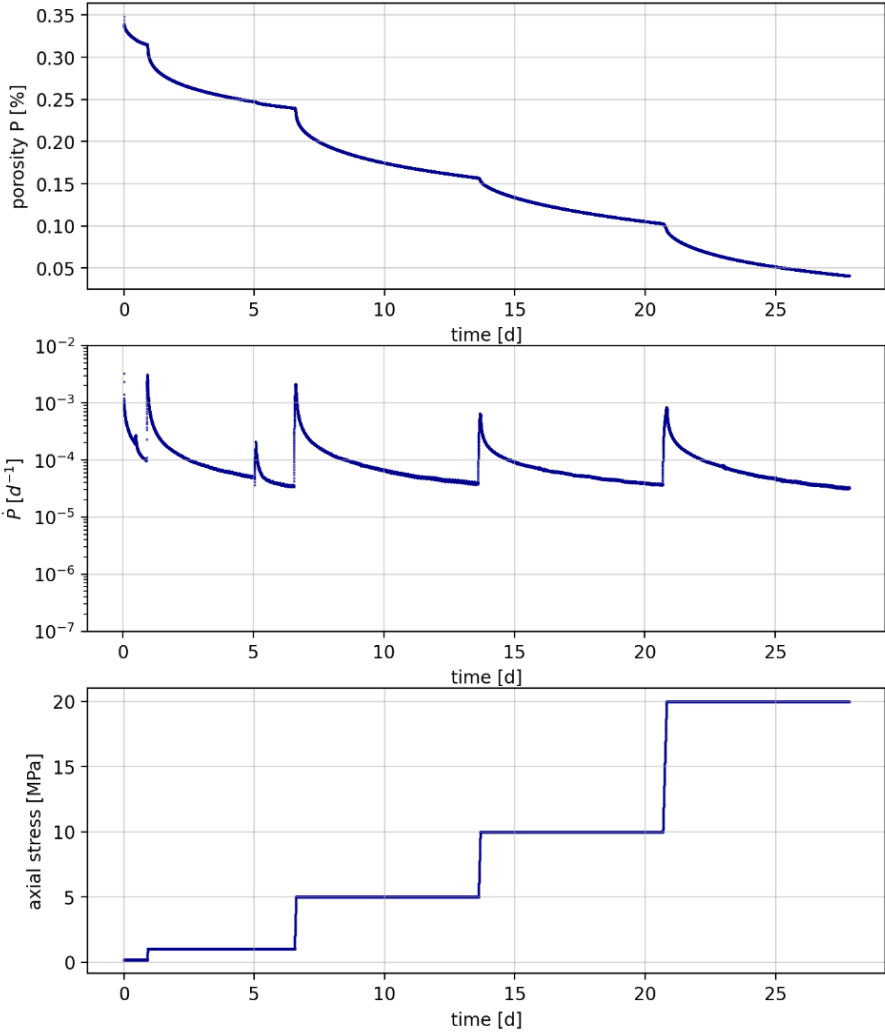


Fig. 3.21 Porosity (top), Compaction rate, i.e., porosity reduction rate (middle), and axial stress (bottom) of experiment GV4 (wet 3)

Each load stage was kept for 7 days. Again, note the initial stage of 0.25 MPa, which is not part of the “official” load stage design, but clearly has an initial compaction effect

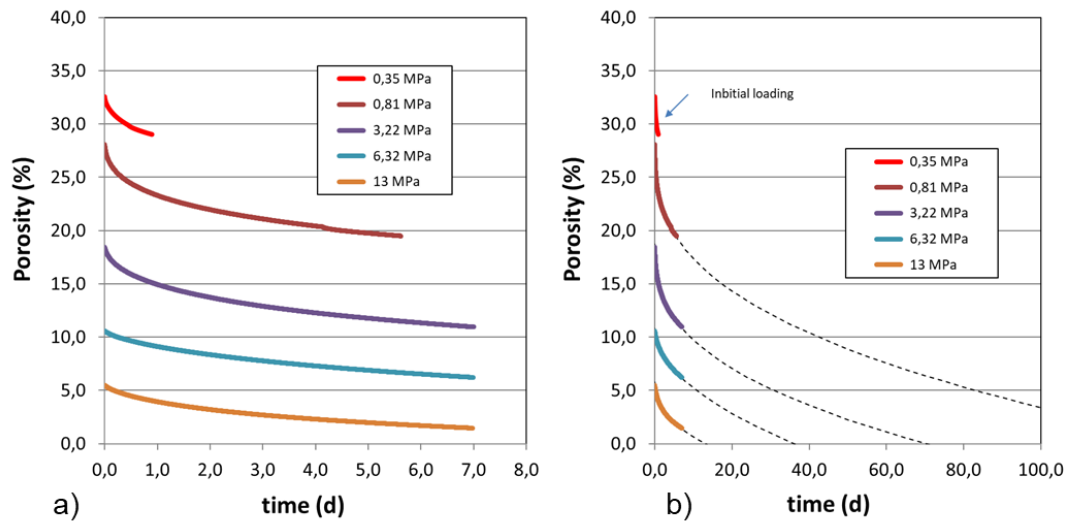


Fig. 3.22 Compaction creep of crushed salt experiment GV 4 (wet 3): (a) Creep phases with porosity reduction vs. creep time per load stage (calculated mean load = average of p_{AX} , middle and lower strain gauges); (b) Fit and extrapolation of creep curves using a power law ($bx^c + a$), indicating short expected times to full compaction

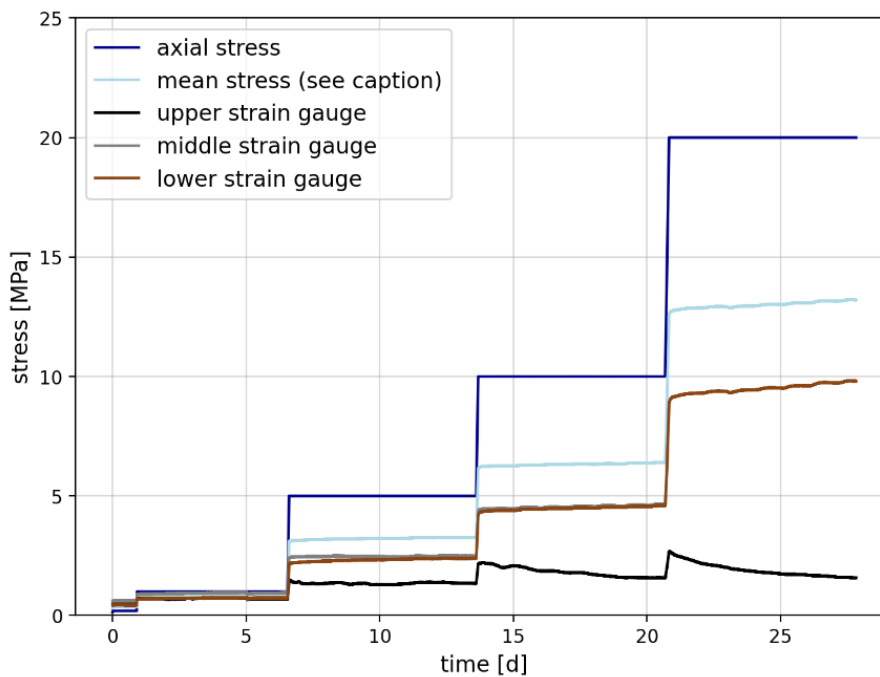


Fig. 3.23 Stress evolution for experiment GV4 (wet 3). Mean stress is calculated as the arithmetic average of axial stress, two times lower strain gauge



Fig. 3.24 The compacted body was pressed out from the cell after finishing the test. From this large-scale sample several smaller sized cylindrical samples ($l = 80\text{mm}$, $d = 40\text{mm}$) were prepared by sawing small segments and machining with a lathe

Experiment GV5 (wet 4, ongoing)

The GV5 (wet 4) compaction test was prepared in layers, following the procedure explained in Section 3.2.2.1. The layer parameters are summarized in Tab. 3.6 and the cumulative and layer densities are visualized in Fig. 3.25. Cumulative dry density was 1.378 g/cm^3 , and layer densities varied between $1.27 - 1.46\text{ g/cm}^3$. Accordingly, the nominal starting porosity was 36.2 %. GV5 (wet 4) was conducted according to the correct duration of all load stages and was therefore the second complete and successful compaction experiment in the new large oedometric cell of IfG. In addition, the two last load stages contained several loading-unloading loops to obtain elastic parameters.

Tab. 3.6 Layer and bulk sample preparation parameters for of experiment GV5 (wet 4)

	Crushed salt mass	H ₂ O-mass	Total mass	Layer	Fill height - total	Fill height - Layer	Total Volume	Layer Volume	Layer density	Total density
no.	(kg)	(g)	(kg)	Nr.	(cm)	(cm)	(cm ³)	(cm ³)	(g/cm ³)	(g/cm ³)
1	15.00	150	15.15	1	5.00	5.00	10415	10415	1.455	1.455
2	15.00	150	30.30							
3	15.00	150	45.45	2	16.0	11.0	33329	22914	1.322	1.364
4	15.00	150	60.60							
5	15.00	150	75.75	3	26.0	10.0	54160	20831	1.455	1.399
6	15.00	150	90.90							
7	15.00	150	106.05	4	36.0	10.0	74991	20831	1.455	1.414
8	15.00	150	121.20							
9	15.00	150	136.35	5	47.5	11.5	98946	23955	1.265	1.378
10	15.00	150	151.50							
11	15.00	150	166.65	6	57.5	10.0	119777	20831	1.455	1.391
12	15.00	150	181.80							
13	15.00	150	196.95	7	68.5	11.0	142690	22914	1.322	1.380
14	15.00	150	212.10							
15	15.00	150	227.25	8	79.0	10.5	164563	21872	1.385	1.381
16	5.24	50	232.54	9	81.0	2.0	168729	4166	1.270	1.378

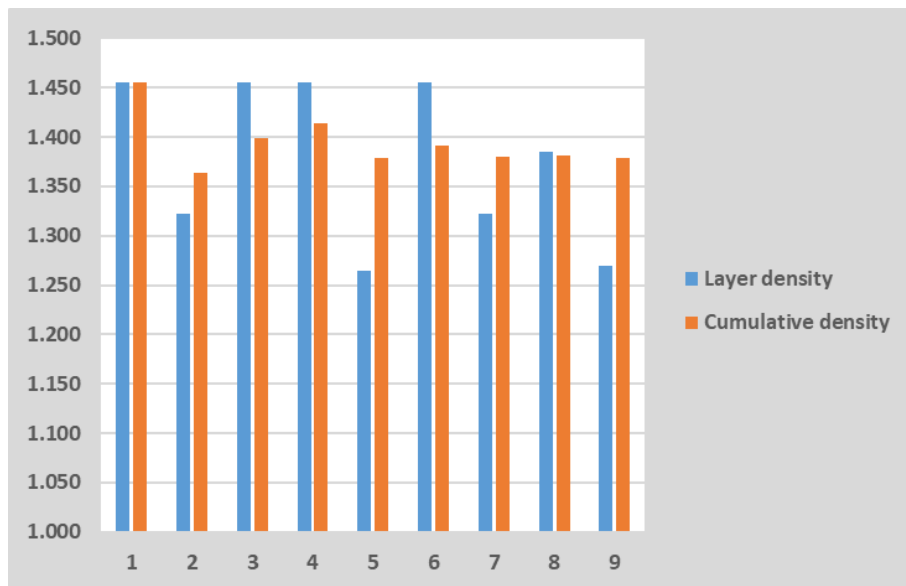


Fig. 3.25 Diagram of layer and cumulative density distribution in experiment GV5 (wet 4)

The load stages load stages of GV5 (wet 4) were kept almost identical to experiment GV4 to maintain comparability, but with some small changes to pursue the following objectives:

- (1) Conduct a force-controlled loading test in 4 stages, including loading and unloading cycles, to determine the system stiffness and elastic behaviour of the moistened salt gravel in relation to the deformation rate. This serves as a basis for possible back-calculation.
- (2) Verify existing uncertainties regarding the stress state within the large sample. To overcome this problem, additional hydraulic pressure cushions will be installed in the cell centre. This allows measurement of the stress state perpendicular to the axial loading direction, which is critical information for the verification of future modelling results.
- (3) Verify the extent to which a final porosity on the order of a few percent can actually be achieved (reproducibility of results from GV4 (wet 3). To achieve this, the experiment will be continued until a steady-state condition is reached, paying particular attention to the possible release of solution (due to pore space saturation).
- (4) Test the homogeneity of the samples and the distribution of the solution and provide sample material for microstructural investigations.

Fig. 3.26 shows the position of the installed pressure cushions in the crushed salt filled cell of test GV5 (wet 4).



Fig. 3.26 Two hydraulic pressure cushions were installed in the lower third of the filled cell while filling it with the crushed salt material. One records the horizontal, the other records the vertical acting pressure

Fig. 3.27 and Fig. 3.29 show the experimental data for the test GV5 (wet 4). Note here that, in contrast to GV3 and GV4, there was no initial stage with very small stresses. The first load stage (1 MPa) therefore starts at the original infill porosity of 36.2 %. The porosity of the end

of each load stage is 32 % (1 MPa), 25 % (5 MPa), 20 % (10 MPa), and 14 % (7 days of last load stage), respectively. The extended last load stage showed a porosity of 8.4 % at the time of this report (the GV5 test is still ongoing).

In the beginning of each load stage, high compaction rates are measured, starting from ca. 10^{-3} d^{-1} immediately after each load increase and reaching 10^{-4} d^{-1} after 1 – 2 days. The compaction rates then decline to values of $2 - 3 \cdot 10^{-5} \text{ d}^{-1}$ at the end of all load stages except for the extended final stage. Again, it is remarkable that the compaction rates at the end of each 7-day load stage are nearly the same despite the marked differences in porosity and stress conditions during each stage.

The strain gauges were used to monitor horizontal stresses and yielded a horizontal to vertical stress ratio of 0.3 – 0.5, and thus a mean stress of 0.6 – 0.7 times the axial stress of each load stage (Fig. 3.29). Note again that first the upper and later also the middle strain gauge does not provide meaningful values once the top of the compacting crushed salt is below the strain gauge. Therefore, mean backfill stress is calculated from the axial stress and values of the lower strain gauge. The last creep stage shows a steady increase in mean stress from 12.8 MPa to 14.4 MPa.

The pressure cushions, which were added to monitor the stresses inside of the backfill bodies provide currently somewhat not explainable values. For instance, the cushion measuring vertical stress measures only half of the applied axial stress or less (Fig. 3.29). The horizontal stress measurements of the other pressure cushion are also very small compared to the strain gauge data and show about $\frac{1}{4}$ of the vertical stress value for each stage. Thus, even for 20 MPa vertical stress, the measured values from the cushions are ca. 8 MPa (vertical stress) and 4 MPa (horizontal stress).

At the moment, we suggest two possible explanations for these unexpected and possibly erroneous measurements:

(1) a strongly heterogeneous compaction, where the upper part of the sample is more compacted and experiences clamping. Thereby, not all of the vertical load is transferred to the bottom of the sample containing the pressure cushions. In addition, due to the significant drainage of pore fluids, as described below, stress relaxation may take place in the upper part.

(2) Stress redistribution due to the presence of the pressure cushions, creation pressure shadow around them and leading to too low stress measurements. The investigation of this issue is not yet conclusive.

The final stage shows a steady but slow decrease in compaction rate which does not follow the exponential decrease of the first three stages, indicating that long holding times are required to reach steady state compaction. Thus, the porosity did not follow the extrapolated curve of GV4 (wet 3). Nevertheless, a very low final porosity is expected at the end of this (ongoing) experiment.

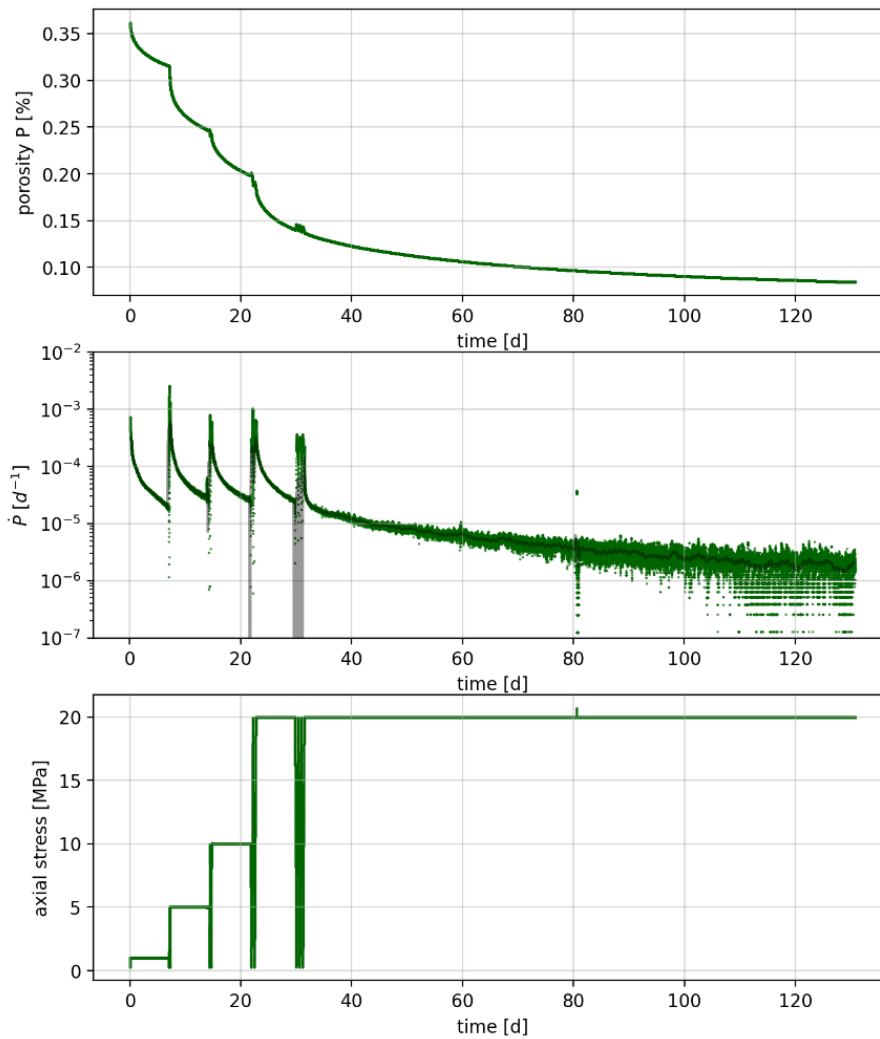


Fig. 3.27 Porosity (top), Compaction rate, i.e., porosity reduction rate (middle, moving 12 h average added as grey line), and axial stress (bottom) of experiment GV5 (wet 4) Note that the stages at 5 MPa and 10 MPa were unintentionally shortened due to an error in the machine control. Again, note the initial stage of 0.25 MPa, which is not part of the “official” load stage design, but clearly has an initial compaction effect

At the time of reporting, the calculated residual porosity after 132 days of testing was 8.4 %, and 1.6 l of solution had been squeezed out (Fig. 3.28). The solution density was measured at 1.22 g/cm³, i.e., the NaCl solution is saturated. Outflow of solution started at a strain-derived porosity of 10.5 %, i.e., at significantly higher porosity than in the GV4 (wet 3) experiment. The rate of outflow per unit porosity change first showed a linear trend and then started to decrease markedly at around 9 % porosity. Since there appears to be considerable uncertainty around the measured porosity, it can be helpful to consider a conservative estimate for porosity at the onset of outflow assuming complete pore space saturation. This results in a porosity ≥ 2.3 % as a lower boundary. Additional measurements to cross-check the measured porosity will be performed once the test is completed.

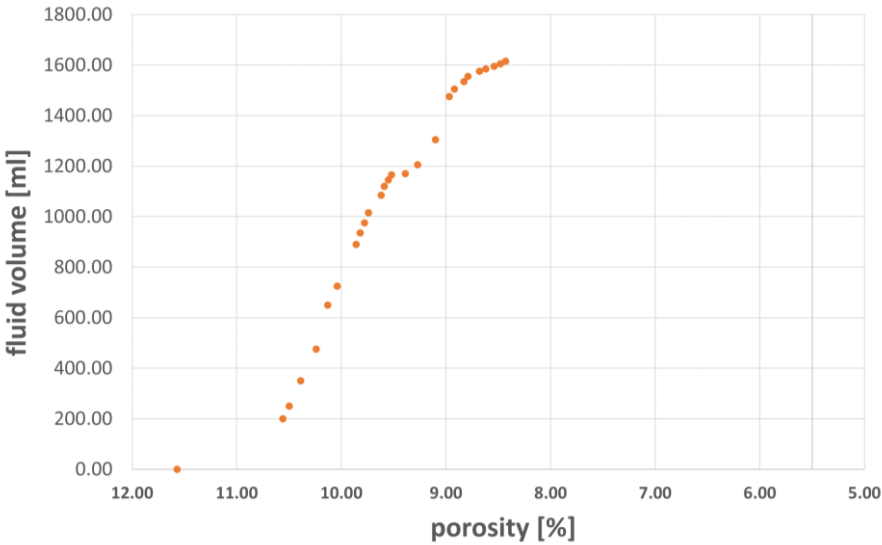


Fig. 3.28 Fluid volume squeezed out from the crushed salt test GV (wet 4) vs. calculated porosity

Comparing to the previous test GV4 (wet 3) which did not have an extended final load stage, the GV5 data show a different porosity evolution with much less overall compaction (i.e., higher final porosity), although the compaction rates are similar in magnitude. Due to the similarity of the experimental procedure, the differences would be expected to be much smaller, and therefore evaluation of the ongoing GV5 test is not deemed complete.

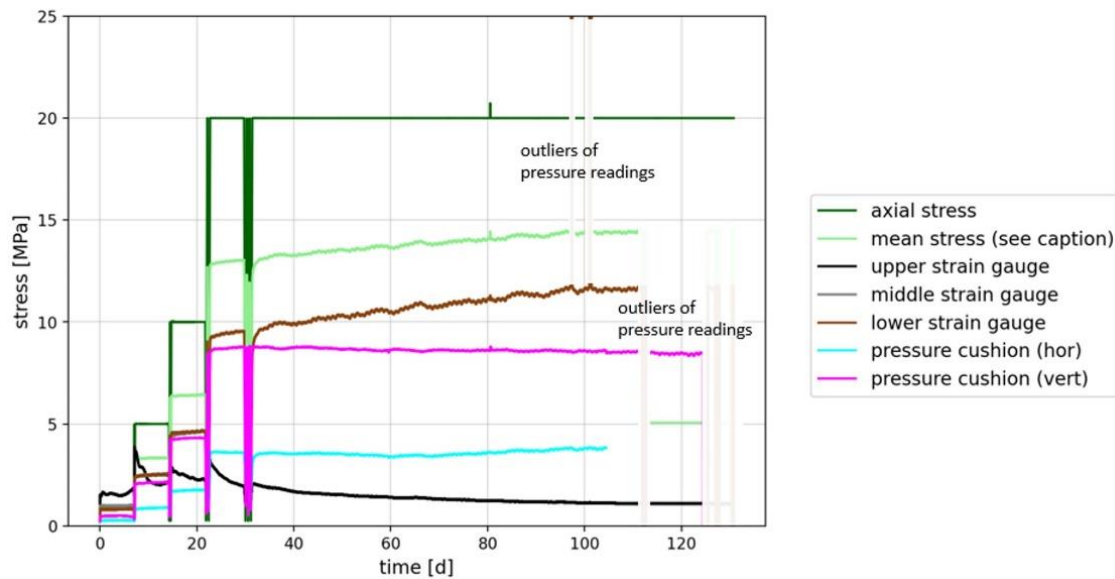


Fig. 3.29 Stress evolution for experiment GV5 (wet 4). Mean stress is calculated as the arithmetic average of axial stress, two times lower strain gauge. The naming of the pressure cushions corresponds to the measured stress (pressure cushion hor = horizontal stress measured, pressure cushion vert = vertical stress measured)

Conclusion and discussion of IfG large oedometric test results

The large IfG oedometric cell has the goal to provide experimental data for compaction tests on a scale that is more comparable to in-situ conditions. This should contribute to closing the scale gap between the laboratory and in-situ scales and provide confidence that experimental results can be transferred to the application case. With the successful completion of both dry tests (KOMPASS-I, /KOM 20/) and wet tests (KOMPASS-II, this report), quantitative data are now available for comparison to previous compaction tests with the KOMPASS reference crushed salt, which will ultimately be used as a sealing in a HAW in rock salt.

Effect of added water (wet vs dry)

The data allow an assessment of the impact of added water on the compaction processes, as well as the experimental procedure in general, but also highlight further need for investigations.

The addition of 1 wt.-% of H₂O generally has an accelerating effect on the compaction process, but there is large scatter in the data. The porosity after 28 days was 15.6 % for GV1 (dry), while wet experiments GV4 and GV5 compacted to 4.1 % and 14.1 %, respectively. Despite this scatter, we observe that the compaction rates in the wet experiments are reduced less

over time, leading to much more compaction in each creep phase compared to dry (non-wetted) crushed salt (Fig. 3.30). Probably as a consequence of the relatively small creep compaction, the plastic, i.e., time-independent, compaction during the load ramps is then stronger during the load ramps of the dry test.

The strong difference in porosity evolution and final compaction between GV4 and GV5 was surprising, as the test conditions were very similar. Much of the observed differences in porosity is established in the first load stage at high residual porosity (> 25 %). Also, the derivation of porosity based on axial strain is highly dependent on an accurate measurement of the initial porosity. This might lead to uncertainties in the measured porosity over time and one should treat the absolute values with caution. On the other hand, the data are consistent within each experiment, i.e., final porosities from axial strain and density measurements show similar values (Tab. 3.3). After the initial stage, the compaction behaviour in terms of compaction rate evolution is very similar (Fig. 3.30). One possible explanation is that the engineered KOMPASS material is still inhomogeneous in the delivered big bags. IfG did not repeat the sieving and remixing of the crushed salt due to the large amount of material used in the big cell and because it will not be done in-situ. In contrast to the smaller experiments in isotropic compaction cells or small oedometers where the crushed salt is carefully sieved and thus very well defined, full repeatability of the material's grain size distribution may not be given for the large IfG cell or in situ applications. However, since (1) grain size distribution has a strong effect on compaction creep and (2) repeatability is a prerequisite for scientific evaluation, the IfG is strongly considering homogenization of the samples prior to future experiments.

Based on the data from GV5 (wet 4), we interpret that most of the constant-stress load stages represent a transition from plastic compaction processes (grain rearrangement to reach optimal packing, grain sliding or breakage) to "steady-state" compaction creep (illustrated in Fig. 3.32). This interpretation is based on the development of more or less constant slopes in compaction rates against both time and porosity (Fig. 3.22, Fig. 3.27, Fig. 3.30).

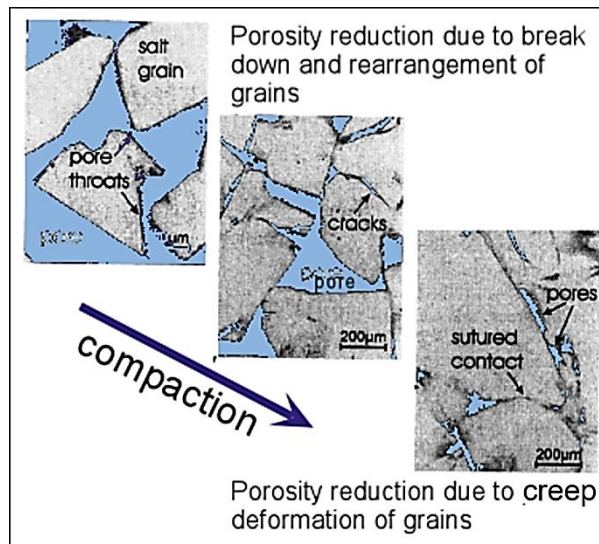


Fig. 3.30 Different processes of progressing crushed salt compaction, edited from /SPA 98/. With decreasing porosity, the dominant processes shift from stress-dependent grain rearrangement and breaking to time-dependent creep deformation

From the extended final load stage of experiment GV5 (wet 4), we can see that the creep rate reduces linearly in the logarithmic plots (i.e., follows an exponential or power law function), only after ca. 8 – 10 days (corresponding to ca. 12 % porosity for this test). This would imply that most load stages in previous tests probably did not, or barely, reach a state where compaction was mainly due to compaction creep by salt creep mechanisms (pressure solution and dislocation creep).

The evolution of mean backfill stress vs. porosity during the creep stages (see Fig. 3.30) seems to support this idea. Only the final creep stage of wet experiments GV4 and GV5 show an increase of mean backfill stress towards the axial stress value with ongoing compaction. This could be interpreted as the expression of deviatoric creep within the backfill body which would lead to an isotropic stress state in the long term. In the GV4/GV5 experiment's final stage, this transition occurs at < 10 % porosity.

Overall, the investigation of crushed salt compaction creep, and thereby the long-term safety and barrier function, likely requires much longer holding times also in the large-scale experiments than the 7 days per load stage. For future experiments, IfG thus aims to either perform very long single stage tests, or two-stage tests with much longer holding times per stage. Also, observation of long-term creep behavior is likely only possible for wet samples if time scales for experiments are to be kept in an acceptable range (weeks to months). Extrapolations based on fitting functions to relatively short load stages have proven to greatly underestimate total compaction times and are therefore of very limited use. If attempted at all, such fits should be

based on long load stages. One should additionally consider that significant deviatoric stresses act in oedometric compaction experiments. This increases compaction rates compared to isotropic stress conditions that might be expected for long-term in-situ compaction of crushed salt.

Storage vs outflow of added water in the pore space

Another central finding of the tests performed at IfG is that NaCl brine was squeezed out in the final stages of experiments GV4 and GV5. The onset of flow was at very different porosities of 4.2 % and 10.5 %, respectively. While GV4 was stopped shortly after outflow of brine began, around 70 % of the added water was squeezed out of the backfill body (1.6 out of 2.3 L) of experiment GV5 (Fig. 3.28). Importantly, the outflow appeared to reduce significantly after ca. 60 % of the added water had been released. Assuming that outflow will more or less stop at the current final value (experiment ongoing), this would result in a residual moisture content of ca. 0.7 L, or 0.3 wt.-%. This is comparable to natural rock salt. This observation highlights the necessity of finding the right balance between accelerating compaction creep through adding water and limiting the volume of water that might be squeezed out of the backfill body as NaCl solution into the neighbouring parts of a future repository. Obviously, an amount of around 0.5 wt.-% water could be sufficient to initiate fluid assistant creep, which enhances the deformability. In addition, the observed range of porosities for the onset of fluid outflow is surprisingly large (4 – 10 %) and needs to be better understood given its potential significance to the long-term safety.

Stress state in the backfill

Measuring the stress state in the backfill body in oedometer tests remains challenging. The unexpectedly low stress measurements from the pressure cushions point towards a possible shielding effect of highly compacted parts of the backfill body, or an influence of the cushions on the stress field itself. To assess this hypothesis, additional sensors for an independent characterization of the pore space and compaction status are needed. These could include sensors for electric conductivity and P-wave speeds to obtain porosity and saturation distributions within the sample. Although the pressure cushions did not deliver satisfactory data on internal backfill stresses in this project, they remain an important part of future experiments once the technical issues are better understood. Overall, the preliminary results from experiment GV5 highlight the need for improved characterization techniques of the spatial heterogeneity of compaction.

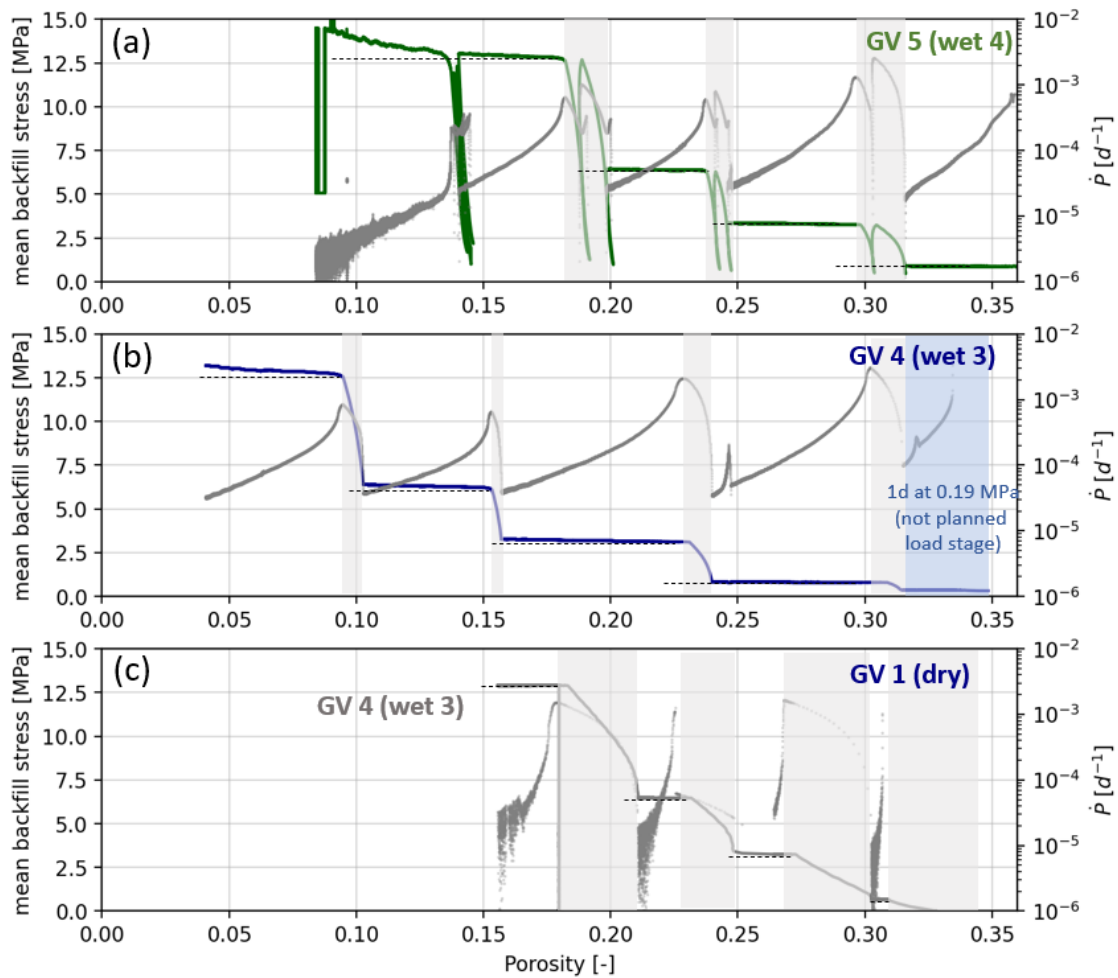


Fig. 3.31 Co-plot of mean backfill stress and compaction rate vs. porosity for experiments (a) GV5 (wet 4), (b) GV4 (wet 3) and (c) GV1 (dry), which all have the same load history. Load ramps are shown with gray background. Thin dotted lines indicate the mean backfill stress level (average of axial stress and lower strain gauge) at the beginning of each creep phase

3.2.3 Plain-strain pre-compaction (TUC)

3.2.3.1 Pre-compaction method

Technique

Pre-compaction tests performed by TUC are characterized by plain-strain loading conditions. The main advantage and purpose of this type of pre-compaction is to achieve true in-situ loading and deformation conditions as closely as possible (in case of shaft or drift sealing). This type of the pre-compaction was first proposed, developed and applied in the framework of the

joint project KOMPASS-I, hence the final report of the KOMPASS-I has additional information about the technical realization of this method of pre-compaction /KOM 20/.

Aims

In the framework of the current project KOMPASS-II, the following methodology was used to perform following tasks:

- further refinement of pre-compaction approach to improve the precision and reliability and consequently to reduce the failure rate and the bandwidth of results;
- systematic series of tests with variation of control parameters to identify the best suitable load conditions for various moisture contents to reach a target porosity of usually 15 % – 20 %;
- creation of pre-compacted samples with target porosity for further investigations: micro-structural investigations (samples produced for SANDIA and BGR) and long-term compaction tests (samples produced for TUC and GRS).

Challenges and further optimization steps

The following problems that led to sample loss or poor sample quality were discovered during the pre-compaction experiments (see Fig. 3.32):

- Oil penetration into the sample due to leakage in the pre-compaction vessels, caused by high deformations of the sample;
- Restricted drainage of the sample during the test due to a clogged sintering plate with moistened crushed salt.

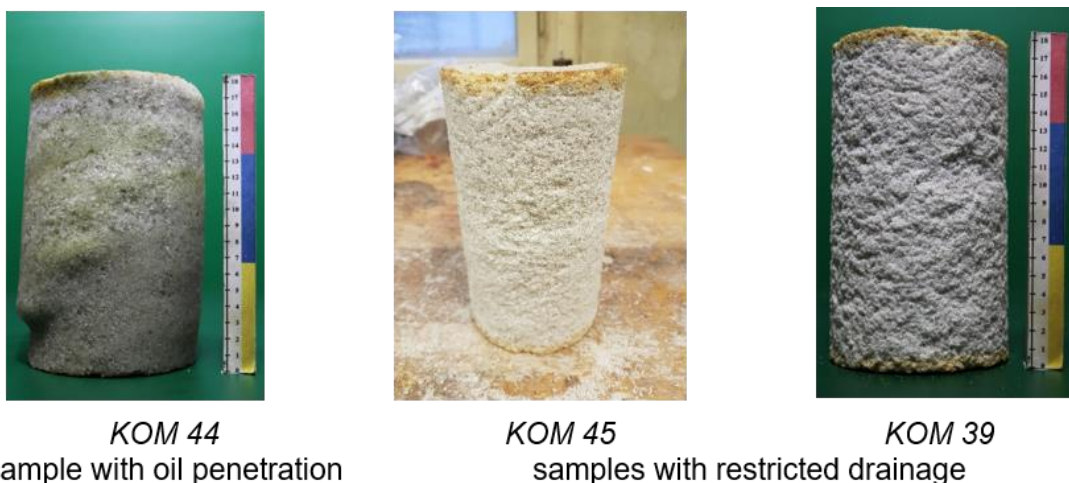


Fig. 3.32 Challenges in the framework of the plain-strain pre-compaction

In an effort to lower the failure rates, different types of fixations of the rubber jacket to the pressure pieces as well as different cleaning and preparation techniques for the sintering plates were used during the realization of the pre-compaction program.

In addition, the following issues were identified during the pre-compaction tests, which led to uncertainties and, as a consequence, to a wide range of results in terms of target porosity:

- The crushed salt which was initially supplied and mixed to a specified grain size distribution directly in the mine, is no longer accurate enough to meet the necessary grain size distribution due to transport and storage conditions.
- The initial porosity varies due to a manual filling of the loose crushed salt into the rubber jacket by the operator manually applying varied pressure.
- The calculation of the initial porosity after the sample has been installed in the equipment and compressed to a predefined sample height is inaccurate because the bulging of the sample is unknown and has to be assumed.

To reduce the magnitude of the aforementioned uncertainties and the spread of results, the following actions were carried out:

- Before performing the pre-compaction tests, the originally supplied material was dried and re-sieved to the target sieve line and thereafter the desired moisture content was added by saturated brine (manually stirred). Since this sieve line inaccuracy was discovered in the middle of the project runtime, the above-mentioned procedure of drying, re-sieving and moistening was only done starting from sample KOM49, see Tab. 3.7.
- During the manual filling of the loose crushed salt into the rubber jacket, the weight of the material to be filled in is fixed with a specified range of 3,300 g – 3,400 g. This specification is valid from sample number KOM79. Previous uncontrolled bandwidth ranged between 3,130 g – 3,720 g.
- Additional tests were performed in order to calculate the initial porosity more precisely after the sample has been installed in the apparatus or to confirm afterwards the assumed initial porosity (due to the presumed bulging of the sample). The diameter of the samples due to the bulging was assumed to be uniform and characterized by an average diameter of 124 mm (by initial sample diameter of 120 mm and a change in height from 210 mm to the target value of 185 mm). After installation and pre-compression to the required height, the specimen was removed and its diameter, bulge, and form were measured. The measurement from tests exemplifies the real bulging of two samples, one of which was pre-

compressed to a height of 200 mm and the other to a height of 188 mm. On the one hand, an expected deviation from the ideal cylindrical shape can be observed, which makes it more difficult to calculate the initial volume precisely. On the other hand, the numerical values of the average bulging diameter with 120.9 mm and 122.4 mm indicate that the preliminary estimate of 124 mm \pm 2 mm is applicable. Therefore, the initial porosity presented in Tab. 3.7 should be considered as a good guideline with an inaccuracy of \pm 2 % (e.g., initial porosity of \approx 30 % means 30 % \pm 2 %).

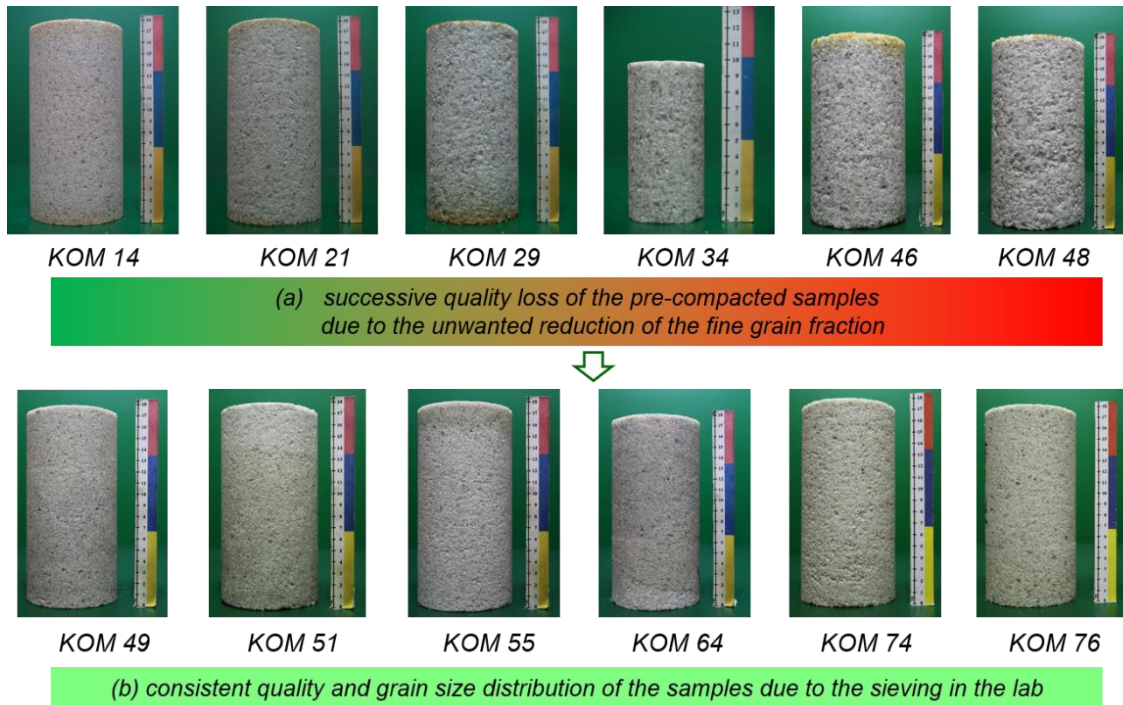


Fig. 3.33 Sample quality without sieving in the lab compared to the sample quality by sieving in the laboratory

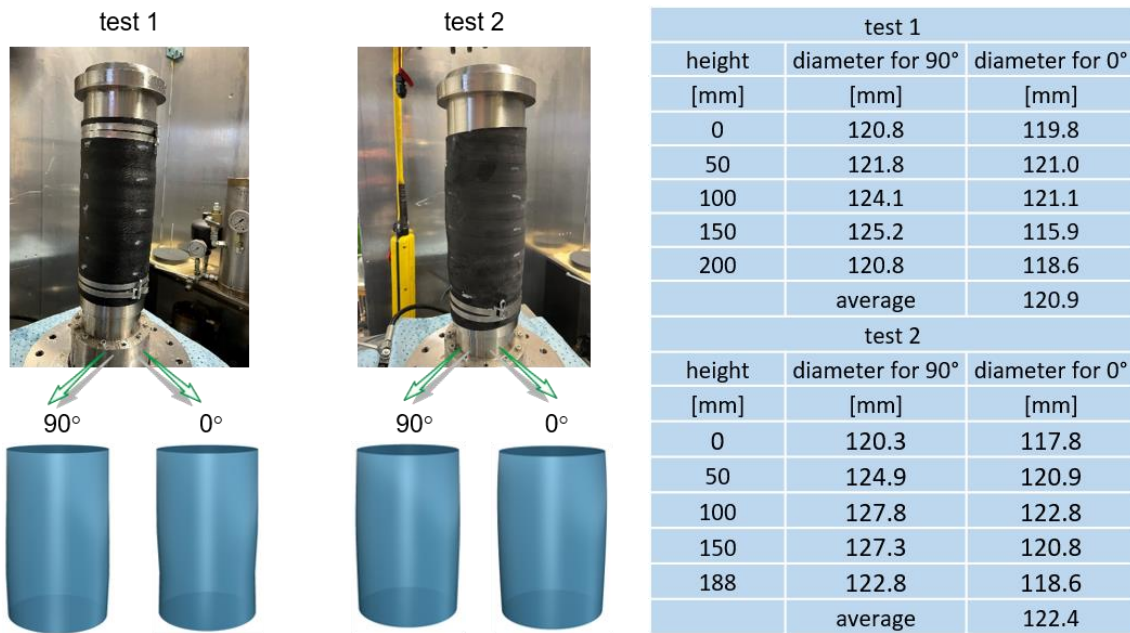


Fig. 3.34 Measurement of the bulging of sample after pre-compression to the required height before performing the pre-compaction test

Representativeness

To verify the representativeness of the samples pre-compacted in laboratory scale of time and condition, for a crushed salt subjected to in situ compaction rate, microstructural comparative analysis must be performed for in situ and lab samples. In preparation for this investigation, the microstructure of the samples, pre-compacted by different methods (from laboratories BGR, IfG and TUC), were compared by Sandia and BGR. Section 4 provides thorough information on the findings of this study.

Homogeneity

To verify and demonstrate the homogeneity of pre-compacted samples, specific tests were performed for samples with two different moisture contents (a 'wet' sample characterized by a water content of $w = 1\%$ and a 'dry' sample characterized by a water content of $w = 0.1\%$). For this purpose, each pre-compacted sample was lathed multiple times to five different sample sizes (180 mm × 90 mm, 160 mm × 80 mm, 140 mm × 70 mm, 120 mm × 60 mm, 100 mm × 50 mm), and the porosity for each sample size was determined. The positive results of these tests (more details in the following subsection) demonstrate a clear homogeneity of the sample.

3.2.3.2 Investigations

In the framework of the KOMPASS-II, the following series of investigations were planned for and carried out:

- Test series to analyze the impact of duration of pre-compaction;
- Test series to analyze the impact of confining pressure → this series was repurposed to create samples for further investigations by GRS demanding requirements for target porosity of 16 % – 19 % and specific small sample size of 100 mm × 50 mm;
- Test series to analyze the impact of moisture content.

Tab. 3.7 gives an overview of the performed pre-compaction tests and prepared samples. Fig. 3.35 and Fig. 3.36 show results of tests for confirmation of homogeneity of pre-compacted samples.

Tab. 3.7 Overview of pre-compaction tests and prepared samples performed by TUC (colored by aims)

sample No.	conf. stress [MPa]	duration [d]	water content [%]	start porosity [%]	end porosity [%]	end_size D/H [mm]	sieving in lab	Aim / Availability
KOM 24	2	10	0.1	≈25	19.4	90/177	-	available
KOM 25	2	10	0.1	≈29	21.7	90/180	-	reserved for compaction test by TUC
KOM 28	2	90	0.1	≈29	20.6	90/180	-	reserved for compaction test by TUC
KOM 29	2	176	0.1	≈28	20.9	90/180	-	reserved for compaction test by TUC
KOM 32	4	5	0.1	≈28	17.6	50/100	-	available
KOM 34	5	4	0.1	≈23	18.6	50/100	-	used for compaction test by GRS
KOM 35	5	4	0.1	≈24	17.8	50/100	-	used for compaction test by GRS
KOM 36	5	4	0.1	≈29	18.1	50/100	-	used for compaction test by GRS
KOM 37	5	4	0.1	≈26	16.5	50/100	-	used for compaction test by GRS
KOM 49	5	4	0.1	≈27	14.9	90/180	+	available
KOM 51	5	4	0.1	≈27	19.8	90/180	+	available
KOM 54	5	4	0.1	≈29	20.6	90/180	+	weight differences?, unknown reason
KOM 55	4	20	0.1	≈31	17.6	90/180	+	available
KOM 59	4	5	0.1	≈31	21.5	90/180	+	available
KOM 60	4	5	0.1	≈26	20.5	90/180→50/100	+	used for check of the homogeneity by TUC
KOM 62	4	5	1	≈34	21.8	90/180→70/140	+	used for check of the homogeneity by TUC
KOM 63	4	5	0.3	≈29	19.7	90/180	+	available
KOM 64	4	5	0.3	≈30	17.9	90/180	+	available
KOM73	4	5	1	≈28	18.1	90/180	+	quality?
KOM74	4	5	1	≈28	17.9	90/180→50/100	+	used for check of the homogeneity by TUC
KOM75	4	5	0.8	≈30	19.2	90/180	+	available
KOM76	4	5	0.8	≈31	16.4	90/180	+	available
KOM79	4	5	1	≈31	19.8	185.5/114	+	brocken during lathing to size
KOM80	4	5	1	≈32	21.4	90/180	+	quality?, problem with drainage?
KOM81	4	5	0.8	≈32	17.9	90/180	+	quality?
KOM82	4	5	0.8	≈31	17.3	90/180	+	available
KOM85	4	5	0.5	≈30	20.2	90/180	+	available
KOM86	4	5	0.5	≈30	19.7	90/180	+	reserved for compaction test by TUC
KOM87	2	20	0.1	≈31	19.4	90/180	+	oli entry
KOM88	2	20	0.1	≈31	18.4	90/180	+	oli entry

Results for test series to analyze the impact of (a) test duration as well as of (b) water content of samples can be found in the Fig. 3.37. It can be observed that compaction stagnates after a certain period due to the very low load (compare results for 90 d vs 176 d). However, as Fig. 3.37a shows, this result is not unambiguous due to the fluctuations of the results: in the representation of the porosity change (start porosity – end porosity), the compaction does not seem to have completely slackened. It is visible, that a higher load level

has to be applied to reactivate the compaction. Furthermore, it can be seen from Fig. 3.37 that a variation of water content, as expected, has a significant influence on the compaction rate. At the same time, it can be seen that the scattering of results observed in different pre-compaction tests is very large, indicating that a more precise determination of the influence of water content on compaction should be investigated in long-term compaction tests considering more precise deformation measurement and stress control. This demand is planned to take into account in the framework of the follow-up project (experiments TUC-V6 to TUC-V8). All pre-compaction tests were performed by room temperature.

Fig. 3.38 shows a photographic view of pre-compacted samples KOM34 to KOM37 that were created for GRS to perform further macroscopic investigations in long-term compaction tests.

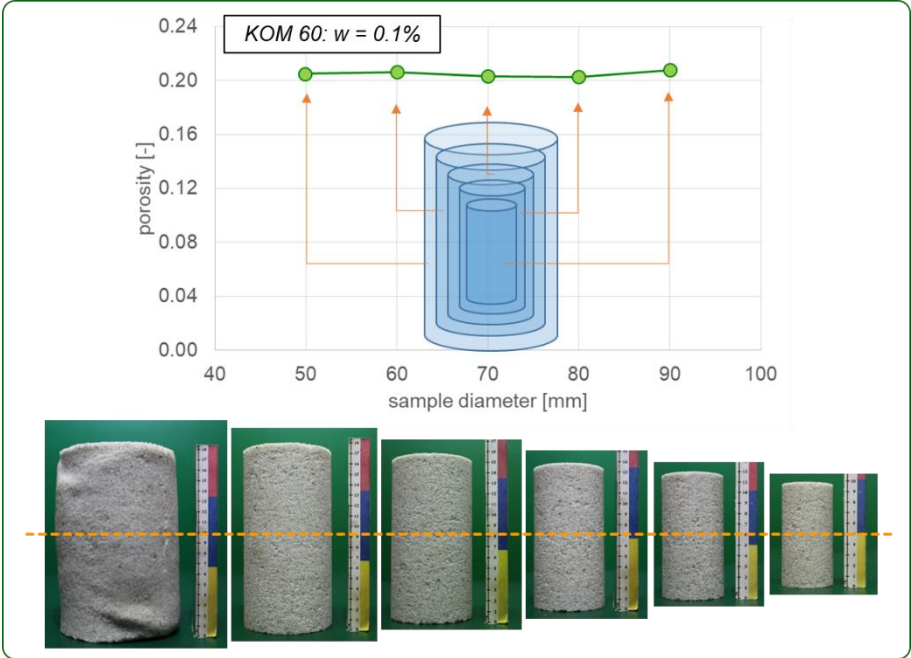


Fig. 3.35 Verification of homogeneity of pre-compacted dry sample (w = 0.1%)

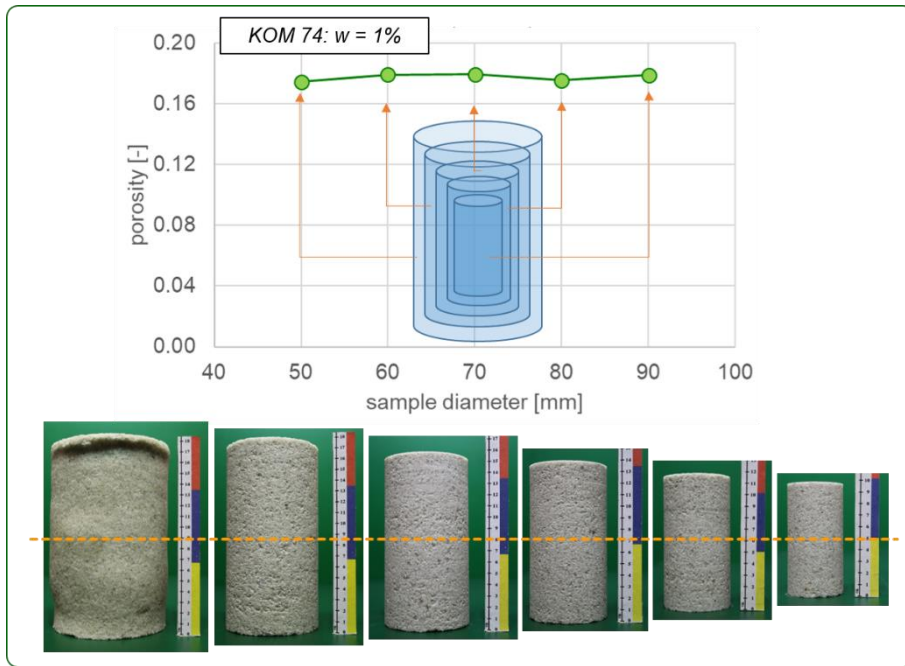


Fig. 3.36 Verification of homogeneity of pre-compacted wet sample ($w = 1\%$)

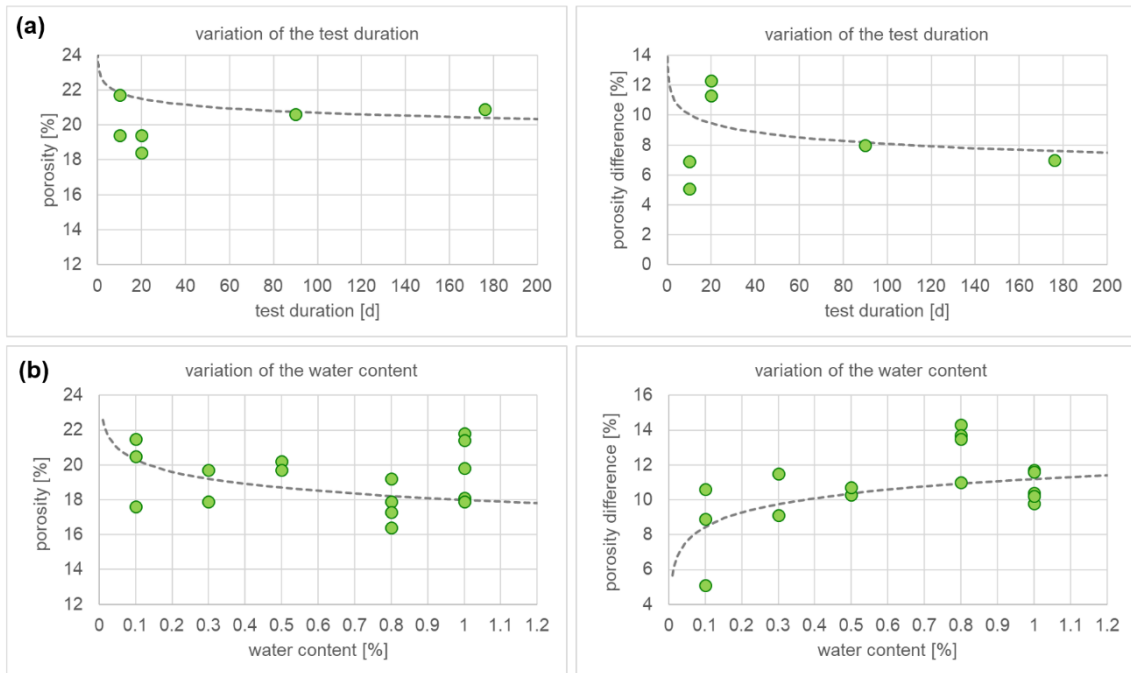


Fig. 3.37 Results of test series considering (a) a variation of pre-compaction duration and (b) a variation of water content of samples (porosity difference means $\phi_{\text{start}} - \phi_{\text{end}}$). The dashed line indicated the trend

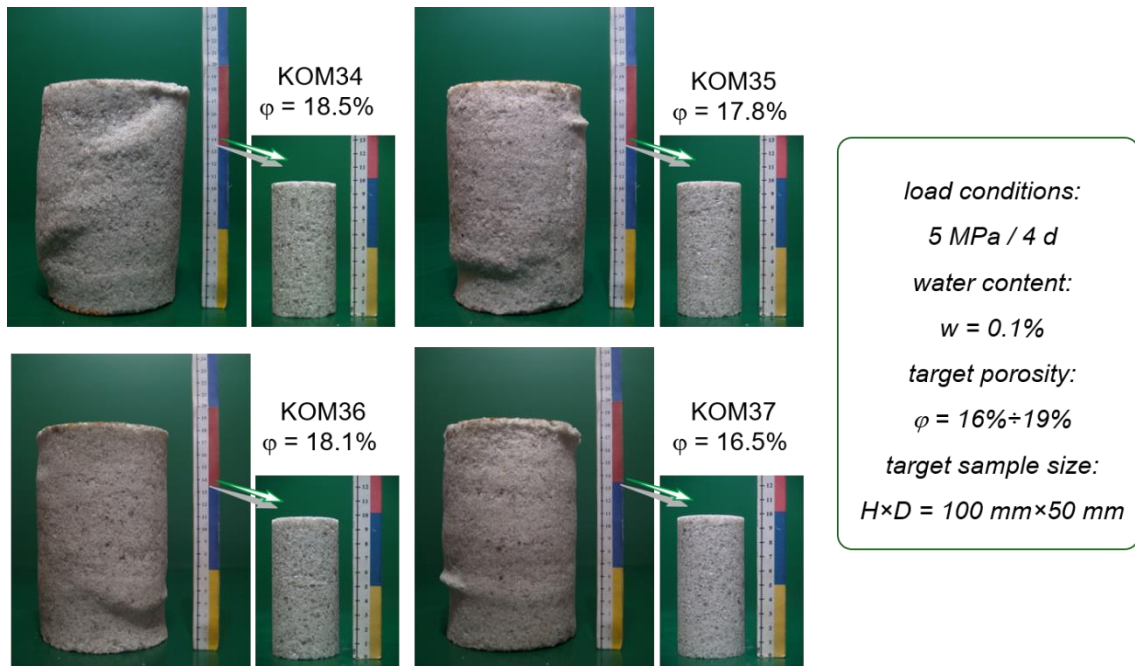


Fig. 3.38 Creation of four samples pre-compacted under plain-strain conditions considering target porosity and sample size for further compaction tests by GRS

Finally, Fig. 3.39 displays the measurement results of the ultrasonic wave velocity belonging to pre-compacted samples of the projects KOMPASS-I, KOMPASS-II as well as for the sample, which has been compacted in the long-term test TUC-V4 (with a slightly non-linear trend).

The following can be obtained from Fig. 3.39:

- a) on the one hand, a good agreement of the punctual measurements in the pre-compaction (at the end of each pre-compaction experiment) with the continuous measurements during the long-time compaction;
- b) on the other hand, comparatively large scatter of the measured values in the pre-compaction, which is caused by the inaccuracies and deficiencies in the pre-compaction realization procedure described previously, which have so far only been partially remedied.

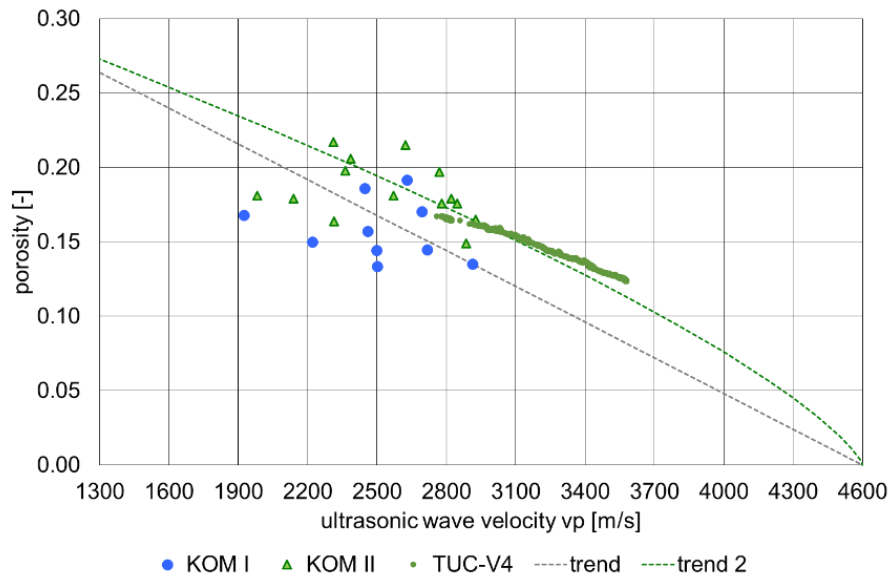


Fig. 3.39 Measurements of ultrasonic wave velocity belonging to pre-compacted samples from the projects KOMPASS-I, KOMPASS-II as well as the sample, which has been compacted in the long-term test TUC-V4

In summary, it can be stated that the plain-strain crushed salt pre-compaction methodology has been successful in generating repeatable results and demonstrating the homogeneity of the samples. Major questions regarding the representativeness of samples in comparison to in-situ pre-compacted material have not yet been definitively answered and will be further explored within the framework of the follow-up projects. In addition, as a technical point, it is also possible to mention improvement in the bandwidth reduction of the results in relation to the final porosity, which is also reasonable to continue in the context of the follow-up investigations.

3.3 Long-term compaction tests

Long-term compaction tests are needed for the characterization of the rheological behavior and the evolution of porosity/permeability with ongoing compaction of crushed salt. In KOMPASS-I, influencing parameter were identified and started to be addressed in the laboratory /KOM 20/. In this project, the ranges of the influencing factors are extended in the experiments and new influencing factors are under investigation. The long-term tests are designed with the aim to extend the process understanding of crushed salt compaction and to deliver a systematical database for the improvement of the constitutive models. In the following the test programs of the different laboratories are presented.

3.3.1 Oedometric compaction tests (BGR)

In the laboratory, a complete simulation of the salt compaction under repository conditions with low reaction rates is not possible due to time constraints. Displacement-controlled oedometric compaction tests mimic the long-term in-situ behavior of crushed salt and give a qualitative impression of the influencing parameters for compaction behavior. There is a long history of oedometric tests at the BGR laboratory since 1993, which examined crushed salt from various origins and with differing temperature conditions. Most tests focused on material from the Asse mine, revealing a variation in the material response during compaction depending on the materials' humidity, temperature, grain size distribution and bentonite as additive. This amount of test results provided a basis for barrier material design. The newest experiments include salt from bedded salt formations: two tests with salt from Teutschenthal reported in /KOM 20/ and six tests with salt from the Sondershausen mine.

Scaling effects and the influence of moisture on the oedometric compaction tests were now addressed in the KOMPASS-II project. For that, a total of 12 multistage tests with different diameters (seven with 300 mm, four with 200 mm and one with 100 mm) were performed. They follow the load path of the GV1 and GV2 compaction tests conducted by the IfG in /KOM 20/ (see also Section 3.2.2). The moisture content was varied in every experiment.

3.3.1.1 Test setup

The displacement-controlled oedometric compaction tests mimic the long-term in-situ behavior of crushed salt. The extensive amount of oedometric compaction tests carried out in the past identified important influencing factors of the compaction process. Therefore, a rough quantitative assessment of the respective influencing factor on the compaction behavior can be made. In the past, the research in the field of a final disposal for radioactive waste was focused on domal salt (Asse and Gorleben mine). With the KOMPASS reference material from the Sondershausen mine, the newer results of the oedometric compaction tests focus on the bedded salt formations. The contribution of oedometric compaction tests is limited to a certain extent. The limitation is true for the validation of functional relationships, for the determination of constitutive model-related parameters and for the (further) development of constitutive models. However, oedometric compaction tests allow almost a qualitative determination of the influencing parameters.

The tests at BGR are carried out in the heatable oedometer cell TRE-3002 "M5", shown in Fig. 3.40. The diameter of the cell is 300 mm and the height is ~150 mm. The sample is confined laterally by a friction-reducing coated steel ring and loaded by the main piston from

the top. Therein, the uniaxial force is servo-controlled by the LVDT-signal. The axial compaction displacement is measured by three inductive displacement transducers. The friction force resulting from friction between the sample or pressure plate and the steel ring is measured independently by three load cells beneath the steel ring and subtracted from the applied axial force as the wall friction do not contribute to compaction. In order to compare the results of the tests, the compaction stress, the so called 'backfill resistance', was calculated from resulting force and constant cross section middle (Fig. 3.40) (for a more detailed description check /STÜ 17/; DAkkS No.: D-PL-20434-01-00).

The compaction of loose crushed salt in an oedometric cell causes unwanted stress inhomogeneities and hence an uneven compaction grade throughout the sample. As a countermeasure, the crushed salt material was filled in stepwise in three portions. Each section was slightly compacted by hammer strokes to a fitting metal disk before filling in the next section. The resulting overall filling height was 145 – 146 mm. With the cells diameter (300 mm), the resulting in an initial sample volume was approximately 10,200 cm³. The initial sample mass was approximately 15,000 g.

To investigate moisture and scaling effects a further test series is carried out on a smaller oedometric cell (200 mm diameter, maximum filling height 120 mm) with TRE-3001 "M4", see Fig. 3.40, on the right. The resulting initial sample volume in the smaller cell is approximately 3,700 – 3,850 cm³, with a sample mass of 5,300 g.

The sample is confined laterally by a coated steel ring and loaded uniaxial servo-controlled by the main piston. The axial displacement is measured by three inductive displacement transducers, similar to the setup in the heatable oedometer cell TRE-3002 "M5". However, friction force can't be measured. A PTFE foil is emplaced between the wall and the loose crushed salt to reduce the friction force and the corrosion of the cell as well.

A third test was carried out with the pre-compaction cell (see Section 3.2.1): the diameter of the pre-compaction cell is 100 mm and the used filling height is approximately 60 mm, resulting in an initial sample volume of approximately 484 cm³ and a sample mass of 650 g.

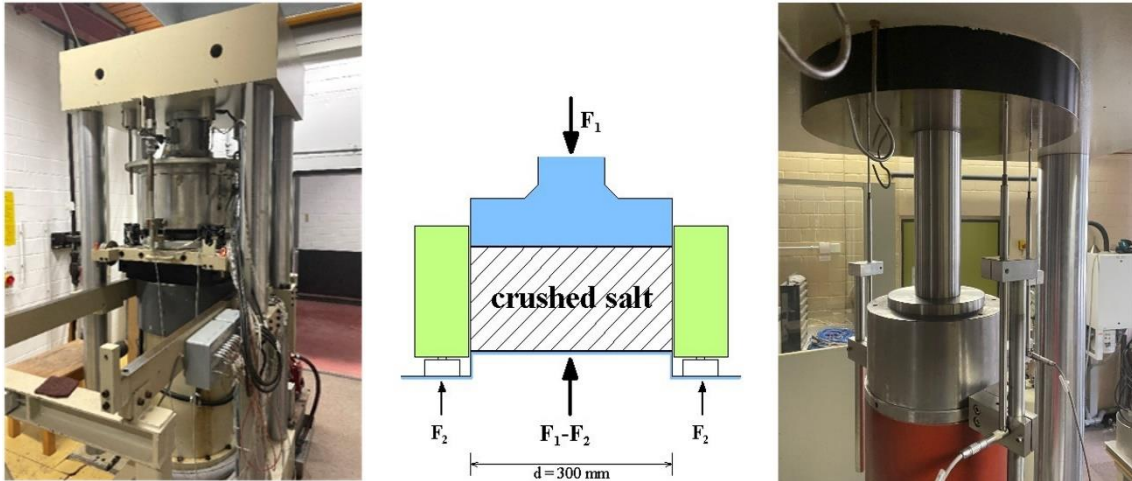


Fig. 3.40 M5 - Load frame with cell and principal sketch (with F_2 = friction force and F_1 = axial force) and M4 – smaller oedometric cell (200 mm diameter)

Material, humidity and test temperature

The experiments carried out within the KOMPASS-II project and described in this section of the report were produced with the KOMPASS reference material from the Sondershausen salt mine (bedded salt formation) /KOM 20/. The KOMPASS reference material from the Staßfurt formation consists of approximately 98 % NaCl accompanied by a small amount of Anhydrite. Moisture content was measured with ~ 0.1 wt.-%. To be able to reproduce the initial KOMPASS reference material and to optimize the production of smaller samples at the BGR, the first ready-mixed delivery from 2017 /KOM 20/ was further characterized. A refined sieving curve named “Son1” was created and used for all future tests (6.9 % > 4 mm; 52.3 % > 2 mm; 17.2 % > 1 mm; 7.2 % > 0.5 mm; 2.8 % > 0.4 mm; 4.4 % > 0.25 mm; 6.4 % > 0.125 mm; 2.8 % > 0.063 mm).

To determine the influence of moisture on the compaction, two sets of experiments with different moisture contents were carried out. The first set of experiments consisted of displacement-controlled tests (OE-117, OE-118, OE-119 and OE-123). The first two experiments (OE-117 and OE-118) were carried out with the “natural” moisture content of the KOMPASS reference material (0.1 wt.-%). Two further oedometric compaction tests were carried out with a moisture content of 0.35 wt.-%, which corresponds to the natural moisture measured in the crushed salt from the Teutschenthal mine (also in a bedded salt formation). Therefore, a comparison to the former oedometer tests OE-112 and OE-113 on the Teutschenthal crushed salt /KOM 20/ seems reasonable. Further, two oedometric compaction tests with a moisture content of 0.45 wt.-% were carried out. The desired moisture was achieved here by adding the saturated brine to the stored salt with natural moisture content without drying the large quantities of salt

beforehand. The moisture of the stored crushed salt is determined regularly and fluctuates slightly within the measurement accuracy. The temperature in those six oedometric compaction tests were set to 50 °C with two exceptions. The test OE-119 was carried out at 100 °C and the test OE-123 had two stages at different temperatures (first stage 50 °C and second stage 100 °C). In order to provide parameters, a multidimensional overview is presented in Fig. 3.41, which shows the selected test parameters and achieved residual porosities for the experiments. The Fig. 3.41 includes also the test parameters from the former oedometric compaction tests OE-112 and OE-113 on the Teutschenthal crushed salt from the first KOMPASS phase /KOM 20/.

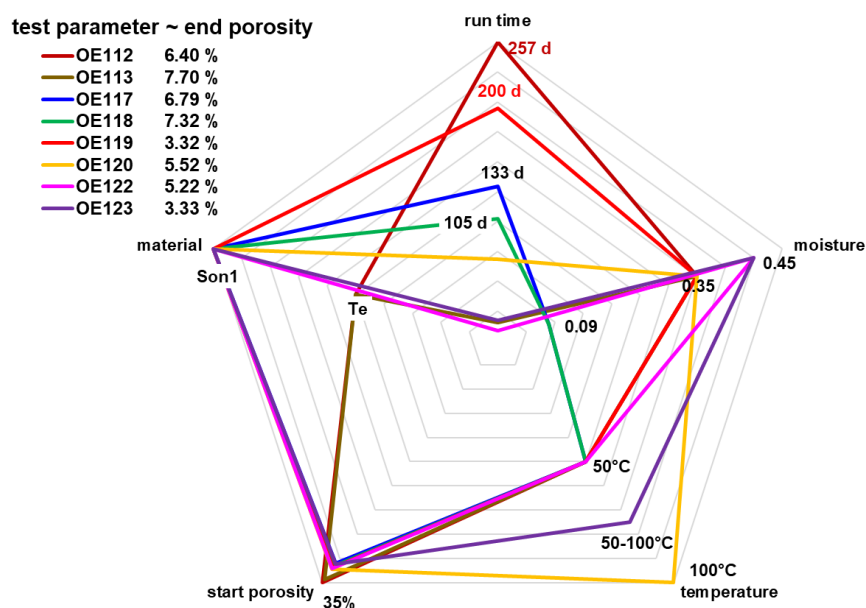


Fig. 3.41 Displacement controlled oedometric tests – test parameter: run time, moisture content, temperature, starting porosity and material

The second series of oedometric compaction tests consisted of multistage tests. In the larger oedometric cell M5 (diameter of 300 mm) two compaction tests with different moisture content were carried out (OE-124 with 0.5 wt.-% and OE-125 with 0.1 wt.-%). Both tests had a constant temperature of 50 °C.

In the smaller oedometric cell (200 mm, no heating, no measuring of friction force), four compaction tests with different moisture contents were carried out (0.1 wt.-%, 0.5 wt.-%, 0.01 wt.-% and 2 wt.-%). To achieve the moisture content of 0.01 wt.-%, the crushed salt was dried at 105 °C, before implemented in the cell.

Test procedure

To keep clear, the test procedure is divided into displacement-controlled tests and multistage tests.

Displacement controlled tests:

A constant displacement rate is selected for loading the specimen, analogous to a constant drift convergence. The compaction behavior of crushed salt is a function of the compaction rate. Compaction rates comparable to the in-situ case (for Asse-conditions approximately 10^{-10} s^{-1} or slower /BEC 99/) cannot be used in the laboratory for an entire experiment because no significant compaction is achieved within a reasonable period of time. The runtime of an in-situ realistic experiment with a strain rate of 10^{-10} s^{-1} would yield to about 13 years. This compaction speed was set in an alternating, multi-step manner, ranging from 0.36 mm/h to 0.00036 mm/h for the tests in steps of an order of magnitude. Corresponding to the initial sample height $\sim 145 \text{ mm}$, this speed resembles strain rates from $6.7 \cdot 10^{-7} \text{ s}^{-1}$ to $6.7 \cdot 10^{-10} \text{ s}^{-1}$.

After inserted periods of higher compaction speeds relaxation intervals were added, to allow any possible impact of foregoing rapid phases to decay. This test procedure with changing compaction speeds and relaxation phases in between was used for the oedometric compaction tests OE-117 – OE-120.

In the last years (2012 – 2021) of experimental time the proportion of friction force to axial load increased due to the wear of the cell surfaces and to chemical reaction on the cell walls. This is also visible in the coloring of the finished test specimens. Therefore, the procedure was adapted, and a PTFE (Polytetrafluoroethylene) foil was implemented to reduce the friction force between the material and the cell walls.

Multistage tests:

Every multistage test OE-124, OE-125, OEK-003 – Oek-006 was performed with four axial loading steps: 10 MPa, 20 MPa, 30 MPa and 40 MPa. Every axial loading step runs for one week.

3.3.1.2 Test results of the displacement controlled oedometric tests

Depending on the boundary conditions, compacted test specimens with residual porosities of 3 % to 8 % were produced. The porosity is determined from the geometric dimensions of the

samples, the weight, and the solid density. The solid density of the material is of decisive importance for the calculation of the porosity. The density of the dry raw material should be the same as for the reference material. The moisture in the sample impacts the density of the material. Therefore, the moisture content is part of the calculation. However, depending on the test duration and temperature, drying out of the sample is assumed. Therefore, a change of density and thus an uncertainty in the residual porosity is expected.

The weight loss after removal is in the magnitude of the initially added moisture. It is not clearly detectable if moisture is lost during the compaction or if the weight loss is mainly due to the loss of individual salt crumbs during the dismantling process. To address this issue in the future, the samples will be jacketed with PTFE foil to prevent material loss during the dismantling. However, the disadvantage for this procedure is the amalgamation of sample and foil.

The selected parameters of the compaction tests are not simply coupled. This includes the effect of an individually changed boundary condition on the overall compaction behavior of the sample. Tab. 3.8 gives an overview of the oedometric compaction tests.

Tab. 3.8 Displacement controlled oedometric tests – parameter and end porosity

Name	Material	Moisture [wt%]	Duration [d]	Temperature [°C]	Porosity [%]	Friction [%]
OE112	Teutschenthal	0.35	257	50	6.40	16.09
OE113		0.35	16	50	7.70	8.75
OE117	Son1	0.06	133	50	6.79	15.8
OE118		0.06	105/187	50	7.32	6.54
OE119		0.35	200	50	3.32	15.98
OE120		0.35	70	100	5.52	30.26
OE122		0.45	9	50	5.22	4
OE123		0.45	18	50	3.33	1.5

The individual results for the evolution of backfill resistance for the new strain-controlled oedometric tests (OE 117 – OE 123) with the KOMPASS reference material are presented in Appendix A.1. For each experiment, the backfill resistance is shown a) as a function of time and b) as a function of porosity. Additionally, the experimental phases and the resulting quantities are presented in two tables for each sample separately. The alternating compaction speed (Section 3.2.1.1) corresponding to strain rates from $6.7 \cdot 10^{-7} \text{ s}^{-1}$ to $6.7 \cdot 10^{-10} \text{ s}^{-1}$ are color coded, untraceable speeds are greyed out. In addition to the backfill resistance, the friction is indicated in the figures.

The following two figures Fig. 3.42 and Fig. 3.43 show a comparative presentation of all tests presented in Appendix A.1 including the former test data performed on crushed salt from Teutschenthal /KOM 20/. Within the individual tests, phases of high compaction speed alternated with phases of lower compaction speed. The change from a high to a low compaction speed was separated by an individual relaxation phase.

In the past, a characteristic stress curve for each compaction rate was determined by interpolating and extrapolating the curves, taking into account the transition phase after changing to another compaction rate. In the oedometric compaction tests with higher moisture contents, the transition phase between the different compaction rates takes longer. In the earlier test OE-112, the relaxation phases were too short and have not yet decayed sufficiently, before the next, higher compaction stage was started. In this former test, reloading was initiated when the relaxation rate corresponded to the new loading rate. This also influences the transition phases between different compaction rates. Both processes, relaxation, and loading, overlap each other. In later tests, a new stage with lower compaction speed than in the stage before, was not started until the backfill resistance was relaxed to 1/4 of the former maximum.

From the test data for backfill resistance evolution versus porosity and the comparison part in the Fig. 3.42, it can be seen, that compaction tests with rather dry material (OE-117 and OE-118) had short transition phases, while the compaction tests with rather wet material (OE-199 and OE-120) had long transition phases.

For the highest compaction rate corresponding to a deformation rate of 10^{-7} s^{-1} , parallel lines were obtained for the same moisture content. The relation between porosity and displacement is similar in the compaction tests OE-119, OE-122 and OE-123 and reaches up to 15 % porosity. The backfill resistance of the compaction test OE-120 (100 °C) is shifted parallel to higher backfill resistance. The shift to higher back fill resistance occurred despite otherwise identical conditions (moisture content). Due to the increased temperature, the salt crust has presumably dried up from the edge to the center and therefore increased the lateral frictional forces. In the short-time test OE-123 (12 days), this parallel line has shifted to lower offset resistances due to the temperature increase during the running test.

The oedometric compaction tests OE-117 and OE-118, which were carried out with the same moisture content (0.35 wt.-%), showed parallel but not congruent lines. One reason for the differences might be the proportion of frictional forces: after oedometric compaction test OE-117, the corroded cell wall was repolished. Since subsequent compaction tests with even higher moisture contents would have caused further corrosion of the cell, an insulating

intermediate PTFE-layer was placed between the cell wall and the crushed salt for the following tests (as of test OE-122). The film reduces the friction component from a maximum of ~ 20 % to ~ 3 %, resulting in a wider measuring range for the backfill resistance (to 41 MPa) at the load limit of the machine of 3000 kN.

Fig. 3.44 shows the relaxation curves for all oedometric compaction tests. The decrease of the backfill resistance over time for each relaxation phase is shown. The dry compaction tests OE-117 and OE-118 (0.1 wt.-%) show approximately parallel relaxation curves for each compaction stage. For wet compaction tests, such as OE-119 (0.35 wt.-%), the decrease of backfill resistance is dependent on the degree of compaction and faster, compared to dry samples.

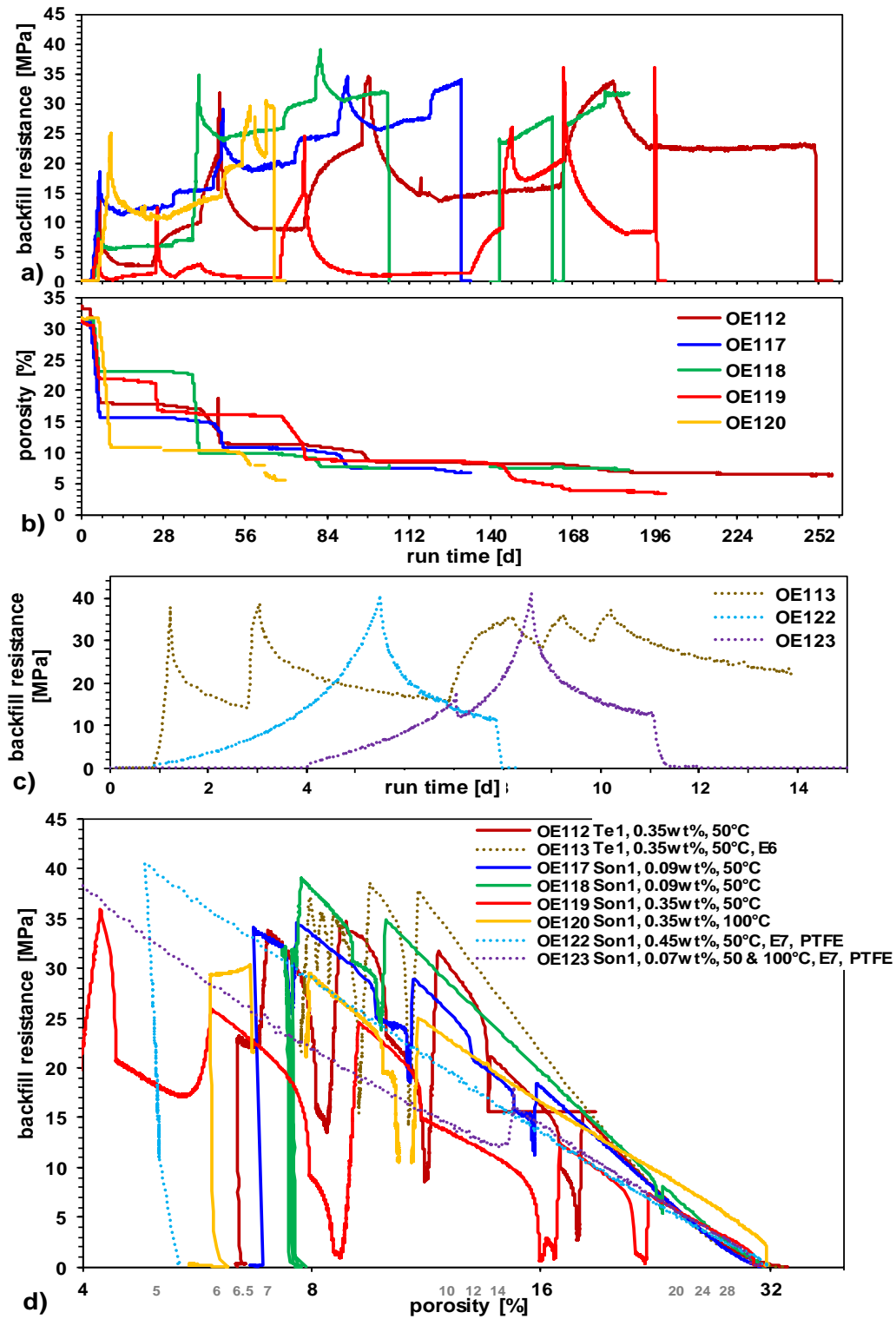


Fig. 3.42 Comparison of strain-controlled oedometer tests – evolution of a) backfill resistance; b) porosity; c) evolution of backfill resistance for the short tests; d) relation porosity ~ backfill resistance for all tests

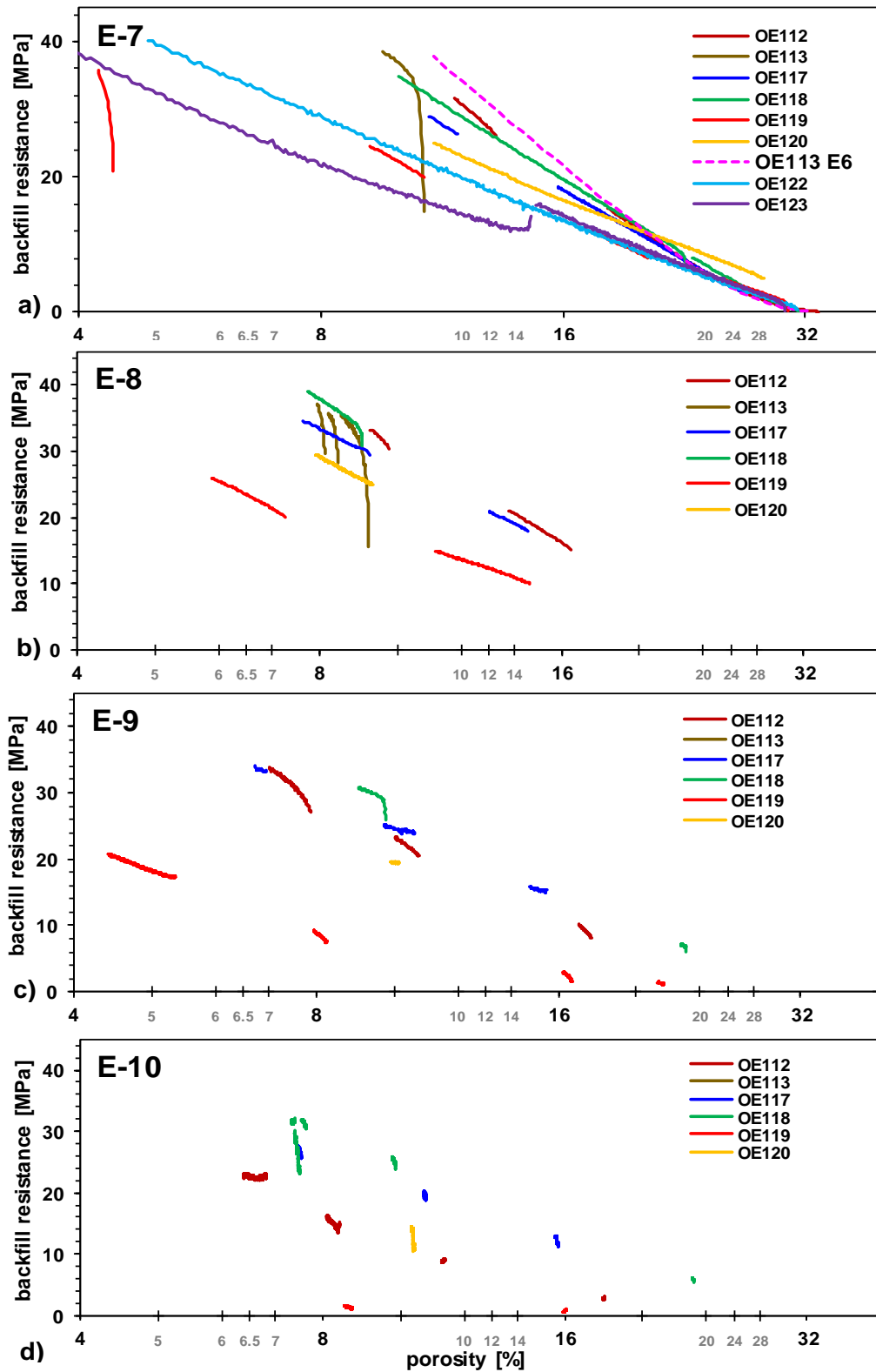


Fig. 3.43 Backfill resistance ~ Porosity for different strain rates: a) 0.36 mm/h = $6.7E^{-7}$ 1/s; b) 0.036 mm/h = $6.7E^{-8}$ 1/s; c) 0.0036 mm/h = $6.7E^{-9}$ 1/s; d) 0.00036 mm/h = $6.67E^{-10}$ 1/s

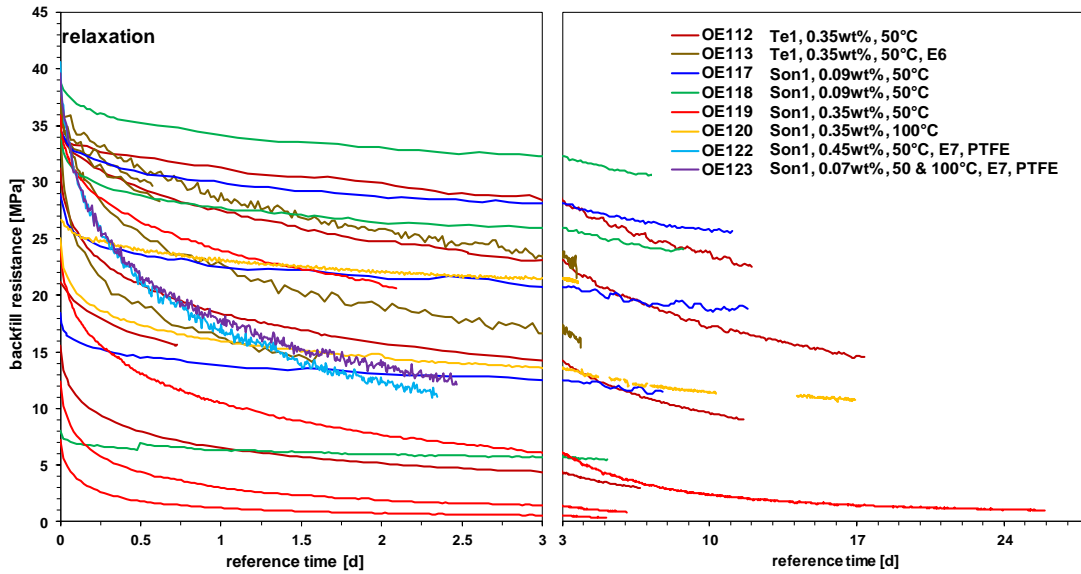


Fig. 3.44 Decay of backfill resistance ~ reference time of relaxation phase for different compaction levels, note different time scales

3.3.1.3 Test results of multistage oedometric compaction tests

To provide parameters, an overview of all boundary conditions and residual porosities for the multistage compaction tests (loading with 10, 20, 30, 40 MPa) with different cell diameters (300 mm, 200 mm, 100 mm) is shown.

Tab. 3.9 shows the moisture content, the test duration, temperature, final porosity, and the deformation rate (uniform for all tests at the end of the second loading step of 20 MPa – the value is available for all tests and is calculated from a potential trend function of deformation rate between one and seven days after loading, Fig. 3.45).

Fig. 3.46 shows the results (porosity and deformation rate) for a series of compaction tests with the small oedometric cell (diameter 200 mm). Due a procedural error, the 3rd loading stage was skipped for the wet (0.5 wt.-%) and the dry (0.1 wt.-%) experiment. The “extra wet” experiment (2 wt.-%) achieved a final porosity of 3.9 %. The final porosity of the “extra dry” compaction test reached 9.1 %. The differences between the samples in the deformation rate decreases with higher loadings.

Tab. 3.9 Multistage oedometric test – parameter, porosity, deformation rate after 20 MPa

Name	Cell	Moisture [wt%]	Duration [d]	Temperature [°C]	Porosity [%]	Rate [1/s] 2. step 20 MPa after 7d
OE 124	Ø 300 mm h 150 mm	0.5	35	50	32 - 1.8	2.3E-08
OE 125		0.1	35	50	31.5 - 7.6	8.8E-09
OEK 003	Ø 200 mm h 120 mm	0.5	34	22	35 - 4.4	2.3E-08
OEK 004		0.1	31	22	36.7 - 8.5	1.2E-08
OEK 005		0.01	42	22	36.7 - 9.1	1.1E-08
OEK 006		2	34	22	37 - 3.9	2.5E-08
OEsk 001	Ø 100 mm h 60 mm	0.1	34	22	38.3 - 8.9	6.1E-09

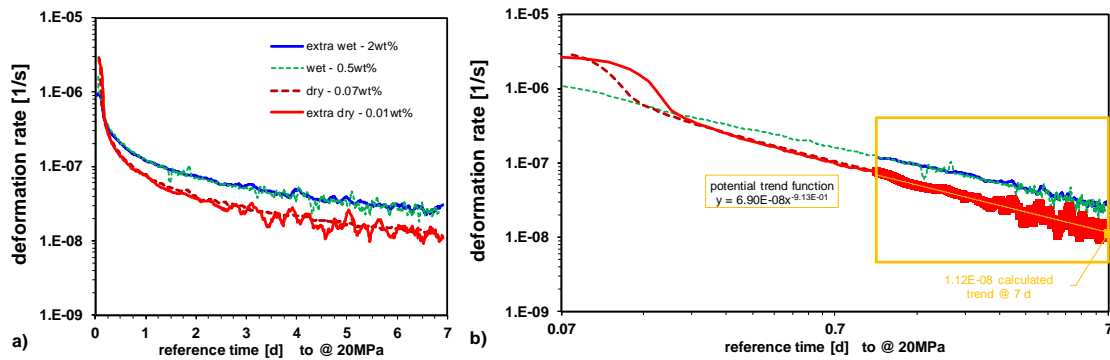


Fig. 3.45 Oedometric multistage creep test – Estimation of deformation rate after 20 MPa
a) Deformation rate for 2nd load stage to reference time for the 20 MPa stage
b) Deformation rate to logarithmic time axis, yellow time range for calculating the potential trend function and the value calculated from it for day 7

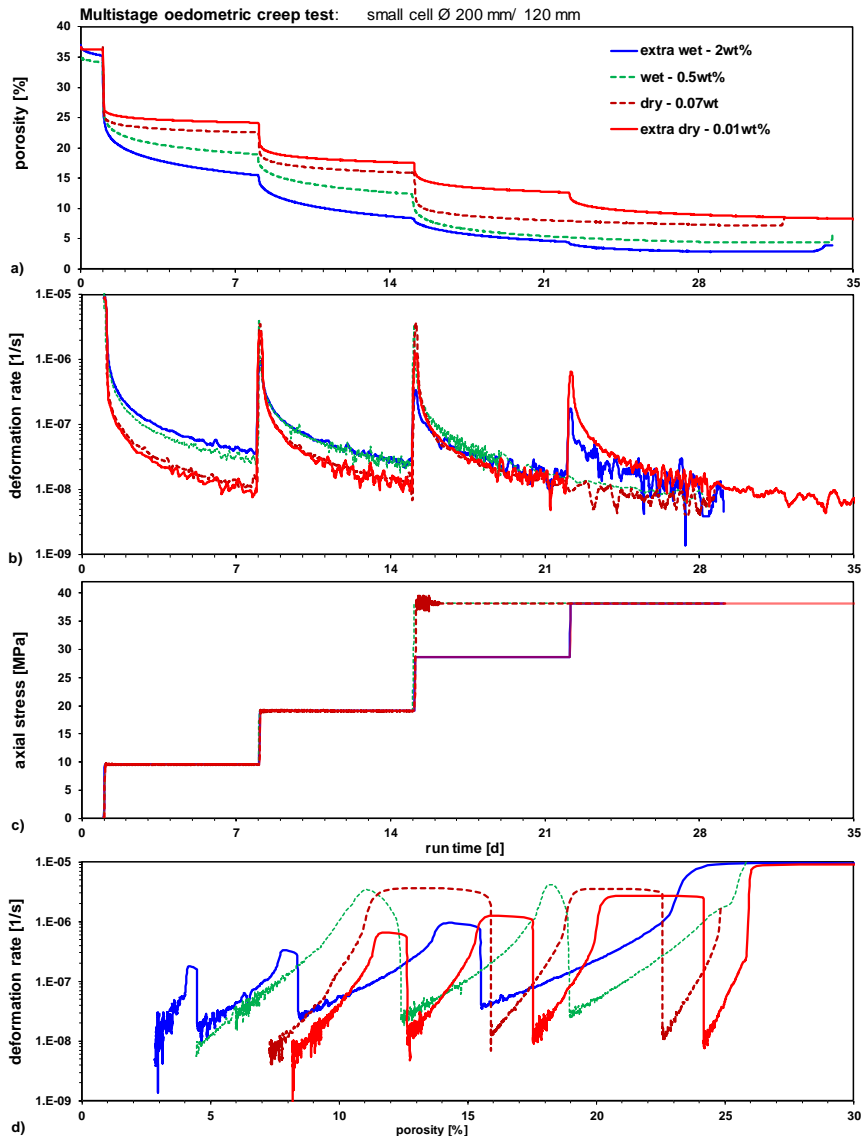


Fig. 3.46 Oedometric multistage creep test - small cell Ø 200 mm - different moisture: a) porosity, b) deformation rate, c) stress regime, d) deformation rate vs. porosity

Fig. 3.47 shows the scaling effects on samples with different sample sizes but same geometric ratio and two different moisture contents (wet: 0.5 wt. %; dry: 0.1 wt.-%). Until an axial stress of 10 MPa is reached, small differences in porosities for dry samples were recognized and more differences for the wet samples. At stresses higher than 20 MPa no differences in the porosities could be recognized for the dry samples. In the pre-compaction cell (Ø 100 mm) the final porosity was higher, compared to the other two cells. The differences occur with filling and with load application in the first phase. The ratio of largest grain size to sample size and with this, the inhomogeneity of grain size distribution during of filling especially for wet material influence the process.

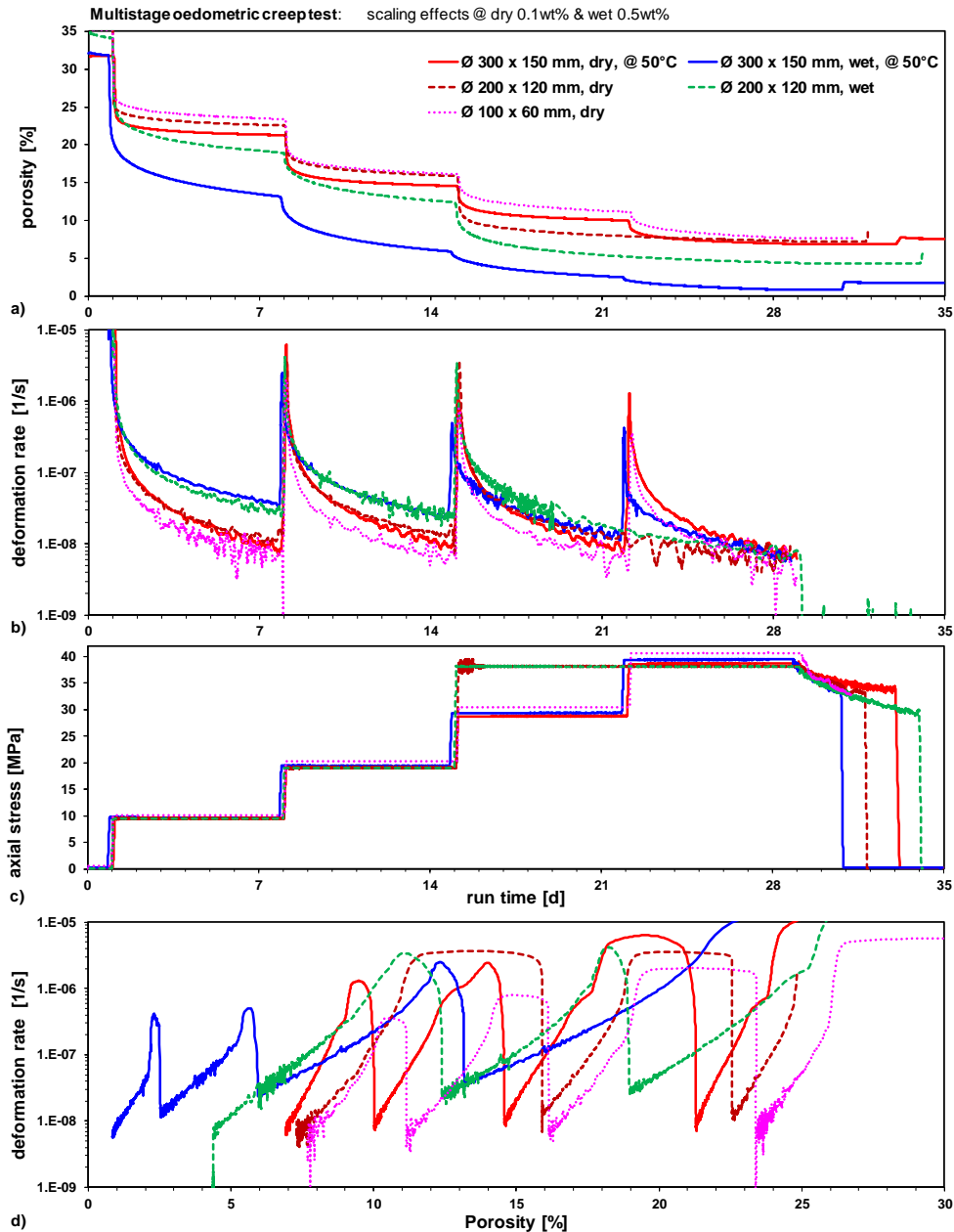


Fig. 3.47 Oedometric multistage creep test – scaling effects for dry and wet crushed salt with different cell diameter Ø 300, 200, 100 mm: a) porosity; b) deformation rate; c) stress regime; d) deformation rate vs. porosity

Due to a procedural error, the 3rd loading stage was skipped for the wet (300 mm, 0.35 wt.-%) and the dry (200 mm, 0.1 wt.-%) experiment. In Fig. 3.48b, the deformation rates are considered as uniform after the 20 MPa loading stage.

The oedometric tests identified important factors influencing the compaction process. Higher amounts of moisture content in the samples influences the compaction process as well as the relaxation process.

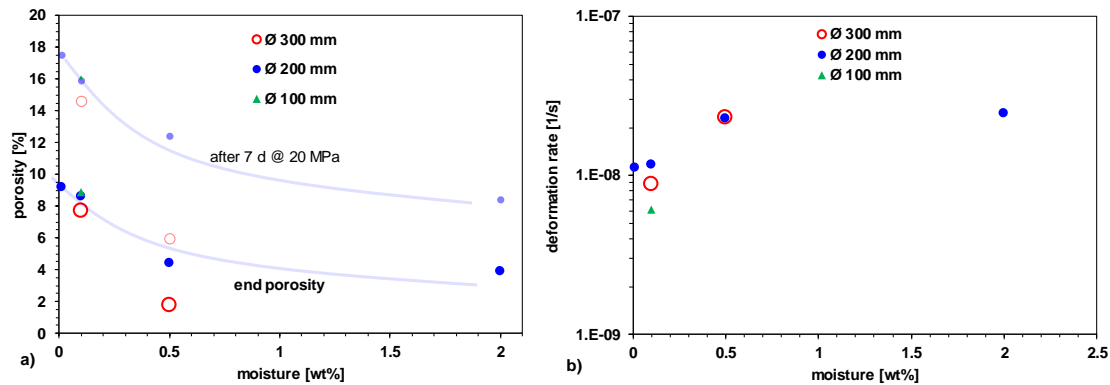


Fig. 3.48 Oedometric multistage creep test – moisture and scaling effects for different cell diameter \varnothing 300, 200, 100 mm: a) porosity end and after 20 MPa; b) deformation rate for 20 MPa after 7 days – end of second loading step

3.3.2 Triaxial compaction tests (BGR)

To support and independently assess the results of the displacement-controlled oedometric compaction tests, triaxial compaction tests with knowledge of the triaxial stress state were performed. Test series of triaxial compaction tests address the samples response to variations in confining pressures and contribute to identify generalized constitutive equations for crushed salt. Both types of compaction procedures at BGR (oedometric and triaxial compaction), are accredited by the German accreditation body (DAkkS).

Triaxial creep tests with wet crushed salt (> 0.1 wt.-%) had not been carried out yet. Therefore, the influence of moisture on the compaction behavior, the achievable final porosities and creep rates are an essential aspect of introduced triaxial test series. All previous tests were carried out on crushed salt from domal salt (Asse mine). In the KOMPASS-I project, the KOMPASS reference was introduced. In bedded salt formations, the moisture content is higher compared to domal salt, due the different stresses during halokinesis /ROE 81/. During the triaxial compaction test, the aim was to compact the samples as far as possible, without exceeding the maximum formation pressure expected in-situ (20 MPa).

For the triaxial compaction tests, the pre-compacted samples were used (see Tab. 3.2 in Section 3.2.1 and Tab. 3.10). In total six long-term compaction tests (one with moistened Asse Speisesalz and five with the KOMPASS reference material with different moisture contents) evaluate the rheological behavior (foremost the creep rate) and the development of porosity during compaction. The series of triaxial compaction tests on crushed salt will expand the previous database to investigate the thermal-hydro-mechanical (THM) processes in moistened crushed salt for an improved description of the compaction behavior by means of constitutive laws.

3.3.2.1 Test setup

All triaxial compaction tests were performed in a triaxial apparatus (test unit: "M6", Fig. 3.49). The M6 is a cell based on the Kármán principle with a burette system to measure the gas outflow during the experiment (reflecting changes in porosity). The unit holds samples with $D = 100 \text{ mm}$ and $H \leq 250 \text{ mm}$ and can be loaded with a confining pressure p_i of up to 50 MPa. This internal cell pressure is supplied by an external pressure intensifier. The axial force F_1 (max. 1,000 kN) is generated by the master cylinder below the pressure cell. The oil in the cell can be heated up to 100 °C. The test temperature is controlled by three independent heating baths and the laboratory was air conditioned (for more detailed description see /STÜ 13/ and /STÜ 17/; DAkkS No.: D-PL-20434-01-00).

In Tab. 3.10 the parameters of all six triaxial tests carried out by BGR in the time period 2019 – 2022 are shown.

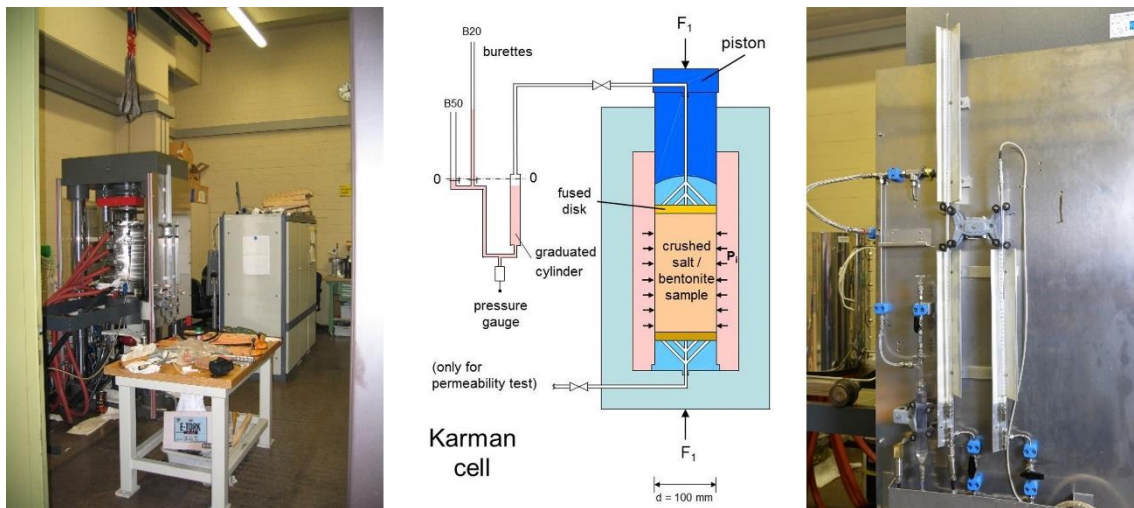


Fig. 3.49 Triaxial testing system with load frame, sketch of the pressure cell and the burette system

Tab. 3.10 Test parameter for the triaxial compaction tests by BGR

Name	Material	Moisture	Temperature	Duration [d]	Pressure steps [MPa]	Pre-compaction			
						VK Nr.	Controlled by	Sig _{max} [MPa]	Porosity [%]
TK-037	Asse Speisesalz z2SP DEBORAH < 8mm	0.15wt%	50°C	141	5, 10, 15, 20	26	strain	25	17.1
TK-038	Sonder-shausen z2 Son1 < 8mm	0.1wt.-%	50°C	34	5, 10,	28	strain	24	16.7
TK-041		0.35wt.-%	50°C	145	5, 10, 15, 20	32		13	17.4
TK-042		0.35wt.-%	50°C	72	10, 15,	34	stress 6 kN/min	14	17.4
TK-044		0.5wt.-%	33°C	144	4, 8, 12, 16, 20	45		14	17.7
TK-045		0.5wt.-%	50°C	220	4, 8, 20	47		15	13.2

Material and Density

Crushed salt from the Asse mine (Germany):

The crushed salt used in the TK-037 experiment originates from the Asse mine (As-z2SP; Asse Speisesalz) and consists of more than 99 % halite with a calculated solid density in the storage-dry state of 2.169 g/cm³. The grading curve was chosen following the sieve line “DEBORA” with a maximum grain size of 8 mm /KRÖ 09/,/STÜ 13/ (10.6 % > 4 mm; 32.3 % > 2 mm; 23.2 % > 1 mm; 13.7 % > 0.5 mm; 8.2 % > 0.25 mm; 6.3 % > 0.125 mm; 4 % > 0.063; 1.7 % < 0.063 mm). The moisture content of the untreated stored salt was measured with 0.06 wt.-% by drying in a thermal cabinet at 105 °C. In difference to former BGR test (TK-031 and TK-033) at untreated dry conditions, saturated brine was added to reach an average moisture content of w = 0.15 wt.-%. The bulk density of the moist crushed salt was calculated with 2.17 g/cm³.

Crushed salt from the Sondershausen mine (Germany):

For the other tests (TK-038 – TK-045), the KOMPASS reference material from bedded formation (Steißfurt Formation) with the refined sieve curve “Son1” was used (Section 3.3.1.1).

Preparation of the test specimens

- Preparation of a crushed salt mixture according to the sieving curve Son1
- Determination of the moisture on 3 x 50 g samples
- Moistening of the crushed salt mixture by spraying with saturated brine to a certain, controlled moisture content
- Mixing
- Filling the salt mixture into the pre-compaction cell in 5 layers and leveling

Pre-compaction (see Section 3.2.1.1)

- oedometric pre-compaction 2 – 4 weeks with target void ratio $e = 0.2$, sample size 200 mm in height, 100 mm in diameter
- compaction at room temperature
- TK-037, TK-038, TK-041 displacement-controlled with linear force build-up
- TK-042 to TK-045 force-controlled with load rate 6kN/d specifying maximum axial load

The exact final sample height and porosity at the beginning of the triaxial test underly uncertainties due to the possible settling induced by contact closure of piston and sample, which occurs before the start of force build-up.

Fig. 3.50 shows the stress curve of the displacement- or force-controlled oedometric pre-compaction tests and the porosity development. The scattering of the filling porosity for the loose fill, influenced by the sample moisture and the deviations from the target final porosity of 16.7 % due to technical reasons, is evident.

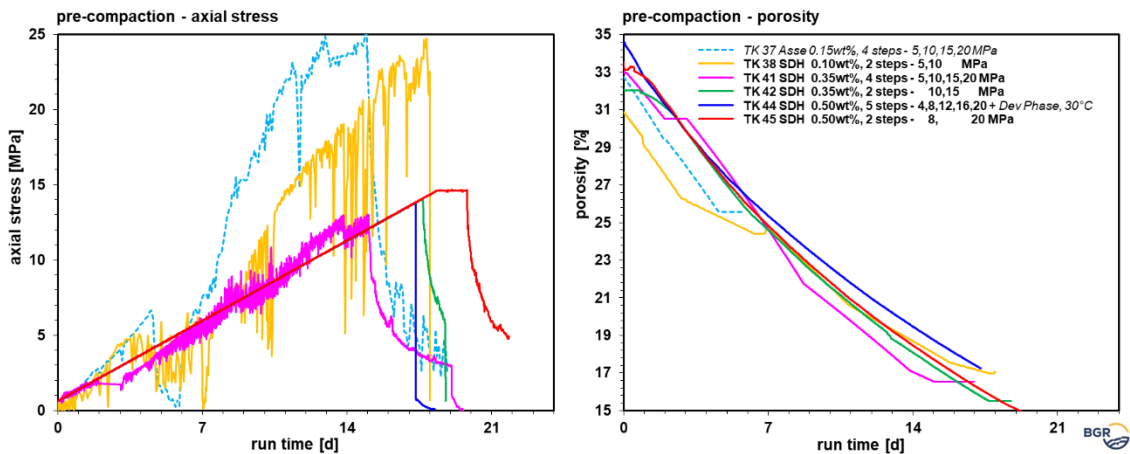


Fig. 3.50 Pre-compaction triaxial test – axial stress and porosity

Humidity and test temperature

The experiments described here are performed with three different moisture contents. The TK-037 (Asse salt) had a moisture content of 0.15 wt.-%. TK-038 is carried out on the storage-dry material with a moisture content of 0.1 wt.-%. The triaxial compaction tests TK-041 and TK-042 had a moisture content of 0.35 wt.-%, which corresponds to the natural moisture values of the salt from the Teutschenthal mine (in a bedded salt formation). Therefore, a comparison with the oedometer tests OE-112 and OE-113 with crushed salt from the Teutschenthal mine /KOM 20/ was carried out. TK-044 was designed as batch test similar to the first phase of TUC-V2 within this project (Fig. 3.66 with a moisture content of 0.5 w.-%). The temperature for all triaxial compaction tests was 50 °C except TK-044 which was carried out at 30 °C.

Stress control

The triaxial compaction tests were carried out as multistage loading tests with isotropic load conditions (with a technical necessary axial overload of 0.5 MPa).

The triaxial tests TK-037 with crushed salt from the Asse mine (0.15 wt.-% moisture) and TK-041 with the KOMPASS reference material (0.35 wt.-% moisture) include both four different loading steps (5, 10, 15 and 20 MPa). The next loading step was initiated after the gradient in strain rate has subsided sufficiently.

The test TK-038 was terminated after 2 load steps of 5 and 10 MPa aiming to examine the specimen in a low loaded state, especially with regard to its microstructure. The TK-042 ended at the load level of 15 MPa, but also had a higher moisture (0.35 wt.-%).

The batch test TK-044 has an average ten-day phase with deviatoric loading of 8 MPa in each of the five isotropic loading stages (4, 8, 12, 16 and 20 MPa; duration of one month each). However, both tests experienced different pre-compaction procedures, its will be investigated within the scope of the project (Section 3.3.6). The TU Clausthal produces their pre-compacted samples with fixed axial strain and constant radial loading. Afterwards, the sample is trimmed to size (Section 3.2.3). In contrast the BGR pre-compacted sample was loaded oedometrically (Section 3.2.1). Due to the use of different pre-compaction methods, differences in the pre-loading and homogeneity of the respective specimen may occur.

The last test described here, TK-045, started with two short phases of 4 MPa and 8 MPa and continued with a long load phase of 20 MPa. Thus it has comparable load phases to TK-033 from the benchmark study in the KOMPASS-I project (Asse dry 50 °C) /KOM 20/.

3.3.2.2 Experimental results

Depending on the boundary conditions (see above), compacted test specimens with residual porosities of 4 % to 15 % were produced. The boundary conditions are not linearly coupled. To provide parameters for numerical models, a multidimensional overview is presented in Fig. 3.51.

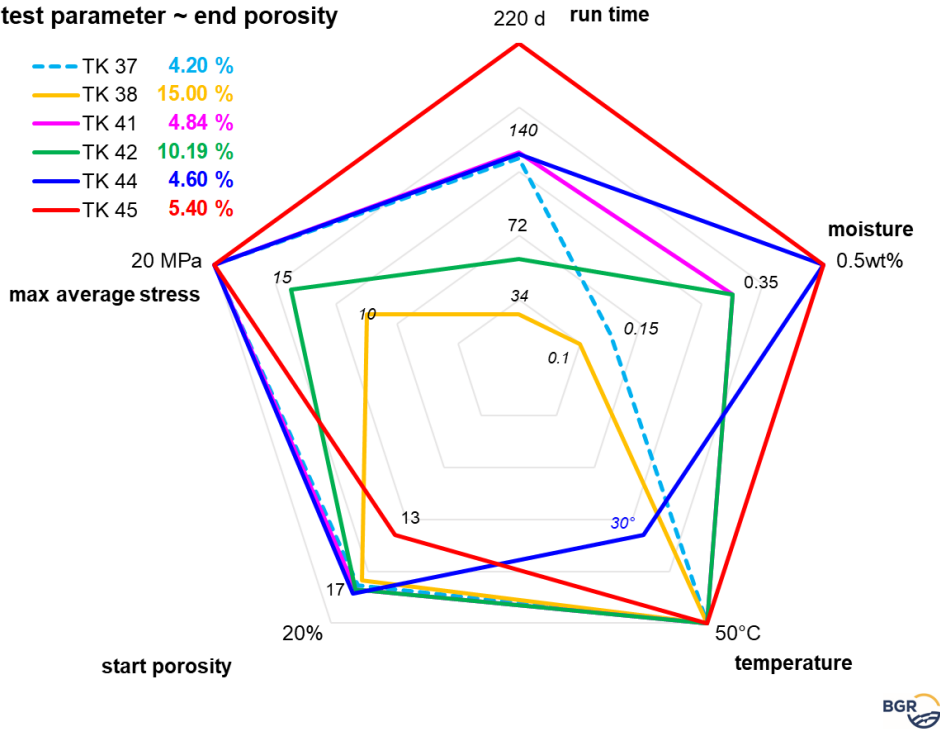


Fig. 3.51 Test parameters of BGR triaxial test including run time, initial moisture content, temperature, starting porosity and max. average stress. The final porosity is given in the legend

The test conditions influence – besides the residual porosity – also the compaction rate of the crushed salt. Tab. 3.11 shows the final porosity and the axial deformation rates achieved in the final loading step for all six triaxial compaction tests. The porosity was determined from the geometric dimensions, the weight of the sample and the solid density.

The deformation rates are determined by a moving average of the slope of axial or volumetric strain, which leads to smearing in areas of large change. The sampling rate is adapted to the test sequence, i.e., a higher sampling rate was used during the change of a load stage. In the volumetric rate, atmospheric pressure and venting of the burette system are reflected as larger fluctuations despite the applied corrections. The final values of the axial deformation rates were calculated from the trend in the reciprocal time domain (power function – straight line in a log-log plot see Fig. 3.52).

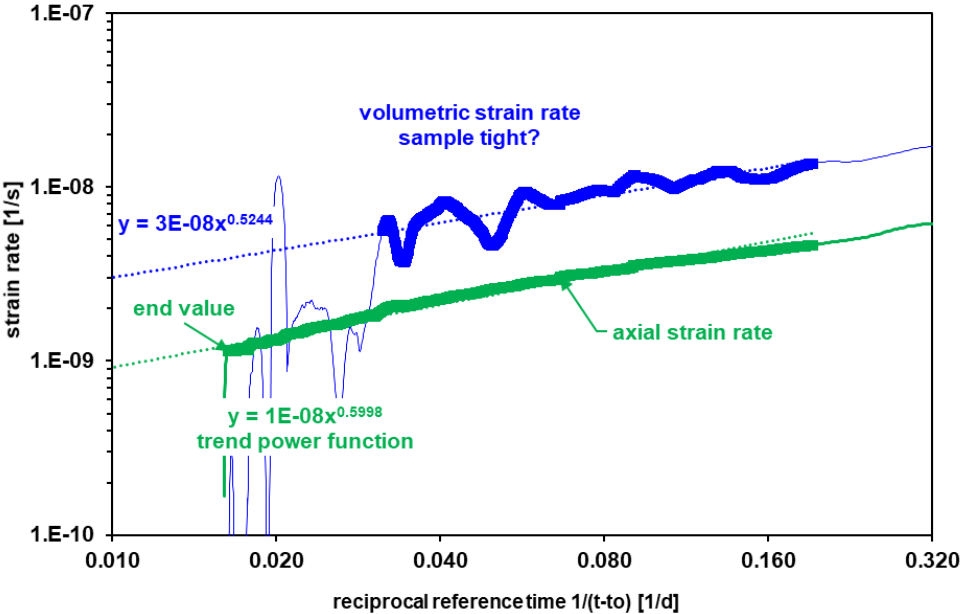


Fig. 3.52 Example for determination of end values for the axial deformation rate: thin line data, thick line used data area for trend

Tab. 3.11 Test parameter and end porosity

Name	Material	Moisture	Duration [d]	Pressure steps [MPa]	Sample high [mm]		Porosity [%]		End value axial Deformation rate [1/s]
					Start	Ende	Start	Ende	
TK-037	Asse	0.15wt%	142	5, 10, 15, 20	200.7	190.6	17.1	4.2	1.12E-09
TK-038	Son1	0.1wt%	34	5, 10	198.1	197.1	16.7	15.0	7.03E-10
TK-041		0.35wt%	145	5, 10, 15, 20	200.3	191.4	17.4	4.84	1.02E-09
TK-042		0.35wt%	72	10, 15	197.3	193.5	17.4	10.2	1.10E-09
TK-044		0.5wt% @30°C	144	4, 8, 12, 16, 20	202.2	185.5	17.7	4.6	~ 5E-10
TK-045		0.5wt%	220	4, 8, 20	195.1	188.9	13.20	5.4	3.20E-10
TK-031		Asse	0.05wt%	298	10,12,15,18, 20	196.5	190.8	17.1	7.7
TK-033	402			16, 20	197	188.3	16.77	5.1	1.7E-010

In KOMPASS-I /CZA 20/ the two dry tests (TK-031 and TK-033, also in /STÜ 13/, /KRÖ 17/) (moisture content 0.1 wt.-%) with crushed salt from the Asse mine have already been discussed. These tests can be compared with the dry test. The results of these two tests are therefore appended in addition to the six triaxial tests presented in this report (Tab. 3.11). The triaxial tests TK-037, TK-041, TK-044 and TK-045 were compacted up to 4 – 5 % porosity. At this porosity, no longer a continuous outflow of air could be recorded by the burette system. This means, the volumetric compaction is not in the same relation to the axial compaction as before. Furthermore, the volumetric compaction stops as the axial reaction increases. The results are an indication of the achieved isolation capacity of the hydrostatically loaded samples.

The triaxial tests TK-038 and TK-042 were terminated at lower load levels (TK-038 after 10 MPa and TK-042 after 15 MPa) aiming to investigate intermediate compaction steps microstructurally. TK-038 reached a final porosity of 15 % at the end of the loading level and was completed after 34 days. The compaction rate achieved in this test was about $7 \cdot 10^{-10} \text{ s}^{-1}$. TK-042 was completed after 72 days and reached a final porosity of 10 %. The compaction rate was about 10^{-9} s^{-1} .

Tab. 3.12 summarizes the results, the details obtained from the six triaxial compaction tests which are presented in Appendix A.2. For all tests, five graphs are shown:

- a) The stress regime (the axial and radial stress components, mean stress) applied to the specimen over time and sample temperature. The slightly higher axial stress is required

for mechanical-technical reasons to ensure a solid connection between the sample and the upper pressure plate.

- b) The measured volume change of the sample determined from the air volume squeezed out in the burette system and the change of sample height.
- c) The volumetric and the axial strains and smoothed rates for both. Because of the measurement accuracy achievable for these volume measurements, the oscillation of the volumetric deformation rates is strongly dependent on the selected time interval and is influenced by venting of the burette system or clocking of the sample.
- d) The detailed experimental course, the loading rates, achieved porosity and sample height with data for the mean stress and temperature.
- e) The relation of the well definable axial strain to the axial and volumetric strain rate.

Remarks on technical problems and qualitative error analysis of the measured values

The sample height is recorded with high accuracy via the three axial displacement transducers with a compensation of the machine deformation at 21 MPa of 0.0815 mm. The initial and final porosity is calculated from the geometric dimensions of the sample (caliper measurement) and the material density of the salt. For the caliper measurement, three sample diameters with an offset of 120 °C are determined every 10 mm of height. The total volume is calculated from the assembled sample disc with the average diameter. In this process, surface roughness and imperfections caused by loose crumbs lead to errors in the final volume determination. The volume loss of the sample corresponds to the pressed-out air volume, which is subject to corrections /STÜ 17/.

During heating and the first load step of 4/5 MPa, the volumetric changes of the sample are not clearly detectable and can therefore usually not be considered as a compaction rate. The surface roughness of the pre-compacted sample and the compressing of the Teflon tubing leads to volumetric changes that have nothing to do with the compaction. At low burette levels, even in the initial phase, high air pressure fluctuations can lead to underflow of the burette.

The deformation rates are determined by a moving average of the slope because the small-scale scatters during experiment course within the measurement accuracy. That leads to smearing in areas of large variations at load change. The sampling rate is adapted to the test sequence, i.e., a higher sampling rate at load change. The large scatter of the volumetric rate reflects insufficient corrections for air pressure and venting as larger variations.

The possible change in the humidity of the specimens during the entire course of the test, i.e., the drying, especially of the extra moistened specimen, is not sufficiently known and can change unnoticed during the test. A traceability via the difference in sample weight is not constructive, as the removal of the sample after the pre-compaction is accompanied by "crumb losses". Installation and removal in the triaxial machine can also lead to material loss, just as moisture can be carried away by the displaced pore air volume. Changes in the material moisture also change the bulk density for the porosity calculation.

It should also be noted that the sample underwent an axial load of more than 13 MPa during the oedometric pre-compaction; the average stress acting in this case, considering the friction in the pre-compaction cell, is probably above 4 – 5 MPa, which means that this load level causes little "virgin" reaction creep.

- TK-037 – pre-compacted core two years storage time in welded aluminum jacket, clogging ~ 100d
- TK-038 – no
- TK-041 – air-conditioning failure room
- TK-042 – air-conditioning system, central hydraulics failure = complete unloading, temperature control problems
- TK-044 – air-conditioning system, central hydraulics failure = complete unloading, temperature control problems
- TK-045 – central hydraulics failure = complete unloading, unknown axial misalignment

Tab. 3.12 Results – deformation and deformation rate at the end of every creep phase

Pressure step [MPa]	Duration [d]	achieved porosity [%] ab 17.11%	Calculated from trend for reference time				
			Deformation [-]		Deformation rate [1/s]		Reference time [d]
			volumetric	axial	volumetric	axial	
TK-037							
5.2	4	16.27	0.014	0.006	2.3E-09	3.7E-09	10
10.2	32	11.20	0.062	0.024	1.0E-08	2.6E-09	30
15.3	34	7.27	0.101	0.037	8.1E-09	2.7E-09	30
20.3	60	4.18	0.129	0.047	5.5E-09	2.1E-09	60
TK-038							
5.2	8	16.42					
10.2	19	14.79	0.023	0.005	1.6E-09	7.0E-10	20
TK-041							
5.2	11	16.3	0.012	0.004		4.2E-09	10
10.2	33	9.3	0.096	0.025	6.9E-08	2.2E-09	30
15.3	48	5.1	0.131	0.037	4.5E-09	1.7E-09	30
20.3	34	4.7	0.134	0.045		1.0E-09	30
TK-042							
10.2	21	14.1	0.039	0.008	8.2E-09	1.3E-9	24
15.3	21	10.1	0.077	0.019	8.7E-09	1.8E-9	24
TK-044							
4.2	5			0.002		2.0E-9	
8.2	31	11.1	0.073	0.043	1.1E-08	1.3E-09	
12.3	31	7.1	0.112	0.064	1.0E-08	1.1E-09	
16.2	32	4.8	0.135	0.077		6.6E-10	
20.2	35	4.1	0.141	0.084			
TK-045							
4.2	5	13.3					
8.2	17	12.3	0.011	0.005	1.7E-07	9E-10	20
20.2	180	5	0.088	0.033	3.7E-10	3.2E-10	200

Moisture influence

To understand the impact of moisture content on the compaction, three of the new tests are compared with two former tests (Fig. 5.52):

- TK-041 (0.35 w.-%) & TK-045 (0.5 w.-%) with the KOMPASS reference material – bedded formation
- TK-037 with moistened Asse salt (0.15 w.-%) – domal salt
- TK-031 & TK-033 with dry Asse salt (0.05 w.-%) – domal salt /STÜ 13/, /KRÖ 17/, /KOM 20/

All tests were performed at the same temperature (50 °C). TK-033 and TK-045 had only two isotropic loading steps, where the second step was of long duration (TK-033: 346 days and TK-045: 183 days) at 20 MPa. For the other three triaxial tests, the pressure was increased stepwise. The duration of the last loading phase was 204 days for the TK-031, 62 d for the TK-037 and 36 d for the TK-041 (20 MPa). The pre-compaction for TK-045 had a low maximum axial stress (15 MPa), but also a low final porosity (13 % vs ~ 17 %).

Fig. 3.53a shows the deformation rates in the final loading phase of 20 MPa with a reciprocal reference time axis. At the final loading step a time-dependent decrease process was observed. Fig. 3.53b shows the compaction rate in dependency of porosity. Fig. 3.53a and b in combination allow warily an estimation of the further course of compaction. For comparability, the deformation rate was used for an approximation of the further compaction to 5 % porosity in all tests. This was averaged from the exponential trend and presented in Fig. 3.53c. There is no direct correlation, as the boundary conditions are not linearly coupled. Multi-stage test, test duration, loading history, pre-compaction and nature starting material have a strong influence on the results.

It can be assumed that the moisture content of the material has a subordinate influence on the compaction rate at high mean stresses. However, moisture related dissolution effects and re-crystallization become more important at low mean stresses and slow compaction rates. The complex, non-linear coupling of the parameters is currently under investigation. The experimental data presented in this report may contain valuable information on this topic.

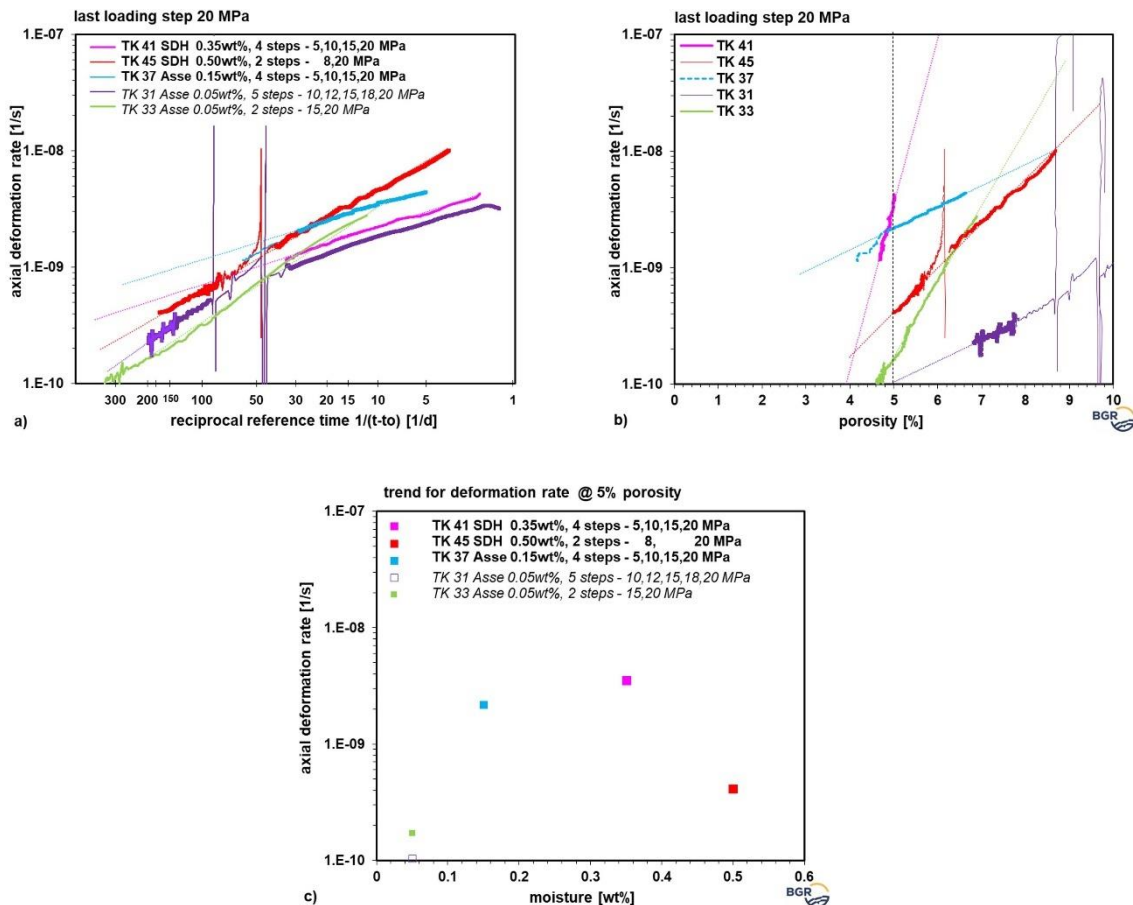


Fig. 3.53 Axial deformation rates last loading step 20 MPa for TK-037, TK-041, TK-045 & old TK-031, TK-033. a) in relation to the reciprocal reference time from start 20 MPa step; b) in relation to the porosity; c) axial deformation rate for 5 % porosity from trend in b)

3.3.3 Triaxial compaction tests addressing pre-compaction and mean stress (GRS)

GRS is not participating in the process of producing pre-compacted samples but relies on the methods and results of the project partners mentioned in Section 3.2. The test program at GRS aims at the investigation of the deformation behavior of pre-compacted crushed salt cylinders dependent on mechanical load (isotropic and deviatoric). GRS received pre-compacted samples from all the three project partners BGR, IfG and TUC. Before comparing their compaction behavior, the samples were investigated in a non-destructive way. The investigation method, test execution, results and discussion are to be found in the following Sections.

3.3.3.1 Non-destructive investigations on pre-compacted samples

Tab. 3.13 gives an overview about the pre-compacted samples which are used by GRS for their investigations.

Tab. 3.13 Overview about crushed salt samples for compaction tests at GRS

Name		Pre-compaction method
BGR sample	VK-048	Pre-compaction in oedometer cell
IfG Sample	Trocken 1 unten	Pre-compaction in "Big" oedometer cell
TUC sample	KOM37	"plain-strain" compaction

Before installation in the test setup, dimensions and weight of samples were measured and the density and porosity of each sample was calculated. The highest density and lowest porosity own the sample of BGR, while the lowest density and highest porosity is shown by the sample of TUC (Tab. 3.14).

Tab. 3.14 Sample properties before testing

	BGR sample	IfG sample	TUC sample
Length [mm]	100.003	100.260	100.006
Diameter [mm]	50.009	50.280	50.060
Volume [cm³]	196.426	199.071	196.939
Weight [g]	368.500	365.660	354.600
Density [g/cm³]	1.876	1.837	1.801
Initial porosity [%]	13.5	15.4	17.0
Water content [m-%]	0.07	dry	0.1

Additionally, the samples were scanned in a computer tomography (CT) (Fig. 3.54). Black areas in the CT scan define gaps filled with air, while dark grey structures show areas with low and light grey structures areas with high density. The singular compaction sections are clearly marked by the horizontal black dotted structures in the BGR (Fig. 3.54, left) and IfG sample (Fig. 3.54, middle). Additionally, the IfG sample shows two dark grey areas (left, near the bottom and right in the middle of the sample). These dark grey areas may mark agglomerations of crushed salt powder within the pre-compacted crushed salt sample and own low densities. The TUC sample (Fig. 3.54, right) shows the highest homogeneity and only small areas with gaps compared to samples of BGR and IfG.

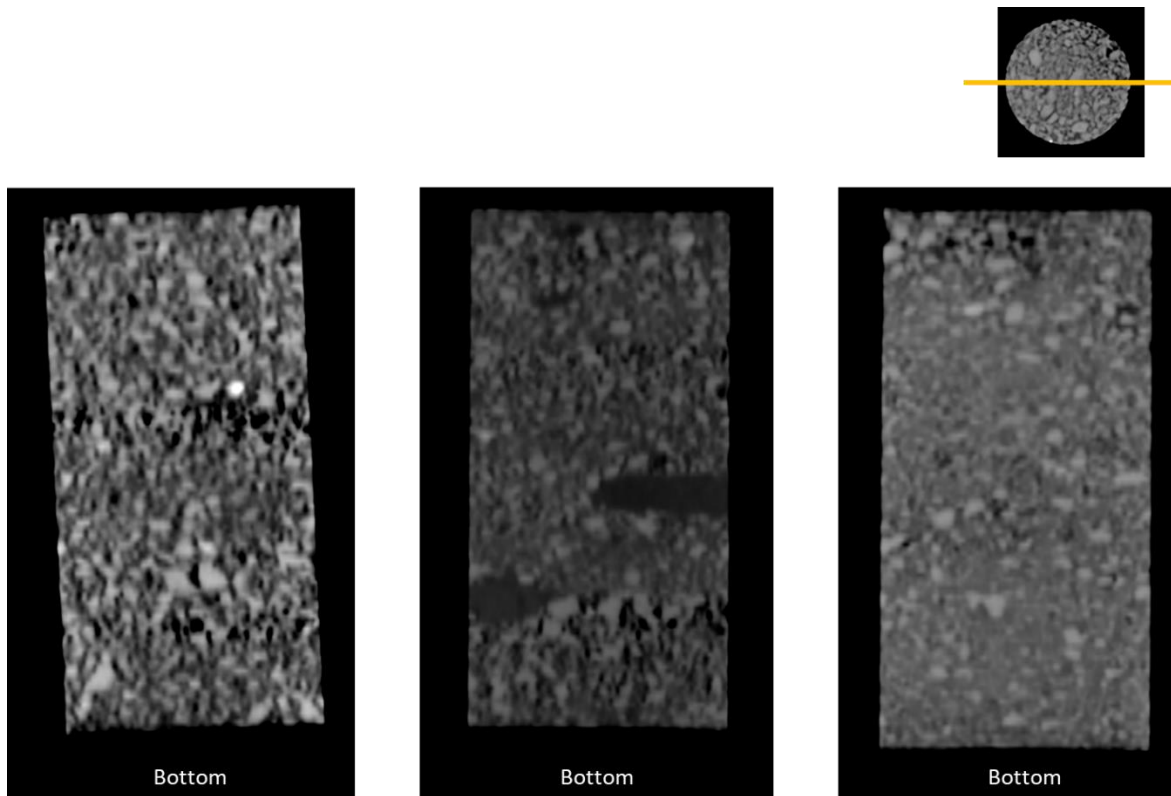


Fig. 3.54 Cross section of BGR (left), IfG (middle) and TUC sample (right) with CT before triaxial compression test

The small picture top right shows the front side of a sample with the cross section marked in yellow. Black areas define gaps. The lighter the colors in the CT picture are the higher is the density at this point. CT scans were done with a conventional CT in human radiology

3.3.3.2 Test setup

The triaxial compression tests are executed in triaxial cells of Kármán type, which allow an independent axial and radial compression to the sample. The sample is placed in a jacket and then put between the pistons at the top and at the bottom of the end covers of the cell. Around the jacket with the sample inside the circumferential transducer is fixed in the middle of the sample (Fig. 3.55, bottom right). This construction is inserted in the tubing. The triaxial cell has several inlets. The inlet at the bottom and at the top aims at injection/outflow of fluids for permeability measurements. Permeability is determined by measuring the displaced water volume in a burette per time.

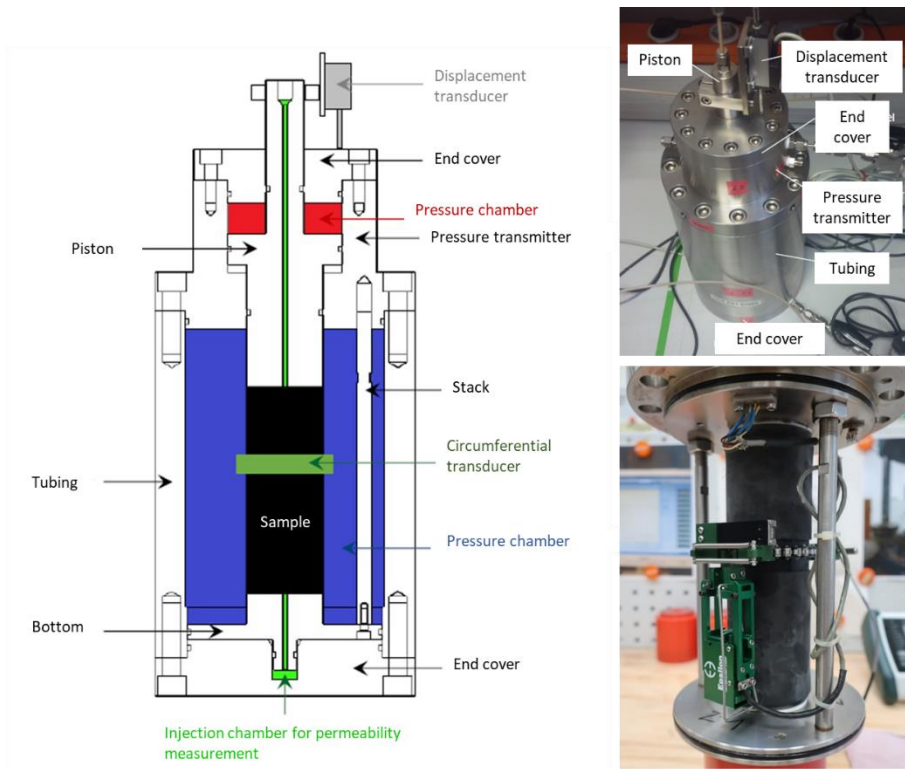


Fig. 3.55 Configuration of the triaxial cell at GRS

The axial and radial pressure is regulated by the two pressure chambers. The blue pressure chamber in Fig. 3.55 generates the radial pressure via an oil pressure, which is induced by a hydraulic pump. The radial pressure is generated by one pump for all three triaxial cells. The axial pressure is also generated by oil with a hydraulic pump (red pressure chamber). Indeed, the 1:2 pressure transmitter doubles the axial pressure of the pressure chamber to the sample. Both pumps (axial and radial) can keep the pressure constant by regulation of the oil volume which is pressed in the pressure chambers.

The test procedure shall be executed in two approaches. The isotropic approach aims at investigation of the dependence of porosity and mean stress to compaction of crushed salt while the deviatoric approach investigates the dependence of porosity and effective stress to compaction of crushed salt. This report refers in follow only to the isotropic approach because the deviatoric approach needs to be conducted in future. The isotropic approach is conducted in 5 nearly isotropic stress states (Tab. 3.15, Fig. 3.56).

Tab. 3.15 Stress states of triaxial compaction tests in GRS lab

Stress state	σ_z [MPa]	σ_x [MPa]	σ_m [MPa]	σ_v [MPa]
1	4.5	4.0	4.16	0.5
2	6.5	6.0	6.16	0.5
3	10.5	10.0	10.16	0.5
4	14.5	14.0	14.16	0.5
5	18.5	18.0	18.16	0.5

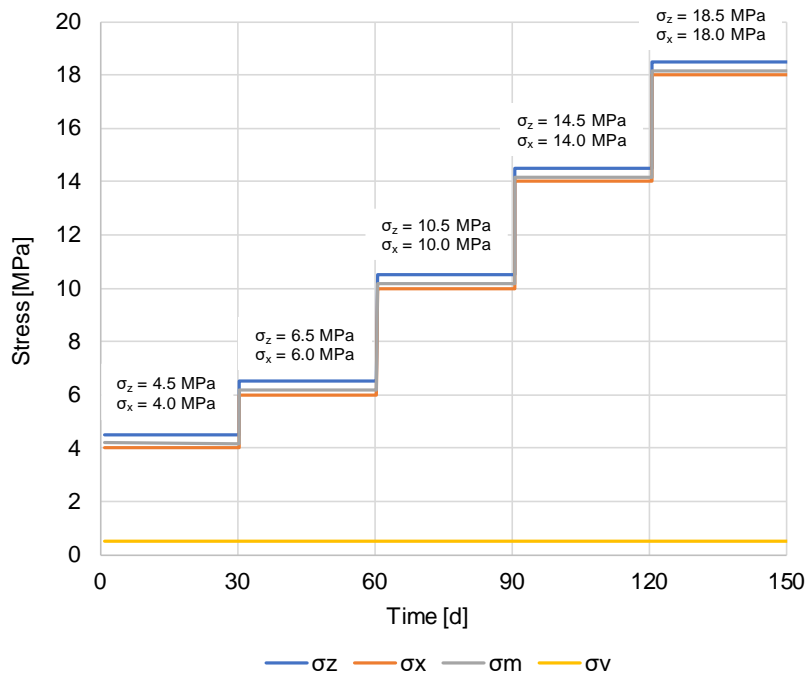


Fig. 3.56 Distribution of stress for the isotropic approach

Each stress state is kept for 30 days. In the beginning and in the end of the stress state permeability is measured.

In general, following measurements are determined:

Direct	Indirect
<ul style="list-style-type: none"> ○ Axial / radial stress ○ Axial / radial deformation ○ Axial percolation 	<ul style="list-style-type: none"> ○ Volumetric deformation ○ Porosity ○ Strain rate ○ Permeability

The volumetric deformations were estimated on assumptions of BGR and IfG. BGR estimated the volumetric deformations by $\varepsilon_v = \varepsilon_1 \cdot 3$. IfG assumes that this value may be too high and specifies the ratio of $\varepsilon_v/\varepsilon_1$ varies between 1.9 and 2.6 /KOM 20/. The real volumetric deformations may lie between these values and needs to be investigated more detailed for crushed salt. Following, volumetric deformations were estimated on the lowest ($\varepsilon_v = \varepsilon_1 \cdot 1.9$) and highest ($\varepsilon_v = \varepsilon_1 \cdot 3$) $\varepsilon_v/\varepsilon_1$ ratio given by IfG and BGR respectively.

The variation of density and porosity while triaxial compaction test needs to be estimated, too, because all samples are still integrated in the test set up. Hence, density and porosity cannot be measured directly now. Primarily, the volume of the samples in course of the compactions tests was calculated by:

$$V_i = V_0 - \Delta V \quad (3.1)$$

V_i volume at time i
 V_0 initial volume
 ΔV volume change

An upper and a lower limit of the volume were calculated based on the assumption, that the ratio of $\varepsilon_v/\varepsilon_1$ varies between 1.9 and 2.6 (see above).

The bulk density was calculated with $\rho_b = m/V_i$. Together with the grain density of salt ($\rho_b = 2.17 \text{ g/cm}^3$) the change in porosity while the compression test can be estimated by

$$\varphi = 1 - \left(\frac{\rho_b}{\rho_g} \right) \quad (3.2)$$

ρ_b bulk density
 ρ_g grain density

The bulk density and porosity were also calculated for the highest and lowest estimated volumetric deformations as mentioned before. The real values may lie between the upper and lower values.

The permeability K was calculated with Darcy's law for compressible fluids:

$$K = \frac{Q \cdot n \cdot p_1 \cdot L}{\Delta p \cdot p^* \cdot A} \quad (3.3)$$

K	permeability [m ²]
Q	volume flow [m ³ /s]
n	dynamic viscosity of solution [kg/(m*s)]
p_1	gas pressure at the outflowing surface [kg/(m*s ²)]
p_2	gas pressure at the inflowing surface [kg/(m*s ²)]
Δp	difference pressure ($p_1 - p_2$) [kg/(m*s ²)]
p^*	average internal pressure in the pores ($((p_1 - p_2)/2)$) [kg/(m*s ²)]
A	sample cross section [m ²]

3.3.3.3 Test results

The following diagrams show the development of axial and radial strains of the BGR (Fig. 3.57), IfG (Fig. 3.58) and TUC (Fig. 3.59) samples in the triaxial compression test at GRS lab in the five stress states. Additionally, volumetric strains and porosity are depicted as spread values because they are only estimated from axial and radial deformations. Diagrams of the BGR and IfG samples show additionally gas permeability data. The TUC sample is currently too permeable for measuring the permeability.

The five load steps are clearly to identify in the diagram by the steps in the curves of axial, radial and volumetric strains and are also reflected in the porosity development. The BGR sample showed the lowest initial porosity of the three samples with 13.5 %. During the experiment porosity decreases to values between 6 – 9 %. In general, the sample is compacted: Axial and radial deformation increase to 2.4 % (axial) and 3.1 % (radial). Volumetric deformations lie between 4 – 7 % in the end. After 140 days sample is sufficient compacted for determining permeability to gas. The volumetric deformation is between 3 – 5 % and porosity is around 9 – 11 % in this time step. Permeability is $4.5 \cdot 10^{-12}$ m². Permeability decreases with increasing compaction of the sample and reach values around $5.4 \cdot 10^{-16}$ m² ($\epsilon_v = 4 - 7$ %, $\phi = 6 - 9$ %) up to now. The lab test is still on-going.

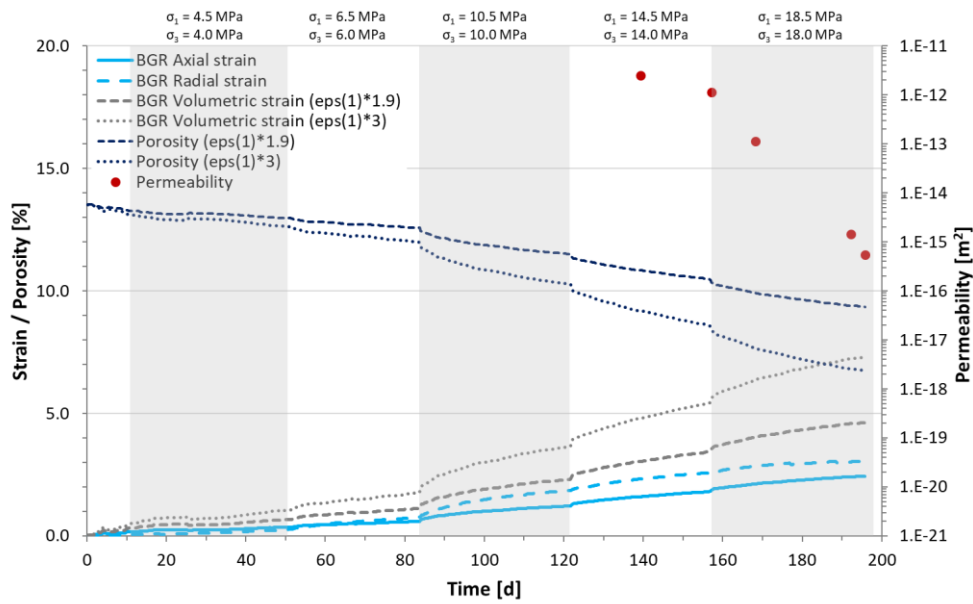


Fig. 3.57 Development of axial, radial and volumetric strain in BGR sample

Axial strain is measured by a circumferential transducer and radial strain by a displacement transducer. Volumetric strains are estimated by assumptions of BGR ($\epsilon_v = \epsilon_1 \times 3$) and IfG ($\epsilon_v = \epsilon_1 \times 1.9$) from axial strains. The development of porosity was calculated from volumetric deformations. Permeability describes permeability to gas (helium)

The initial porosity of the IfG sample is 15.4 % and decreases to 4 – 8 % while experiment. This sample is also compacted and shows final axial strain of 4 % and radial strain of 4.5 %. The volumetric deformation is between 8 – 11 % after 200 days. A permeability is measurable for the first time after round 120 days and is at $2.1 \cdot 10^{-14} \text{ m}^2$. The volumetric deformation is between 5 – 9 % and porosity between 7 – 10 % currently. After 175 days permeability decreases to $9.4 \cdot 10^{-21} \text{ m}^2$ ($\epsilon_v = 7$ to 11 %, $\phi = 4 - 9$ %). Afterwards, permeability is too low for determination. Additionally, axial and radial strains increase very slowly, and consequently volumetric deformations and porosity changes are very small.

In the third load level (around 100 days) a sharp bend in the curve of the axial and radial strains is visible. Therefore, a significant change is in the curve development of volumetric strains and porosity at the same time, because as mentioned before both values are calculated from the axial strains. Potential, the sample structure in Fig. 3.58 explains this course: the CT-scan of the IfG sample shows areas which may consist of agglomerated crushed salt powder. Probably this inhomogeneity lost its stability within the third load step and induces a step-in deformation.

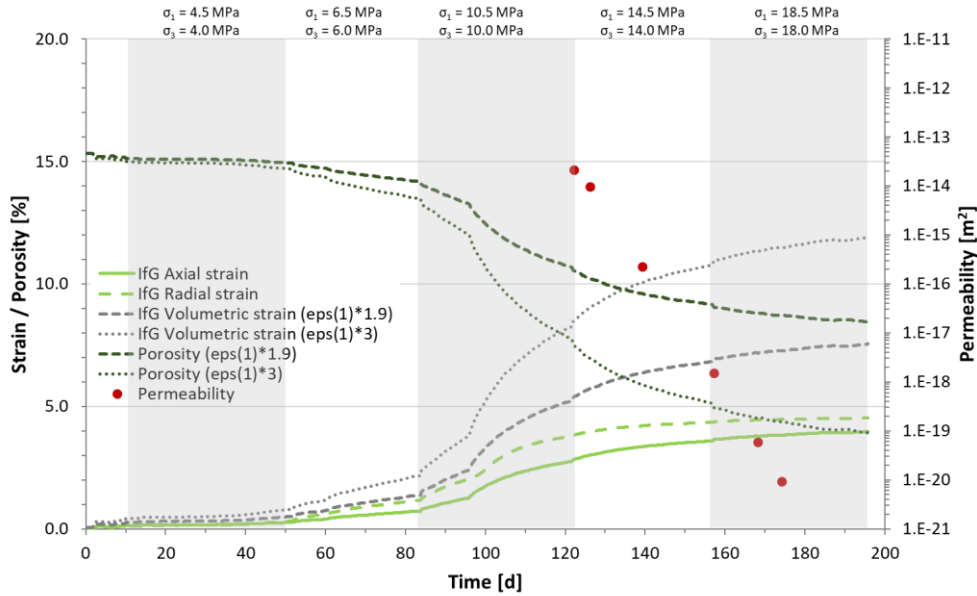


Fig. 3.58 Development of axial, radial and volumetric strain in IfG sample.

Axial strain is measured by a circumferential transducer and radial strain by a displacement transducer. Volumetric strains are estimated by assumptions of BGR ($\epsilon_v = \epsilon_1 \times 3$) and IfG ($\epsilon_v = \epsilon_1 \times 1.9$) from axial strains. The development of porosity was calculated from volumetric deformations. Permeability describes permeability to gas (helium)

The sample of TUC has the highest initial porosity with 17 %. During the experiment porosity decreases to 4 – 9 %, while axial strains are around 4.7 % and radial strains around 1.8 % in the end. The volumetric deformations are between 9 – 14 % after 200 days. Although the TUC sample has the highest volumetric deformation and consequently the highest percentual compaction, no permeability is measurable up to now. The test will be continued until permeability is measurable.

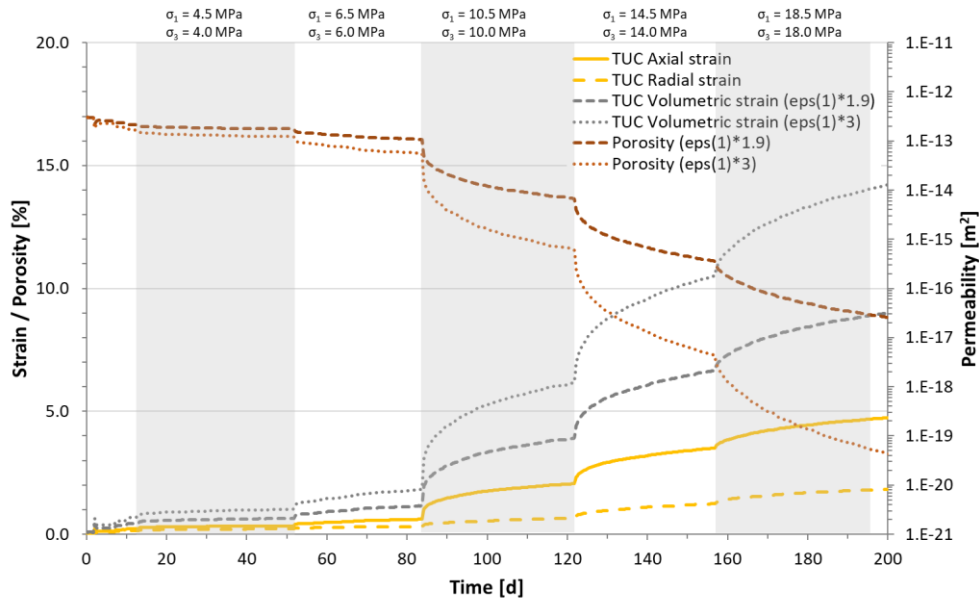


Fig. 3.59 Development of axial, radial and volumetric strain in TUC sample

Axial strain is measured by a circumferential transducer and radial strain by a displacement transducer. Volumetric strains are estimated by assumptions of BGR ($\epsilon_v = \epsilon_1 \times 3$) and IfG ($\epsilon_v = \epsilon_1 \times 1.9$) from axial strains. The development of porosity was calculated from volumetric deformations. Currently, permeability to gas could not be measured because the sample is too permeable. The test is ongoing

In general, samples of BGR, IfG and TUC show different compaction behavior in axial and radial direction. While the samples of BGR and IfG show the highest deformations in radial direction, the TUC sample deforms higher in axial direction. With a view to the pre-compaction, this varying compaction behavior is comprehensible: the samples of BGR and IfG were compacted by oedometric approaches in axial direction while the TUC sample were compacted radial with the plain-strain compaction method. Radial deformations in the BGR and IfG samples and axial deformations in the TUC sample, respectively, were prohibited by the wall of the compaction cell. But there was no active compaction in these directions. Following, samples react in an isotropic stress state with higher compactions in those direction, which were not active compacted before.

Fig. 3.60 and Fig. 3.61 show the development of axial and radial strains in the samples of BGR, IfG and TUC. The separate load steps are clearly to identify in the depiction of axial strain rate versus axial strain (Fig. 3.60). The first two load steps ($\sigma_1 = 4.5$ MPa, $\sigma_3 = 4$ MPa and $\sigma_1 = 6.5$ MPa, $\sigma_3 = 6$ MPa) show similar axial deformation behavior in all samples. Essentially, deformations are generated directly with increasing stress, the time dependency is low. In the following load steps, deformation behavior became more different between the samples. The BGR sample shows the lowest axial deformations. The strain rate increases with each

load step in the beginning, but in general the strain increases within one load step only a little. The strain rates between the load step three ($\sigma_1 = 10.5 \text{ MPa}$, $\sigma_3 = 10 \text{ MPa}$), four ($\sigma_1 = 14.5 \text{ MPa}$, $\sigma_3 = 14 \text{ MPa}$) and five ($\sigma_1 = 18.5 \text{ MPa}$, $\sigma_3 = 18 \text{ MPa}$) don't change significantly. The time-dependent deformation of BGR sample is small. The IfG sample shows a clearly time-dependent deformation behavior in load steps three and four. The discontinuity in load step three, as mentioned above, is also shown in Fig. 3.60: the strain rate increases again at a strain of 1.3 % without increasing the axial and radial stress. Thus, the sample significantly deforms time dependent. In load step five the IfG sample shows only less time dependent deformations. The TUC sample has in the beginning of load step three clearly increased strain rates versus load steps before. Following, the sample deforms time dependent until an axial strain around 2 %. Ongoing deformation starts not until load is increased to $\sigma_1 = 14.5 \text{ MPa}$, $\sigma_3 = 14 \text{ MPa}$ in time step four. The deformation behavior of TUC sample is clearly time dependent in step four and five. To summarize, the TUC sample shows the highest axial strain of 4.7 % in the end while the BGR sample shows the lowest (2.5 %). The final axial strain of IfG sample is around 4 %.

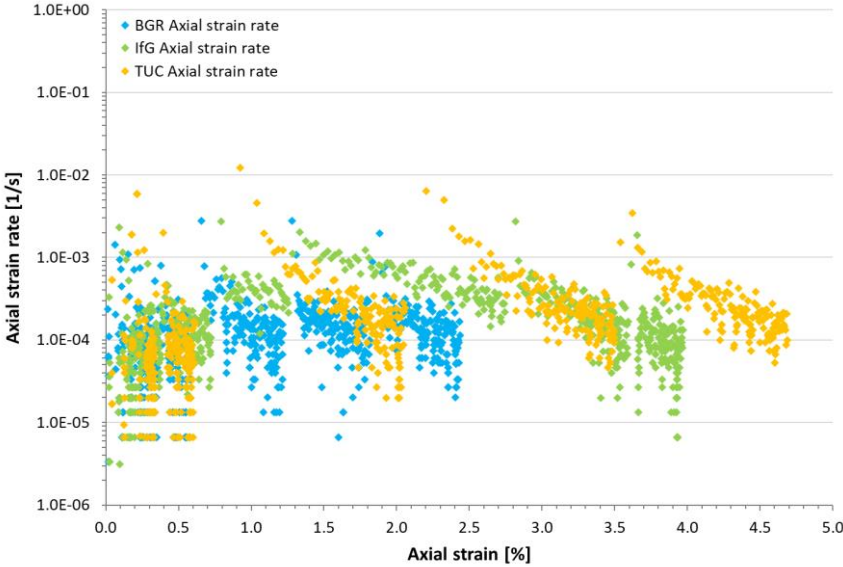


Fig. 3.60 Axial strain rate [1/s] versus axial strain [%] of the BGR, IfG and TUC samples in the triaxial compression test at GRS

The radial strains of the BGR sample are in a range between $1 \cdot 10^{-3}$ and $1 \cdot 10^{-4}$ 1/s. The increasing stress don't influence the dimension of the strain rate visible, but the general deformation behavior is time dependent and reach a radial strain of 3 % in the end. The IfG sample deforms in the load steps one and two up to 1.2 % with a small time-dependent component. In load step three the discontinuity of deformation is to identify by the increasing strain rate at a strain of 2.1 %. Based on the increasing strain rate a volume increase in radial direction can

be assumed for a short time interval. Later, strain rates decrease again. All in all, deformation behavior of the IfG sample is time dependent in load steps three, four and five. The load steps one and two in the TUC sample don't differ significantly and are not explicit to differentiate from each other in Fig. 3.60. The increase of radial strain is mainly induced by load increase and shows only small time-dependent deformations.

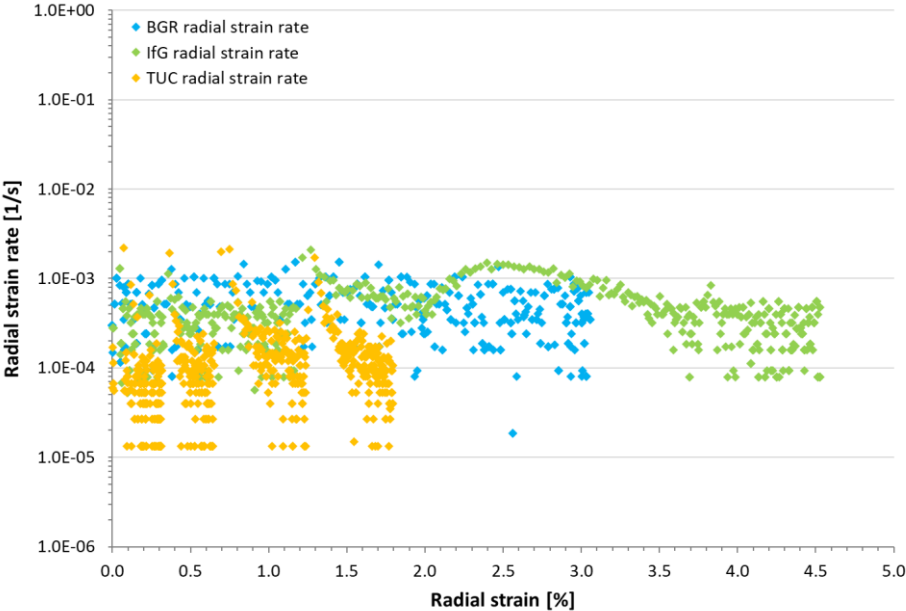


Fig. 3.61 Radial strain rate [1/s] versus radial strain [%] of the BGR, IfG and TUC samples in the triaxial compression test at GRS

3.3.3.4 Interpretation of the triaxial test results

Tab. 3.16 summarizes final parameters after 200 days compaction of the BGR, IfG and TUC samples. Results show similar ranges of porosity in all samples, while permeability and volumetric strains divide significantly.

Tab. 3.16 Parameters after 200 days compaction

	BGR sample	IfG sample	TUC sample
Volumetric strain [%]	4 – 7	8 – 11	9 – 14
Porosity [%]	6 – 9	4 – 8	4 – 9
Permeability [m ²]	5.4*10 ⁻¹⁶	gas tight	permeable

To understand the similar porosities resulting in a completely different percolation behavior, the sample preparation needs to be considered. The samples of BGR and IfG were pre-compacted in oedometer cells. Crushed salt was filled in layers in the cells and was compacted by

hand before the next layer was filled in /KOM 20/. These procedure results in inhomogeneities as CT-scans (Fig. 3.54) show: the crushed salt is more compacted in the upper part of the individual layer caused by the direct load input. In the lower part of the layers the load is less and following porosity is higher than in the upper part. If the sample is percolated by a fluid from the bottom, the fluid can spread in the loosely compacted section below, but a higher injection pressure is needed for the breakthrough to the more closely compacted section above. Afterwards the fluid can spread in the next loosely compacted section but needs higher injection pressure again to breakthrough to the next tight section. At the same time the samples are volumetric compacted and following the high compacted sections become tighter again. In this way only one preferred pathway is generated in the samples of BGR and IfG because the pathway has the lowest percolation resistance.

The TUC sample was also filled in layers /KOM 20/ but subsequent the sample were compacted with the plain-strain method. Hence, compaction follows not in direction of filling but in vertical. Consequently, the layering is not increased, and sample is compacted more homogeneous. The higher homogeneity versus oedometric compaction is significant in the CT-Scans (Fig. 3.54). While TUC sample is percolated, the sample is passed integral which results in significant higher permeability versus the percolation by pathways in samples of BGR and IfG.

3.3.4 Long-term compaction test in the „New IfG crushed salt compaction cell“

The newly designed isostatic compaction cell has been built and is operational (Fig. 3.62). During the use of the long-term compaction cell with combined transmission/permeability measurement, the automatic pressure control failed, which is why the ongoing tests could not be continued. The preliminary results are presented in Section 3.3.4.2.

Therefore, the experimental focus is on the continuation of the ongoing compaction test in the large offset pressure cell. In contrast to the original planning, long-term tests (with a duration of up to several months) were now also achieved with compaction values with end porosities significantly less than 10 %, so that beyond the provision of sample material for further compaction tests, additional results on long-term compaction were obtained.

3.3.4.1 Test setup

The newly designed isostatic compaction is shown in Fig. 3.62. The overall system consists of:

- (1) The hydraulic pressure cell (up to 20 MPa).
- (2) The cell cover with sample holder (the cover and base plate have conduits for permeability measurements); in addition, pressure and shear wave transducers (p-wave and s-wave) are installed in the plungers close to the sample.
- (3) The hydraulic system, based on a demand control principle, supplies oil to the pressure cell through a pressure intensifier to maintain a constant pressure and compensate for volume compaction of the material. The displacement of the pressure intensifier is measured using a potentiometric displacement sensor. The volume change of the sample is determined by considering the cross section and accounting for the pressure-dependent system stiffness.
- (4) The measurement systems for determining permeability (for gas or NaCl solution).

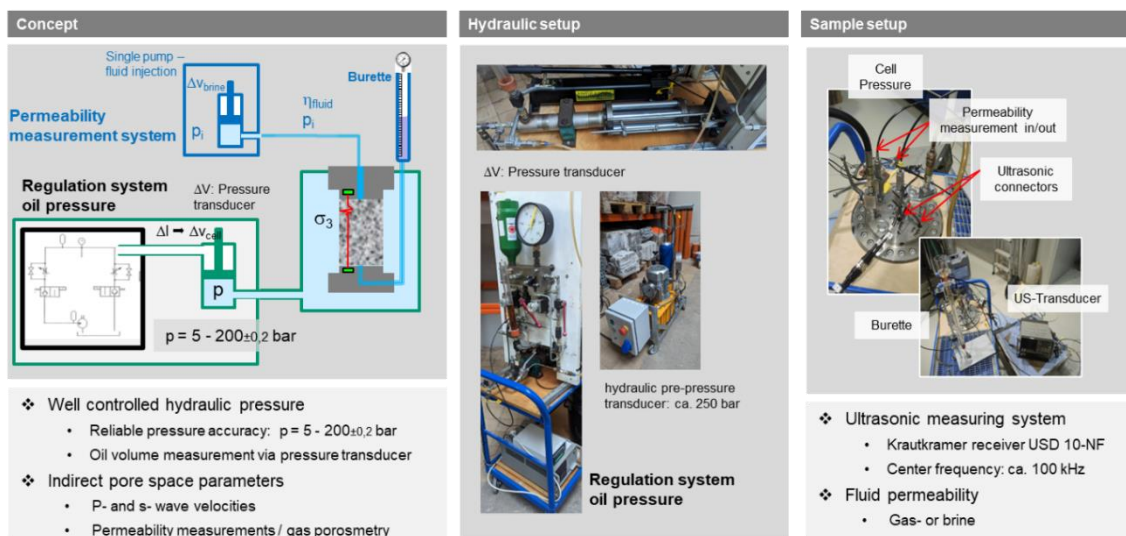


Fig. 3.62 Setup „New IfG crushed salt compaction cell“

3.3.4.2 Test results

In the previous project, KOMPASS-I, isotropic creep tests were found to be qualitatively suitable for documenting the time-dependent compaction creep. These tests involved loading cylindrical creep samples in a triaxial deformation apparatus under isostatic conditions ($\sigma_1 = \sigma_3$).

For similar experiments in this study, samples were prepared from large experiment 3 (Exp. wet 2) with dimensions of $d = 60 \text{ mm}$ and $l = 120 \text{ mm}$. The nominal moisture content during sample preparation was 1 wt.-%. After installation in the cells and isostatic loading at 2, 4 and 8 MPa (see results in Fig. 3.63, Fig. 3.64), the samples were subjected to intensive drying with dry air over a period of 30 days to dehydrate and dry them.

Starting from initial porosities of 6 – 8 %, gas permeability in the range of $3 \cdot 10^{-9} \text{ m}^2$ was determined, which is a typical value for crushed salt in this porosity range. The isostatic steady-state compaction rates ranged from approximately $1 - 5 \cdot 10^{-5} \text{ d}^{-1}$, depending on the external load.

Subsequently, the samples were dismantled, and approximately 0.5 wt.-% water was added to the gap between the jacket and the sample. The samples were then reassembled. After reapplying the load with identical constraints, isostatic compaction rates on the order of $2 - 6 \cdot 10^{-4} \text{ d}^{-1}$ were measured, representing an increase by a factor of $> 10x$. In particular, the sample subjected to an 8 MPa load achieved very low porosity values, although the absolute value has an estimated error of + 3 % (due to uncompensated system deformations in the creep testing apparatus during the loading phase).

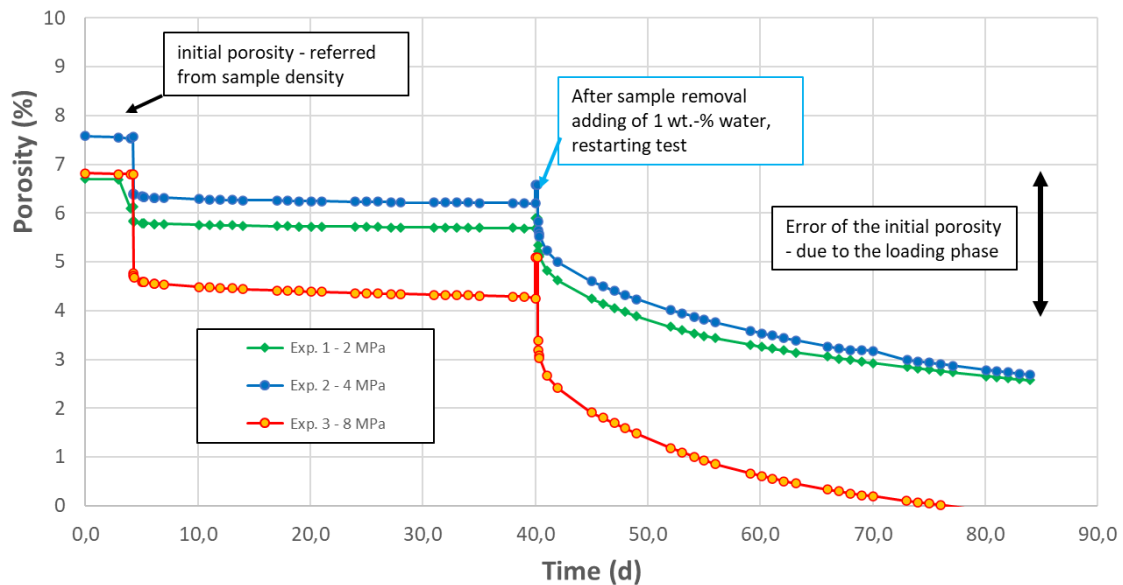


Fig. 3.63 Isotropic creep tests were conducted to demonstrate the influence of moisture (Note: due to the challenging correction of elastic system de-formation, the error for the initial porosity is estimated to be approximately 3 vol.-%. As a consequence, only a qualitative effect is represented here)

The isostatic compaction experiments will be continued as a new series of tests with comparable loads, following verification/calibration of the system stiffness. In addition, gas or solution permeabilities will be measured.

An initial short-term test was conducted, where simultaneous measurements of volume compaction, ultrasonic velocities (P- and S-waves), and permeability were performed. The preliminary results are summarized in Fig. 3.64.

To accurately determine the volume through the injected oil volume, it is necessary to determine the system deformation, which depends on the stiffness of the hydraulic system with pressure cell and sample, based on rapid loading and unloading cycles at the end of the experiment. In this test, a volume reduction from 11.4 % initial porosity to approximately 7.7 % was observed after increasing the pressure to 20 MPa and holding that time for approximately 70 hours. At the same time, the P-wave travel times decreased by around 10 % (with significantly lower S-wave travel times), i.e., the respective velocities increased accordingly. However, the final values are still lacking because system calibration (determination of lead times in the plungers) is pending. After system calibration, long-term measurements with several months of holding time will be conducted.

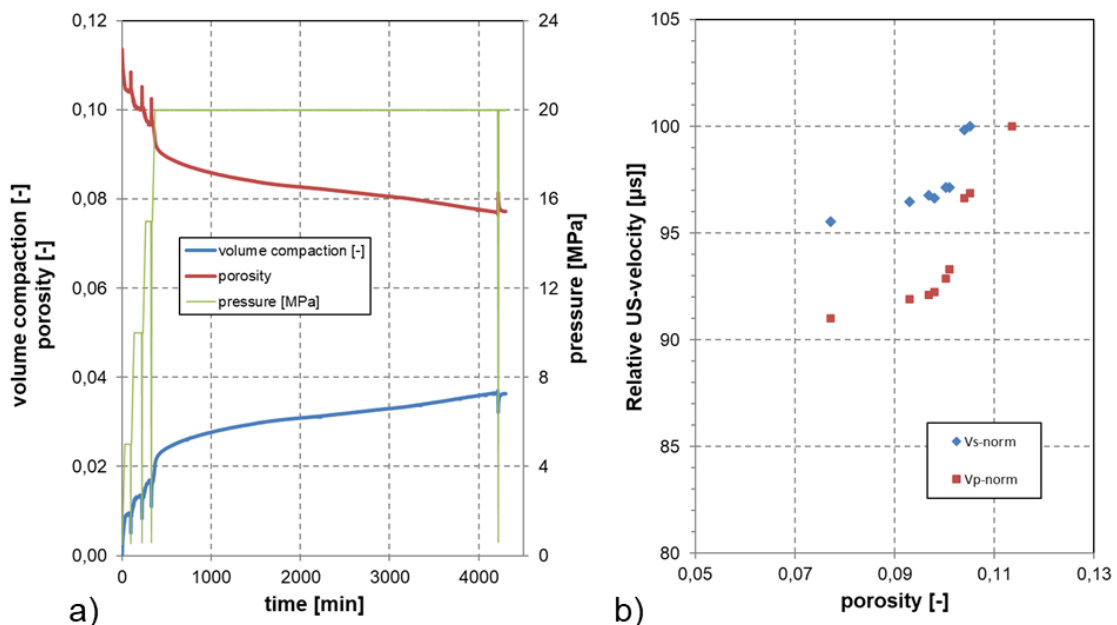


Fig. 3.64 Test experiment for crushed salt compaction in the “new IfG compaction cell”. (a) Compaction curve (system stiffness compensated) with the various load stages and the calculated porosity evolution. (b) Relative change of ultrasonic travel times, normalized to the initial value (note: S-wave was likely detected with some delay)

3.3.5 Long-term triaxial compaction tests addressing the dependency of compaction rate on porosity, mean stress, deviatoric stress and temperature (TUC)

Fig. 3.65 shows the test bench, that has been employed to perform both long-term tests. With respect to Fig. 3.65, the test bench is characterized by a two-column loading frame, a triaxial cell, a computer-controlled hydraulic system to realize an axial and a confining pressure cycle independently of each other. Due to the integration of the so-called EMC-System (Electro Mechanical Cylinder) into the confining pressure cycle, the volume change of the samples can be controlled. The EMC cylinder is continuously variable and therefore allows very precise quantification of the oil volumes transported into or out of the triaxial cell. Considering the pressure and temperature dependent stiffness of the test bench as well as the temperature and pressure dependent compressibility of the confining pressure oil, the confining pressure oil volume, fed in and out of the triaxial cell, can be used to quantify sample's volume changes during the test. Thus, the precision of the calibrations, which is clearly less accurate than the equipment accuracy, determines the final accuracy of the deformation measurement.

The sample volume change is determined from the readings of axial specimen deformation and change in the oil volume in the triaxial cell.

The oil volume displaced from the triaxial cell during the test is fed into a cylinder, which is connected to the continuously variable electro-mechanical drive of the EMC-System. A one millimeter movement of the piston in the measuring cylinder corresponds to a volume of 2.6 ml. Assuming a measurement accuracy of 1/100 mm of the piston of the EMC-System, the system outlined here can record changes in volume of the order of 0.0025 % in the specimen volume.

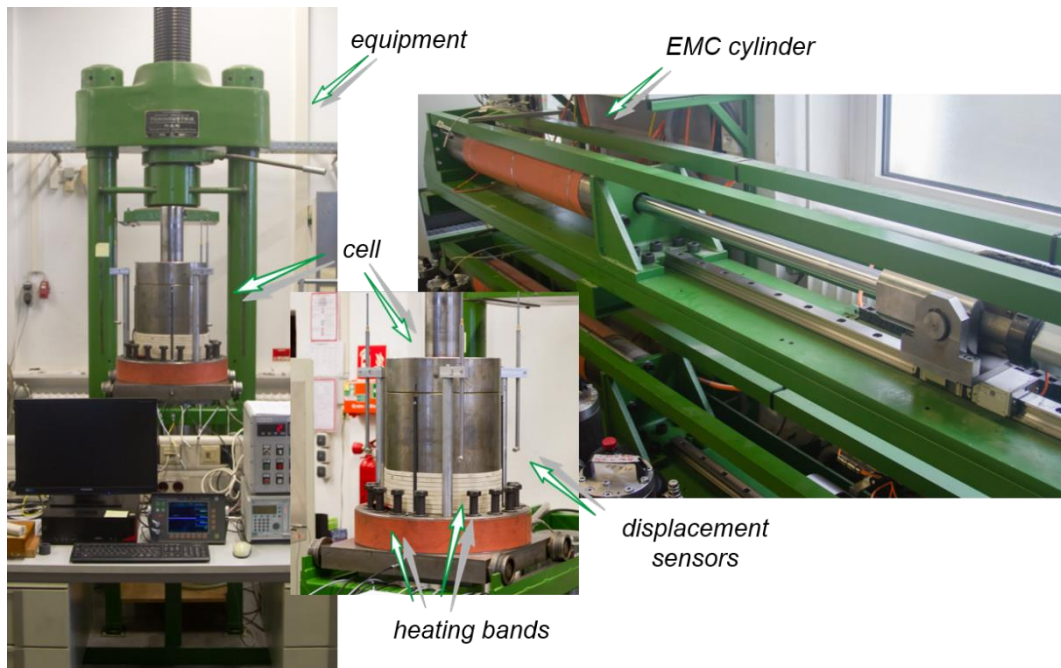


Fig. 3.65 Test bench at TUC employed to perform long-term compaction tests and the EMC system for volume change measurement

The triaxial compaction test TUC-V2 is in fact a series of five tests, here referred to as phases, due to the high number of influencing factors (Fig. 2.1). Each phase has a duration of 150 d and contains its own objectives. Fig. 3.66 shows, in a schematic overview, the most important information on test TUC-V2, as used for a benchmark back-analysis for all project partners (see Section 5.3). As depicted in Fig. 3.66, impacts of five influencing factors designated as InF1, InF2, InF3, InF4 and InF5 can be analyzed from the measured data:

- InF1: dependency of compaction rate on porosity,
- InF2: dependency of compaction rate on mean stress,
- InF3: dependency of compaction rate on temperature,
- InF4: dependency of compaction rate on deviatoric stress (only one level),
- InF5: dependency of volume-preserving creep rate on porosity.

With regard to the usability of the measurements, the following aspects of test TUC-V2 should be highlighted:

- The large number of influencing factors investigated: porosity (regarding the influence on the compaction), porosity (regarding the influence on the creep), mean stress, deviatoric stress and temperature;

- Use of a sufficient number (six) of mean stress levels, allowing reliable investigation of the dependency on mean stress;
- a relatively wide range of investigated porosity between $\phi = 16.7\%$ and highly compacted state of $\phi \approx 3\%$;
- a long test duration of 750 d to analyze the long-term behavior;
- a selection of load conditions that allows the isolation of the investigated factors, especially the dependency of creep behavior on porosity as well as the dependency of compaction behavior on deviatoric stress, the last one only index-like. The demand of the investigation regarding the dependency of creep rate on porosity originated from analytical benchmark calculations in REPOPERM II research project, which showed significant differences in predictions depending on the choice of constitutive model. This means that the currently available constitutive models must contain deficits regarding to the validation of the dependence between creep rate and porosity.

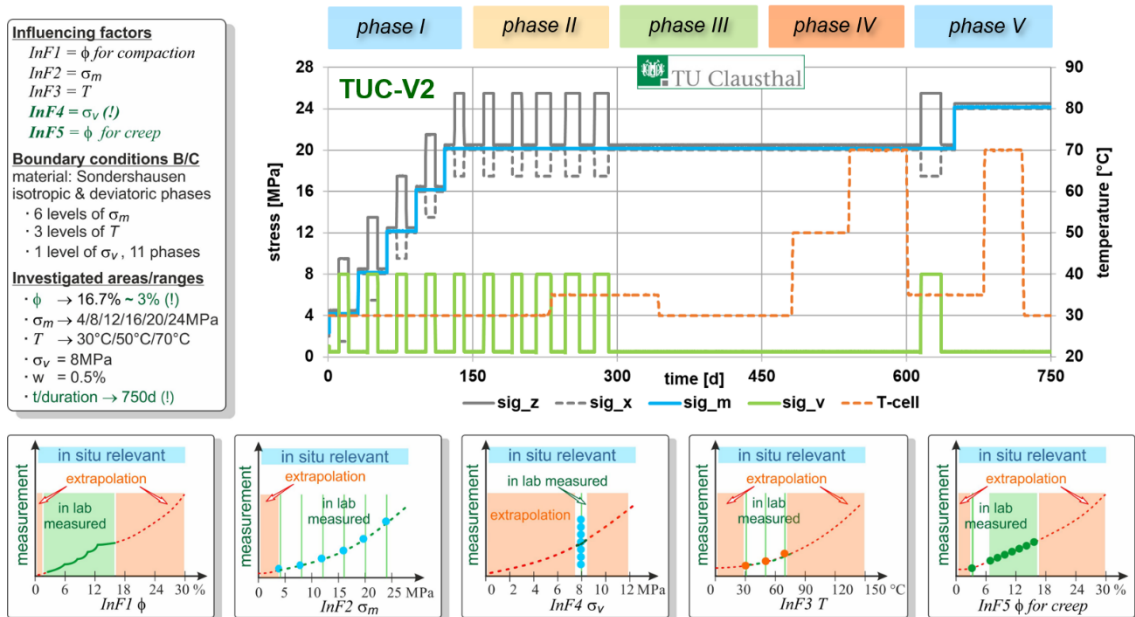


Fig. 3.66 Test TUC-V2 – boundary conditions and investigated ranges for influencing factors in relation to in situ relevant ranges (σ_z – axial stress, σ_x – confining stress, σ_m – mean stress, σ_v – deviatoric stress)

Fig. 3.67 shows a schematic overview of the most important information pertaining to test TUC-V4, which is planned to form the database (combined with the TUC-V2 test data) for the benchmark analysis in the framework of the follow-up project. The investigation of the impact of deviatoric stress on the compaction behavior at different stress levels is the main aim of this

test. As depicted in Fig. 3.66, impacts of following influencing factors designated as InF1, InF2 and InF3 can be analyzed from the measured data:

- InF1: dependency of compaction rate from porosity (however, for a relatively small range of porosity values of ~ 17 % to ~ 12 %),
- InF2: dependency of compaction rate from mean stress (only one level, except the short pre-phase),
- InF2: dependency of compaction rate from deviatoric stress.

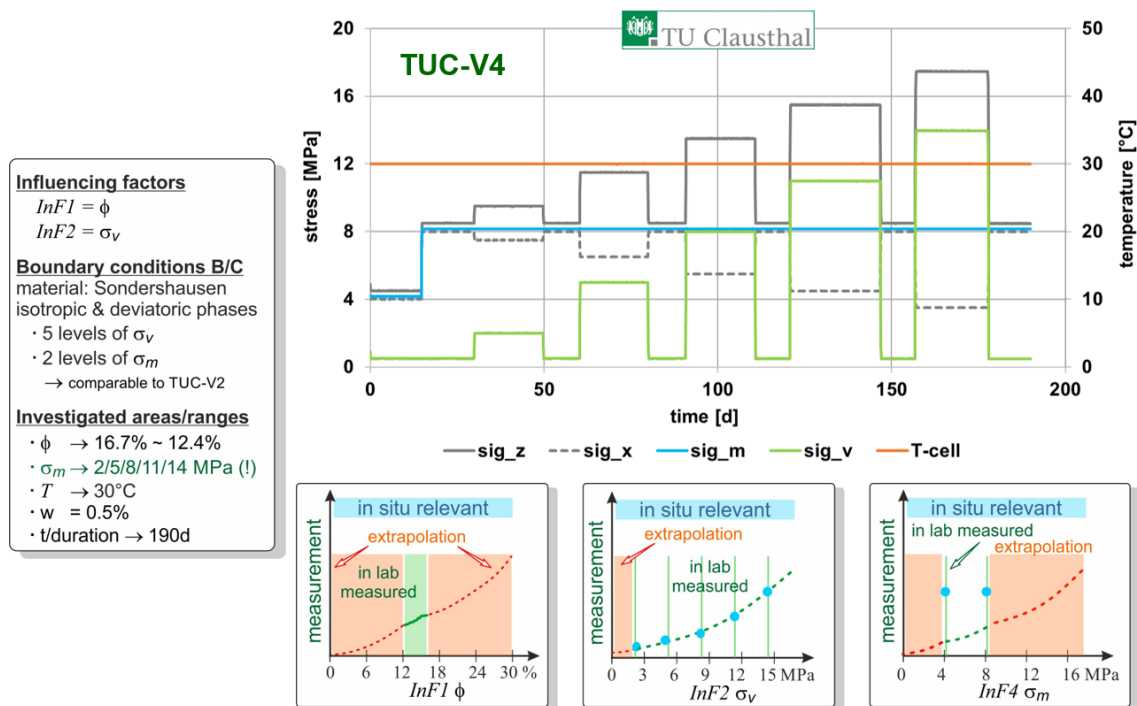


Fig. 3.67 Test TUC-V4 – boundary conditions and intervals for investigated influencing factors in relation to in situ relevant ranges

With regard to the usability of the measurements, the following aspects should be highlighted:

- the realized number of five deviatoric stress levels is sufficient and allows us to reliably investigate the dependency on the deviatoric stress;
- 190 test-days document a relatively long test duration for the analysis of long-term behavior.

Remark: The level of mean stress in the pre-phase of test TUC-V4 (4 MPa) and in the main phase (8 MPa) are chosen to be identical to the first two load phases of test TUC-V2 to check the comparability of the samples. For test TUC-V2 the plain-strain pre-compacted sample KOM 7, and for test TUC-V4 the plain-strain pre-compacted sample KOM 16, were used. Both

pre-compacted samples were prepared in the framework of the project KOMPASS-I (without sieving in the lab).

Despite the complexity and markedly long total duration of the two experiments TUC-V2 and TUC-V4 and correspondingly substantial data obtained regarding the possibilities of development and validation of the constitutive models, the following disadvantageous characteristics remain to be mentioned:

- The experimental analysis of the temperature influence is limited to only three load levels in a relatively low interval for the temperature 30/50/70 °C, and thus insufficient database to determine or validate a reliable relation in this respect.
- The impact of the influencing factors on the compaction behavior is investigated only for the porosity area from middle to the low range (~ 17 % – 3 %), and thus the area from high to middle is still not investigated for the KOMPASS reference material. Correspondingly, the very low stresses have not yet been investigated (< 4 – 8 MPa), which would be relevant with regard to final disposal as one of the foreseen future applications. Thus, further optimizations and modifications of the functional relations in the framework of the constitutive models established so far are to be expected after obtaining further laboratory data.
- The deformation behavior of crushed salt is a combined reaction of several deformation mechanisms each reacting differently to the influence of influencing factors (external variables as well as internal state variables). Different combinations of the investigated factors studied may cause different mechanisms being dominant. Thus, further experiments are necessary for the investigation of correlating factors, as well as deepening of the understanding of the dominance ranges for different deformation mechanisms, see Figure 3.3.

3.3.5.1 Test results

Results of test TUC-V2, regarding deformations, deformation rates and porosity, are presented in Fig. 3.68 and Fig. 3.69.

Fig. 3.70 gives additional information on the maximum bandwidth of results, i.e., is an estimation of maximum possible uncertainties. This estimation is based on experience, the measurement precision, the deformation values as well as the temperature fluctuations within the two years of test duration. The usual precision of the vertical deformation measurement produces a maximum of 0.1 mm inaccuracy. In this case, a deviant inaccuracy of ca. 0.3 mm was considered for the bandwidth calculation since a calibration done after the test TUC-V2 was finished has shown some irregularities. Due to that, the three deformation sensors were replaced

afterwards. The inaccuracy of the volumetric strain was calculated based on the comparison of the test results with the final manual measurement of the sample after end of test (subtracting the assumed value for the elastic relaxation). For this measured value, the inaccuracy totaled to some 0.7 % in absolute difference. The same procedure could not be applied to compare the vertical and horizontal measurement with the final manual measurement, since the sample underwent for a short period during test termination at an unwanted deviatoric stress higher than 8 MPa (not presented in Fig. 3.70). This event changed the shape of the sample due to additional shear deformations.

Further information on all five test phases of TUC-V2, including analysis and interpretation, is described in Section 5.3.

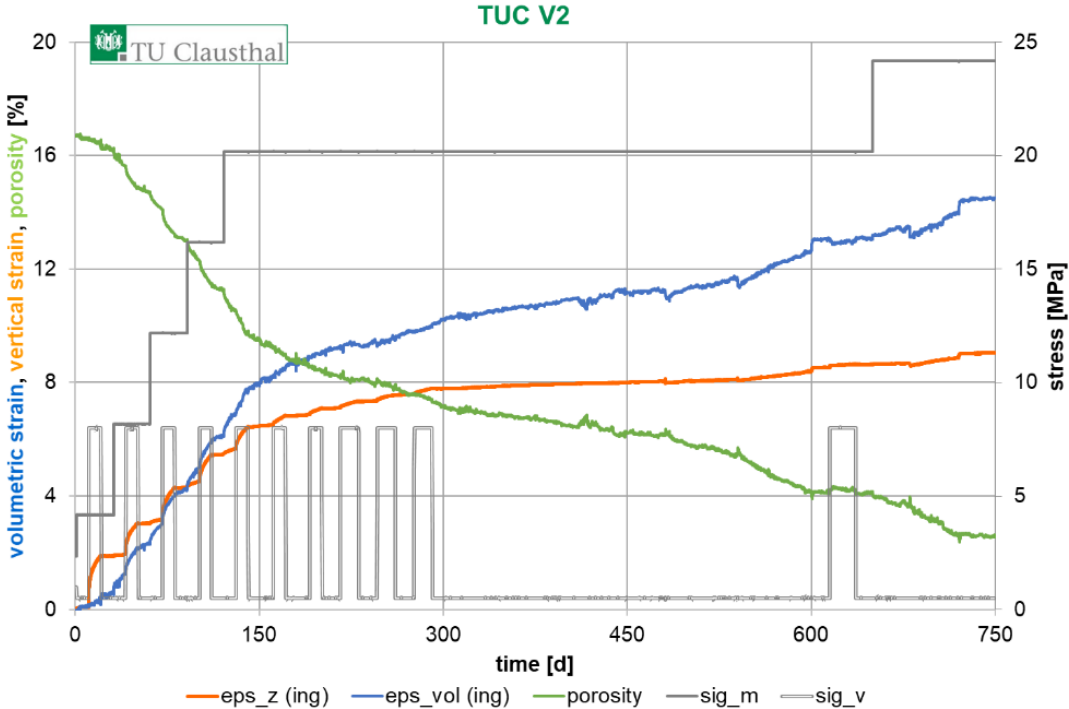


Fig. 3.68 Test TUC-V2 – measurements of vertical strain, volumetric strain and porosity (derived from the volumetric strain)

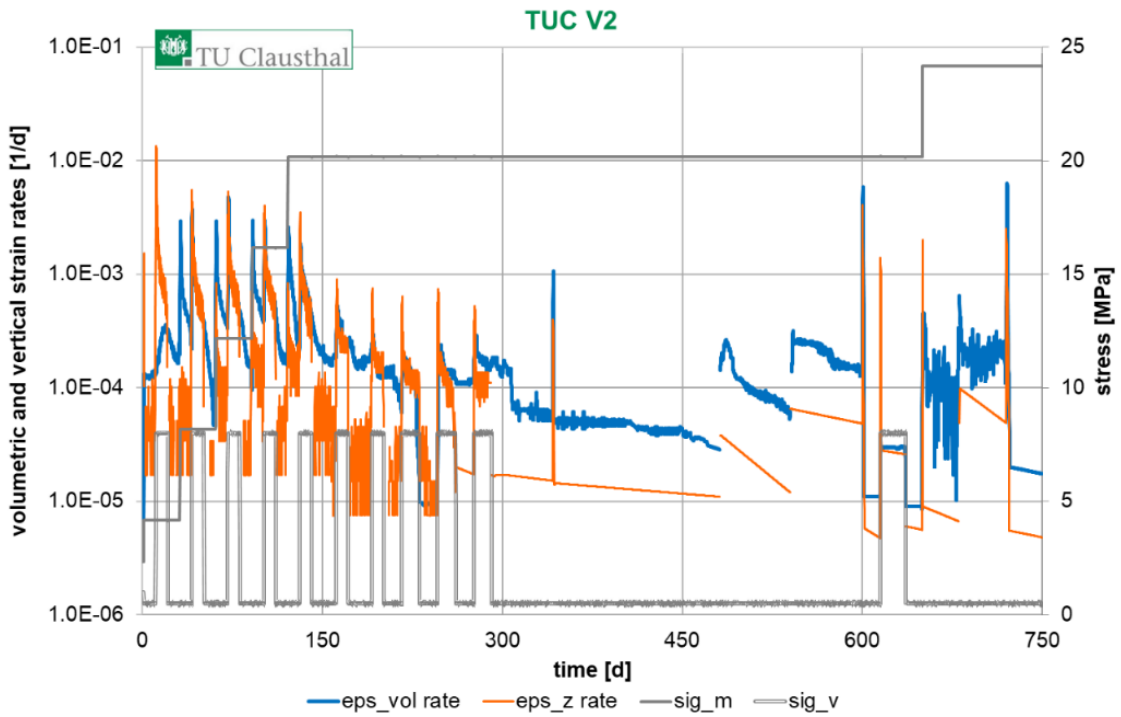


Fig. 3.69 Test TUC-V2 – measurements of vertical and volumetric strain rates

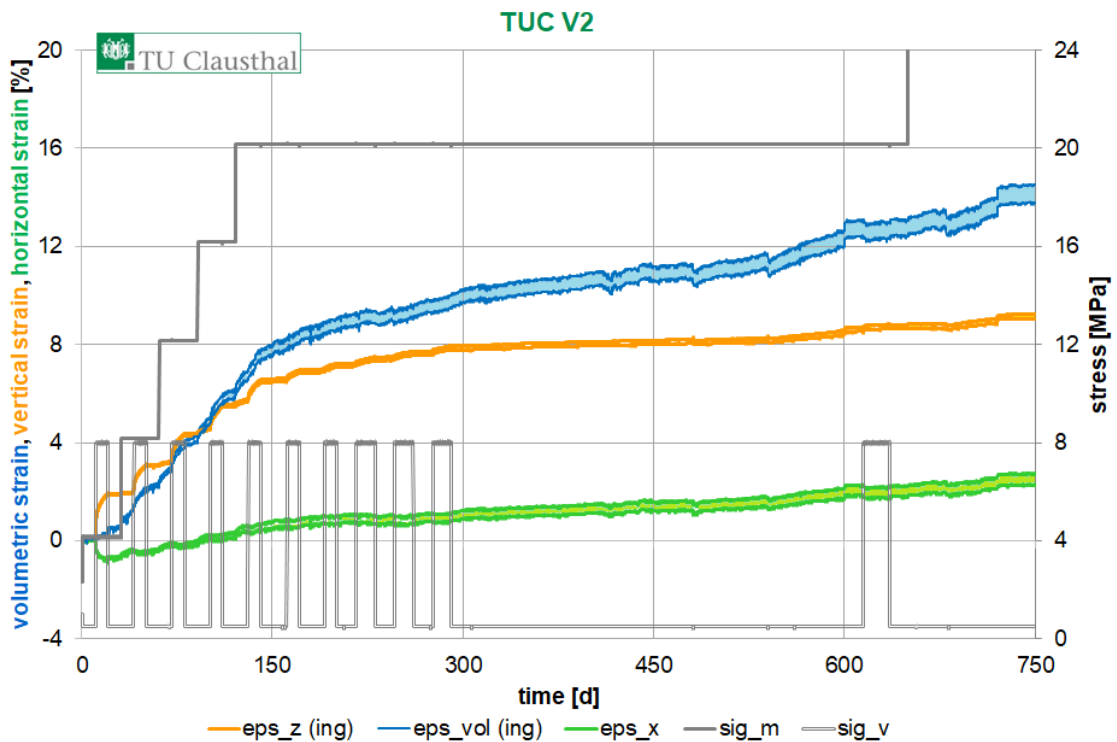


Fig. 3.70 Test TUC-V2 – bandwidth of measurements of vertical strain, volumetric strain and horizontal strain, including measurement and calibration uncertainties as well as the influence of temperature fluctuation

Results of test TUC-V4, regarding deformations, deformation rates and porosity, are presented in Fig. 3.71 and Fig. 3.72.

Note: Plotted results for strains are engineering values (in relation to the initial size of the sample). In case of calculating load conditions *Cauchy* stresses were used (force divided by current cross-sectional area of the sample). The measurement inaccuracies mentioned previously with regard to test TUC-V2 also relate to test TUC-V4 (with the exception of one unreliable deformation sensor by TUC-V2 not more used here, and in contrast to TUC-V2 successful test termination of the test without unwanted events).

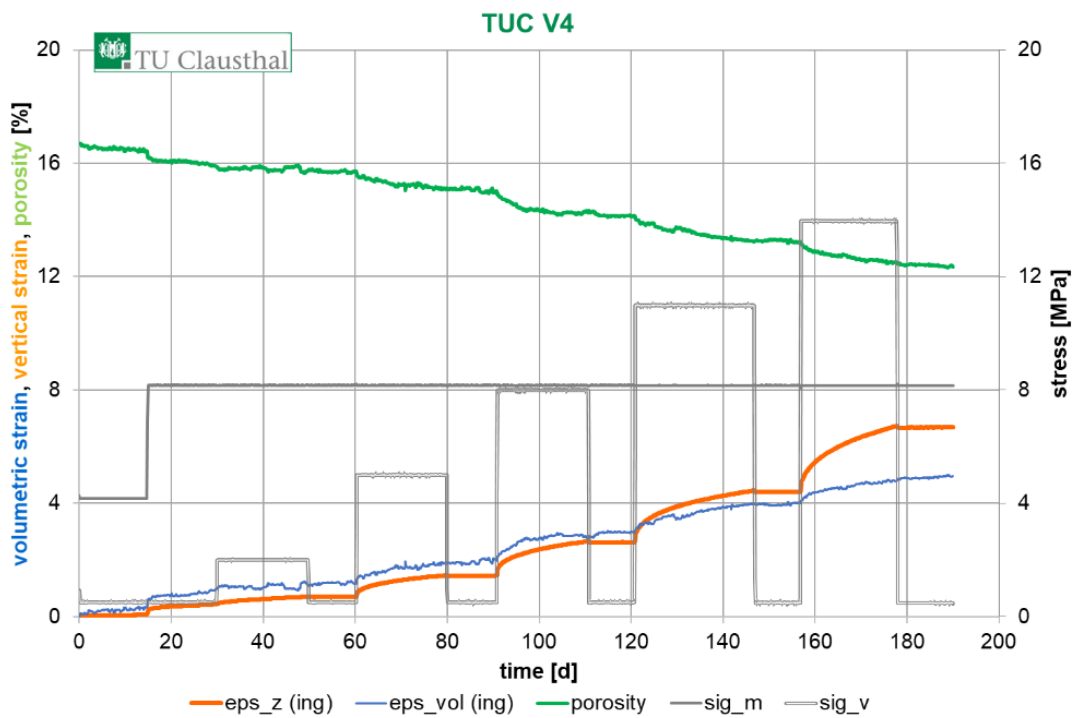


Fig. 3.71 Test TUC-V4 – measurements of vertical strain, volumetric strain and porosity (derived from volumetric strain)

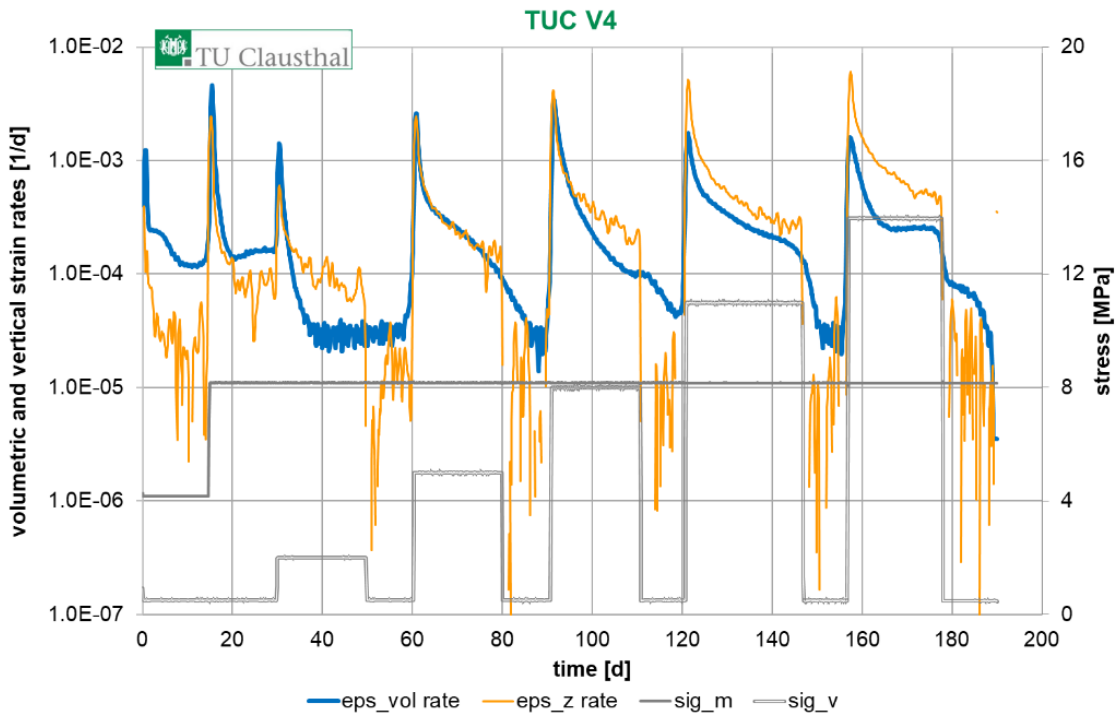


Fig. 3.72 Test TUC-V4 – measurements of vertical and volumetric strain rates

Focusing on the dependency of the compaction on the deviatoric stress, it can be generally stated that experiment TUC-V2 was aimed at providing information on whether there is a dependence on deviatoric stress or not. Since this was clearly answered with a ‘yes’ in the results, experiment TUC-V4 focused on investigating this dependence in detail for different load levels. In the next step, depending on the needs of each constitutive model, the database will be applied to validate, optimize or to develop the missing functional relationship in regard to the factor deviatoric stress.

Fig. 3.73 shows the initial comparison between the results of the two tests TUC-V2 and TUC-V4, with the aim of checking the suitability of the two samples and of verifying the usability of both test results as one coherent unified database. As can be seen in Fig. 3.73, the volumetric strain rate results agree with each other in areas of similar load conditions and porosities (highlighted areas). Ultrasonic wave velocity results cannot be directly compared, due to lack of overlap in the variables space investigated (ultrasonic wave velocity measurements in TUC-V2 were successful merely during a few small periods). However, both test data sets can be viewed as part of the same curve, thus the results are considered in good agreement.

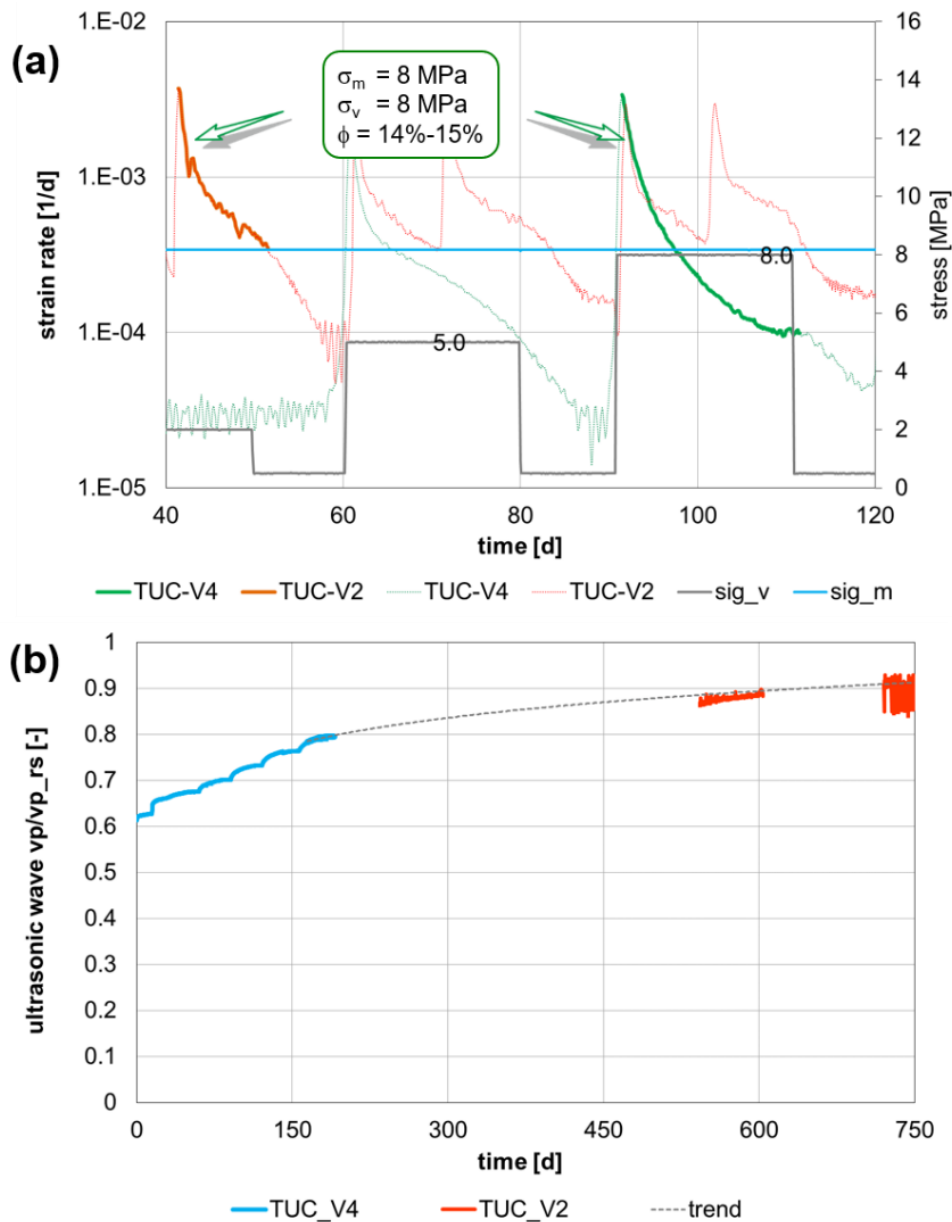


Fig. 3.73 Initial comparison of test results TUC-V2 and TUC-V4 – measurements of volumetric strain rates and ultrasonic wave velocities (normalized to the assumed rock salt value of 4500 m/s)

3.3.6 Results of the Laboratory Benchmark

A benchmark study was carried out between the laboratories of TUC and BGR. For this purpose, the load conditions of test TUC-V2 – phase I (150 days) were selected. TUC-V2 – phase I is characterized by relatively complex load conditions involving a total of 15 load steps (5 isotropic levels and one deviatoric intermediate phase in each isotropic load level, Fig. 3.74) /KOM 20/.

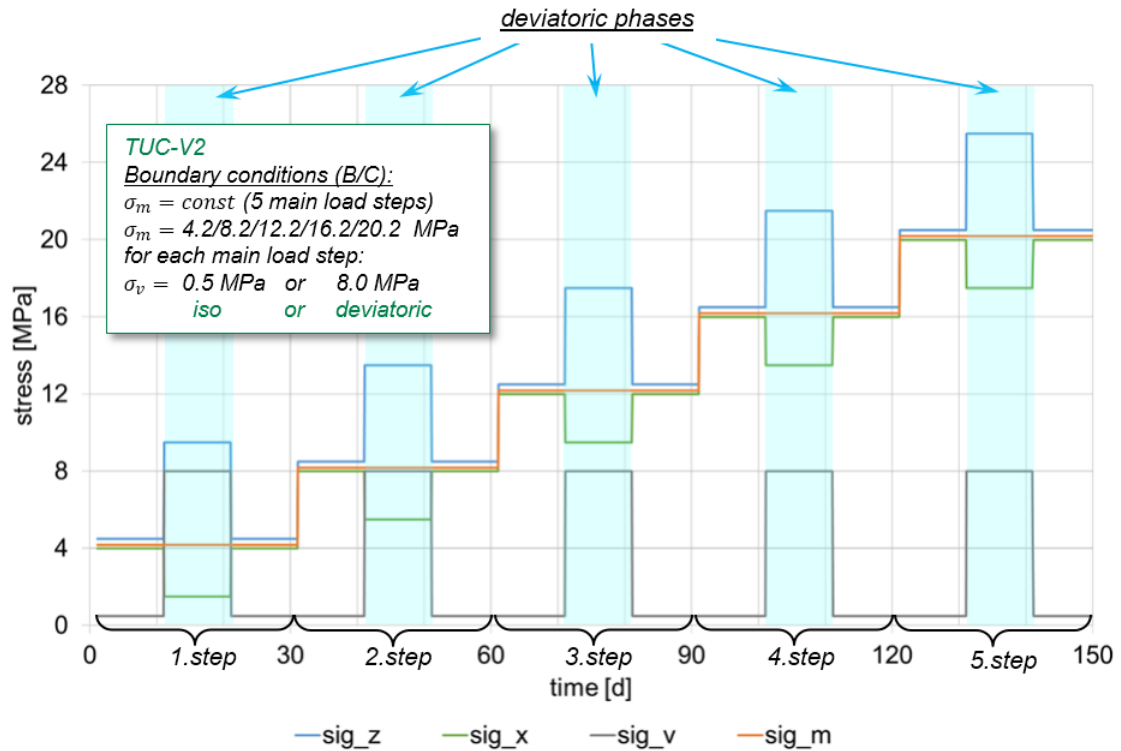


Fig. 3.74 Loading history for the multi-stage long-term test TUC-V2 (phase I – 150 d)

It has been aspired to provide identical conditions for both samples as far as possible. Both samples were prepared with a moisture content of 0.5 wt.-%, the initial porosity of 17.7 % (BGR) and 16.7 % (TUC) is sufficiently close together, as is the test temperature 33 °C (BGR) and 30 °C (TUC). The mean stress is shown in Fig. 3.75. In the later realized test BGR TK-044, the observations taken from test TUC-V2 that hardly any compaction has taken place in the first isotropic phase at a level of 4 MPa (since the samples have already experienced a higher load in the pre-compaction), were taken into account, and the duration of the stage was shortened. To allow a direct comparison of test results, a fictitious time (moved forward by 18 days) was used for test TUC-V2 and the entire measured curves were shifted in such a way, that the load phases of the two tests approximately coincided. The comparison of the test results after this adjustment is shown in Fig. 3.75.

There is a clear difference between the results of the two laboratories to be noticed. While the difference in the vertical deformations can still be described as moderate at some 2 %, it amounts to a considerable 6 % for volumetric deformations.

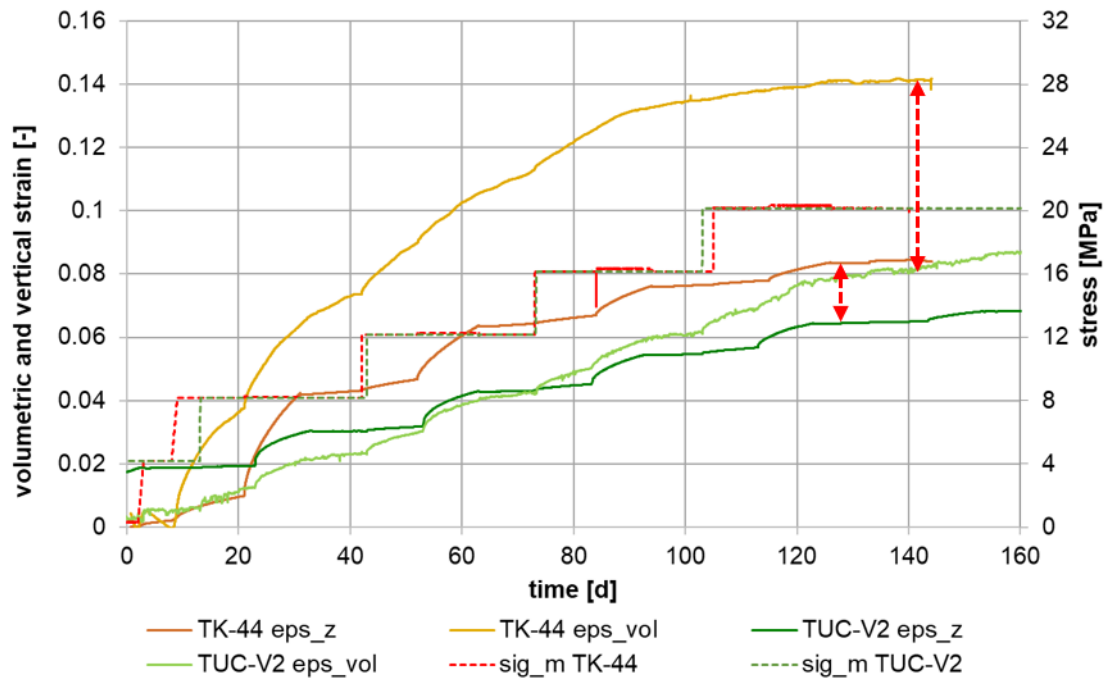


Fig. 3.75 Comparison of the test results for TUC-V2 - phase I and TK-044 – volumetric and vertical strains

Since this result did not correspond to expectations, possible reasons for the differences were searched for. Firstly, to localize the areas with significant differences in behavior of the specimens, the deformation rates against time were compared, see (a) and (b) in Fig. 3.76. This gives the impression that only the first half of the test shows significant differences whereas in the second half of the test samples behave quite similar. However, the plot of results against porosity (c) in Fig. 3.76 shows that the behavior of each specimen at any given current state of compaction (i.e., sample porosity) differs throughout the entire duration of the experiments. Therefore, no stress level or porosity range for this purpose could be localized.

As an additional idea, a further test, TK-045 from BGR, was used for comparison since in this test a sample with same water content of $w = 0.5$ w.-% was used. However, the isotropic load was greater than or equal to the load level of the two benchmark tests for most of the test duration. With reference to Section 3.2.1 and Section 3.2.3, a thorough explanation of BGR and TUC long-term compaction tests and their load histories is not provided here. Since a significant difference can now be seen when comparing the two tests TK-044 and TK-045 within one laboratory as well as between laboratories, this additional comparison, which can be seen in Fig. 3.77 exemplarily on volumetric and vertical strains, has thus far not clarified the previous questions but also raised new ones. Despite being under higher isotropic load, the sample from test TK-045 compacts far more slowly than sample TK-044.

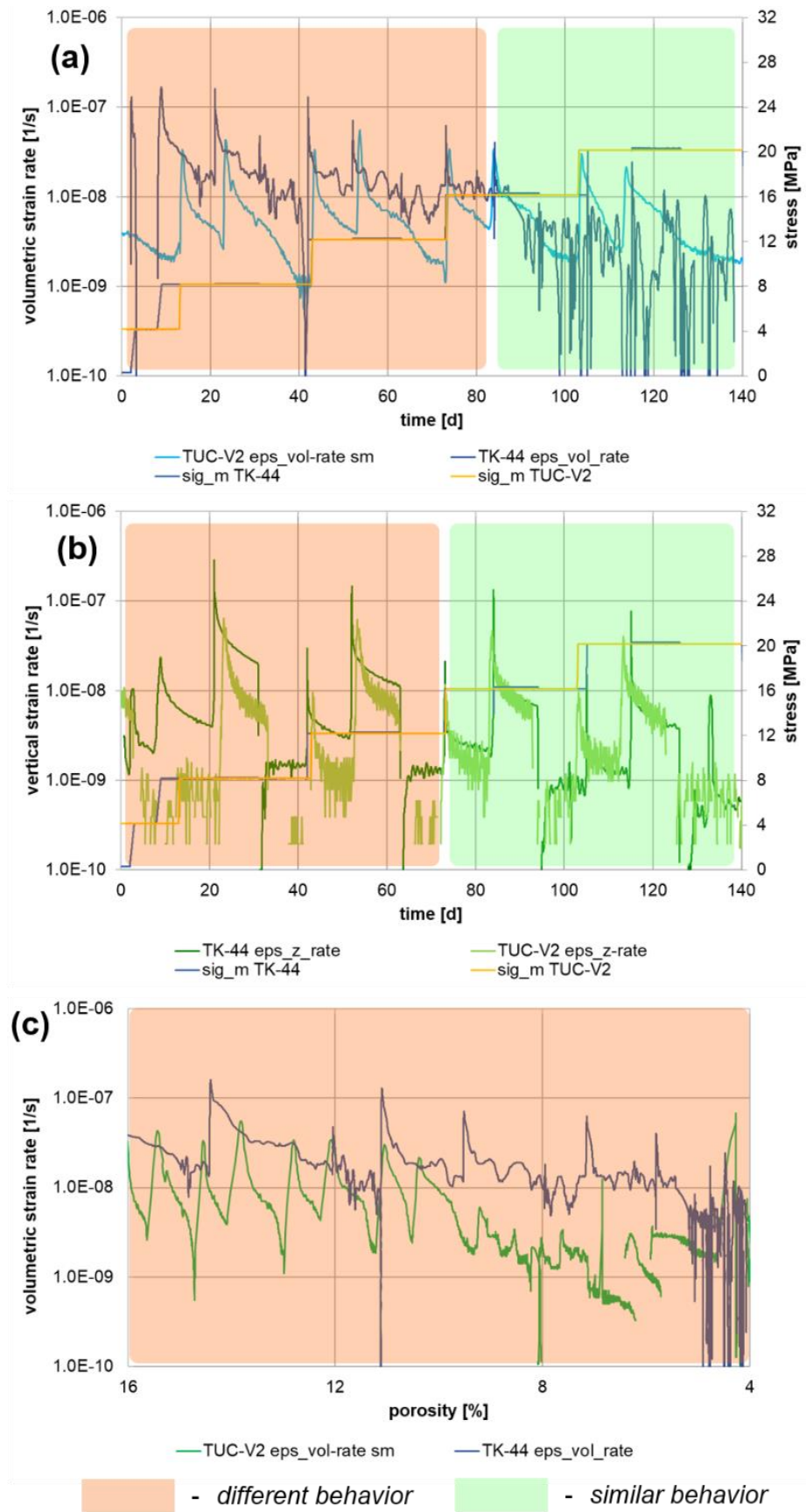


Fig. 3.76 Comparison of the test results for TUC-V2 – phase I and TK-044 – volumetric and vertical strain rates

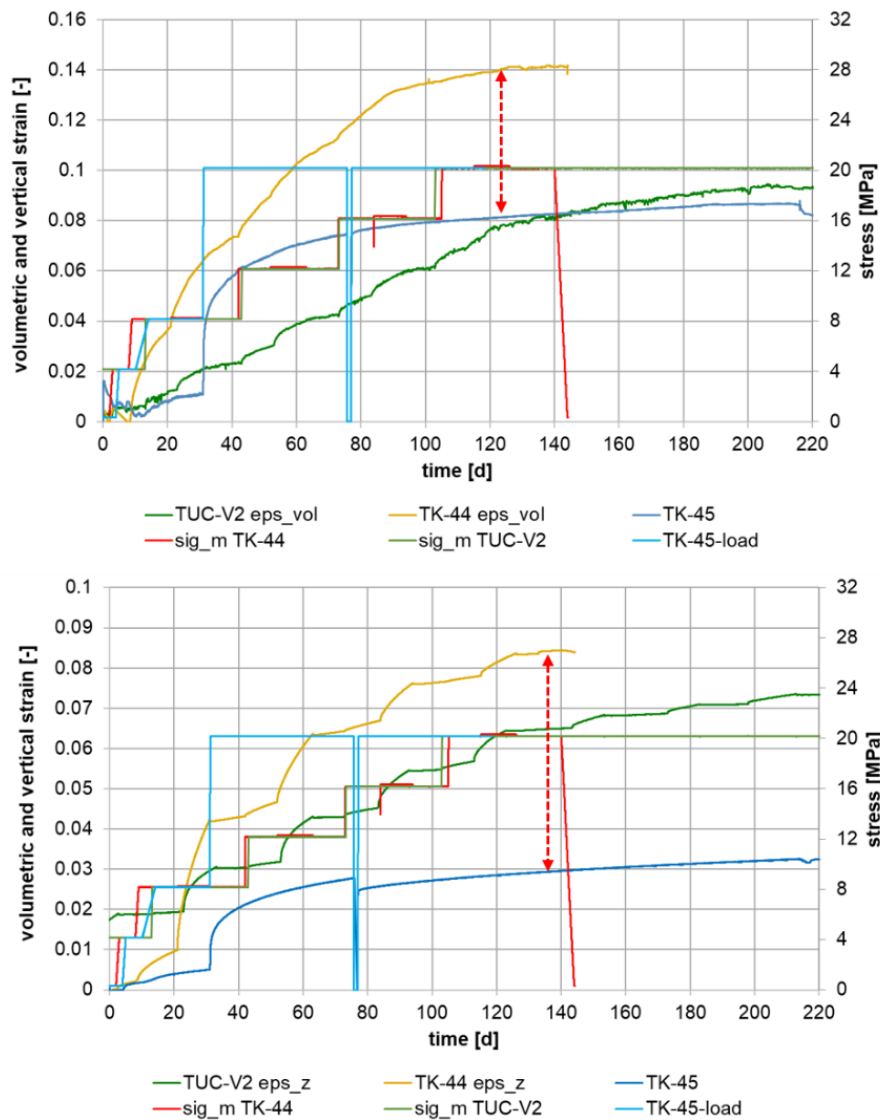


Fig. 3.77 Comparison of the test results for TUC-V2 - phase I, TK-044 and TK-045 – volumetric and vertical strains

Potential explanations for the differences between the three tests can be:

- Material differences (?)
- Sample for test TUC-V2 KOM7 was pre-compacted in the framework of the KOMPASS-I project and no sieving was done in the lab. Therefore, slight differences between the materials cannot be excluded.
- Different microstructure (?)
- Samples for tests TK-044 and TUC-V2 were pre-compacted on two different principles: oedometer pre-compaction with a constant deformation rate and plain-strain pre-compaction with a constant confining stress.

- Measurement uncertainties (?)
- The disparities in the measurements cannot be accounted for by the measurement uncertainties, at least not entirely, since both laboratories have verifiably high measurement accuracy that cannot cause a difference between the curves of up to 6% (absolute value of porosity).
- Different processes (?)
- The reason for the difference between the tests TK-044 and TK-045 may be caused by distinct microstructural processes that predominate in each test as a result of the deviatoric and isotropic load conditions. The areas of the processes' dominance are still not understood in their entirety; hence it remains here as a vague assumption rather than a concrete explanation.

The real cause of the differences is still unknown and could not be clarified in the current project. That is, whether one of the reasons mentioned above drives the differences or others that have not yet been identified and are not listed here is not known.

3.4 Indexed permeability tests (TUC)

Permeability tests were carried out at TUC on the compacted samples TK-031 (BGR), TK-033 (BGR), TUC-V2 and TUC-V4. They serve as indexed preliminary tests to determine the permeability of the KOMPASS reference material, per se, as well as to compare with the earlier preferred material ASSE GSD "DEBORA" /KRÖ 17/.

Permeability tests were carried out with nitrogen at constant gas pressure difference (inflow and outflow). Measurements of the flow rate were used to determine the permeability. For each test, the permeability was measured multiple times for various gas pressure differences and various confining stress levels to identify any potential influencing effects of these variables. Primary and secondary measurements were tuned to each other before the test and a steady state without gas flow was established to assure the precision of the gas pressure difference measurement (which was comparatively small due to the high permeability of the samples). This preliminary step lasted from a few hours to two weeks, depending on the sample. The mechanical load with maximum values of $\sigma_1/\sigma_3 = 6/5$ MPa, was selected in such a way that the samples did not compact further, and the porosity remained constant during the entire test period, which was between 10 – 20 days depending on the test. The stress level was assumed as not causing ongoing compaction since all three samples experienced significantly higher

stress levels for relatively longer periods of time in the preceding long-term compaction tests. The measurement of the vertical deformations of the sample during the permeability tests has confirmed this assumption (→ measured deformations were negligible). Tab. 3.17 gives an overview of the sample characteristics and the permeability test results.

Tab. 3.17 Overview of the permeability test results

sample	lab	material	porosity, test	porosity, manual	water content	test duration	mechanical load		hydraulic load	permeability
			%	%	%	d	σ_1 , MPa	σ_3 , MPa	dp, bar	m ²
TK-31	BGR	ASSE GSD DEBORA	7.8	6.6	0.05	15	6	5	0.05/0.1/0.1 5/0.2/0.25/0 .3/0.35/0.44	1.8E-14÷2.8E-15
TK-33	BGR	ASSE GSD DEBORA	5.1	3.8	0.05	20	6	5/3	5/6/7/8/9/1 0	2.8E-19÷1.5E-19
TUC-V2	TUC	KOMPASS reference material	2.6	3.5	0.5	19	6	5/3	1.3/3/4	2.1E-18÷1.2E-18
TUC-V4	TUC	KOMPASS reference material	12.4	12.5	0.5	10	6	5	0.03	5E-15 (?)

Note: For samples TK-33 and TK-031, the range of porosity is obtained from the value for porosity given by BGR and from the porosity measured at TUC after lathing the sample down from a size of 190 mm x 95 mm to 180 mm x 90 mm. The achievement of the target water content in the samples is described in the final report KOMPASS-I in the pre-compaction procedure /KOM 20/.

Fig. 3.78 shows in some representative examples of results obtained for samples TK-031 and TK-033 that the permeability did not depend on either the confining stress or the pore pressure difference. Interesting to note, however, is that the permeability was time-dependent and that a steady-state value was reached until about 5 – 10 days. Each of the four samples demonstrated their independence from the confining stress and the pore pressure difference, but not all of them consistently showed a clear time dependency. Fig. 3.79 shows a comparison of permeability measurement results with measurements performed in the framework of REPOPERM II project /KRÖ 17/.

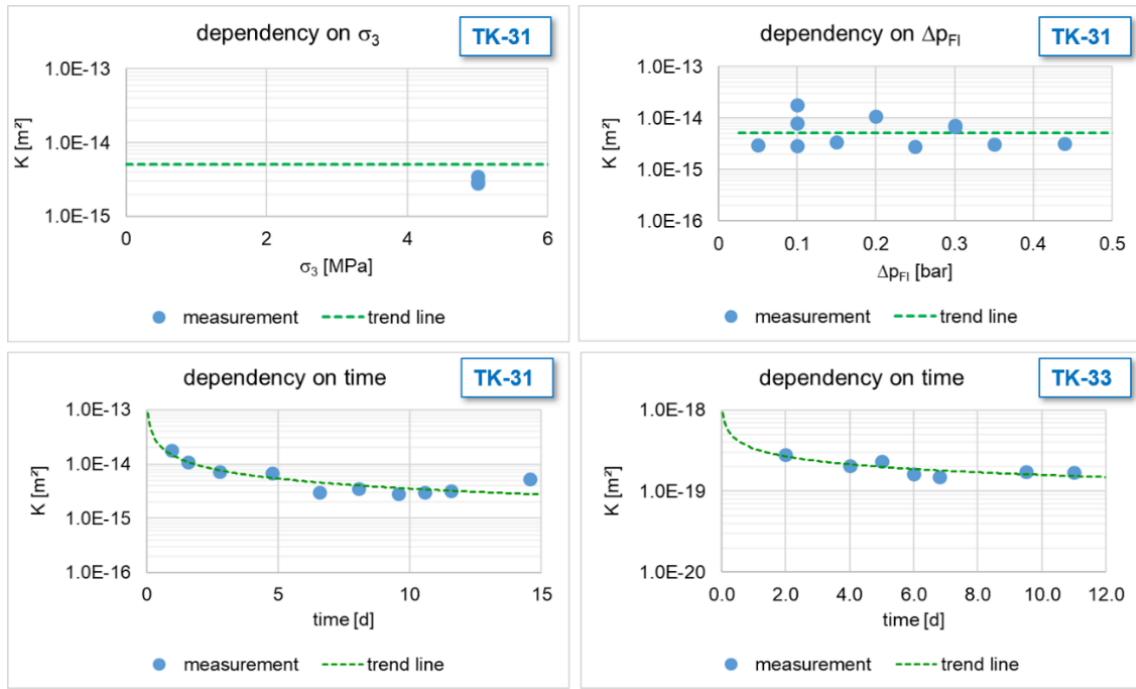


Fig. 3.78 Representative examples of permeability measurement results obtained for samples TK-031 and TK-033 in regard to the influence of confining pressure, gas pressure difference and gas flow time

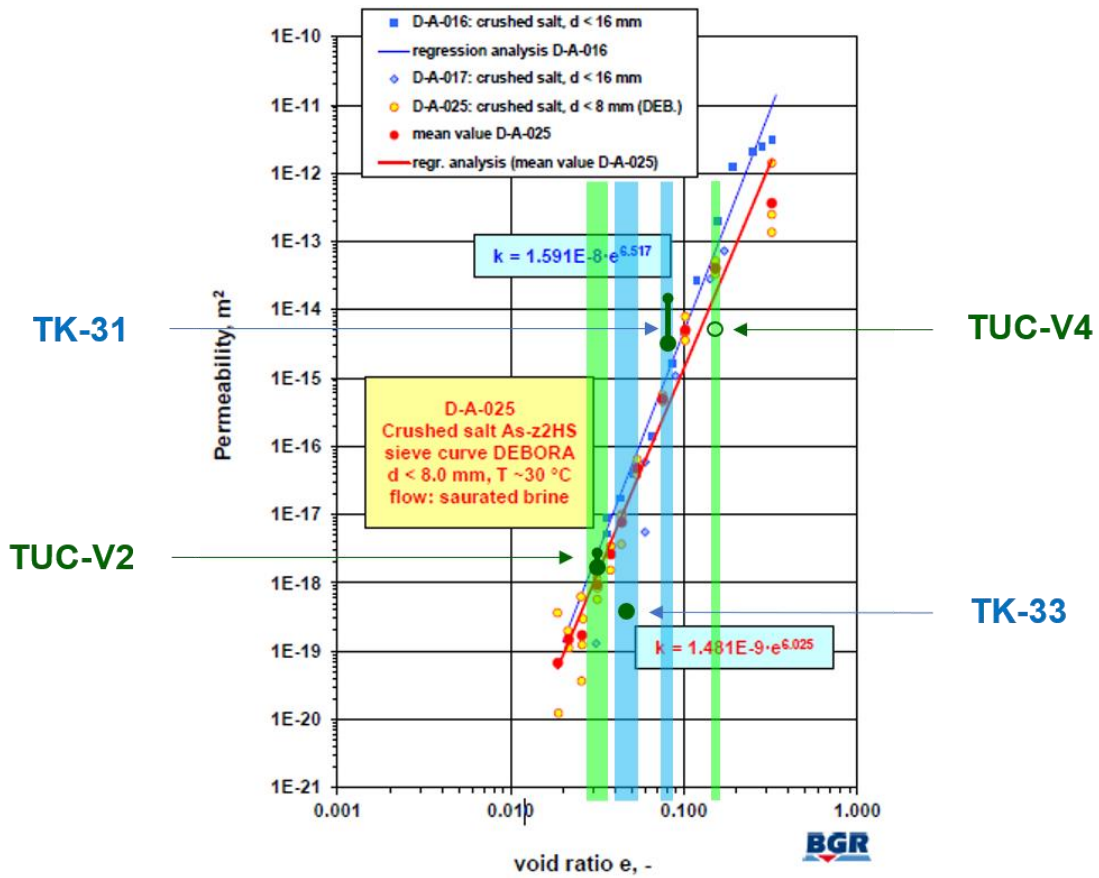


Fig. 3.79 Comparison of permeability results of KOMPASS-II and REPOPERM II /KRÖ 17/

In conclusion, the following statements can be deduced from the results obtained:

- The permeability of the two different materials does not appear to differ significantly (DEBORA vs KOMPASS): TUC-V2 results compared with the REPOPERM II measurements. Measurements of permeability from different laboratories seem to be generally consistent and in relatively good agreement with each other: TUC-V2 and TK-031 results compared with the REPOPERM II measurements. It should be emphasized that this comparison is indicative, as it is based on a few experiments, and thus not yet truly robust. The following two points make it obvious. It is also important to mention that different media used for the KOMPASS and DEBORA samples tested here (gas, saturated brine) could have influenced the permeability data obtained.
- The permeability of sample TK-033 is conspicuous: TK-033 results compared to TUC-V2 and to REPOPERM II measurements. As was shown in KOMPASS-I final report, the mechanical behavior also was non-conform to the TK-031. The sample must probably be considered as an outlier.
- The permeability measurement results for sample TUC-V4 are substantially lower than expected from previous data and from comparison with sample TK-031, which has much lower porosity. This may be due to the high porosity of the sample combined with the limit of measurability reached with the equipment employed. The sample required an extremely low gas pressure difference to accurately record the gas flow. In conclusion, it can be stated that, at TUC, permeabilities of crushed salt samples are measurable at porosities lower than 10 % with the current equipment. The permeability of samples with higher porosity cannot be precisely captured.
- Permeability does not seem to be dependent on either confining pressure or gas pressure difference but takes up to 10 days to reach a constant level.
- However, the investigations carried out are only indicative, meaning that the created preliminary database is obviously insufficient to make any conclusive claims. Systematic, more extensive investigations are necessary in the future. Investigations in the range of low porosity of 1 % – 5 % are crucial, as is the continuation of the investigation of other potential influencing factors (confining stress, pore pressure difference, water content). Furthermore, not only investigations with gas but also with fluid are relevant regarding the in-situ application. TUC-V2 and TUC-V4 samples tested here could potentially have affected the permeability data obtained, e.g., because of drying during the flow of N₂ gas.

To the extent that the mechanical and thermal behavior has been investigated so far that reliable predictions as well as understanding for the pore space structure of the material are possible for the low porosity range, subsequently systematic investigations of hydraulic behavior must be carried out.

4 Microstructural Investigations

4.1 Introduction

In many previous empirical tests, crushed salt was compacted from initial porosities of about 35 % down to 5 % and presumably even less /BEC 99/, /BEC 04/, /KRÖ 09/, /KRÖ 17/, /KOM 20/, albeit that the measurement inaccuracy at such small porosities is high. It became evident that compaction rate and/or resistance depend on many environmental factors (e.g., temperature, stress), boundary conditions (e.g., rate of cavity convergence and drainage conditions), intrinsic material controls (e.g., microstructural state variables, such as grain size, porosity, moisture content and impurity phase content), and initial conditions (such as emplacement porosity as determined by emplacement method). The relationships determining how these controls affect compaction are often highly non-linear, such that the influence of individual factors is variably dependent on the state of others. A rise in moisture content, for instance, might not come into effect when stresses are high (i.e. when microstructural processes such as crystal plasticity dominate compaction), but it may contribute significantly to enhancing compaction when stresses are low (i.e. when processes such as pressure solution become important - sensu /SPI 86/, /SPI 90/. An understanding of crushed salt compaction and permeability evolution, based on the physical processes that operate at the microscale, hence microstructure, is therefore essential for underpinning constitutive models.

In this work, the abundance of indicators for microscale deformation mechanism were related to the compaction conditions, focusing on the different pre-compaction methods, the influence of humidity and grain size.

4.2 Comparison of pre-compacted samples (BGR)

To resolve the various complex and non-linear dependencies, the KOMPASS-II partners agreed on a set of different compaction tests, using the same starting material: crushed salt from Sondershausen mine with a grain size distribution resembling the Fuller grading curve (maximum packing density curve) for granular aggregates (KOMPASS reference material).

To achieve cohesive samples in the first place, all partners employ an initial rapid compaction phase, a.k.a. "pre-compaction". This imparts cylindrical samples with about 15 vol.-% porosity. However, the pre-compaction phase is not standardized, and each project partner uses a somewhat different technique (Tab. 4.1).

Our work aims to distinguish if the differences in pre-compaction technique are manifested in microstructural differences. Such differences, in turn, would imply a bias introduced by the pre-compaction technique with respect to further compaction behavior below 15 %. A future need will be to establish which of these techniques resembles the real-use-case of an underground backfill best and in how far the associated microstructure still differs from the real case scenario.

The following three working hypotheses were formulated: (1) the type and abundance of microstructural deformation indicators as well as (2) the grain size distribution (GSD) and grain shape parameters (GSP) differ in the differently pre-compacted samples. Moreover, (3) all pre-compaction techniques result in samples with a distinct GSD and GSP compared to the starting material, that is the loose, uncompacted crushed salt supplied to all participating in the experimental compaction program.

4.2.1 Method

4.2.1.1 Material and general approach

We investigated a total of four polished thick sections (S1, S2, S3 and S4 – Tab. 4.1) for their microstructure. They were made from the same starting material, i.e., run-of-mine material (i.e., the same loose, unprocessed, mined material) from Sondershausen salt mine. Their origin and their mineralogical composition are described in Section 3.2 of this report.

The samples S2, S3 and S4 were retrieved from different types of compaction tests (Tab. 4.1), performed during the KOMPASS-I project phase /KOM 20/. Sample S1 acts as an uncompacted reference standard (loose crushed salt) S2 derives from the oedometric BGR test VK-043, S3 from the plain strain test TUC-14 by TUC and S4 from the oedometric test IfG-684 from IfG. All samples were investigated qualitatively for their microstructural deformation indicators. Moreover, three samples (S1, S2 and S3) were quantitatively studied by a statistical evaluation of hand-segmented grains, as observed in optical micrographs.

In each sample, the GSD was expected to resemble the GSD of earlier studies on crushed salt, originating back to /BEC 99/, where the state of the art was: “[...] the material for backfilling drifts will consist of crushed salt as received by drift excavation, i.e., a coarsely grained material with a maximum grain size of 60 mm”. However, for the samples S1 to S4, the objective to use a consistent, distinctive GSD, is fulfilled with a differing quality of fit. The samples S3 (TUC) and S4 (IfG) used the run-of-mine material as received, with a rough differentiation into three

bins caused by the on-site processing of the crushed salt (0.03 mm to 0.3 mm, 0.4 mm to 4 mm and 0.1 mm to 1 mm, Fig. 4.1). The starting GSDs for samples S1 and S2 (BGR) got refined from 10 bins. Fig. 4.1 displays the starting GSDs of the samples.

Tab. 4.1 Overview of microstructurally investigated samples by BGR

Sample name (origin)	Compaction type	Maximum load	Compaction time	Porosity	Moisture
		[MPa]	[d]	[%]	[%]
S1 (-)	loose	---	---	31 - 42	0.1
S2 (BGR VK-043)	Oedometric	20	28	15	0.35
S3 (TUC-14)	Plain strain	5	2	14	0.5
S4 (IfG-684)	Oedometric	20	28	10 - 20	0.1

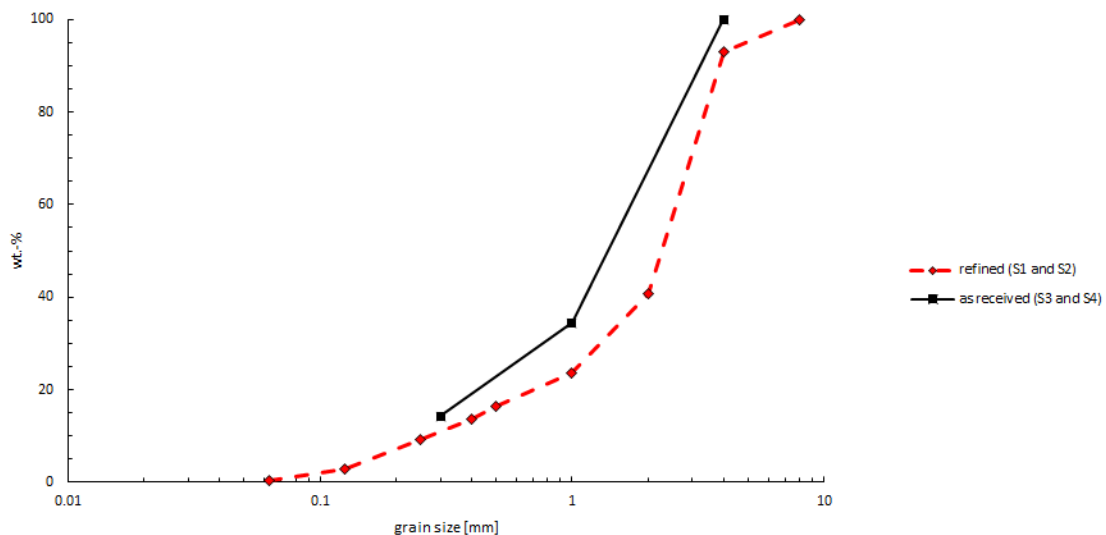


Fig. 4.1 Sum-curves for the different starting GSD

4.2.1.2 Thick section preparation

Sample S1 (loose crushed salt) was poured into a bowl, saturated with yellow-dyed two-component resin (Araldite 2020 A / B, comp. Huntsman with EpoDye, comp. Struers) and subsequent fully hardened at 35 °C. The samples S2 (BGR VK-043) and S3 (TUC-14) were prepared from the surface of cylinder halves (Fig. 4.2). Sample S4 (IfG-684) was selected from a cubic subsample (Fig. 4.2), such that it contained a region where fine material accumulated into a lense of 1 – 2 cm in width and 3 – 5 cm in length (white arrow in Fig. 4.2).

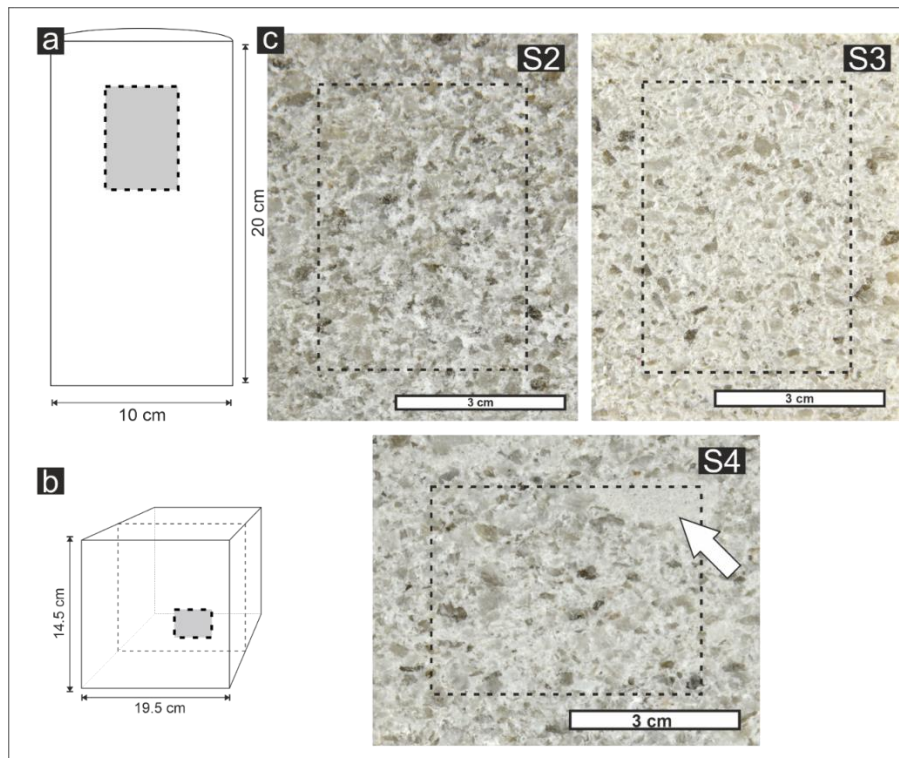


Fig. 4.2 Sketches of the sampled locations for the sections used. Samples S2 (BGR VK-043), S3 and (TUC-14) were prepared from cylinder halves; (a) Sample S4 (IfG-684) was prepared from a more cubic shaped sample; (b) The dotted lines in the sketches and the images exemplary show the size of the prepared thick section. Scale bars are 3 cm. White arrow in c S4 point to lenses of fine-grained material

Polished thick sections (~5 x 7 cm, ~200 μm thickness) were prepared for reflected light microscopy from all four samples. All sawing (band saw) and polishing (polishing machine TF 250, comp. JEAN WIRTZ) were performed dry. The pre-compacted samples were saturated with colored two-component resin (Araldite 2020 A / B, comp. Huntsman with EpoDye, comp. Struers) under low vacuum (~30 minutes).

Subsequently, the dried samples (24 h drying time) were glued (24 h at 35 $^{\circ}\text{C}$, using an adhesive press) onto polished glass slides, then cut (fine band saw, comp. EXAKT) and polished (Mikroschleifsystem 400CS, comp. EXAKT). The samples were etched to decorate subgrain boundaries, using a slightly undersaturated, 5.5-molar NaCl-brine (40 s etching time) and n-hexane for cleaning and to stop the reaction /URA 87/, /SPI 86/, /LIN 16/, /BÉR 23/, /URA 87/.

4.2.1.3 Microscopy

The full sections were scanned in reflected and transmitted light (RL, TL), at a resolution of approximately 20 μm , using a computer-automated sample stage, mounted in the Axio Imager M2m microscope from ZEISS. Each scan consists of approximately 500 individual images that were stitched using the ZEN Blue software also from ZEISS. Subsequent, the scans were transferred to the program QGIS /QGI 22/ where they were spatially referenced to enable a prompt switch between the different recordings of each sample (RL, TL scans as well as individual inset micrographs).

4.2.1.4 Statistical analysis

For each sample studied quantitatively (S1, S2 and S3), a representative area of interest (AOI) was chosen, which fully contained more than 8 of the largest grains. Subsequently, all grains falling fully within the AOI were segmented by hand using the polygon tracing tool in QGIS (Fig. 4.3, Fig. 4.4, Fig. 4.5). The acquired data (area, perimeter, maximum width and maximum length for each grain as well as the total grain number) was used to determine each samples' GSD and GSFs, i.e., circularity and axial ratio (AR). To analyze and compare the GSDs, we follow the fractal-dimension-approach given in /BON 01/. Therein, the density GSDs follow a power-law equation, in which the number of grains (N_i) within each individual bin i was normalized by the bins' width b_{wi} and by the area of the AOI S_{AOI} :

$$\frac{N_i}{b_{wi} * S_{AOI}} = C * bc_i^{-D} \quad (4.1)$$

C is a constant of proportionality and bc_i is the bin center of each bin. For each sample, the power-law exponent D was derived by the least-squares method and describes the dimension of self-similarity, i.e., the ratio of small to large grains that can be used to point out grain breakage when compared to D of the starting material (sample S1).

For each segmented grain, circularity, and axial ratio (AR) are defined as:

$$circularity = \left(\frac{4\pi * area}{perimeter^2} \right) \quad (4.2)$$

$$AR = \left(\frac{1}{\left(\frac{length}{width} \right)} \right) \quad (4.3)$$

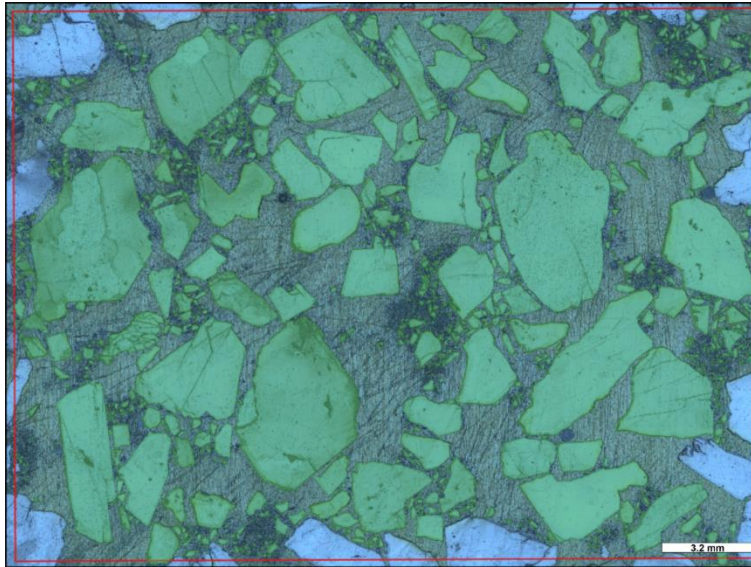


Fig. 4.3 The AOI (red boundary) in sample S1 (loose crushed salt). 1547 grains (marked in green) were segmented. Scale bar is 3.2 mm and image width is 24.5 mm

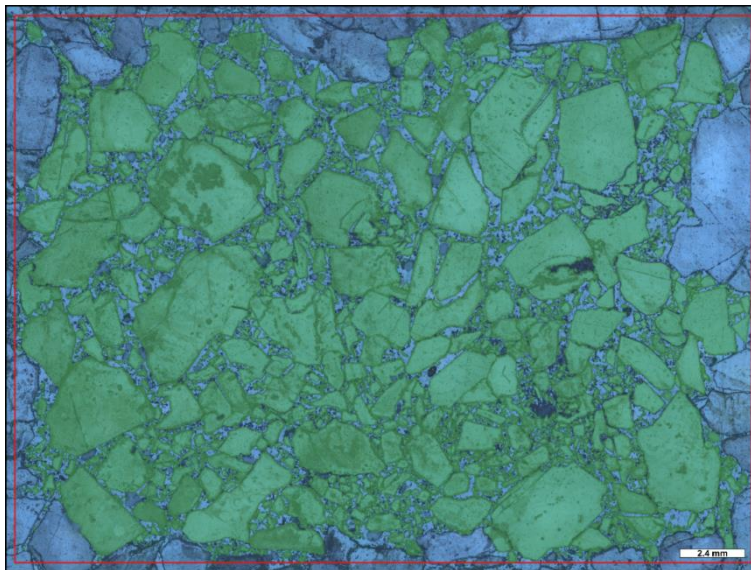


Fig. 4.4 Overview of the AOI (red boundary) in sample S2 (BGR VK-043). 2677 grains (marked in green) were segmented. Scale bar is 2.4 mm and image width is 27 mm

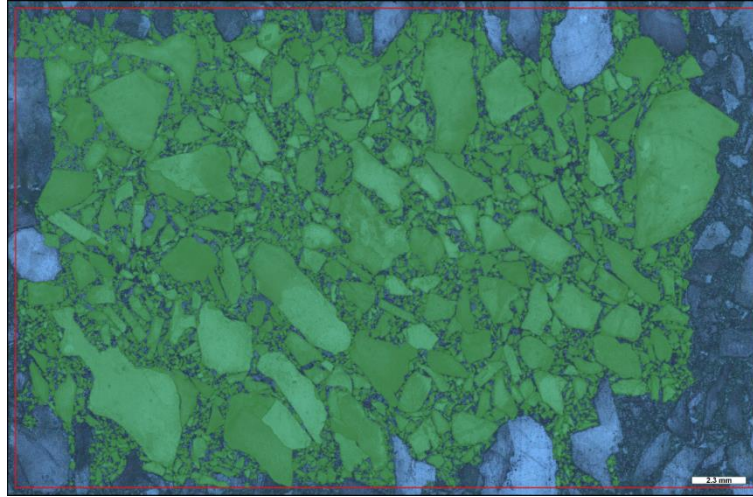


Fig. 4.5 Overview of the AOI (red boundary) in sample S3 (TUC-14). 5491 grains (marked in green) were segmented. Scale bar is 2.3 mm and image width is 30 mm

4.2.2 Results

First, we present a qualitative analysis, describing the samples' general appearance (Samples S1, S2, S3 and S4) and subsequently list the microstructural deformation indicators found. We then present the quantitative data obtained on GSD and GSP (Samples S1, S2 and S3).

4.2.2.1 General microstructural appearance

By visual estimate, the observed size of the grains in sample S1 (starting material) varies between approximately $130 \mu\text{m}^2$ and approximately 16.2 mm^2 . The fine grains tend to accumulate between the larger ones (Fig. 4.6a, top middle).

The grains show a blocky, angular shape and grain-to-grain contacts are scarce, as expected in this loose crushed salt. Yet, if observed at all, they appear between small and large grains, likely due to a static or water aided adhesion during the sample preparation. Especially the larger grains show internal substructures, such as fractures (Fig. 4.8), fluid inclusions, often arranged in trails (Fig. 4.9) and subgrains (Fig. 4.10).

The size of the grains in the sample S2 (originating from test BGR VK-043) varies between approximately $72 \mu\text{m}^2$ and approximately 14.4 mm^2 . Compared to S1 (Fig. 4.6a), grains are closely aligned and grain-to-grain contacts are ubiquitous (Fig. 4.6b),

resembling a moderately sorted, clast supported fabric with pores in stress shadow regions between larger grains. By visual estimate, the porosity is > 20 vol.-%, hence somewhat larger than given in the BGR VK-043 test recordings (15 vol.-%). Fractures, fluid inclusions and subgrains are abundant throughout the sample. The grain boundaries, however, hold additional deformation indicators, such as dense slip bands (Fig. 4.11), tight, indenting, truncating or interpenetrating grain boundaries (TITIGB, Fig. 4.17). Moreover, there are some occurrences of recrystallized (Fig. 4.20) and entirely bent grains (Fig. 4.14).

The grain sizes in the sample S3 (originating from test TUC-14) varies between approximately 36 μm^2 and approximately 17.5 mm^2 . Compared with S2, the fabric is more matrix supported with even more grain-grain contacts and with less and finer pore space (Fig. 4.6c).

The porosity is visually less than in sample S2, resembling the TUC-14 test recordings of 14 vol.-%. Again, the grains comprise fractures, fluid inclusions and subgrains as well as dense deformation/slip bands (Fig. 4.12), bent grains (Fig. 4.15), TITIGB (Fig. 4.18) and recrystallized grains (Fig. 4.21).

With sample S4 (originating from test IfG-684), there are lenses of accumulated, well sorted, fine grains (Fig. 4.7) embedded within a moderately sorted fabric, the latter more similar to the fabric in the other samples. Outside the lenses, grains vary between approximately 13 μm^2 and approximately 8 mm^2 in size. Similar to S2 and S3, grain-to-grain contacts are common (Fig. 4.6d).

Despite the apparent moderate sorting, the fabric is matrix supported with some-what less touching of larger grains than in S2. Fractures, fluid inclusions and subgrains, dense deformation/slip bands (Fig. 4.13), bent grains (Fig. 4.16), TITIGB (Fig. 4.19) and recrystallized grains (Fig. 4.22) were observed, too.

Fig. 4.7 displays the fabric of the fine-grained lenses. Therein, the grains exhibit no fractures, rarely subgrains and no visible fluid inclusions. Also, dense deformation/slip bands and recrystallized grains are absent. However, tight, indenting, and interpenetrating grain boundaries (TITIGB) and bent grains were observed (Fig. 4.7).

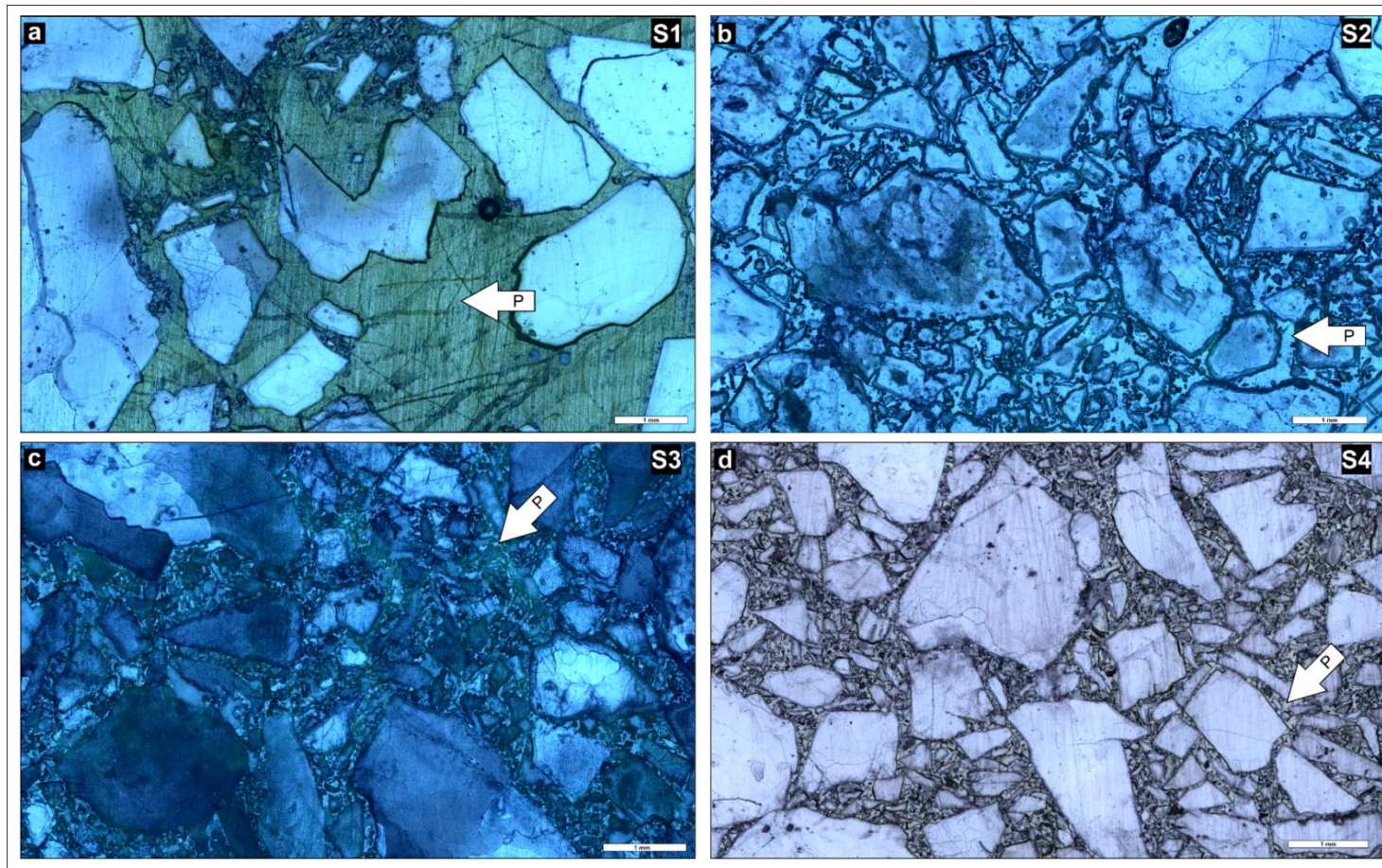


Fig. 4.6 Sections of polished thick sections, made of the Samples S1 (a: originating from the starting material), S2 (b: originating from test BGR VK-043), S3 (c: originating from test TUC-14) and S4 (d: originating from test IfG-684). White arrows mark porosity and scale bars in each micrograph are 1 mm

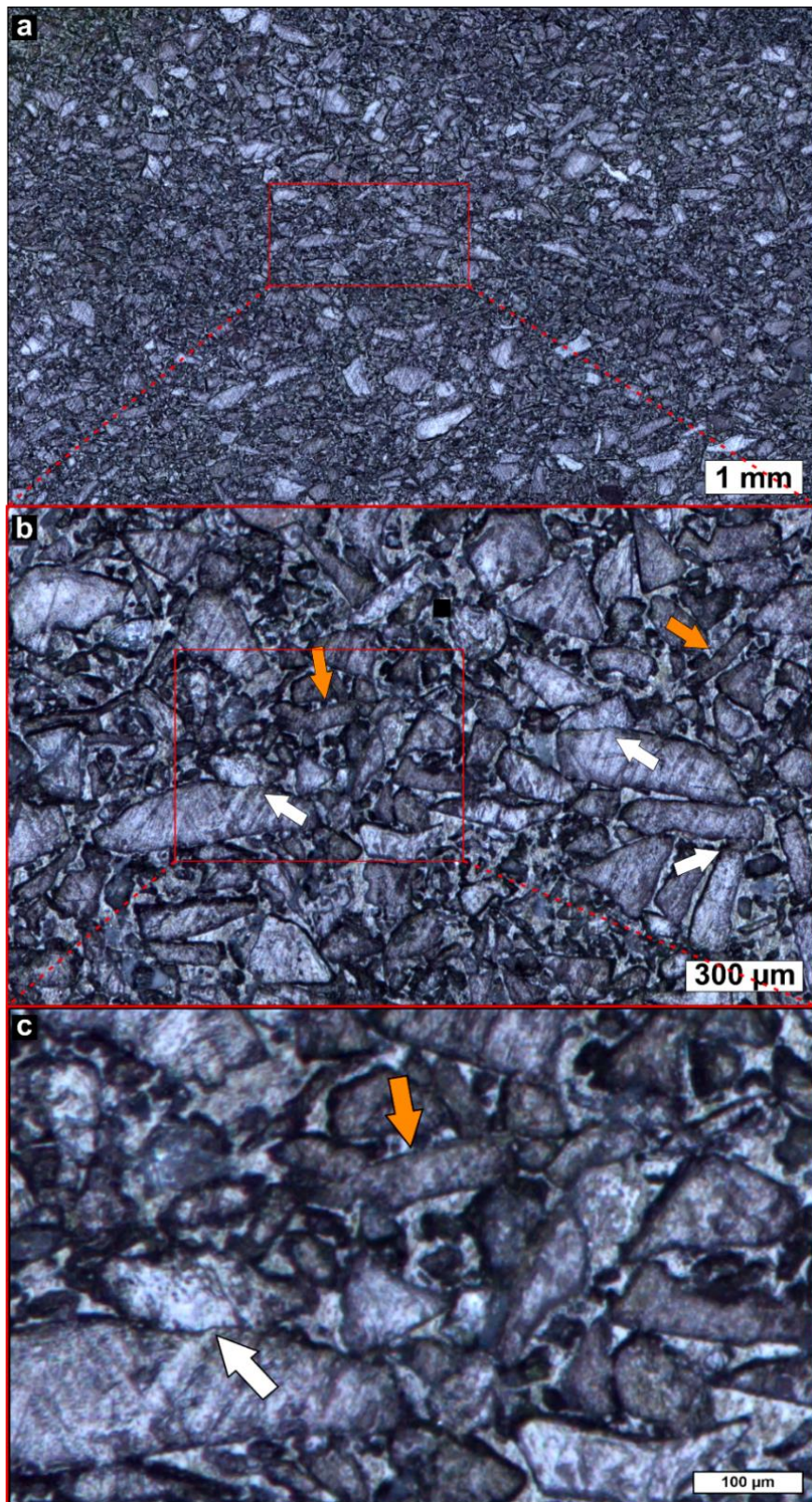


Fig. 4.7 Micrograph and zoom-in on a lens of fine grained material in S4. White arrows mark tight, indenting grain boundaries (c) and orange arrows mark bent grains

4.2.2.2 Microstructural deformation indicators

Within the investigated sections, several microstructural indicators for different types of deformation mechanisms were distinguished (Tab. 4.2). The samples contain all these indicators in a similar abundance, making a clear assignment of any micrograph to its specific test impossible. The only exception is sample S1 (loose crushed salt), which displays almost no indicators at the grain boundaries. However, this loose starting material already shows plenty of substructure-rich grains, in advance of any compaction testing, meaning that a large quantity of deformation indicators is a-priori inherent to the material. These a-priori indicators make it difficult to firmly distinguish the microstructural impact of any of the compaction tests. Tab. 4.2 tags the most likely cause for each indicator (inherent/induced). This differentiation is based on the subjective increase of an indicators abundancy when compared to the uncompacted, loose crushed salt in sample S1. Four types of microstructural indicators, (1) dense deformation/slip bands, (2) bent grains, (3) tight, indenting, truncating, or interpenetrating grain boundaries and (4) recrystallized grains were present in the compacted samples only. They all have in common, that they appear close to direct grain-to-grain contacts, which implies significant local deviatoric stress.

Tab. 4.2 List of distinguished microstructural indicators and corresponding deformation mechanisms, after /BLE 02/

Microstructural deformation indicators	Mechanism	Sub-mechanism	Inherent / test induced	Example in micrograph
Fractures (intragranular, transgranular, intergranular)	Cataclasis	Grain breakage	inherent and test induced	Fig. 4.8
Tight, indenting, truncating, or interpenetrating grain boundaries (TITIGB)	Diffusive mass transfer	Pressure solution and grain boundary migration (GBM)	Test induced	Fig. 4.17 Fig. 4.18 Fig. 4.19
Recrystallized grains	Diffusive mass transfer	Dynamic recrystallization	Test induced	Fig. 4.20 Fig. 4.21 Fig. 4.22
Fluid inclusions	Diffusive mass transfer	Healing, pressure solution, GBM	inherent and test induced	Fig. 4.9
Subgrains	Intracrystalline plasticity	Dislocation creep	inherent (and test induced?)	Fig. 4.10
Dense deformation/slip bands	Intracrystalline plasticity		Test induced	Fig. 4.11 Fig. 4.12 Fig. 4.13
Bent grains	Intracrystalline plasticity		Test induced	Fig. 4.14 Fig. 4.15 Fig. 4.16

Cataclasis

Indicators for cataclasis include fractures, which can be divided into (1) intragranular, (2) transgranular or (3) intergranular (sensu /BLE 02/, /PAS 05/). Transgranular and intergranular fractures, whereby one fracture effects multiple grains, are not observed.

However, grains are occasionally shattered, marked by multiple intragranular fractures. Such a grain is illustrated in sample S1 (upper left corner in Fig. 4.8), which shows that the crushed salt processing itself creates fractures as a-priori, inherent microstructural indicator.

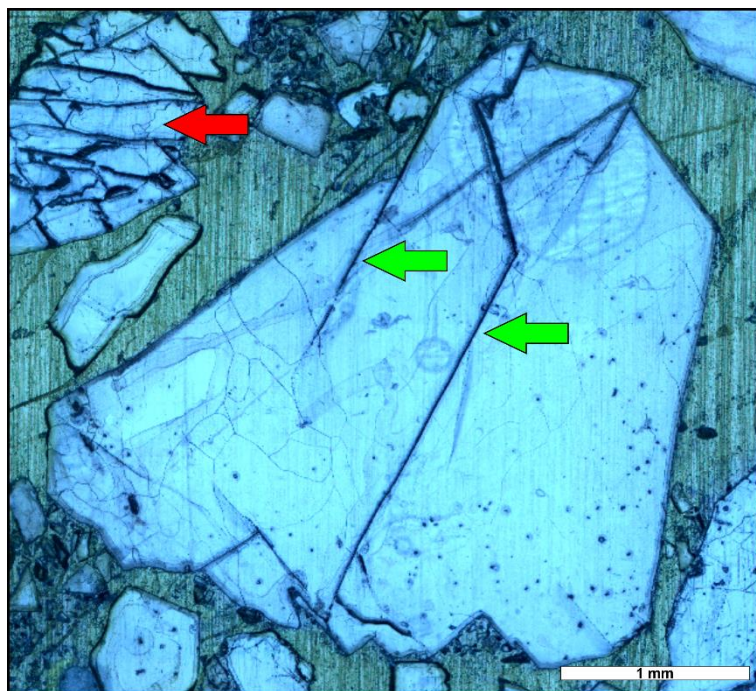


Fig. 4.8 Grain with intragranular (green arrows) fractures in sample S1. Note also the fully shattered grain, partly offset along its fractures (red arrow). Scale bar is 1 mm

Fluid Inclusions

Fluid inclusions (Fig. 4.9) can be an indicator for diffusive mass transfer (DMT) and grain boundary migration (GBM), with most noticeable fluid inclusions marking old, healed fractures (Fig. 4.14), or ghost-boundaries, i.e., former grain-grain contacts /URA 86/. Thin, continuous brine films along grain boundaries enable solution-precipitation

processes, such as pressure solution (PS) and fluid-assisted grain boundary migration (GBM), when dislocation activity is important /SPI 86/.

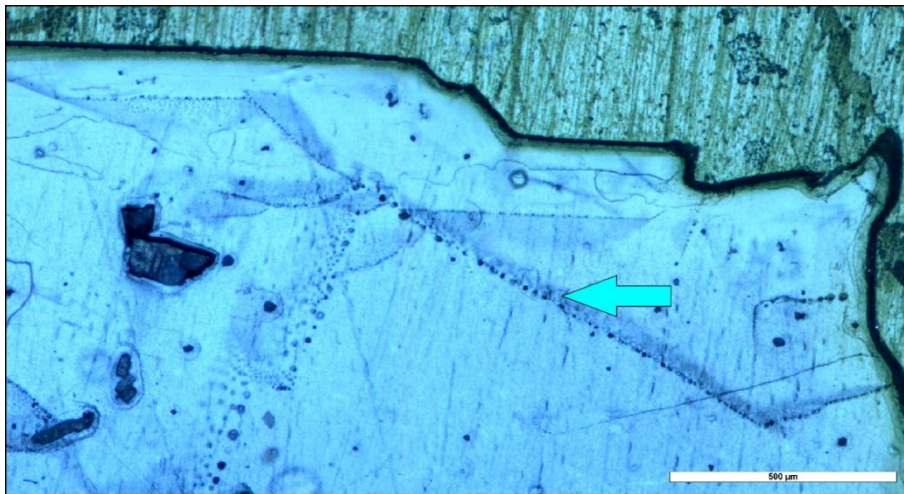


Fig. 4.9 Grain with lines of fluid inclusions (light blue arrow) in the sample S1. Scale bar is 500 μm

Subgrains

A subgrain is a volume of a grain that comprises a homogenous crystal lattice orientation, which is at a low-angle mismatch to the lattice orientation of adjacent grain parts. At misorientation angles $> 10^\circ$, the subgrain boundary can be regarded as a new grain boundary, pointing to subgrain rotation recrystallization /PAS 05/. Commonly, the boundary of a subgrain is associated with an accumulation of dislocations, which pile up and rearrange in walls, eventually leading to the dynamic subgrain rotation recrystallization /URA 86/. The lattice orientations and subgrain boundaries in halite can be determined using, e.g., electron backscatter diffraction (e.g. /PEN 05/). However, the swifter approach by etching as described above yielded easily distinguishable decoration of subgrain boundaries (Fig. 4.10).

In natural rock salt, subgrains are often studied as deformation indicators for intracrystalline plasticity by dislocation creep /CAR 83/, /KNE 18/, /SCH 22a/, /MER 23/. The relation between subgrain size D and differential stress σ due to /CAR 83/, for example, can be used as a piezometer:

$$\sigma \text{ (MPa)} = 107 D^{-0.87} (\mu\text{m}) \quad (4.4)$$

We used the equivalent circular area diameter (ECAD) D_A , calculated from the segmented area of the subgrains (Equ. 4-5, /LI 05/, /HEI 14/):

$$D_A = 2 \sqrt{\frac{A}{\pi}} \quad (4.5)$$

A crude subgrain structure indicates a climb-controlled recovery, with areas of small subgrains documenting stress concentrations /SPI 86/. Such concentrations can often occur close to grain-grain contacts, where deviatoric stress is locally high in (isostatic) compaction. However, elongated subgrains at grain boundaries indicate recrystallization by fluid-assisted grain boundary migration /URA 07/.

Tab. 4.3 lists the number of subgrains found per sample and gives the corresponding differential stress range. Generally, the values are similar with a large range from 0.5 MPa to 22.7 MPa and allow no strict relation of subgrain abundance or size to compaction method. The abundance and average size hold true also for loose crushed salt in sample S1, indicating that all subgrains are found inherent and of tectonic origin. Note that outliers were included in this analysis and that the differential stress, particularly in sample S1 has not been this high. Regardless, the calculated differential stresses (Tab. 4.3) showed no clear trend.

Tab. 4.3 Spot checked subgrain extent with size of the spot-checked region (number of subgrains), minimum and maximum ECAD (Equ. 4-5) and calculated differential stress (according to Equ. 4-4). Calculated differential stress shows the lowest value, than the arithmetic average, than the highest value. Note: outliers are included

Sample	Number of subgrains [-]	Minimum ECAD [μm]	Maximum ECAD [μm]	Calculated differential stress [MPa]
S1 raw-material	240	7.3	257.6	0.9 > 4.3 < 19
S2 BGR VK-043	502	5.9	331.5	0.7 > 4.5 < 22.7
S3 TUC-14	251	6.3	450.7	0.5 > 3.8 < 21.5
S4 IfG-684	267	8.5	263	0.8 > 4.9 < 16.6

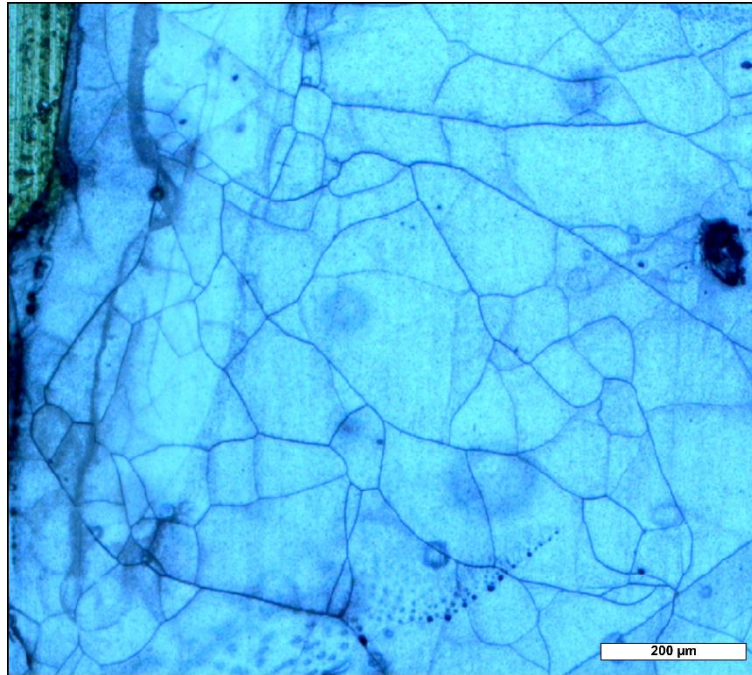


Fig. 4.10 Grain with subgrains (thin black lines) in the sample S1. Scale bar is 500 μm and image width is 1.5 mm

Dense slip bands

Dense slip or deformation bands (Fig. 4.11, Fig. 4.12, Fig. 4.13) are areas with increased presence of dislocations and significant dislocation mobility within the crystal /CAR 83/ and are indicators for high stresses (> 10 MPa /SPI 86/). Slip bands occurring in samples cored from mine galleries may be associated with gallery closure after mining in rock salt /SPI 86/.

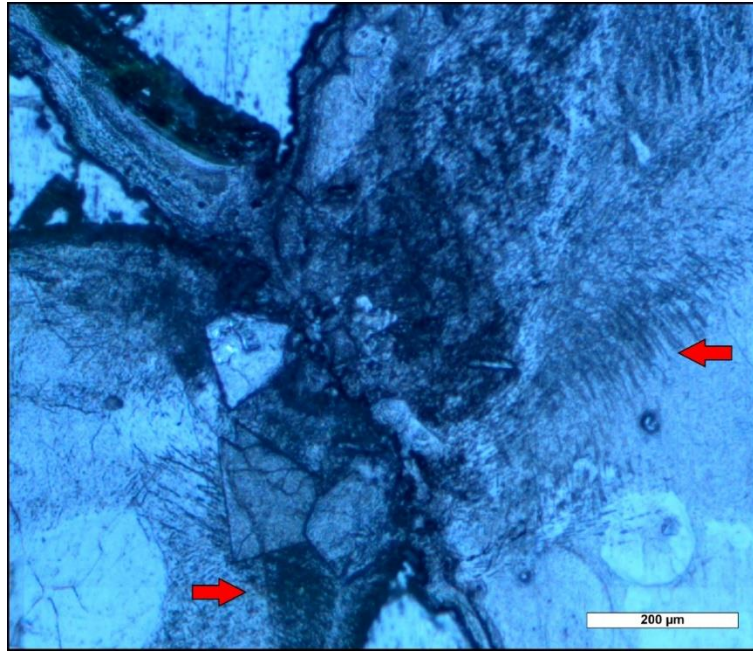


Fig. 4.11 Contact area between grains showing dense deformation/slip bands (red arrows) – sample S2. Recrystallized grains are also visible at the contact. Scale bar is 200 μm and image width is 1 mm

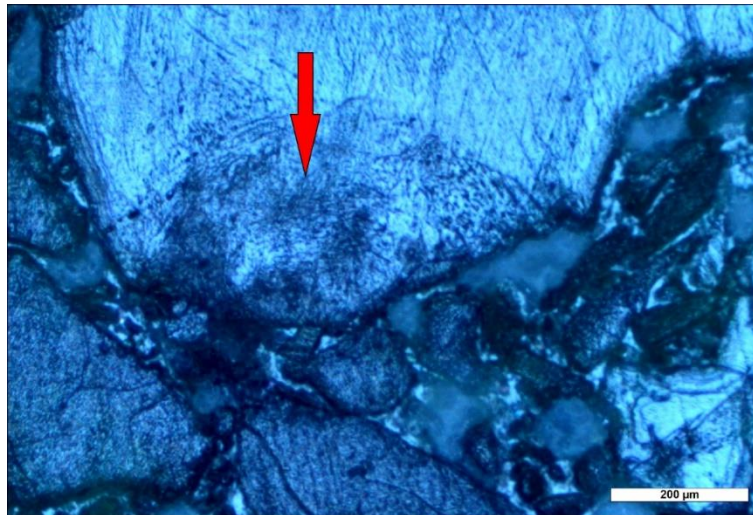


Fig. 4.12 Contact area between grains with dense slip bands (red arrow) in the larger, upper grain – sample S3. Scale bar is 200 μm and image width is 1 mm

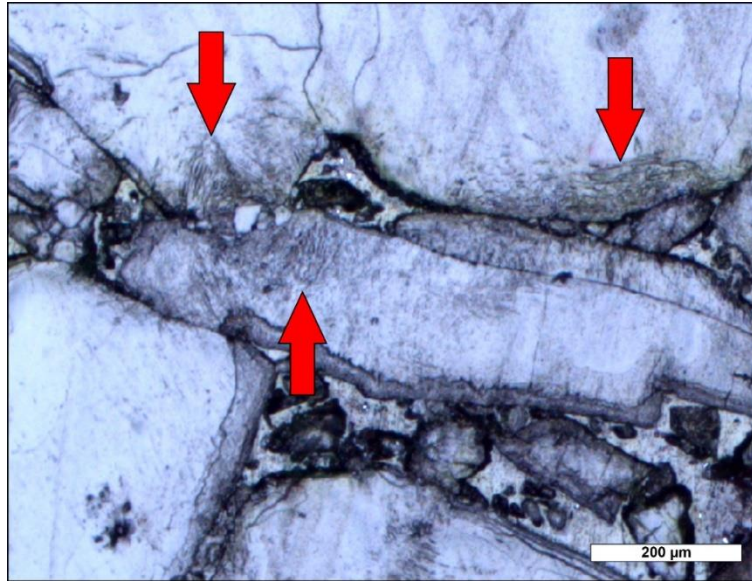


Fig. 4.13 Contact area between grains showing dense slip bands (red arrows) in the upper and central grains in the image – sample S4. Scale bar is 200 μm and image width is 1 mm

Grains with a bent shape

Bent grains and undulating grain/pore boundaries indicate intracrystalline plasticity (Fig. 4.14, Fig. 4.15, Fig. 4.16) and occur at certain conditions only. According to /JOF 24/, bending of unconfined salt crystals (i. e., adjacent to pore walls here) is only possible, if a temperature of 200 °C is exceeded, or if sufficient moisture is present.

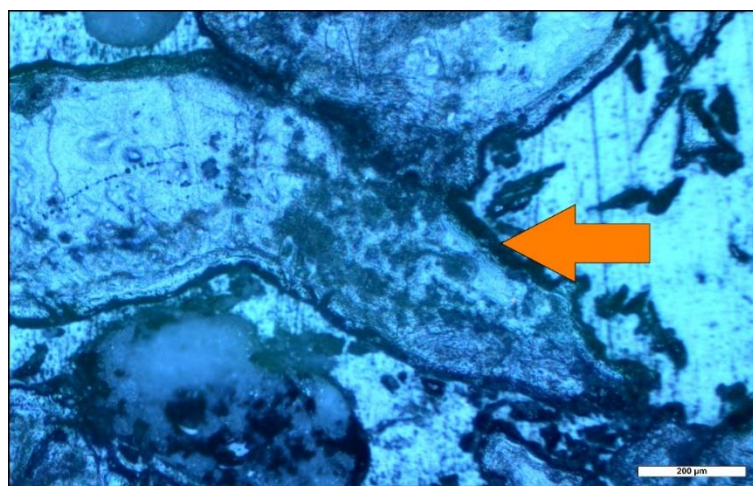


Fig. 4.14 Bent grain (orange arrow) from sample S2. Scale bar is 200 μm and image width is 1.4 mm

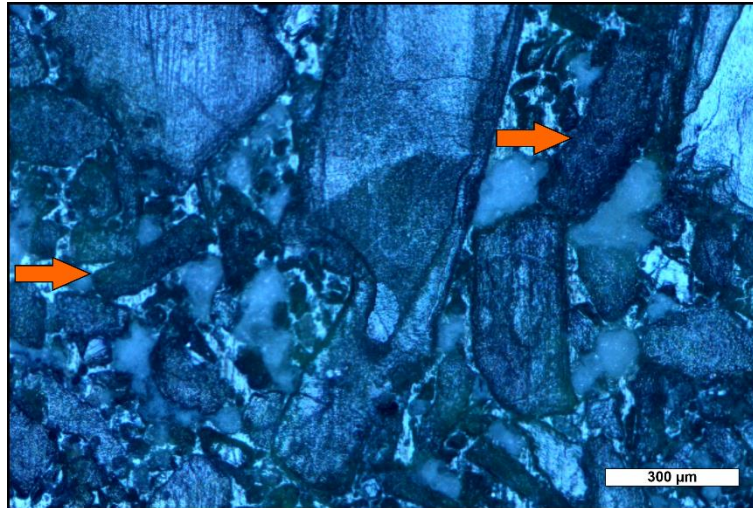


Fig. 4.15 Bent grains (orange arrows) in sample S3. Scale bar is 300 μm and image width is 1.7 mm

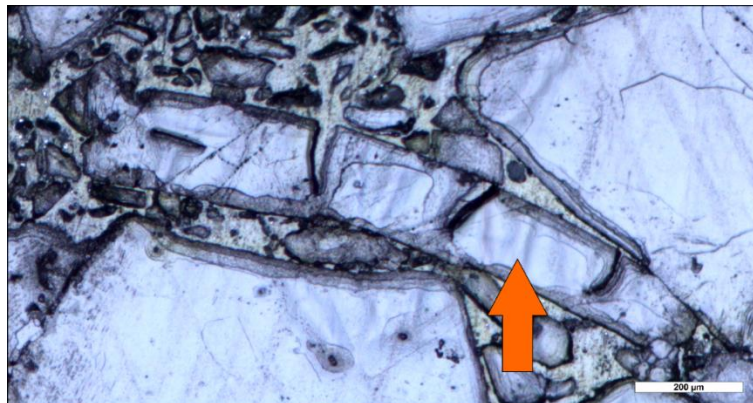


Fig. 4.16 Bent and fractured grain locked (orange arrow) between two others in sample S4 (IfG-684). Scale bar is 200 μm and image width is 1.4 mm

Tight, indenting, truncating, or interpenetrating grain boundaries (TITIGB)

Tight, indenting, truncating or interpenetrating grain boundaries (TITIGB) are indicators for the operation of solution-precipitation processes (pressure solution, overgrowth, fluid-assisted grain boundary migration) between two adjacent, loaded grain surfaces in a porous material, when evidence of crystal plastic deformation is absent at these sites (i.e., no local deformation/slip bands, no local subgrains). They can be formed by fluid-assisted grain boundary migration (recrystallized grains at grain boundaries) and overgrowth at pore walls (see below). The grain boundary migration is likely driven by the reduction of dislocation density. Solution-precipitation is a combined process in the field of deformation by diffusive mass transfer (DMT). DMT is generally facilitated by fine grain

size and involves material removal, transport and deposition at stresses too low to drive fracturing or dislocation motion plus lattice distortion /BLE 02/. Fluid inclusion planes within natural halite rock, as a relic of former, now healed grain boundaries, demonstrate that DMT finds small but sufficient amounts of soluble fluid to be active under natural conditions /URA 86/, /URA 08/. The term solution-precipitation-creep (or “pressure solution creep”) is sometimes referred to as fluid-enhanced, diffusion-driven grain boundary deformation /SPI 86/, /SPI 89/, /SPI 90/. The driving force for pressure solution creep (mass transfer around grains) is provided by (small) differences in the surface potential of the solid on the grain-scale. This depends on the local stress in such a way that solid dissolves at grain contacts under high intergranular stress, then diffuses to and precipitates at the interfaces or pore walls under lower normal stress. Compaction creep results. Moreover, a difference in mean stress, between one region of material and another, causes dissolution and a higher concentration of solute solution in the more highly stressed regions, versus a lesser one in stress shadow regions, hence generating an ionic diffusion over a larger length scale. This diffusion, in turn, leads to precipitation in stress shadow regions, where the solution phase becomes supersaturated. In salt, these and other dissolution-precipitation effects need only very small quantities of water to be present on grain boundaries in the system (a few tens of ppm /HEE 05a/). Correspondingly, only in carefully dried laboratory material (< 5 ppm water) do solution-precipitation processes not operate in NaCl /HEE 05a/. The amount of DMT-derived strain is coupled to grain surface area. The activity of pressure solution accordingly increases rapidly with decreasing grain size (intergranular pressure solution creep rate increases with the inverse cube of the grain size), as well as increasing with increasing temperature, moisture content and applied stress, at least until other processes, such as dislocation creep become dominant /SPI 86/.

We found TITIGB in all samples. Fig. 4.17 to Fig. 4.19 show examples in samples S2, S3 and S4.

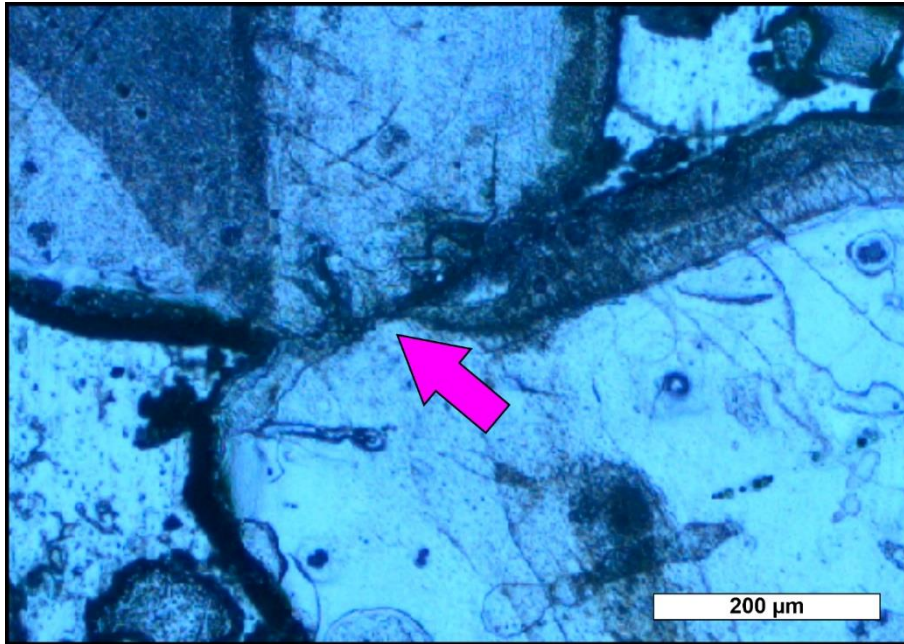


Fig. 4.17 Tight, indenting/truncated grain boundary (magenta arrow) in sample S2. Scale bar is 200 μm and image width is 0.8 mm

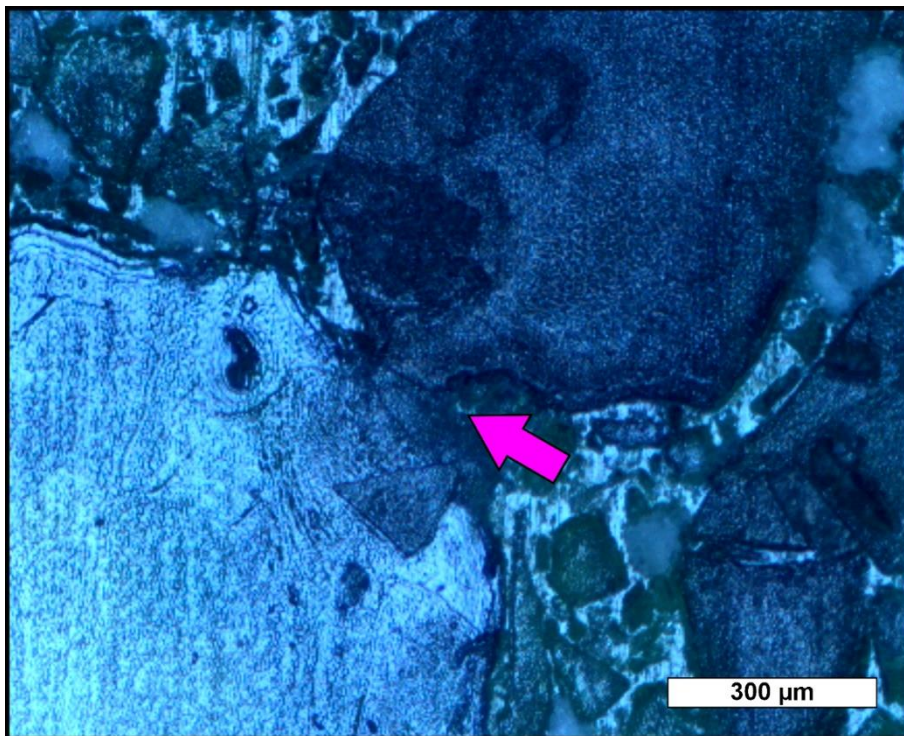


Fig. 4.18 Tight, indenting/truncated grain boundary (magenta arrow) in sample S3. Scale bar is 300 μm and image width is 1.3 mm

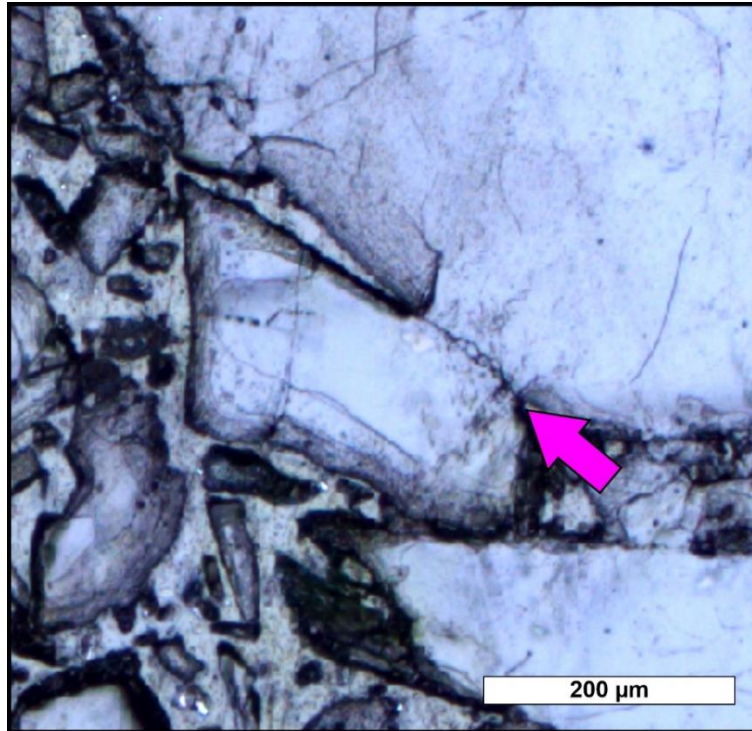


Fig. 4.19 Tight, indenting/truncated grain boundary with small, recrystallized grains (magenta arrow) in the sample S4. Scale bar is 200 μm and image width is 1 mm

Recrystallized grains

Recrystallized, idiomorphic grains with little or no visible internal substructures are characteristic of fluid-assisted recrystallization /URA 86/, /PEA 01/. These can be observed in all compacted samples (Fig. 4.20, Fig. 4.21, Fig. 4.22) but were not seen in the loose starting material (S1). They occur in particular next to heavily strained regions, such as within a set of dense deformation/slip bands along grain-grain contacts. Recrystallization is enhanced by the presence of already low concentrations of fluid /SPI 86/, /SPI 90/, /HEE 05a/.

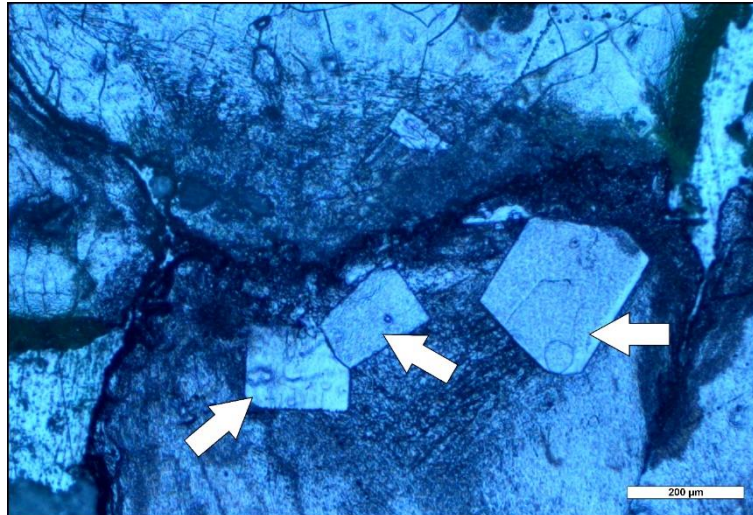


Fig. 4.20 Contact area between two large grains with recrystallized, microstructure-free grains (white arrows) in sample S2. Image width is 1.3 mm

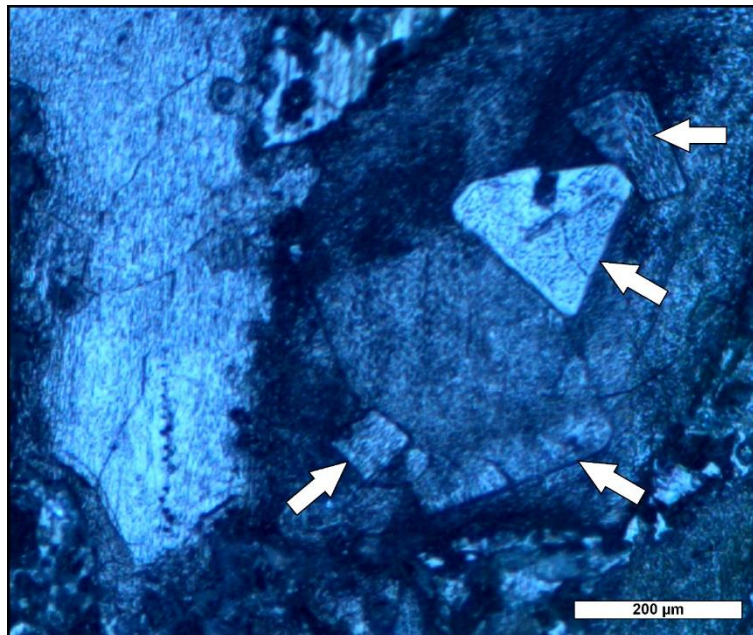


Fig. 4.21 Contact area between two large grains with recrystallized, microstructure-free grains (white arrows) in sample S3. Image width is 0.7 mm

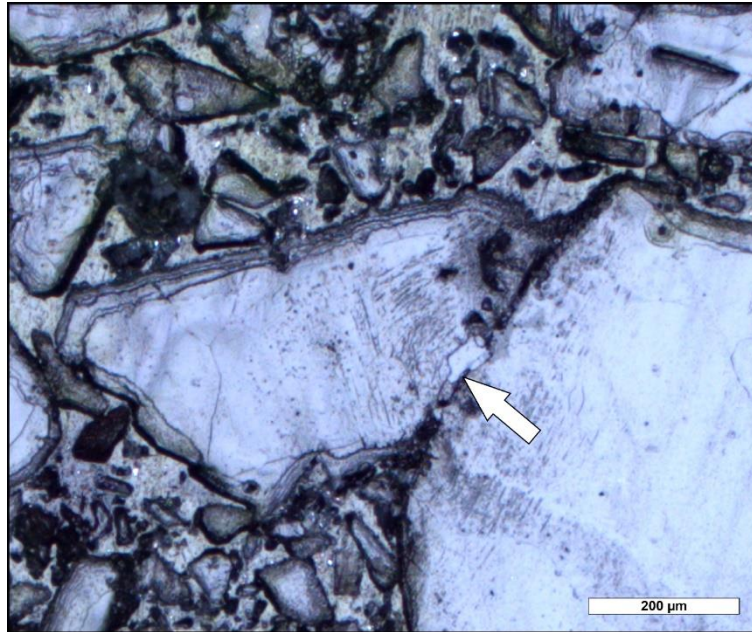


Fig. 4.22 Truncated contact area between two large grains with recrystallized, microstructure-free grains (white arrows) in sample S4. Image width is 0.8 mm

4.2.2.3 Semi- quantitative evaluation of the microstructural indicators

We subjectively quantified the abundance of the above-described indicators. The bar chart in Fig. 4.23 illustrates the complex interplay of the many deformation mechanisms. However, we would like to stress that the abundance of a given deformation process indicator does not necessarily reflect its contribution to the overall sample deformation, i.e., compaction.

A firm relation between the indicators and the compaction test procedures cannot be established. This drawback is due to (1) too many of the available indicators are already present in the loose crushed salt and (2) only marginal differences in abundancies were found between the compacted samples.

However, sample S2 (originating from test TUC-14) seems to exhibit slightly fewer fractures, less dense slip bands and fewer/less bent grains than the other samples. We discuss the potential cause for this marginal difference below.

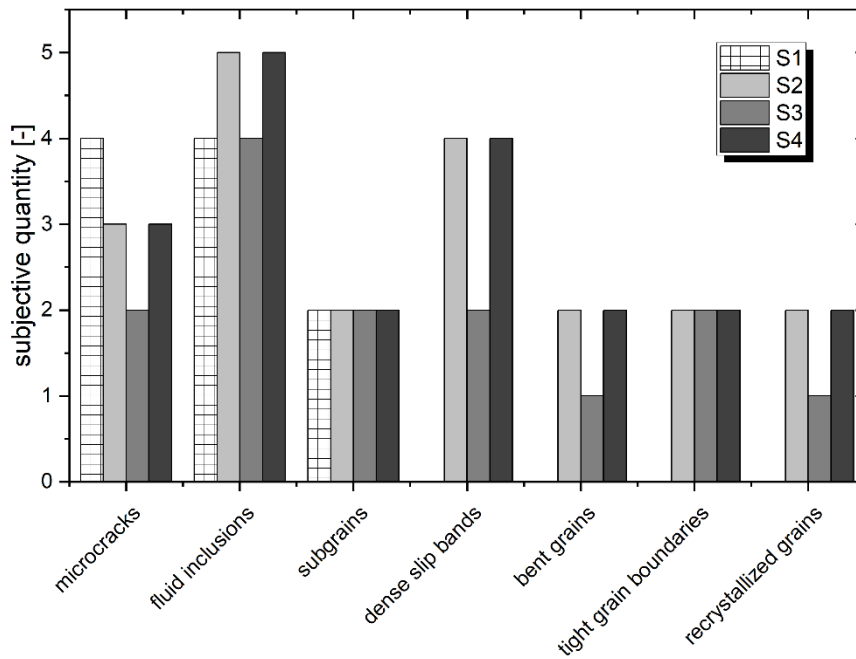


Fig. 4.23 Results of semi-quantitative (subjective) evaluation of microstructural indicators for deformation mechanisms. The term “tight grain boundaries” refers to tight, indenting, truncating or interpenetrating grain boundaries /SVE 22/

4.2.2.4 Statistical evaluation of segmented grains

A total of 9,715 grains were segmented by hand (S1 = 1547; S2 = 2677; S3 = 5491). The segmentation provided data on area (μm^2), perimeter (μm), max. length (μm) and max. width (μm) of each segmented grain, the aim of this feat being to identify differences in GSD and GSP that have being imposed by laboratory compaction.

Grain size distribution (GSD)

Fig. 4.24 shows in log-log space the number of grains or grain frequency normalized to individual bin width and AOI vs. the grain size. The diagram exhibits the lower limit of resolution at a grain area of 0.001425 mm^2 ($\log(S_i) = 3.9 \mu\text{m}^2$ in Fig. 4.24), below which many grains remain undetected, leaving their corresponding bins underrepresented. Therefore, we only used grains larger than this threshold for the following statistical analysis. An individual sample's slope of regression gives the relation between its small to large grains, i.e., its order of self-similarity D (S1: $D = -1.56$; S2: $D = -1.55$; S3: $D = -1.73$). The compacted samples' D -values are slightly larger than of those of the loose crushed salt, suggesting a rework of larger grains into smaller ones at all scales, such that a self-similarity is still maintained.

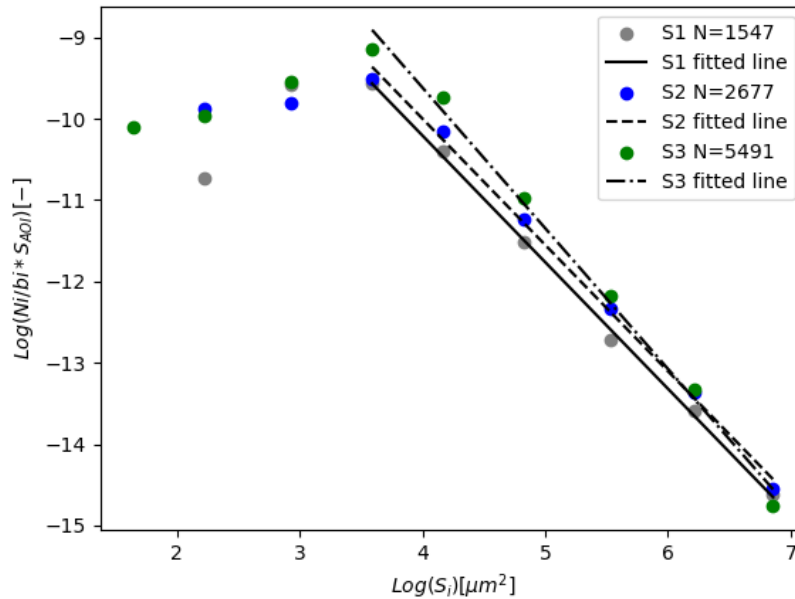


Fig. 4.24 The slopes of the regression lines (S1: $D = -1.56$; S2: $D = -1.73$; S3: $D = -1.55$) illustrate the differences in self-similarity of the samples' grain sizes

Next to the fractal-dimension approach, we present a plot showing the cumulative area of the grains vs. grain size (Fig. 4.25). Therein, the cumulative area is normalized for the total AOIs area. This plot type allows to relate the segmented GSDs to the generalized sieving curve above (Fig. 4.1) more easily, except that the x-Axis shows precise grain sizes instead the mesh width of sieves. Note that the cumulative curves are not summing up to a total of 100 area-%, as porosity and non-segmented grains need to be considered, too. The non-segmented area is per sample: S1 = 48 %; S2 = 35 %; S3: 31 %), with many grains being too small to be recognized and some larger ones that do not fall completely within the AOI, being not considered in the grain size analysis. Moreover, the compacted samples have a fair amount of porosity as seen from the calculated porosity due the compaction of the samples (S1 = loose material; S2 = 15 %; S3 = 14 %).

Deliberately ignoring these area misfits, we can see a firm shift to an increase in smaller grains in the samples S2 and S3 compared to the sample S1 (Fig. 4.24, Fig. 4.25).

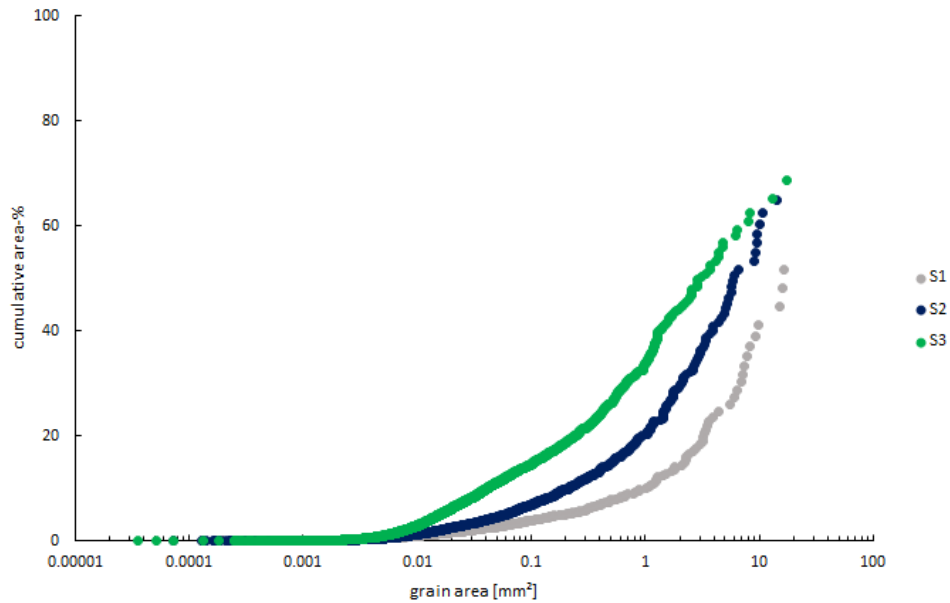


Fig. 4.25 Cumulative GSD of the three investigated AOIs

Grain shape parameters (GSP)

Two GSP were calculated: (1) normalized axial ratio (AR_{Norm} ; Equ. 4-3) and circularity (Equ. 4-2). Fig. 4.26d gives a general idea of the GSPs informative value by illustrating the ratio of the GSPs for some generic shapes.

The results for the samples S2 and S3 look quite similar to the result for the raw material (S1). However, we observed a shifting to lower circularities in both compacted samples, compared to the raw material. The peak of the data stays more or less at similar regions in the accompanying histograms. These plots suggest a test induced (i.e., compaction-induced) trend towards more angular grains.

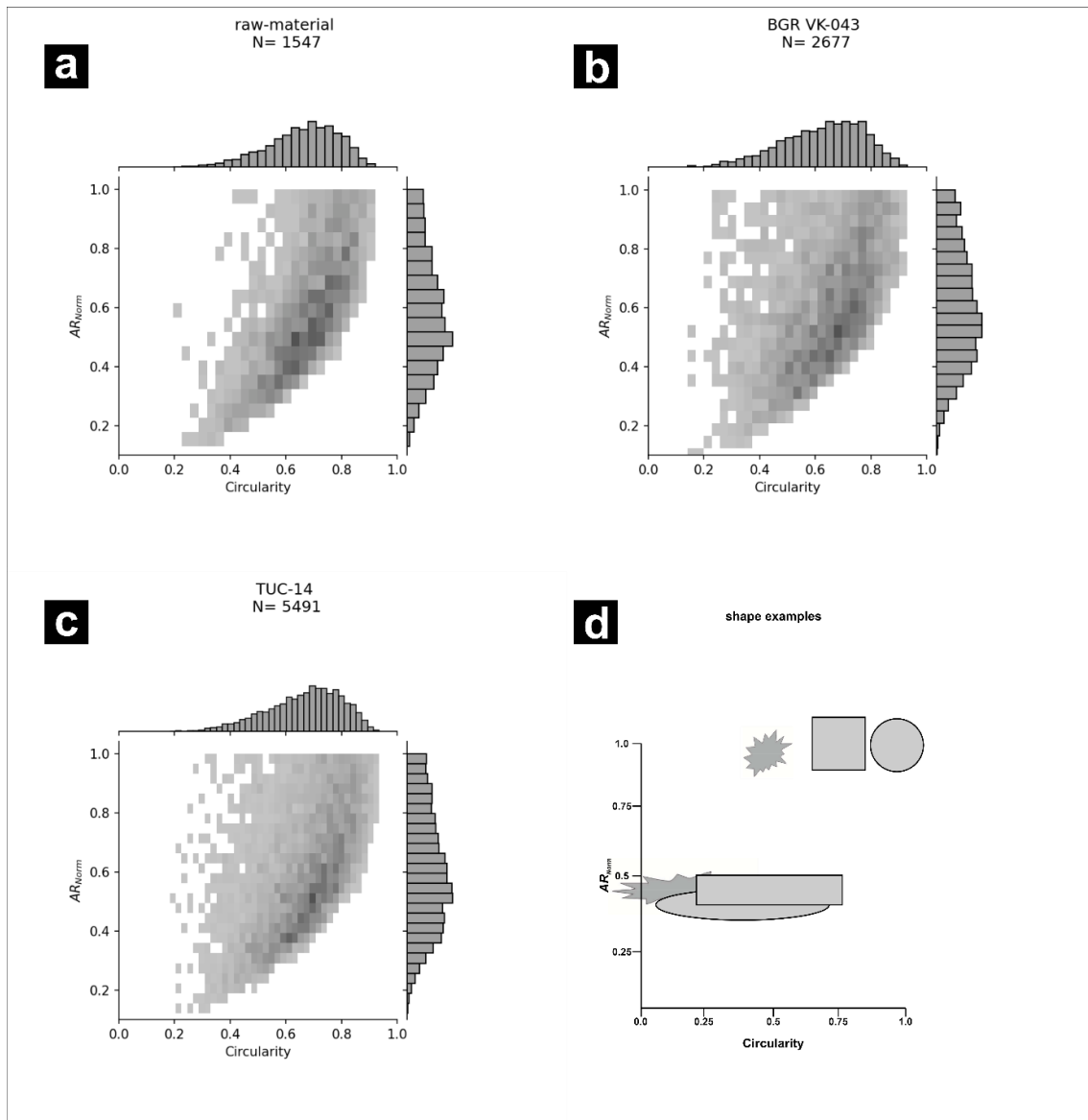


Fig. 4.26 Grain size parameters (GSP) axial ratio (ARNorm) and circularity calculated and plotted for the samples S1 (a), S2 (b) and S3 (c). Darker color illustrates higher quantity of grains. Shape examples (d) GSPs' ratio of some generic shapes (for illustration)

4.2.3 Discussion

In the introduction to this chapter, we formulated the following three working hypotheses: (1) the microstructural indicators for deformation mechanisms differ in the differently pre-compacted samples, (2) the grain size distribution (GSD) and grain shape parameters (GSP) differ in the differently pre-compacted samples (S2 and S3) and (3) the pre-compaction methods alter the GSD and GSP of the loose crushed salt (S1). Only subtle

differences between the samples were found (Fig. 4.20). An exception are the 3 – 5 cm wide lenses of fine material that are solely present in sample S4 (Fig. 4.2 – Fig. 4.7).

No compaction test caused an explicit, dominant abundance of any microstructural deformation indicator that can be related to strain contribution. Hence, it was not possible to point out a dominant deformation mechanism that governs the laboratory-driven compaction (Fig. 4.23). Moreover, a firm relation between microstructural appearance to sample origin, i.e., compaction type (S2 = oedometric, S3 = plain strain, S4 = oedometric) was not discernible.

The GSD and GSP are similar for all samples (Fig. 4.24). However, a subtle trend in grain size decrease with increasing compaction speed can be spotted for the samples S2 and S3 (28 days and 2 days, respectively, Tab. 4.1) and both pre-compacted samples show a grain size reduction compared to the loose material (S1). We interpret this reduction to be caused by brittle grain fracturing, which was observed in both cases.

Albeit, the sample S3 (originated from TUC-14) shows a more distinct grain size reduction, it shows fewer intragranular, fewer, and less dense slip bands and bent grains, compared to S2 and S4. This might be due to reduced stress on the grain-grain contacts, as the applied force is (1) acting in plain-strain, being distributed over a larger number of grains simultaneously instead of applying the force over the smaller area of the axial piston surfaces. This force distribution allowed (2) a much smaller maximal stress during compaction (S3: $\sigma_{\text{radial}} = 5 \text{ MPa}$ versus S2 and S4: $\sigma_{\text{axial}} = 20 \text{ MPa}$; Tab. 4.1).

The median of grain circularity is quite similar for all samples. However, the pre-compacted samples (S2 and S3) show more grains with a less circular shape than the loose material (S1) (Fig. 4.26). We interpret this lowered circularity (the loose material is a priori not particularly circular) as a product of (further) grain breakage during the laboratory compaction tests.

To a minor part, angular and less-circular grain shapes detected in the analysis can also be explained by recrystallization. Idiomorphic, recrystallized grains were observed in all compacted samples (S2, S3 and S4).

Please note that within the laboratory compacted samples (S2, S3 and S4) a complex interplay of several deformation mechanisms has been identified, with severe deformations localized particularly at grain edges. For instance, the dense deformation/slip

bands manifest quite large differential stresses (> 10 MPa, /SPI 86/) at the grain contacts, while subgrain sizes within the grains attest similarly low differential stresses for all samples (3.8 – 4.9 MPa). This finding suggests that these subgrains are inherent to the starting material and of tectonic origin. We propose that in a few cases, the enriched dislocation density within the deformation/slip bands even resulted in the dynamic recrystallization of new grains, e.g., in Fig. 4.20, Fig. 4.21 and Fig. 4.22. It remains untested if the recrystallization occurred during or after the compaction (~10 weeks of storage, versus 2 days to 4 weeks of test duration).

4.2.3.1 Laboratory test versus real-case emplacement of crushed salt

For in-situ, long-term compaction, after initial phases of grain settlement, contact-stress built-up and accompanied stress-redistribution, we expect less differential stress at the grain edges than in laboratory tests. This condition must result from the much slower deformation of the converging cavity walls (about $1 \cdot 10^{-10} \text{ s}^{-1}$ at early stages of convergence, /BEC 99/, /KRÖ 09/), in which viscous mechanisms govern, such as dislocation creep and pressure solution creep. Particularly for the relatively small-grained crushed salt and based on the pressure solution compaction law and deformation mechanism maps for salt constructed by /SPI 90/ (or the low creep rate data published by /BÉR 19/), we expect pressure solution to dominate the compaction behavior (see also Section 4.4). At the same time, dislocation creep might act in earlier stages of the real-case compaction, particular in regions of higher differential stress and convergence rate, such as in the cavity corners (Section 5.4).

Studies of pure pressure solution suggest the formation of much less angular grains that have a xenomorphic, pore space-consuming appearance /SPI 93/, /URA 07/. Such xenomorphic grains should exhibit a larger surface-to-volume ratio than broken grains from (rapid) laboratory studies, which is a promising line of research for upcoming compaction tests exploring pressure solution.

Tight, indenting, truncating or interpenetrating grain boundaries (TITIGB) are indicators for pressure solution and grain boundary migration (GBM). We observed them in every pre-compacted sample. Pressure solution is expected to be the main deformation mechanism in small grains /SPI 86/, /SPI 90/. Since smaller grains and moisture will be present in a real case scenario, it is expected that pressure solution will be a part of the active deformation mechanisms in a real case. If smaller grains accumulate locally, it can easily become the dominant deformation mechanism at those areas. This phenomenon

is clearly visible in Fig. 4.7, where the boundaries of fine grains in the accumulation lenses of sample S4 show many TITIGB indicators.

Just as for undisturbed, in-situ rock salt, diffusive mass transfer (DMT) is a relevant, relatively rapid deformation mechanism in crushed salt, too, even at a small grain size /SPI 90/. Even quick laboratory experiments (> 2 days) show DMT-indicators, such as truncated grain boundaries and idiomorphic recrystallized grains within dense bands of dislocations at grain contacts (see sample S3). Bending of salt crystals by crystal plasticity was described by /JOF 24/. They concluded that either temperatures above 200 °C or moisture must be present for bending without brittle failure. Unfortunately, the minimal threshold in moisture content for bending has not been identified, so we must consider grain bending as likely to occur in a real case scenario, too. However, bent grains can also originate from the starting material, as has been demonstrated for samples from Gorleben /KÜS 10/ and Morsleben /MER 23/.

Recrystallized grains were observed in the contact areas between larger grains (Fig. 4.20, Fig. 4.21, Fig. 4.22). Dynamic recrystallization is supported by the presence of moisture /SPI 86/, /SPI 90/, which indicates it will be present in a real case scenario.

We observed at least two test-caused indicators (dense deformation/slip bands and grain breakage), which we do not expect to be widely present much in a real case scenario.

4.2.4 Summary and Outlook

We investigated four crushed salt samples for their microstructural deformation indicators. The samples suffered differing load paths: (S1) loose crushed salt, (S2) oedometric compacted crushed salt, (S3) plain-strain compacted crushed salt and (S4) oedometric compacted crushed salt for a large oedometric cell (0.514 m in diameter and 0.780 m in height /KOM 20/). Please refer to Section 3.2 for detailed descriptions of the pre-compaction procedures. All sample material originates from the Sondershausen mine. A-priori to the tests, the material in samples S1 and S2 was mixed from 10 grain size fractions (Fig. 4.2). The material in the samples S3 and S4 was used as received (three grain size fractions, Fig. 4.2).

Our analyses were twofold: (1) qualitative impression on grain substructures and (2) quantitative measurement on GSD and GSP.

By qualitative analysis, we found:

- All samples show microstructural deformation indicators that are relicts either from geological evolution or from underground mining. Hence, attesting a strict laboratory cause of the observed structures like fluid inclusions, fractures and subgrains found is not possible. Subgrain piezometry indicates the same paleodifferential stress for all samples (~ 4.3 MPa), regardless of the laboratory loading style.
- Microstructural deformation indicators at individual grain-grain contacts, however, are likely caused by the laboratory tests. Those indicators are: dense deformation or slip bands, bent grains (which can also be relicts of the starting material), tight indenting, truncating or interpenetrating grain boundaries (TITIGB) and recrystallized grains.
- The differing laboratory compaction tests produced the same types and similar abundance of indicators at grain-grain contacts.

By quantitative analysis we found:

- All three quantitatively investigated samples display a roughly similar GSD and GSP, with a trend for grain size reduction by all compaction methods. This reduction is accompanied by a change towards less circular grain shapes.

We demonstrated the strong similarity of microstructures resulting from the different compaction tests.

In the in-situ real case, the compaction rates are thought to be in the range of $1 \cdot 10^{-10} \text{ s}^{-1}$ /KRÖ 09/, /KRÖ 17/ and below. Hence, we suspect much less cataclastic deformation than in the rather rapid laboratory pre-compaction tests. Significant deformation by dislocation movement is likely for regions of higher differential stress, i.e., in larger grains in the excavation damaged zone (EDZ). In stress shadow regions, we suspect pressure solution to be the dominant deformation mechanism, in particular, in the finer grains of the backfill material and when the backfill is supported by fine matrix.

However, more work is necessary to justify our assumptions and conclusions. This endeavor might be achieved in two ways: (1) by comparison to real-used backfill and (2) by a set of single-stepped laboratory experiments on juvenile salt grains, i.e., without any a-priori substructures.

To date, real-used backfill with a known a-priori microstructure is lacking. However, recent sampling of a 40-year-old backfilled gallery provides encouraging primary results, with a strong abundance of pressure solution indicators. Moreover, the current backfill emplacement within the Sondershausen mine seems promising for a later analysis /SCH 22b/.

Juvenile salt grains have been investigated in the past /SPI 90/, /FRA 90/. However, with the focus on general salt rheology and less to quantitatively understand the mechanisms in compaction behavior of crushed salt.

4.3 The impact of moisture content, compaction speed and compaction stress on microstructure (Sandia)

When crushed salt includes small amounts of moisture, solution precipitation processes, such as fluid-assisted creep, help reduce dislocation densities in the crystal lattice and influence grain boundary migration leading to recrystallization /URA 07/. Fluid-assisted creep, or the more commonly known as pressure solution, is described above (Section 4.2.2 in this report). It enhances the densification of granular salt at ambient temperature /SPI 90/, /CAL 96/, /CAL 98/. Hence, added moisture in synthetic, juvenile salt /URA 07/ and natural granular rock salt /URA 86/, /BRO 96/ has shown rapid recrystallization at grain boundaries from fluid-assisted creep.

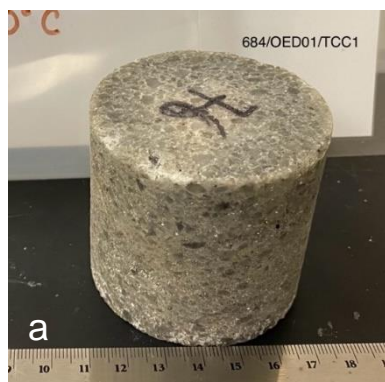
4.3.1 Method

To determine effects of added moisture to compaction, multiple samples from IfG and TUC were sent to Sandia over the course of the KOMPASS-II phase and investigated for microstructural deformation indicators, such that respective deformation mechanism can be derived, i.e., Tab. 4.2. As described in /KOM 20/ and as well in Section 3.2.2, IfG samples were pre-compacted oedometrically (“Pre-comp Oedom.”), in big cell vessels ($d = 500$ mm and $h = 620$ mm). Following pre-compaction, sub-samples (nomenclature “TCC”) were cored from OED01 (dry big cell) and subjected to long-term isostatic compaction (“Comp Isos.”) tests at various conditions (see /KOM 20/, Section 4.6.2.1 for additional test details). Two original block samples from the big cell pre-compaction tests, OED01-dry and OED03-wet, were also obtained from IfG. Additionally, samples were obtained from TUC of pre-compacted plain strain tests (Section 3.2.3) at shorter

durations. For samples with added moisture, pure water at associated weight % was added. Sample details are summarized in Tab. 4.4 and shown in Fig. 4.27 a – g.

Tab. 4.4 Summary of samples and associated experimental test conditions

Partner	Sample	Test Type	Added moisture	Temperature Range (°C)	Stress Range (MPa)	Total Duration (days)	Initial porosity (%)	Final porosity (%)
IfG	684/OED01/TCC1	Pre-comp Oedom. → Comp Isos.	dry	25 to 60	5 to 20	197	14.39	11.09
	684/OED01/TCC2	Pre-comp Oedom. → Comp Isos.	dry	25 to 60	10 to 30	197	15.6	7.77
	684/OED01/TCC3	Pre-comp Oedom. → Comp Isos.	dry	25 to 60	1 to 10	197	12.9	11.7
	684/OED01/TCC5	Pre-comp Oedom. → Comp Isos.	wet (1%)	25	5 to 20	28	16	1.3
	684/OED01/TCC6	Pre-comp Oedom. → Comp Isos.	wet (1%)	25	1 to 10	28	16.21	0.88
	684/OED01/Dry "Big Cell" Block	Pre-comp Oedom	dry	25	0.4 to 8	28	33.75	12
	684/OED04/Wet 3 "Big cell" Block	Pre-comp Oedom	wet (1%)	25	0.4 to 12.8	28	33.3	2
TUC	TUC14	Pre-comp Plain strain	wet (0.5%)	25	5	2	26	14
	TUC15	Pre-comp Plain strain	wet (0.5%)	25	5	2	27	14
	TUC18	Pre-comp Plain strain	dry	25	2	2	22	17
	TUC21	Pre-comp Plain strain	wet (1%)	25	5	4	27	18



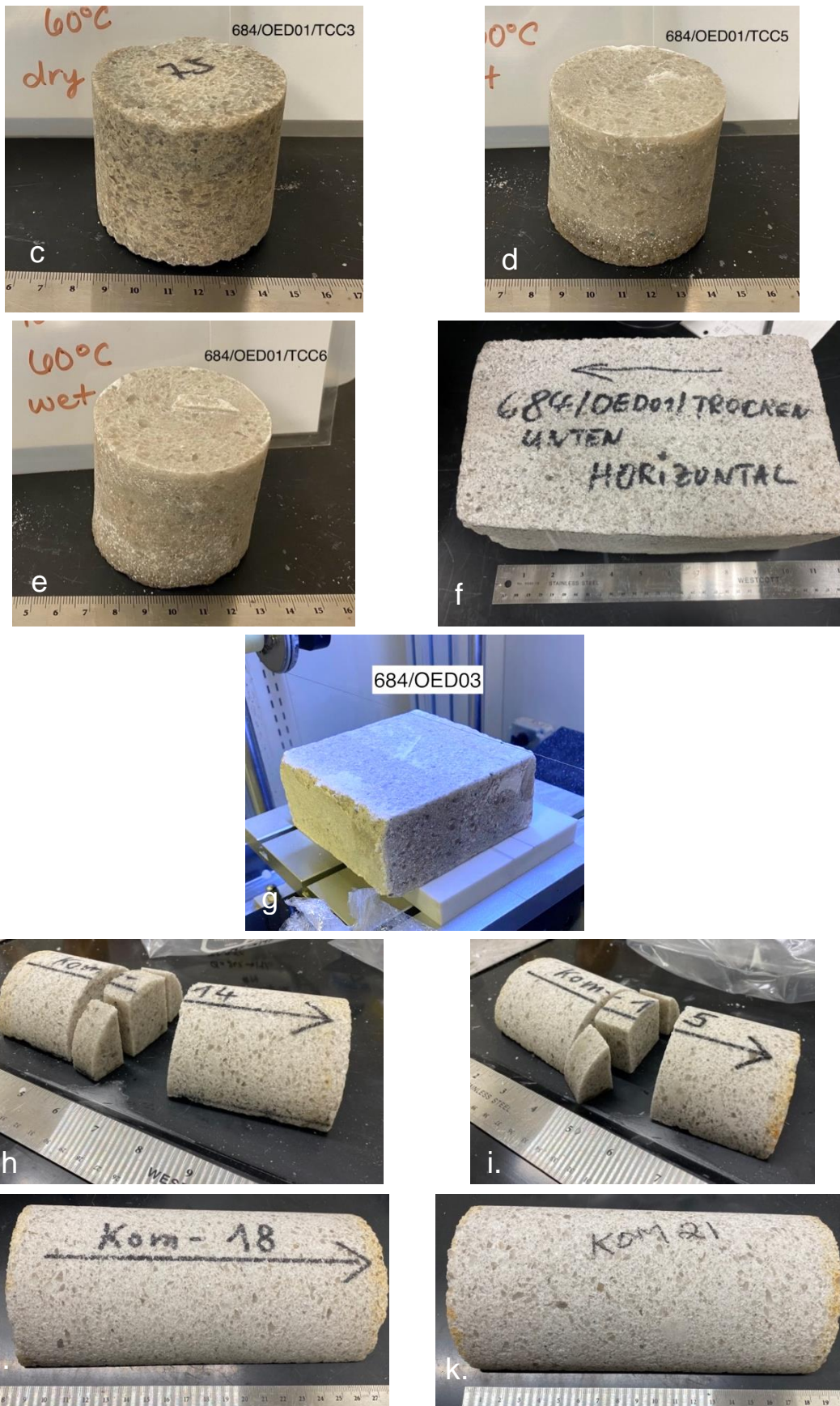


Fig. 4.27 Pre-compacted and compacted granular salt samples from oedometric tests at IfG (a through g) and triaxial tests at TUC (h through k)

4.3.1.1 Sample preparation

Samples with diameters less than 10 cm were cut into billets, typically from center locations, using a low damage IsoMet1000 saw (Buehler) with isopropanol as the cutting fluid. Larger sample blocks from big oedometer (IfG) were cut using a low damage diamond wire saw (MTI Corp.), also with HPLC grade isopropanol as the cutting fluid. Each billet was then vacuum impregnated with a two-part epoxy doped with rhodamine B dye for contrast, glued to a glass slide, and cut a few mm thick. A semi-automatic grinder/polisher (Buehler Ecomet) was used first with 400 grit diamond embedded resin plate for coarse grinding, followed by 1000 grit for fine grinding, and polishing with 9, 3 and $\frac{1}{4}$ μm diamond suspensions all with alcohol-based lubricant (Struers). After polishing, thick sections were also etched in a solution of methanol saturated with PbCl_2 for several seconds followed by submergence in butanol for several seconds and thoroughly dried with compressed air.

4.3.1.2 Microscopy

All thick sections were examined under a ZEISS AxioScope 5 optical microscope, equipped with ZenCore imaging software, in both reflected and transmitted light (RL, TL). Reflected light was utilized to observe grain sizes, shapes, boundaries, and pore structures, where transmitted light to view fluid inclusion planes and bands with any attributable microcracks in the grain structure from deformation.

4.3.2 Microstructure results

To determine effects of moisture on compaction, it is important to perform a direct comparison of microstructures of wet and dry samples with similar magnifications, light source, and etched surfaces. Additionally, comparing samples with the least amount of differing test conditions is key to associate the cause of the alteration (ideally only one). Therefore, the following micrographs are grouped with one or two changed test conditions (moisture addition and time) and arranged side-by-side to show examples of grain shapes, fluid inclusions, and subgrain features.

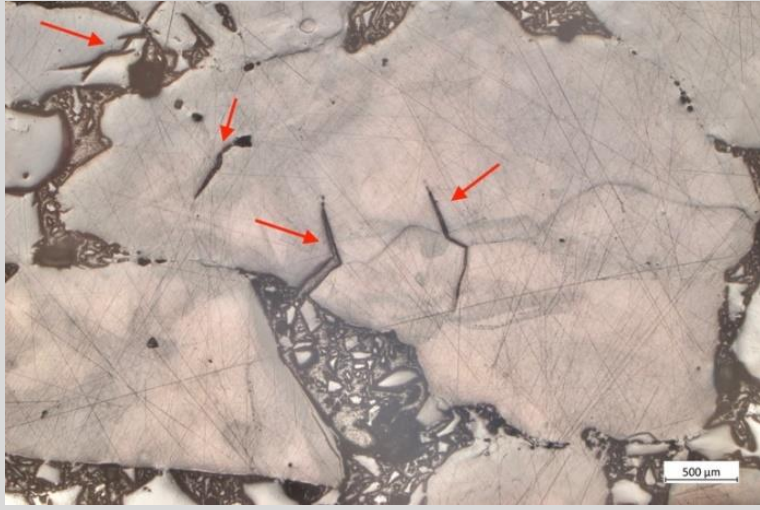
Annotations are provided to highlight several deformation indicators and have the following color key:

- Red → fractures (intragranular, transgranular, intergranular)
- Blue → fluid inclusion bands and arrays
- Green → tight, indenting, truncating and intruding grain boundaries (TITIBG)
- Yellow → areas of dense deformation/slip bands
- White → recrystallized grains

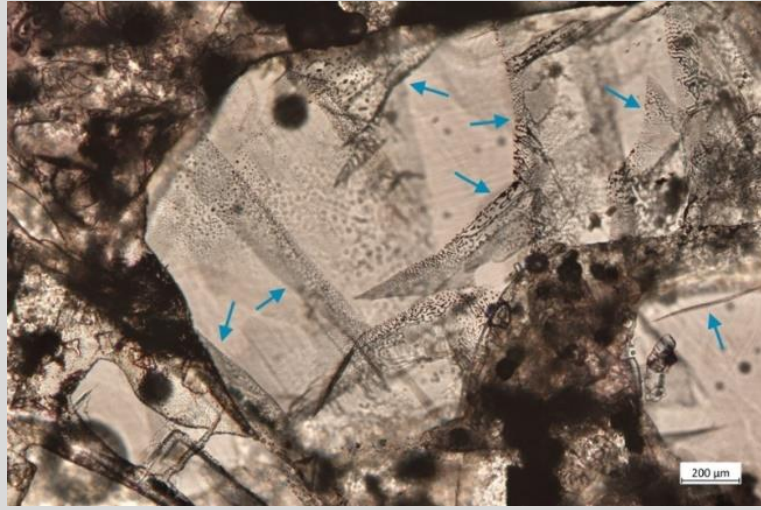
4.3.2.1 IfG “Big Oedometer cell” pre-compaction blocks

Photomicrographs from the “Big Oedometer cell” pre-compaction blocks are shown in Fig. 4.28a – h. The left column are images from the “dry” (~ 0.1 w.-%) pre-compacted sample, and on the right, with 1 % added moisture (“wet”). The “dry” sample experiences angular grain shapes and multiple areas of cataclasis and grain breakage with intragranular fractures (Fig. 4.28a) along with bands of fluid inclusions (Fig. 4.28c). In contrast, the “wet” sample has more rounded grain shapes while grain contacts indicate pressure solution creep with tightly fitting grain boundaries and areas of overgrowth (Fig. 4.28b). Fluid inclusion bands are also evident (Fig. 4.28d). An example of an interpenetrating grain in the “wet” sample is shown in Fig. 4.28f, promoted by plasticity-coupled dissolution-precipitation creep /SPI 93/ typically seen in “wet” samples. Etched surfaces can be seen in Fig. 4.28e,g and h. The “dry” sample experiences crystal plastic deformation, marked by areas of dense slip bands (Fig. 4.28e), but also areas of recrystallized, dislocation-free grains (Fig. 4.28g). Fig. 4.28h displays a very tight grain boundary at center in the “wet” sample with no apparent deformation/slip bands in the substructure. Fluid-assisted grain boundary migration is evident by recrystallized, cubic, strain-free grains.

684/OED01/Dry "Big Cell" Block

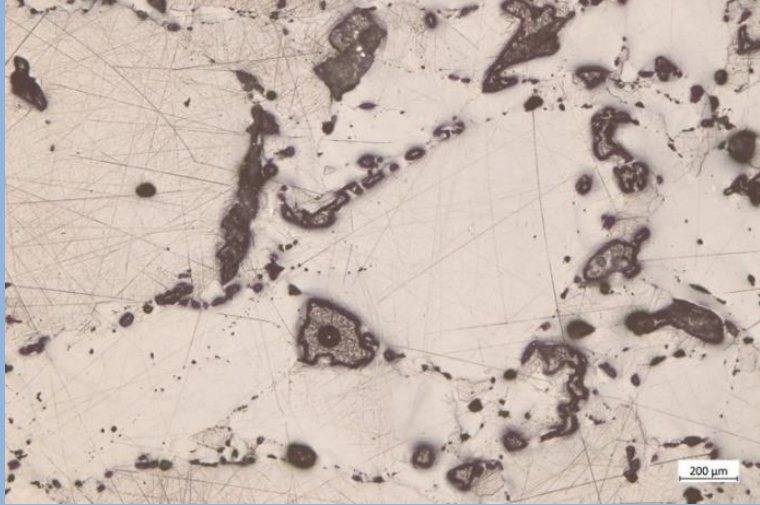


a

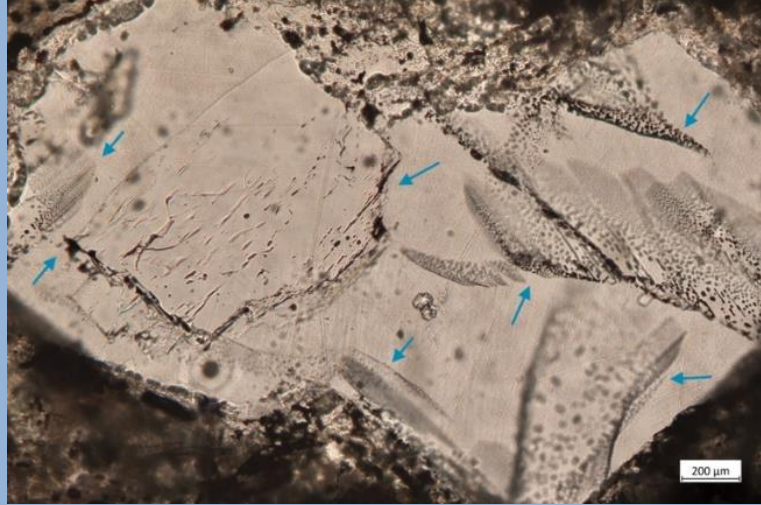


c

684/OED04/Wet 3 "Big Cell" Block



b



d

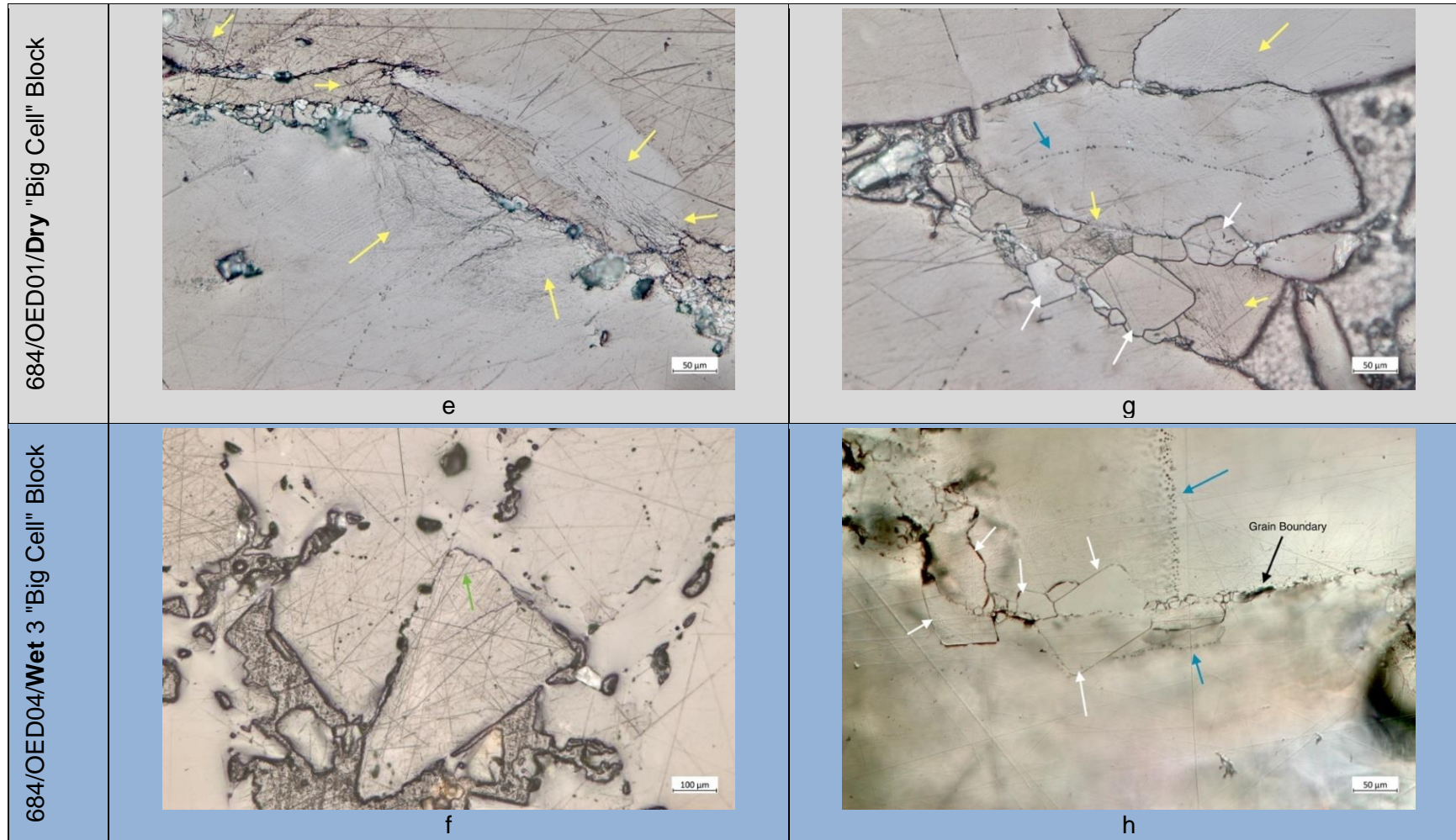
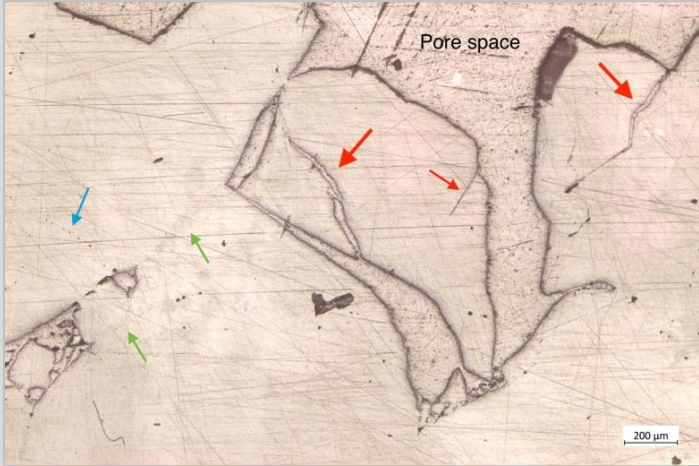
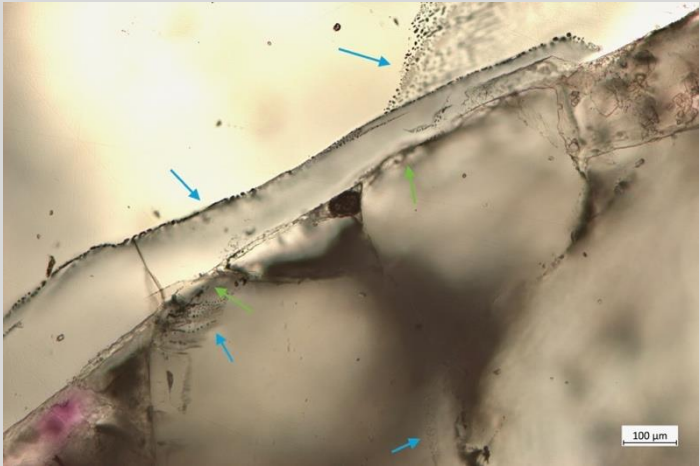
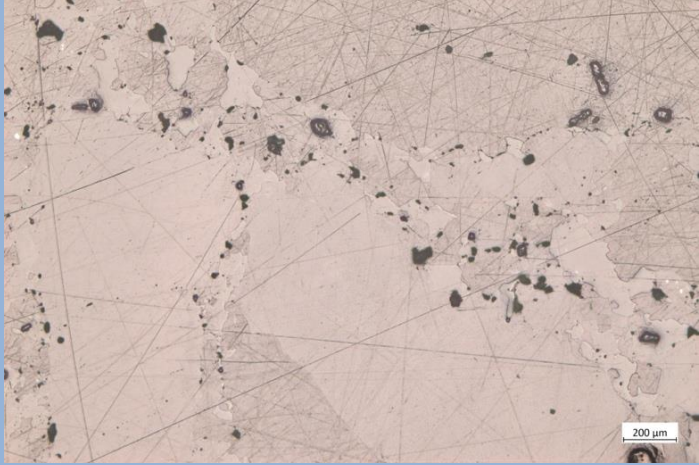
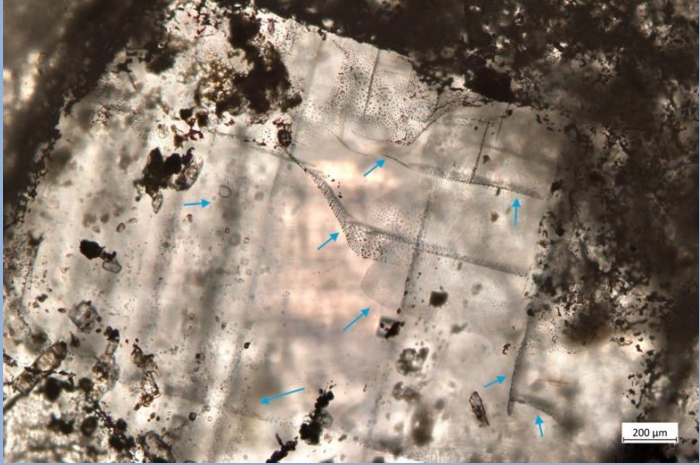


Fig. 4.28 Photomicrographs from “Big Cell” pre-compacted samples under “dry” (a, c, e, g,) and “wet” (b, d, f, h) conditions. Arrows: fractures (red), fluid inclusions (blue), TITIGB (green), deformation bands (yellow), recrystallization (white)

4.3.2.2 IfG isostatic long-term compaction samples

The microstructures of the long-term compaction samples from IfG are compared in Fig. 4.29, Fig. 4.30 and Fig. 4.31. It is important to note that the “dry” samples were subject to stresses much longer than “wet” samples; 197 days for “dry” and 28 days for “wet”, porosity 11.7 % and 0.88 %, respectively. Nonetheless, the “wet” samples reached a much lower porosity in a shorter time and had different deformation indicators apparent in their microstructure. For samples compacted at 10 MPa (Fig. 4.29a – h), the “dry” sample still displays intragranular fractures with angular shaped grains (Fig. 4.29a), but at some grain contacts, diffusion-driven grain boundary deformation enhanced by natural fluid content (Fig. 4.29c) can be seen. The microstructure of the “wet” sample shows mostly isolated pore spaces (Fig. 4.29b) with no apparent grain fractures, more rounded grain shapes, and tight grain boundaries. Fluid inclusions are present in both samples (Fig. 4.29c and d).

Etched surfaces are presented in Fig. 4.29e – h. Similar to the “dry” pre-compacted sample, the “dry” long-term compacted sample experiences areas of dense deformation/slip bands with cross-slip controlled dislocation creep (Fig. 4.29e and g). Yet, new strain-free grain areas are seen, showing static recrystallization by fluid-assisted grain boundary migration. In particular, Fig. 4.29g displays two grains squeezing and plastically deforming the center grain. Over time, this deformation produces dislocation glide/creep mechanisms, followed by recrystallization from natural fluid (pressure solution). In the wet long-term compacted sample, the substructure is more recovered, with little evidence of stressed slip bands, and more strain-free grain areas (dynamic recrystallization).

<p>6 TCC3 ("dry", 10 MPa)</p>	 <p>Pore space</p> <p>200 μm</p> <p>a</p>	 <p>100 μm</p> <p>c</p>
<p>684/OED04/Wet 3 "Big Cell" Block</p>	 <p>200 μm</p> <p>b</p>	 <p>200 μm</p> <p>d</p>

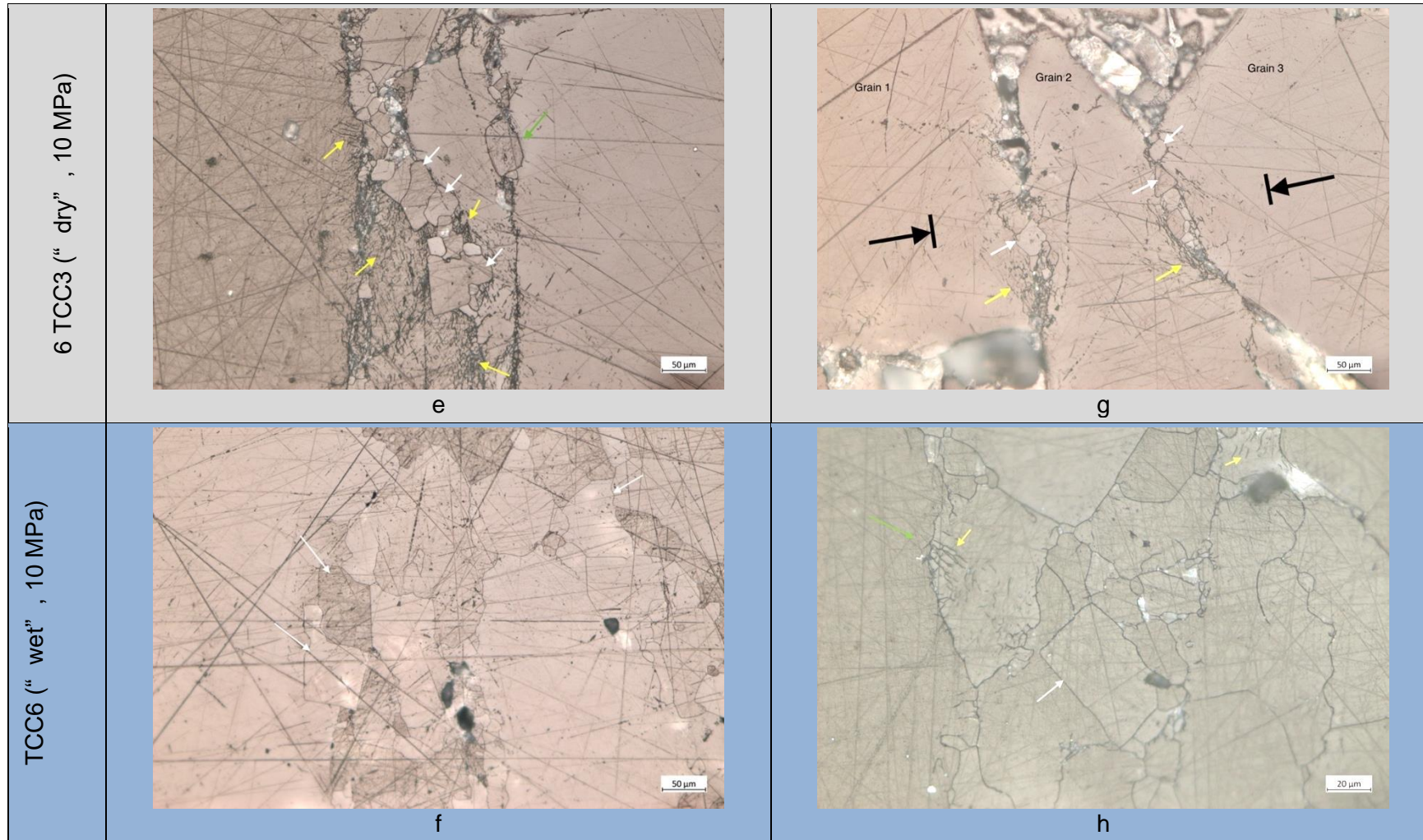
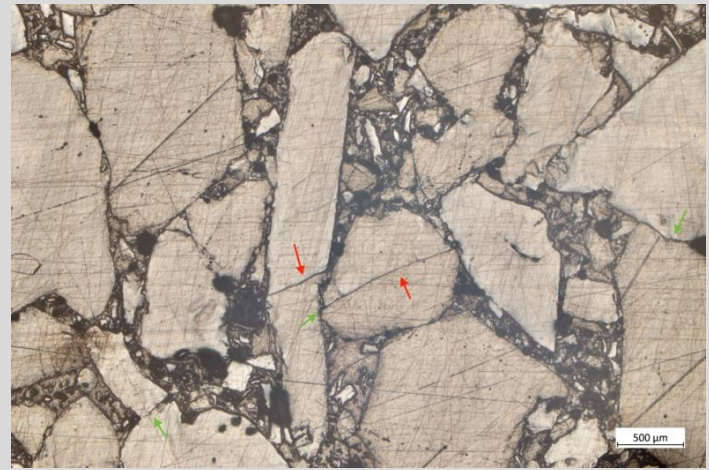


Fig. 4.29 Photomicrographs from IfG long-term compacted samples at 10MPa under dry (a, c, e, g) and wet (b, d, f, h) conditions. Arrows: fractures (red), fluid inclusions (blue), TITIGB (green), deformation bands (yellow), recrystallization (white)

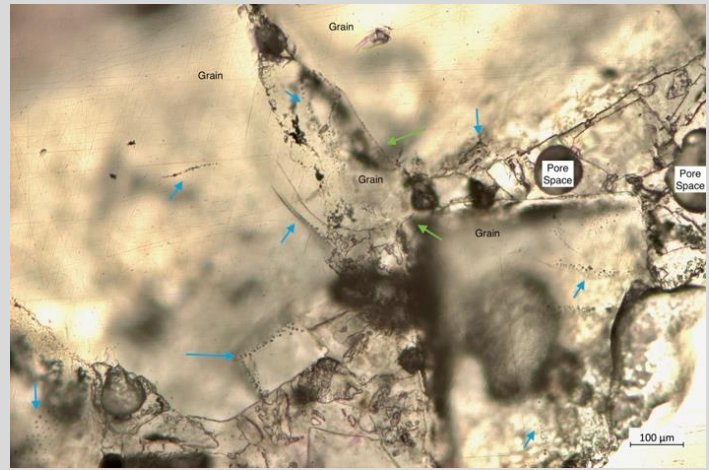
An increase in stress to 20 MPa, as seen in sample name (days of compaction, porosity) produces more transgranular fractures under “dry” compaction conditions (Fig. 4.30a) with angular grain shapes remaining. For added moisture conditions, a similar microstructure to the 10 MPa “wet” sample is seen, with tight grain boundaries, little to no fractures (only scratches from polishing) and rounded grains (Fig. 4.30b). For fluid inclusions, in Fig. 4.30c and d, results are comparable to 10 MPa samples. For etched faces, static recrystallization aided by pressure solution is once again seen in the “dry” sample (Fig. 4.30e and g), surrounded by high dislocation density areas (deformation/slip bands) with elongated subgrains indicative of high stress regions. The wet sample, on the other hand, exhibits strong dynamic recrystallization by fluid assisted grain boundary migration with subgrain rotation creating new grain boundaries (left of Fig. 4.30f) and irregular subgrain shapes (Fig. 4.30h) /PEA 01/.

Though there was no wet sample tested at 30 MPa to compare directly, the microstructure of the “dry” sample in Fig. 4.31 still provides information on the effect of high stress conditions on compaction. Again, angular grain shapes are observed even with reduced porosity (Fig. 4.31a). Though, more abundance of grain contacts experiencing TITIGB indicators, indicating pressure solution. Static recrystallization is apparent as well (substructure-free grain in Fig. 4.31b), yet large areas of deformation/slip bands also indicate strong plastic deformation with glide, cross-slip, and climb controlled dislocation creep exhibited in one grain (center to left, Fig. 4.31c).

TCC1 ("dry", 20 MPa)

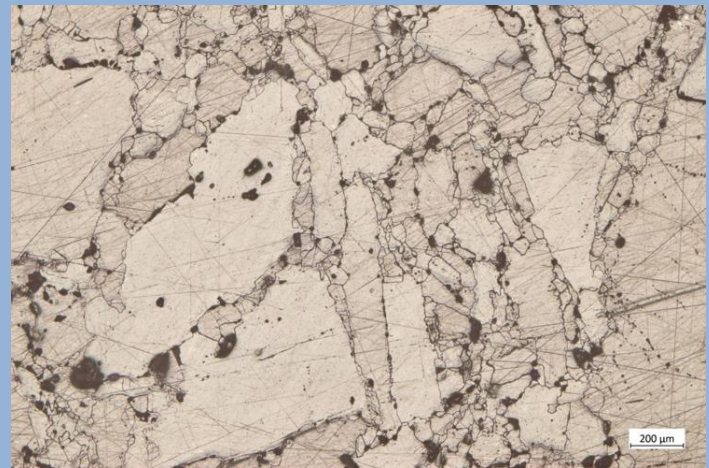


a

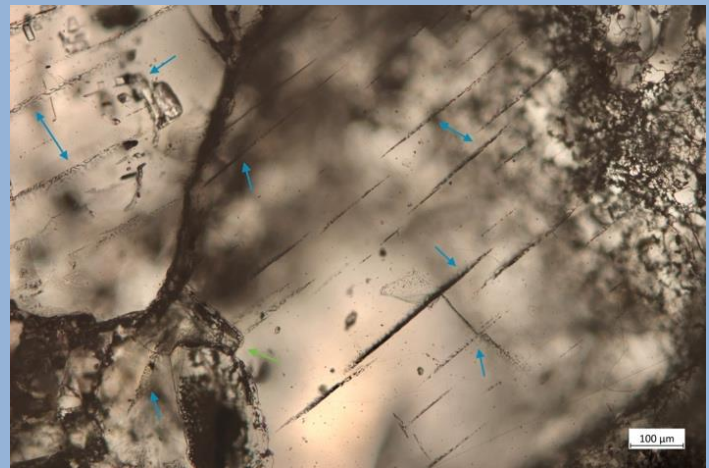


c

TCC5 ("wet", 20 MPa)



b



d

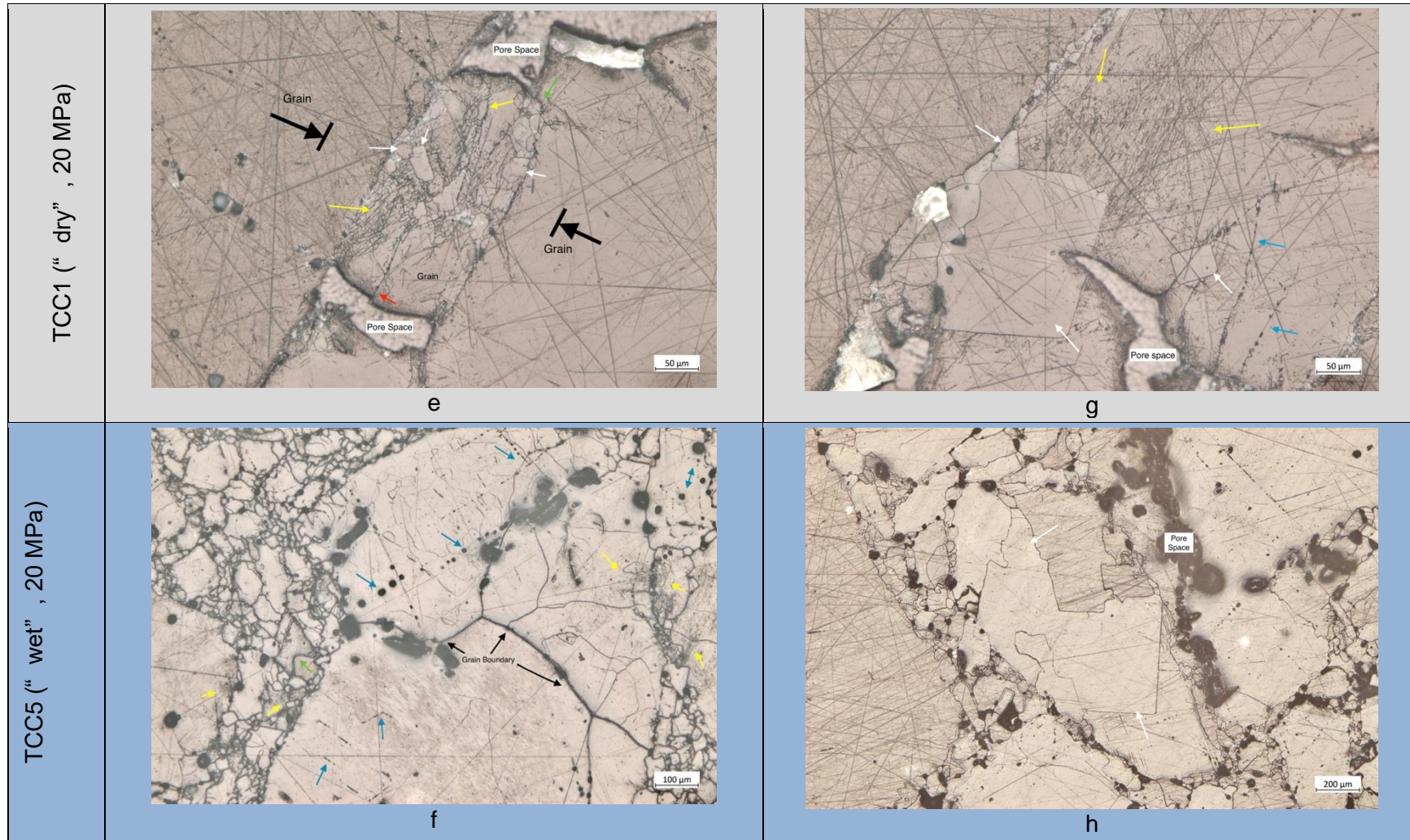


Fig. 4.30 Photomicrographs from IfG long-term compacted samples at 20MPa under "dry" (a, c, e, g) and "wet" (b, d, f, h) conditions

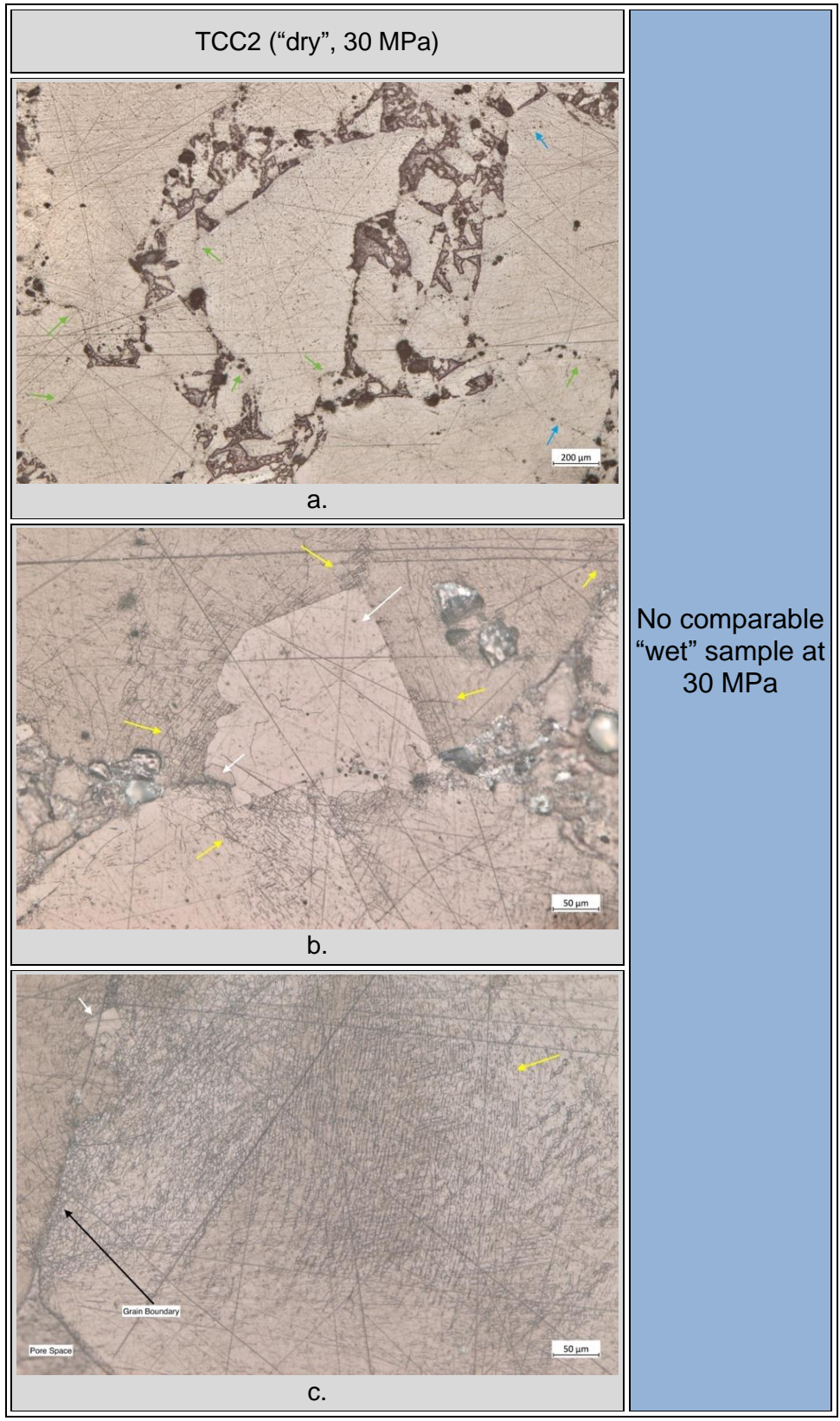
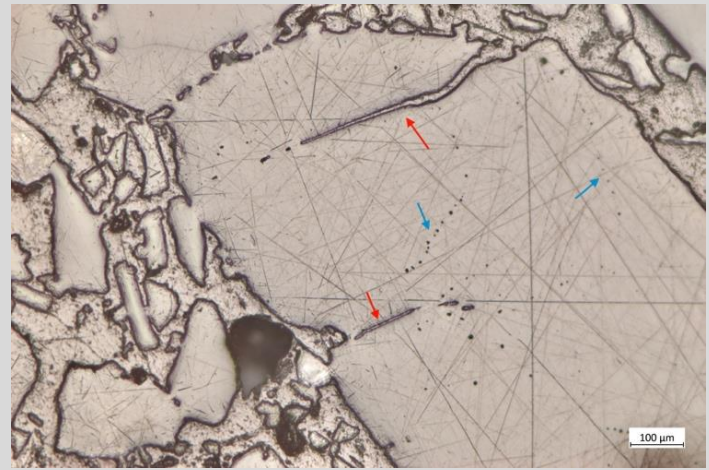


Fig. 4.31 Photomicrographs from IfG long-term compacted sample at 30 MPa under dry conditions. Arrows: fluid inclusions (blue), TITIGB (green), deformation bands (yellow), recrystallization (white)

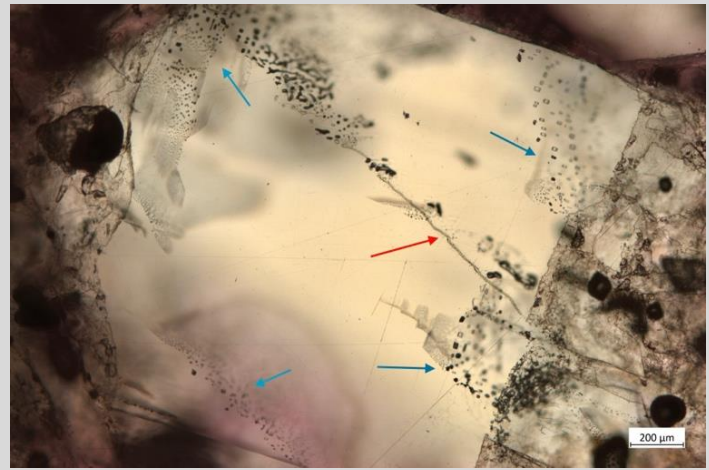
4.3.2.3 TUC pre-compaction samples

Due to time constraints, only two of the TUC samples, pre-compacted under triaxial methods, could be investigated. These samples experienced lower stress regimes and test durations as compared to the IfG pre-compacted samples in Section 3.2.2. Microstructures for the analyzed TUC samples are shown in Fig. 4.32. Once again, the “dry” pre-compacted sample experiences intragranular fractures (Fig. 4.32a and c), however there are still transgranular fractures apparent in some grains for the “wet” pre-compacted sample (Fig. 4.32d and f). This most likely relates to the lesser compaction duration (i.e., 2 days, 18 % porosity) where there was not enough time for pressure solution mechanisms to fully heal those fractures. Nonetheless, there is evidence of pressure solution at some grain contacts as shown in Fig. 4.32b. The etched surface of the “dry” compacted sample in Fig. 4.32e shows an area of glide-controlled work hardening creep in the center grain. For the “wet” sample (Fig. 4.32f), the subgrains are elongated in a more linear arrangement, an indicator of a progressed deformation process of cross-slip controlled dislocation creep.

TUC 18 ("dry", 2 MPa)

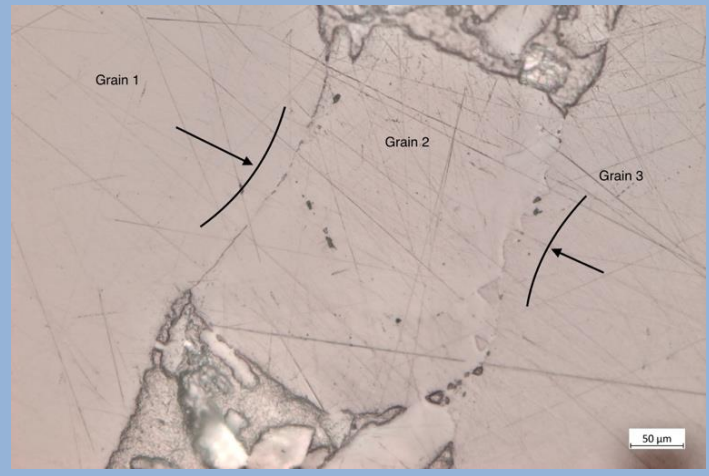


a

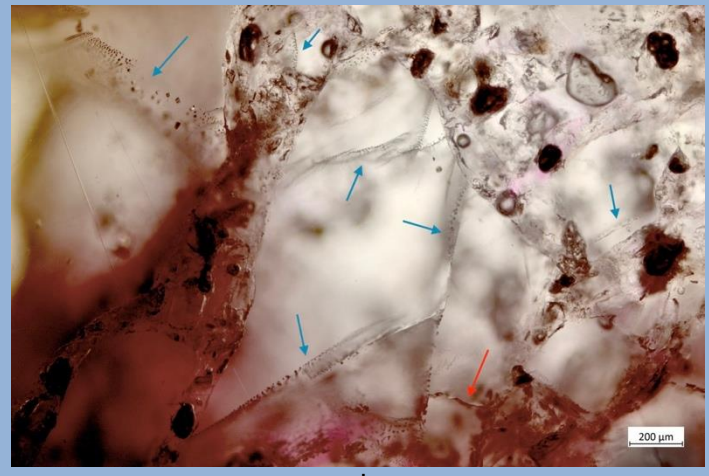


c

TUC 21 ("wet", 1%, 5 MPa)



b



d

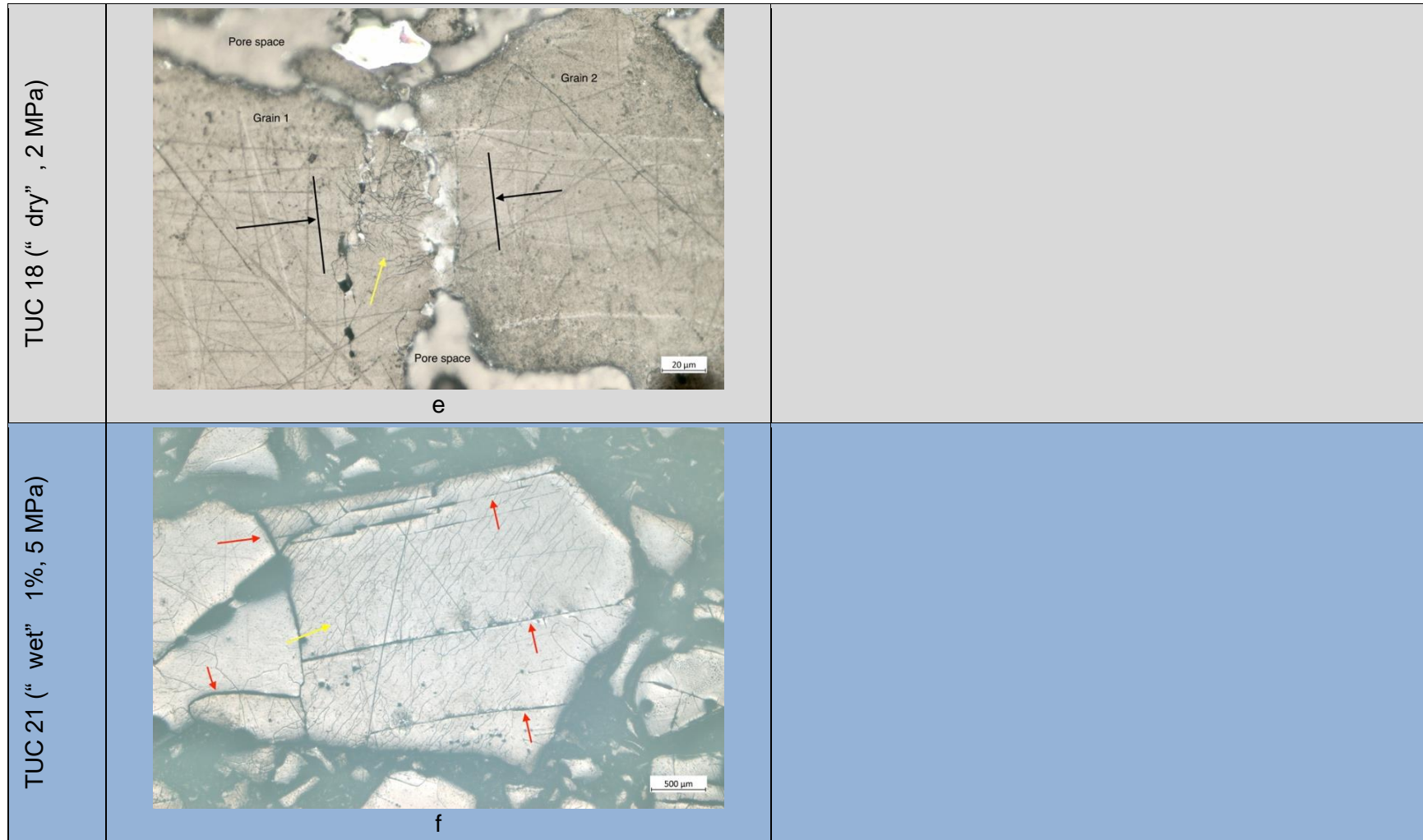


Fig. 4.32 Photomicrographs from TUC pre-compacted samples under dry (a, c, e) and wet (b, d, f) conditions. Arrows: fractures (red), fluid inclusions (blue), TITIGB (green), deformation bands (yellow), recrystallization (white)

4.3.3 Summary

From the presented comparison of microstructures for dry and wet samples (pre-compacted and compacted), the effect of additional moisture and time on compaction is evident. However, due to the different testing conditions between the IfG and TUC pre-compacted samples, and having fully compacted samples, it is difficult to have a direct comparison and conclusion amongst those samples. Therefore, only samples subjected to the most alike conditions should be compared. IfG pre-compacted and compacted samples without added moisture had larger amounts of fractures, angular grain shapes, and areas of dense deformation/slip bands (i.e., areas of higher stress). When 1 wt.-% moisture was added, there were fewer fractures, grain shapes were more rounded, pressure solution creep at grain contacts, and more abundant areas of recrystallization. While the TUC pre-compacted sample with added moisture still had evidence of fractures, the elongated subgrain structures shows a more progressive regime of deformation into a cross-slip dislocation creep, as opposed to the "dry" sample. Additional moisture promotes healing during compaction, more so with longer duration tests, as shown here and noted in several other granular salt compaction studies /URA 86/, /SPI 93/, /BRO 96/, /MIL 18/. Although, it remains untested, if even longer deformation times and low stresses with this material (e.g., emplaced as in-situ backfill) will have similar results for "dry" samples or if indicators shown in "wet" samples begin to be observed. Thus, by microstructural analysis of samples investigated here, it cannot be guaranteed that the laboratory "dry" compaction methods correctly mimic a real-case scenario.

4.4 Effect of grain size and its distribution on backfill compaction (UU)

Identifying and quantifying the grain-scale mechanisms controlling compaction of the granular salt backfill material in a radioactive waste repository is crucial to accurately predict the porosity-permeability evolution of the converging cavity. In this context, the High Pressure and Temperature Laboratory at Utrecht University (the Netherlands) is collaborating with the Dutch Central Organisation for Radioactive Waste (COVRA). Many of the aims within this project align with those of the KOMPASS project and therefore, we share data, results and in-sight with the KOMPASS partners. In this contribution, we provide a summary of our recent studies relevant to the KOMPASS-II project, which will be published in full in the scientific literature in the future.

4.4.1 Introduction

There is a lot of data available on compaction creep of backfill at high and intermediate porosity (> 10 %) /SPI 90/, /KOR 98/, /KOM 20/, but at low porosity (< 10 %) there is relatively little experimental data available and most of the data is obtained at stresses higher than expected during in-situ convergence. While in long-term experiments, to keep the experiment time reasonable, the applied stress typically is increased to 20 MPa around 10 % porosity (e.g. TK-031 /KOM 20/ and TUC-V2, Section 3.3), the models for convergence indicate that an effective stress of 5 – 15 MPa can be expected between 10 % and 0 % porosity (e.g., see the results of the virtual demonstrator comparison in Section 5.4, Fig. 5.63). At high stresses, compaction of (wet) granular salt is likely dominated by dislocation creep, while at lower stresses stress-induced dissolution-precipitation (intergranular pressure solution) will take over. Hence, the grain-scale deformation mechanisms that dominate under realistic in-situ stresses and porosity are not necessarily targeted in typical long-term experiments.

To date, most compaction experiments performed at lower stresses have focused on granular material with a single grain size /SPI 90/, /ZHA 07/. Low-stress experiments on single grain size aggregates indicate that compaction creep is very sensitive to grain size, with rates increasing with smaller grain sizes (compaction rate $\propto d^\beta$ /SPI 90/, /ZHA 07/). However, real backfill material, such as the KOMPASS mixture, covers a distributed grain size distribution. Yet, constitutive laws predicting compaction of aggregates with a distributed grain size (i.e., mixtures) take a single value for grain size to describe the mechanical behavior /MIN 07/. Such laws either take the average grain size or use grain size such that the experimental data fits the model /MIN 07/. Hence, the contribution of the individual grain size fractions to the overall creep rate in these mixtures are not well understood or included in predictions. This results in uncertainties when extrapolating the results of these mixtures beyond laboratory conditions. Therefore, we have developed two models that aim to predict the upper and lower bound for the pressure solution strain rates in a mixture based on its grain size distribution and the rates obtained from experiments on their single grain size endmembers.

4.4.2 Method

We have carried out stress relaxation experiments in 1D compaction mode on analytical 99.9 % pure NaCl of single grain sizes (mean grain sizes of 115, 137, 165, 225, 325 and 450 μm) and mixtures with a distributed grain size (Fig. 4.33). Samples were pre-compacted rapidly to a fixed porosity in the range of 20 – 25 %. The stress on the sample was then allowed to relax by setting the piston to a fixed height. Strain rates were obtained at a continuously decaying stress. The effects of applied stress ($\sim 0.3 - 80$ MPa), grain size and porosity (20 – 15 – 10 – 5 – 1 %) were systematically investigated on brine-saturated samples under drained conditions (atmospheric pressure, 0.1 MPa). The plastic strain rate during stress relaxation can be calculated using:

$$\dot{\epsilon}_p = \dot{\epsilon}_m - \left(\frac{A}{L(t)} C_a(F) + C_s \right) \frac{d\sigma}{dt} \quad (4.6)$$

$\dot{\epsilon}_p$	plastic strain rate [s^{-1}]
$\dot{\epsilon}_m$	measured strain rate [s^{-1}]
A	sample area [mm^2]
L	sample length [mm]
t	time [s]
F	force [kN]
C_a	elastic compliance of the testing machine as a function of stress [$\text{mm} \cdot \text{N}^{-1}$]
C_s	elastic compliance of the sample [MPa^{-1}]
$\frac{d\sigma}{dt}$	rate of effective stress change with time [$\text{MPa} \cdot \text{s}^{-1}$]

The machine was carefully calibrated to allow for correction of the strain rate calculation based on the elastic response of the testing machine under a decaying load.

A local linear velocity displacement transducer (LVDT) was installed between the top piston and the top of the vessel, to measure the displacement and hence strain rate ($\dot{\epsilon}_m$) of the sample during compaction. A second fixed LVDT was located in the INSTRON testing machine, that was used to determine the absolute length of the sample at any instant in time, correcting for machine distortion. For each experiment, a fixed weight of sodium chloride (6.24 g) was used. This amount of material corresponds to a fully dense sample (0 % porosity) with a length of 9.83 mm, taking a density of 2170 kg/m^3 . Hence, the absolute length of the sample during the experiment can be used to determine the porosity, where the length of the sample was obtained with an error of 0.0294 mm. This corresponds to an absolute error in porosity of 0.27 %.

For more information about the stress relaxation technique see /LEE 71/, /RUT 78/. A clear advantage of stress relaxation tests is that one can obtain the relation between stress and plastic flow rate of a sample within a single test, for near-constant porosity. In addition, this allows us to measure the plastic flow rate at low stresses (down to ~ 5 MPa) in samples with a low porosity (5 – 10 %).

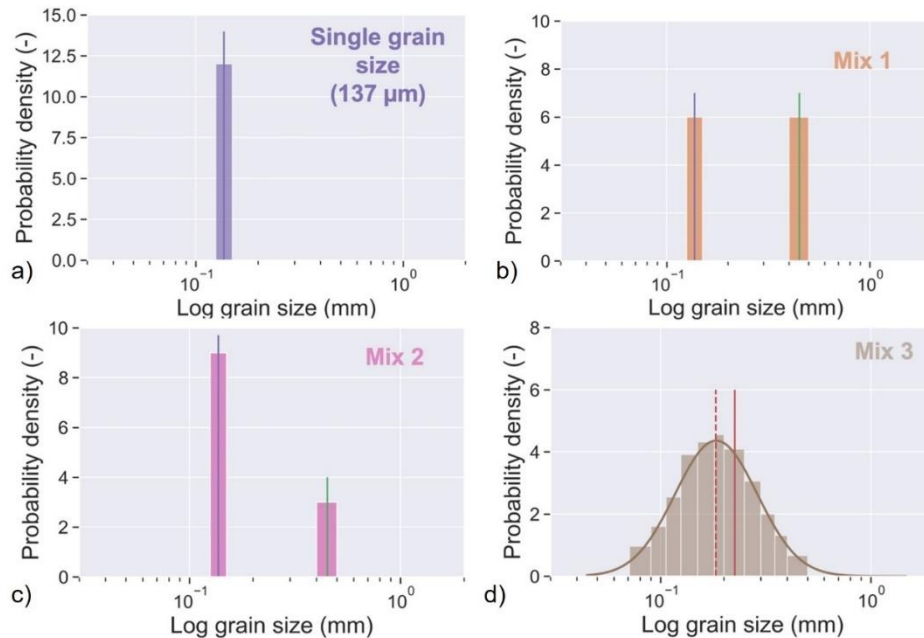


Fig. 4.33 Overview of grain size mixtures used in this study for (a) a single grain size fraction of 137 μm , (b) a 50 – 50 % mixture of 137 and 450 μm grains (Mixture 1), (c) a 75 – 25 vol-% mixture of 137 and 450 μm grains (Mixture 2), and (d) a log-normal volume distribution with a mean of 225 μm , a mode of 183 μm and a standard deviation of 0.45. For Mixture 3, a mixture was constructed using the available sieves that approached the same distribution as the continuous distribution shown in d (solid line). Note that the y-axis indicates the volume probability, for which the scales in a, b, c and d are different

4.4.3 Results

4.4.3.1 Compaction creep in single grain sizes

For a representative experiment (137 μm grain size), the effect of aggregate porosity on the compaction rate is shown as a log strain rate versus log stress plot (Fig. 4.34). To evaluate the effect of grain size, experiments on aggregates with average grain sizes of 115 μm , 165 μm , 225 μm , 325 μm and 450 μm at near-constant porosity of 10 % are shown in Fig. 4.35.

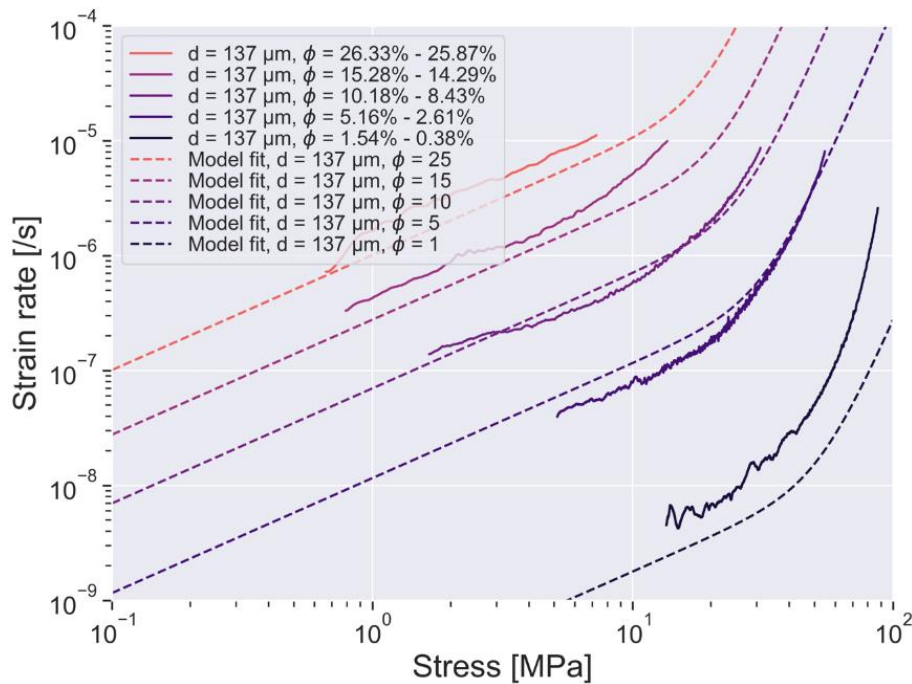


Fig. 4.34 Strain rate versus stress data obtained from relaxation steps on a brine-saturated sample with a mean grain size of 137 μm

Note the change in slope when going from high ($n > 3$) to low stress ($n \sim 1$) in a single experiment, as well as the decrease in strain rate by 3 orders of magnitude going from high porosity (25 %; orange curve) to low porosity (~ 1 %; dark blue curve). Strain rate versus stress data predicted by the constitutive law of /OOS 23/ for $d = 137 \mu\text{m}$ and the different tested porosity's is indicated by the dotted lines

At low stress ($< 10 - 30 \text{ MPa}$, depending on grain size and porosity), the compaction creep rate was linearly proportional to stress ($\dot{\epsilon} \propto \sigma^1$) and showed a near-cubic inverse dependence on grain size (d) ($\dot{\epsilon} \propto \frac{1}{d^3}$). This type of behavior is typically associated with pressure solution, which relies on dissolution-precipitation diffusional transport through the grain boundaries /SPI 90/. At higher stresses, a transition to non-linear creep was observed, with apparent power law stress exponents (n) of 3-7 ($\dot{\epsilon} \propto \sigma^{3-7}$). This is generally attributed to dislocation-dominated mechanisms /CAR 93/, /KOR 98/. However, this does not explain the grain size dependence observed in this study in this domain, which indicates a grain size dependence of around 1.8 ($\dot{\epsilon} \propto \frac{1}{d^{1.8}}$). Based on the results of both the linear (pressure solution) and non-linear (dislocation) creep domain we have developed a constitutive law that can be used to describe the compaction rate of backfill as a function of stress, grain size and porosity, which is described in more detail in the COVRA deliverable 2 (under embargo until peer-reviewed publication of this work /OOS 23/). The results for this constitutive law are presented in Fig. 4.34 and Fig. 4.35. Given the

observed grain-size sensitivity in the dislocation creep-regime, we have modified the dislocation creep part of this relationship to account for this grain size sensitivity /KOR 98/. In Section 4.4.4.1, this constitutive law, together with a two-component flow law for the surrounding host rock, is used to predict the convergence of a backfilled repository.

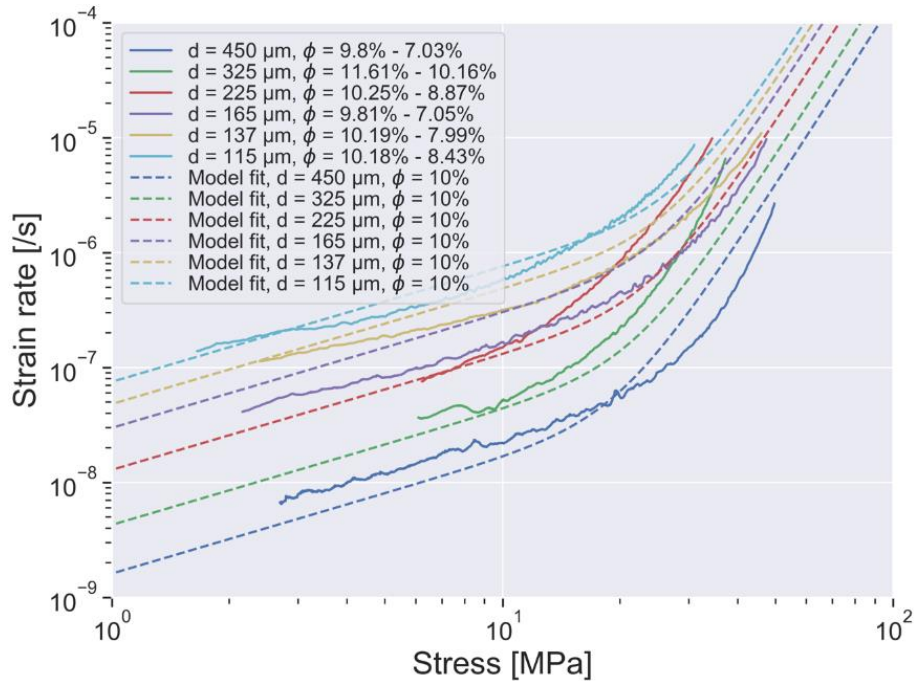


Fig. 4.35 Strain rate versus stress data obtained during brine-saturated experiments on aggregates with grain sizes between 115 and 450 μm at a porosity of 10 % (solid lines). Strain rate versus stress data predicted using the constitutive law of /OOS 23/ is indicated using the dotted-lines for all of the tested grain sizes

4.4.3.2 Compaction creep in mixtures (samples with distributed grain size)

In addition to the single grain size experiments, stress relaxation experiments were performed on samples with a mixed grain size distribution (Fig. 4.33). Fig. 4.36 shows the strain rate-stress behavior of mixtures 1 and 2 (75:25) at 5 % porosity together with single grain size experiments (137 and 450 μm) at the same porosity for comparison. The results on the mixtures show similar behavior as the single grain size aggregates with a high stress exponent of 3 – 6 at high stress and near-linear behavior at low stress.

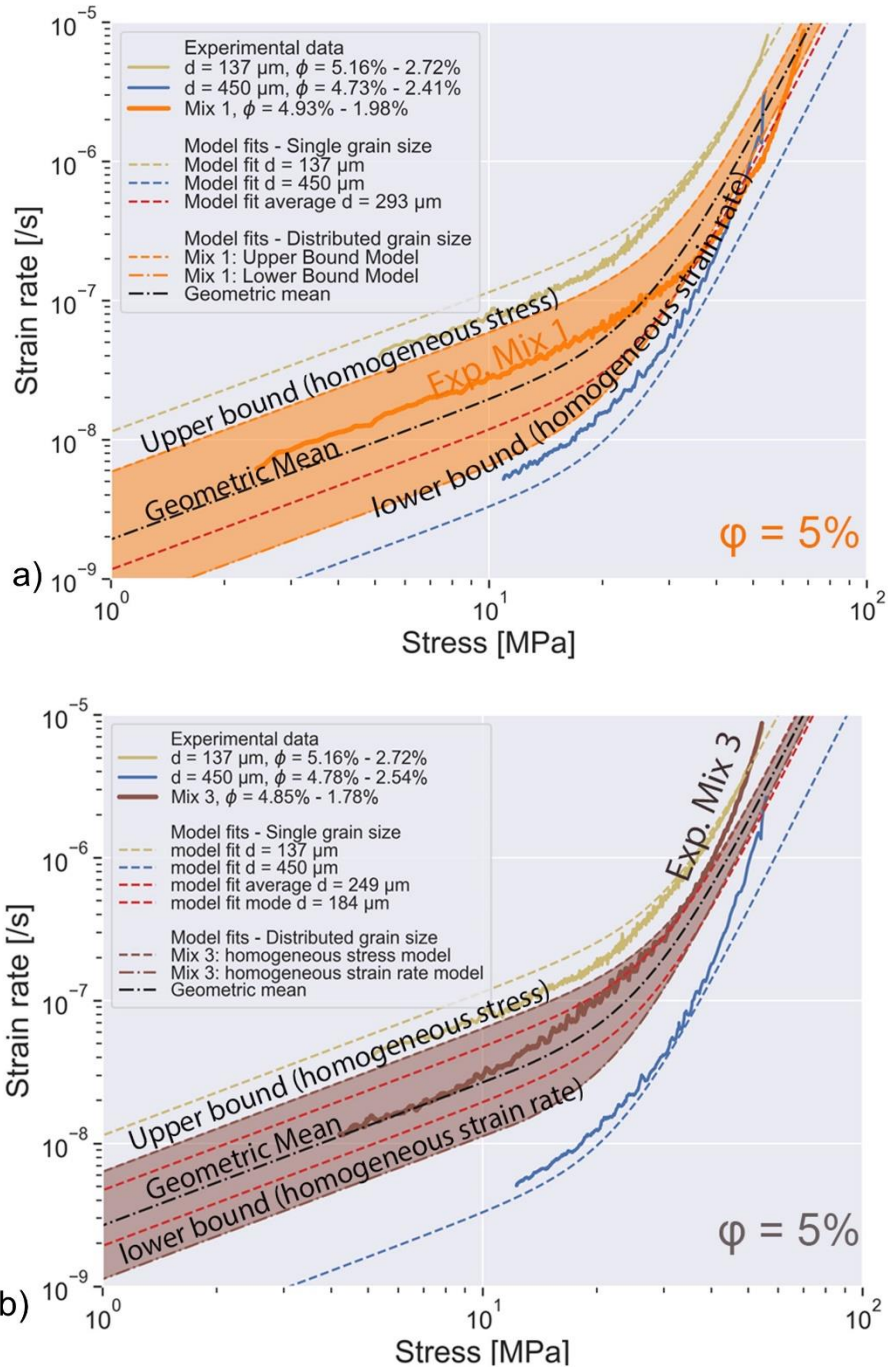


Fig. 4.36 Strain rate versus stress for the experiments on (a) Mixture 1 and (b) Mixture 2 and single grain size aggregates (137 and 450 μm) at 5% porosity (solid lines)

Dotted lines represent the model results of pressure solution creep in single grain size aggregates of 137 μm and 450 μm and the upper and lower bound of mixture 2 based on the model for compaction creep in a mixture assuming compaction by the constitutive law obtained from the experiments conducted with single grain sizes

Based on the experiments on single grain size fractions, we derived a constitutive law. When plotting the predicted strain rate as a function of stress, this law shows a linear branch at low stress, representing compaction by pressure solution, and a non-linear branch at high stress, representing dislocation creep. As the maximum stress in the backfill is expected to be around 15 MPa. Based on the constitutive law for backfill compaction obtained for the single grain size fractions, we have developed two models that aim to predict the upper and lower bound for the pressure solution strain rates in a mixture based on its grain size distribution and the rates obtained from single grain size-fraction experiments. The upper bound assumes that stress is distributed homogeneously (i.e., a homogenous stress model), and all grain size classes can deform at the strain rate obtained from single grain size fraction experiments. The total strain rate is subsequently calculated by multiplying the strain rate of each grain size fraction by its volume fraction. The lower bound assumes that strain rate is homogeneously distributed (i.e., a homogeneous strain rate model). For this bound, the total strain rate is calculated by obtaining the stress on each grain size fraction and multiplying the stress of each grain size fraction by its volume fraction to obtain stress as a function of strain rate (for a similar approach see /HEE 05b/).

As can be seen in Fig. 4.36, the geometric mean of these two models can be used to predict the creep rate of a mixture. Note that for mixture 2 (75:25 vol-% fine:coarse mixture), the geometric mean is very similar as taking the average grain size and calculate the compaction rate. However, for mixture 1 (50:50 vol-% fine:coarse mixture), taking the average grain size results in an underestimation of the compaction rate by 50 %. It should be noted that the grain sizes used on our experiments ranged from 0.1 to 0.5 mm, whereas a realistic backfill mixture, such as the one used by KOMPASS, has a range of 0.1 to 4 mm. Hence, uncertainties remain whether this approach can be applied to mixtures with a much broader grain size distribution.

4.4.4 Discussion

4.4.4.1 Coupled convergence model

Based on the experimental results of this study we have derived a constitutive equation that described the compaction creep of the backfill as a function of mean stress, porosity and grain size. We have used this equation, together with a two-component flow law for the intact dense rock salt surrounding the repository /MAR 16/, /HUN 99/, /SPI 90/ to make predictions regarding the closure of the cavity and the densification of the backfill.

For the intact rock salt, we take a grain size of 5 mm and assume that brine is present. Using a far-field hydrostatic stress of 15 MPa (corresponding to a depth of 700 m), we have calculated the mean effective stress, the compaction rate and the porosity reduction as a function of time/porosity for a backfill grain size of 0.3 mm, 1.0 mm and 3.0 mm. Fig. 4.37a and b show the evolution of mean stress and compaction creep as a function of backfill porosity and Fig. 4.37c shows backfill porosity as a function of time.

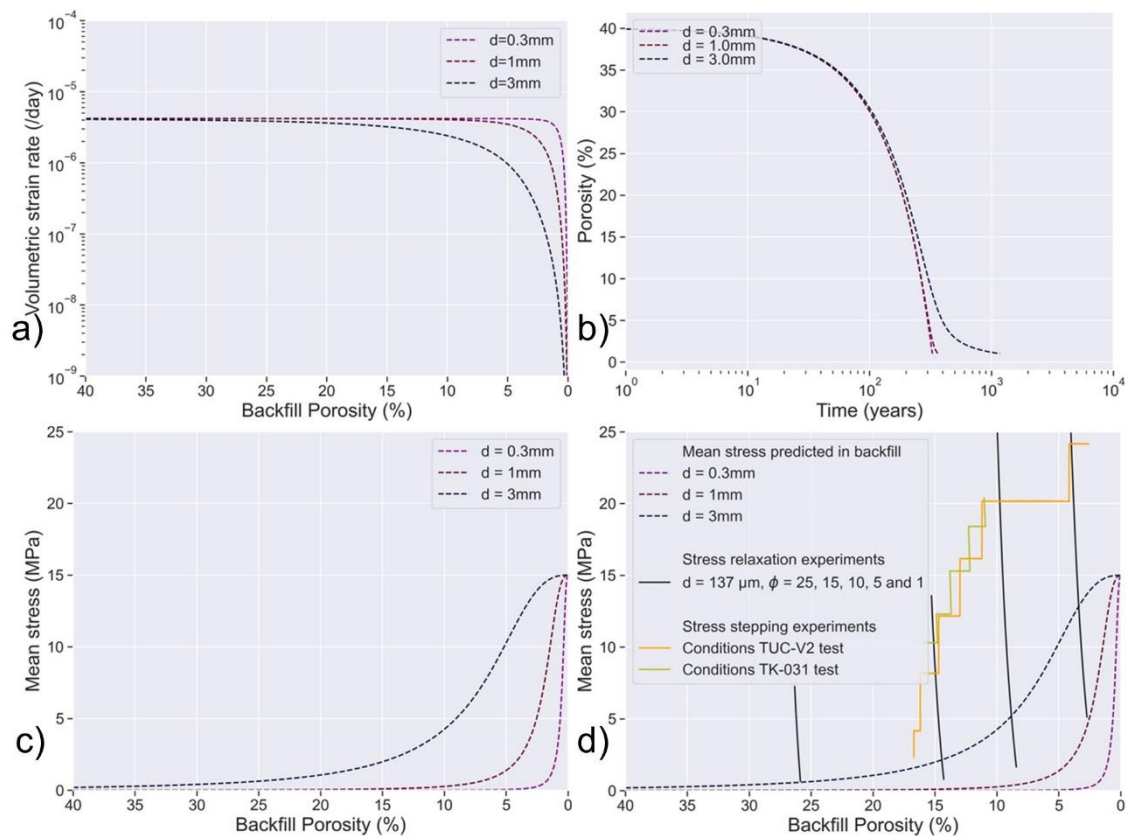


Fig. 4.37 (a) Volumetric strain (/day) versus backfill porosity (%) for a backfilled repository in rock salt grain size of 0.3, 1.0 and 3.0 mm, using an analytical solution for coupled-convergence. b) Backfill porosity (%) versus time (years) until a porosity of 1 % is reached. c) Predicted mean stress evolution versus backfill porosity and (d) Mean stress versus backfill porosity in-situ (model) and during typical long-term experiments /KOM 20/ and stress relaxation experiments (example of experiment on sample with 137 μm)

Based on the experimental results in this study and this coupled convergence model, a backfill porosity of 1 % is reached after 330 years for a grain size of 0.3 mm up to 1200 years for a grain size of 3.0 mm (Fig. 4.37c). Note that the volumetric strain rate down to 20 % porosity is near constant and purely governed by the convergence of the repository walls, with virtually no resistance by the relatively weak backfill (Fig. 4.37b).

The mean stress shows that for a grain size of 0.3 and 1.0 mm, the stresses/porosity conditions remain within the linear part (i.e., pressure solution domain) of the creep curve (see the left part of Fig. 4.37a). For a coarse-grained backfill with grains of 3.0 mm diameter, below about 4 % aggregate porosity the stress/porosity conditions are such that the transition of linear to non-linear creep is observed.

4.4.4.2 Implications for targeted experiments

This study indicates that the effect of grain size on compaction creep rates in the backfill is significant, especially at low stress (< 10 – 15 MPa). Extrapolating these results to larger grain sizes and including a constitutive law for the surrounding host rock, shows that the stresses in the backfill remain very low (< 5 MPa) during most of the convergence and only increase to 15 MPa when porosity is just a few percent. This indicates that pressure solution, the mechanism, which is dominant in these experiments at low stress, is governing compaction creep during in-situ conditions. Except for the final stages of porosity reduction (< 3 %) and when the grain size is very coarse (> 3 mm).

Although the KOMPASS material is a mixture with a grain size up to 4 mm, the mean grain size is around 1.5 mm /KOM 20/. Therefore, based on our model, it can be expected that during in-situ stress conditions, pressure solution is the dominant mechanism leading to compaction of the KOMPASS mixture. Other models for convergence of a backfilled gallery that consider pressure solution to take place, such as the IfG-CWIPP and the Sandia-Callahan model (see Section 5.4 and Fig. 5.62), agree that the mean stress in the backfill remains low (< 10 MPa) until porosity drops below 2 – 5 % (see Fig. 5.62). However, in most long-term experiment the stress is increased towards 20 – 25 MPa around a porosity of 10 % (e.g. TK-031 /KOM 20/ and TUC-V2, see Section 3.3 of this report). Thus, moving it into the regime where non-linear creep is dominant.

Based on the experimental results and the in-situ stresses predicted from our model, the IfG-CWIPP model and Sandia-Callahan model (described in Section 5.4), we advise to perform long-term experiments at low stresses (e.g., mean stress of 5 MPa and porosity of 5 %). This may help in reducing the discrepancy in behavior that is observed under predicted in-situ stress and porosity conditions (see Fig. 5.62) and the current experimental conditions during the long-term compaction tests (e.g., at the calibrated conditions at 20 – 25 MPa during the long-term compaction tests TUC-V2 and TK-031, where all models of Section 5.4 agree).

4.4.5 Conclusion

- At low stresses ($< 10 - 15$ MPa), the compaction creep experiments show a linear dependence of compaction rate on stress and near inverse cubic dependence on grain size indicating that pressure solution creep is the main mechanism under these conditions.
- At high stress ($> 10 - 15$ MPa), the stress exponent varies from 3 – 7. Although this is typically associated with grain size insensitive dislocation creep mechanisms, we do observe some dependence on grain size in our experiments and the exact deformation mechanism(s) remain unclear.
- Experiments on a mixture containing multiple grain size fractions indicate that the same mechanisms operate in mixtures as in single grain size aggregates. The rates can be approximated by taking the geometric mean of the upper and lower bound method described here.
- Our coupled convergence model indicates that during backfill convergence, the stresses remain within the linear creep/pressure solution domain, except for the final few percent of porosity reduction, and only when the average backfill grain size is very coarse (3.0 mm or larger).

5 Numerical Modelling

5.1 Introduction

If the verification of a HAW repository is considered from the current point of view, even against the background of a decades-long operation phase, a physical demonstration of long-term safety in the area of crushed salt would not be possible and not be permissible. The demonstration of long-term safety therefore has to be carried out numerically. A reliable numerical demonstration of long-term safety requires that all components of the numerical calculation can be described sufficiently well. "Sufficient" is to be seen in the context of the objective of the demonstration of long-term safety and not solely against the background of a representation of reality. The components of the numerical calculation are the geological model, the model of the mine, the model of material behavior, the initial and boundary conditions, and the schedule of events with e. g., construction, operation, and post-operation phases of the HAW repository. The constitutive model for the material behavior of crushed salt is therefore, beside the other components, a central element for the modeling of a HAW repository. The need for computational demonstration of long-term safety, combined with the state of knowledge and computational capabilities for crushed salt compaction, provides the basis for this project.

From a modeling point of view, it would in principle be possible to describe the material behavior of a granular and a solid rock salt with different constitutive models. In such a case, the constitutive model could thus be changed at complete compaction. However, the ultimate goal of developing a constitutive model for the crushed salt should be a unified formulation. Differences between a granular and a damaged rock salt with comparable porosity must be accounted for in the individual deformation processes, since the pore structure and grain structure, as well as grain boundaries and subgrain boundaries, differ. The complexity of the geometry description will be addressed in Section 5.1.2, but such complex functions with their evolution equations are not part of the current project. Likewise, the current formulations of the crushed salt do not yet reach the level of the solid rock salt, as documented e.g., in /HAM 22/.

The complexity of the deformation mechanisms of the crushed salt behavior /KOM 20/ is taken up again in Section 5.1.1. This degree of complexity is not yet supported by all constitutive models used in the project. However, not all processes have been investigated experimentally yet. Therefore, not all complexities have to be explicitly included in

a material model in order to achieve satisfactory results. As already described in the case of rock salt /HAM 16/, similarly acting processes can be modeled in a common approach and thus be well represented by a suitable parameterization. However, such an integrated process fails if the physical conditions in the system behavior to be calculated do not exist for one of them.

Although the work of the project cumulates in the constitutive model and the constitutive model is based on the accompanying work. These accompanying works are the experimental and the microstructural investigations, which give the data basis for the parameter identification and the basis of the physical processes to be represented. Two specific aspects should be pointed out in advance: Section 5.1.1 deals with acting deformation mechanisms and the different terminology used in microstructural analysis and continuum mechanics describing the mechanisms. The scope of processes presented in Section 5.1.1 is relativized against the background of the currently available or evaluated experimental basis, so that for some project partners a reduced scope of processes in the constitutive model is currently sufficient. Such a behavior of complex overall state but simplified description is also reflected in the geometry description of grain and pore structure, Section 5.1.2. The real complex structures are currently represented by one or two quantities, depending on the constitutive model. The current state of the constitutive models involved here is described in Section 5.2. These models are used for the parameter identification of the triaxial tests (Section 5.3). Finally, Section 5.4 demonstrates the achieved state of the art for the prediction capability of the compaction behavior of a distance offset at a repository-related application example.

5.1.1 Deformation mechanism

In this project, there is an interaction between geological materials science and engineering mechanics. Not all terms used in the two disciplines have the same meaning, and competing terms exist within a single discipline. Possible discrepancies in individual definitions of the two disciplines are not resolved here. Rather, the different definitions remain side by side because they are established in their respective disciplines and the assignment is clear to the reader from the disciplinary context. One differently defined term is plasticity. In geology, this term describes a ductile material behavior in contrast to a brittle one /BLE 02/; in the context of a constitutive model in mechanics, it is the lack of reversibility of a deformation component. Therefore, plasticity in mechanics includes brittle fracturing. Ductility would be another aspect. In /BLE 02/, the quantification of a

ductile deformation in a laboratory test and the lack of quantification in a geological field study are discussed. Field observations, however, are not an issue in this project.

According to /BLE 02/, the deformation behavior in geology is classified according to a geological deformation mode. Three elements characterize such a deformation mode: the deformation mechanism, its spatial continuity, and its spatial extent. As the spatial resolution of the object size changes from microscale (< 1 cm) to mesoscale (1 cm – 10 m) to macroscale (> 10 m), a geologic deformation mode can change, /BLE 02/. The structural studies conducted in this project are at the microscale. If these three elements are considered from the perspective of continuum mechanics, ensuring continuity or discontinuity of deformation behavior is not a task of the constitutive model, but a requirement of the structural model being computed. In mechanics, the spatial extent of a deformation mechanism is a computational result or, if the deformation mechanism is reflected in the material properties, an input value or initial condition. Deformation mechanisms are considered in microstructural analysis at the microscale. This scale, e.g., in terms of grain structure and lattice orientation, is quite accessible to the continuum mechanical codes used in this project, but the real target in the application of these codes is the mesoscale, possibly in the outer regions of the computational model with a transition to the macroscale.

This difference in the microstructural observation level between the scales may play a role in transferring the quantitative results of the microstructural analysis to the constitutive models. At present, however, the focus is on qualitative findings with the finding of the essential deformation mechanisms and their mathematical description in the constitutive model, so that the difference in the observation scale with its influence on the deformation mode is of rather secondary relevance. The formulation of the deformation processes in some constitutive models is inspired by or even derived from microscale process models, while others are conceived from a phenomenological point of view.

The deformation mechanism is the quantity transferable from microstructural analysis. Since deformation mechanism and deformation microstructure are bijective, sometimes the microstructure is called instead of the mechanism. In mechanics, the deformation mechanism of microstructure analysis is given a scheme consisting of a temporal component and an evaluation of the reversibility of the deformation. In the temporal context, "time-independent" is seen in terms of the temporal behavior of the load application. A deformation is defined as time-independent if it is sufficiently rapid and complete to a generalized load application. The aspect of reversibility describes the deformation

process as fully traceable to the initial state when the deformation causing load is removed again. However, the time-dependent material behavior of the granular salt leads to a change in microstructure as a result of the compaction process. If such a process is assumed, a deformation gap remains at the end of a corresponding loading and unloading loop. Fig. 5.1 shows the relationship between the two classification schemes used for deformation mechanisms in crushed salt. The gray blocks represent the deformation behavior from a mechanical point of view, while the yellow blocks contain the microstructural deformation mechanisms. In addition to the general mechanism, several specific mechanisms are shown in the respective block, highlighted in blue when moisture is present on the microstructural mechanism. The absence of a microstructural mechanism in elastic deformation is not a question of its existence, but the result of its lack of microscopic observability in thin sections /BLE 02/. No microstructural mechanism in the salt can be attributed to the viscoelastic deformation behavior.

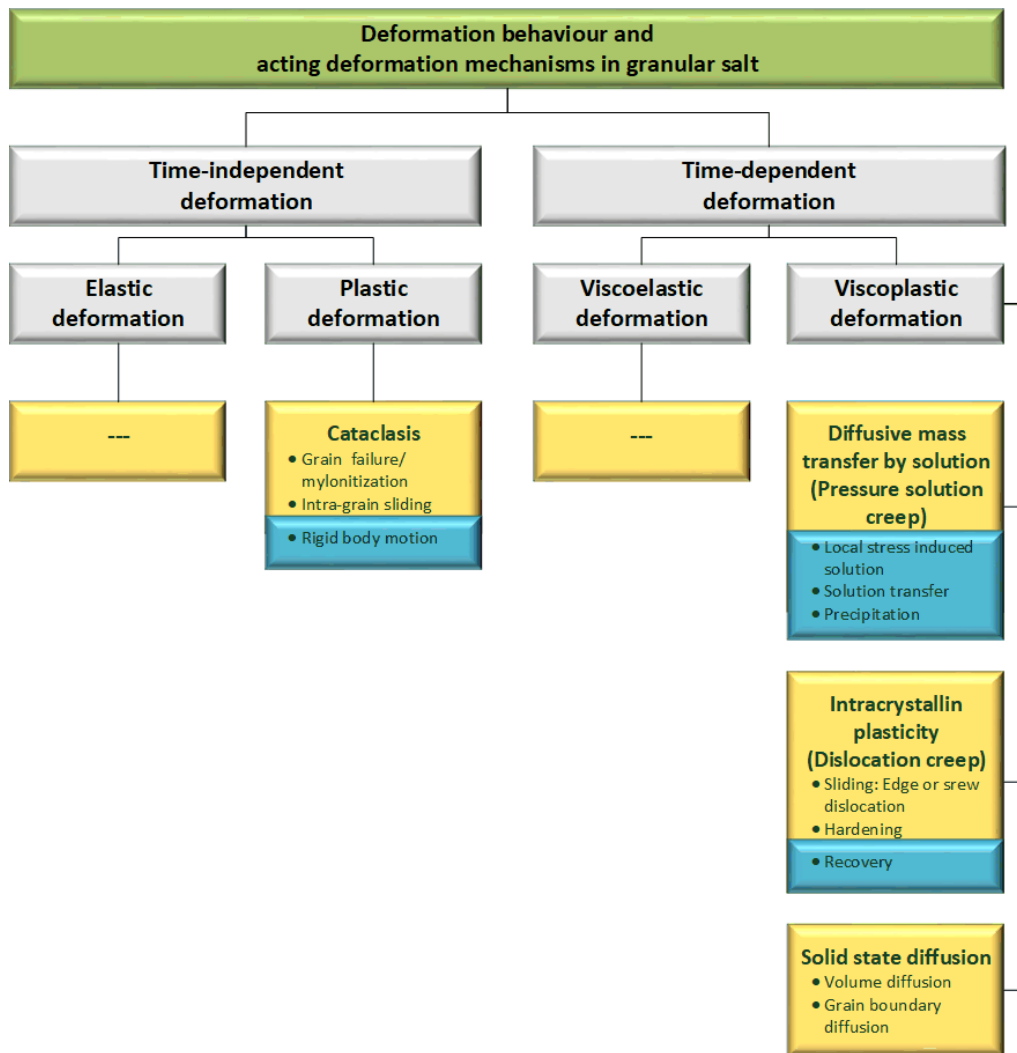


Fig. 5.1 Classification schemes of deformation behavior in salt - Assignment in mechanics and microstructure analysis (according to /ELL 04/)

Already /BLE 02/ pointed out that mechanisms may occur in combination with each other. The reason for this is caused in the conservation laws of mechanics since external loads and internal material reaction have to be in equilibrium. Individual processes carry a limited number of loads, so further processes are required to reach equilibrium, resulting in a reaction with multi-mechanism response.

/KOM 20/ describes how the degree of compaction significantly influences the possibility or at least the extent of the occurrence of a mechanism in crushed salt. At the beginning of deformation, intergranular stresses are expected to be low, so that rigid-body motions are easily possible. Similarly, contact will occur by fracture-sensitive grain tips, so grain fractures will occur even more readily at these locations than later at subsequent low porosity conditions. As compaction progresses, the pore space becomes smaller and the confinement of a grain higher. Thus, the possibility of rigid body movement is more limited and, if it occurs, may result in dilation or compaction depending on the stress conditions. The possibility of grain fracture is also reduced by increasing the contact areas, since the stress acting in the grain is closer to the global stress. Although these two processes are combined as time-independent processes in the microstructural process of cataclase, they are nevertheless independent mechanisms. This independence is already evident when considering the active surfaces, the grain surface during rigid-body motions and the fracture surface in the grain during a fracture process, as well as the different influence of moisture on the mechanisms. Further deformation mechanisms have been discussed in /KOM 20/.

In the isotropic and deviatoric decomposition of the stress tensor, the statistical distribution of the grain arrangements and the contact areas between the grains and the resulting direction of the forces between the grains must be taken into account, at least at the beginning of the deformation process of a loose material. A purely hydrostatic or purely deviatoric stress state from a global point of view is represented at the loose grain level as a combination of isotropic and deviatoric stress components. Therefore, at least in the high porosity region, a stress-based deformation mechanism should exhibit a dependence on both stress invariants with similar intensity.

In Fig. 5.1, the influence of moisture has been pointed out for the deformation mechanisms of inter-crystalline rigid-body motion, pressure solution creep, and recovery and re-crystallization. Small amounts of moisture are sufficient for processes at the grain surface. The equilibrium moisture content for rock salt has been determined to be less than 1 % by mass. The influence must be designed accordingly. Further hydraulically

motivated processes occur when a larger amount of moisture is added and compaction results in low porosity. The resulting pore pressure development is part of a hydromechanically coupled consideration, which is not considered in the current project phase.

5.1.2 Influence of Geometry

The deformation behavior of a material is determined by external quantities such as stresses, temperature, and deformation rate. In addition, internal state variables are added, and possibly their evolution equations. An internal state variable of crushed salt is the description of grain structure and pore space, which may be summarized as "geometry". The importance and effect of the external quantities varies depending on the process under consideration. The influence of geometry itself must be considered in all processes. A good description of the geometric influence is necessary for the respective sub-process, so that no redistribution of an in fact geometric behavior to functions of the external quantities occurs during the experimental fitting. Such a redistribution may lead to incorrect, possibly even unphysical parameters. Therefore, it is one of the tasks in the development of the constitutive models to describe the geometric behavior in a suitable way.

Technically produced crushed salt is usually a mixture of different mineral components, so that the geometry may have to be considered separately for each fraction. However, the variability of this component mixture is largely excluded in this project by the choice of a reference mixture. The principle influence of geometric quantities has already been pointed out in /KOM 20/, e.g., the influence of maximum grain size and sieve line on the deformation behavior. As desirable as such a delimitation of geometric variables of influence is, it is difficult to differentiate them even in the laboratory. In an industrial process of production and processing crushed salt, the interferences are likely to increase compared to the laboratory mixture. Currently, the constitutive models used in this project are based solely on the geometric quantities' porosity, void fraction or fractional density and mean grain size.

The constitutive models of individual project partners are based on a specific geometry model. Such a geometry model represents a single crystal geometry. Such an approach can be helpful as it allows a spatial assignment of individual deformation processes. The deformation process of pressure solution is assigned to the surface, dislocation creep takes place primarily in the outer area of the grain before the contact areas expand during compaction, thus, the stress distribution in the grain is homogenized. However, the

material is not as ideal as the geometry model requires. Therefore, the geometry models are extended by correction terms. However, the knowledge gained from the extended geometry models can be used to develop empirical geometry approaches. The other constitutive models are based on empirical models to describe the geometric behavior.

From a geometric point of view, two structures are to be considered: the grain structure and the pore space structure. Both structures can be described by the size distribution (referred to as sieve line), the maximum size, the cross-sectional dimensions, the shape, and the number of junctions (also referred to as coordination number) of their components. Both structures are independent of each other and are only linked to each other by the compatibility of their volumes with respect to the total volume. Integral quantities are, from the point of view of the pore structure, the porosity, and the void fraction and, from the point of view of the grain structure, the fractional density. The porosity is the ratio of the current pore space to the current total space and the void ratio is the ratio of the current pore space to the solid volume. The fractional density is the ratio of the current density to the solid density. The advantage of using the void ratio or fractional density is that the denominator is constant assuming an invariant solid fraction. Therefore, only the respective numerator must be considered in a derivation.

For individual geometric quantities mentioned above, there are approaches that establish a relationship between the quantity itself and, for example, the porosity. Based on such a relationship, a constitutive model could be developed depending on external quantities, which, for example, describes the rigid-body motion or the intracrystalline fracture as a function of the coordination number, the contact area size, and the stress level. Approaches of different authors to the mean coordination number are given in /HEI 91/. The coordination number is the number of contacts of a grain with the surrounding grains. A valid approach for such a coordination number should provide a finite positive number for realistic values of porosity. The approaches considered in /HEI 91/ (Tab. 5.1) can be divided into a porosity-independent group with crystallographic geometry and thus constant coordination number and a group with porosity-dependent coordination number. Crystallographic geometries are not able to depict a real deformation process with fracture processes and deviatoric creep and some of the porosity-dependent approaches violate the expectation value at complete compaction and are therefore limited downward in porosity (Tab. 5.1). Compared to non-negative coordination numbers, the porosity may also be upper bounded. In one case, a porosity range is mentioned in

/HEI 91/ caused by identification. Work on the influence of geometrical quantities are topics of other projects.

Tab. 5.1 Functional dependencies between mean coordination number and porosity /HEI 91/

Crystallographic geometry	Coordination number M	Porosity η
Cubic	6	0.476
Orthorhombic	8	0.395
-	8.84	–
Tetragonal	10	0.302
Rhombohedral	12	0.259
-	$3.183^{2.469 - \frac{\eta}{1-\eta}}$	–
-	$26.486 - \frac{10.726}{1-\eta}$	$\eta \leq 0.595$
-	$\frac{3.1}{\eta}$	$0.0 < \eta$
-	$12 \cdot (1 - \eta)$	–
-	$3.824 \left(\frac{\eta}{1-\eta} \right)^{-1.09}$	$0.0 < \eta$ /HEI 91/ $0.286 \leq \eta \leq 0.565$
-	$0.5 \left(1 + \frac{3}{\eta} \right) \left(1 + \sqrt{1 - \frac{16\eta}{(3+\eta)^2}} \right)$	$0.0 < \eta$
Mean from cryst. geometries	$18.44 - 26.35 \eta$	$\eta \leq 0.7$

5.2 Constitutive Models for Crushed salt

5.2.1 BGR-CRUSHED SALT3 model (BGR)

The BGR-CRUSHED SALT3 model considers elastic and creep deformation of crushed salt as well as deformation due to grain rearrangement and humidity creep. The constitutive model as well as its implementation in BGR's proprietary FEM code JIFE have been reviewed both from a theoretical point of view and an updated version is currently under development. Here a condensed version of the detailed documentation published in /KRÖ 17/ is given.

The formulation of the compaction behavior within the constitutive model BGR-CRUSHED SALT3 is based on the geometrical idealization (Fig. 5.2) of the salt

grains presented in /STE 85/. Starting point of the model is an additive decomposition of the strain rate tensor according to the underlying deformation mechanism:

$$\dot{\epsilon}_{ij} = \dot{\epsilon}_{ij}^{elastic} + \dot{\epsilon}_{ij}^{crushed} + \dot{\epsilon}_{ij}^{frac} + \dot{\epsilon}_{ij}^{humidity} + \dot{\epsilon}_{ij}^{dislocation} \quad (5.1)$$

where the elastic component of the deformation is described by an isotropic Hooke's law. Here, the Young's modulus E is piecewise linearly related to the void ratio e . Besides the elastic contribution the model includes a compaction creep rate of the grain peaks $\dot{\epsilon}_{ij}^{crushed}$, a grain rearrangement creep rate $\dot{\epsilon}_{ij}^{frac}$, a contribution for pressure solution creep $\dot{\epsilon}_{ij}^{humidity}$ and a contribution for dislocation movements $\dot{\epsilon}_{ij}^{dislocation}$. The tensor valued creep rates $\dot{\epsilon}_{ij}^{cr}$, with $cr \in \{crushed, frac, humidity, dislocation\}$ are derived from a scalar valued creep function $\dot{\epsilon}^{cr}$ with the following formalism:

$$\dot{\epsilon}_{ij}^{cr} = \dot{\epsilon}^{cr}(\sigma^{eq}) \frac{\partial \sigma^{eq}}{\partial \sigma_{ij}} \quad (5.2)$$

The equivalent stresses $\sigma^{eq} \in \{\sigma^{local}, q\}$ are scalar quantities, which take into account the micro structural stress distribution within the idealized grain of Fig. 5.2. For each deformation mechanism in Equ. (5.1) the underlying theory and the evolution equations are sketched in the following sections.

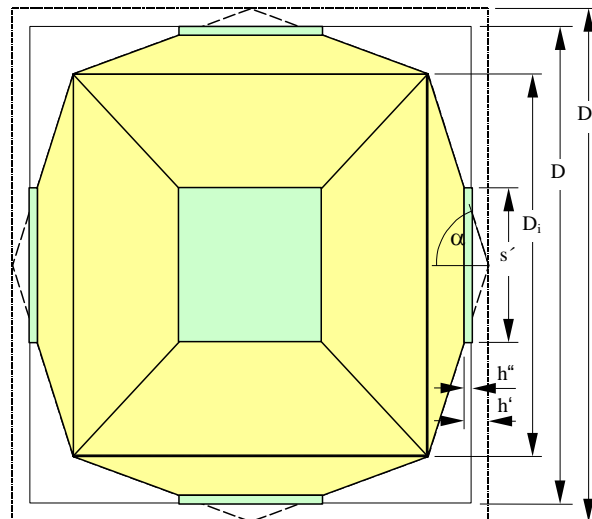


Fig. 5.2 Idealized model of a unit crystal with peak-to-peak contact to six adjoining crystals

5.2.1.1 Compaction Creep

The creep rate $\dot{\epsilon}^{crushed}$ of the crushed salt depends on the stress difference between the local equivalent stress σ^{local} and a dynamically developing frictional hardening stress σ^{RV} , which in a stationary state tends to $\sigma^{RV} \rightarrow z \sigma^{local}$. The local stress at the contact zones is computed from the hydrostatic pressure p , the deviatoric stress q (= von Mises equivalent stress) and the extended relative contact area U' . The relative grain contact area U and its extension U' satisfy the following functions of initial and current void ratio derived from the geometrical idealization ($U = 0$ for virgin uncompacted crushed salt and $U \rightarrow 1$ for complete compaction):

$$U = \left(\frac{3}{2} \frac{1}{\cot(\alpha)} \right)^2 \left(\left(\frac{1 + ke_0}{1 + ke} \right)^{\frac{1}{3}} - 1 \right)^2 \quad (5.3)$$

$$U' = (\kappa U)^\gamma \quad (5.4)$$

$$\cot(\alpha) = \sqrt{1 + ke_0} - 1 \quad (5.5)$$

- κ, γ artificial fit parameters close to 1 [-]
- α Peak angle [-]
- e_0 initial void ratio [-]
- e void ratio [-]

The compaction creep rate then is defined by:

$$\dot{\epsilon}^{crushed} = 2A \exp\left(-\frac{Q}{RT}\right) \left(\frac{\sigma^{local} - \sigma^{RV}}{(1-z)\sigma^*} \right)^n \cot(\alpha) \sqrt{U} \frac{\frac{1}{k} + e}{1 + e} \quad (5.6)$$

$$\sigma^{local} = \sqrt{\left(\frac{p}{U'}\right)^2 + b \left(\frac{q}{U'\beta}\right)^2} \quad (5.7)$$

- β, b fit parameters close to 1 [-]
- σ^* normalization stress [MPa]
- z ratio of frictional stress over local stress [-]
- A structural parameter for Norton law [d⁻¹]
- Q activation energy for Arrhenius term [kJ mol⁻¹]
- n stress power for Norton law [-]
- R universal gas constant [kJ mol⁻¹ K⁻¹]
- T temperature [K]

where $\frac{1}{k}$ is the fraction of total solid mass of the crushed salt that is mainly contributing to this deformation mechanism as described e.g. in /KOM 20/. The compaction creep rate decreases linearly with void ratio thus fulfilling theoretical expectation and avoiding negative porosity. The differential equation for evolution of the frictional hardening stress σ^{RV} in the contact zone, which can also be interpreted as a geometric hardening, is described with an exponential hardening law /HOL 45/:

$$d\sigma^{RV} = \frac{z \sigma^{local} - \sigma^{RV}}{m \epsilon_{vol}} d\epsilon_{vol} \quad (5.8)$$

m fit parameter [-]

5.2.1.2 Grain Rearrangement Creep

Fracturing occurs when the local stress in the contact zone exceeds a given stress limit σ^{frac} . The following scaling has been suggested based on experimental results which indicate that this limit is inverse proportional to the root of grain diameter:

$$\sigma^{frac} = \sigma_F \sqrt{\frac{0.01m}{D_i}} \quad (5.9)$$

σ_F fit parameter [MPa]

D_i grain width [m] (Fig. 5.2)

For a diameter of about 1 cm, the parameter σ_F should be about that of fracture stress for compact rock salt. As a reference value for the grain diameter the fraction with the lowest grain diameter must be taken.

Hence, deformation due to fracture and grain rearrangement will happen as soon as the function $\langle \sigma^{local} - \sigma^{frac} \rangle$ is getting positive. The local effect due to fracturing is given by:

$$\epsilon^{frac} = B^{frac} \left\langle \frac{\sigma^{local} - \sigma^{frac}}{\sigma^*} \right\rangle \cot(\alpha) \sqrt{U} \frac{\frac{1}{k} + e}{1 + e} \quad (5.10)$$

B^{frac} structural parameter [MPa]

5.2.1.3 Humidity Creep

Humidity creep is a deformation mechanism which takes place at the grain boundaries to model the pressure precipitation mechanism. Usually, this mechanism is decomposed

into the phases dissolution of the salt ions from the contact surface, diffusion of these ions within the intercrystalline space and precipitation of the ions. The focus in the modelling of pressure precipitation creep is the diffusion phase analogue to Olivella and Gens /OLI 02/, because it is assumed to be the slowest process which therefore dominates the creep rates. The modelling of humidity creep is assuming diffusion of salt ions having a pressure gradient on the contact areas between the grains as driving force. The macroscopic creep rate is then given by:

$$\dot{\epsilon}^{humidity} = \frac{D^{diff}}{R^{contact} D_i [1+\cot(\alpha)]^{\frac{1}{3}}} \cdot \frac{(1+ke)^{\frac{2}{3}}}{k(1+e)} \cdot \exp\left(-\frac{Q^{diff}}{RT}\right) \cdot \sinh\left(\frac{3\kappa'\sigma^{local}}{TR^{contact}}\right) \quad (5.11)$$

Q^{diff} activation energy for diffusion process [kJ mol⁻¹]

D^{diff} Diffusion coefficient [m² d⁻¹]

κ' parameter [K m MPa⁻¹]

Within this equation the radius $R^{contact}$ results from a radial symmetric capture of the contact area:

$$R^{contact} = \zeta \frac{s'}{2} = \zeta \frac{3 D_i [1+\cot(\alpha)]}{4 \cot(\alpha)} \left[1 - \left(\frac{1+ke}{1+ke_0} \right)^{\frac{1}{3}} \right] \quad (5.12)$$

ζ fit parameter [-]

s' width of the contact area [m]

5.2.1.4 Dislocation Creep

The mechanism of dislocation creep is modelled with a standard Norton-Hoff power law:

$$\dot{\epsilon}^{dislocation} = A \exp\left[-\frac{Q}{RT}\right] \left(\frac{q-\sigma^{RN}}{(1-z)\sigma^*}\right)^n \quad (5.13)$$

If dislocations pile up, the hardening stress σ^{RN} increases and the creep rate decreases. Transient creep can be interpreted as the competing mechanism of dislocation storage and recovery. In /KOC 76/ or in /HEE 89/ an evolution equation of the dislocation density is derived. Based on this, a micromechanical motivated isotropic hardening model was established which leads to the evolution equation for the hardening stress σ^{RN} :

$$\frac{d\sigma^{RN}}{d\dot{\epsilon}^{dislocation}} = \kappa_{RN} \left[\frac{q-\sigma^{RN}}{\sigma^{RN}} - \left(\frac{1-z}{z}\right)^2 \frac{\sigma^{RN}}{q-\sigma^{RN}} \right] \quad (5.14)$$

κ_{RN} hardening modulus [MPa]

5.2.2 Callahan model (Sandia)

This description of the Callahan crushed salt constitutive model is primarily based on information provided in /CAL 99/. For further information and analysis of the formulation, a critical assessment of the Callahan model can be found in /COU 23/. Most of the model is presented in an infinitesimal strain setting for simplicity, but, in actual practice, the model is extended into the finite deformation realm using hypoelasticity as described in Section 2.4 of /REE 18/. Note that the following description uses the convention that tensile stresses and strains are positive.

The final report of KOMPASS phase I /KOM 20/ contains several notation errors due to typesetting and formatting issues. The formulation presented in this section corrects these errors and employs notation that slightly differs from the notation in /CAL 99/.

5.2.2.1 Model equations

The total strain rate is additively decomposed into elastic strain rate $\dot{\varepsilon}_{ij}^e$ and inelastic (creep) strain rate $\dot{\varepsilon}_{ij}^c$ contributions, as shown:

$$\dot{\varepsilon}_{ij} = \dot{\varepsilon}_{ij}^e + \dot{\varepsilon}_{ij}^c \quad (5.15)$$

Thermal expansion is not considered in the original formulation but a thermal strain ε_{ij}^{th} could be readily added to the strain decomposition Equ. (5.15).

5.2.2.2 Elastic behavior

The elastic strain rate may be decomposed into deviatoric $\dot{\varepsilon}_{ij}^e$ and volumetric $\dot{\varepsilon}_{kk}^e$ contributions:

$$\dot{\varepsilon}_{ij}^e = \dot{\varepsilon}_{ij}^e + \frac{1}{3} \dot{\varepsilon}_{kk}^e \delta_{ij} \quad (5.16)$$

In this model the stress rate $\dot{\sigma}_{ij}$ is related to the elastic strain rate by the isotropic linear-elastic relation:

$$\dot{\sigma}_{ij} = 2G\dot{\varepsilon}_{ij}^e + K\dot{\varepsilon}_{kk}^e\delta_{ij} = 2G(\dot{\varepsilon}_{ij} - \dot{\varepsilon}_{ij}^c) + K(\dot{\varepsilon}_{kk} - \dot{\varepsilon}_{kk}^c)\delta_{ij} \quad (5.17)$$

With G and K the shear and bulk modulus of crushed salt, respectively.

Following the work of /SJA 87/, these elastic moduli are assumed to be functions of the crushed salt density ρ . No temperature dependency is included in the functional form of the elastic moduli. The functional forms for these elastic moduli are:

$$G = G_0 \exp(G_1 \rho) \quad (5.18)$$

$$K = K_0 \exp(K_1 \rho) \quad (5.19)$$

G_0, K_0 , material parameters [Pa]
 G_1, K_1 , material parameters [m^3/kg]

These parameters are typically determined from laboratory testing.

5.2.2.3 Inelastic (creep) behavior

The total creep strain rate $\dot{\varepsilon}_{ij}^c$ contains contributions from two deformation mechanisms – dislocation creep $\dot{\varepsilon}_{ij}^{\text{dc}}$ and grain boundary diffusional pressure solution $\dot{\varepsilon}_{ij}^{\text{ps}}$:

$$\dot{\varepsilon}_{ij}^c = \dot{\varepsilon}_{ij}^{\text{dc}} + \dot{\varepsilon}_{ij}^{\text{ps}} \quad (5.20)$$

The model assumes that the crushed salt has compacted enough that grain rearrangement is negligible, and the stresses are low enough that grain breakage is also negligible.

The following flow rules describe the evolution of these two creep strains

$$\dot{\varepsilon}_{ij}^{\text{dc}} = \dot{\varepsilon}_{\text{eq}}^{\text{dc}}(\sigma_{\text{eq}}^f) \frac{\partial \sigma_{\text{eq}}}{\partial \sigma_{ij}} \quad (5.21)$$

$$\dot{\varepsilon}_{ij}^{\text{ps}} = \dot{\varepsilon}_{\text{eq}}^{\text{ps}}(\sigma_{\text{eq}}^f) \frac{\partial \sigma_{\text{eq}}}{\partial \sigma_{ij}} \quad (5.22)$$

The terms $\dot{\varepsilon}_{\text{eq}}^{\text{dc}}$ in Equ. (5.21) and $\dot{\varepsilon}_{\text{eq}}^{\text{ps}}$ in Equ. (5.22) are the equivalent creep strain rates for dislocation creep and grain boundary diffusional pressure solution, respectively. The notation used in Equ. (5.21) and Equ. (5.22) indicates these equivalent creep strain rates are scalar functions of the equivalent stress measure σ_{eq}^f , which is defined in Equ. (5.23). The non-associated creep flow potential σ_{eq} is defined in Equ. (5.24). The partial derivative term $\frac{\partial \sigma_{\text{eq}}}{\partial \sigma_{ij}}$ appearing in Equ. (5.21) and Equ. (5.22) is the normal to the flow potential, which determines the creep flow direction.

Equivalent stress and flow potential

The equivalent stress and flow potential used in Equ. (5.21) and Equ. (5.22) are given by:

$$\sigma_{\text{eq}}^f = \left[\eta_0 \Omega_f^{\eta_1} \sigma_m^2 + \left(\frac{2-D}{D} \right)^{\frac{2n_f}{n_f+1}} \sigma_t^2 \right]^{\frac{1}{2}} \quad (5.23)$$

$$\sigma_{\text{eq}} = \left[\kappa_0 \Omega^{\kappa_1} \sigma_m^2 + \left(\frac{2-D}{D} \right)^{\frac{2n}{n+1}} \sigma_t^2 \right]^{\frac{1}{2}} \quad (5.24)$$

where

$$\Omega_f = \left[\frac{(1-D)n_f}{[1 - (1-D)^{1/n_f}]^{n_f}} \right]^{\frac{2}{n_f+1}} \quad (5.25)$$

$$\Omega = \left[\frac{(1-D_v)n}{[1 - (1-D_v)^{1/n}]^n} \right]^{\frac{2}{n+1}} \quad (5.26)$$

$$D_v = \begin{cases} D_t & \text{if } D \leq D_t \\ D & \text{if } D > D_t \end{cases} \quad (5.27)$$

- D current fractional density = $\frac{\rho}{\rho_{\text{int}}}$ [-]
- ρ_{int} intact salt density [kg/m³]
- σ_m mean stress = $\frac{1}{3} \sigma_{kk}$ [Pa]
- σ_t Tresca equivalent stress = $\sigma_{\text{max}} - \sigma_{\text{min}}$ [Pa]
- σ_{max} maximum principal stress [Pa]
- σ_{min} minimum principal stress [Pa]
- $\eta_0, \eta_1, \kappa_0, \kappa_1, n_f, n, D_t$ = material parameters [-]

The functional forms of Equ. (5.23) and Equ. (5.24) are identical, but each has independent parameters so that one can specify different mean stress and deviatoric stress dependence to the equivalent stress and flow potential. This non-associated formulation allows one to control the ratio of dilation strain to distortional strain without affecting the equivalent stress definition. As crushed salt approaches full consolidation ($D \rightarrow 1$), Ω_f and Ω both approach zero and the mean stress influence on the creep strain rate is eliminated. This is consistent with observed inelastic isochoric deformation characteristics of intact salt. When the salt is fully consolidated, $D = 1$, Equ. (5.23) and Equ. (5.24) reduce to the Tresca equivalent stress:

$$\sigma_{eq}^f = \sigma_{eq} = \sigma_t = \sigma_{max} - \sigma_{min} \quad (5.28)$$

Graphically, the flow potential surface is a closed hexagonal ellipsoid whose major axis is aligned with the hydrostat in when $D < 1$ (Fig. 5.3a), but evolves to a Tresca hexagonal prism whose surface normals are perpendicular to the hydrostat when $D = 1$ (Fig. 5.3b). An expanded expression for the flow potential normal $\frac{\sigma_{eq}}{\sigma_{ij}}$ is provided in Section 2.2.1 of /CAL 99/.

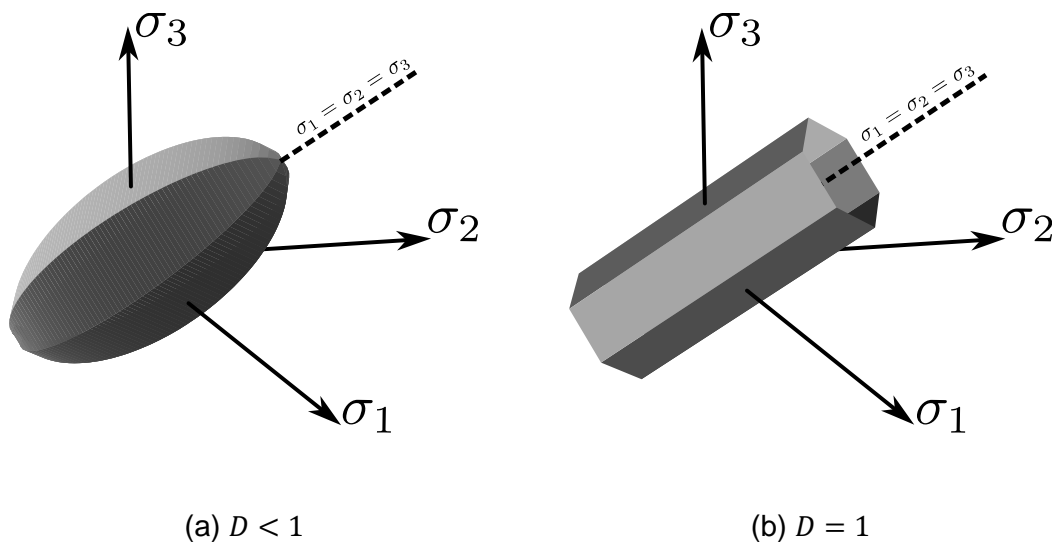


Fig. 5.3 Flow potential at two different relative densities

To complete the description of the creep strain rate, the kinetic equations (i.e., equivalent creep strain rate equations) for dislocation creep $\dot{\epsilon}_{eq}^{dc}$ and grain boundary diffusional pressure solution $\dot{\epsilon}_{eq}^{ps}$ need to be defined.

Kinetic equation for dislocation creep

The dislocation creep model, known as the Multi-mechanism Deformation model (MD model) originally developed by /MUN 79/ and later extended by /MUN 89/, provides the dislocation creep component of the crushed salt model. /REE 18/ recently extended the MD model to account for creep at low equivalent stress and exchanged the Tresca equivalent stress for the Hosford equivalent stress. The creep at low equivalent stress has been incorporated into the Callahan model, but the equivalent stress has been left as Tresca for now.

The kinetic equation for dislocation creep in the MD model is given by

$$\dot{\epsilon}_{\text{eq}}^{\text{dc}} = \dot{\epsilon}^{\text{ss}} + \dot{\epsilon}^{\text{ts}} \quad (5.29)$$

$\dot{\epsilon}^{\text{ss}}$ steady state dislocation creep strain rate [-]

$\dot{\epsilon}^{\text{ts}}$ transient dislocation creep strain rate [-]

In the current MD model, four steady state dislocation mechanisms are considered. The steady state dislocation mechanism associated with low equivalent stress is denoted $\dot{\epsilon}_0^{\text{ss}}$. Several experimental observations indicate that the micro-mechanical origin for the low stress behavior is pressure solution redeposition along the grain boundaries /BÉR 19/. The other three steady state dislocation mechanisms are the same as in the legacy MD model: dislocation climb $\dot{\epsilon}_1^{\text{ss}}$, an unidentified but experimentally observed mechanism believed to be cross-slip $\dot{\epsilon}_2^{\text{ss}}$, and dislocation slip $\dot{\epsilon}_3^{\text{ss}}$. Because these mechanisms are assumed to act in parallel, their contribution to the steady state dislocation creep strain rate is simply the sum of the four:

$$\dot{\epsilon}^{\text{ss}} = \sum_{i=0}^3 \dot{\epsilon}_i^{\text{ss}} \quad (5.30)$$

$$\dot{\epsilon}_i^{\text{ss}} = A_i \left(\frac{\sigma_{\text{eq}}^{\text{f}}}{\mu} \right)^{n_i} \exp\left(-\frac{Q_i}{RT}\right) \text{ for } i < 3 \quad (5.31)$$

$$\dot{\epsilon}_3^{\text{ss}} = H(\sigma_{\text{eq}}^{\text{f}} - \sigma_0) \sum_{i=0}^2 B_i \exp\left(-\frac{Q_i}{RT}\right) \sinh\left[q \left(\frac{\sigma_{\text{eq}}^{\text{f}} - \sigma_0}{\mu} \right)\right] \quad (5.32)$$

$A_0, A_1, A_2, B_0, B_1, B_2$	structure factors [1/s]
n_0, n_1, n_2	stress exponents [-]
Q_0, Q_1, Q_2	activation energies [J/mol]
R	universal gas constant = 8.31446 [J/(mol K)]
T	absolute temperature [K]
q	stress constant [Pa]
σ_0	stress limit [-]
μ	shear modulus of intact salt [Pa]
$H(\cdot)$	Heaviside function with argument $(\sigma_{\text{eq}}^{\text{f}} - \sigma_0)$

The low stress mechanism “0” has the same functional form as mechanisms “1” (dislocation climb) and “2” (unidentified). Mechanisms “0” (low stress) dominates at low equivalent stress and low temperature. It characterizes pressure solution at crystal boundaries *within the grains* of intact salt, which differs from the grain boundary diffusional pressure

solution creep mechanism *between the grain*, presented in the next section. This difference can be important if the crystal size is much smaller than the size of the crushed salt grains. In the present work, pressure solution within the grains is neglected for simplicity and Mechanism “0” is not used Mechanism “1” (dislocation climb) dominates at low equivalent stress and high temperature. Mechanism “2” (unidentified or unnamed) dominates at medium equivalent stress and low temperature. Mechanism “3” (dislocation glide) is only active at high stress when $\sigma_{eq}^f > \sigma_0$, as reflected by the Heaviside function $H(\cdot)$.

The evolution of the transient strain is given by:

$$\varepsilon^{ts} = (F - 1)\varepsilon^{ss} \quad (5.33)$$

Where the transient function F has three branches: a work hardening branch ($F > 1$), an equilibrium branch ($F = 1$), and a recovery branch ($F < 1$)

$$F = \begin{cases} \exp \left[\Delta \left(1 - \frac{\varepsilon^{ts}}{\varepsilon^{tl}} \right)^2 \right] & \text{if } \varepsilon^{ts} < \varepsilon^{tl} & \text{Transient Branch} \\ 1 & \text{if } \varepsilon^{ts} = \varepsilon^{tl} & \text{Equilibrium Branch} \\ \exp \left[-\delta \left(1 - \frac{\varepsilon^{ts}}{\varepsilon^{tl}} \right)^2 \right] & \text{if } \varepsilon^{ts} > \varepsilon^{tl} & \text{Recovery Branch} \end{cases} \quad (5.34)$$

delimited by the transient strain limit ε^{tl} , prescribed by /REE 18/ as:

$$\varepsilon^{tl} = \sum_{i=0}^1 \varepsilon_i^{tl} \quad (5.35)$$

$$\varepsilon_i^{tl} = k_i \exp(c_i T) \left(\frac{\sigma_{eq}^f}{\mu} \right)^{m_i} \quad (5.36)$$

k_i	material parameter [1/s]
c_i	material parameter [1/K]
m_i	material parameter [-]
T	absolute temperature [K]
μ	shear modulus of intact salt [Pa]

The transient strain ε^{ts} acts as an internal variable (written ζ in the original formulation). The choice of the particular branch depends on the transient strain limit ε^{tl} and the

internal variable ε^{ts} . The legacy MD model used a single mechanism to describe the stress and temperature dependence of the transient strain limit. /REE 16/, however, analyzed the data from /SAL 15/ and /DÜS 15/ and discovered larger transient strain limit values for equivalent stress < 8 MPa than would be expected from extrapolating from higher stresses. Therefore, an additional mechanism of identical form to the legacy model was added to capture the transient creep at low equivalent stress”: subscript “0” identifies the low stress transient strain limit term and subscript “1” the legacy transient strain limit term. The quantities Δ and δ , appearing in Equ. (5.34), are the work hardening and recovery parameters and are given by:

$$\Delta = \alpha_h + \beta_h \log_{10} \left(\frac{\sigma_{\text{eq}}^f}{\mu} \right) \quad (5.37)$$

$$\delta = \alpha_r + \beta_r \log_{10} \left(\frac{\sigma_{\text{eq}}^f}{\mu} \right) \quad (5.38)$$

$\alpha_h, \beta_h, \alpha_r, \beta_r$ material parameters

The recovery parameter δ is often taken to be constant (i.e., $\beta_r = 0$) because of insufficient data.

Kinetic equations for grain boundary diffusional pressure solution

This section transitions from the earlier infinitesimal strain presentation to a finite strain presentation in order to more accurately define the logarithmic volumetric strains in terms of densities and fractional densities. The kinetic equation for grain boundary diffusional pressure solution between the grains, used in the Callahan model, is a modified version of the /SPI 93/ model for moist crushed salt:

$$\varepsilon_{\text{eq}}^{\text{ps}} = \frac{r_1 w^a}{d^p} \exp(-\bar{\varepsilon}_v) \left(\frac{\exp(r_3 \bar{\varepsilon}_v)}{|\exp(\bar{\varepsilon}_v) - 1|^{r_4}} \right) \frac{\exp\left(-\frac{Q_s}{RT}\right)}{T} \Gamma \sigma_{\text{eq}}^f \quad (5.39)$$

- r_1 material parameter [$\text{m}^p \text{K}/(\text{Pa s})$]
- r_3, r_4 material parameters [-]
- a, p material parameters [-]
- Q_s material parameter [J/mol]
- T absolute temperature [K]
- R universal gas constant 8.31446 [J/(mol K)]
- d salt grain size [m]
- w moisture fraction by weight [-]
- $\bar{\varepsilon}_v$ logarithmic shifted volumetric strain [-]
- Γ large consolidation function [-]

Note that if the crushed salt is dry ($w = 0$) the grain boundary diffusional pressure solution contribution to the total strain rate vanishes i.e., $\dot{\varepsilon}_{eq}^{ps} = 0$. Also note that the term $\exp(-\bar{\varepsilon}_v)$ should not be present, it is an error due to accidental conversion between engineering strain and logarithmic strain measures in the original formulation. This error is purposely maintained in the current formulation and implementation for consistency purposes with /CAL 99/.

Equ. (5.39) contains the term $e^{\bar{\varepsilon}_v} - 1$ in the denominator, which could cause problems when the volumetric strain is zero at the start of a calculation. To avoid that issue, a fictitious initial volumetric strain ε_v^* is introduced to shift the actual volumetric strain ε_v so that the shifted volumetric strain $\bar{\varepsilon}_v$ is always negative:

$$\bar{\varepsilon}_v = \varepsilon_v + \varepsilon_v^* = \ln\left(\frac{\rho^*}{\rho}\right) = \ln\left(\frac{D^*}{D}\right) \quad (5.40)$$

$$\varepsilon_v^* = \ln\left(\frac{\rho^*}{\rho_0}\right) = \ln\left(\frac{D^*}{D_0}\right) \quad (5.41)$$

D_0	initial crushed salt fractional density [-]
D^*	fictitious reference fractional density [-]
ρ_0	initial crushed salt density [kg/m ³]
ρ^*	fictitious reference density [kg/m ³]

The shifted strain is defined relative to the fictitious reference configuration at density $\rho^* < \rho_0$, or fractional density $D^* < D_0$. According to /CAL 99/, a value of the fictitious fractional density $D^* = 0.64$ is typically set and corresponds to the random close packing of monodisperse spheres. The following relationships between porosity, density, and fractional density are useful:

$$D = \frac{\rho}{\rho_{int}} = 1 - \phi \quad (5.42)$$

$$D_0 = \frac{\rho_0}{\rho_{int}} = 1 - \phi_0 \quad (5.43)$$

$$D^* = \frac{\rho^*}{\rho_{int}} = 1 - \phi^* \quad (5.44)$$

ϕ	current crushed salt porosity [-]
ϕ_0	initial crushed salt porosity [-]
ϕ^*	fictitious reference porosity ($\phi^* = 0.36$) [-]

The large consolidation function Γ used in Equ. (5.39) has two branches: a small consolidation branch, and large consolidation branch, depending on the magnitude of the volumetric strain.

$$\Gamma = \begin{cases} 1 & \text{small consolidation } (\exp(\bar{\varepsilon}_v) > 0.85) \\ \left[\frac{\exp(\bar{\varepsilon}_v) + \phi^* - 1}{\phi^* \exp(\bar{\varepsilon}_v)} \right]^{n_s} & \text{large consolidation } (\exp(\bar{\varepsilon}_v) < 0.85) \end{cases} \quad (5.45)$$

n_s material parameter

For compressive engineering volumetric strains less than 15 %, a constant value of $\Gamma = 1$ is used. For compressive engineering volumetric strains greater than 15 %, a value of $\Gamma = (\phi/\phi^*)^{n_s}$ is used: as the crushed salt density approaches the density of intact salt, the value of Γ approaches zero; therefore, $\varepsilon_{eq}^{DS} = 0$ when the salt is fully consolidated.

5.2.3 CODE_BRIGHT model (GRS)

The finite-element code CODE_BRIGHT was designed to handle thermal-hydraulic-mechanical coupled problems in porous media. The code, as well as the pre- and post-processor GiD is developed at the Polytechnical University of Barcelona /GID 23/.

The crushed salt model is based on an additive approach including an elastic, viscoplastic and creep part. The latter combines the fluid assisted diffusional transfer mechanism and the dislocation creep mechanism.

$$\dot{\varepsilon} = \dot{\varepsilon}_{el} + \dot{\varepsilon}_c + \dot{\varepsilon}_{vp} \quad (5.46)$$

$$\dot{\varepsilon}_c = \dot{\varepsilon}_{FADT} + \dot{\varepsilon}_{DC} \quad (5.47)$$

5.2.3.1 Linear Elasticity

The elastic behavior for crushed salt is described by the Generalized Hook's law in combination with a variation of Young's modulus with porosity:

$$E = E_0 + (\Phi - \Phi_0) \frac{dE}{d\Phi} \geq E_{min} \quad (5.48)$$

E_0 Initial value for Young's modulus [MPa]

Φ Porosity [-]

Φ_0 Initial porosity [-]

$dE/d\Phi$ Variation of Young's modulus with porosity [MPa]

E_{min} Minimum value for Young's modulus [MPa]

5.2.3.2 Grain rearrangement

To capture effects of grain reorganization and sliding which causes changes in the structure of the material, a viscoplastic part was added. The approach is based on the critical state theory /OLI 02/.

$$\dot{\varepsilon}_{vp} = \Gamma \langle \sigma(F) \rangle \frac{\partial G}{\partial \sigma} \quad (5.49)$$

Γ Inverse viscosity
 $\sigma(F)$ stress function
 F viscoplastic yield function
 G flow rule

$$\sigma(F) = F^m \quad (5.50)$$

$$G = F = q^2 - \delta^2(p_0 p' - p'^2) \quad (5.51)$$

$$\Gamma = \Gamma_0 \exp\left(-\frac{Q}{RT}\right) \quad (5.52)$$

$$dp_0 = p_0 \frac{1+e}{\lambda-\kappa} d\varepsilon_v = p_0 \frac{1+e}{X} d\varepsilon_v \quad (5.53)$$

$$p = \sigma_{oct} = \frac{1}{3} I_1 = \frac{1}{3} (\sigma_x + \sigma_y + \sigma_z) \quad (5.54)$$

$$q = \frac{3}{\sqrt{2}} \tau_{oct} \quad (5.55)$$

$$= \frac{1}{\sqrt{2}} \sqrt{(\sigma_x - \sigma_y)^2 + (\sigma_y - \sigma_z)^2 + (\sigma_z - \sigma_x)^2 + 6(\tau_{xy}^2 + \tau_{yz}^2 + \tau_{zx}^2)}$$

m power in the stress function
 δ parameter in flow rule
 p_0 initial value of hardening parameter
 Γ_0 initial value for fluidity
 Q activation energy
 R gas constant
 T temperature
 X parameter in hardening law

5.2.3.3 Fluid assisted diffusional transfer mechanism

The fluid assisted diffusional transfer (FADT) mechanism describes the humidity induced creep including dissolution and precipitation processes. Dissolution occurs in areas with

high stresses, the salt migrates through the liquid phase and will be precipitated in areas of lower stress /CZA 20/, /OLI 95/.

$$\varepsilon_{ij}^{FADT} = \frac{1}{2\eta_d^{FADT}} (\sigma'_{ij} - p' \delta_{ij}) + \frac{1}{3\eta_v^{FADT}} p' \delta_{ij} \quad (5.56)$$

$$\sigma'_{ij} = \sigma_{ij} + \delta_{ij} P_f \quad (5.57)$$

$$p = \frac{1}{3} (\sigma'_x + \sigma'_y + \sigma'_z) \quad (5.58)$$

$$P_f = \max (P_g, P_l) \quad (5.59)$$

σ'_{ij}	effective stress
p	mean effective stress
P_f	fluid pressure

The definitions for the volumetric and deviatoric viscosities, the temperature dependent parameter and the geometrical functions are given as:

$$\frac{1}{2\eta_d^{FADT}} = \frac{16B(T)\sqrt{S_l}}{d_0^3} g_d^{FADT}(e) \quad (5.60)$$

$$\frac{1}{\eta_v^{FADT}} = \frac{16B(T)\sqrt{S_l}}{d_0^3} g_v^{FADT}(e) \quad (5.61)$$

$$B(T) = \frac{A_B}{RT} \exp \frac{g^2}{(1+e)} \quad (5.62)$$

$$g_d^{FADT}(e) = \frac{(1+e)}{(\sqrt{1+e} - \sqrt{2e/\lambda_v})^4} \quad (5.63)$$

$$g_v^{FADT}(e) = \frac{3e^{3/2}(1+e)}{(\sqrt{1+e} - \sqrt{2e/\lambda_v})^4} \quad (5.64)$$

5.2.3.4 Dislocation creep mechanism

The dislocation creep (DC) mechanism covers several mechanisms related to the dislocation theory, e.g., dislocation glide and climb. It is described by a creep power law which is known from rock salt investigations /OLI 95/.

$$\dot{\epsilon}_{ij}^{DC} = \frac{1}{\eta_{DC}^d} \Phi(F) \frac{\partial G}{\partial \sigma'_{ij}} \quad (5.65)$$

G flow rule
F stress function
 Φ scalar function

The following functions are used for specifying the flow rule and stress function, the volumetric and deviatoric viscosities, the geometrical relations in dependence of void ratio, as well as the temperature dependence.

$$F = G = \sqrt{q^2 + \left(\frac{-p}{\alpha_p}\right)^2} \quad (5.66)$$

$$\Phi(F) = F^n \quad (5.67)$$

$$\alpha_p = \left(\frac{\eta_{DC}^v}{\eta_{DC}^d}\right)^{\frac{1}{n+1}} \quad (5.68)$$

$$\eta_{DC}^v = A(T) g_{DC}^v(e) \quad (5.69)$$

$$\eta_{DC}^d = A(T) g_{DC}^d(e) \quad (5.70)$$

$$g_{DC}^v(e) = 3(g - 1)^n f \quad (5.71)$$

$$g_{DC}^d(e) = \left(\sqrt{\frac{1 + g + g^2}{3}}\right)^{n-1} \left(\frac{2g + 1}{3}\right) f + \frac{1}{\sqrt{g}} \quad (5.72)$$

$$A(T) = A_A \exp\left(\frac{-Q_A}{RT}\right) \quad (5.73)$$

$$g = \frac{1}{(1 - f)^2} = \frac{d^2}{x^2} \quad (5.74)$$

$$f = \frac{\sqrt{2e}}{\sqrt{3(1 - e^{\frac{3}{2}})(1 + e)}} = \frac{\sqrt{2}s}{d} \quad (5.75)$$

$$q = \sqrt{3J_2} \quad (5.76)$$

$$p' = \frac{1}{3}(\sigma'_x + \sigma'_y + \sigma'_z) \quad (5.77)$$

q deviatoric stress [MPa]
 p' mean net stress [MPa]
 J_2 second invariant of the deviatoric stress tensor [MPa]

5.2.4 EXPO-COM (TUC)

5.2.4.1 Selection of the database for the development of a constitutive model

Originally, TUC used the C-WIPP model to represent the behavior of crushed salt. In the framework of KOMPASS-I shortcomings of the model C-WIPP were detected and the model was partially improved by addition of the missing influencing factor deviatoric stress as well as due to reformulation of the flaw in deformation distribution in the 3D-space which caused implausible results for some load configurations. This modified model was referred to as C-WIPP-TUC. More detailed information to this model variation can be found in the final report of KOMPASS-I project.

The model development C-WIPP-TUC was based on experimental data from test TK-031 from BGR (crushed salt from Asse mine, not KOMPASS material) and from test TUC-V2 - phase I (KOMPASS reference material). The model development was evolutionary, i.e., due to minor changes. The database was so small that comparatively minor changes in the model formulation were sufficient to accurately reproduce the measured data.

The remaining shortcoming and deficiencies of the model C-WIPP-TUC were, however, so significant and substantial that it made more sense leaving the evolutionary way of model development (→ small changes) and creating a brand-new model with the acronym EXPO-COM (exponential and power functions for the compaction behavior of crushed salt). This newly developed approach is still purely phenomenological.

The development of model EXPO-COM as well as the determination of the material parameter set was based on extended experimental database including 5 additional phases of test TUC-V2 with a total duration of 750 days. Since this database, generated so far from the entire planned laboratory program, is still insufficient to develop a new model with all relevant influencing factors, especially with regard to the influence of water content on compaction behavior, three tests from GRS (crushed salt from Asse mine) performed in the REPOPERM II /KRÖ 17/ project were temporarily used. The tests TUC-V5 and TUC-V6 to TUC-V8, to be performed at KOMPASS reference material, planned for the follow-up project will replace this GRS database of three tests in the future.

As a consequence, the following five long-term tests were selected from the currently available database: TK-031 from BGR, TUC-V2 and three tests GRS-dry/GRS-

0.1%/GRS-wet. Detailed information about test TUC-V2, including the load history and investigated factors of influence, is provided in Section 3.3.5. Detailed information about test TK-031 can be found in the final report of KOMPASS-I /KOM 20/. Detailed information about the tree tests from GRS is given in the final report of REPOPERM II /KRÖ 17/. Fig. 5.4 and Fig. 5.5 show in a schematic overview the most important information regarding the tests TK-031 as well as GRS-dry, GRS-0.1% and GRS-wet that were used for the analysis. In this context, it has to be emphasized that one central objective of the modeling approach is to capture the functional relationships between the influencing factors and compaction stain rate (derived from a measured quantity).

The selected database can thus be characterized on the one hand as insufficient, not systematic, heterogeneous (different labs with measurement principles and equipment) and not uniform (different materials) with respect to the development and validation of a constitutive model for crushed salt compaction, but on the other hand it is best alternative until the completion of all tests planned for KOMPASS-I, KOMPASS-II and following projects.

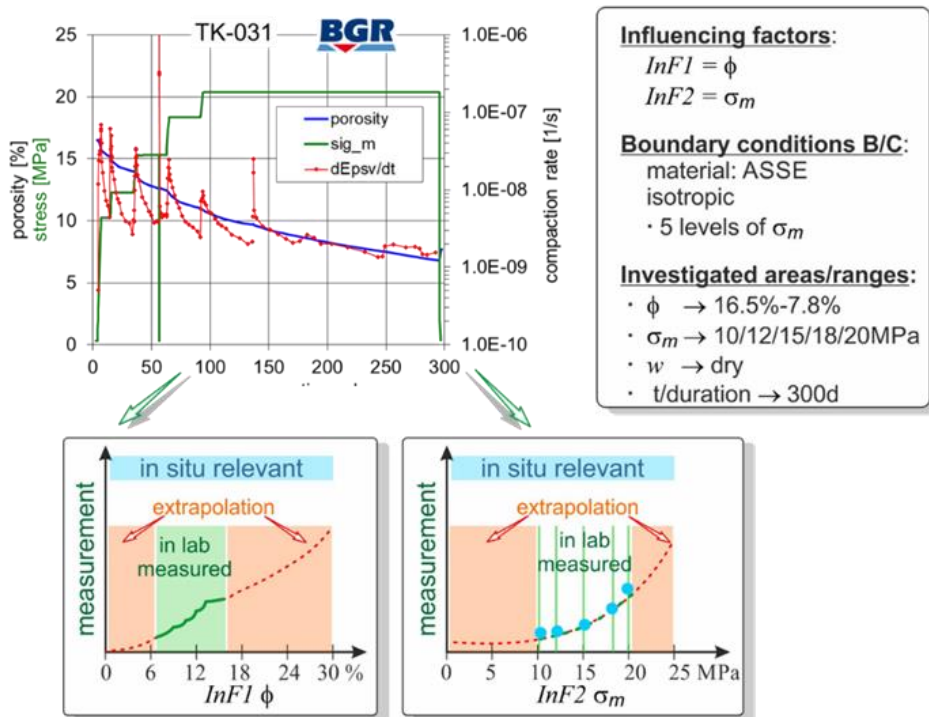
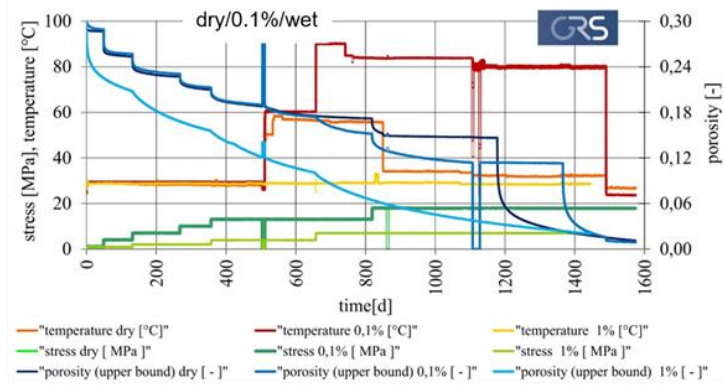


Fig. 5.4 Test TK-031 from BGR – measurements for compaction rate and porosity, boundary conditions and investigated ranges of the influencing factors in comparison to the in situ relevant ranges



Influencing factors	Boundary conditions B/C	Investigated ranges
$Inf1 = \phi$ $Inf2 = \sigma_m$ $Inf3 = T$ $Inf4 = w (!)$	$\sigma_z = \text{const}, \varepsilon_x = 0$ • 4-6 levels of σ_z • 1-3 levels of T • 3 samples with diff. w	• $\phi \rightarrow 30\% - 1\% (!)$ • $T \rightarrow 30^\circ\text{C}/\sim 60^\circ\text{C}/\sim 80^\circ\text{C}$ • $\sigma_z \rightarrow 1/2/4/7\text{MPa}$ • $w \rightarrow \text{dry}/ 0.1\%/ 1\%\text{-wet}$ • $\sigma_z \rightarrow 1/4/7/10/13/18\text{MPa}$ • $t/\text{duration} \rightarrow 1600\text{d} (!)$ • $\sigma_m \rightarrow (?)$

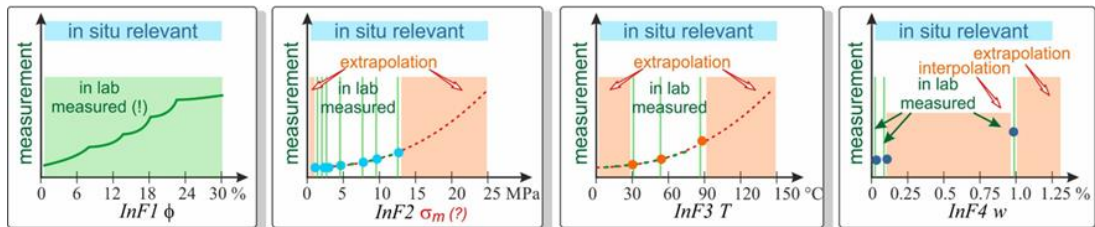


Fig. 5.5 Tests GRS-dry/GRS-0.1%/GRS-wet from GRS – measurements for porosity, boundary conditions and investigated ranges of the influencing factors in comparison to the in situ relevant ranges

5.2.4.2 Analysis of database, development strategy and development of the new model

There are two main objectives for the analysis of the experimental database:

1. For the model development phase, establish a clear-cut analysis and unambiguous identification of the functional relationships to be defined.
2. For the model calibration phase, process data in a way that is directly applicable for a distinct and possibly explicit determination of the model parameters.

The measured values are usually available in the form of displacements and volumes, from which strains can be determined (e.g., axial strain, volumetric strain). However, the constitutive model should be formulated in terms of strain rate as a function of multiple influencing factors (e.g., mean stress, deviatoric stress etc.). For this reason, it is purposeful to first calculate the strain rates from the measured data and then to plot and analyze the rates as a function of the currently investigated influencing factor instead of

time. This procedure is independent from the specific assumptions of an individual constitutive model and therefore generally applicable and valid.

Furthermore, within the framework of the applied methodical approach for the model development, in the first step the decision about the choice of the model strategy is to be made: model justification (microstructural or phenomenological type) and the model structure. For the optimal application of the model and the optimal possibility of parameter determination for the model (with the possibility of process isolation (activation and deactivation) and isolation of individual influencing factors) model structure with an additive superposition of the processes and a multiplicative superposition of the impact of the influencing factors is recommended is considered sensible/appropriate.

For the phenomenological model, the following (exemplarily) structure would result:

$$\dot{\varepsilon}^{total} = \dot{\varepsilon}^{elast} + \dot{\varepsilon}^{viscous\ shear} + \dot{\varepsilon}^{viscous\ compaction} \quad (5.78)$$

For the microstructural based modeling approach respectively, following (exemplarily) structure would result:

$$\dot{\varepsilon}^{total} = \dot{\varepsilon}^{grain\ rearrangement} + \dot{\varepsilon}^{dislocation\ creep} + \dot{\varepsilon}^{pressure\ solution} \quad (5.79)$$

Within the framework of this selected overall model structure, the structure for individual processes can then be chosen/determined as follows (here exemplified for the phenomenological model for the sub-process of viscous compaction):

$$\dot{\varepsilon}^{viscous\ compaction} \sim f(\phi) \cdot f(T) \cdot f(\sigma) \cdot f(w) \quad (5.80)$$

If this definition of the model structure proves to be well applicable in the course of the lab database analysis, it remains, however, if it cannot represent the test results correctly and contradicts these, the structure must be modified in the concerned model section in favor of the realism at the expense of the practicability. In the EXPO-COM material model, for example, the dependence of the compaction behavior on the moisture content was reformulated, as a simple multiplicative overlay for this influence factor was insufficiently accurate to represent the selected laboratory database (see Fig. 5.7 for the final model structure).

Fig. 5.6 demonstrates the practical realization of the comparative analysis of the data obtained from the five chosen compaction tests. Fig. 5.6a shows the original measurements for the individual tests (measured deformations normalized to the initial sizes): green – TUC-V2, blue – TK-031 from BGR, yellow/orange/red – GRS-dry/GRS-0.1%/GRS-wet. Fig. 5.6b the result of the first step of the database preparation can be seen: the rates are derived from the volume strains and plotted versus time. In Fig. 5.6c the volumetric strain rates are now plotted versus porosity. Fig. 5.6d depicts the rates normalized with respect to the mean stress (the normalization stress levels are listed in the diagram). The normalization is done as follows: the jumps in the strain rate caused by stress change are leveled, thus the normalization has the goal to represent/approximate a strain rate progression for the case of only one level of the stress without any changes for the entire duration of the experiment. An alternative way of normalization, by using the function of stress was deliberately avoided in order to avoid the negative influence of the uncertainties in the stress function on the normalization of the strain rates. In the chosen version of the normalization the influence of the model assumptions and uncertainties in the assumptions for the stress dependency is avoided, the impact of transient effects after the stress changing is however still there. Finally, Fig. 5.6e and f present the comparison between the processed and normalized data and the analytical curves from the new constitutive model EXPO-COM for the dependency from porosity $\dot{\epsilon}_{com} \sim f(\text{porosity})$. Fig. 5.6e represents the tests TUC-V2 and TK-031 and Fig. 5.6f represents the tests GRS-dry, GRS-0.1% and GRS-wet. In these diagrams, some jumps were intentionally left unnormalized to additionally accent the effects caused by the changes in temperature, deviatoric stress and moisture content.

In this regard, the following aspects should be mentioned in particular:

- Regardless of backfill material, moisture content and temperature being different, tests TK-031 and TUC-V2 show similar behavior with respect to the curve shape (the slope of the curves) for the dependence between volume strain rate and porosity. It is therefore to be expected, that the constitutive model parameters for the characterization of specimen TK-031 and TUC-V2 will have a similar order of magnitude.
- A comparison of tests TUC-V2 and TK-031 with the oedometer tests GRS-dry and GRS-0.1% shows significant differences. Therefore, the parameter sets can be expected to differ considerably.

- The influence of temperature on the compaction behavior is similar for both TUC and GRS samples (indicated by similar sizes of jumps).
- The influence of moisture content on the compaction behavior is evidently significant. Clear difference in the inclinations for the dry and wet samples of GRS can be distinguished.
- The difference between the results from GRS-dry and GRS-0.1% is nearly undetectable on the other hand. Considering the previous statements, therefore the dependence on moisture content has to be represented in the model with clearly non-linear correlations.

As a result of the systematic comparison of normalized quantities (to represent individual dependencies between the volumetric strain rate and influencing factors), it was evidently possible to define functional relations that qualitatively and quantitatively represent the compaction behavior of crushed salt with sufficient accuracy for all different levels of all investigated influencing factors.

Remarks:

- 1) This kind of analysis of measured values serves not only for the development of the EXPO-COM model but is more generally valid and can be used for the development and validation of other constitutive models (rather phenomenological type).
- 2) The applied methodology of the analysis serves not only to establish the functional forms in the modeling approach, but also to calibrate the model. That also means the model is calibrated against multiple different materials.

Additional information to the analysis methodology for the lab measurements can be found in /DÜS 21/.

Lab database: preparation, isolation, normalization
for individual and comparative analysis

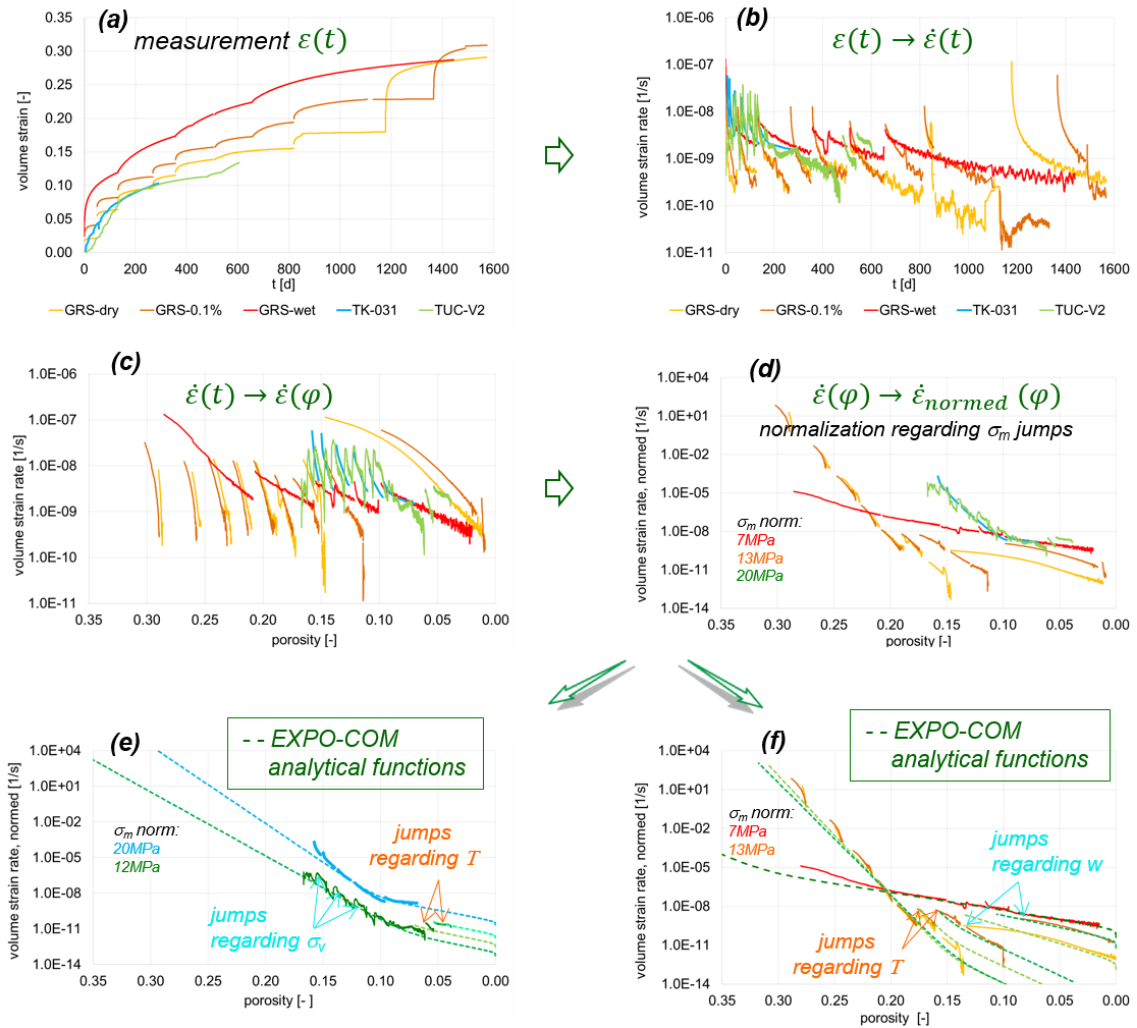


Fig. 5.6 Database preparation for the five chosen tests and comparison of measurements with analytical curves for the dependency of compaction from porosity in the newly developed constitutive model EXPO-COM

5.2.4.3 Structure and the functional relations of the model EXPO-COM

The structure of the newly developed constitutive model EXPO-COM is schematically shown in Fig. 5.7.

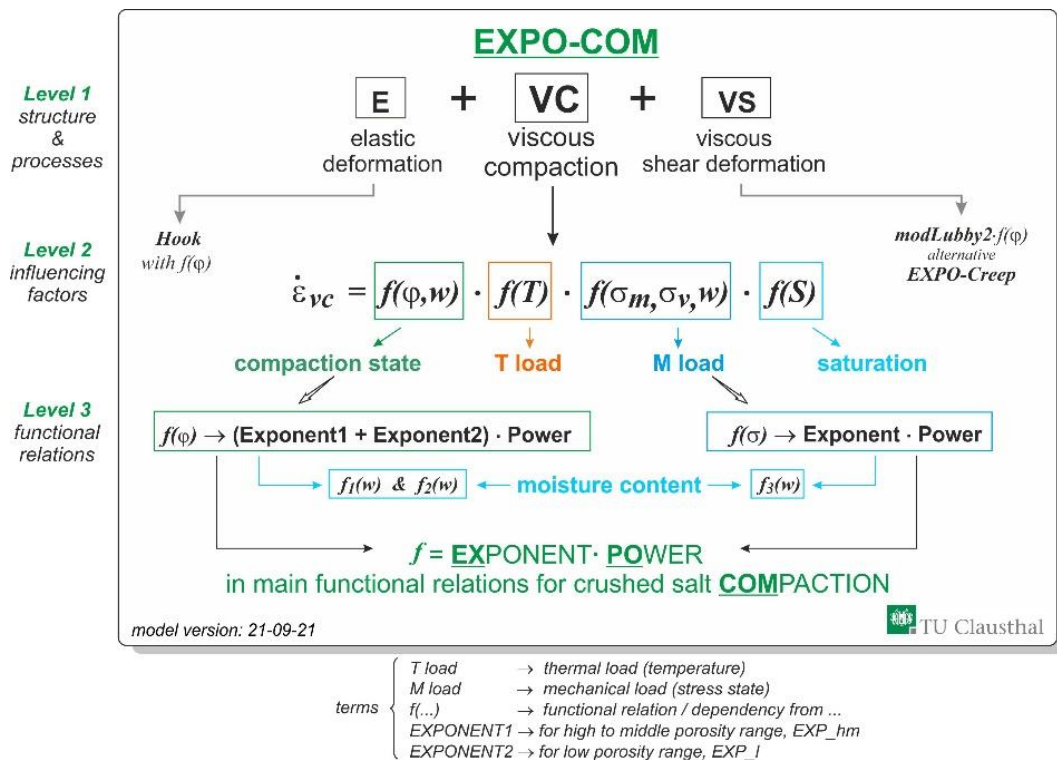


Fig. 5.7 Structure of the new constitutive model EXPO-COM for the material behavior of crushed salt

According to the description in Fig. 5.7, in contrast to the C-WIPP model which is characterized by merely two influencing factors (mean stress and porosity), all relevant experimentally detected influencing factors are now implemented in the EXPO-COM model – mean stress, porosity, deviatoric stress, temperature and moisture content with the exception of grain size distribution (since only KOMPASS reference material with defined grain size distribution will be used in the framework of KOMPASS-I, KOMPASS-II and the follow-up project, thus no information in regard to this factor is available so far). The pre-factors in functional relations regarding the stress and the porosity were formulated as variables dependent from moisture content, designated here as the functions $f_1(w)$, $f_2(w)$ and $f_3(w)$. Thereby the two main dependencies, expressed by the **exponential** and **power** functions to characterize the relations regarding the influencing factors stress and porosity, inspired the name of the new constitutive model. Furthermore, a significant modification is the incorporation of modLubby2 as the creep term into the EXPO-COM model. The term modLubby2, representing the creep behavior of rock salt, /LER 12/ is additionally multiplied by a porosity-function, which is adopted from the accelerated damage part of the constitutive model Lux/Wolters/Lerche /LUX 18/. Additionally, a new creep term EXPO-Creep is currently being developed for the crushed salt model to capture the transient creep phase more realistically.

The new model EXPO-COM involves following formulations:

Elastic deformation part

The formulation for the elastic deformation in the model is currently adopted from the model C-WIPP since no additional specific tests have been performed with the KOMPASS reference material so far in this regard. The formulations for the elastic part of the C-WIPP model can be found in the KOMPASS-I report /KOM 20/.

Viscous shear deformation part

The formulation for the viscous shear deformations is adopted from the model mod-Lubby2 for rock salt /LER 12/, /HAM 07/. The representation of the formulation of mod-Lubby2 is presented in detail in /LER 12/ and not recalled here. The functional relations take into account the higher rate of creep deformation of crushed salt in contrast to the rock salt are represented by the following functional relations:

$$\dot{\varepsilon}_{ij}^{vp} = \dot{\varepsilon}_{ij}^{tr} + \dot{\varepsilon}_{ij}^{st} = [f(\bar{\eta}_k, \bar{G}_k) + f(\bar{\eta}_m)] \cdot s_{ij} \quad (5.81)$$

$$\bar{\eta}_m = \bar{\eta}_m(\text{modLubby2})/f_{vs_st}(\varphi) \quad (5.82)$$

$$\bar{\eta}_k = \bar{\eta}_k(\text{modLubby2})/f_{vs_tr}(\varphi) \quad (5.83)$$

$$\bar{G}_k = \bar{G}_k(\text{modLubby2})/f_{vs_tr}(\varphi) \quad (5.84)$$

$$f_{vs_st}(\varphi) = \exp(c_{2_cr_st} \cdot \varphi) \quad (5.85)$$

$$f_{vs_tr}(\varphi) = \exp(c_{2_cr_tr} \cdot \varphi) \quad (5.86)$$

Viscous compaction deformation part

Structure forming relations:

$$\dot{\varepsilon}_{ij}^{vc} = \dot{\varepsilon}_{vol}^{vc} \cdot RV^{vc}_{ij} \quad (5.87)$$

$$\dot{\varepsilon}_{vol}^{vc} = -3 \cdot f(\sigma_m, \sigma_v, w_g) \cdot f(\varphi, w_g) \cdot f(T) \cdot f(S) \quad (5.88)$$

$$RV^{vc}_{ij} = \left[\frac{\delta_{ij}}{3} - f(\alpha) \cdot \frac{s_{ik} \cdot \delta_{kj}}{\sigma_v} \right] \quad (5.89)$$

Main functional relations:

$$f(\sigma_m, \sigma_v) = \exp\left(C_{1e}^{iso} \cdot \frac{\sigma_m}{\sigma_*} + C_{1e}^{dev} \cdot \frac{\sigma_v}{\sigma_*}\right) \cdot \left(\frac{\sigma_m}{\sigma_*} + \frac{\sigma_v}{\sigma_*}\right)^{C1p} \quad (5.90)$$

$$f(\varphi) = (EXP_{hm} + EXP_l) \cdot POWER_h \quad (5.91)$$

$$EXP_{hm} = C_0^{hm} \cdot (\exp(C_{2e}^{hm} \cdot \varphi_{eff}) - 1) \quad (5.92)$$

$$EXP_l = (C_0^l \cdot \exp(C_{2e}^l \cdot \varphi_{eff}) - 1) \quad (5.93)$$

$$POWER_h = \left[1 - \frac{(\varphi - \varphi_{crit}(w_g))}{\varphi_0}\right]^{C2p_h} \quad (5.94)$$

$$f(T) = \exp\left(l_{com}(\varphi) \cdot \frac{T - T_0}{T_0}\right) \quad (5.95)$$

$$f(S) = (1 - S)^{h3} \quad (5.96)$$

Additional supporting functional relations:

$$C_0^{hm} = f_1(w_g) = C_0^* \cdot \exp(h0 \cdot F_w) \quad (5.97)$$

$$C_{2e}^{hm} = f_2(w_g) = C_2^{dry} - (C_2^{dry} - C_2^{wet}) \cdot F_w^{h2} \quad (5.98)$$

$$C_{1e}^{iso} = f_3(w_g) = C_{1e}^{dry} - (C_{1e}^{dry} - C_{1e}^{wet}) \cdot F_w^{h1} \quad (5.99)$$

$$F_w = \frac{w_g - w_{min}}{w_{max} - w_{min}} \quad (5.100)$$

$$\varphi_{eff} = \varphi - \varphi_{rs} \quad (5.101)$$

$$\varphi_{crit} = \varphi_{crit_dry} - (\varphi_{crit_dry} - \varphi_{crit_wet}) \cdot F_w \quad (5.102)$$

$$l_{com}(\varphi) = l_{com_rs} + \left(\frac{\varphi_{eff}}{\varphi_0 - \varphi_{rs}}\right)^{t1} \cdot (l_{com_0} - l_{com_rs}) \quad (5.103)$$

$$f(\alpha) = \beta_1 \cdot [\text{tg}(\alpha)]^{\beta2} \quad (5.104)$$

List of designated symbols:

$\dot{\varepsilon}_{ij}^{vc}$	individual components of the viscous compaction strain rate tensor [1/s]
$\dot{\varepsilon}_{vol}^{vc}$	scalar volumetric compaction strain rate [1/s]
S_{ik}	deviatoric stress tensor [MPa]
σ_v	von Mises equivalent stress [MPa]
σ_m	mean stress [MPa]
σ_*	scaling stress [MPa]
δ_{ij}	Kronecker symbol
φ	porosity [-]
φ_0	initial porosity (for the loose crushed salt) [-]
φ_{rs}	porosity of undisturbed rock salt [-]
φ_{eff}	effective porosity, defined as the difference between the current crushed salt porosity and the porosity of undisturbed rock salt [-]
φ_{crit}	critical porosity (for the end of the impact of the POWER function for the high porosity range) [-]
φ_{crit_dry}	critical porosity for dry material [-]
φ_{crit_wet}	critical porosity for wet material [-]
RV^{vc}_{ij}	term determining directional distribution of individual strain components for viscous compaction [-]
β_1, β_2	material parameters for directional distribution of individual strain components for viscous compaction [-]
C_0^{hm}	pre-factor for the function of the porosity influence (for the range of high to middle porosity) [1/s]
C_0^l	pre-factor for the function of the porosity influence (for the range of low porosity) [1/s]
C_{2e}^{hm}, C_{2e}^l	material parameters for inclination of the exponential function for the porosity influence (high to middle porosity range as well as for low porosity range) [-]
C_{2p_h}	material parameters for inclination of the exponential function for the porosity influence (high porosity range) [-]
C_{1e}^{dev}	material parameters for inclination of the exponential function for the influence of deviatoric stress (the high to middle range of stress) [-]
C_{1e}^{iso}	material parameters for inclination of the exponential function for the influence of mean stress (the high to middle range of stress) [-]
C_{1p}	material parameter for inclination of the power function for the influence of the mean as well as of the deviatoric stress (low range of stress) [-]

T	temperature of the material [K]
T_0	reference temperature of the material [K]
l_{com}	material parameter for inclination of the exponential function for the temperature influence [-]
$l_{com,rs}$	material parameter for inclination of the exponential function for the temperature influence for rock salt [-]
$l_{com,0}$	material parameter for the initial inclination of the exponential function for the temperature influence – for loose crushed salt [-]
t_1	material parameter for the dependency of the factor l_{com} from the porosity [-]
S	degree of saturation ($S = 1$ for fully saturated pores, $S = 0$ for completely dry pores [-])
F_w	support function for the dependency from water content [-]
$w = w_g$	water content based on weight [-]
w_{min}	minimum water content [-]
w_{max}	maximum water content [-]
C_0^*	material parameter for the dependency of the factor C_0^{hm} from the water content [1/s]
$C_{1e}^{dry}, C_{1e}^{wet}$	material parameters for the dependency of the factor C_{1e}^{iso} from the water content [-]
C_2^{dry}, C_2^{wet}	material parameters for the dependency of the factor C_{2e}^{hm} from the water content [-]
h_0, h_1, h_2, h_3	material parameters for the dependency from water content [-]
$\bar{\eta}_m$	Maxwell viscosity for the steady state creep [MPa*s]
$\bar{\eta}_k$	Kelvin viscosity for the primary creep [MPa*s]
\bar{G}_k	Kelvin shear modulus for the primary creep [MPa]
$c_{2_cr_st}$	material parameter for the dependency of the steady state creep from the porosity [-]
$c_{2_cr_tr}$	material parameter for the dependency of the primary creep from the porosity [-]

The majority of influencing factors were considered as normalized quantities, i.e., without a physical unit. The main functional relations in the model are functions of porosity, stress, and temperature. The function of moisture content is built into the coefficients C_0^{hm} , C_{1e}^{iso} and C_{2e}^{hm} . Furthermore, the dependence on porosity is realized in terms of effective porosity, where effective porosity is defined as a difference between actual porosity of crushed salt and minimum reachable porosity that corresponds to the natural porosity of intact rock salt. Consequently, the compaction rate becomes zero when minimum porosity (φ_{rs} of rock salt) is reached and only a deformation rate corresponding to the volume-preserving creep behavior of intact rock salt remains. This ensures a smooth transition between the compaction behavior of crushed salt and the creep behavior of rock salt. The function of saturation is currently not determined on the basis of experiments but serves only for the plausible consideration that the compaction process in the moist strongly compacted crushed salt is terminated with the degree of saturation $S = 1$ even if the final porosity φ_{rs} is still not reached.

5.2.4.4 Back-analysis of selected laboratory tests to verify and validate the functionality of the new constitutive model

To demonstrate and verify the functionality of the new constitutive model EXPO-COM, the compaction tests GRS-dry, GRS-wet, TK-031 and TUC-V2 were calculated, and the calculation results were compared with the measurements. The aim of the back-analysis is neither a development of the material model nor a determination of the material parameter sets. Rather, the back analysis is intended to show or verify whether the influence of individual factors based on the clear-cut analysis, represented in Section 5.2.4.2, has been correctly implemented to the extent that the evaluated dependencies are in principle suitable for representing the material behavior observed in the experiment. The result of the back-analysis displayed in Fig. 5.8 demonstrates for example that the calculated porosity evolution agrees comparatively well with the measured porosity evolution.

Although the constitutive model incorporates all influencing factors currently considered to be relevant for the compaction behavior of crushed salt, its validation quality can still be characterized as insufficient. While the influence of mean stress and porosity on the compaction behavior could be validated by higher number of the tests (sufficient systematic database), performed with the same material (as it is planned for the KOMPASS reference material), the experimental database to ensure sufficiently valid statement

regarding the influence of moisture content, temperature and deviatoric stress is not yet available.

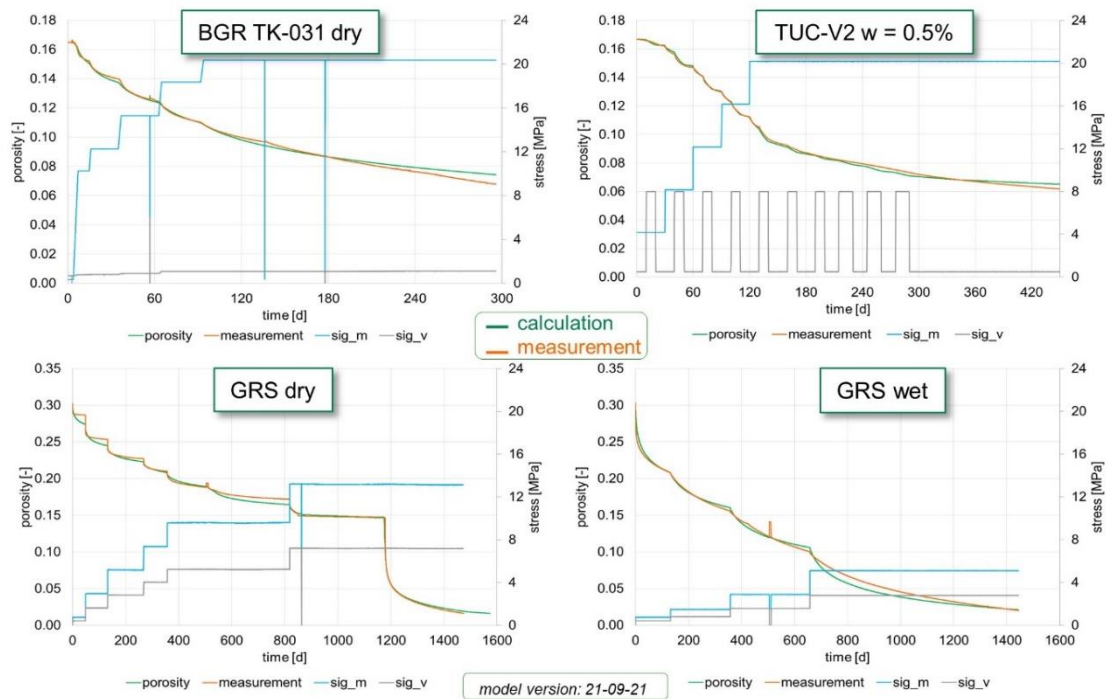


Fig. 5.8 Back-analysis of selected tests used to develop the new constitutive model EXPO-COM from TUC

5.2.4.5 Validation state and first numerical applications

In conclusion, the constitutive model EXPO-COM can be considered successfully validated on the basis of the available laboratory tests, in principle for almost all in situ relevant influencing factors (with the exception of grain size distribution), but only for a partial range of the in situ relevant load conditions (areas of the influencing factors). By considering most relevant factors influencing the compaction behavior of crushed salt and by the successful back-analysis of selected tests, the functionality and suitability of the constitutive model for the prognostic analysis of the long-term behavior of repository excavations backfilled with crushed salt in salt formation can be expected. However, the small number of suitable tests for the analysis of most influencing factors regarding the compaction behavior of crushed salt has evidently shown the necessity for systematic expansion of the experimental database, since the validation status still requires significant increase by supplementary tests in order to guarantee the robustness and reliability of the model predictions required in the research field of final disposal.

The next essential step is to implement the constitutive model in the numerical calculation tools such as FLAC3D (software used by TUC). This numerical equipment must be practical, robust and stable on the one hand and deliver plausible calculation results on the other. First successful results in this regard with several numerical calculations and series of sensitivity analyses for a drift, a chamber as well as a generic mine layout in 3D are documented in /DÜS 22/.

5.2.5 Hein-Korthaus (BGE-TEC)

A general description of the process classes is given in /KOM 20/ and a description of the processes from a continuum mechanical point of view and from a microstructural point of view is given there also and at Section 5.1. The internal and external field variables that influence the processes were also discussed in /KOM 20/. Against this background the constitutive model is as follows: On the side of the process classes, only the mechanical and the thermal class are supported, although the thermal class is only briefly discussed in this work because the parameter identification is done analytically and the calculations in the demonstrator are isothermal.

The hydraulic process class is not yet supported by the constitutive model meaning that not only external hydraulic field variables such as hydraulic flow, pore pressure and saturation are not taken into account, but also that internal state variables such as moisture acquire the character of a constant material parameter. Therefore, at the current state of the material model, material parameters that are related to the hydraulic process class are not resolved separately. The thermal process class is included in the constitutive model with heat conduction as its thermal process, although - if at least with high porosity – an additional effect caused by radiation can be seen /WIE 12/. Parameter identification is finally the aspect that makes the difference in the treatment of hydraulic and thermal process class. Due to the temperature control in TUC-V2, the temperature influence in the temperature-sensitive parts of the constitutive model must be resolved explicitly. Therefore, heat capacity and thermal conductivity are material functions of temperature and porosity. Thermomechanical coupling is used in connection with parameter identification. Thermal expansion is used as its material function, which is linear depending on temperature.

The focus is currently on the mechanical part of the constitutive model. The constitutive model by Hein is an elastic-viscoplastic model, which describes the material behavior of naturally dry crushed salt /DÜS 15/, /HEI 91/. While in the constitutive model the elastic

material behavior and two viscoplastic parts, namely one called grain deformation and the other called grain displacement, are described, in the simulation only the elastic part and the viscoplastic grain deformation part are used. However, the formulation of all three parts is described herein.

Compared to the multitude of micromechanical processes and their representation in continuum mechanics /KOM 20/ and in Section 5.1, the constitutive model presented here and in particular the further one used in the application, represents a significant process reduction. This limited physical load capacity acts directly on the extrapolation quality. With the experimental availability of the corresponding process states, additions must be made. Against the background of the process classes, the above-mentioned designation of a naturally dry crushed salt is to be understood as a crushed salt with constant moisture. Due to the naturally dry crushed salt, processes strongly influenced by moisture, such as pressure solution creep, are not considered as independent processes in the current state of the constitutive model. The remaining processes must therefore cover this influence in the overall behavior. Hence, the influence of moisture is not explicitly included in the constitutive model, but only implicitly in the parameterization of the remaining deformation processes. In contrast, as mentioned above, the thermal influence is explicitly taken into account in the corresponding parts of the constitutive model.

Only in the completely dry state of the salt does the viscoplastic part of the grain deformation with the displacement creep find its direct counterpart in the processes mentioned above. Under the influence of moisture, the pressure solution creep is also included. The intention for the grain displacement part is also to combine several micromechanical processes. These are grain fracture and rigid body motion of the grains as well as a highly transient deformation process immediately after loading. In contrast to the micromechanical processes, grain fracture and rigid body motion are instantaneous parts from continuum mechanical point of view. Even though such a conglomerate of processes could be mapped with a viscoplastic approach from a microstructural point of view, it should be separated according to continuum mechanical aspects in the sense of physically justifiable approaches. Therefore, this approach is only described in Section 5.2.5.3. If this approach is omitted in the application, this means that at least the viscoplastic influence is included in the grain deformation fraction.

The fundamental equation is the kinematic description of the additive decomposition of the strain rate tensor $\dot{\epsilon}$ into an instantaneous thermoelastic part $\dot{\epsilon}^{thel}$ and a viscoplastic

part $\dot{\boldsymbol{\varepsilon}}^{vpl}$. The viscoplastic part itself is an additive decomposition into a part of grain deformation $\dot{\boldsymbol{\varepsilon}}^{gd}$ and a part of grain displacement $\dot{\boldsymbol{\varepsilon}}^{ga}$ (Equ. (5.105)). As noted above, an instantaneous plastic proportion is not taken into account.

$$\dot{\boldsymbol{\varepsilon}} = \dot{\boldsymbol{\varepsilon}}^{thel} + \dot{\boldsymbol{\varepsilon}}^{vpl} = \dot{\boldsymbol{\varepsilon}}^{thel} + \dot{\boldsymbol{\varepsilon}}^{dc} + \dot{\boldsymbol{\varepsilon}}^{ga} \quad (5.105)$$

5.2.5.1 Thermoelastic behavior

The thermoelastic behavior is additively composed of the linear stress-strain relationship according to Hooke and a linear temperature strain relationship, each in a rate formulation and each with non-constant coefficients.

$$\dot{\boldsymbol{\varepsilon}}^{thel} = \mathbb{D}(\eta) : \dot{\boldsymbol{\sigma}} + \alpha_{th}(T) \dot{T} \mathbf{I} \quad (5.106)$$

α_{th} is the thermal expansion coefficient, depending on temperature T /WIE 14/. The compliance tensor \mathbb{D} is the inverse tensor to the fourth-order elasticity tensor \mathbb{C} . It depends on porosity η . For an isotropic material behavior, these tensors are described by two elastic properties, for example the bulk modulus K and the shear modulus G . Regardless of whether they are bulk or shear modulus, a common feature is their structure $P = P_{RS} f_P(\eta)$, where P stands for the function of the elasticity quantity K or G , the index RS denotes the corresponding parameter of rock salt and f_P is the respective porosity function. There are three different functional descriptions in the constitutive model for this porosity function. The first approach $f_{1,P}$ is a linear function on void ratio, thus non-linear in porosity in the range $[0; 1]$ (Equ. (5.107)). The second approach $f_{2,P}$ is an empirical one (Equ. (5.108)) in the range $[e^{-c_P \eta_0}; 1]$. The material parameter c_P is determined from the two limit states, thus, $c_P = \ln(P_{RS}/P_0)/\eta_0$. Compared to the previous approach, the initial value P_0 must be different from zero. The third approach $f_{3,P}$ is derived from a sphere model with Hertzian contacts by taking into account the coordination number M (Equ. (5.109)). The relative contact area $b(\eta)/R$ is given by $b(\eta)/R = (1 - ((1 - \eta_0)/(1 - \eta))^{2/3})^{1/2}$. The material parameter k_1 is given by the final state, where $\eta = 0$: $k_1 = (R/b_{fin})^{k_2}/M_{fin}$ with $b_{fin}/R = (1 - (1 - \eta_0)^{2/3})^{1/2}$. As a note on the initial state x_0 : This state is not the state at the beginning of the experiment, but it is a state, possibly only thought theoretically, of loose bulk of the crushed salt. Otherwise, the values of the function of quantity x would depend on x_0 . Thus, two experiments with different initial porosity would lead to different functions, which is not permissible.

$$f_{1,P}(\eta) = \frac{\eta_0 - \eta}{\eta_0(1 - \eta)} \quad (5.107)$$

$$f_{2,P}(\eta) = e^{-c_P \eta \frac{1-\eta_0}{1-\eta}} \quad (5.108)$$

$$f_{3,P}(\eta) = k_1 M(\eta) \left((1 - \eta) \frac{b(\eta)}{R} \right)^{k_2} \quad (5.109)$$

While the first and third models have the value zero in the initial state, i.e., there is no contact between the grains, the initial value in the empirical model is always greater than zero.

A graphical representation of the models from Equ. (5.107) to Equ. (5.109) is shown in Fig. 5.9. As a note: The last function from Tab. 5.1 was used for the graphical representation in Fig. 5.9. A wide range of behavior between the different models as well as the different parameterizations is observed. On the path from initial porosity, a value of 0.56 was used, to complete compaction, a degressive behavior, an almost linear behavior and a progressive behavior are possible. For the empirical approach, two different parameterizations are given. The variant f_2 with $P_{RS}/P_0 = 1/10^{-4}$ can be well approximated by the Hertzian model using a suitable parameterization e. g. $k_2 = 4$. A parameterization with $k_2 < 1.0$ leads - after a strong initial increase - to a more linear behavior on the remaining compression path. This general behavior of the Hertzian model is independent of the coordination number approach used.

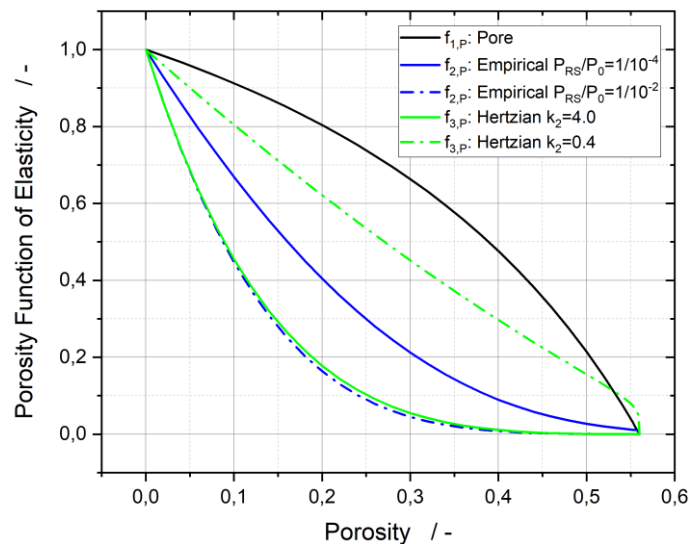


Fig. 5.9 Variants of the porosity function of elasticity

The application of the porosity functions to the elastic moduli influences the Poisson's ratio /HEI 91/. Based on the relationship between the bulk modulus K , shear modulus G

and the Poisson's ratio ν (Equ. (5.110)) the relationship between the Poisson's ratio of crushed salt ν_{CS} and that of rock salt ν_{RS} results in a correlation between the porosity functions of shear modulus and bulk modulus (Equ. (5.111)). If crushed salt has the same Poisson's ratio as rock salt, the porosity function for the two moduli must be identical. The pore model in the first approach fulfills this condition by construction; the other two approaches only meet this requirement through identical parameterization. If a porosity dependence of the Poisson's ratio is assumed, the parameterization is limited in order to preserve the range of the Poisson's ratio $[0; 0.5]$. Although there are also materials with a behavior outside this range, in the case of crushed salt it is assumed that measurements leading to such values involve inelastic deformation processes.

$$G = 3K \frac{(1 - 2\nu)}{2(1 + \nu)} \quad (5.110)$$

$$\frac{(1 + \nu_{CS})(1 - 2\nu_{RS})}{(1 - 2\nu_{CS})(1 + \nu_{RS})} = \frac{f_{i,K}(\eta)}{f_{i,G}(\eta)} \quad (5.111)$$

5.2.5.2 Grain deformation

The viscosity approach for grain deformation is currently a combination of viscous effects, preferably those coming from pressure solution and dislocation creep processes. If the solidifying effect from the porosity decrease is not taken into account, the process can be described as a steady state. The mathematical description employs a Perzyna formulation:

$$\dot{\epsilon}^{gd} = \gamma \langle \phi(F - F_0) \rangle \frac{\partial G}{\partial \sigma} \quad (5.112)$$

- $\langle X \rangle$ Macaulay brackets $\langle X \rangle = X \forall X > 0 \wedge \langle X \rangle = 0 \forall X \leq 0$
- F yield function: $F = \hat{\sigma}^{dc2} [MPa^2]$
- $\hat{\sigma}$ equivalent stress [MPa]
- F_0 hardening function: $F_0 = 0 [MPa]$
- G viscoplastic potential: $G = F$ (associated flow rule) [MPa²]
- T temperature [K]
- γ fluidity coefficient: $\gamma = \frac{A}{2} e^{-\frac{Q}{RT}}$ (Arrhenius term)
- A pre-exponential factor $\left[\frac{1}{d MPa^n} \right]$
- Q activation energy $\left[\frac{J}{mol} \right]$
- R gas constant $\left[\frac{J}{mol K} \right]$
- $\phi(F)$ scalar over stress function: $\phi(F) = F^{\frac{n-1}{2}}$
- n stress exponent [-]
- σ stress tensor [MPa]

The mean stress and the deviatoric stress both act on the deformation process. Therefore, their effect is summarized in the equivalent stress with corresponding weighting functions h_1 and h_2 :

$$\hat{\sigma}^{gd} = \sqrt{h_1 \sigma_0^2 + h_2 q^2} \quad (5.113)$$

- h_1, h_2 material function [-]
 q deviatoric stress invariant [MPa] $q = \sqrt{\mathbf{S}:\mathbf{S}}$
 \mathbf{S} deviatoric stress [MPa] $\mathbf{S} = \boldsymbol{\sigma} - \sigma_0 \mathbf{I}$
 σ_0 mean stress [MPa] $\sigma_0 = \frac{1}{3} \text{tr}(\boldsymbol{\sigma})$
 \mathbf{I} identity tensor of second rank [-]

Equ. (5.113) used in Equ. (5.112) leads to Equ. (5.114). As with the stress tensor, invariants can be determined from the strain rate tensor. The volumetric strain rate $\dot{\epsilon}_0^{gd}$ is given in Equ. (5.115), a representation of equivalent strain rate $\hat{\epsilon}^{gd}$ in Equ. (5.116). The deviatoric strain rate tensor is given by $\dot{\epsilon}^{gd} = \dot{\boldsymbol{\epsilon}}^{gd} - \dot{\epsilon}_0^{gd} / 3 \mathbf{I}$. If the grain deformation process is the only acting time-dependent process, these two quantities also describe the volumetric and isochoric time-dependent deformation capacity over all. A third quantity derived from the strain rate tensor is the viscoplastic Poisson's ratio ν^{gd} , which is determined analogously to the elasticity (Equ. (5.117)). From Equ. (5.115) and Equ. (5.116) the ratio h_1/h_2 can be determined, which leads to the last term in Equ. (5.117).

$$\dot{\boldsymbol{\epsilon}}^{dc} = A e^{-\frac{Q}{RT}} (h_1 \sigma_0^2 + h_2 q^2)^{\frac{n-1}{2}} \left(\frac{1}{3} h_1 \sigma_0 \mathbf{I} + h_2 \mathbf{S} \right) \quad (5.114)$$

$$\dot{\epsilon}_0^{dc} = \text{tr}(\dot{\boldsymbol{\epsilon}}^{dc}) = A e^{-\frac{Q}{RT}} (h_1 \sigma_0^2 + h_2 q^2)^{\frac{n-1}{2}} h_1 \sigma_0 \quad (5.115)$$

$$\hat{\epsilon}^{dc} = \sqrt{\dot{\boldsymbol{\epsilon}}^{dc} : \dot{\boldsymbol{\epsilon}}^{dc}} = A e^{-\frac{Q}{RT}} (h_1 \sigma_0^2 + h_2 q^2)^{\frac{n-1}{2}} h_2 q \quad (5.116)$$

$$\nu^{dc} = -\frac{\dot{\epsilon}_3^{dc}}{\dot{\epsilon}_1^{dc}} = \frac{3 - \frac{h_1}{h_2}}{6 + \frac{h_1}{h_2}} = \frac{3 - \frac{\dot{\epsilon}_0^{dc}}{\hat{\epsilon}^{dc}} \frac{q}{\sigma_0}}{6 + \frac{\dot{\epsilon}_0^{dc}}{\hat{\epsilon}^{dc}} \frac{q}{\sigma_0}} \quad (5.117)$$

General conditions can be defined for the course of the weighting functions h_1 and h_2 (Fig. 5.10). In the range of initial porosity, high deformation velocities result from over-stresses due to the shape of contact between the grains. As a result of this deformation process (and the corresponding porosity reduction), the contact peaks flatten and at the local level the stress homogenizes, so that at the same external stress the deformation speed is drastically reduced; the gradient in the weighting functions must also be

correspondingly steep. In the region of high porosity, it is not possible to distinguish at local grain level whether an average stress state or a purely deviatoric stress state is present globally. Therefore, in this region, the two materials must be similar. On the other side of the porosity development, the two weighting functions diverge. If compaction is complete, $\eta \rightarrow 0$, the volumetric deformation rate has to become zero. This can only be achieved if h_1 becomes zero too, $h_1(\eta \rightarrow 0) \rightarrow 0$. The remaining part of dislocation creep for rock salt is a J_2 based power law $\hat{\varepsilon}^{gd} = A e^{-\frac{Q}{RT}} h_2^{\frac{n+1}{2}} q^n$. The minimum requirement would be a positive value for h_2 , ideally $h_2(\eta \rightarrow 0) \rightarrow 1$. Thus, the viscoplastic Poisson's ratio (Equ. (5.117)) in that state is 0.5, $v^{gd}(\eta \rightarrow 0) \rightarrow 0.5$. Based on experiments /KOR 96/ assumes the initial value of v^{dc} at the Poisson's ratio of elastic behavior. A shown scattering around the assumed function, /KOR 96/ attributes to anisotropic grain arrangements.

There are five different representations for the material functions h_1 in Equ. (5.118) to Equ. (5.121). The original approach h_1^H (Equ. (5.118)) is given in /HEI 91/. This approach is based experimentally on short-term compaction, p_{max} , and a reduction function from long-term creep. With the reference to individual effects - short- and long-term compaction tests - only a few parameters are always assigned to the individual test arrangements, so that parameter identification is easily possible. Thus, the parameter ϕ as the angle of internal friction can therefore be determined separately. The h_1^H approach by Hein shows the limitation that its volumetric compaction rate does not disappear in the state of complete compaction. Thus, with complete compaction, not only a volumetric compaction rate deviating from zero remains, but assuming the same parameterization as for the rock salt, there would also be a multiplicative factor in the isochore deformation rate between rock salt and fully compacted crushed salt. The modified approach h_1^{mH} fulfills the above-mentioned requirements for the material functions (Equ. (5.119)). /KOR 96/ overcame the limitation in h_1^H with an empirical approach h_1^{HK} (Equ. (5.120)). With respect to high initial porosities, he slightly modified the approach in /KOR 99/ to h_1^{mK} (Equ. (5.121)). As it can be easily seen, this is just a reparameterization of the pre-factor $a \eta_0^{r \cdot m} = a \eta_0^{(r-c) \cdot m} \eta_0^{c \cdot m}$. Hence, $h_1^{m^2K}$ is just a reallocation compared to h_1^{mK} , in that the porosity in the numerator has the deviating exponent applied to it, not the initial porosity (Equ. (5.121)). The material function h_2 is always the same (Equ. (5.122)).

$$h_1^H = \frac{1 - a_1 \tan^2(\phi) e^{a_2 \eta}}{p_{max}^2} = \frac{1 - a_1 \tan^2(\phi) e^{a_2 \eta}}{\left(\frac{c_1}{c_2} \left(\left(\frac{1 - \check{\eta}}{1 - \eta_0} \right)^{c_2} - 1 \right) \right)^2} \quad (5.118)$$

$$h_1^{mH} = \eta h_1^H \quad (5.119)$$

$$h_1^{HK} = a \left(\frac{\eta_0^c \eta^c}{\eta_0^c - \check{\eta}^c} \right)^m \quad (5.120)$$

$$h_1^{mK} = a \left(\frac{\eta_0^r \eta^c}{\eta_0^c - \check{\eta}^c} \right)^m \quad (5.121)$$

$$h_2 = 1 + b h_1 \quad (5.122)$$

- a, a_1, a_2 material property
- b material property
- c, c_1, c_2 material property
- m, r material property
- $\check{\eta}$ porosity to prevent singularity [-] $\check{\eta} = \min(\eta; \eta_0 - \Delta)$
- Δ small value of porosity to prevent singularity [-]
- ϕ angle of inner friction [-]

Fig. 5.10 shows the behavior of the material functions h_1 and h_2 for the above mentioned variants. The functions shown in Fig. 5.10 are mainly based on parameter identification, but their parameters remain unnumbered at this point because the focus is a qualitative one. The deviation from the target values of h_1 and h_2 can be clearly seen in the model h^H . All the other approaches meet the requirements. The models h^{mH} and h^{HK} basically show comparable characteristic crushed salt. The difference between h^{HK} , h^{mK} and h^{m^2K} results from the change of parameter r with respect to parameter c , here $c = 0.7$ and $r = 1.2$.

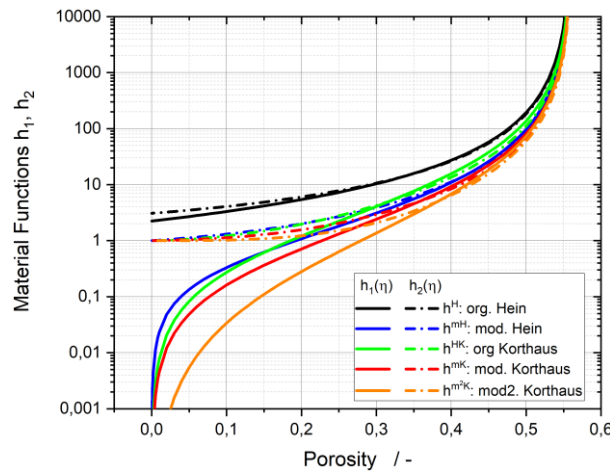


Fig. 5.10 Variants of the Functions h_1 and h_2 of Grain Deformation; h^{HK} , h^{mK} and h^{m^2K} with $c = 0.7$ and if required $r = 1.2$

5.2.5.3 Grain displacement

For the grain displacement, an approach comparable to grain deformation (Section 5.2.5.2) is used /HEI 91/. The deformation process of grain displacement involves three mechanisms: the ordinary grain displacement, which occurs after overcoming the intergranular friction, the rearrangement of fragments after grain fracture into existing pore spaces and a short-term deformation after load change. With increasing compaction, it is expected that the individual grains are more strongly clamped (this requires higher frictional forces); that local stress and pore space is reduced (hence, less fractures and it is more difficult for fragments to fill gaps between grains). Thus, a hardening of the grain displacement mechanism takes place.

Both sliding and fracture mechanisms, which are instantaneous processes from a continuum mechanics point of view, are active, at least in the area of greater porosity, transient creep in the whole range of porosity. To what extent the friction limit and the fracture limit can be considered together is still unresolved. With increasing compaction, the space for movement for the ordinary grain displacement disappears. However, fracture processes as well as transient creep during load changes can occur in the fully compacted rock salt. Therefore, the transition to rock salt must be ensured analogous to the process of grain deformation.

The mathematical description is the same as for grain deformation (Equ. (5.112)). Compared to grain deformation, it can be assumed that temperature does not influence either the frictional or the fracture behavior. The influence of moisture can also be disregarded for these two mechanisms at present. Unfortunately, temperature and moisture are properties that should be noticeable in the third mechanism.

In /HEI 91/ a linear stress approach with associated flow rule is used. The equivalent stress is given in Equ. (5.123) and the total approach in (5.124).

$$\hat{\sigma}^{ga} = k|\sigma_0| + q \quad (5.123)$$

$$\dot{\epsilon}^{ga} = gh_3 \langle k|\sigma_0| + q - F_0 \rangle \left(\frac{k}{3} \text{sign}(\sigma_0) \mathbf{I} + \frac{1}{q} \mathbf{S} \right) \quad (5.124)$$

- k material property [-]
- gh_3 fluidity coefficient [1/d*MPa]

If a common action of the time dependent deformation processes is assumed, a separate allocation of volumetric and isochoric parts is only of limited use. Certainly, the quantities can be determined mathematically and possibly for comparison purposes between the different processes:

$$\dot{\varepsilon}_0^{ga} = tr(\dot{\varepsilon}^{ga}) = sign(\sigma_0)gh_3k\langle k|\sigma_0| + q - F_0 \rangle \quad (5.125)$$

$$\hat{\varepsilon}^{ga} = \sqrt{\dot{\varepsilon}^{ga} : \dot{\varepsilon}^{ga}} = gh_3\langle k|\sigma_0| + q - F_0 \rangle \quad (5.126)$$

For the development in a repository, largely damage free processes are assumed. However, this does not necessarily apply to tests in a laboratory, which may be carried out faster and with higher loads. Here, fracture processes are not only to be expected, but have been detected in the microstructural analysis of samples, Section 4. However, the material used is the result of a mechanical working process, so grain fracture is an inherent part of the starting material from a microstructural point of view. But this also applies to the material in-situ. Even if the process of grain displacement is more important in the initial phase of deformation, it should be taken into account for the analysis of laboratory samples, since it has an influence on the different quantities of geometry and it may lead to a redistribution between deformation processes. For this purpose, the mechanisms should be separated on the basis of the continuum mechanical background and the influence of the external and internal state variables in order to be able to determine the material functions g and h_3 , which have been undetermined so far.

5.2.6 CWIPP model (modified by IfG)

The IfG currently uses a variant of the empirical CWIPP crushed salt model /SJA 87/ that has been modified in several aspects. In general, this IfG-CWIPP model is still of the same form described and used in /KOM 20/, but with additional terms for temperature and deviatoric stress dependence. We therefore keep our model discussion concise and present only the most important equations describing compaction creep, deviatoric creep, and elastic behavior.

Compaction creep in this model is given by:

$$(\dot{\epsilon}_c)_{ij} = -C_0 (e^{-C_1 \sigma_0} - 1) \frac{e^{C_2 P} - 1}{1 - P} \left(1 + \frac{C_3 \sigma_{eff}}{\sigma_0} \right) e^{-\frac{Q_c}{RT}} \left[\frac{1}{3} \delta_{ij} - \frac{2}{\sqrt{\zeta_{iso} \sigma_0^2 + \zeta_{eff} \sigma_{eff}^2}} \cdot \sigma_{ij}^d \right] \quad (5.127)$$

Where σ_0 is the mean stress, σ_{eff} is the effective stress, σ_{ij}^d denotes the deviatoric stress tensor, T is temperature, R is the universal gas constant and P is porosity. C_0 represents an overall factor of creep magnitude, while C_1 and C_2 describe the dependency on mean stress and porosity, respectively. Compared to the original CWIPP model, the porosity dependence has been changed such that the compaction rate goes to zero for small porosities. Thus, full compaction (zero porosity) is attained only asymptotically for long timescales.

The term containing C_3 is new compared to the KOMPASS-I version of the model and introduces a simple deviatoric stress dependency of the compaction rate, normalized by the mean stress. In addition, we added a temperature dependency using an Arrhenius term with an activation energy Q_c .

The tensor structure allows for a general deviatoric component of compaction creep (or, in other words, an additional porosity-dependent creep term). The coefficient of the stress deviator has two additional parameters ζ_{iso} and ζ_{eff} . This leads to a smooth transition between uniaxial and isotropic stress and includes flexibility to accommodate a range of deformation behaviors for general triaxial stress states.

The model only retains the compaction creep term and the porosity dependence of the elastic moduli of the CWIPP model. To include intact rock salt behavior, i.e., creep and damage, these terms are coupled to the visco-elasto-plastic constitutive model for rock salt /MIN 07/, /LÜD 14/.

Additionally, the model is reformulated in terms of porosity rather than density. While this does not change the physical behavior, the interpretation is more intuitive and there are fewer conversions required when changing systems of units. The parameters in the new formulation are renamed C_0 to C_3 to avoid ambiguity with original CWIPP parameters.

Elastic behavior is described by the usual Hooke law, with elastic moduli depending on porosity as

$$K = K_S e^{-\kappa P}, \quad G = G_S e^{-\gamma P} \quad (5.128)$$

Note that a porosity-dependent bulk modulus (increasing with decreasing porosity) implies that after a loading–compaction creep–unloading cycle, there will be a “frozen elastic” contribution to volumetric strain proportional to

$$\Delta\sigma \left(\frac{1}{K(P_{ini})} - \frac{1}{K(P_{final})} \right) \quad (5.129)$$

Transient and stationary creep are given by, in rheological terms, Kelvin and modified Maxwell elements. The stationary creep rate is enhanced by a hyperbolic sine,

$$\left(\dot{\epsilon}_{creep,stat} \right)_{ij} = \frac{1}{\eta} e^{-\frac{Q}{RT}} \sinh m \sigma_{eff}^n \cdot \sigma_{ij}^d \quad (5.130)$$

Finally, plastic deformation, dilatancy and softening are governed by the Minkley yield function.

$$\sigma_{diff}^{yield} = -\sigma_D - \frac{\sigma_{MAX} - \sigma_D}{\sigma_\phi - \sigma_3} \quad (5.131)$$

and a non-associated plastic potential. The parameters of the yield function are all functions of plastic strain (as an equivalent representation of damage), where σ_D is the uniaxial compressive strength, σ_{MAX} is the maximum shear strength and σ_ϕ governs the curvature of the non-linear yield function. However, since rock salt damage does not play an important role in this project, we will not go into further detail here.

5.3 Benchmarking of TUC-V2

5.3.1 Introduction

A comparative analysis of the capabilities of the different constituent approaches with respect to the realistic representation of the compaction process is the major goal of the benchmark based on the re-analysis of the existing laboratory database.

In the current project phase KOMPASS-II, only the test TUC-V2 has been used for the benchmark analysis. Extension of the benchmark to further tests TUC-V4 (performed in

the framework of KOMPASS-II and to include in the benchmark for the follow-up project phase) as well as TUC-V5 to TUC-V8 (to be executed in the follow-up project phase) is planned in the framework of the follow-up project phase.

The TUC-V2 test offers the opportunity to validate large number of influencing factors in relatively broad areas for a total test duration of 750 days. While the test by itself is insufficient for a complete validation of the models, it already represents a sizeable amount of database due to its five distinct phases, each with a duration of 150 days and a different investigation focus.

- In **Phase I**, the effects of mean stress (for 5 levels), deviatoric stress (1 level with 5 on/off cycles) and porosity at constant temperature are investigated.
- In **Phase II**, the range of validity in regard to the porosity for the influencing factor deviatoric stress (with another 5 on/off cycles) at constant temperature and mean stress is extended.
- In **Phase III**, the long-term behavior is observed when all controllable influencing factors (stress and temperature) are kept constant, thus extending the validity range for the influencing factor porosity.
- In **Phase IV**, the effect of the temperature is investigated when the mean stress is kept constant under isotropic load, thus extending the validity range for the influencing factor porosity.
- In **Phase V**, the influencing factors deviatoric stress, mean stress and temperature are re-activated in order to observe their effect for a range of low porosity, thus extending the validity range for these factors to the broad range of 'medium to low porosity' (for approx. 17 % → 3 %).

In the framework of the KOMPASS-I project, test TK-031 from BGR was utilized for modeling benchmark. Only two influencing factors, mean stress and porosity, were investigated in the test for comparatively narrow areas, moreover it was not the KOMPASS reference material. The switch to the new database, first represented by test TUC-V2, is thus already an essential milestone in the development and validation process of the constitutive modeling. Fig. 5.11 illustrates the significant increase of the database as a result of using TUC-V2 test, and consequently, the improvement in the models' the validation status after the application of this database for model development, validation or calibration (parameter determination). Here, the term "**validation status**" refers to the entirety of the ranges of state variables and influence factors for which a experimental database and the successful validation of the models are available.

Accordingly, the benchmark of the TUC-V2 experiment can be utilized to provide answers to the following questions regarding the **capability** of each model's approach:

- Is the approach capable to accurately represent the dependency of the compaction behavior on **isotropic stress** for a wide range of stresses (4 MPa to 20 MPa)?
- Is the approach capable to represent the dependency of the compaction behavior on the **deviatoric stress** at all?
- Is the approach capable to accurately represent the dependency of the creep behavior (viscous shear deformations) on the **porosity**?
- Is the approach capable to accurately represent the dependency of the compaction behavior on **temperature** for a wide range of porosity (medium to low porosity)?
- Is the approach capable to accurately represent the dependency of the compaction behavior on the porosity for a wide range of **porosity** (medium to low porosity)?

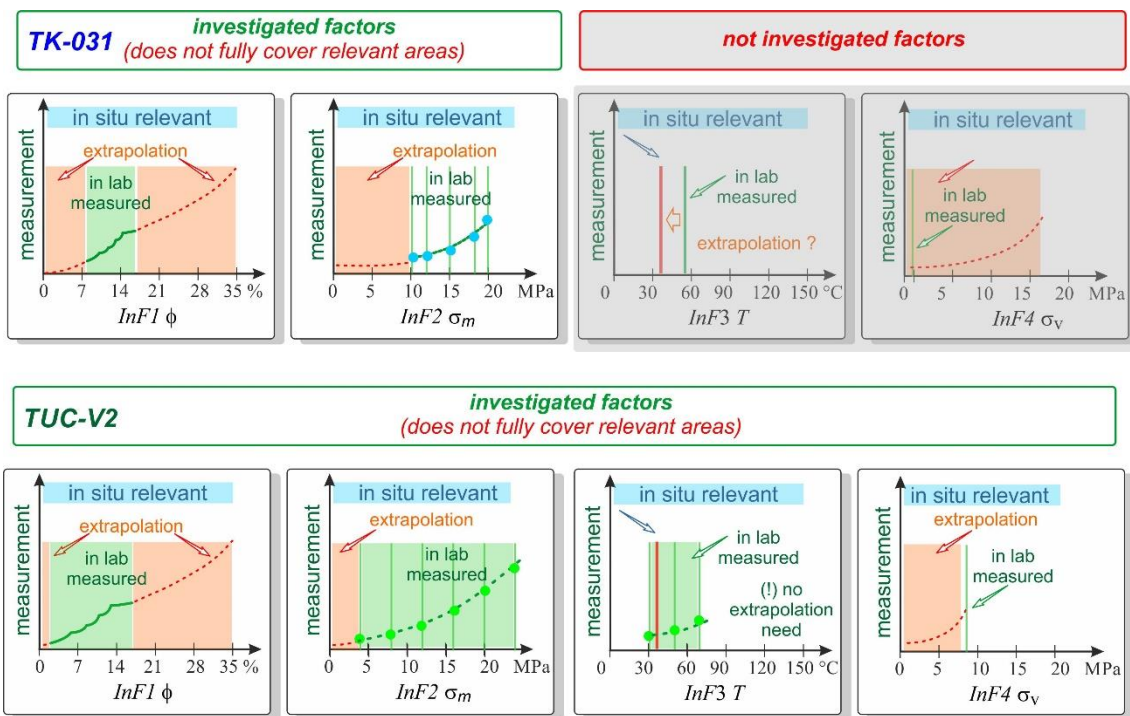


Fig. 5.11 Increase of the models' validation status by the usage of the measurement database from test TUC-V2 (KOMPASS reference material)

It should be emphasized, however, that despite the majority of information obtained from the measurement data on the test TUC-V2, these data have strong limitations in terms of capturing long-term behavior: the released investigation of the multitude of influencing factors in the series connection (not superimposed, but isolated) can only be done at the

cost of the duration of each individual load stage. Thus, only one really long-term phase for the mean stress level of 20 MPa with over 150 days duration is involved in the test, for the reason that otherwise using 150 days for each of the load stages of the test TUC-V2 would lead to a total duration of the experiment of over 8 years. As a consequence, it is very important to be aware of the limitations of the validation. With reference to Fig. 2.3 for the long-term strategy, the investigated areas for individual influencing factors must be extended in the future (with respect to other areas of porosity, to longer time scale, to larger dimension) to increase the robustness and quality of the validation of modelling approaches and thus of the long-term predictions.

5.3.2 Modelling approaches

5.3.3 BGR-CRUSHED SALT3 (BGR)

The TUC-V2 laboratory test is modelled with the in-house finite element analysis program JIFE. Since the solution is homogeneous, a single finite element is sufficient to obtain a convergent solution. However, the specimen is discretized with 32 elements within a two dimensional axisymmetric set up as shown in Fig. 5.12 to ensure that there is no artificial localization. The simulation was performed first in a geometrical linear context and later successfully extended to a total Lagrangian finite deformation context. The boundary conditions are also displayed in Fig. 5.12. The bottom and the symmetry axis are fixed in normal direction and on the top and right face traction boundary conditions are prescribed according to the measured stresses. The material model described in Section 5.2.1 is applied. During the creep phases the time step size for the fully implicit time discretization schemes is automatically increased based on the number of solver iterations in the previous step.

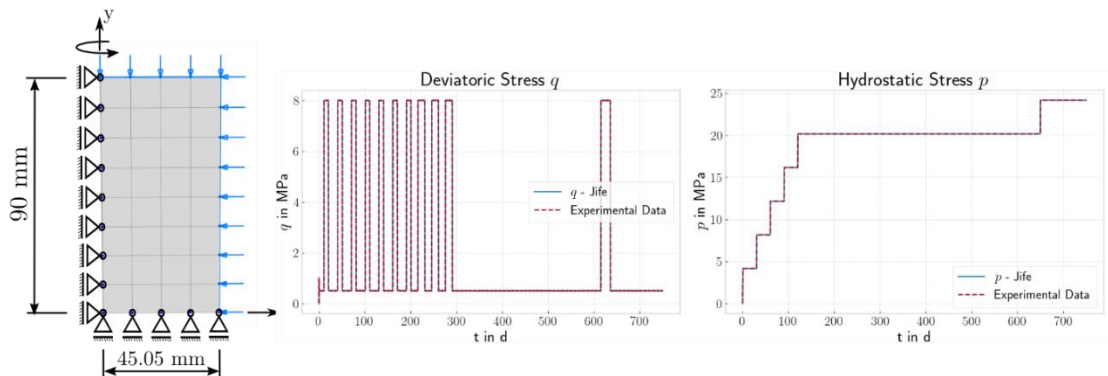


Fig. 5.12 Discretization of the TUC-V2 laboratory test and validation of the boundary conditions.

In Tab. 5.2 the material parameters used in the simulation of the numerical experiment are listed. This set of parameters could not be determined in a deterministic way with only a single experiment. Instead, the parameters were found by considering datasets from past experiments and a subsequently variation of a few key parameter. Especially the stress ratio parameter b was tuned for a good agreement of radial and axial strains with the laboratory measurements.

Tab. 5.2 Material parameters for TUC-V2 simulation in the BGR-CRUSHED SALT3 framework

Parameter	Description	Unit	Value
Physical			
E_{Salt}	Young's modulus	MPa	25000
ν	Poisson's ratio	-	0.27
Q	Activation energy	kJ/mol	54
σ^f	Fracture stress	MPa	8
Q^{Diff}	Activation energy	kJ/mol	25
e_0	Initial void ratio	-	0.2005
e_{pre}	Precompaction void ratio	-	0.23
Physicly derivable			
n	Stress exponent	-	6
κ^{RN}	Hardening modulus	MPa	100
$\sigma_{\text{init}}^{RN}$	Initial hardening stress	MPa	2
$\sigma_{\text{init}}^{RV}$	Initial hardening stress	MPa	10
D_i	Grain diameter	mm	0.3
D_{s0}	Reference grain size	mm	10
D^{diff}	Diffusion coefficient	mm ² /d	5000000.0
Fitting Parameter			
A	Structure parameter	d ⁻¹	2×10^{-5}
k	Grain size distribution	-	4
b	Stress ratio	-	3.075
β	Parameter	-	0.755
z	Saturation parameter	-	0.65
m	Parameter	-	0.7
ζ	Parameter	-	10
κ'	Parameter	K m MPa ⁻¹	1.151
B^{frac}	Structure parameter	d ⁻¹	0.0005

In Fig. 5.13 different strain measures are plotted against the experimental observation. Over the entire load history, the slope of the strain components and the strain component itself show a good agreement with the measured data. The axial strain ϵ_y slightly

overestimates the measurement and therefore the volumetric strain is a little bit too high as well.

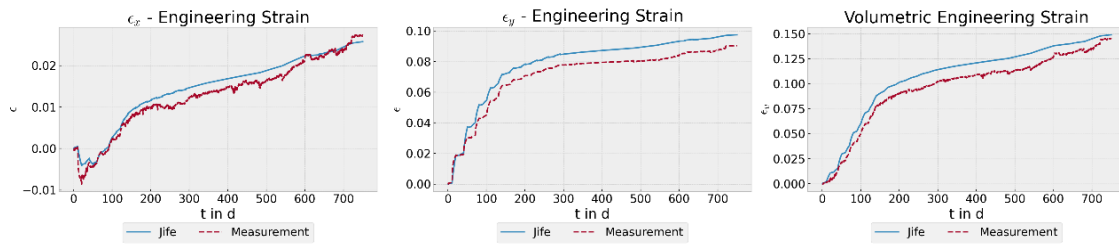


Fig. 5.13 Comparison of simulation and laboratory measurements for different strains

In Fig. 5.14 on the left-hand side the measured void ratio is plotted against the simulated one. Both curves show a good agreement over the entire load path. On the right-hand side of Fig. 5.14 the different contributions to the creep strain are shown. Where in the first 300 days the compaction creep strain plays a dominant role the humidity creep is more pronounced afterwards. The fracture creep rate plays a significant role only in the beginning 200 days when high deviatoric stresses are applied and the local stresses are high compared to the fracture stress.

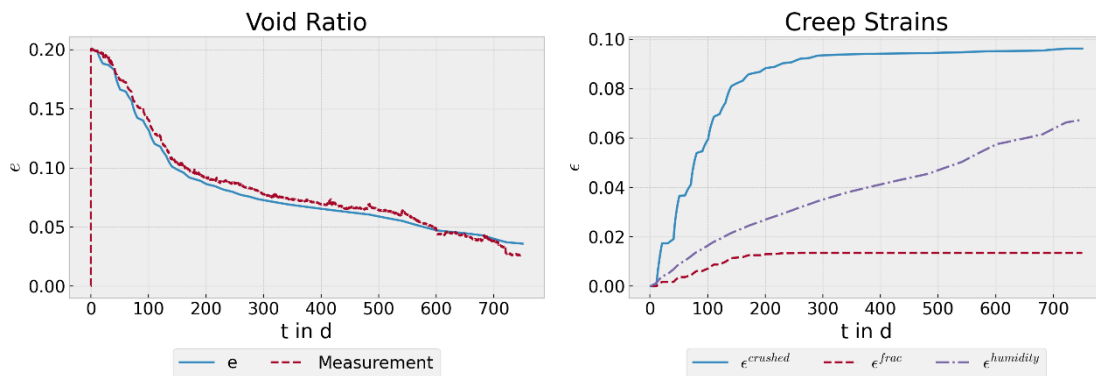


Fig. 5.14 Simulated void ratio against measurement (left) and decomposition of the creep strain (right)

5.3.4 Callahan model (Sandia)

This section describes the modelling and calibration efforts by Sandia National Laboratories (SNL). We have applied the Callahan crushed salt constitutive model /CAL 99/ to simulate test TUC-V2. The relevant equations and description of the model are provided

in Section 5.2.2 of this report. Recall that that tensile stresses and strains are positive by convention.

During the first phase of the KOMPASS project /KOM 20/, we did not attempt to calibrate the Callahan model against TUC-V2. Instead, we created a preliminary model calibration that combined two pre-existing parameter sets. The first was a legacy parameter set provided by /CAL 99/ for the grain boundary diffusional pressure solution mechanism and porosity-dependence of the model, obtained by calibration against WIPP crushed salt experiments. The second was a parameter set provided by /DEV 11/, obtained by calibration against Sonderhausen intact salt experiments to inform the dislocation creep mechanism and fully-reconsolidated behavior of the model. The predictions from this preliminary model calibration differed substantially from the test data of TUC-V2 and were considered a starting point from which an improved calibration of the model to the test data would begin. A proper calibration against TUC-V2 has now been conducted and documented in greater detail in /COU 23/ and supports the present work.

In this section, we describe the calibration procedure employed to obtain the material parameters, the numerical modelling assumptions and analyses performed, and a comparison of the model predictions to the experimental data. Further comparison of our results and the other models results to the experimental data can be found in Section 5.3.9.

5.3.4.1 Intact salt parameters for the Callahan model

As described in Section 5.2.2, pressure solution and dislocation creep are the only viscoplastic modes of deformation considered in the model. The dislocation creep mechanism of the Callahan model /CAL 99/ is built upon the Munson-Dawson (MD) model for dislocation creep of intact salt. Therefore, the 24 material parameters for the dislocation creep part of the Callahan model are identical to those of the Munson-Dawson model and are obtained from calibration against intact salt experimental data. Calibration of these parameters for Sonderhausen intact salt was performed by /DEV 11/ and discussed in more detail in /KOM 20/. Due to the limited number of tests available for analysis, some of the parameters could not be directly determined and were chosen to be the same as previously determined for Waste Isolation Pilot Plant (WIPP) salt by /MUN 89/. The values of the parameters are given in Tab. 5.3. Note that the low stress mechanism, which is a recent addition to the MD model, was not used in this work, i.e., a value of zero is chosen for parameters A_0 , B_0 , Q_0 , k_0 , c_0 , and m_0 .

Tab. 5.3 Model parameters for intact Sondershausen salt /DEV 11/

Parameter	Sondershausen	Units
ρ_{int}	2160	kg/m ³
μ	9.85×10^9	Pa
A_0	0.0	1/s
A_1	3.02×10^{21}	1/s
A_2	3.48×10^{11}	1/s
B_0	0.0	1/s
B_1	2.23×10^9	1/s
B_2	9.89×10^{-4}	1/s
Q_0/R	0.0	K
Q_1/R	12,589	K
Q_2/R	5035.5	K
n_0	0.0	-
n_1	5.5	-
n_2	5.0	-
q	1500	-
σ_0	20.57×10^6	Pa
m_0	0.0	-
m_1	3.49	-
k_0	0.0	-
k_1	2.48×10^6	-
c_0	0.0	1/K
c_1	9.198×10^{-3}	1/K
α_h	-10.88	-
β_h	-7.738	-
α_r	0.58	-
β_r	0.0	-

5.3.4.2 Crushed salt parameters calibration

There are 18 model parameters beyond those listed in Tab. 5.3 that specify the behavior of crushed salt and must be calibrated. Four parameters (K_0 , K_1 , G_0 , and G_1) describe the porosity-dependent elasticity. Four parameters (κ_0 , κ_1 , n , and D_t) describe the flow potential, while three parameters (η_0 , η_1 , and n_f) describe the equivalent stress σ_{eq}^f . The

grain boundary diffusional pressure solution model has 7 parameters ($r_1, r_3, r_4, n_s, a, p,$ and Q_s) that describe the dependence on moisture, grain size, temperature, and porosity.

Modelling assumptions and numerical settings

The specifics of how the laboratory test TUC-V2 was performed are described in Sections 3.3.5. In this section, we describe how the tests were modelled. Simulations of TUC-V2 performed with the legacy calibration during KOMPASS phase 1 /KOM 20/ showed that:

1. Taking into account the hardening due to pre-compaction by adjusting the initial value of the internal variable ε^{ts} (transient strain) at the beginning of test TUC-V2 had only a minor influence on the response.
2. Results obtained by modelling the cylindrical geometry and friction with the loading frame did not significantly differ from those obtained using a single element with frictionless boundary conditions.

For these reasons, the present analysis does not attempt to model the pre-compaction phase (the initial value of the internal variable is taken as $\varepsilon^{\text{ts}} = 0$) and calibration is performed on a single cubic finite element of unit dimensions.

The Finite Element Analysis code Sierra/SolidMechanics 5.12 /SIE 23/ developed by Sandia National Laboratories was used. An 8-node hexahedral element using a mean quadrature integration was employed. The quasi-static equilibrium equations (without inertia terms) are solved implicitly using a non-linear pre-conditioned conjugate gradient technique. For a given timestep, the solution is considered converged when the relative residual $\hat{R} = \|\mathbf{R}\|_2 / \|\mathbf{F}\|_2$, where \mathbf{R} is the discretized equilibrium residual vector, \mathbf{F} is the boundary condition reaction force vector, and $\|\cdot\|_2$ is the discretized L_2 norm of a quantity, is below 5×10^{-4} . Initial runs indicated that specifying a tighter relative residual tolerance of 1×10^{-5} did not change the results. An adaptive time-stepping strategy is employed, with an initial time step size of 1,000 s at each change in loading, and a maximum time step size increase of 5 % for each subsequent step. To perform the triaxial compression test, the displacements normal to the faces $X = 0$ m, $Y = 0$ m, and $Z = 0$ m are fixed (roller boundary conditions) while axial stress is applied to the face $Z = 1$ m and confining pressure is applied to the faces $X = 1$ m and $Y = 1$ m. The logarithmic strains $\varepsilon_x, \varepsilon_y, \varepsilon_z$, are computed as the average logarithmic strain for the element in the X, Y and Z directions, respectively. The volumetric and radial strains are computed as: $\varepsilon_v = \varepsilon_x + \varepsilon_y + \varepsilon_z$,

and $\varepsilon_r = \frac{\varepsilon_x + \varepsilon_y}{2}$ (this formula can help smooth out potential minor deviations from $\varepsilon_x = \varepsilon_y$, it was always verified that such differences were negligible). Similarly, the strain rates $\dot{\varepsilon}_x$, $\dot{\varepsilon}_y$, $\dot{\varepsilon}_z$, were directly obtained from the rate of deformation in the X , Y and Z directions computed in the hypoelastic formulation and did not require numerical differentiation of the strain histories.

In /KOM 20/, an engineering axial stress, i.e., constant total axial force, was mistakenly used. The experimental axial force applied during test TUC-V2 was adjusted as the cross-sectional area of the sample varied in order to maintain a constant axial Cauchy stress. In the present model, radial Cauchy stress $\sigma_x = \sigma_y = \sigma_r$ and axial Cauchy stress σ_z are applied to the single element. The simulations use the axial and radial stress histories given in Tab. 5.4 and the temperature history given in Tab. 5.5. The material properties are chosen to match the properties of the KOMPASS reference material and the state of the sample after pre-compaction, yet before TUC-V2: grain size $d = 8$ mm, water content $w = 0.05$ %, and initial porosity $\phi_0 = 16.7$ % (fractional density $D_0 = 83.3$ %, density $\rho_0 = 1799$ kg/m³).

The Callahan model cannot be entirely calibrated against a single experimental test. Test TUC-V2 does not cover the entire parameter space, e.g., grain size and moisture content are not varied, and systematic optimization methods may fail. A heuristic exploration of the parameter space is used instead in order to establish a satisfactory and practical calibration for the benchmarking of TUC-V2.

Tab. 5.4 Loading history for TUC-V2. The stress is linearly interpolated between the given times

t	σ_z	σ_r	t (continued)	σ_z	σ_r
[d]	[MPa]	[MPa]	[d]	[MPa]	[MPa]
0	-3	-2	141.0	-25.5	-17.5
1	-3	-2	141.1	-20.5	-20.0
1.1	-4.5	-4.0	161.5	-20.5	-20.0
11.0	-4.5	-4.0	161.6	-25.5	-17.5
11.1	-9.5	-1.5	171.4	-25.5	-17.5
21.0	-9.5	-1.5	171.5	-20.5	-20.0
21.1	-4.5	-4.0	191	-20.5	-20.0
31.0	-4.5	-4.0	191.1	-25.5	-17.5
31.1	-8.5	-8.0	201	-25.5	-17.5
41.0	-8.5	-8.0	201.1	-20.5	-20.0
41.1	-13.5	-5.5	216	-20.5	-20.0
51.0	-13.5	-5.5	216.1	-25.5	-17.5
51.1	-8.5	-8.0	231	-25.5	-17.5
61.0	-8.5	-8.0	231.1	-20.5	-20.0
61.1	-12.5	-12.0	246	-20.5	-20.0
71.0	-12.5	-12.0	246.1	-25.5	-17.5
71.1	-17.5	-9.5	261	-25.5	-17.5
81.0	-17.5	-9.5	261.1	-20.5	-20.0
81.1	-12.5	-12.0	276.3	-20.5	-20.0
91.0	-12.5	-12.0	276.4	-25.5	-17.5
91.1	-16.5	-16.0	290.9	-25.5	-17.5
101.0	-16.5	-16.0	291	-20.5	-20.0
101.1	-21.5	-13.5	615.1	-20.5	-20.0
111.0	-21.5	-13.5	615.2	-25.5	-17.5
111.1	-16.5	-16.0	636.1	-25.5	-17.5
121.0	-16.5	-16.0	636.2	-20.5	-20.0
121.1	-20.5	-20.0	650	-20.5	-20.0
131.0	-20.5	-20.0	650.1	-24.5	-24.0
131.1	-25.5	-17.5	750	-24.5	-24.0

Tab. 5.5 Temperature history for TUC-V2. The temperature is linearly interpolated between the given times

t	T
[d]	[°C]
0	30
228	30
232.1	35
342	35
343.7	30
481	30
482	50
540	50
541.2	70
600	70
602	35
680.1	35
681.8	70
720	70
722.8	30
750	30

Calibration of the flow potential

Following /CAL 99/, the four flow potential parameters κ_0 , κ_1 , n , and D_t are determined by fitting the radial-to-axial strain rate ratio $\mathcal{R} = \dot{\epsilon}_r/\dot{\epsilon}_z$. For triaxial compression, the ratio is given by:

$$\mathcal{R} = \frac{\kappa_0 \Omega^{\kappa_1} \sigma_m / 3 + \left(\frac{2-D}{D}\right)^{\frac{2n}{n+1}} \sigma_t / 2}{\kappa_0 \Omega^{\kappa_1} \sigma_m / 3 - \left(\frac{2-D}{D}\right)^{\frac{2n}{n+1}} \sigma_t} \quad (5.132)$$

The experimental radial-to-axial strain rate ratio shows values larger than unity during phases of hydrostatic stress (Fig. 5.15). That behavior is currently unexplained and might be attributed to anisotropy and transient effects upon load changes or porosity non-uniformity induced by temperature gradients /OLI 11/. It remains however surprising to observe $\mathcal{R} > 1$ for long periods of time during which no change in loading or temperature occurs, e.g., between 350 and 475 days. The radial-to-axial strain rate ratio for the Calahan model is bounded by the hydrostatic loading of porous crushed salt and the deviatoric loading of fully reconsolidated salt: $-0.5 \leq \mathcal{R} \leq 1$. Calibration is performed by attempting to best match the low values of \mathcal{R} during the deviatoric loading phases of the test. The calibrated values of the flow potential parameters thereby obtained are given in Tab. 5.6.

Tab. 5.6 Calibrated flow potential parameters for TUC-V2

Parameter	Legacy value /CZA 20/	Calibrated Value	Units
κ_0	10.119	11.629	-
κ_1	1.005	1.005	-
n	1.331	1.331	-
D_t	0.896	0.970	-

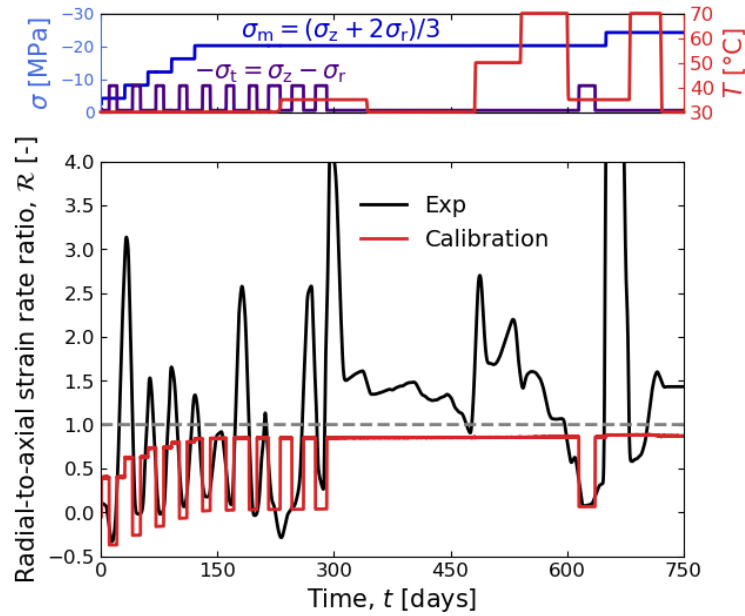


Fig. 5.15 Calibration of the flow potential parameters against the radial-to-axial strain rate ratio. The experimental strain rate ratio is smoothed using a LOWESS algorithm with a smoothing window of 15 days (shorter windows only affect the magnitude and fluctuations around the large peaks where $\mathcal{R} > 1$, which does not affect the calibration)

Calibration of the equivalent stress and grain boundary diffusional pressure solution

There remain 14 parameters to be calibrated while holding the 4 flow potential parameters fixed. The parameter space is reduced based on the following considerations:

- Elasticity parameters K_0 , K_1 , G_0 , and G_1 cannot be obtained from TUC-V2 and the legacy values, based on the work of /SJA 87/ are used.
- The grain size and water content are not varied during TUC-V2 and the legacy values for the associated parameters p and a are used.
- The theoretical values of the geometric exponents $r_3 = 1/3$ and $r_4 = 2$ are used because the values of the legacy calibration are considered to deviate too much from these theoretical values.
- The original value proposed by /SPI 93/ for the activation energy for grain boundary diffusional pressure solution $\frac{Q_s}{R} = 3000$ K is used for consistency.

- A large value of the exponent $n_s = 2.75$ is used to decay the contribution of grain boundary diffusional pressure solution over time, under the assumption that this mechanism dominates the initial, low-stress, stage of the test, while dislocation creep dominates the later, high stress, stage of the test.

The 4 parameters left, r_1 , η_0 , η_1 , and n_f , are calibrated to best match the axial and radial strain response (Fig. 5.15) and their values are presented in Tab. 5.7.

Tab. 5.7 Calibrated creep consolidation parameters for TUC-V2

Parameter	Legacy value /CZA 20/	Calibrated Value	Units
K_0	1.76×10^4	1.76×10^4	Pa
K_1	6.53×10^{-3}	6.53×10^{-3}	m ³ /kg
G_0	1.06×10^4	1.06×10^4	Pa
G_1	6.53×10^{-3}	6.53×10^{-3}	m ³ /kg
η_0	0.1029	5.0	-
η_1	3.9387	1.2	-
n_f	3.5122	1.55	-
a	0.3147	0.3147	-
p	1.6332	1.6332	-
n_s	0.5576	2.75	-
r_1	1.041×10^{-12}	3.165×10^{-12}	(m ^p K)/(Pa s)
r_3	15.1281	1/3	-
r_4	0.1678	2	-
Q_s/R	1077.46	3000	K

Discussions on the calibrated response and comparison to experimental data

The volumetric compaction response is satisfying up to about 450 days (Fig. 5.16a). The fractional density at the last stages of the test deviate from the experimental measurements when higher temperatures are imposed. The directional response agrees rather well with the experiments, even though the axial strain is underestimated (Fig. 5.16b) and the radial strain overestimated (Fig. 5.16c). This is the result of the model not being able to capture high values of $\mathcal{R} > 1$ since the error in strain rate ratio inevitably leads to deviation in strain for at least one of the directions.

The measured and predicted volumetric strain rate, and the predicted breakdown into grain boundary diffusional pressure solution (PS) and dislocation creep (DC) contributions are shown in Fig. 5.16d. The strain rate measurements in the first 150 days have a greater degree of nonlinearity (in semi-logarithmic space) than could be captured with

pressure solution creep alone. Pressure solution creep in the Callahan model does not include an internal hardening variable, such that the pressure solution strain rate, at a given density, immediately adjusts to changes in the loading conditions. When the loading conditions are held fixed, the predicted pressure solution strain rate remains nearly linear in Fig. 5.16d. This nearly linear decrease in rate is solely due to the pressure solution strain rate's dependence on the volume strain (density), which characterizes micro-scale changes to the grain contact geometry over time. Dislocation creep in the Callahan model, on the other hand, includes an internal hardening variable, the transient strain. This transient strain variable requires a significant time (and strain) to reach saturated conditions after an initial rapid response to a load change. Accordingly, the predicted dislocation creep strain rate in Fig. 5.16d evolves nonlinearly during each loading phase during the first 150 days. Combining pressure solution and dislocation creep allows the model to more accurately capture the high initial transient after a load change and the gradually varying, yet high, strain rate thereafter. Other plastic mechanism such as grain rearrangement and breakage are expected to play a negligible role in the transient response upon stress changes.

The relative contributions of pressure solution and dislocation creep after 150 days are less straightforward to select. In Fig. 5.16d, the model predicts dislocation creep dominates when the deviatoric stress is high and/or the temperature is above 60°C (except for one period between 650 and 680 days). Otherwise, the model predicts pressure solution creep dominates. We considered adjusting parameters to increase the dislocation creep at the expense of the pressure solution creep later in the test, but eventually decided to retain the partition shown in Fig. 5.16d.

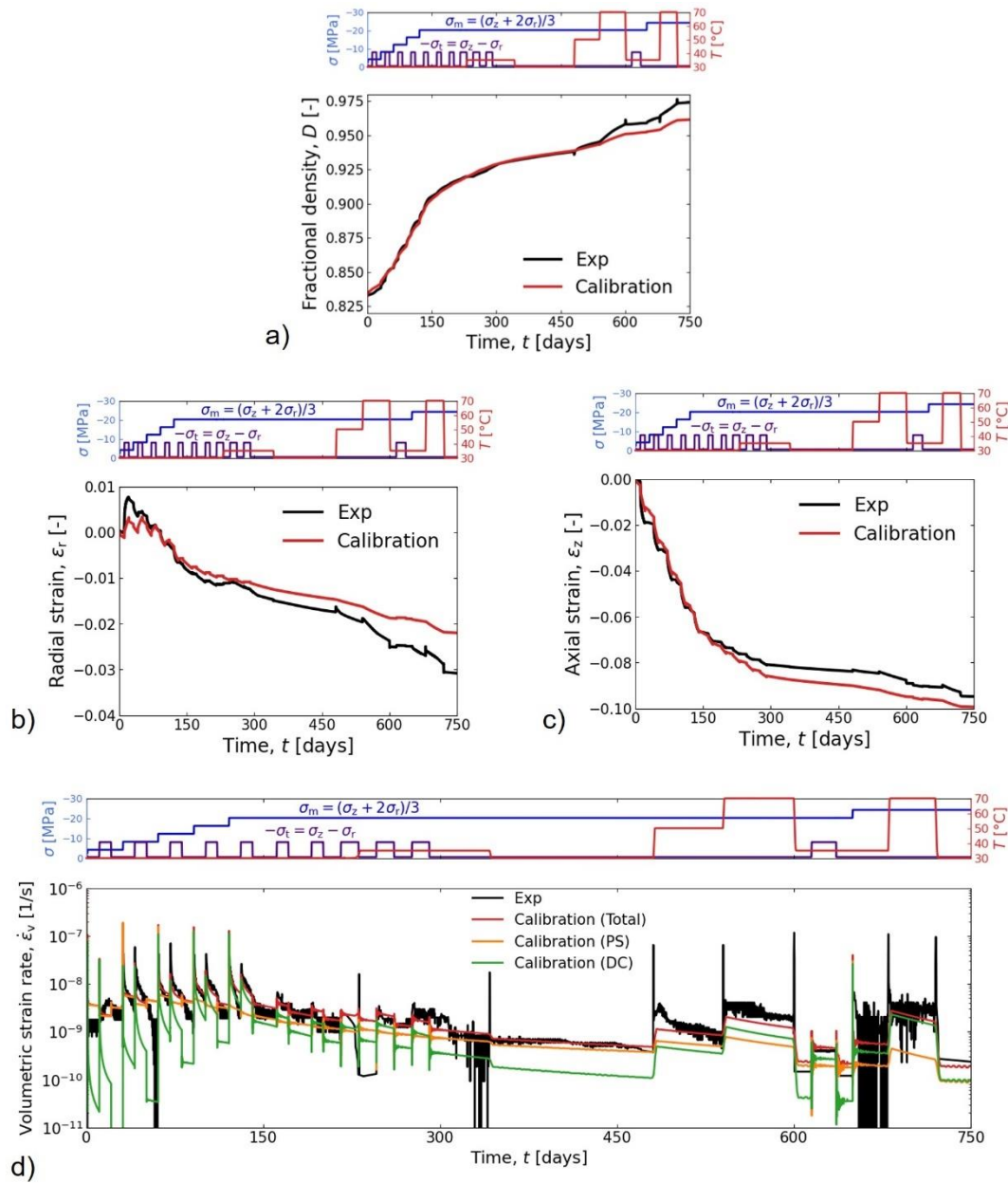


Fig. 5.16 Calibrated response of the Callahan model to TUC-V2

Numerical simulation of pre-compaction

The pre-compaction phase of test TUC-V2 is simulated with the calibrated model to verify our assumption that pre-compaction does not cause significant hardening for the Callahan model. To perform the pre-compression test, the displacements normal to the faces $X = 0$ m, $Y = 0$ m, $Z = 0$ m and $Z = 1$ m are fixed (roller boundary conditions), while Cauchy stresses $\sigma_x = \sigma_y = \sigma_r = -5$ MPa are applied to the faces $X = 1$ m and $Y = 1$ m.

The temperature was assumed to be $T = 30 \text{ }^\circ\text{C}$ and the initial value of the internal variable is taken as $\varepsilon^{\text{ts}} = 0$.

Pre-compaction is dramatically underestimated by the Callahan model: it takes more than 100 days to reach the fractional density of $D_0 = 83.3 \%$ instead of the 2 days required experimentally (Fig. 5.17). This poor prediction is likely due to the model not accounting for grain rearrangement and cataclasis, expected to be important deformation mechanisms during pre-compaction of loose cohesionless crushed salt. The model develops very little hardening: when fractional density reaches $D = D_0 = 83.3 \%$, the internal variable has a value of $\varepsilon^{\text{ts}} = 7.7 \times 10^{-4}$. This is significantly smaller than the value of $\varepsilon^{\text{ts}} = 0.0248$ obtained with the preliminary calibration in /KOM 20/, and simulating test TUC-V2 with the initial value of $\varepsilon^{\text{ts}} = 7.7 \times 10^{-4}$ (not presented herein) causes virtually no change to the response presented in Fig. 5.16 which validates our assumption to consider $\varepsilon^{\text{ts}} = 0$ for the simulations of TUC-V2.

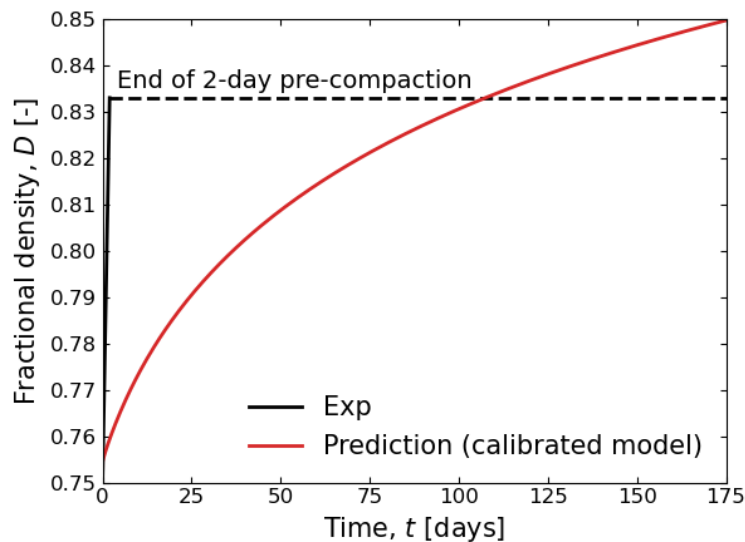


Fig. 5.17 Simulation of the pre-compaction test with the calibrated model

Summary

We calibrated the constitutive model developed by /CAL 99/ against the experimental data from test TUC-V2 using Sandia National Laboratories finite element code Sierra/SolidMechanics /SIE 23/. The flow potential is first calibrated against the radial-to-axial strain rate response, before calibrating the equivalent stress and grain boundary diffusional pressure solution parameters to best match the magnitude of the axial and radial strain responses.

Our new calibration provides a significant improvement in comparison to the preliminary calibration employed in /KOM 20/ and a satisfactory characterization of the experimental response. The predicted fractional density agrees very well with the experimental data, except for the very late stages of the test at high temperature, and the predicted directional response is acceptable, in spite of the radial-to-axial strain rate ratio being calibrated only on the deviatoric phases with $-0.5 \leq \mathcal{R} \leq 1$, which make up less than half of the test duration. Pre-compaction was modelled and showed negligible evolution of the dislocation hardening variable as well as a strong underestimation of the deformation, likely due to the absence of grain rearrangement and cataclasis mechanisms in the model. Nevertheless, the model predicts reasonable behavior for test TUC-V2 at fractional densities above 0.85 when deformation is mostly due to grain boundary diffusional pressure solution and dislocation creep mechanisms.

5.3.5 CODE_BRIGHT model (GRS)

The triaxial compaction test TUC-V2 is simulated using the finite element code CODE_BRIGHT. Based on the simulations for the first 150 days of TUC-V2 done in KOMPASS-I, it could be seen that the reproduction of the crushed salt compaction process is not yet satisfying /KOM 20/, /FRI 23/. In the second phase of KOMPASS, the focus was to develop a strategy to improve the constitutive model formulation in CODE_BRIGHT using the extended information from the TUC-V2 test.

Fig. 5.18 shows the model together with its mesh which is used in the simulation. The stress history and the boundary conditions follow the test execution (Section 3.3.5) and the constitutive model applied is described in Section 5.2.3.

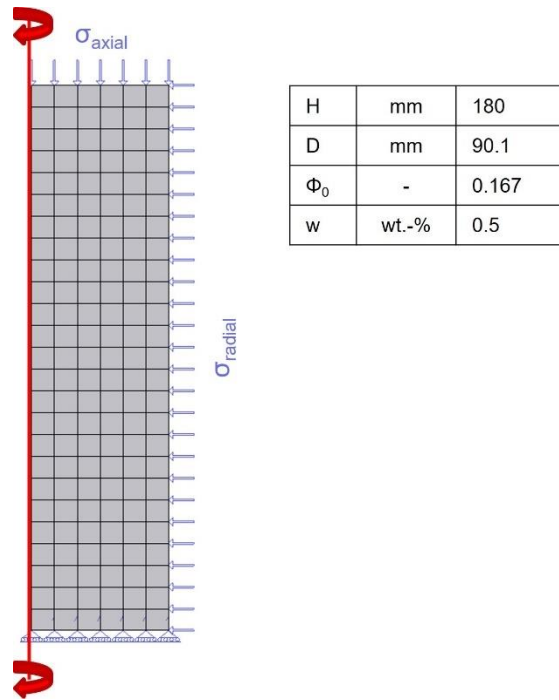


Fig. 5.18 CODE_BRIGHT model with mesh of the TUC-V2 test

Based on the outcomings of the investigations in KOMPASS-I which showed that issues regarding the reproduction of volumetric strain rates exist when simulating variations in mean and deviatoric stress, the strategy for the improvement of the constitutive model formulations is focused on the creep equations first. Therefore, it was started with the dislocation creep part. Dislocation creep is assumed to be the dominating creep mechanism based on the creep mechanism map from /OLI 02/.

The constitutive model for creep in CODE_BRIGHT is based on an idealized geometry of grains and pores /OLI 95/. The functions $g_{DC}^v(e)$ and $g_{DC}^d(e)$ in the dislocation creep model are geometrical functions which depends on the pore space but are generally fixed implemented. The blue curves in Fig. 5.19 show the course of the functions $g_{DC}^v(e)$ and $g_{DC}^d(e)$ for the void ratios $0 < e < 0.3$. With the experimental data of the TUC-V2 test, it is possible to derive the functions for the test. The yellow curve in Fig. 5.19 shows the function $g_{DC}^v(e)$ for the TUC-V2 data. Comparing both $g_{DC}^v(e)$ functions the accordance is not quite high, and the trend differs. This leads to the step of adapting the geometrical functions.

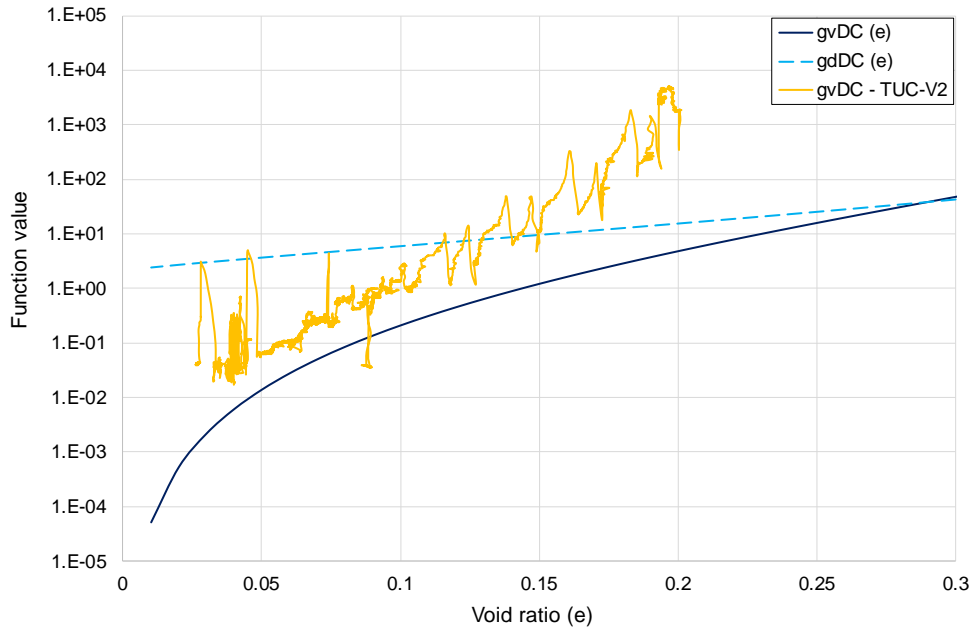


Fig. 5.19 Auxiliary functions $g_{DC}^v(e)$ and $g_{DC}^d(e)$ as implemented in CODE_BRIGHT (modified after /OLI 02/) and the function g_{DC}^v as derived from the experimental data of the TUC-V2 test /FRI 23/

In the current state, the possibility to modify the geometrical function is provided by calculating an equivalent void ratio following:

$$e_{equ} = e + \frac{e^3}{e_0^3} (e_{max} - e_0) \quad (5.133)$$

- e_0 initial void ratio
- e_{max} maximum void ratio
- e current void ratio

The comparison of the implemented function versus the experimental derived function and the one derived by using the equivalent void ration are presented in Fig. 5.20. The modified function matches the experimental function very well.

For the simulation the approach from the KOMPASS-I project was followed /KOM 20/. Thus, a simulation with the initial dataset from the TK-031 test was carried out for the whole test duration of 750 days first (Fig. 5.21, blue curve). The simulation results underestimate the compaction process strongly. By including the equivalent void ratio in the dislocation creep model, the simulation result for porosity improves notably (Fig. 5.21, red curve).

As discussed in the KOMPASS-I final report /KOM 20/ for the simulation with CODE_BRIGHT the reproduction of strain rates have to be included in the evaluation of results. Fig. 5.22 presents the volumetric strain rate over time for the measurements, the simulation with the initial dataset and the simulation including the equivalent void ratio. For the first 150 days of the test, the volumetric strain rates of the simulation using the equivalent void ratio reproduce the changes in mean stress and deviatoric stress well. The initial dataset on the other hand provides no satisfying results. For the phase from 150 days to 300 days with constant mean stress of 20 MPa and variations in deviatoric stress, the model with equivalent void ratio captures the jumps in the volumetric strain rates and shows a good accordance with the measurements. For the influence of temperature (300 – 600 days, Fig. 5.22) the model shows in general a good predictability. For the increase of mean stress at 650 days the volumetric strain rates could not be reproduced by the model, though the increase of temperature (680 days) is captured well. All in all, the modification of the constitutive model by using an equivalent void ratio in the geometrical function for the volumetric part of the dislocation creep model improves the numerical results for porosity, volumetric strain and volumetric strain rate. The equivalent void ratio is also used in the definition for $g_{DC}^d(e)$, but not for the geometrical functions in the FADT part of the model. Further investigations are needed for the other results as shown in Section 5.3.9.

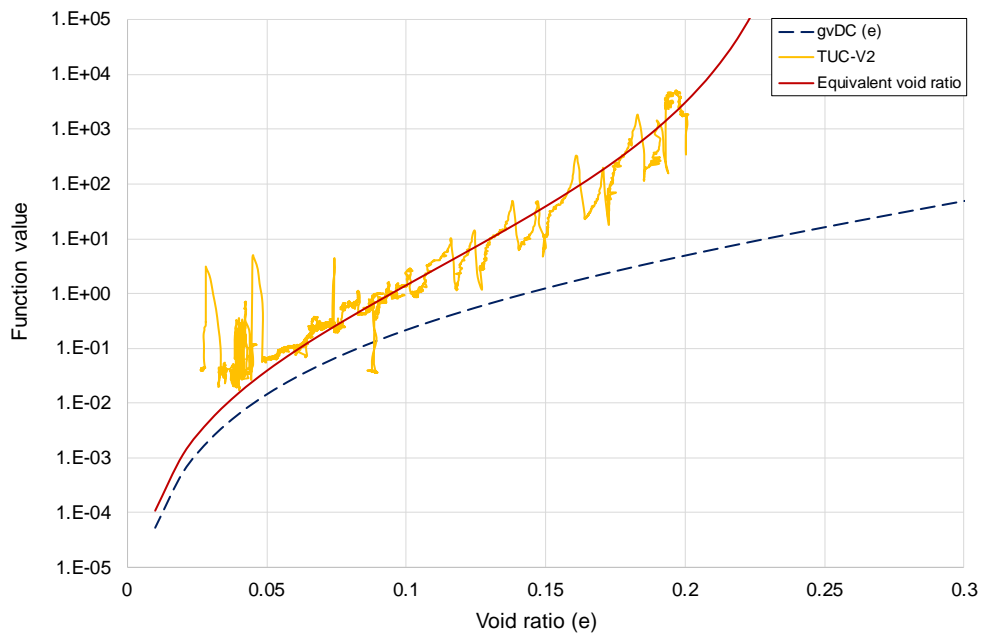


Fig. 5.20 Function $g_{DC}^v(e)$. Blue: as implemented in CODE_BRIGHT, yellow: as derived from the experimental data of TUC-V2, red: as derived from the modification using an equivalent void ratio

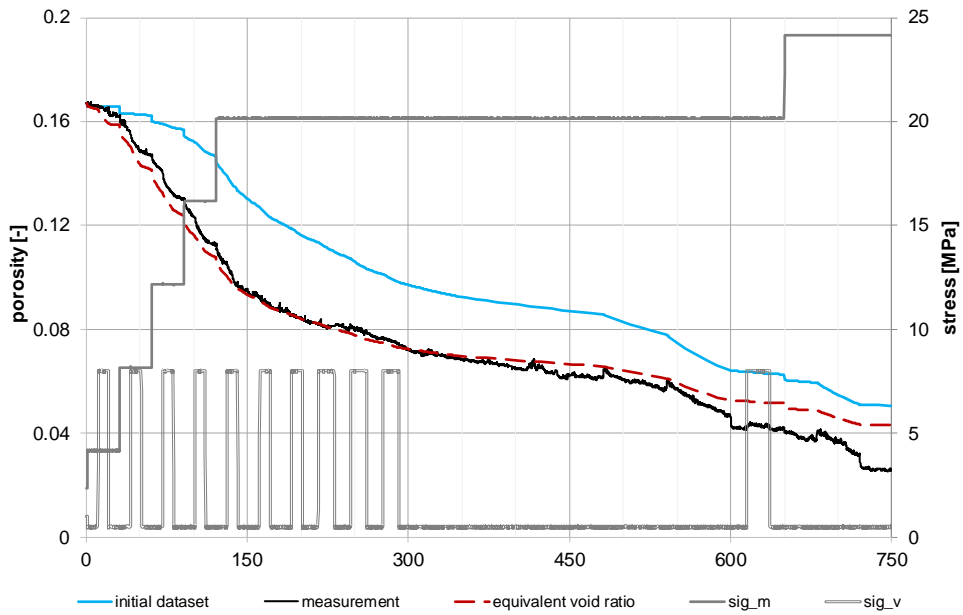


Fig. 5.21 Porosity for the TUC-V2 test. Black: measurement, blue: simulation with initial data set /KOM 20/ and red: simulation with equivalent void ratio

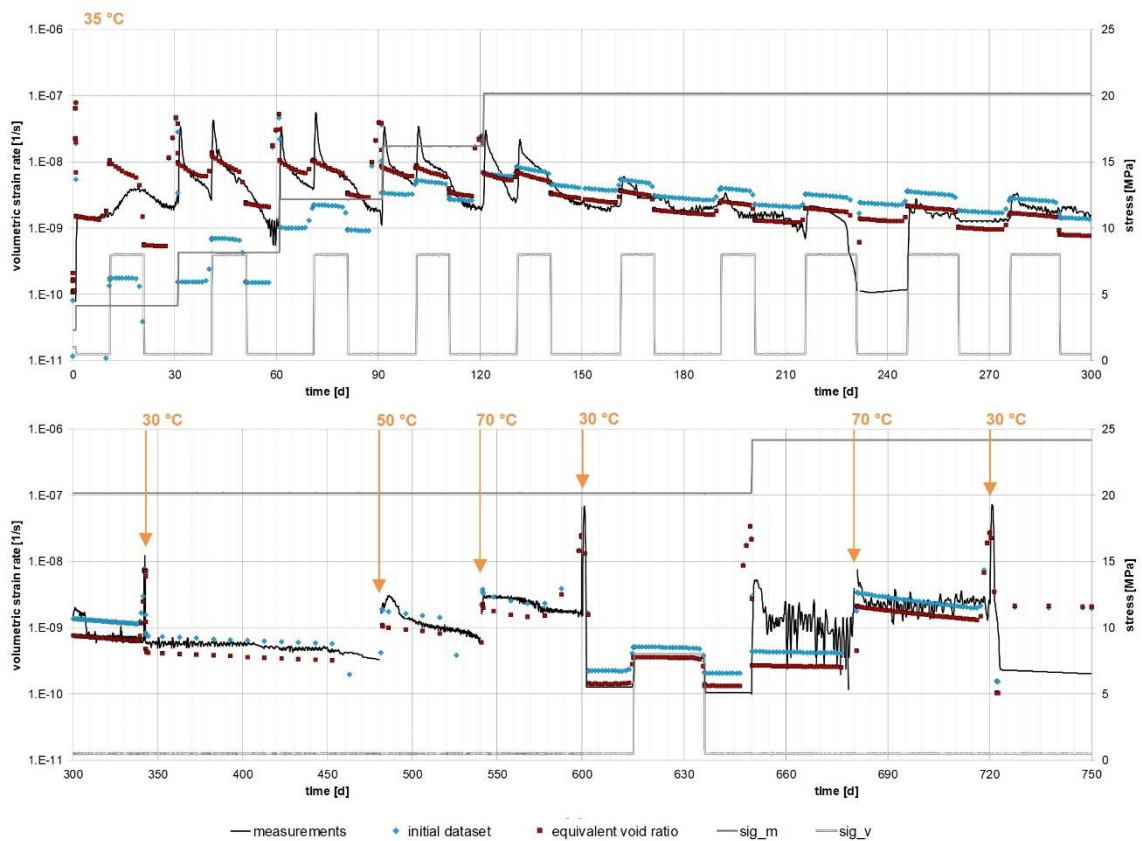


Fig. 5.22 Volumetric strain rate for the TUC-V2 test. Black: measurement data, blue: simulation with the initial dataset, red: simulation using the equivalent void ratio, grey: mean stress and deviatoric stress

5.3.6 EXPO-COM (TUC)

The methodology used to analyze the measured values for the development and validation of the constitutive model was presented in Section 5.2.4. This chapter specifically addresses the determination of individual functional relationships and associated material parameters.

Fig. 5.23 shows an overview of all individual functional relationships and influencing factors in correspondence to the TUC-V2 test phases from which the information can be derived.

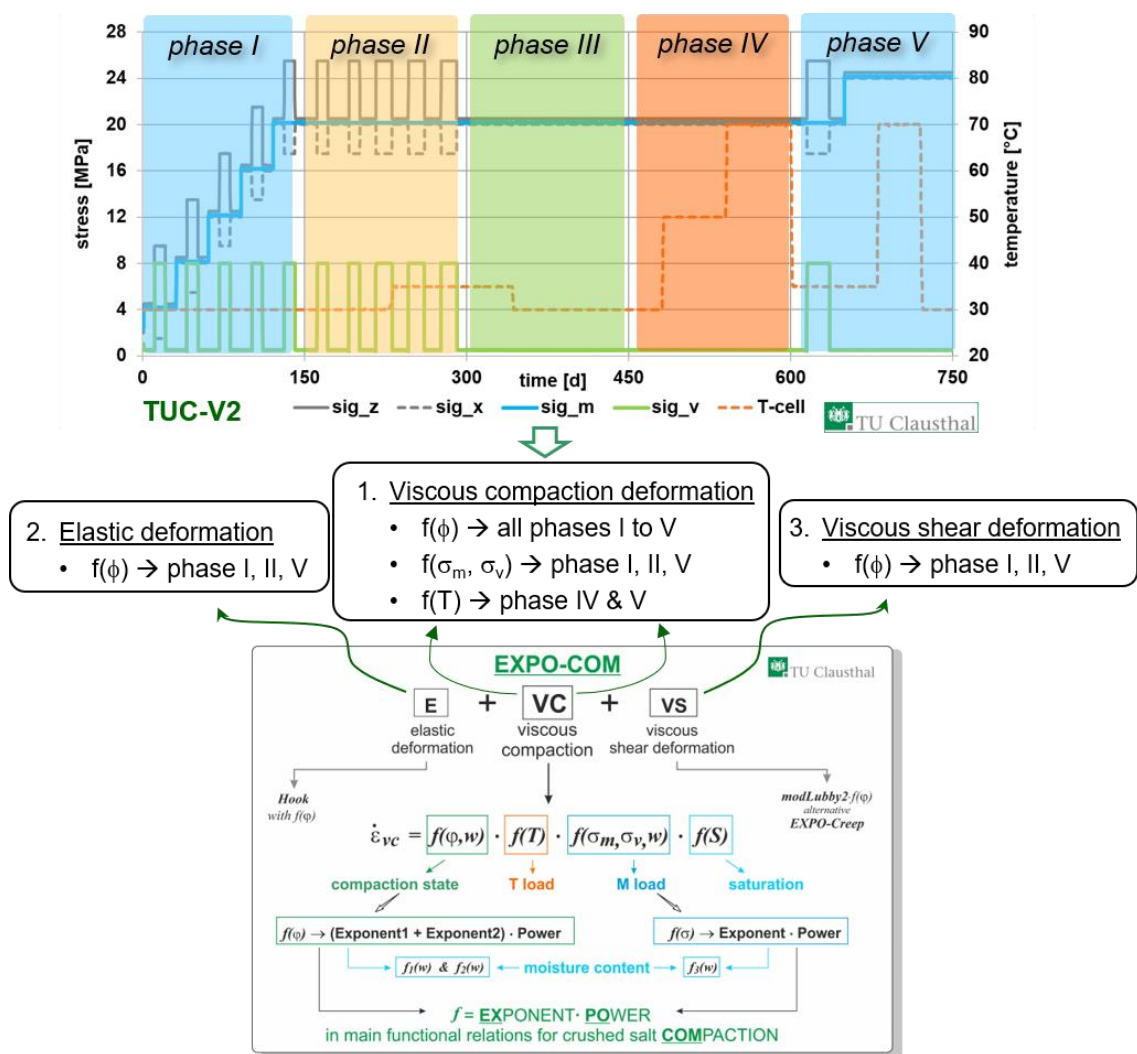


Fig. 5.23 Overview of all individual functional relationships and influencing factors with the corresponding phases of test TUC-V2

Fig. 5.9 shows a diagram for one of the main influencing factors, porosity, with the measured values (normalized), the theoretical curve from EXPO-COM with a tripartite approach and the corresponding material parameters for the functional relations. In the area highlighted in red, assumptions are currently required for the functional relation and corresponding parameters. After the successful realization of the experiment TUC-V5 in the future (next project phase) and incorporating its results in the analysis and validation, the functional relationships and parameters for the red area will be determinable.

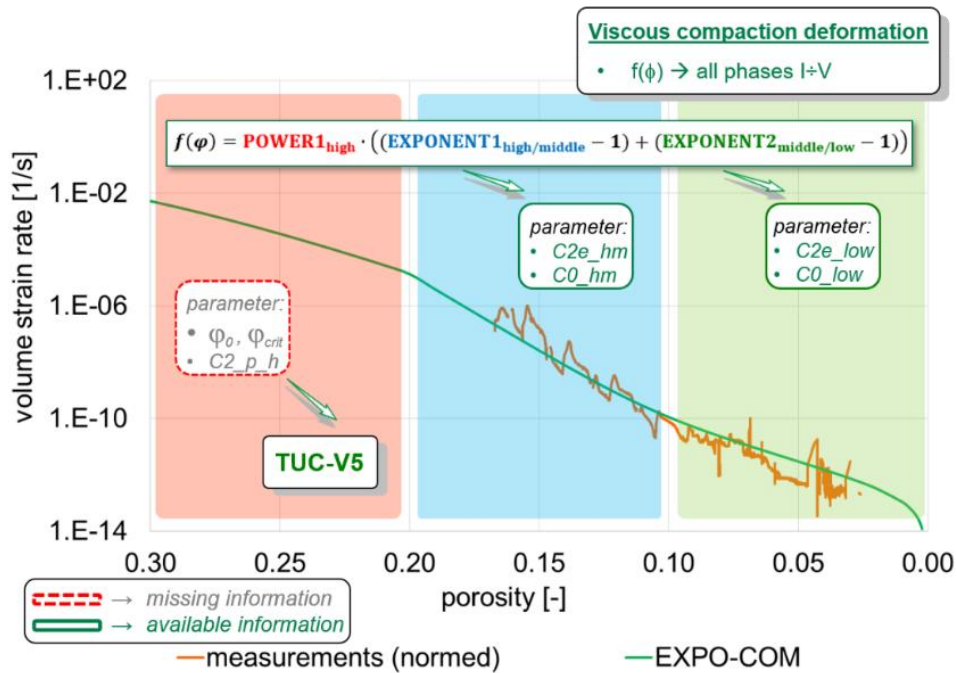


Fig. 5.24 Influence of porosity on the compaction rate: measured values (normalized), theoretical curve from EXPO-COM with a tripartite approach and with the corresponding material parameters for the functional relations

Fig. 5.25 furthermore shows a diagram of the other main influencing factor mean stress. For this purpose, the jumps in the volumetric strain rate caused by the load change are quantified and the appropriate functional relations and the associated material parameters are determined (see also Fig. 5.6). In the figure, the area is again additionally marked in red, for which a functional relation and associated parameters must be assumed so far.

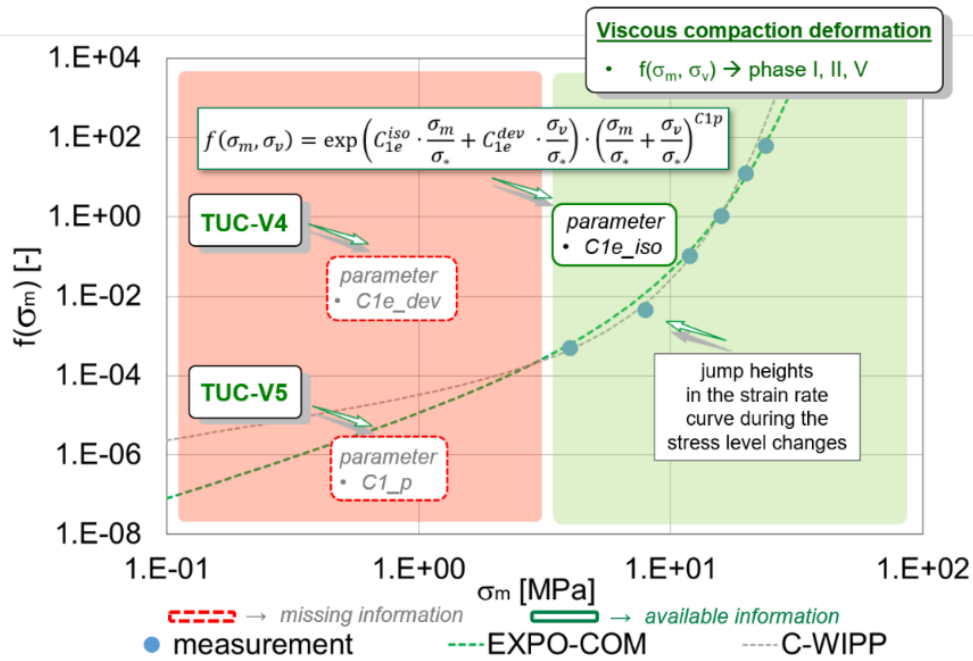


Fig. 5.25 Influence of mean stress on the compaction: measured values, theoretical curve from EXPO-COM and corresponding material parameters

Fig. 5.26 shows the next step of validation and parameter determination. Here, the temperature dependency of the compaction behavior is analyzed. In analogy to the mechanical load changes in the previous step, the jumps caused by the change in temperature level are quantified here. In addition, Fig. 5.27 illustrates different observed intensity of the reaction of the sample on the temperature change in different states of compaction, i.e., for different porosities (in the model EXPO-COM, the parameter $l_{com}(\phi)$ is formulated as a function of porosity). However, the database is clearly insufficient to see or derive a distinct dependency and must be extended for the range of high porosity.

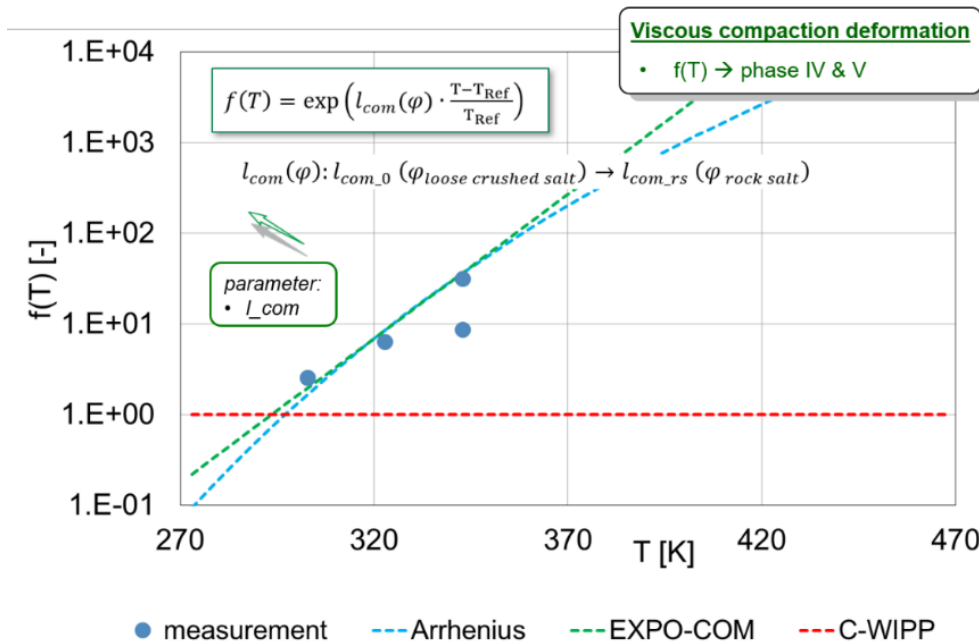


Fig. 5.26 Influence of temperature on the compaction: measured values and theoretical curve from EXPO-COM in comparison to the model approaches Arrhenius and C-WIPP (no dependency from temperature)

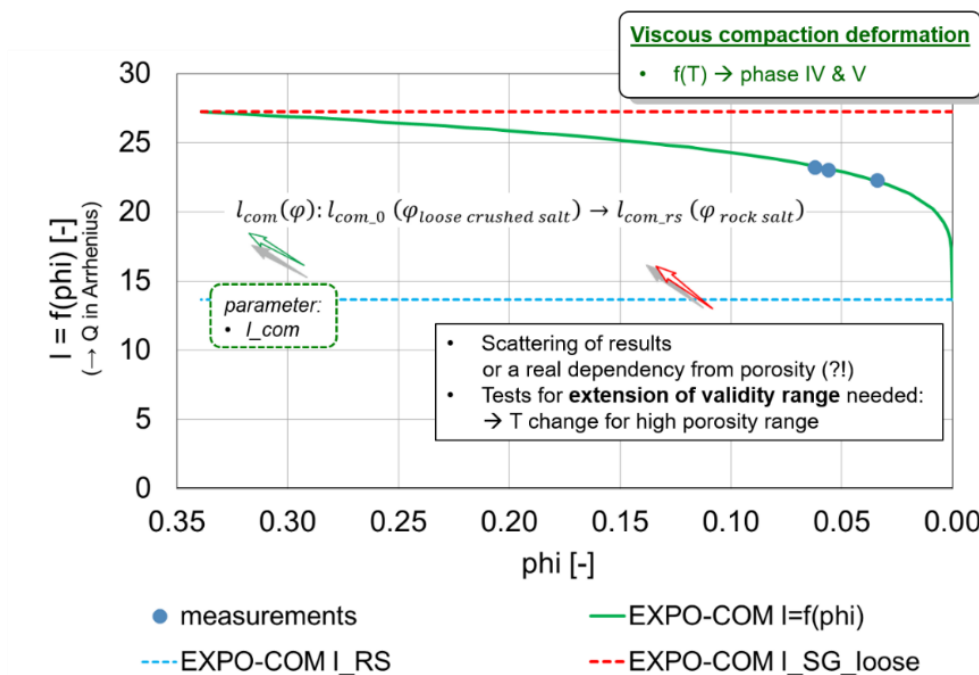


Fig. 5.27 Diagram for the temperature dependence of the compaction behavior: measured points and theoretical curves from EXPO-COM compared to the model approaches Arrhenius and C-WIPP (no dependency from temperature)

Finally, Fig. 5.28 shows the plot to determine the dependence of shear creep deformation on porosity. For this purpose, the effective strain rates were derived from the measurements and plotted against the porosity. Since the macroscopic deviatoric stress in the test was at the same level in all switch-on cycles and the transient creep can be assumed to have almost completely declined after 2 – 3 cycles, the porosity remains as the only and therefore well-isolated influencing factor that can change the magnitude of the shear creep strain rates from cycle to cycle. In the graph, in addition to the measured values, the level (range) of creep for rock salt is also shown, which is used as target value for the theoretical curve of EXPO-COM for a final porosity near zero. The information on the creep behavior of the Sondershausen rock salt was derived from the creep tests that were carried out in the IfG laboratory within the framework of the joint project for rock salt and can be found in the final report /HAM 07/.

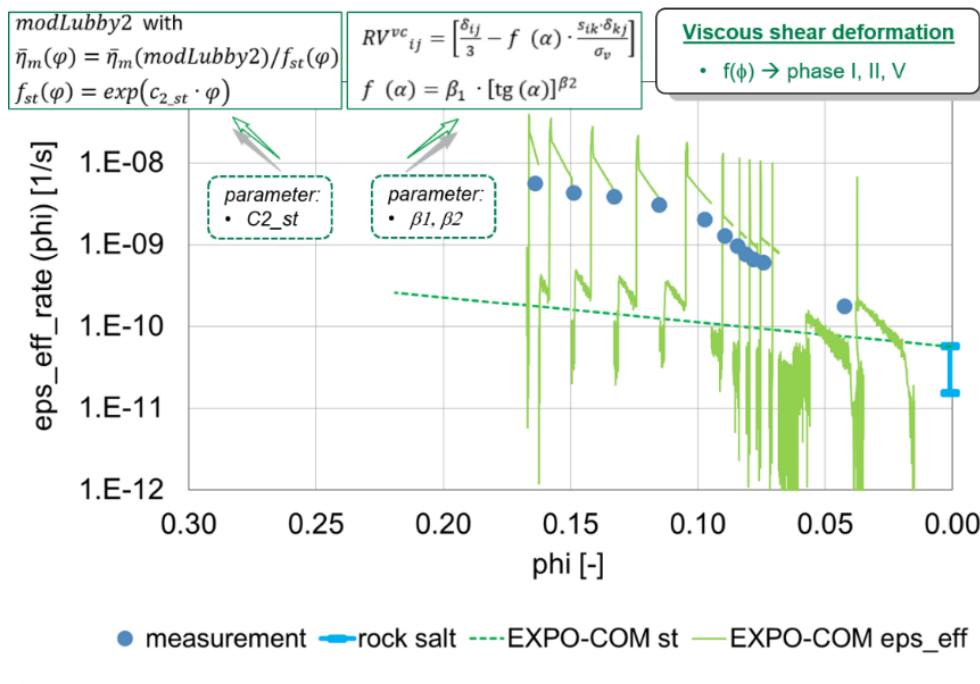


Fig. 5.28 Influence of porosity on the shear creep rate: measured values and theoretical curves from EXPO-COM ('EXPO-COM st' in the modLubby2 part of the model and 'EXPO-COM_eff' for the total effective strain rates from the both model parts producing volume true

After determination of the parameter set for the model EXPO-COM, the back-analysis of the measured strains was done. Fig. 5.29 shows the back-analysis results exemplarily for the volumetric strains. As a result, a good agreement of the calculated curves with the measurement results can be recognized. Two different calculated curves designated

as UB (upper-bound) and LB (lower-bound), with nearly no differences in the agreement in regard to the measurements, are shown. The use of two different parameter sets in regard to the influencing factor porosity was caused by the different possible extrapolations of the theoretical curve in unstudied region of porosity (high to middle values), see Fig. 4.22. The current spread of the parameter set will be reduced by the execution of the planned test TUC-V5 in the follow-up project and the use of the results for additional model validation.

Tab. 5.8 shows the determined parameter sets, used for the back-analysis. Fig. 5.31 shows additional calculation results from a single element model as well as for a cylinder-segment model. To recognize is a similarity of the results. Since the sample does not significantly bulge, this result is as expected and plausible. More detailed results for the back-analysis of the measurements in comparison to the other model approaches can be found in the summarized Section 5.3.9.

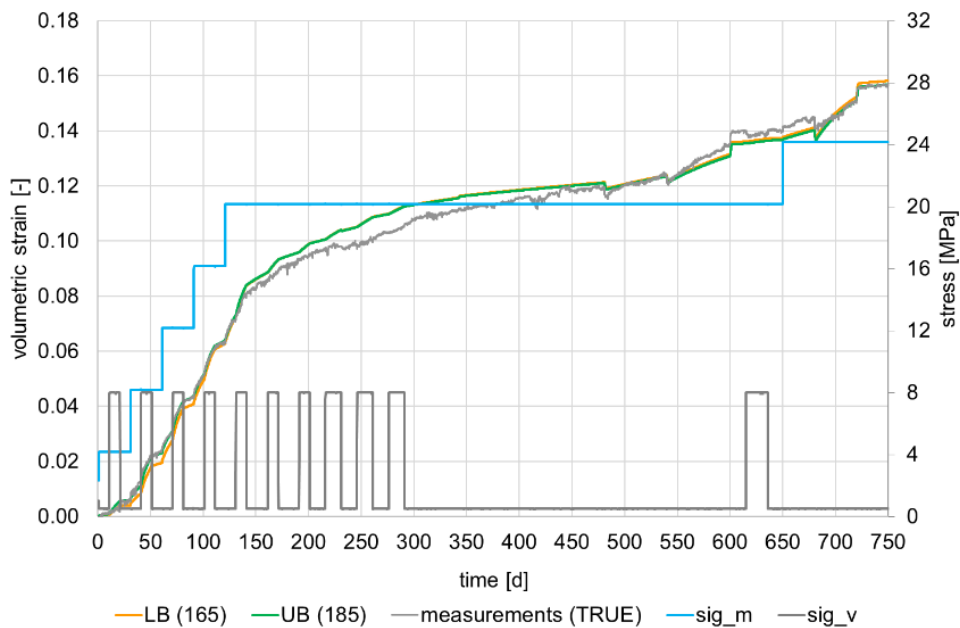


Fig. 5.29 Back-analysis results for the volumetric strains with two different parameter sets for EXPO-COM: UB (upper-bound) and LB (lower-bound)

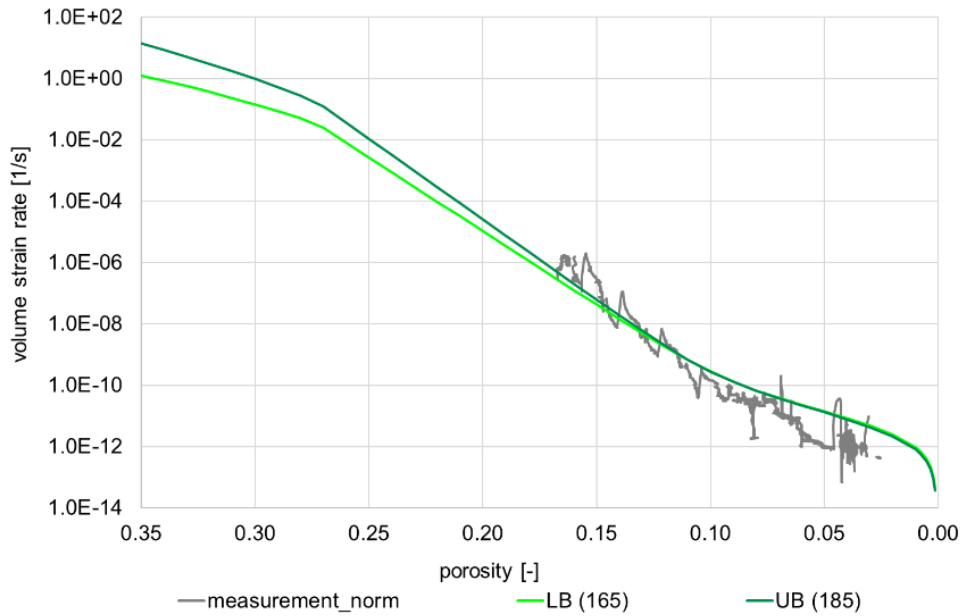


Fig. 5.30 Scattering of the parameter set UB and LB produced in regard to the influencing factor porosity due to different extrapolations of the theoretical curve in the not investigated ar-rea of porosity (high to middle range)

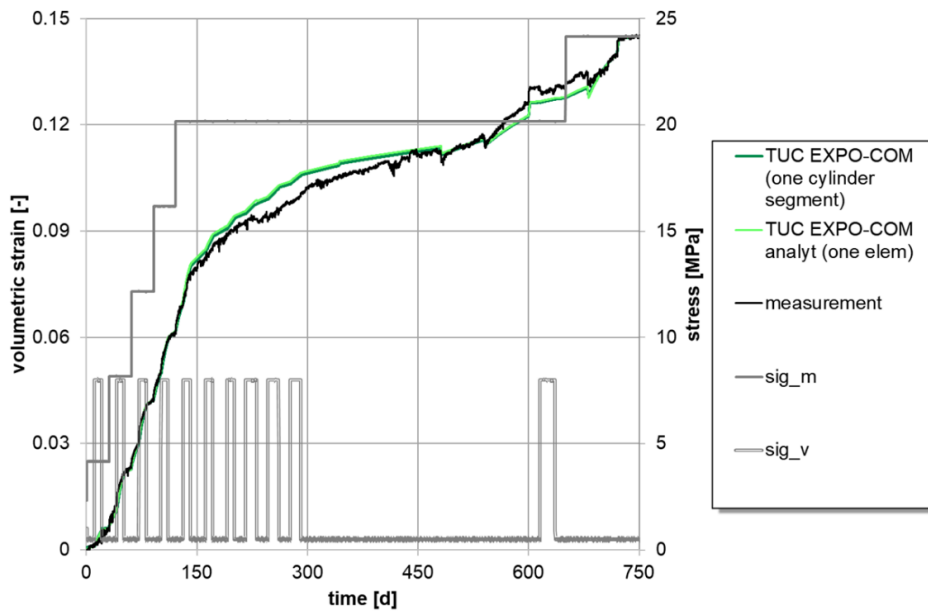


Fig. 5.31 Comparison of the back-analysis results from EXPO-COM performed on a single element model as well as for a cylinder-segment model

Tab. 5.8 Parameter sets for EXPO-COM model determined from the test TUC-V2

parameter	description	unit	value, UB (185)	value, LB (165)
elastic parameter				
K	current/start elastic bulk modulus	Pa	5.42E+09	5.42E+09
G	elastic shear modulus	Pa	2.50E+09	2.50E+09
E	E-modulus	Pa	6.50E+09	6.50E+09
ν	poisson ratio	-	0.3	0.3
K_f	final, intact salt, bulk modulus	Pa	2.33E+10	2.33E+10
G_f	final, intact salt, shear modulus	Pa	1.08E+10	1.08E+10
E_f	final, intact salt, E-modulus	Pa	2.80E+10	2.80E+10
ν_f	final, intact salt, poisson ratio	-	0.3	0.3
K	creep compaction parameter	Pa	4.05E-03	4.05E-03
G	creep compaction parameter	Pa	4.05E-03	4.05E-03
r_f	final, intact salt, density	kg/m ³	2.16E+03	2.16E+03
r	density	kg/m ³	1799.28	1799.28
ϕ	initial porosity for the test	-	0.167	0.167
viscous compaction parameter				
f(σ)				
$c0$	pre-factor	1/s	1.555E-29	5.070E-29
$c1e_dry$	exp-factor dry	-	0.43	0.43
$c1P$	power-factor	-	2.0	2.0
$c1e_dev$	exp-factor for dev.stress	-	0.055	0.055
$c1e_wet$	exp-factor dry	-	0.38	0.38
σ^*	norm. factor	Pa	1.0E+06	1.0E+06
f(ϕ)				
ϕ_{rs}	porosity of rock salt	-	0.001	0.001
ϕ_0	porosity if loose crushed salt	-	0.35	0.35
$c2_dry$	exp-factor dry	-	185.0	165.0
$c2_low$	exp-factor for phi low	-	45.0	40.0
$c0_low$	pre-factor for phi low	1/s	1.06E-18	1.46E-18
$c2e_wet$	exp-factor wet	-	53.0	53.0
ϕ_{crit_dry}	critical porosity for start of power_high	-	0.2	0.2
$c2_p_h$	power-factor	-	20.0	20.0
ϕ_{crit_wet}	critical porosity for start of power_high	-	3.50E-01	3.50E-01
f(w)				
w_min	minimum water content (natural dry)	-	3.0E-04	3.0E-04
w_max	maximum water content	-	1.0E-02	1.0E-02
w	current water content	-	5.0E-03	5.0E-03
$h1, h2$	power factor for water content influence	-	1.0	1.0
$h0$	exp-factor for water content influence	-	36.0	36.0
$h3$	power factor for water saturation influence	-	0.0	0.0
f(T)				
l_com_0	proportionality factor for temperature influence	-	19.1	19.1
T_Ref	reference temperature	K	273.15	273.15
T	temperature	K	303.0	303.0
l_rs	proportionality factor for rock salt	-	6.01	6.01
$t1$	power-factor	-	0.2	0.2
deformation distribution in 3D-space				
$\beta1$	pre-factor	-	3.70	3.90
$\beta2$	power-factor	-	1.00	1.00
viscous shear parameter				
rock salt parameter				
G_k^*	transient creep parameter	MPa	4.80E+04	4.80E+04
k_1	transient creep parameter	1/MPa	-0.06	-0.06
b	transient creep parameter	-	-0.7	-0.7
η_k^*	transient creep parameter	MPa*s	3.46E+09	3.46E+09
k_2	transient creep parameter	1/MPa	-0.07	-0.07
η_m^*	steady state creep parameter	MPa*s	6.05E+18	6.05E+18
m	steady state creep parameter	1/MPa	-0.12	-0.12
a	steady state creep parameter	-	-0.7	-0.7
l	steady state creep parameter	1/K	-0.05	-0.05
T	steady state creep parameter	K	303	303
f(ϕ)				
$c2_cr_st$	st. state creep parameter for porosity influence	-	10.0	10.0
$c2_cr_tr$	transient creep parameter for porosity influence	-	10.0	10.0

In relation to the functionality and validation state of the model EXPO-COM, the conclusions from the development, findings and still remaining flaws can be summed up as follows:

- The reaction of the sample for all researched influencing factors in the database can be build up with the use of the model EXPO-COM with a high degree of agreement. Thus, the level of validation corresponding the current available database (TUC-V2, KOMPASS reference material) is accomplished.
- Next steps will be the improvement of the validation state due to the expansion of the database (TUC-V4, TUC-V5).
- In addition, it is anticipated that the current formulations will need to be significantly modified to account for the influence of water content, which will result in a wider validation state as a result of further database's expansion (with TUC-V6 to TUC-V8).
- For the remote future, depending on the results of the widened database and the respective findings, the transformation of the current formulations into an additive approach of the individual microstructural deformation processes to account for grain fracture and rearrangement, pressure solution creep as well as dislocation creep could prove to be reasonable and more effective than the current purely phenomenological approach.

5.3.7 Hein-Korthaus (BGE-TEC)

The constitutive model is presented in its structure and with its components as well as their different expressions in Section 5.2.5. It is used in the form of Equ. (5.105), with the components from Equ. (5.108) and Equ. (5.120).

$$\dot{\varepsilon} = \dot{\varepsilon}^{\text{thel}} + \dot{\varepsilon}^{\text{dc}} \quad (5.134)$$

Tab. 5.9 Material parameters for the TUC-V2 simulation with the material model Hein-Korthaus

Parameter	Description	Unit	Value
	General parameters		
ρ_{RS}	Density of intact salt	kg/m^3	2170
η_0	Porosity of loose crushed salt	–	0.42
	Thermo-mechanical parameter		
α_T	Thermal expansion coefficient	$1/K$	$48 \cdot 10^{-6}$
	Mechanical parameters: Elasticity		
E_{RS}	Young's modulus of intact salt	MPa	$27 \cdot 10^3$
E_0	Young's modulus of loose crushed salt	MPa	$2 \cdot 10^3$
ν	Poisson ratio	–	0.3
	Mechanical parameters: Viscoplasticity		
A	Pre-factor	$1/d MPa^n$	0.692
Q	Activation energy	kJ/mol	52.8
n	Stress exponent	–	3.3
a	Material parameter	$1/MPa^2$	$580 \cdot 10^{-9}$
c	Material parameter	–	$13 \cdot 10^{-3}$
m	Material parameter	–	4.0
b	Material parameter	MPa^2	1.7

A focus of the project phase was the identification procedure. If the structure of the material model becomes more complex because it consists of several, partly competing, sub-processes, it might be difficult to find a clear solution within an acceptable time frame. Up to now, Excel has been used as a solver for an analytical solution that can be applied here. The identification procedure was performed in two stages. In the first stage, the implemented evolutionary algorithm is used. Beginning with any start vector, the parameter vector is brought close to a minimum. In the second stage the parameter vector is further improved to the target vector by means of the GRG nonlinear solver.

The handling of large amounts of data, as in the present multi-stage experiment, is time-consuming with Excel. Therefore, an identification method was set up with the help of the program R - R denotes both the code and the code's own programming language. The overall process is also set out in two stages. In the first stage, a particle swarm algorithm is used. In order to assess the clarity of the solution and the optimality, a cluster procedure is used in the second stage together with a gradient procedure afterwards. The cluster method evaluates the solution vectors of the particle swarm according to their cluster affiliation and the best solution of each cluster is then iterated with the gradient method. In case of equivalent solutions from several clusters, a selection would be made by assessing the values of the solution vector and a graphical representation. It

has been shown that although several clusters were formed from the solution vectors of particle swarm optimization, they belong to the same target area during post-iteration. As an example, the relationship between the two parameters a and c of the constitutive model (Equ. (5.120)) is shown in Fig. 5.32, the color represents the error value. Since the other material parameters of the constitutive model are also varied, there are also less good solution vectors in the target area.

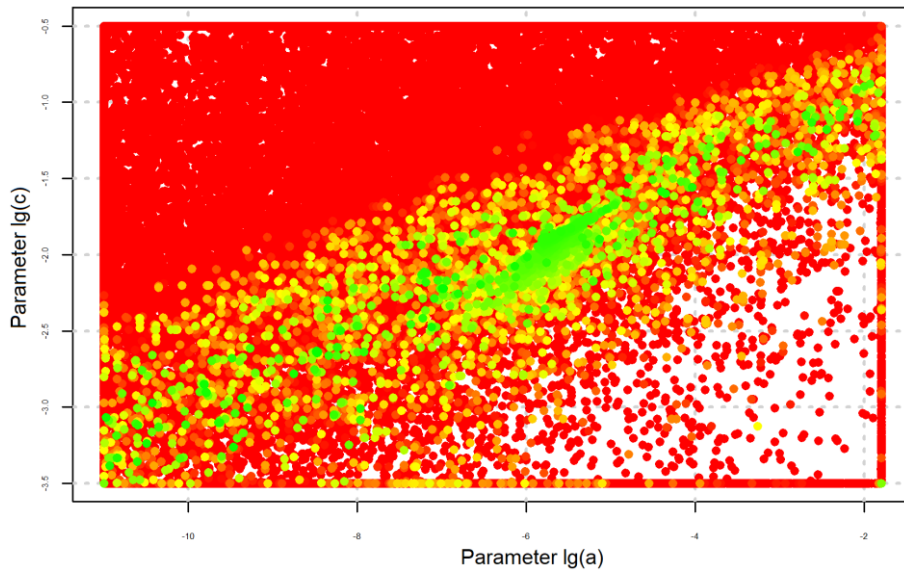


Fig. 5.32 Relationship between the logarithmic values of the material parameters a and c of the constitutive model to the solution

Another aspect of the identification is whether the behavior of individual constitutive models can be separated from the measured overall behavior. Even if the constitutive model used is simple in its structure, there are starting points with respect of the mechanical and the thermal load change. In the test evaluation, a differentiation is made between load steps and load cycles. While steps go in one direction only, cycles include a loading and an unloading step in the same height and type of load. For cycles, the creep phase between loading and unloading is neglected for the following consideration. The test TUC-V2 includes six steps of mechanically almost isotropic loading, $\Delta\sigma_0(1) \dots \Delta\sigma_0(6)$, and eleven deviatoric load cycles ΔS_x . The first five of these eleven cycles take place at an ascending isotropic load level, $\Delta S_{\sigma_0}(1) \dots \Delta S_{\sigma_0}(5)$, the fifth load cycle and the remaining six take place at a comparable mechanical isotropic load level of $\sigma_0 = 20 \text{ MPa}$, $\Delta S_{20}(1) \dots \Delta S_{20}(7)$, but at two slightly different temperature levels and with two different creep durations. Hence, the load cycle denoted by $\Delta S_{\sigma_0}(5)$ and $\Delta S_{20}(1)$ is the same. The thermal load change can be roughly summarized in three temperature cycles,

$\Delta T(1) \dots \Delta T(3)$ (Fig. 3.66). The independent measured quantities are the axial and the radial stress, the axial and the volumetric deformation and the temperature; calculated from the measured quantities are the circumferential stress and the radial and the circumferential deformation (Section 3.3.4.)

The measured deformation behavior in the stages of isotropic load increase is shown in Fig. 5.33. The mean stress is used as the stress quantity in this figure. Within the steps of load increase, the test control between the axial and the radial stress components was carried out with good constancy of 0.5 MPa . The first load stage is seen as preload and is therefore not shown here. Since the state of compaction has an influence on the material properties, the porosity η at which the load change took place is also indicated in the legend of the diagrams. It is assumed that temperature has no influence on the elastic behavior, but it may have an influence on other processes. Therefore, the temperature at which the load change took place is also indicated.

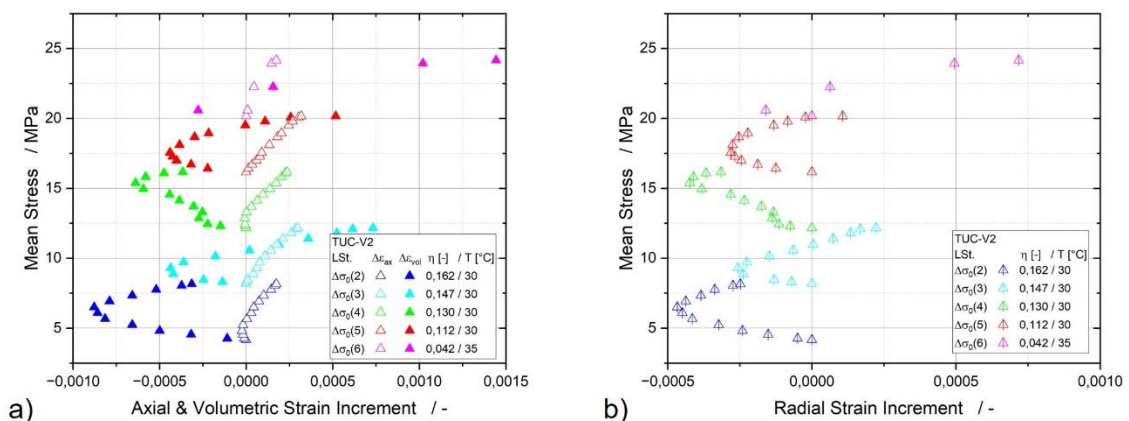


Fig. 5.33 Mean stress vs. change in deformation within the stage of isotropic load increase $\Delta\sigma_0$ (2) to $\Delta\sigma_0$ (6) – a.) Measured axial and volumetric strain increment; b.) Calculated radial expansion increment

The cyclic deviatoric behavior is shown in Fig. 5.34 and Fig. 5.35. Fig. 5.34 gives the behavior of the deviatoric load cycles during the phase of isotropic load increase, Fig. 5.35 shows the behavior during the constant isotropic load level of $\sigma_0 = 20 \text{ MPa}$. Lines between the measuring points serve to clarify the deformation path in Fig. 5.35.

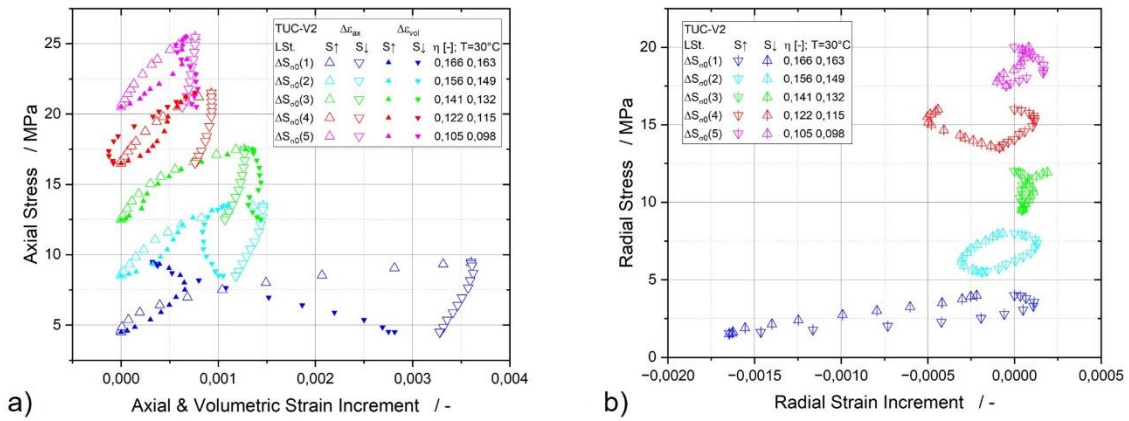


Fig. 5.34 Stress deformation behavior of the deviatoric load cycles $\Delta S_{\sigma_0}(1)$ to $\Delta S_{\sigma_0}(5)$ during the phase of isotropic load increase – a.) Measured axial stress vs. measured axial and volumetric strain increment; b.) Measured radial stress vs. calculated radial stress

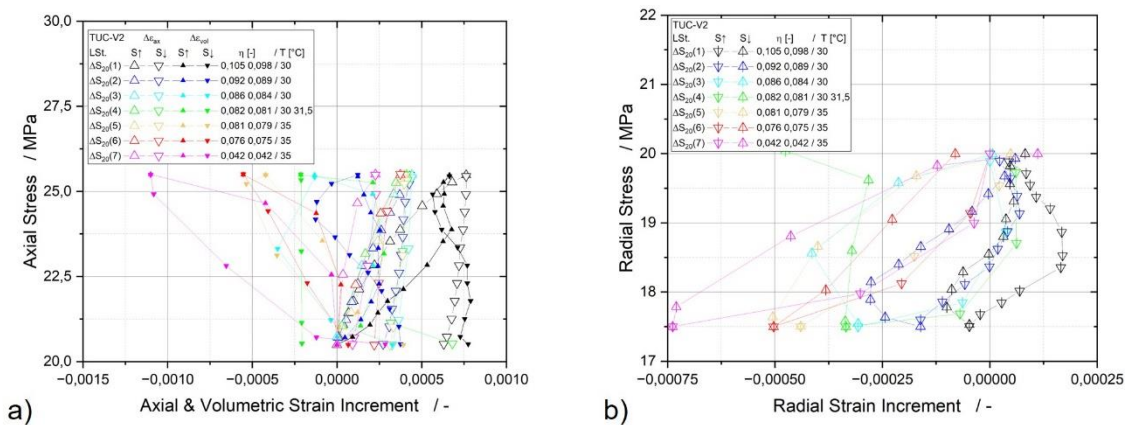


Fig. 5.35 Stress deformation behavior of the deviatoric load cycles $\Delta S_{20}(1)$ to $\Delta S_{20}(7)$ during the phase of constant isotropic load – a.) Measured axial stress vs. measured axial and volumetric strain increment; b.) Measured radial stress vs. calculated radial stress

At the beginning of the isotropic load increase, the measured deformation behavior runs counter to its expected behavior (Fig. 5.33). A delay of the reaction or an after-effect from the previous load cannot be used to explain this behavior, since the previous deformation did not run counter to the load increase. During the load increase phase, the direction of movement reverses into the direction of expectation. The moment in time of reversal motion occurs earlier in case of axial strain than in case of volumetric deformation.

The deviatoric load cycles show a behavior on the axial branch which, in addition to the instantaneous elastic behavior, could possibly be attributed to a time-dependent behavior (Fig. 5.34). On the other hand, the volumetric deformation behavior shown in the same figure cannot be fully explained. This applies in particular to the behavior on the unloading path and correspondingly to the calculated behavior in the radial direction. The discrepancy between axial and radial behavior is particularly evident when comparing the remaining plastic deformation at the end of a load cycle. If the behavior in the axial direction is classified as trustworthy, a decreasing plastic deformation can be seen over the individual load cycles; On the other hand, the remaining plastic deformation at the end of the cycles is rather indifferent in the case of radial deformation. The described cyclic behavior shown in Fig. 5.34 can be applied to the load cycles shown in Fig. 5.35. Compared to the load cycles with increasing load level shown in Fig. 5.34, the cycles in Fig. 5.35 are performed at the same stress level. The first cycle shows a greater plastic deformation at the end of the cycle than the subsequent cycles, which show a relatively constant degree. The last two cycles, $\Delta S_{20}(6)$ and $\Delta S_{20}(7)$, which were carried out at slightly elevated temperatures, differ slightly from the characteristic behavior of the previous cycles.

Three mechanisms are considered probable as the cause of the measured behavior:

- re-arrangement of the grain structure, possibly in conjunction with grain breakage;
- grain breakage, primarily acting on the first path to a new, increased load level, both in terms of the isotropic and deviatoric load path;
- lack of equilibrium in dislocation climbing resp. the different velocities at which the generation and annihilation of dislocation react to load changes.

These three deformation mechanisms are not yet considered in the current version of the constitutive model resp. only as equilibrium state in the case of displacement climbing (Equ. (5.112)). In the implementation of these mechanisms, time behavior will need to be considered in even more detail.

In addition to the above-mentioned time-dependent mechanisms, a load change is accompanied by an instantaneous elastic behavior. For the load cycles and load steps, the measured and calculated incremental behavior – load change in axial direction vs. deformation change – is shown in Fig. 5.36. The origin (0; 0) is in the initial state for the load path as in Fig. 5.33 to Fig. 5.35, but in the final state for the unloading path. The

cycle's unloading path $\Delta S_{20}(4)$ has been corrected for a meaningful behavior by its end-point value. In addition to the measured behavior, a thermo-elastic fit is shown. Obviously, further processes play a role beside these two mechanisms of thermo-elasticity. The time for the load changes in the experiment was approx. 2.5 h. While the behavior near the origin of the deviatoric cycles in these mechanisms reduced approach could still be mapped in a plausible way, the calculated behavior in the isotropic load increase stages shows a clear deficit. Therefore, it is yet not possible to assess the different functions of the elastic material approach (Section 5.2.5.1).

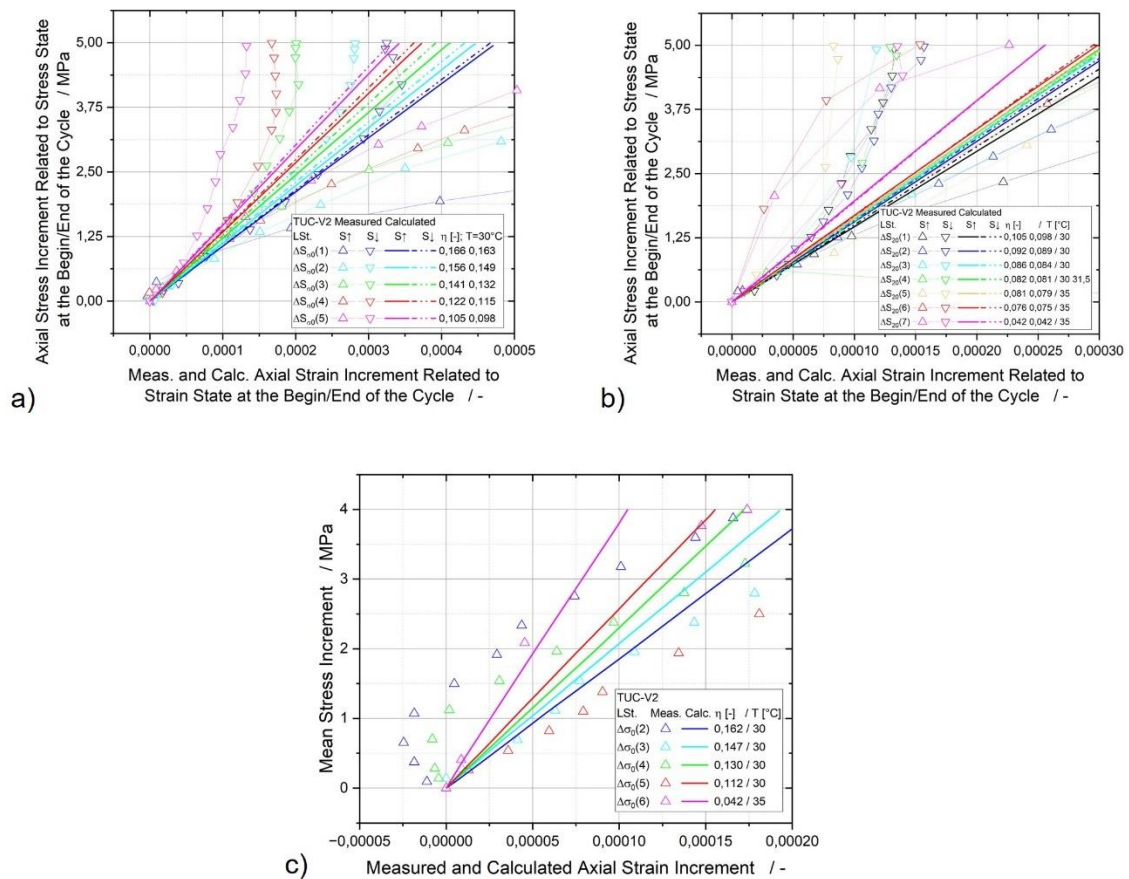


Fig. 5.36 Measured and calculated deformation behavior in axial direction – a.) Increment of axial stress in the deviatoric load cycles $\Delta S_{\sigma_0}(1)$ to $\Delta S_{\sigma_0}(5)$; b.) Increment of axial stress in the deviatoric load cycles $\Delta S_{20}(1)$ to $\Delta S_{20}(7)$; c.) Increment of the mean stress during the phase of isotropic load increase $\Delta \sigma_0(2)$ to $\Delta \sigma_0(6)$

The importance of elastic behavior for the material model does not result from its contribution to the overall deformation behavior (which is small), but from the determination of the stress state in deformation driven processes. Processes of this kind are the case in the compaction of crushed salt in underground openings of a salt mine. Porosity, velocity

of loading, stress ratio between the stress components and load height would be the main influence parameters to be investigated in order to achieve an assignment in the deformation mechanisms also with respect to short-time properties.

The axial and volumetric deformation behavior within the temperature cycles is shown in Fig. 5.37. In the temperature cycle, only the deformation behavior during heating and cooling phase is considered. According to the mechanical cycles, the creep phase between is not taken into account. Hence, the initial value of the deformation in the cooling phase has been shifted to the final value of the heating phase. Due to the sign convention of deformation with compressions as positive values and extension as negative values, the deformation increment with temperature increase is negative. The measured deformation behavior during a phase of temperature change corresponds only partially with the expected behavior (Fig. 5.37). At the beginning of a changing phase, a behavior occurs which is not solely due to thermal expansion. In the case of volumetric deformation, such a behavior also occurs at the end of the phase. Accordingly, when a complete cycle is considered, the initial state is not reached.

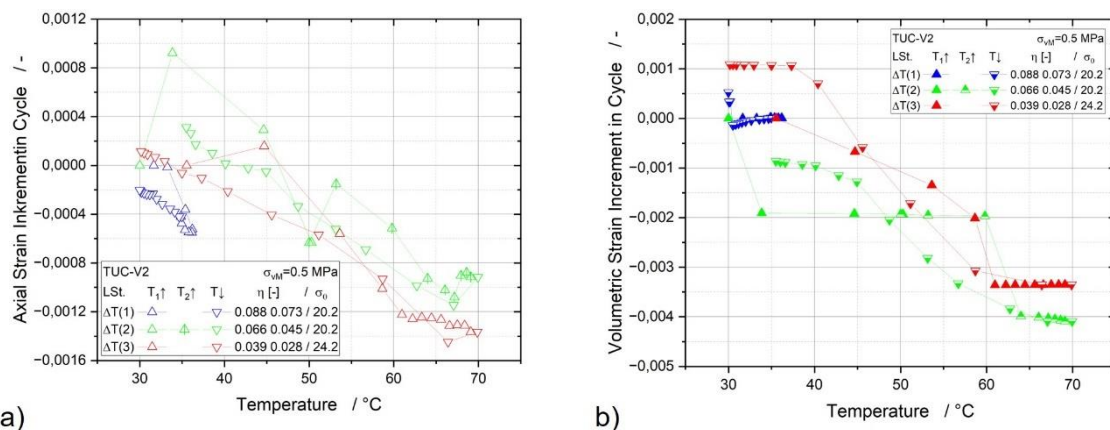


Fig. 5.37 Measured deformation behavior in the thermal load cycles $\Delta T(1)$ to $\Delta T(3)$ as a function of temperature – a.) Axial strain increment; b.) Volumetric strain increment

Because of the variability in the strain difference at the end of a cycle, no additional mechanism, such as it is called in connection with mechanical load changes, can be attributed to this behavior. Whether the duration of the individual temperature change phases is sufficient is to be investigated when the model is completed in the area of transient displacement behavior. The amount of thermal activation must also be considered.

The coefficient of the thermal expansion depends on temperature. However, this influence is covered by other effects in the measured behavior here and is therefore not considered. So only a constant value of $\alpha_{th} = 48 \cdot 10^{-6}$ has been determined (Fig. 5.38). This value tends to be at the upper limit of the expectation range of salt, so it can be assumed that time-dependent processes and thermally activated processes have to be taken into account. The initial value, visible in the calculated behavior in Fig. 5.38, is attributable to the identification process and has no physical significance.

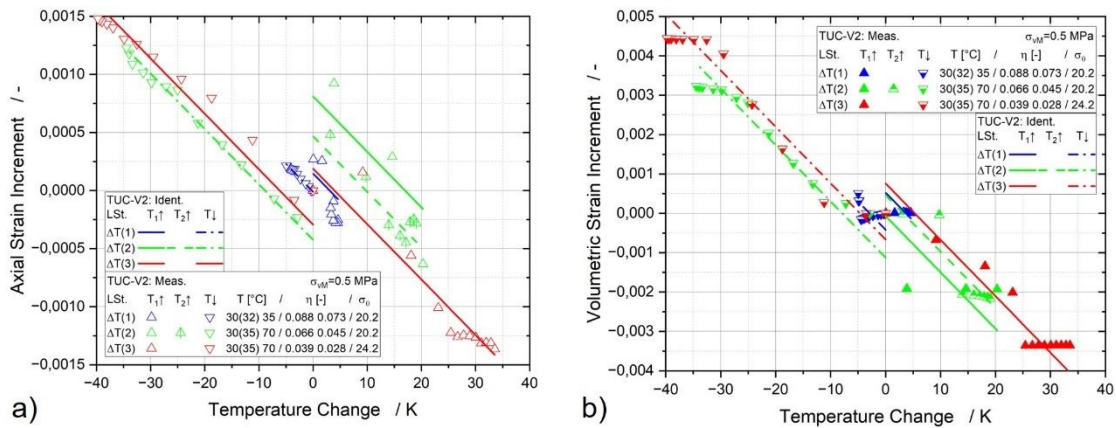


Fig. 5.38 Comparison of measured and calculated thermal deformation in the thermal load cycles $\Delta T(1)$ to $\Delta T(3)$ depending on temperature – a.) Axial strain increment; b.) Volumetric strain increment

As shown above, a separation of sub-processes has been successful only to a limited extent. Therefore, an over-all fit was performed. The overall time behavior can be represented well (Fig. 5.39) even if not all the individual acting processes of crushed salt compaction are included in the constitutive model. The reason therefore is a shift of physical processes to different processes in the model. A differentiated look at individual phases of the compaction process shows the limitation that results from the reduced number of processes considered. If experiments were conducted under altered boundary conditions, this could result in larger deviations.

A comparison of measured and calculated behavior (Fig. 5.39) leads to the following results for the model:

- a shift from time-dependent processes to instantaneous processes;
- a joint action of creep processes, what is seen in a stress exponent between the expected values for the time-dependent behavior of pressure solution creep and dislocation creep in the constitutive model;
- an underestimation of creep behavior under the influence of thermal activation,
- a shift in creep behavior from the porosity-dependent geometry function to the stress function;
- a limited time-dependent behavior in the event of a change in external condition;
- over-estimation of isochoric behavior, especially in the first half of the experiment.

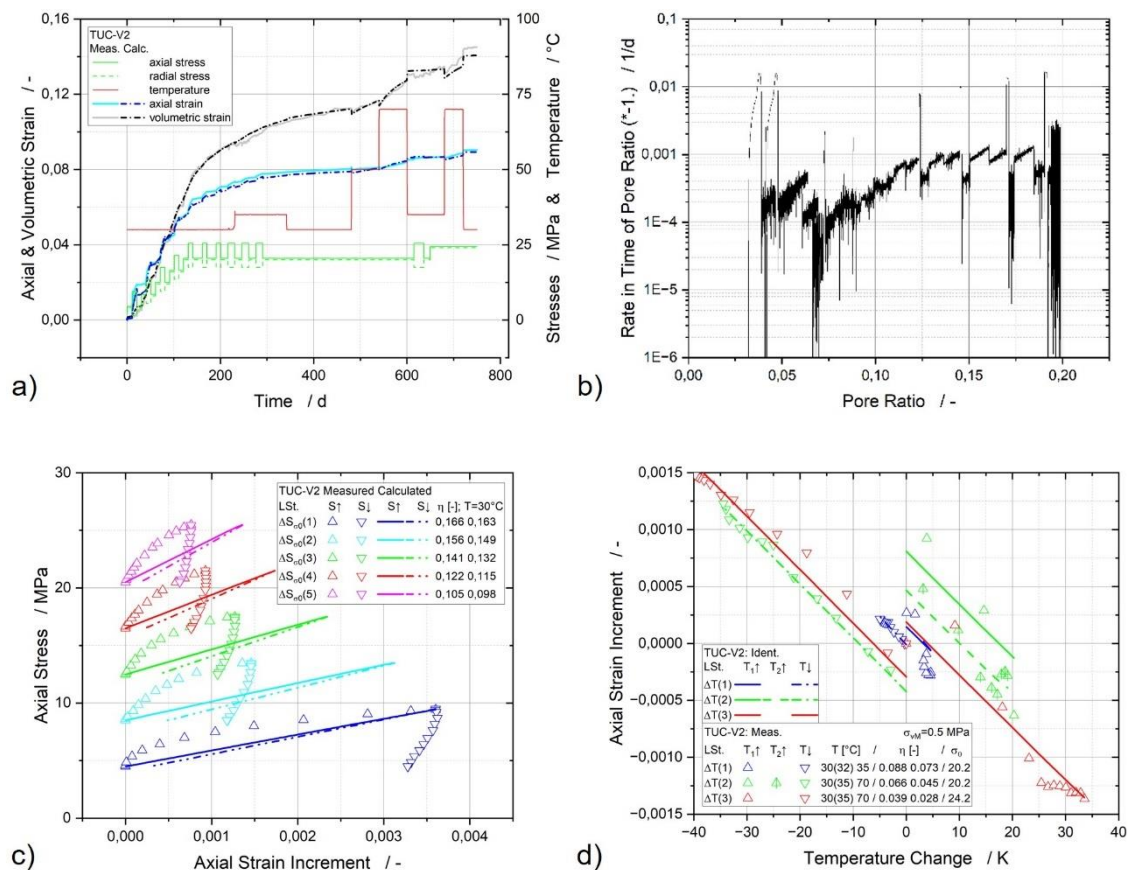


Fig. 5.39 Comparison of measured and calculated deformation behavior – a.) Deformation behavior over time; b.) Rate of pore ratio over pore ratio based on calculation; c.) Axial stress over axial strain increment during deviatoric load cycles $\Delta S_{\sigma_0}(1)$ to $\Delta S_{\sigma_0}(5)$; d.) Axial strain increment over temperature change in the thermal load cycles $\Delta T(1)$ to $\Delta T(3)$

5.3.8 Modified CWIPP (IfG)

To derive parameters for the benchmark tests, the IfG has employed an algorithm that focuses on the creep (i.e., constant stress) phases. There is an additional elastic compaction component, and likely also a “plastic” contribution to volumetric strain during the ramps that is not covered by the creep law (Equ. (5.127)).

However, during the isotropic creep phases, where stress is constant and to a good approximation isotropic and there are no deviatoric stresses, the volume strain is given by the trace of (Equ. (5.127)). For this simple situation, the porosity as function of time can be computed analytically,

$$P(t) = -\frac{1}{C_2} \ln[1 - (1 - e^{C_2 P_0}) \exp(-C_0(e^{C_1 \sigma_0} - 1) C_2 (t - t_0))] \quad (5.135)$$

with initial value $P(t=t_0) = P_0$ and constant compressive isotropic stress σ_0 (where compressive stress is positive). This expression still is a nontrivial function. A set of compaction parameters is obtained in three steps:

- 1) Fix a value of C_2 .
- 2) For each creep phase, calculate the factor $A = C_0(e^{C_1 \sigma_0} - 1)$ from the known phase duration $T = t - t_0$. Compare the curves of $P(t)$ to the experimental data and adapt the value of C_2 if necessary.
- 3) From a plot of A_{calc} vs. σ_0 for each isotropic creep phase, the parameters C_0 and C_1 can be determined by a fit.

The above procedure is illustrated in Fig. 5.40. In the left panel (Fig. 5.40a), porosity evolution is plotted for the six isotropic creep phases (blue dotted line represents laboratory data) as well as the intermittent deviatoric creep phases. An offset is applied such that the porosity loss during the deviatoric phase is ignored for the derivation of the model parameters $C_{0,1,2}$. We justify this with the strong “transient” compaction component associated with the beginning of each deviatoric phase. The data additionally show that in the second isotropic creep phase of each load stage, the volumetric strain rates almost immediately return to values like those at the end of the first. Nevertheless, this treatment will lead to an underestimation of the compaction rate.

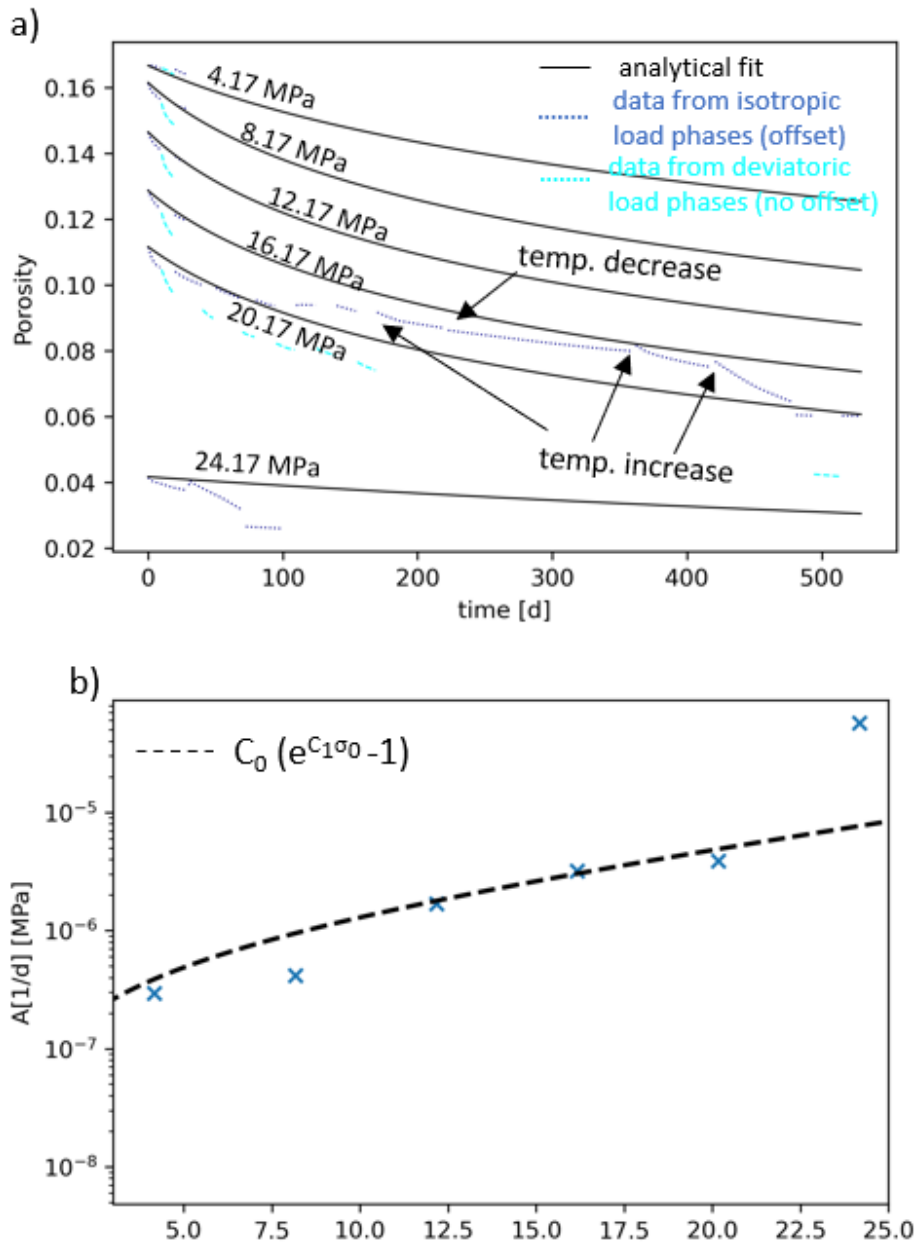


Fig. 5.40 Illustration of analytical procedure for parameter determination for IfG CWIPP. (a) Data and model fit for porosity-time curves for each isotropic load stage (data: blue, model: black). Cyan curves show intermittent deviatoric load phases. These phases are compensated for by an offset. (b) Analytical fit term containing C_0 and C_1

In the first step, the analytical curves have with individual values A_{calc} for a chosen value of $C_2=37.0$. This ensures that the initial and final porosities for each isotropic load stage are correctly reproduced. The choice of C_2 just determines the curvature of the $P-t$ curve. The right panel plots (Fig. 5.40b) then shows the computed values A_{calc} and the analytic

fit of A , indicating a reasonable the agreement. Since the final values of C_0 and C_1 are determined from this fit, the replotted analytical P-t curves displayed in Fig. 5.40a do not match the end of the data perfectly anymore.

Overall, the analytic solution is too flat for all phases, although a direct comparison is not straightforward, because each isotropic phase is “interrupted” by a deviatoric creep phase. Additionally, several temperature changes were included in the longest creep phase, which clearly impacts the creep rates.

Once these steps are completed and C_0 and C_1 are known, A_{calc} can be recalculated for deviatoric creep phases (at same mean stress) and compared to the isotropic values. C_3 is taken as the average value, and its effect can be inspected visually similar as in step 2 of the parameter determination. For the future, we aim to obtain better results for mixed isotropic-deviatoric triaxial compaction tests such as TUC-V2 by an iterative fitting procedure, where steps 2 and 3 are repeated for known values of C_3 , leading again to a new C_3 value.

Fig. 5.41 shows the Arrhenius plot to obtain the activation energy for the temperature dependence, based on the temperature changes during the last load stage. Porosity dependence was ignored for this analysis (i.e., no correction was made), and volumetric strain rates are taken at the end of each phase of constant temperature. The result is and activation energy of around 24 kJ/mol, which is approximately the value found for pressure solution creep by /SPI 90/.

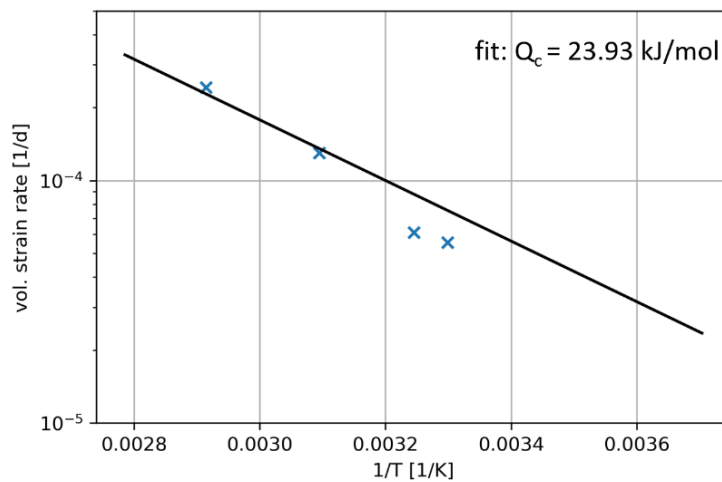


Fig. 5.41 Arrhenius plot of temperature dependent volumetric strain rates and analytical fit

The parameters of the IfG-CWIPP model obtained from the TUC-V2 experiment are presented in Tab. 5.10.

Tab. 5.10 IfG-CWIPP parameters relevant for compaction creep based on TUC-V2.

Parameter	Value [unit]
C_0	$7.5 \cdot 10^{-7}$ [-]
C_1	0.1 [MPa ⁻¹]
C_2	37 [-]
C_3	1.2 [-]
κ	11.8
ζ_{iso}	0.025
ζ_{eff}	0.0085

We now summarize the approach and results to the numerical back-calculation of the TUC-V2 experiment.

The calculation was performed using FLAC3D and the model geometry was implemented to scale as a quarter-cylinder with ca. 1500 zones, exploiting rotational symmetry. We followed the laboratory schedule for load stages closely and also included loading and unloading ramps as step functions (5 steps) as they were recorded. Stress boundary conditions were set at the top and lateral boundaries to reproduce axial and confining stresses from the laboratory.

The back-calculation of the TUC-V2 compaction test is presented in terms of the evolution over time of porosity (Fig. 5.42, derived from volumetric strain), effective (deviatoric) strain (Fig. 5.43), as well as volumetric strain (Fig. 5.44). Both porosity and effective strain evolutions show a reasonable fit, especially in the long isostatic creep phase at 20 MPa. Note that the strong jumps in volumetric strain rates during the loading ramps are a result of relatively fine sampling of time steps, which was smoothed out in the experimental data.

As opposed to the version used in the KOMPASS-I benchmark calculations, the constitutive model now reacts to changes in both deviatoric stress and temperature. This results in an overall reasonable fit for the porosity evolution and order of magnitude for the volumetric strain rates over most of the experiment's duration (Fig. 5.42, Fig. 5.44).

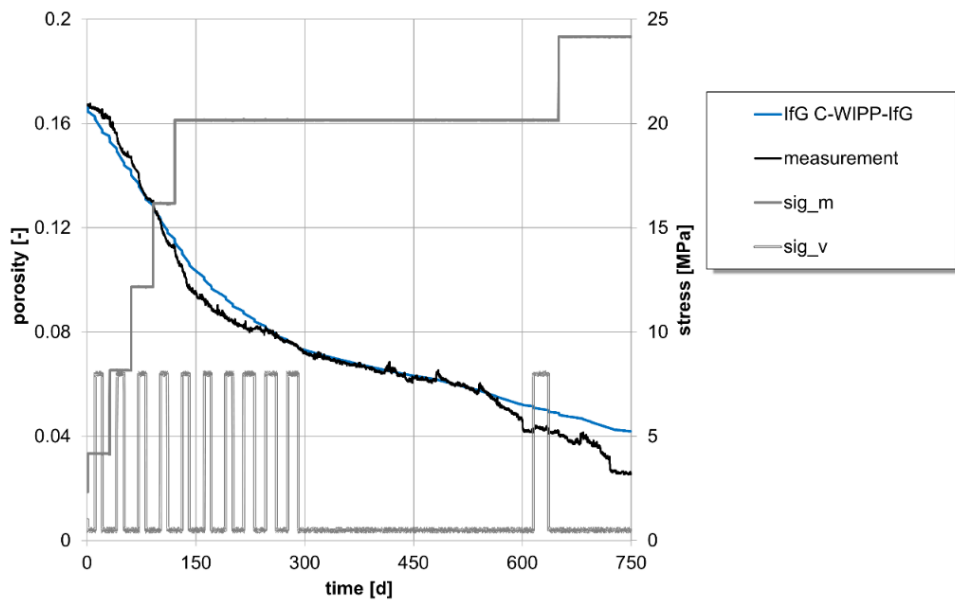


Fig. 5.42 Porosity evolution over time for the Benchmark calculation of the TUC-V2 experiment with numerical result in blue and laboratory measurements in black. The grey curves show load phases and durations

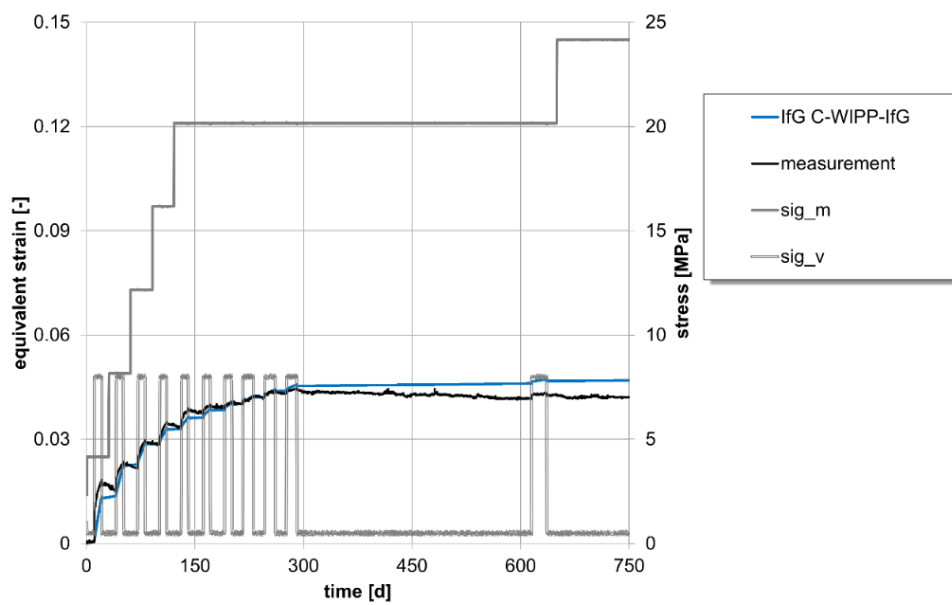


Fig. 5.43 Deviatoric strain evolution over time for the Benchmark calculation of the TUC-V2 experiment with numerical result in blue and laboratory measurements in black. The grey curves show load phases and durations

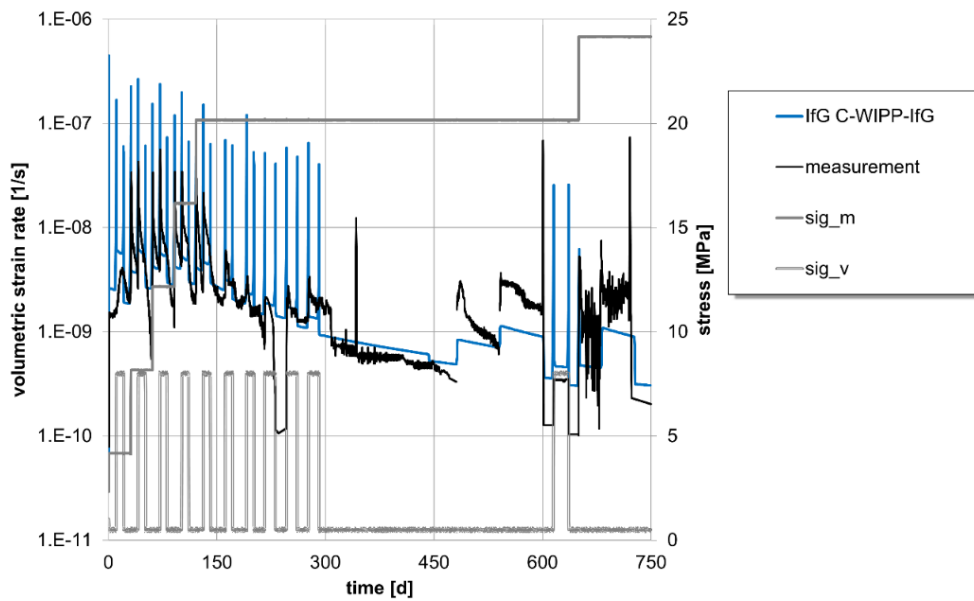


Fig. 5.44 Volumetric strain rate evolution over time for the Benchmark calculation of the TUC-V2 experiment with numerical result in blue and laboratory measurements in black. The grey curves show load phases and durations

Especially the deviatoric strain curve is reproduced nicely (Fig. 5.43). However, probably due to the relatively simple functional implementation, result remains only partly satisfactory.

The volumetric creep rates isotropic creep phases generally show an acceptable fit during the isostatic creep phases but are relatively flat compared to the typical exponential decline in the laboratory data (Fig. 5.44). For the deviatoric stress phases, the volumetric strain rate increases as desired but qualitatively does not show the same exponential decline as the real data, as the mathematical formulation in the model is a linear dependency on deviatoric stress. However, the modelled volumetric strain rates do show a reasonable fit with the final values of the deviatoric creep phases.

The temperature dependency of the volumetric creep rates and thus porosity evolution is underestimated in the results (Fig. 5.44). This could be a result of choosing the final volumetric strain rate as the reference value for fitting the Arrhenius term.

In conclusion, the updated IfG-CWIPP model has an extended range of functionalities that allows it to respond to all changes in boundary conditions that are presented in TUC-V2. In this sense, the model has experienced a valuable upgrade and produces better results. But the inherent weaknesses of the underlying purely empirical CWIPP model

persist (see discussion in /KOM 20/). These prevent both better qualitative fits as well as a more accurate physical description of the compaction process based on the insight gained from experimental and microstructural work. For the future, the IfG therefore aims to develop a crushed salt constitutive model based on its own existing, more physically sound rock salt models.

5.3.9 Summary and Outlook

This chapter presents the benchmark results of each project partner in comparison.

Fig. 5.45 and Fig. 5.46 show an overview of the benchmark results regarding volumetric, vertical and horizontal strains as well as porosity. In general, all models show a relatively good agreement with the measurement. However, a larger deviation in regard to the strain distribution can be noticed in Olivella/Gens (see z-strain and x-strain).

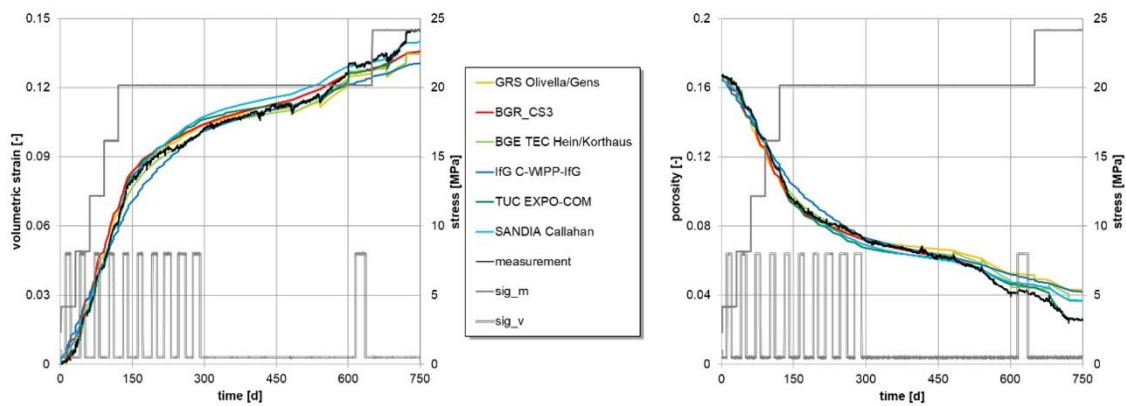


Fig. 5.45 Benchmark results: volumetric strain and porosity

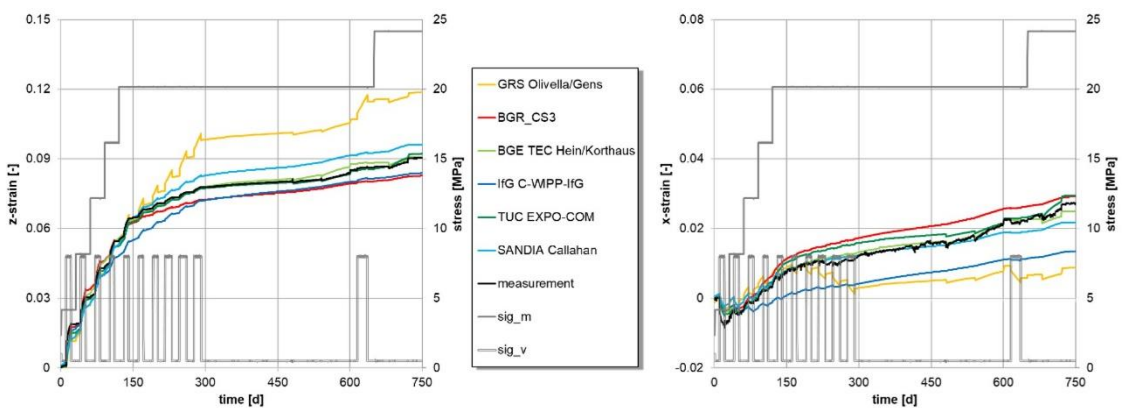


Fig. 5.46 Benchmark results: vertical and horizontal strain

More detailed and precise analysis can be carried out by comparing the strain rates rather than cumulative values (strains). The strain rates are compared and presented phase-wise in the following Fig. 5.47 to Fig. 5.51 in order to more accurately detect how appropriately the impacts of each influencing factor are reproduced in the model approaches. Fig. 5.47 shows the volumetric strain rates for phase I and for the specified time frame of phase I of the test. Additionally, the assessed functionality of model approaches and the criteria for the evaluation of success in imaging of the measurements are listed in Fig. 5.47. In regard to these criteria, following observations can be made:

- Generally, the magnitude of rates is correctly reproduced in all models.
- The reaction to the increase of mean stress is underestimated slightly by BGR_CRUSHED SALT3 and significantly by C-WIPP-IfG (except the nearly instantaneous peaks).
- The reaction on the activation of the deviatoric stress is underestimated by C-WIPP-IfG.
- The development of the rate within each stress level, i.e., the curve progression shape, is mostly appropriate by Callahan model with clearly non-linear tendency (in half logarithmic description), as depicted in the enlarged diagram.

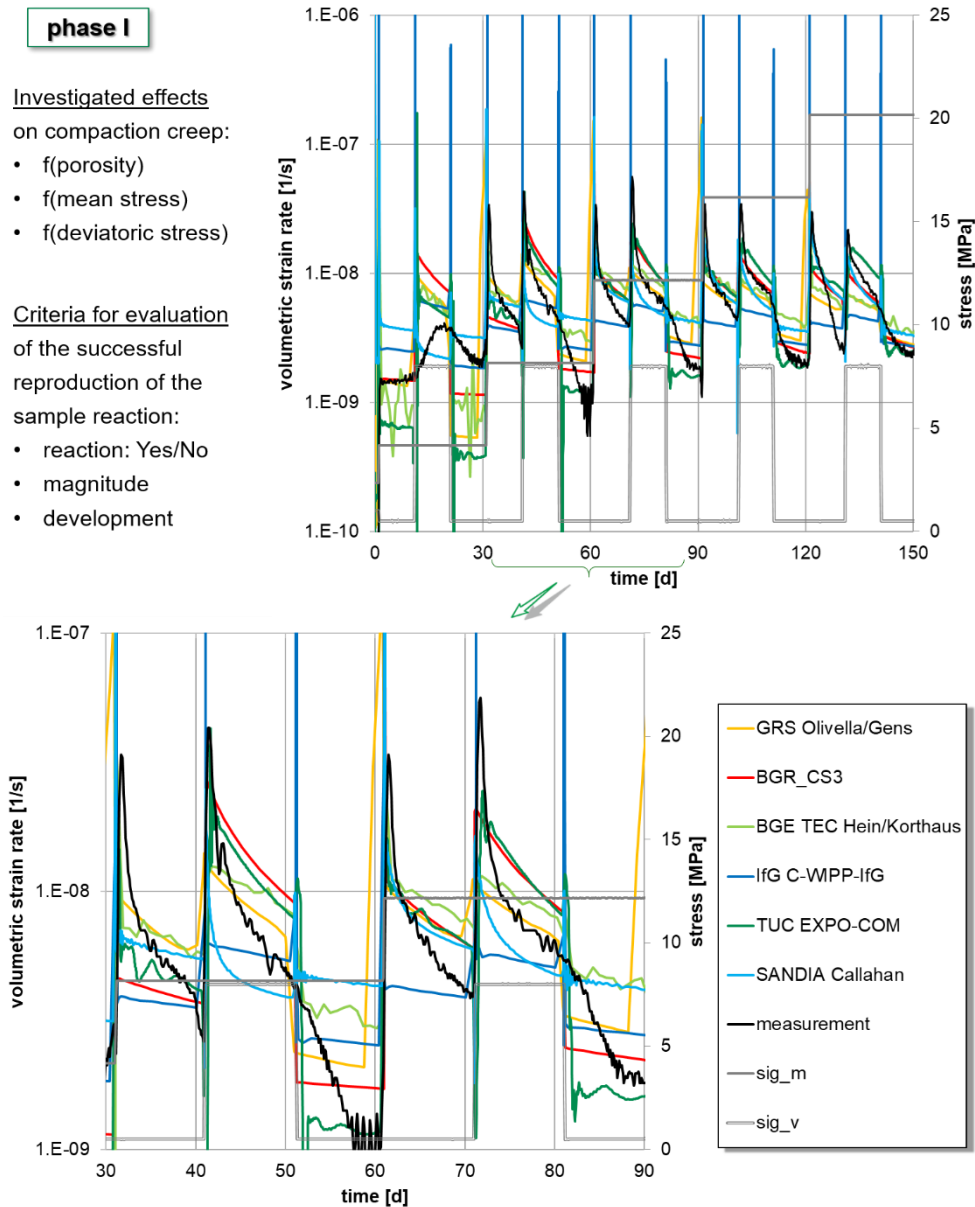


Fig. 5.47 Benchmark results: volumetric strain rates for phase I of the test

Fig. 5.48 (phases I and II) and Fig. 5.49 (phase V) show the effective strain rates with the focus on the impact of porosity on viscous shear deformations. From these Figures following observations can be made:

- For the initial phase of the test, the magnitude of effective strain rates is correctly reproduced in all models. However, the analysis of both phases made the increase of differences between model approaches as well as growing deviation from the measurement clearly visible. The largest deviations can be recognized for BGR_CRUSHED SALT3 and Olivella/Gens.

- Because of the relatively low porosity reached in phase V, the shear creep is observed to be near the creepability of the rock salt. However, a considerable over-estimation of the creepability by the model Olivella/Gens can be noted. Presumably, the specific creep behavior of Sondershausen rock salt was not yet considered precisely in Olivella/Gens. Other models construct a very narrow bandwidth of results and rather well reproduce the creepability in this phase.

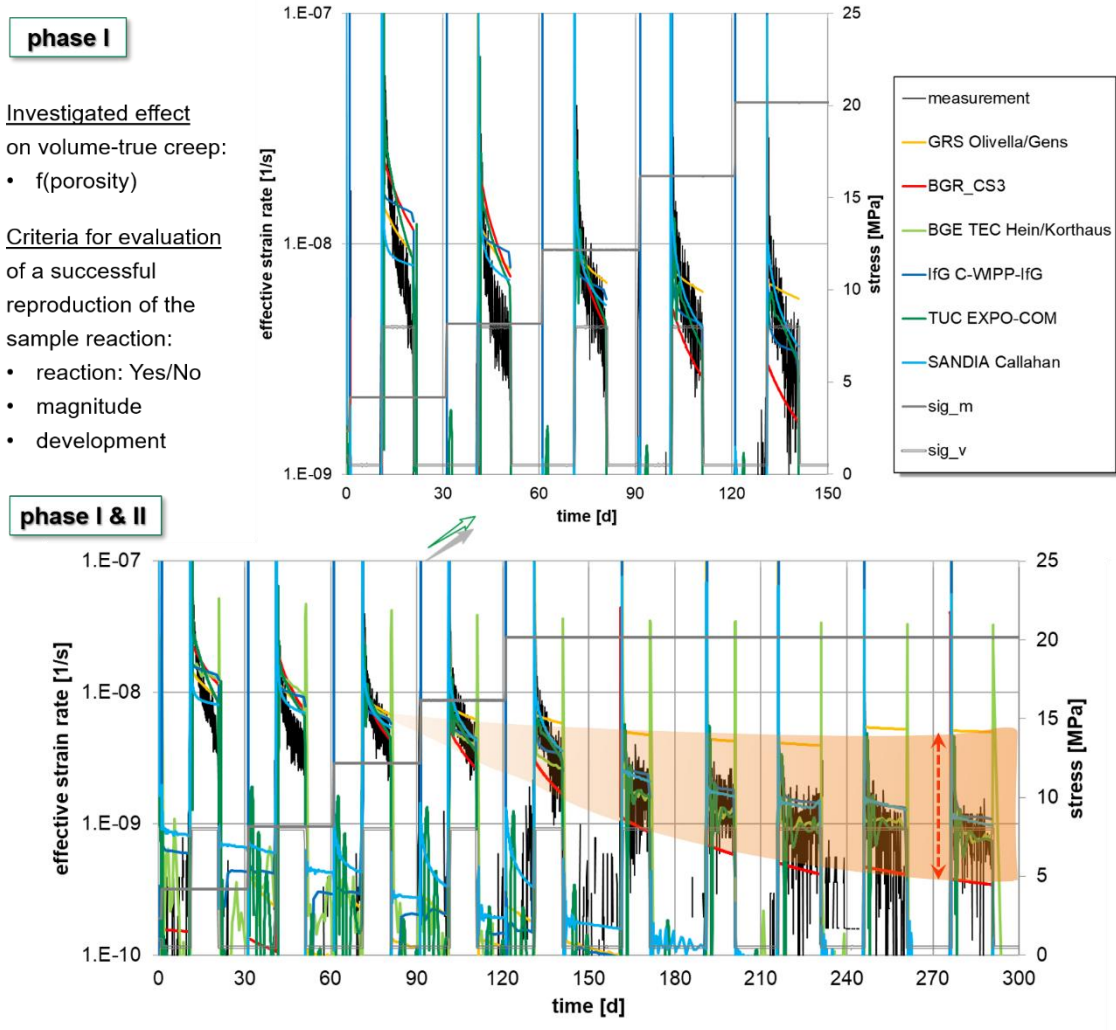


Fig. 5.48 Benchmark results: effective strain rates for phases I and II of the test

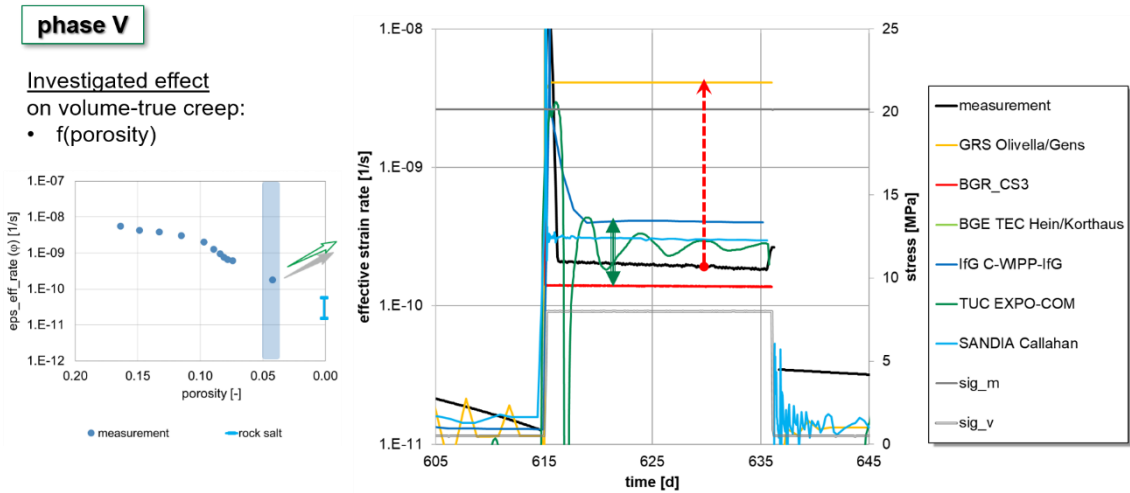


Fig. 5.49 Benchmark results: effective strain rates for phase V of the test

Fig. 5.50 and Fig. 5.51 present the benchmark results for volumetric strains and strain rates for phases IV and V of the test in regard to the temperature effect.

Following findings can be noticed from the figures:

- The compaction rate change caused by the first temperature increase (from 30 °C to 50 °C) is reproduced relatively well by all models.
- The compaction rate change caused by the second temperature increase (from 50 °C to 70 °C) is significantly underestimated by C-WIPP-IfG. The best agreement can be seen in cases of Hein/Korthaus and EXPO-COM.

The compaction rate change caused by the third temperature increase (from 35 °C to 70 °C) is underestimated by most models and slightly overestimated by EXPO-COM. The deviation of the calculation results increases. The best agreement with the measurement can be seen in case of Callahan model.

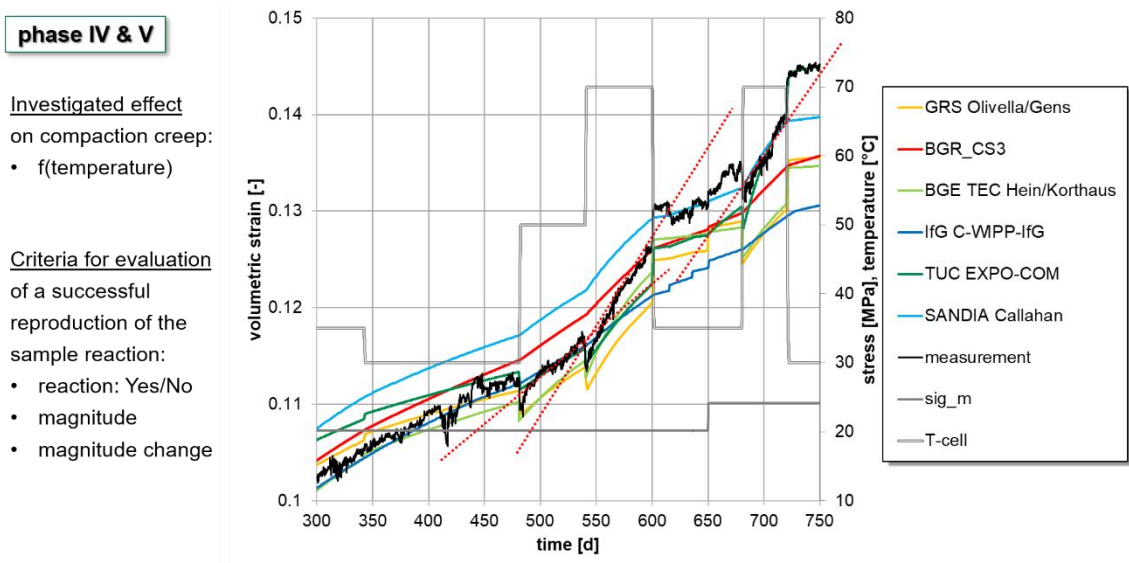


Fig. 5.50 Benchmark results: volumetric strains for phases IV and V of the test in regard to the temperature impact

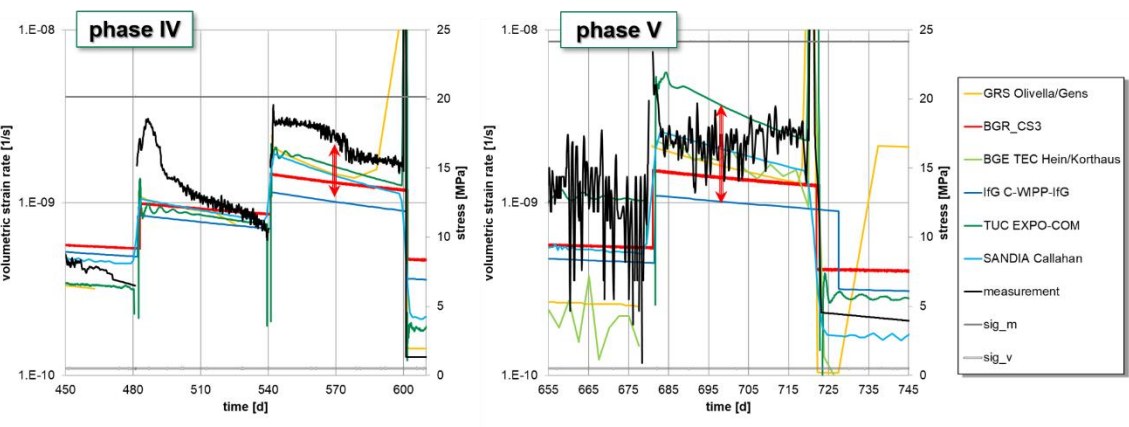


Fig. 5.51 Benchmark results: volumetric strain rates for phases IV and V of the test in regard to temperature impact

In addition, the individual back-analysis results from BGR_CRUSHED SALT3 are presented in Fig. 5.52. The special feature respectively the additional benefit of these results is given by a separation of volumetric strains for different microstructural deformation mechanisms: GF – grain fracture, PSC – pressure solution creep, DC – dislocation creep.

The following model assumptions can be recognized:

- Even for a relatively high level of stress (20 MPa), the pressure solution mechanism is dominant after 300 d (porosity of 7 %). Also, PSC predominates the response to temperature change on the compaction behavior in all three temperature load steps.
- Pressure solution mechanism does not react to the activation of deviatoric stress (in contrast to the dislocation creep mechanisms).
- The impact of grain fracture mechanism on the compaction behavior is relevant (i.e., not negligible) even for the middle range of porosity (< 17 %) for deviatoric load phases or for high mean stress levels (> 12 MPa).

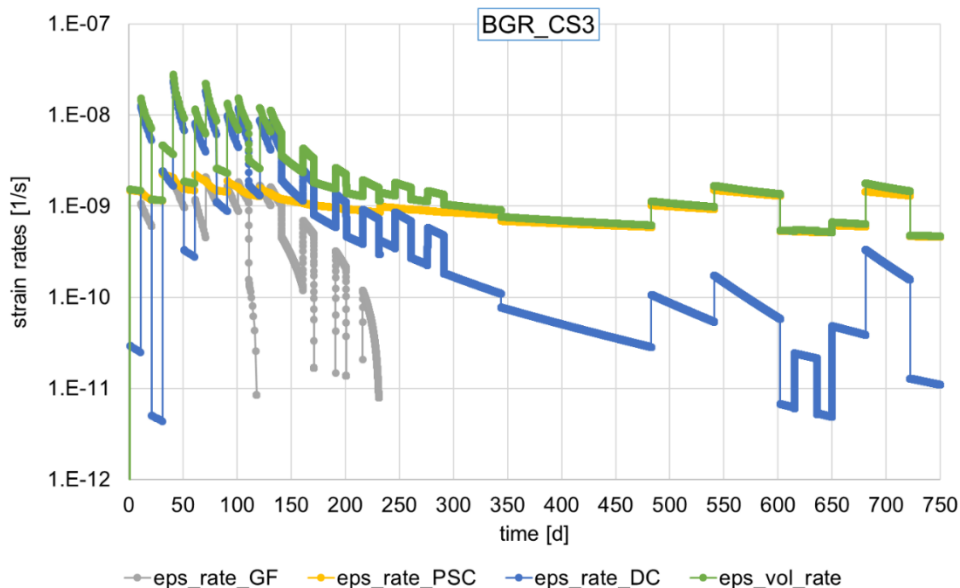


Fig. 5.52 Benchmark results: volumetric strain rates for different microstructural mechanisms from the model BGR_CRUSHED SALT3

5.4 Virtual Demonstrator

5.4.1 Introduction

The virtual demonstrator is a numerical model of a generic backfilled drift in a salt-hosted repository. It is designed to simulate the time-dependent compaction behavior of crushed salt backfill in a converging drift. The virtual demonstrator serves as a tool for constitutive model development and verification because it allows a detailed analysis of the spatial-temporal evolution of important quantities like porosity, stresses, and volumetric

compaction rates at the application scale. This is the foundation of a quantitative comparison of different constitutive models that are available to model crushed salt compaction and helps to identify potential need for improvements in the model formulation, experimental calibration, and validation status (Fig. 5.55). In this context, the demonstrator results over time are also a good way to visualize the progress made in constitutive model development. In lack of an analytical solution, we establish a reference case for comparison by taking the “status-quo” of crushed salt models in KOMPASS-I /KOM 20/ and applying it to the demonstrator.

Note that while the demonstrator aims to approximate in-situ conditions in a realistic manner, it remains a simplified model for development purposes. This means that the results presented here **do not** constitute a prediction of the expected time to full compaction in a potential future nuclear waste repository.

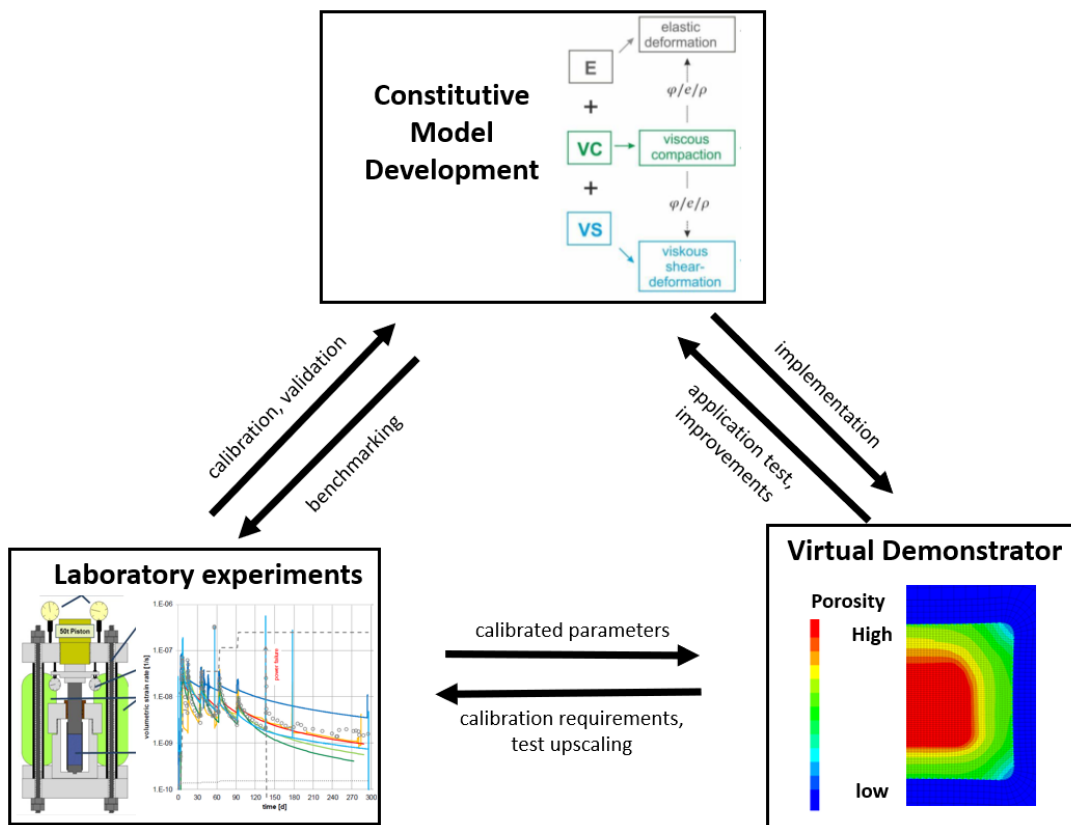


Fig. 5.53 Role of the virtual demonstrator in the constitutive development process

The virtual demonstrator includes two material domains, the host rock (rock salt), and drift (crushed salt backfill). Both model geometry and boundary conditions are based on generic repository concepts for bedded rock salt developed in the KOSINA project (cf. appendix 1 of /BOL 18/). As depicted in Fig. 5.55a, the virtual demonstrator is a 2D plane

strain model, i.e., representing an infinitely long drift, which is justified by the relatively long emplacement drifts in the KOSINA design /BOL 18/. The model is 103.7 m high and 19 m wide in total, including 50 m of rock salt above and below the drift. Through roller boundary conditions along the lateral boundaries, the model makes use of a symmetry axis along the drift center and thus a half drift with dimensions representing a simplified version of a KOSINA emplacement drift is sufficient to represent the repository (Fig. 5.55b, c). With the model symmetry, the dimensions of the model reflect the minimum vertical barrier thickness (50 m) and minimum drift spacing (38 m) deduced from thermal simulations /BOL 18/. Note that the lateral boundary conditions imply the assumption of an infinite number of drifts in the y-direction. The top boundary condition applies a vertical stress of 16.1 MPa, which translates into a depth of the drift floor of 800 m, assuming 2200 kg/m³ overburden density. Gravitational forces are considered in the calculations. Temperature is assumed constant at 307.15 K. Again, this was chosen in reference to the KOSINA project, which proposed a minimum depth of 800 m of a repository in bedded rock salt. Fig. 5.54 depicts the approximate location that would correspond to the conditions chosen for the demonstrator within two reference geological sections of bedded rock salt scenarios (flat-lying and salt pillow) from /BOL 18/. In this project, a 500-year time span has been modelled.

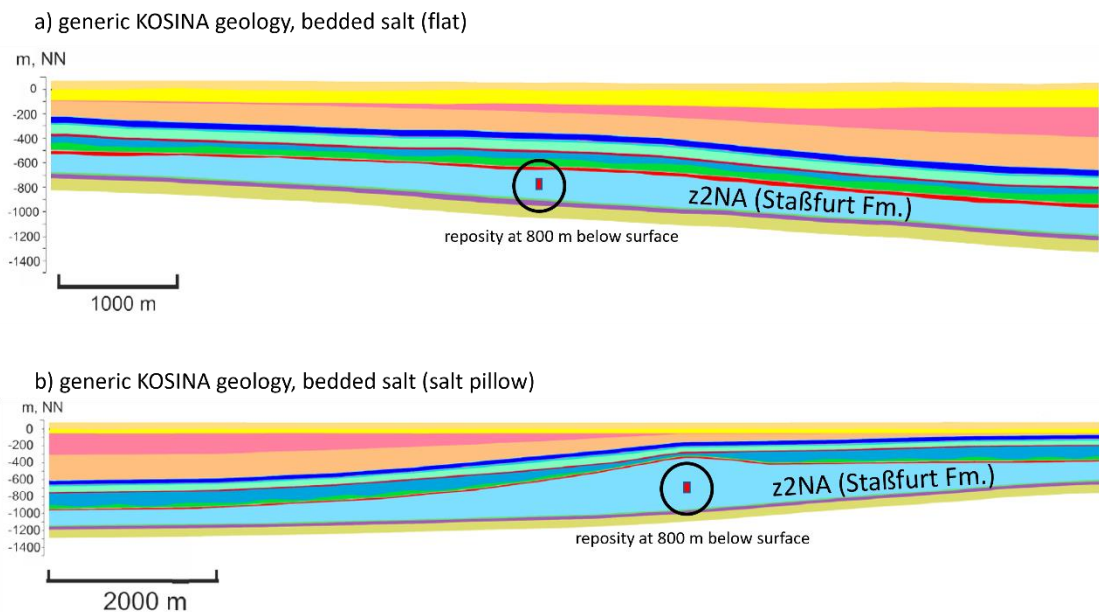


Fig. 5.54 Geological reference sections from /BOL 18/ for a salt-hosted repository in bedded salt. The encircled red rectangle represents a repository at 800 m depth, which would correspond to the boundary conditions chosen for the virtual demonstrator

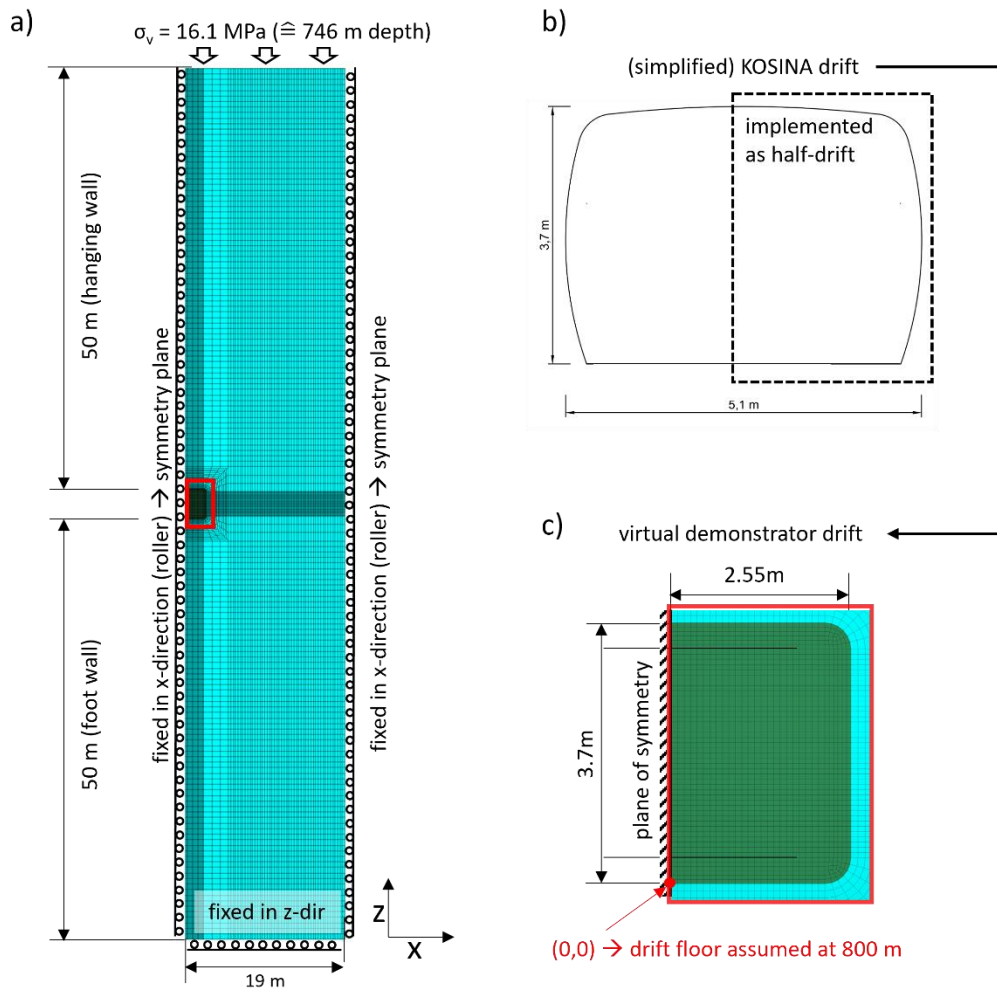


Fig. 5.55 Geometry and boundary conditions of the virtual demonstrator model. (a) Full scale view of the 2D model, (b) simplified technical drawing of a drift from the generic KOSINA repository design (/BOL 18/), (c) close-up view of the implemented drift in the virtual demonstrator

The creep of the rock salt host material is the main driving force of crushed salt compaction over time. In accordance with the current state of research of rock salt deformation /HAM 16/, the partners chose a two-component power law to represent both pressure solution creep (dominant at $\sigma_{eff} < \text{ca. } 8 \text{ MPa}$) and dislocation creep (dominant at $\sigma_{eff} > \text{ca. } 8 \text{ MPa}$).

$$\dot{\epsilon}_{cr} = A_1(T) \sigma_{eff}^1 + A_2(T) \sigma_{eff}^5 \quad (5.136)$$

Here, we used $A_1(T)=5e^{-7}d^{-1}$ and $A_2(T)=10^{-10}d^{-1}$. σ_{eff} denotes von Mises effective stress. Note that these terms remain constant as temperature is assumed constant. The two individual lines as well as the cumulative creep curve along with relevant creep measurements from rock salt samples (from WEIMOS project /HAM 23/) are displayed in Fig. 5.56. For comparison, test runs with a single-component creep law resembling the BGRa creep law /HUN 94/ were also carried out (essentially the same creep law but with the linear stress term switched off, see Fig. 5.56). . Note that we are aware that rock salt behavior also includes primary creep and plastic deformation, but the partners' own more comprehensive constitutive laws for rock salt (/HAM 16/) use different mathematical formulations for the different mechanisms (especially for creep and plastic deformation) which would lead to different rock salt behavior. By using the described two-component creep formulation, the partners ensure that (1) the main rock salt deformation mechanism (i.e., stationary creep) for long-term analysis is taken into account correctly, and (2) the host rock convergence is identical for all partners, in this way, the different crushed salt compaction models can be compared, because the differences in the results are solely due to crushed salt behavior.

The backfill is assumed to completely fill the drift upon emplacement (no initial roof gap) and has an initial porosity of 35 %, which is a typical value used in previous backfill modelling studies /BEC 04/. Crushed salt moisture content is not prescribed specifically but depends on the underlying experimental tests that were used for calibration of the crushed salt constitutive models (0.5 wt.-% in this project). Additionally, the backfill domain is numerically connected to the walls, i.e., friction along the wall surface is not considered (continuum). The mechanical behavior of the crushed salt is modelled using the different constitutive models described in Section 5.2. In this way, the differences in the time-dependent crushed salt compaction are exclusively due to the different model formulations and the respective parameter sets.

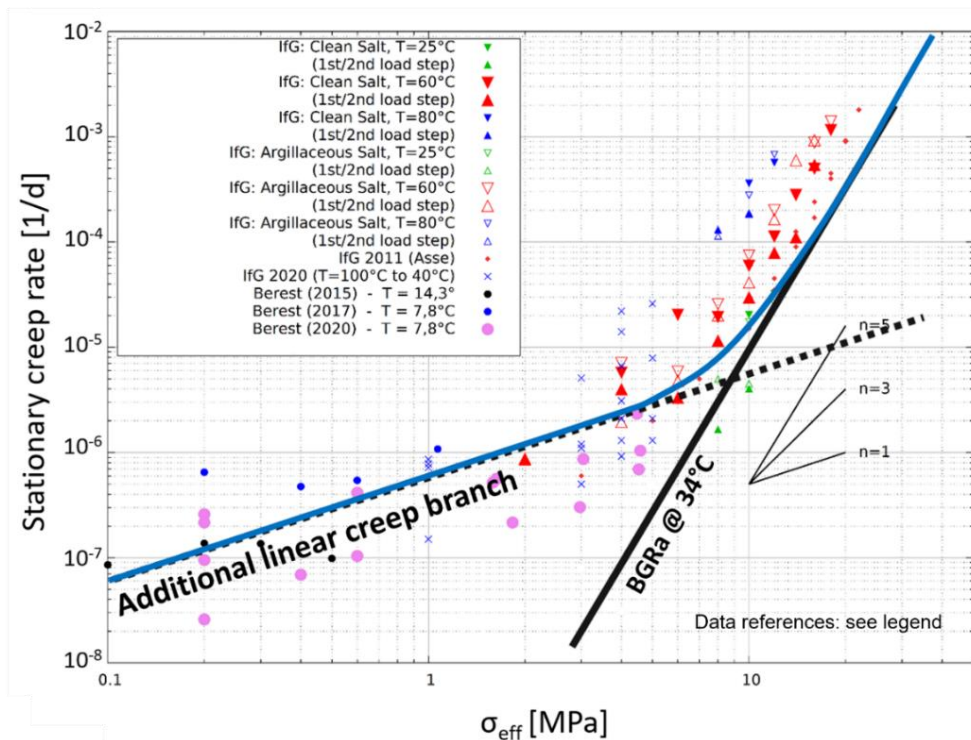


Fig. 5.56 Stationary creep data and curve chosen for the virtual demonstrator (blue curve), representing an additive two-component power law with a linear creep branch for pressure solution creep (dotted black line) and a $n=5$ power law for dislocation creep (\approx BGRa creep law)

5.4.2 Modelling approaches

IfG, TU Clausthal, BGE-Technology

The IfG, TUC and BGE-Tec all used the identical implementation of the virtual demonstrator in the commercial numerical code ITASCA FLAC3D /ITA 19/. Fig. 5.55a, c displays the discretized FLAC3D demonstrator model. For the calculations, the constitutive models IfG-CWIPP (IfG), EXPO-COM (TUC) and Hein-Korthaus (BGE-Tec) were used and parametrized as described in Sections 5.2 and 5.3. Note that initial calculations to establish the “status quo” base case deliberately used parameter sets obtained in the previous KOMPASS-I project.

In FLAC3D the 2D nature of the model was implemented by a 1-Element deep “3D” model with a zero-displacement boundary condition in the third dimension. Time-step calculation was performed using the built-in automatic algorithm with a minimum and maximum timestep of 10^{-6} d and 1 d, respectively. A mesh convergence study was

carried out to ensure sufficient mesh fineness and negligible impact of mesh resolution on the computation results.

BGR

The demonstrator was discretized with a total number of 48,750 bilinear quadrilateral elements. The domain representing the backfilled crushed salt was discretized with 4,626 elements and the host rock with 44,124. In order to avoid locking a simple enhanced assumed strain technique is applied where the volumetric strains are constant within the element. The balance of linear momentum was solved in a quasi-static context and the constitutive law is by default integrated with an implicit Euler backward scheme. The simulation was carried out with the in-house finite element analysis software *JIFE 6.3*.

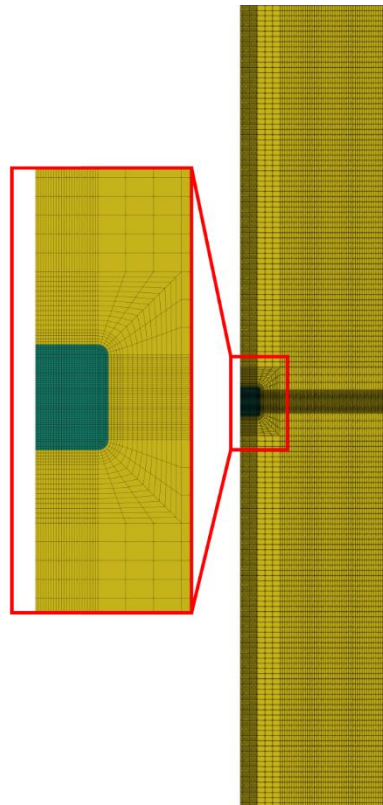


Fig. 5.57 Discretization of the virtual demonstrator with JIFE 6.3

Currently only the small strain version of the crushed salt constitutive model is compatible with initial stresses. Therefore, the simulation was done in a small strain setup. While the implicit integration of the constitutive model worked well for the TUC-V2 test, numerical difficulties occur while integrating the humidity creep rate $\dot{\epsilon}^{humidity}$ within the virtual

demonstrator. Therefore, only results obtained without this creep component are shown in the following sections. The constitutive model reduces in the absence of $\epsilon^{humidity}$ to the BGR-CRUSHED SALT2 model.

GRS

The virtual demonstrator was run using the FEM code CODE_BRIGTH (Section 5.2.3). For the host rock salt, the two-component power law was realized following the specifications. The crushed salt behavior was simulated using the Olivella/Gens described in Section 5.2.3. The model shown in Fig. 5.58 was discretized with 10,106 nodes and 19,801 triangular elements. One of the basic assumptions in CODE_BRIGTH is that small strains and small strain rates are assumed for solid deformation. Therefore, the simulation was done in a small strain setup, making them comparable to BGR.

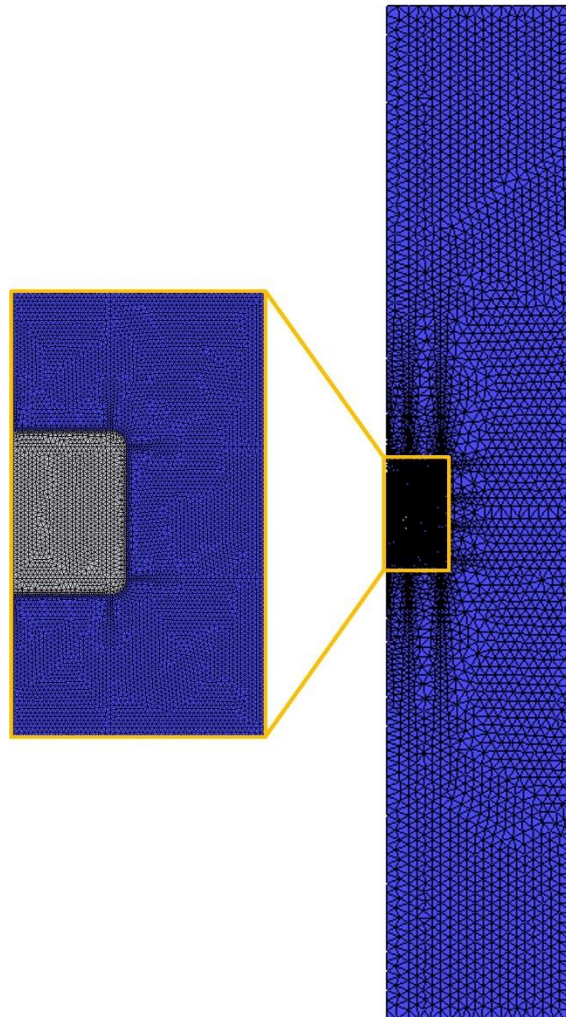


Fig. 5.58 Discretization of the virtual demonstrator in CODE_BRIGTH

Sandia National Laboratories

Sandia National Laboratories Code: The demonstrator model was run using version 5.5.2 of the Sierra/SolidMechanics code developed at Sandia National Laboratories /SIE 23/. Sierra/SolidMechanics is a three-dimensional finite element code for solving solid mechanics problems.

Boundary Conditions: Sierra/SolidMechanics does not include a two-dimensional plane strain element formulation; therefore, the plane strain assumption was enforced through the application of kinematic boundary conditions with zero normal displacement components, $u_y = 0$, on the nodes on the front and back surfaces of the model domain.

Constitutive Models: Two constitutive models were used in the simulations. The MD_Viscoplastic model /REE 18/ was parameterized to be consistent with the host rock salt behavior specified for the virtual demonstrator. The Callahan model, described in Section 5.2.2 was parameterized to simulate the crushed salt backfill, as discussed in Section 5.3.4. The ordinary differential equations in both model implementations were integrated using the implicit, first-order accurate, backward Euler method. Both model implementations included modifications which allowed them to use the viscoplastic rate scaling option discussed below.

Domain Discretization: The simulation domain was discretized using 8-node hexahedral selective deviatoric elements. This element formulation fully integrates the deviatoric stress contribution (8 gauss points in the hexahedral element) but under integrates the volumetric stress contribution to the internal force calculation. This formulation avoids numerical stabilization techniques, like hourglass control, and reduces numerical element locking in nearly incompressible materials like the host rock salt.

A series of simulations were performed to determine how the quantities of interest (ex. Room porosity history) were affected by mesh size. Only minor differences were observed between the nonstructured mesh shown in Fig. 5.59 and one with approximately 4 times fewer elements, so the mesh in Fig. 5.59 was used for all reported simulations. The mesh in Fig. 5.59 included 848 elements to represent the crushed salt backfill and 12,055 elements for the host rock salt. The computational mesh included a total of 26,204 nodes. The domain was discretized so that the majority of the elements were located in a region near the room in order to resolve the expected larger stress gradients during the time period before the crushed salt backfill starts to resist the inward creep of

the host rock salt. The domain was modeled using only 1 element (1 m) through the y-direction dimension.

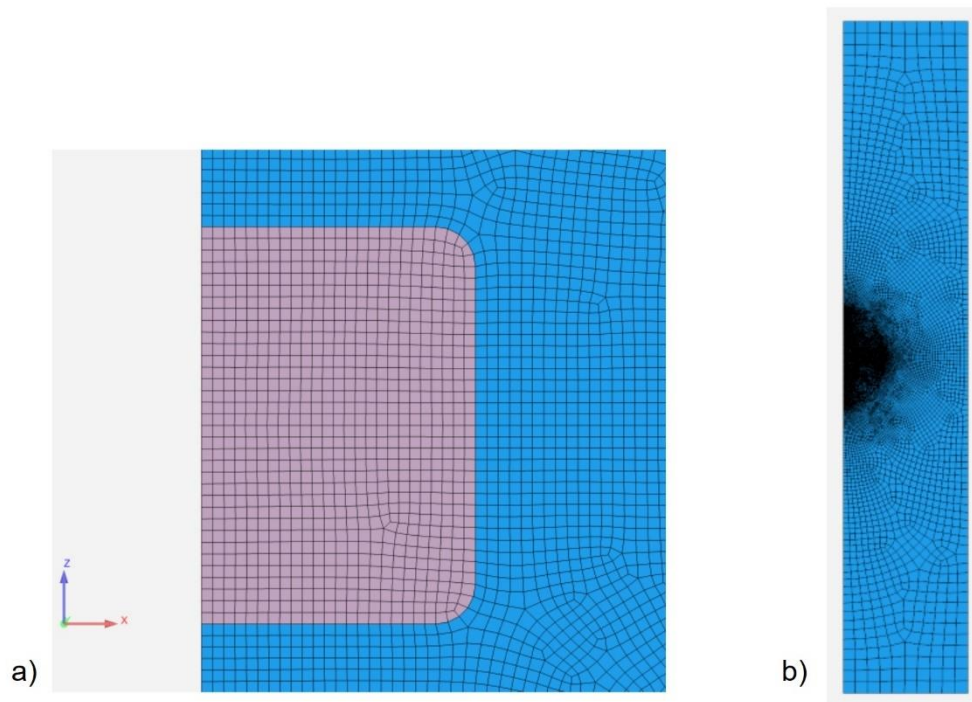


Fig. 5.59 Mesh used in demonstrator simulation. a) Close-up view of backfill and host rock salt mesh and b) view of full model domain

Open drift convergence

The partners performed a benchmark calculation to compare drift convergence for an open drift, i.e., without backfill, and set a range of 10 % deviation of the minimum and maximum convergence/displacement (rates) as the criterion for sufficient comparability. Each benchmark calculation also included a mesh convergence study to ensure that the mesh fineness did not impact the results. Fig. 5.60 shows that the convergence and stresses are nearly identical for most partners after 10 years. The exceptions are GRS and BGR, whose results deviate slightly from the other curves. The reason is that their numerical codes did not support large strain formulations at the time of simulation, and they are therefore using small strain mode. However, the differences are less than 10 % in the benchmark calculations and therefore in the acceptable range to ensure comparability.

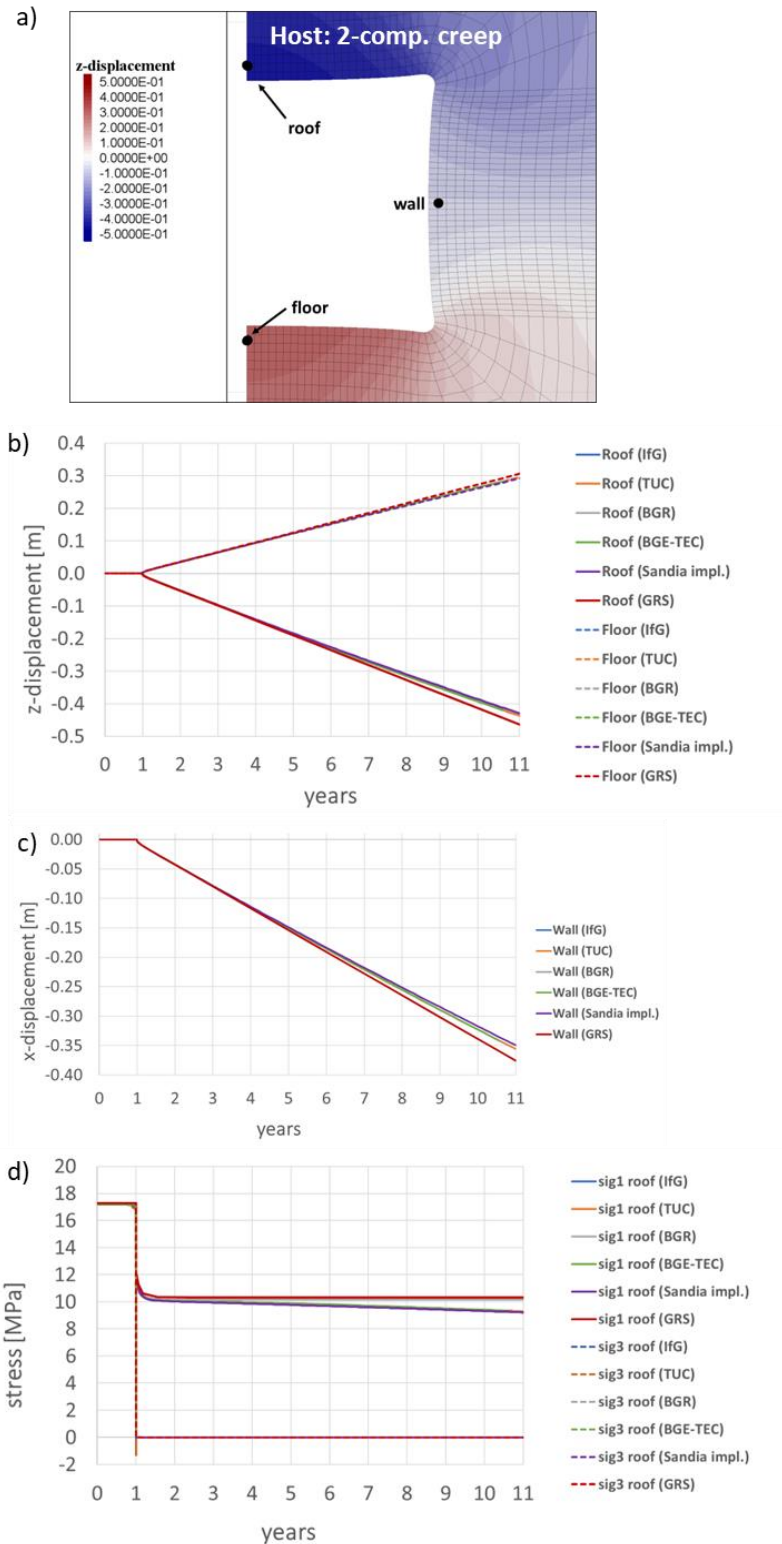


Fig. 5.60 Results from the open drift benchmark calculation. (a) Close-up view of the converging drift showing z-displacement after 10 years and points to document convergence and stresses. (b-d) x/z-displacement, and mean stress curves, respectively, for all 2 partners. Note that GRS and BGR curves lie on top of each other, the same applies to IfG, TUC, BGE-TEC and Sandia

5.4.3 Demonstrator results with TK-031 parameters – “Status quo”

The first objective for the application of the virtual demonstrator was to establish the “status quo”, i.e., to run the simulations with constitutive models and parameter sets obtained during the KOMPASS-I project. These were based on the TK-031 long-term iso-static triaxial compaction test and are documented in /KOM 20/. Thereby, a reference case was established which could be used to analyze the behavior of each constitutive model individually, but also to identify general issues such as in sufficiently calibrated influencing factors (e.g., porosity and mean/deviatoric stresses). For instance, TK-031 only covers the porosity range of 17 – 7.7 % and represents a “dry” crushed salt, i.e., no water or brine was added. In addition, the partners performed simulations using a single-component creep law in the host rock with only dislocation creep (i.e., $A_1 = 0$ in Equation (5.136), cf. Fig. 5.56) to investigate the impact of host rock behavior on the status-quo compaction behavior. Note, however, that this variation of host rock behavior mainly serves to illustrate the importance of using a two-component creep law according to the state-of-the art. It was therefore only carried out for the simulations using TK-031 parameters, while the improved demonstrator results (see Section 5.4.4) only consider two-component creep for the host rock.

Fig. 5.61 displays the average porosity over time for the TK-031-calibrated demonstrator runs with both a two-component and single component creep law acting within the host rock salt. For each of these two sets of simulations, Fig. 5.62 shows the evolution of volumetric strain rates and mean stress vs. porosity. There is a relatively large spread in the results for the different constitutive models, both qualitatively and quantitatively.

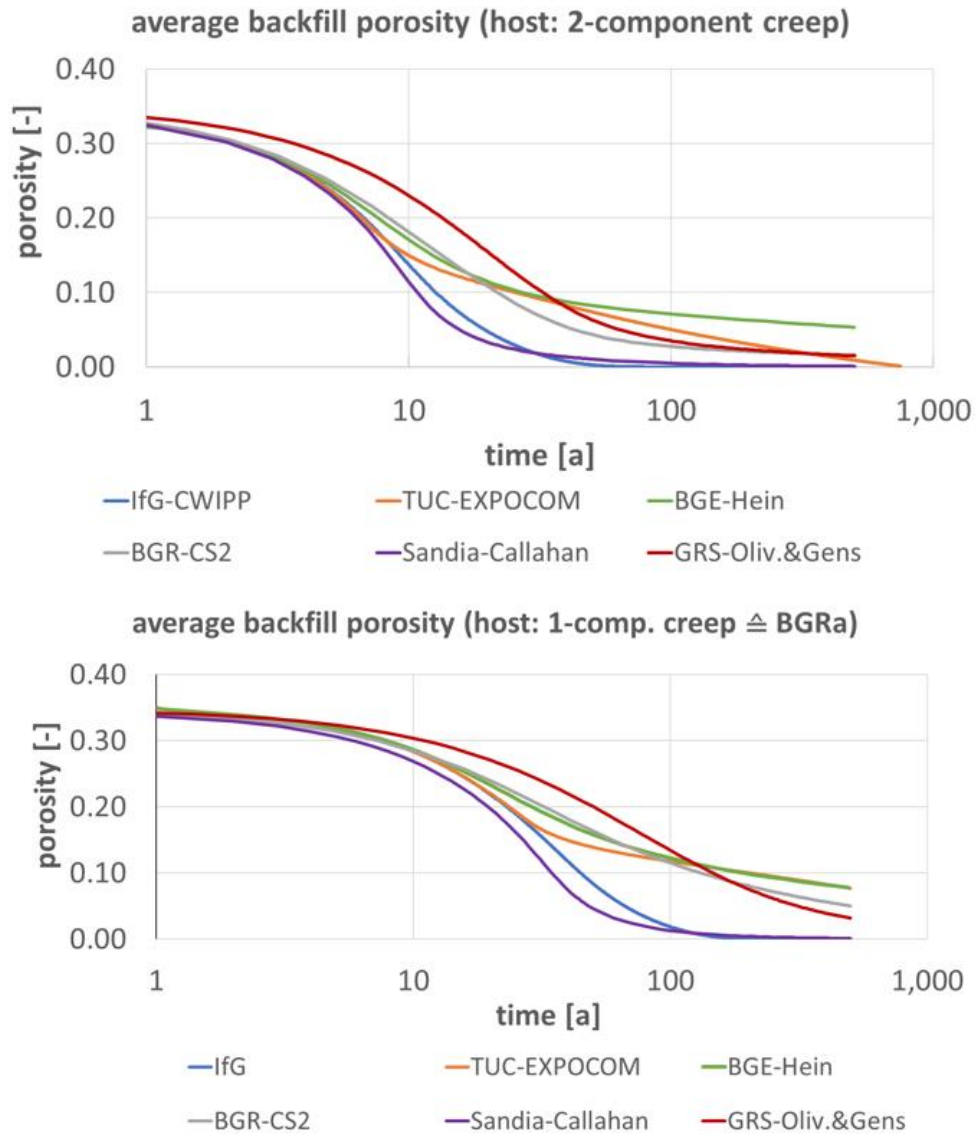


Fig. 5.61 Averaged porosity vs. time curves for demonstrator runs of all partners using the parameter sets derived from the TK-031 compaction experiment. Results for a host with (a) two-component creep, and (b) a single component (BGRa) creep

Already from a porosity of ca. 30 %, the volumetric compaction rates start to diverge, causing the porosity evolution over time to differ significantly. For the IfG-CWIPP and Sandia-Callahan models, compaction rates are slightly reduced from $8 \cdot 10^{-5} \text{ d}^{-1}$ at 30 % porosity to around $4 \cdot 10^{-5} \text{ d}^{-1}$ at 10 %. In contrast the other models show a reduction of volumetric compaction rates by over one order of magnitude over the same porosity range. This behavior and the distinction of these two groups is even more apparent for the host with the slower single component power law creep (BGRa). A “kink” in the curves can be observed at ca. 18 – 20 % porosity, corresponding to values of the mean stresses

larger than 5 MPa in the models predicting slower compaction of the backfill (Fig. 5.62c, d). In these models, the stronger backfill resistance starts to have marked effects on the convergence rates of the drift.

As the porosity is reduced below 10 % and lower, the volumetric strain rate is strongly reduced in all models. However, the pace of this reduction differs markedly, such that the volumetric strain rates diverge even more than before and span more than two orders of magnitude (Fig. 5.62a). For instance, at 5 % porosity, the Hein-Korthaus (BGE-TEC) model shows rates below $< 10^{-7} \text{ d}^{-1}$ while both IfG-CWIPP (IfG) and Callahan (Sandia) models compact with rates above $> 10^{-5} \text{ d}^{-1}$. The other models produce intermediate volumetric strain rates, but still vary about 1 order of magnitude. In a similar fashion, the development of mean stress (“backfill resistance”) with decreasing porosity also shows wide scattering (Fig. 5.62c, d), where the models with highest volumetric strain rates are those with the least, or latest, increase in mean stress vs. porosity. However, note that also that the shape of the mean stress vs. porosity curves differs between the models. The porosity value at which the stresses start to increase markedly vary between approx. 33 % (CRUSHED SALT3 and Olivella/Gens of BGR and GRS, respectively) and 15 % (Callahan model, Sandia). The point at which the mean stress starts to level off towards the background mean stress in the host rock of ca. 17 MPa, lies between ca. 10 % (EXPO-COM, TUC) and 0 % (IfG-CWIPP, IfG) which has no such point for the given parameter set. Note also that the GRS demonstrator run suffers from unrealistically high initial mean stresses of around 1 MPa (numerical causes under investigation), which likely explains the smaller volumetric strain rates in the high-porosity range.

These differences in compaction behavior result in a significant spread in porosity evolution over time (Fig. 5.61). Depending on host rock creep, the faster compacting models (IfG-CWIPP, Callahan model of IfG and Sandia, respectively) reach full or near-full compaction in less than 100 years, while the other models including EXPO-COM (TUC), Hein-Korthaus (BGE-TEC), CRUSHED SALT3 (BGR), Olivella/Gens (GRS) lie between 4 – 7 % and 11 – 12 % porosity after 100 years for the two different host rock models (Fig. 5.61). After 500 years (end of demonstrator simulation), the residual porosity varies between 0 – 5.3 % with a two-component creep law in the host rock (Fig. 5.61a) and 0 – 7.8 % with a BGRa host creep (Fig. 5.61b).

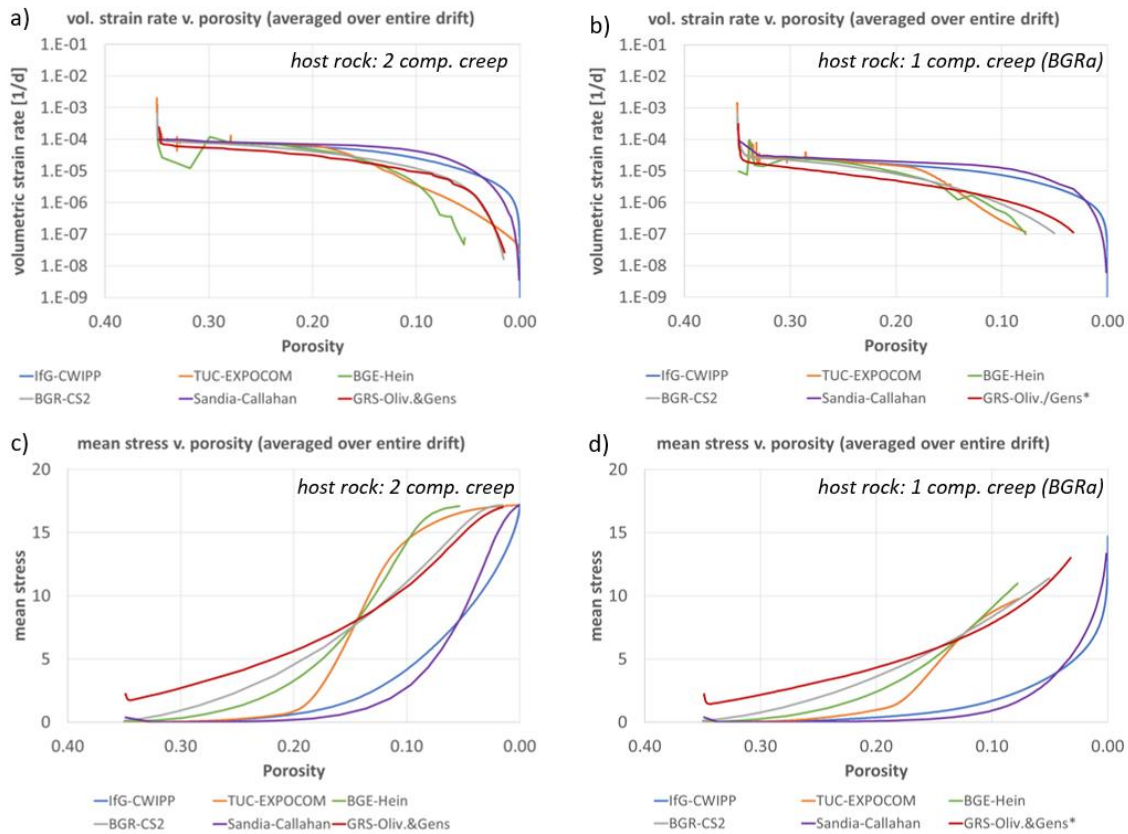


Fig. 5.62 Results for drift-averaged volumetric strain rates (a, b) and mean stress (c, d) vs. porosity for host with two component (left column) and single-component (BGRa) creep (right column) for the TK-031 reference demonstrator simulation

Overall, these “status-quo” simulations demonstrated that despite calibration to the identical triaxial long-term compaction test (TK-031), the spread in the results for an application case (i.e., the demonstrator) was considerable. In particular, the divergence in predicted volumetric strain rates for porosities of less than 10 – 15 % showed that significant improvements in the calibration and validation of the models in the low-porosity range were necessary, as these were not covered in TK-031. While we do not know which result would be accurate or realistic, a spread of strain rates of over two orders of magnitudes suggests either insufficient calibration and/or marked differences in the representation of compaction behavior (e.g., in terms of the dominant processes). Thus, additional laboratory experiments are needed to address these issues.

Although this is not directly related to crushed salt models, the simulations also clearly show the importance of an adequate representation of the host rock creep by state-of-the-art models. These rock salt models must (among others) correctly represent the

different salt creep mechanisms, for instance as a two-component formulation, to avoid underestimation of convergence rates and thus compaction rates.

5.4.4 Demonstrator results with TUC-V2 parameters – Improvements of KOMPASS-II models

This chapter presents the results of the demonstrator runs with the improvements made during the KOMPASS-II projects. Here, improvements mean (1) the updated constitutive model formulations as described in Section 5.2, and (2) the new calibration of these models using the TUC-V2 long-term triaxial compaction test (see Section 5.3). The improved calibration mainly incorporates the expansion of the tested porosity range down to < 3 %, the expanded range of mean stresses to 4 – 20 MPa, and including the impact of effective (i.e., differential) stresses on compaction rates (though only tested for one effective stress level of 8 MPa). Note that TUC-V2 used (moistened) KOMPASS reference crushed salt which will be used in future experiments and differs from the coarser, dryer material used for TK-031.

First, the results of porosity evolution over time as well as volumetric compaction and mean stress vs. porosity are presented as average values over the entire drift. This is used to show the improvements of the constitutive models and their calibration status during KOMPASS-II project in comparison to the “status-quo” in the virtual demonstrator application scenario (cf. Section 5.4.3). Then, a more in-depth analysis is presented, which addresses several remaining challenges such as the spatial variation of compaction behavior, compaction rates at high porosities and the detailed mean and deviatoric stress evolution in the backfill body. Finally, the results are discussed to outline remaining challenges, required future model development and laboratory tests to further improve the constitutive models of crushed salt to a state where reliable predictions can be made.

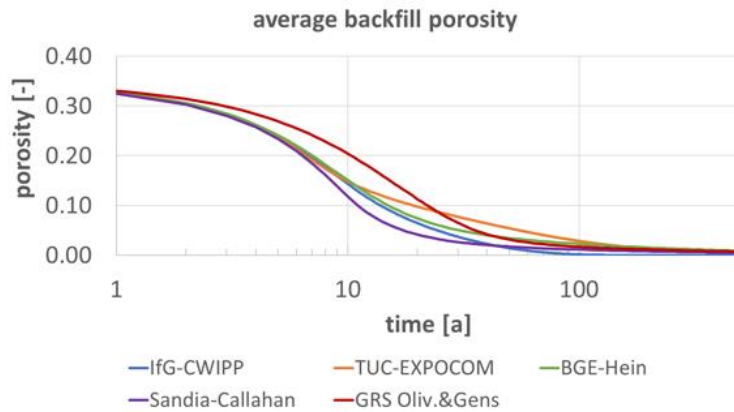


Fig. 5.63 Averaged porosity vs. time curves for demonstrator runs of all partners using the parameter sets derived from the TUC-V2 compaction experiment

Fig. 5.63 and Fig. 5.64 visualize the average evolution of porosity over time and the development of volumetric strain rate and mean stress with decreasing porosity for the TUC-V2 calibrated demonstrator calculations. Comparing to the same curves from the previous demonstrator calculations (Fig. 5.61a, Fig. 5.62a, c), the new results show significantly reduced spread in porosity evolution over time as well as volumetric strain rate and mean stress development. Especially in the low-porosity range below 10 %, the volumetric strain rates lie in a narrower range and within less than one order of magnitude, except for below 3 % porosity. This correlates well with the porosity range covered by the TUC-V2 test. The compaction rates concentrate towards intermediate values previously obtained from the “status quo” calculations, i.e., the fastest compacting models (IfG-CWIPP, Callahan) now show slower compaction rates, while the other models exhibit large (Hein-Korthaus) or small (EXPO-COM, Olivella-Gens) increases in compaction rates. For instance, the range is now $1.3 \cdot 10^{-6} - 9.0 \cdot 10^{-6} \text{ d}^{-1}$ instead of previously $4.7 \cdot 10^{-8} - 1.1 \cdot 10^{-5} \text{ d}^{-1}$ at 5 % porosity.

Despite the better agreement between the models, there are still marked differences, for example in the computed stress build-up in the backfill body. Especially EXPO-COM has a much steeper sigmoidal mean stress evolution compared to the other models (Fig. 5.64b). Until a porosity of ca. 20 %, EXPOCOM shows similar behavior as the IfG-CWIPP and Sandia models in that only about 1 MPa of mean stress is developed compared to 2 – 4 MPa Hein-Korthaus and Olivella-Gens, respectively. But then this value rises to an average mean stress of ca. 12 MPa at 10 % average porosity, which is significantly higher than all other models (4 – 9 MPa at 10 % porosity). This much stronger increase of backfill resistance appears to be correlated with a marked “kink” in the volumetric strain rate development for the EXPO-COM model at ca. 13 % porosity, from

where the volumetric strain rates are diminishing much smaller than those of the other models. However, even with these observations in mind, the scatter in the mean stress-porosity relationships of all models has also decreased markedly (compare Fig. 5.62c and Fig. 5.64b).

Overall, the improvements from the initial calculations using the KOMPASS-I model formulations and parameters result in a much closer range of the models for the prediction of the evolution of average porosity over time. After 100 years, the range of average porosity in the backfill body is 0 – 4 %, and all models have reached < 1 % porosity after the prescribed end of calculation after 500 years. **Note again that this result is not a prediction for a real repository case, but rather an indicator for improvement of the constitutive models and their calibration and validation status.** Nevertheless, the results show that further research is needed. Between 18 – 5 %, i.e., in the important medium to low porosity range, there is still significant spread between the result even though this is part of the now calibrated porosity range. While some variability can be expected when different models are applied, this suggests that the dependency of crushed salt compaction on stress and porosity is still not captured good enough. A possible solution lies in performing (1) repetition of some of the existing experiments to increase reliability and (2) experiments with very long load stage durations to increase the similarity between the chosen boundary conditions in the laboratory (stress-controlled) and the real in-situ conditions.

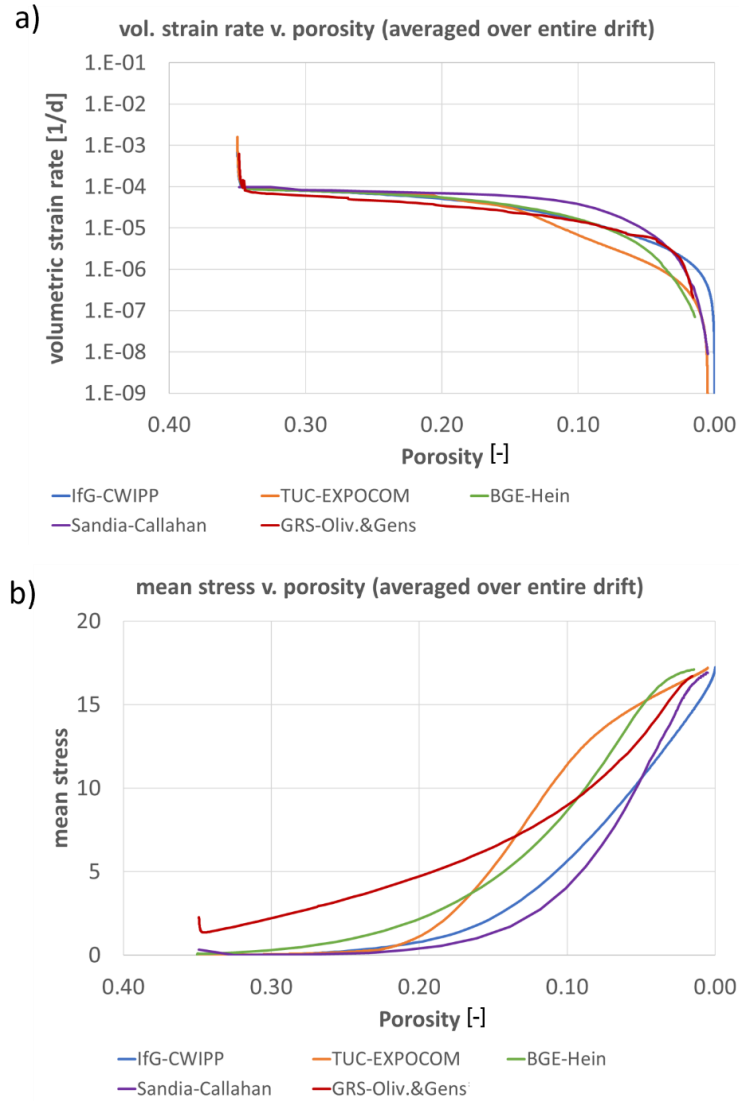


Fig. 5.64 Results of demonstrator runs of all partners using the parameter sets derived from the TUC-V2 compaction experiment. Drift-averaged volumetric strain rate (a) and mean stress (b) vs. porosity

Fig. 5.65 shows volumetric strain rates vs. porosity for two history points at the bottom and top of the backfill body (indicated in insets on the top right). These results highlight that the models still behave rather differently at high porosities, i.e., in the early phase of backfill compaction. For comparison, the dotted black line indicates the closure rate of the open drift benchmark calculation.

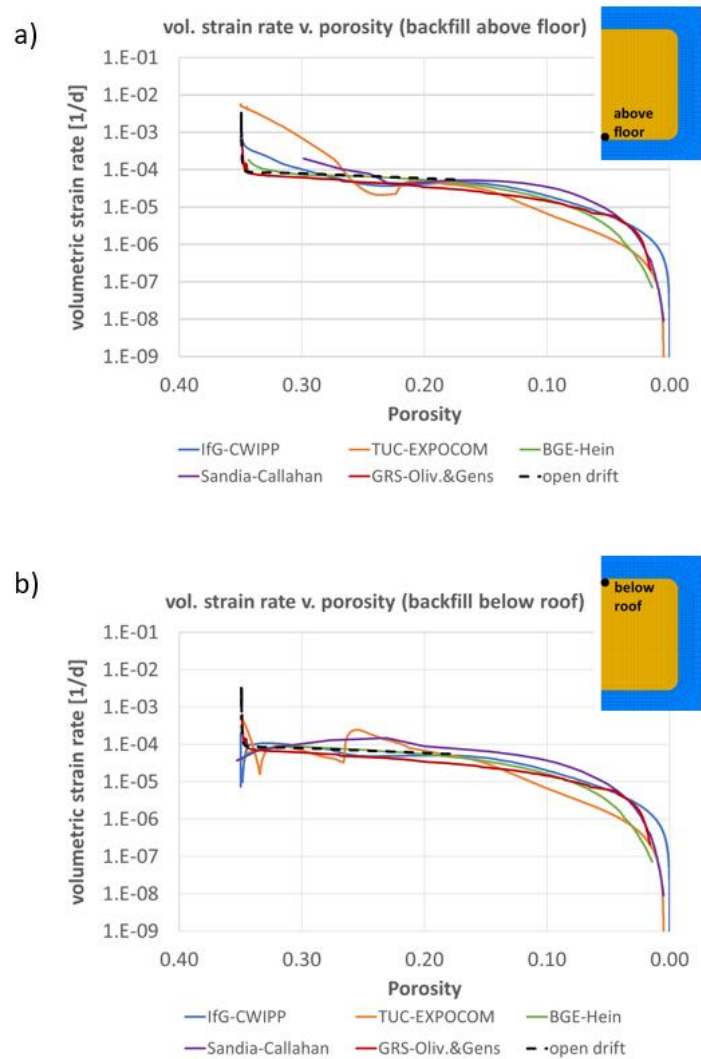


Fig. 5.65 Results of demonstrator runs using TUC-V2 derived parameters. Volumetric strain rate vs. porosity at two locations within the backfill body, (a) centrally above floor (b) centrally below roof

The compaction rates at the bottom and top of the backfill (i.e., above the floor and below the roof, Fig. 5.65a) may vary by over a magnitude between the models in the porosity range above 25 %. At the top of the backfill, the quantitative differences between the volumetric strain rates of the models are smaller, but still follow different paths (Fig. 5.65b). First, it is important to note that this high porosity range was not covered by the laboratory test used for calibration. In the early stages, the main driving force of compaction is the weight of the backfill body itself, indicating that compaction under such small stresses and high porosity differs strongly for the different partners' models. The models showing stronger deviations from the open room closure rates (especially EXPO-COM, but also IfG-CWIPP and the Callahan model), are interpreted to have a more pronounced

settling behavior than those models compacting essentially at the rate of open room convergence. If the (local) volumetric compaction rate exceeds empty room closure, as the case in the bottom of the backfill, the material compacts faster and its own weight than the host rock converges on average. Vice versa, the average empty room closure rate exceeding the (local) volumetric strain rate, means that in this element of the model, some void space is created, indicating for instance the possible creation of a roof gap. This interpretation is supported by the significant reduction of these differences if gravity is set zero, as was found in further test simulations that were carried out by all partners (see Fig. 5.66). These tests are aimed at isolating certain effects and understand potential numerical and modelling issues – note that gravitational effects like self-settling must of course be represented in a plausible way by the constitutive models and the demonstrator model setup.

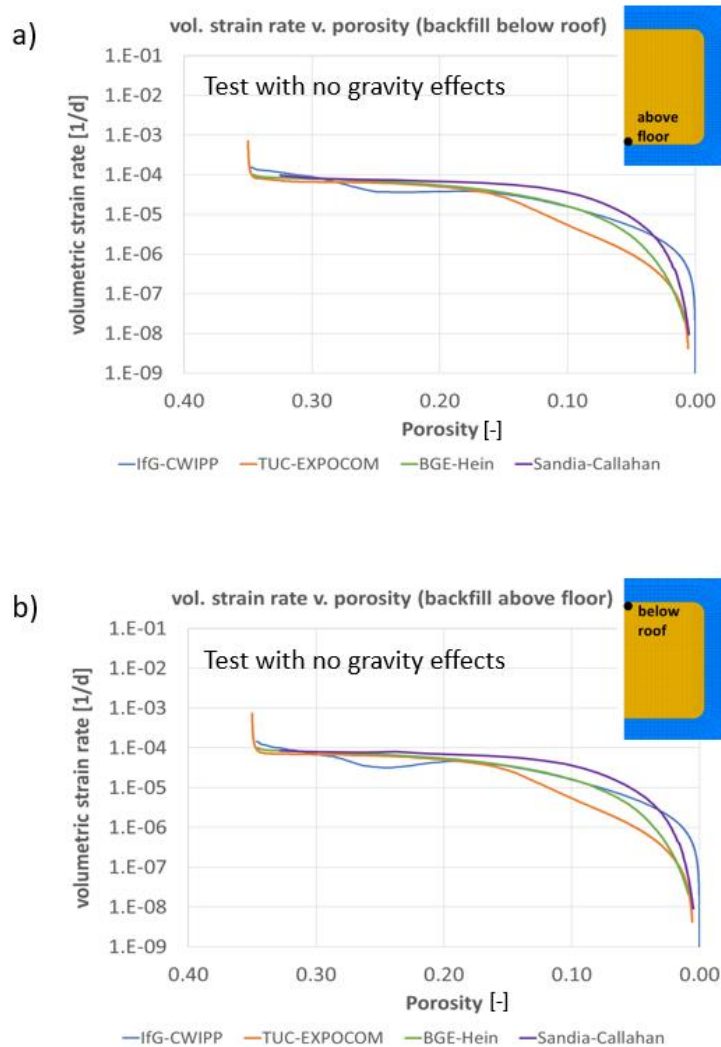


Fig. 5.66 Results of the demonstrator runs using TUC-V2 derived parameters, but without additional gravity (stress boundary conditions remain) to isolate gravitational effects. Note that GRS and BGR could not provide such tests due to their numerical implementation in in-house software. Volumetric strain rate vs. porosity at two locations within the backfill body, (a) centrally above floor (b) centrally below roof

Although, in the context of nuclear waste disposal, the issue of gravitational settling is perhaps of less overall importance to long-term safety compared to the low-porosity compaction rates, the demonstrator results indicate that the compaction under high-porosity, low-stress conditions is not qualitatively consistent in the models. As currently no quantitative data is available to understand the expected behavior in a real drift, we advocate for more research to better understand the characteristics of early-stage compaction. This would enable the modelling groups to improve their models. More insight and

calibration data can be expected from triaxial compaction experiments on material with little pre-compaction, as well as in-situ observations on a backfill body with KOMPASS-material that was recently in the Sondershausen mine.

Finally, Fig. 5.67 shows the stress evolution (mean and von-Mises (deviatoric) stress) over time for all models in different locations for the first 200 years of simulation. While within each model results, the differences are minor between the locations, it is noteworthy that the build-up of effective stresses in the backfill body appears to be strongly dependent on the constitutive model. The Hein-Korthaus and Olivella-Gens constitutive models used by BGE-Tec and GRS, respectively, show almost no effective stresses throughout the calculations. In contrast, the results of the demonstrator calculations using the Callahan, IfG-CWIPP and EXPO-COM predict up to 3 – 6 MPa of effective stress within the backfill. As deviatoric stresses can increase volumetric strain rates significantly (see e.g., Section 3), these results demonstrate that the treatment of deviatoric stresses in the different constitutive models needs to be examined in detail. We point out here that the test TUC-V4 was completed at the end of KOMPASS-II, which yields the necessary data to expand model validation for deviatoric stresses. In addition, it will be critical to obtain data from large-scale laboratory tests and, if possible, in-situ experiments to better constrain the magnitude of expected deviatoric stresses.

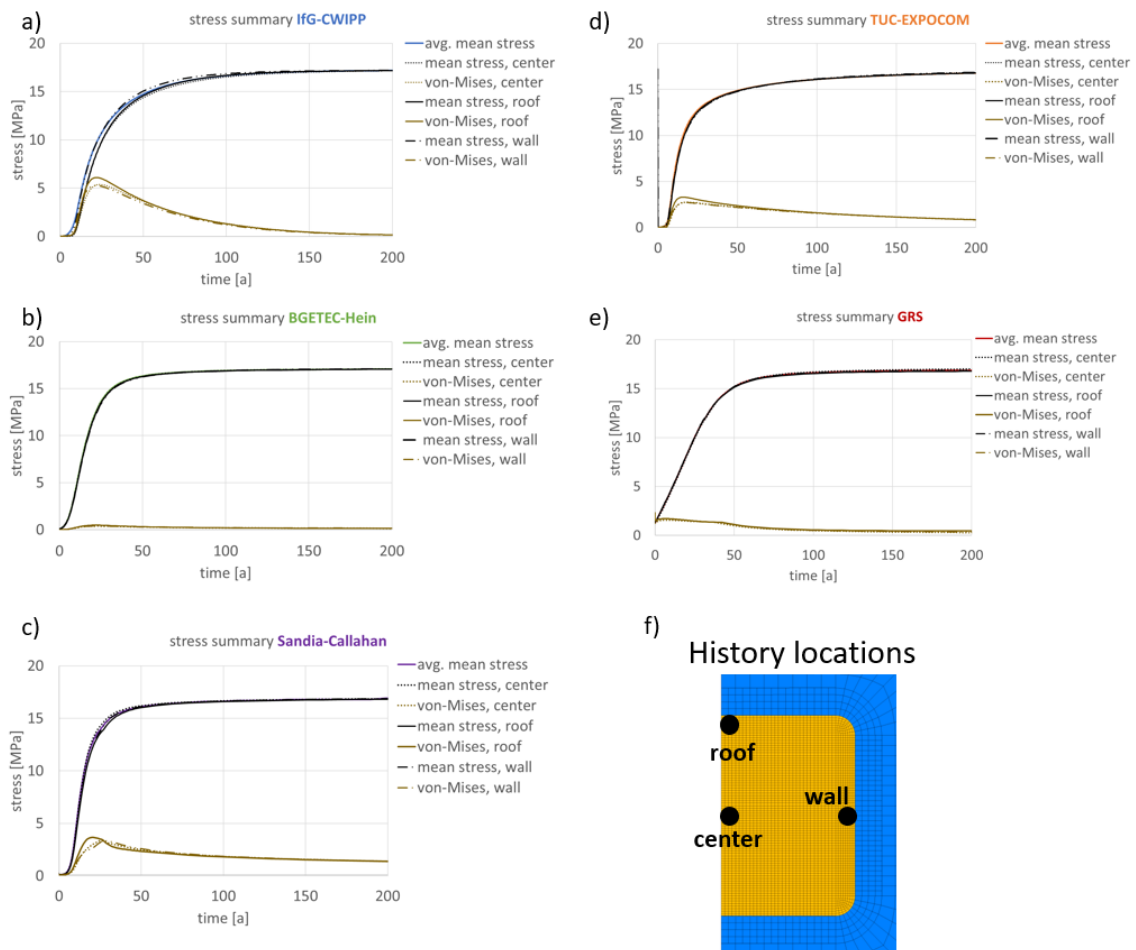


Fig. 5.67 Results of demonstrator runs using TUC-V2 derived parameters. Evolution of mean stress and von-Mises stress (“effective stress”) at the roof, center and wall of the backfill body. Each image represents a different partner (constitutive model): (a) IfG (IfG-CWIPP), (b) BGE-Tec (Hein-Korthaus), (c) Sandia (Callahan), (d) TUC (EXPO-COM), (e) GRS (Olivella-Gens). (f) Indications history locations for numerical time series

In summary, the employment of the virtual demonstrator as a tool for constitutive model development had notable positive impact for improving the constitutive models in the KOMPASS-II project. The demonstrator aided in identifying areas of focus for necessary calibration and model development like the low-porosity regime (implement during KOMPASS-II), high-porosity/low-stress regime and impact of deviatoric stresses (future work required). The partners were able to use the demonstrator to visualize advancements made during this project, especially with respect to the model development and especially the calibration status for porosities smaller than 15 %. As a clear sign of this process, the spread in the volumetric strain rates for this generic application scenario was significantly decreased compared to the “status quo” reference calibration, leading

to an overall better agreement between the different models especially regarding long-term behavior. In addition, it is impossible to stress that further research is urgently needed: It will be critical to quantitatively address the impact of parameter uncertainties on the predicted in-situ compaction behavior, as well as the impact of critical factors such as temperature, moisture content, and deviatoric stresses on the compaction behavior, which are currently not included and/or calibrated in the available constitutive models for crushed salt.

The virtual demonstrator can be easily expanded to evaluate more influencing factors and THM-processes. As a first step, the partners have started to discuss the implementation of temperature effects, which are available in all models. Finally, the demonstrator should be used for developing a methodology to quantify and bound the errors of prognosis for crushed salt compaction (uncertainty quantification).

6 Conclusion and Outlook

6.1 Summary

The KOMPASS-II project contributes to the improvement of the scientific knowledge for using crushed salt as backfill for high-level nuclear waste containment. Within the project, the process understanding of crushed salt compaction is enhanced by experimental studies and microstructural investigations, and the scientific database for the improvement of the constitutive modelling is extended. All these findings join in the development of the constitutive models. The existing constitutive models are evaluated against the experimental studies and their formulation is subsequently improved or re-designed.

One task in the project was the verification and further development of the pre-compaction methods, whereby three different methods were used. All three methods are checked for homogeneity of the samples. The plain-strain crushed salt pre-compaction method by TUC has been successful in generating repeatable results and demonstrating the homogeneity of the samples. For the pre-compaction methods by BGR and IfG, reproducibility was shown, however boundary effects expected from the oedometric test setup were present. For BGR the small sample itself show inhomogeneity in density due to the influence of friction and stress geometry. Because of the very large size of the cell at IfG, there is spatial variability within the big sample. In the beginning of this project this inhomogeneity was expected to be negligible for small samples taken from the large sample. However, the microstructural investigations of BGR showed strong inhomogeneities within the small samples. The effect of inhomogeneity has to be addressed in future research.

The experimental database for crushed salt compaction was extended by the execution of several triaxial compaction tests. The tests addressed influences of pre-compaction, different level of mean and deviatoric stress, moisture content, temperature and test duration. As a result, an extensive amount of data was produced, enhancing the process understanding and providing a solid basis for numerical progress. A comparison of all these tests in a common framework of external load conditions could not yet be achieved within the scope of this project. In addition to the experimental database extension, a laboratory benchmark was executed to determine the variability between different laboratories. The result shows a range of compaction behavior of the samples across the different labs. Potential explanations for these differences were found (e.g., different pre-

compaction, measurement uncertainties, microstructural effects), however, definitive and concluding evidence is not yet identified. Within the project, the newly designed iso-static compaction cell of the IfG became operational. The cell allows a combined measurement of ultrasonic velocity and permeability during the compaction process.

The microstructure investigations in this project focused on the abundance of microscale deformation mechanism effected by pre-compaction (Section 4.2, BGR), moisture content (Section 4.3, Sandia) and grain size/grain size distribution (Section 4.4, UU).

Regarding pre-compaction, the analyses were twofold: (1) qualitative impression on grain substructures and (2) quantitative measurement on GSD and GSP (Section 4.2).

By qualitative analysis, it was found:

- All samples show microstructural deformation indicators that are relicts either from geological evolution or from underground mining. Hence, attesting a strict laboratory cause of the found fluid inclusions, fractures and subgrains found is not possible. Subgrain piezometry indicates the same paleo-differential stress for all samples (~4.3 MPa), regardless of the laboratory loading style.
- Microstructural deformation indicators at individual grain-grain contacts, however, are likely caused by the laboratory tests. Those indicators are: dense deformation or slip bands, bent grains, tight indenting, truncating or interpenetrating grain boundaries (TITIGB) and recrystallized grains.
- The differing laboratory compaction tests produced the same types and similar abundance of indicators at grain-grain contacts.

By quantitative analysis, it was found:

- All three quantitatively investigated samples display a roughly similar GSD and GSP, with a trend for grain size reduction by all compaction methods. This reduction is accompanied by a change towards less circular grain shapes.

The strong similarity of microstructures resulting from the different compaction tests was demonstrated.

From the presented comparison of microstructures for dry and wet samples (pre-compacted and compacted), the effect of additional moisture and time on compaction is evident (Section 4.3). However, due to the different testing conditions between the IfG and TUC pre-compacted samples, and having fully compacted samples, it is difficult to have a direct comparison and conclusion amongst those samples. Therefore, only samples subjected to the most alike conditions should be compared. IfG pre-compacted and compacted samples without added moisture had larger amounts of fractures, angular grain shapes, and areas of dense deformation/slip bands (i.e., areas of higher stress). When 1 wt.% moisture was added, there were fewer fractures, grain shapes were more rounded, pressure solution creep at grain contacts, and more abundant areas of recrystallization. While the TUC pre-compacted sample with added moisture still had evidence of fractures, the elongated subgrain structures shows a more progressive regime of deformation into a cross-slip dislocation creep, as opposed to the "dry" sample. Additional moisture promotes healing during compaction, more so with longer duration tests, as shown here and noted in several other granular salt compaction studies /URA 86/, /SPI 93/, /BRO 96/, /MIL 18/. Although, it remains untested, if even longer deformation times and low stresses with this material (e.g., emplaced as in-situ backfill) will have similar results for "dry" samples or if indicators shown in "wet" samples begin to be observed. Thus, by microstructural analysis of samples investigated here, it cannot be guaranteed that the laboratory "dry" compaction methods correctly mimic a real-case scenario.

The investigations on the effect of grain size and its distribution on backfill compaction led to the following conclusions (Section 4.4):

- At low stresses ($< 10 - 15$ MPa), the compaction creep experiments show a linear dependence of compaction rate on stress and near inverse cubic dependence on grain size indicating that pressure solution creep is the main mechanism under these conditions.
- At high stress ($> 10 - 15$ MPa), the stress exponent varies from 3 – 7. Although this is typically associated with grain size insensitive dislocation creep mechanisms, we do observe some dependence on grain size in our experiments and the exact deformation mechanism(s) remain unclear.
- Experiments on a mixture containing multiple grain size fractions indicate that the same mechanisms operate in mixtures as in single grain size aggregates. The

rates can be approximated by taking the geometric mean of the upper and lower bound method described here.

The coupled convergence model indicates that during backfill convergence, the stresses remain within the linear creep/pressure solution domain, except for the final few percent of porosity reduction, and only when the average backfill grain size is very coarse (3.0 mm or larger).

All these microstructural analysis methods provided meaningful qualitative information on individual deformation mechanisms, but their efficiency still needs to be improved for quantitative application on a broad scale.

In the project, a large number of constitutive models were applied for the simulation of crushed salt compaction. By benchmarking the models against the complex triaxial compaction test TUC-V2, the calibration range for each model was extended and a continuous optimization process took place. For the constitutive models, different methods are used with regard to the geometric representation of the grain structure - geometric equivalent body vs. integral consideration - and the mapping of the deformation mechanisms - microstructural referred vs. phenomenological approach. The models were able to reproduce large parts of the test sufficiently well but showed limitations in capturing the entire response of the test over 750 days. An evaluation of this deviation between test procedure and numerical model requires further analysis together with the additional tests and can therefore only be carried out in the future.

The calibrated crushed salt models were then used to simulate a generic drift within the virtual demonstrator. This demonstrator was developed to act as a tool for model development and verification. The demonstrator highlights the continuous progress in the model development made from the KOMPASS-I project until the end of the KOMPASS-II project. Furthermore, the application of the demonstrator showed new improvement potential for the constitutive models, as well as, calibration requirements which should be implemented in the future.

In summary, the KOMPASS-II project represents a significant effort that achieved progress in experimental characterization, microstructural investigations and numerical modelling of crushed salt.

6.2 Further recommendations

The KOMPASS-II project answered many open questions and shortcomings regarding the process understanding of crushed salt compaction, however, some issues remain, and new ones arose. The most important ones are listed below:

- The Laboratory program is not complete: factors like moisture content have not yet been investigated experimentally. Furthermore, the demonstrator results showed the need for an extension of the parameter range for porosity and deviatoric stress from experimental side and based on this, in parameter identification.
- The effects of laboratory shortcomings (e.g., relaxation transient artefacts when multi-stage strain-rate compaction is used) on the numerical extrapolation of laboratory compaction tests to the real case compaction need to be investigated.
- The hydraulic properties of consolidated crushed are a key factor with respect to its long-term sealing capacity. Accurate permeability measurements, especially in the low porosity range, are still challenging. In the foregoing KOMPASS projects experimental approaches and equipment were developed and manufactured to allow reliable permeability measurements during compaction. However, test duration was not sufficient to reach high compaction levels during the KOMPASS projects.
- During experiments with a moisture content of 1 w.-% a squeezing out of brine could be observed at relatively high porosities (Section 3.2.2). The onset of fluid flow must be better understood and therefore, more investigation is needed.
- A number of tests are available that has been successfully executed to date as part of the extended laboratory program. These tests must be checked for consistency in order to be used as a benchmark for numerical modeling.
- The sample-to-sample variability is not yet characterized.
- The essential investigation of in-situ compacted crushed salt for the quantification of microstructures and the related deformation mechanism is still pending.
- Special experiments focusing on the activation and quantification of the dominant microscale mechanism operating in-situ are needed. This is required to underpin constitutive models describing porosity/permeability reduction and support extrapolation to long time scales by identifying the dominant deformation mechanism for a given set of conditions.
- The results from the virtual demonstrator in KOMPASS showed wide scattering of the predicted crushed salt compaction behaviors over time, such that reliable

long-term predictions for in-situ compaction are not yet possible. Several reasons for these shortcomings were identified:

- Not all models take into account all of the essential influencing factors on the compaction processes. This gap must be closed.
 - The available database of controlled long-term triaxial compaction tests still does not cover the entire range of in-situ relevant conditions for the various influencing parameters.
 - Available triaxial compaction experiments include complex multi-stage tests with relatively short duration for each loading stage. For a better understanding of the long-term behavior, tests with longer stages are needed.
- The KOMPASS backfill body was constructed in January 2023 and will be preserved for several years. To obtain data about the in-situ behavior of the KOMPASS reference material the collaboration with the SAVER project should continue.
 - The permeability reduction with time is considered in current long-term safety analysis approaches on the basis of research work performed for the “vorläufige Sicherheitsuntersuchungen Gorleben” (vSG) /MÜL 12a/. The database reflects the state of knowledge at that time and has not been updated in over 10 years. A coupling of the relevant processes, which is common today and reported in the KOMPASS projects, is not considered, and should be included.

References

- /BEC 99/ Bechthold, W., Rothfuchs, T., Poley, A., Ghoreychi, M., Heusermann, S., Gens, A., Olivella, S.: Backfilling and sealing of underground repositories for radioactive waste in salt (BAMBUS project), Final report. EUR Project report - nuclear science and technology, vol. 19124, EUR-19124-EN, 248 p., ISBN 92-828-7923-2, DOI 0009, Off. for Off. Publ. of the Europ. Communities: Luxembourg, 1999.
- /BEC 04/ Bechthold, W., Smailos, E., Heusermann, S., Bollingerfehr, W., Bazargan Sabet, B., Rothfuchs, T., Kamlot, P., Grupa, J., Olivella, S., Hansen, F. D.: Backfilling and sealing of underground repositories for radioactive waste in salt (BAMBUS II project), Final report. Europäische Kommission, EUR Nuclear science and technology Project report, vol. 20621, EUR-20621-EN, 272 p., ISBN 92-894-7767-9, DOI 00051, Office for Official Publications of the European Communities: Luxembourg, 2004.
- /BÉR 19/ Bérest, P., Gharbi, H., Brouard, B., Brückner, D., DeVries, K., Hévin, G., Hofer, G., Spiers, C. J., Urai, J. L.: Very Slow Creep Tests on Salt Samples. *Rock Mechanics and Rock Engineering*, vol. 52, no. 9, pp. 2917–2934, DOI 10.1007/s00603-019-01778-9, 2019.
- /BÉR 23/ Bérest, P., Gharbi, H., Blanco-Martín, L., Brouard, B., Brückner, D., DeVries, K. L., Hévin, G., Hofer, G., Spiers, C. J., Urai, J. L.: Salt Creep: Transition Between the Low and High Stress Domains. *Rock Mechanics and Rock Engineering*, DOI 10.1007/s00603-023-03485-y, 2023.
- /BLE 02/ Blenkinsop, T.: *Deformation, Microstructures and Mechanisms in Minerals and Rocks*. 1163 p., ISBN 0-306-47543-X, Chapman & Hall: New York, 2002.
- /BMU 10/ Sicherheitsanforderungen an die Endlagerung wärmeentwickelnder radioaktiver Abfälle as amended on 30 September 2010.

- /BOL 18/ Bollingerfehr, W., Bertrams, N., Buhmann, D., Eickemeier, R., Fahland, S., Filbert, W., Hammer, J., Kindlein, J., Knauth, M., Liu, W., Minkley, W., Mönig, J., Popp, T., Prignitz, S., et al.: KOSINA, Concept developmens for a generic repository for heat-generating waste in bedded salt formations in Germany, Synthesis report. Ed.: BGE-TEC: Peine, October 2018.
- /BON 01/ Bonnet, E., Bour, O., Odling, N. E., Davy, P., Main, I., Cowie, P., Berkowitz, B.: Scaling of fracture systems in geological media. *Reviews of Geophysics*, vol. 39, no. 3, pp. 347–383, DOI 10.1029/1999RG000074, 2001.
- /BRO 96/ Brodsky, N. S., Hansen, F. D., Pfeifle, T. W.: Properties of dynamically compacted WIPP salt. Sandia National Laboratories, SAND96-0838C: Albuquerque, NM, July 1996.
- /CAL 96/ Callahan, G. D., Loken, M. C., Hurtado, L. D., Hansen, F. D.: Evaluation of constitutive models for crushed salt. Sandia National Laboratories, SAND96-0791C: Albuquerque, NM, 1996.
- /CAL 98/ Callahan, G. D., Mellegard, K. D., Hansen, F. D.: Constitutive behavior of reconsolidating crushed salt. *International Journal of Rock Mechanics and Mining Sciences*, vol. 35, No. 4-5, pp. 422–423, DOI 10.1016/S0148-9062(98)00045-X, 1998.
- /CAL 99/ Callahan, G. D.: Crushed Salt Constitutive Model. Sandia National Laboratories, SAND98-2680, DOI 10.2172/4127: Rapid City, 1999.
- /CAR 83/ Carter, N. L., Hansen, F. D.: Creep of rocksalt. *Tectonophysics*, vol. 92, no. 4, pp. 275–333, DOI 10.1016/0040-1951(83)90200-7, 1983.
- /CAR 93/ Carter, N., Horseman, S., Russell, J., Handin, J.: Rheology of rocksalt. *Journal of Structural Geology*, vol. 15, No. 9-10, pp. 1257–1271, DOI 10.1016/0191-8141(93)90168-A, 1993.
- /COU 23/ Coulibaly, J. B.: An assessment of Callahan's crushed salt constitutive model, Memorandum. Sandia National Laboratories, SAND, XXX-YYY: Albuquerque, 2023.

- /CZA 20/ Czaikowski, O., Friedenber, L.: Benchmarking for validation and verification of THM simulators with special regard to fluid dynamic processes in repository systems, Project BenVaSim. GRS, vol. 588, 128 p., ISBN 978-3-947685-74-5, Gesellschaft für Anlagen- und Reaktorsicherheit (GRS) gGmbH: Köln, Garching b. München, Berlin, Braunschweig, 2020.
- /DAE 17/ Wieczorek, K., Düsterloh, U., Heemann, U., Lerch, C., Lüdeling, C., Müller-Hoeppe, N., Popp, T., Stührenberg, D., Wolters, R.: Reconsolidation of crushed salt backfill - review of existing experimental database and constitutive models and need for future R&D work, DAEF Stellungnahme. 2017.
- /DEV 11/ DeVries, K. L.: Munson-Dawson Model Parameter Estimation of Sonderhausen and Asse Salt. To Pfeifle, T. W., RESPEC Memo: Albuquerque, 25 January 2011.
- /DÜS 15/ Düsterloh, U., Herchen, K., Lux, K.-H., Salzer, K., Günther, R.-M., Minkley, W., Hampel, A., Argüello, J. G., Hansen, F. D.: Joint project III on the comparison of constitutive models for the mechanical behavior of rock salt III. Extensive laboratory test program with argillaceous salt from WIPP and comparison of test results. In: Roberts, L., Mellegard, K., Hansen, F. D. (Eds.): The Mechanical Behaviour of Salt VIII. ISBN 9781138028401, Taylor & Francis Ltd: [s.l.], 2015.
- /DÜS 21/ Düsterloh, U., Lerche, S.: Methodology of structured development and validation of multiphysical constitutive models using the example of crushed salt compaction under 3D THM load conditions. Safety of Nuclear Waste Disposal, vol. 1, pp. 113–115, DOI 10.5194/sand-1-113-2021, 2021.
- /DÜS 22/ Düsterloh, U., Lerche, S., Saruulbayar, N.: Crushed salt compaction - a new approach for lab test analysis, physical modelling and numerical simulation, Part 1: Development and validation. In: Bresser, J. de, Drury, M. R., Fokker, P. A., Gazzani, M., Hangx, S., Niemeijer, A. R., Spiers, C. J. (Eds.): The Mechanical Behavior of Salt X, Proceedings of the 10th Conference on the Mechanical Behavior of Salt (SaltMech X), Utrecht, The Netherlands, 06 - 08 July 2022. ISBN 9781003295808, DOI 10.1201/9781003295808, CRC Press: London, 2022.

- /ELL 04/ Elliger, C.: Untersuchungen zum Permeationsverhalten von Salzlaugen in Steinsalz bei der Endlagerung wärmeentwickelnder nuklearer Abfälle. Dissertation, Fachbereich Maschinenbau, Technische Universität Darmstadt: Darmstadt, November 2004.
- /FRA 90/ Franssen, R., Spiers, C. J.: Deformation of polycrystalline salt in compression and in shear at 250–350°C. Geological Society, London, Special Publications, vol. 54, no. 1, pp. 201–213, DOI 10.1144/GSL.SP.1990.054.01.20, 1990.
- /FRI 23/ Friedenber, L., Olivella, S., Düsterloh, U.: Numerical analysis for the simulation of crushed salt compaction behavior, ARMA23-0341. In: American Rock Mechanics Association (ARMA) (Ed.): 57th U.S. Rock Mechanics / Geomechanis Symposium. Atlanta, 25 - 28 June 2023, 2023.
- /GID 23/ Centre Internacional de Mètodes Numèrics a l'Enginyeria: GiD Simulation. Barcelona, available from <https://www.gidsimulation.com/>, retrieved on 23 August 2023.
- /HAM 07/ Hampel, A., Schulze, O., Heemann, U., Zetsche, F., Günther, R.-M., Salzer, K., Minkley, W., Hou, Z., Wolters, R., Düsterloh, U., Zapf, D., Rokahr, R., Pudewills, A.: Die Modellierung des mechanischen Verhaltens von Steinsalz: Vergleich aktueller Stoff-gesetze und Vorgehensweisen, BMBF-Verbundprojekt. 2007.
- /HAM 16/ Hampel, A., Herchen, K., Lux, K.-H., Günther, R.-M., Salzer, K., Minkley, W., Pudewills, A., Yildirim, S., Rokahr, R., Missal, C., Gährken, A., Stahlmann, J.: Verbundprojekt - Vergleich aktueller Stoffgesetze und Vorgehensweisen anhand von Modellberechnungen zum thermo-mechanischen Verhalten und zur Verheilung von Steinsalz, Synthesebericht. 30 September 2016.

- /HAM 22/ Hampel, A., Lüdeling, C., Günther, R.-M., Salzer, K., Yildirim, S., Zapf, D., Epkenhans, I., Wacker, S., Gährken, A., Stahlmann, J., Sun-Kurczinski, J. Q., Wolters, R., Herchen, K., Lux, K.-H.: Verbundprojekt: Weiterentwicklung und Qualifizierung der gebirgsmechanischen Modellierung für die HAW-Endlagerung im Steinsalz (WEIMOS), Synthesebericht, Projektlaufzeit: 01.04.2016 - 31.12.2022. Karlsruhe, 2022.
- /HAM 23/ Hampel, A., Argüello, J. G., Hansen, F. D., Günther, R.-M., Salzer, K., Minkley, W., Lux, K.-H., Herchen, K., Düsterloh, U., Pudewills, A., Yildirim, S., Staudtmeister, K., Rokahr, R., Zapf, D., et al.: Benchmark Calculations of the Thermo-Mechanical Behavior of Rock Salt - Results from a US-German Joint Project. In: American Rock Mechanics Association (ARMA) (Ed.): 57th U.S. Rock Mechanics / Geomechanics Symposium. Atlanta, 25 - 28 June 2023, ARMA13-456, 2023.
- /HEE 89/ Heemann, U.: Heemann, U. (1989): Transientes Kriechen und Kriechbruch im Steinsalz. Dissertation, Institut für Baumechanik und Numerische Mechanik, Universität Hannover: Hannover, 1989.
- /HEE 05a/ Heege, J. H. ter, Bresser, J. de, Spiers, C. J.: Rheological behaviour of synthetic rocksalt: the interplay between water, dynamic recrystallization and deformation mechanisms. *Journal of Structural Geology*, vol. 27, no. 6, pp. 948–963, DOI 10.1016/j.jsg.2005.04.008, 2005.
- /HEE 05b/ Heege, J. H. ter, Bresser, J. de, Spiers, C. J.: Dynamic recrystallization of wet synthetic polycrystalline halite: dependence of grain size distribution on flow stress, temperature and strain. *Tectonophysics*, vol. 396, No. 1-2, pp. 35–57, DOI 10.1016/j.tecto.2004.10.002, 2005.
- /HEI 91/ Hein, H.-J.: Ein Stoffgesetz zur Beschreibung des thermomechanischen Verhaltens von Salzgranulat, Ein Beitrag zur Endlagerung wärmefreisetzender radioaktiver Abfälle. Fakultät für Maschinenwesen, RWTH Aachen: Aachen, 1991.
- /HEI 14/ Heilbronner, R., Barrett, S.: *Image Analysis in Earth Sciences*. ISBN 978-3-642-10342-1, DOI 10.1007/978-3-642-10343-8, Springer Berlin Heidelberg: Berlin, Heidelberg, 2014.

- /HOL 45/ Hollomon, J. H.: Tensile Deformation. Transactions of the Metallurgical Society of AIME, Vol. 162, pp. 268–290, 1945.
- /HUN 94/ Hunsche, U., Schulze, O.: Das Kriechverhalten von Steinsalz. Kali und Steinsalz, vol. 11, No. 8/9, pp. 238–255, 1994.
- /HUN 99/ Hunsche, U., Hampel, A.: Rock salt — the mechanical properties of the host rock material for a radioactive waste repository. Engineering Geology, vol. 52, No. 3-4, pp. 271–291, DOI 10.1016/S0013-7952(99)00011-3, 1999.
- /JOF 24/ Joffé, A., Kirpitschewa, M. W., Lewitzky, M. A.: Deformation und Festigkeit der Kristalle. Zeitschrift für Physik, vol. 22, no. 1, pp. 286–302, DOI 10.1007/BF01328133, 1924.
- /KNE 18/ Kneucker, T., Mertineit, M., Schramm, M., Hammer, J., Zulauf, G., Thiemeyer, N.: Microfabrics and composition of Straßfurt and Leine rock salt (Upper Permian) of the Morsleben site (Germany): Constraints on deformation mechanisms and palaeodifferential stress. In: Fahland, S., Hammer, J., Hansen, F. D., Heusermann, S., Lux, K.-H., Minkley, W. (Eds.): The mechanical behavior of salt IX, Proceedings of the 9th Conference on the Mechanical Behavior of Salt (SaltMech IX), Hannover, Germany, 12-14 September 2018. Bundesanstalt für Geowissenschaften und Rohstoffe (BGR), Institut für Gebirgsmechanik (IfG) Leipzig, Technische Universität Clausthal (TUC), Conference on the Mechanical Behavior of Salt, Hannover, 12 - 14 September 2018, ISBN 978-3-9814108-6-0, Federal Institute for Geosciences and Natural Resources (BGR): Hannover, 2018.
- /KOC 76/ Kocks, U. F.: Laws for Work-Hardening and Low-Temperature Creep. Journal of Engineering Materials and Technology, vol. 98, no. 1, pp. 76–85, DOI 10.1115/1.3443340, 1976.
- /KOM 20/ Czaikowski, O., Friedenber, L., Wieczorek, K., Müller-Hoeppe, N., Lerch, C., Eickemeier, R., Laurich, B., Liu, W., Stührenberg, D., Svensson, K., Zemke, K., Lüdeling, C., Popp, T., Bean, J., et al.: KOMPASS, Compaction of crushed salt for the safe containment. GRS-, vol. 608, 320 p., ISBN 978-3-947685-94-3, Gesellschaft für Anlagen- und Reaktorsicherheit (GRS) gGmbH: Köln, Garching b. München, Berlin, Braunschweig, August 2020.

- /KOR 96/ Korthaus, E.: Consolidation and deviatoric deformation behaviour of dry crushed salt at temperatures up to 150 °C. In: Aubertin, M. (Ed.): Mechanical behavior of salt, 4th conference ; Ecole Polytechnique, Montreal, Canada, June 17 and 18, 1996./ [4th Conference on the Mechanical Behavior of Salt] Organized by: Ecole Polytechnique and McGill University. [Ed.: Michel Aubertin. École polytechnique de Montréal, McGill University, Conference Mechanical Behavior of Salt, Series on rock and soil mechanics, vol. 22, pp. 365–378, ISBN 9780878491032, Trans Tech Publications: Clausthal-Zellerfeld, 1996.
- /KOR 98/ Korthaus, E.: Experiments on Crushed Salt Consolidation with True Triaxial Testing Devices as a Contribution to an EC Benchmark Exercise. Institut für Nukleare Entsorgungstechnik, FZKA 6181: Karlsruhe, 1998.
- /KRÖ 09/ Kröhn, K.-P., Stührenberg, D., Herklotz, M., Heemann, U., Lerch, C., Xie, M.: Restporosität und -permeabilität von kompaktierendem Salzgrus-Versatz, REOPERM - Phase 1. GRS, vol. 254, GRS-254, 266 p., ISBN 978-3-939355-29-8, GRS: Köln, 2009.
- /KRÖ 17/ Kröhn, K.-P., Stührenberg, D., Jobmann, M., Heemann, U., Czaikowski, O., Wieczorek, K., Müller, C., Zhang, C.-L., Schirmer, S., Friedenberg, L.: Mechanical and hydraulic behaviour of compacting crushed salt backfill at low porosities, Project REOPERM - phase 2. GRS-, vol. 450, No. 450, 219 p., ISBN 978-3-946607-32-8, Gesellschaft für Anlagen- und Reaktorsicherheit (GRS) gGmbH: Köln, Garching b. München, Berlin, Braunschweig, February 2017.
- /KÜS 10/ Küster, Y., Leiss, B., Schramm, M.: Structural characteristics of the halite fabric type 'Kristallbrocken' from the Zechstein Basin with regard to its development. International Journal of Earth Sciences, vol. 99, no. 3, pp. 505–526, DOI 10.1007/s00531-008-0399-8, 2010.
- /LEE 71/ Lee, D., Hart, E. W.: Stress relaxation and mechanical behavior of metals. Metallurgical Transactions, vol. 2, no. 4, pp. 1245–1248, DOI 10.1007/BF02664258, 1971.

- /LER 12/ Lerche, S.: Kriech- und Schädigungsprozesse im Salinargebirge bei mono- und multizyklischer Belastung. PhD Thesis, Technische Universität Clausthal (TUC): Clausthal-Zellerfeld, 2012.
- /LI 05/ Li, M., Wilkinson, D., Patchigolla, K.: Comparison of Particle Size Distributions Measured Using Different Techniques. *Particulate Science and Technology*, vol. 23, no. 3, pp. 265–284, DOI 10.1080/02726350590955912, 2005.
- /LIN 16/ Linckens, J., Zulauf, G., Hammer, J.: Experimental deformation of coarse-grained rock salt to high strain. *Journal of Geophysical Research: Solid Earth*, vol. 121, no. 8, pp. 6150–6171, DOI 10.1002/2016JB012890, 2016.
- /LÜD 14/ Lüdeling, C., Minkley, W. (Eds.): A Crushed–Salt Model with Creep, Compaction and Strain Softening, and Application to Tailings Heaps. U.S. Rock Mechanics/Geomechanics Symposium, All Days, 2014.
- /LUX 18/ Lux, K.-H., Lerche, S., Dyogtyev, O.: Intense damage processes in salt rocks - a new approach for laboratory investigations, physical modelling and numerical simulations. In: Fahland, S., Hammer, J., Hansen, F. D., Heusermann, S., Lux, K.-H., Minkley, W. (Eds.): *The mechanical behavior of salt IX*, Proceedings of the 9th Conference on the Mechanical Behavior of Salt (SaltMech IX), Hannover, Germany, 12-14 September 2018. Bundesanstalt für Geowissenschaften und Rohstoffe (BGR), Institut für Gebirgsmechanik (IfG) Leipzig, Technische Universität Clausthal (TUC), Conference on the Mechanical Behavior of Salt, Hannover, 12 - 14 September 2018, pp. 47–68, ISBN 978-3-9814108-6-0, Federal Institute for Geosciences and Natural Resources (BGR): Hannover, 2018.
- /MAR 16/ Marketos, G., Spiers, C. J., Govers, R.: Impact of rock salt creep law choice on subsidence calculations for hydrocarbon reservoirs overlain by evaporite caprocks. *Journal of Geophysical Research: Solid Earth*, vol. 121, no. 6, pp. 4249–4267, DOI 10.1002/2016JB012892, 2016.

- /MER 23/ Mertineit, M., Schramm, M., Thiemeyer, N., Blanke, H., Patzschke, M., Zulauf, G.: Paleostress, deformation mechanisms and finite strain related to chocolate-tablet boudinage and folding of a Permian rock salt/anhydrite sequence (Morsleben site, Germany). *Tectonophysics*, vol. 847, pp. 229703, DOI 10.1016/j.tecto.2023.229703, 2023.
- /MIL 18/ Mills, M. M., Stormont, J. C., Bauer, S. J.: Micromechanical processes in consolidated granular salt. *Engineering Geology*, vol. 239, pp. 206–213, DOI 10.1016/j.enggeo.2018.03.024, 2018.
- /MIN 07/ Minkley, W., Mühlbauer, J.: Constitutive models to describe the mechanical behaviour of salt rocks and the imbedded weakness planes. In: Wallner, M., Lux, K.-H., Minkley, W., Reginald Hardy, J. H. (Eds.): *The Mechanical Behavior of Salt - Understanding of THMC Processes in Salt, Proceedings of the 6th Conference (SaltMech6), Hannover, Germany, 22-25 May 2007*. 1. ed., pp. 119–129, ISBN 9781315106502, CRC Press, 2007.
- /MUN 79/ Munson, D. E., Dawson, P. R.: Constitutive model for the low temperature creep of salt (with application to WIPP). Sandia National Laboratories, SAND, 79-1853, DOI 10.2172/5729479: Albuquerque, 1979.
- /MUN 89/ Munson, D. E., Fossum, A. F., Senseny, P. E.: Advances in resolution of discrepancies between predicted and measured in situ WIPP (Waste Isolation Pilot Plant) room closures. Sandia National Laboratories, SAND, 88-948, DOI 10.2172/5784434: Albuquerque, 1989.
- /OLI 95/ Olivella, S.: Nonisothermal multiphase flow of brine and gas through saline media. Dissertation, ETSCCP, Universitat Politècnica de Catalunya (UPC): Barcelona, June 1995.
- /OLI 02/ Olivella, S., Gens, A.: A constitutive model for crushed salt. *International Journal for Numerical and Analytical Methods in Geomechanics*, vol. 26, no. 7, pp. 719–746, DOI 10.1002/nag.220, 2002.

- /OLI 11/ Olivella, S., Castagna, S., Alonso, E. E., Lloret, A.: Porosity Variations in Saline Media Induced by Temperature Gradients: Experimental Evidences and Modelling. *Transport in Porous Media*, vol. 90, no. 3, pp. 763–777, DOI 10.1007/s11242-011-9814-x, 2011.
- /PAS 05/ Passchier, C. W., Trouw, R. A. J.: *Microtectonics*. 2. ed., 366 p., ISBN 3-540-64003-7, Springer: Berlin, Heidelberg, 2005.
- /PEA 01/ Peach, C. J., Spiers, C. J., Trimby, P. W.: Effect of confining pressure on dilatation, recrystallization, and flow of rock salt at 150°C. *Journal of Geophysical Research: Solid Earth*, vol. 106, B7, pp. 13315–13328, DOI 10.1029/2000JB900300, 2001.
- /PEN 05/ Pennock, G. M., Drury, M. R., Spiers, C. J.: The development of subgrain misorientations with strain in dry synthetic NaCl measured using EBSD. *Journal of Structural Geology*, vol. 27, no. 12, pp. 2159–2170, DOI 10.1016/j.jsg.2005.06.013, 2005.
- /POP 98/ Popp, T., Kern, H.: Ultrasonic wave velocities, gas permeability and porosity in natural and granular rock salt. *Physics and Chemistry of the Earth*, vol. 23, no. 3, pp. 373–378, DOI 10.1016/S0079-1946(98)00040-8, 1998.
- /QGI 22/ QGIS: QGIS - Ein freies Open-Source-Geographisches-Informationssystem. Available from <http://www.qgis.org/>, as at 2022.
- /REE 16/ Reedlunn, B.: *Reinvestigation into Closure Predictions of Room D at the Waste Isolation Pilot Plant*. Sandia National Laboratories, SAND, 2016-9665, DOI 10.2172/1333709: Albuquerque, 2016.
- /REE 18/ Reedlunn, B.: *Enhancements to the Munson-Dawson Model for Rock Salt*. Sandia National Laboratories, SAND, 2018-12601: Albuquerque, November 2018.
- /ROE 81/ Roedder, E., Bassett, R. L.: Problems in determination of the water content of rock-salt samples and its significance in nuclear-waste storage siting. *Geology*, vol. 9, no. 11, pp. 525, DOI 10.1130/0091-7613(1981)9<525:PIDOTW>2.0.CO;2, 1981.

- /RUT 78/ Rutter, E. H., Mainprice, D. H.: The Effect of Water on Stress Relaxation of Faulted and Unfaulted Sandstone. In: Byerlee, J. D., Wyss, M. (Eds.): Rock Friction and Earthquake Prediction. pp. 634–654, ISBN 978-3-0348-7184-6, DOI 10.1007/978-3-0348-7182-2_6, Birkhäuser Basel: Basel, 1978.
- /SAL 15/ Salzer, K., Günther, R.-M., Naumann, D., Popp, T., Hampel, A., Lux, K.-H., Herchen, K., Düsterloh, U., Argüello, J. G., Hansen, F. D.: Laboratory testing Joint project III on the comparison of constitutive models for the mechanical behavior of rock salt II. Extensive laboratory test program with clean salt from WIPP. In: Roberts, L., Mellegard, K., Hansen, F. D. (Eds.): The Mechanical Behaviour of Salt VIII. ISBN 9781138028401, Taylor & Francis Ltd: [s.l.], 2015.
- /SCH 22a/ Schmitz, J., Závada, P., Urai, J. L.: Microstructural evolution of glacier salt from the Kuh-e-Namak salt diapir, Iran. In: Bresser, J. de, Drury, M. R., Fokker, P. A., Gazzani, M., Hangx, S., Niemeijer, A. R., Spiers, C. J. (Eds.): The Mechanical Behavior of Salt X, Proceedings of the 10th Conference on the Mechanical Behavior of Salt (SaltMech X), Utrecht, The Netherlands, 06 - 08 July 2022. pp. 46, ISBN 9781003295808, DOI 10.1201/9781003295808, CRC Press: London, 2022.
- /SCH 22b/ Schaarschmidt, L., Friedenber, L.: SAVER/KOMPASS-II collaboration. Presentation, Technische Universität Bergakademie Freiberg (TU BAF), Gesellschaft für Anlagen- und Reaktorsicherheit (GRS) gGmbH, US/German Workshop. Salt Repository Research, Design, & Operation, BGE-TEC, Sandia National Laboratories, Project Management Agency Karlsruhe (PTKA): Braunschweig, 8 September 2022.
- /SCH 23/ Schaarschmidt, L.: Big Scale In-Situ Application of Matrix-stabilized vs. Conventional Backfill With Improved Backfilling Method. Presentation, US/German Workshop. Salt Repository Research, Design, & Operation, Sandia National Laboratories, BGE TECHNOLOGY GmbH, Project Management Agency Karlsruhe (PTKA): Santa Fe, NM, 23 June 2023.
- /SIE 23/ SIERRA Solid Mechanics Team: Sierra/SolidMechanics 5.12 User's Guide. Sandia National Laboratories, SAND, 2023-11993: Albuquerque, Livermore, 2023.

- /SJA 87/ Sjaardema, G. D., Krieg, R. D.: A Constitutive Model for the Consolidation of WIPP Crushed Salt and Its Use in Analyses of Backfilled Shaft and Drift Configurations. Ed.: Sandia National Laboratories, SAND, 87-1977: Albuquerque, October 1987.
- /SPA 98/ Spangenberg, E., Spangenberg, U., Heindorf, C.: An experimental study of transport properties of porous rock salt. *Physics and Chemistry of the Earth*, vol. 23, no. 3, pp. 367–371, DOI 10.1016/S0079-1946(98)00039-1, 1998.
- /SPI 86/ Spiers, C. J., Urai, J. L., Lister, G. S., Boland, J. N., Zwart, H. J.: The influence of fluid-rock interaction on the rheology of salt rock, Final report. Ed.: Commission of the European Communities, Nuclear science and technology, vol. 10399, EUR 10399 EN, 131 p., ISBN 92-825-6214-X, Commission of the European Communities: Luxembourg, 1986.
- /SPI 89/ Spiers, C. J., Peach, R. H., Brzesowsky, R. H., Schutjens, P. M. T. M., Liezenberg, J. L., Zwart, H. J.: Long-term rheological and transport properties of dry and wet salt rocks, Final report. Nuclear science and technology, vol. 11848, EUR-11848-EN, 49 p., ISBN 92-825-9191-3, Office for Official Publications of the European Communities: Luxembourg, 1989.
- /SPI 90/ Spiers, C. J., Schutjens, P. M. T. M., Brzesowsky, R. H., Peach, C. J., Liezenberg, J. L., Zwart, H. J.: Experimental determination of constitutive parameters governing creep of rocksalt by pressure solution. *Geological Society, London, Special Publications*, vol. 54, no. 1, pp. 215–227, DOI 10.1144/GSL.SP.1990.054.01.21, 1990.
- /SPI 93/ Spiers, C. J., Brzesowsky, R. H.: Densification behaviour of wet granular salt: theory versus experiment. In: Kakihana, H. (Ed.): *Seventh Symposium on Salt*. Salt Science Research Foundation, pp. 83–92, ISBN 9780444891433, Elsevier: Amsterdam, 1993.
- /STA 17/ Gesetz zur Suche und Auswahl eines Standortes für ein Endlager für hochradioaktive Abfälle (Standortauswahlgesetz - StandAG) as amended on 5 May 2017 (BGBl. I 2017, Nr. 26, S. 1074-1100), last changed 5 May 2017.

- /STE 85/ Stelte, N.: Analytische Approximation der Konvergenzrate salzgrusversetzter und unter hydraulischem Druck stehender Hohlräume im Salzgestein. 15. ed.: Berlin, 1985.
- /STÜ 13/ Stührenberg, D.: R+D Radioactive Waste Repository, Triaxial Compaction Test TK-031. Federal Institute for Geosciences and Natural Resources (BGR): Hannover, August 2013.
- /STÜ 17/ Stührenberg, D.: Methodenbericht Triaxiale Salzgruskompaktion – Bestimmung der zeitabhängigen Volumenänderung von Salzgrusversatz im triaxialen Kompaktionsversuch, Dokumentation zum Qualitätsmanagement. Federal Institute for Geosciences and Natural Resources (BGR), 2017.
- /SVE 22/ Svensson, K., Laurich, B.: Microstructures in compacted crushed salt. Presentation, Federal Institute for Geosciences and Natural Resources (BGR), US/German Workshop. Salt Repository Research, Design, & Operation, BGE-TEC, Sandia National Laboratories, Project Management Agency Karlsruhe (PTKA): Braunschweig, 8 September 2022.
- /URA 86/ Urai, J. L., Spiers, C. J., Zwart, H. J., Lister, G. S.: Weakening of rock salt by water during long-term creep. *Nature*, vol. 324, no. 6097, pp. 554–557, DOI 10.1038/324554a0, 1986.
- /URA 87/ Urai, J. L., Spiers, C. J., Peach, C. J., Franssen, R., Liezenberg, J. L.: Deformation mechanisms operating in naturally deformed halite rocks as deduced from microstructural investigations. *Geol. en Mijnb*, no. 66, pp. 165–176, 1987.
- /URA 07/ Urai, J. L., Spiers, C. J.: The effect of grain boundary water on deformation mechanisms and rheology of rocksalt during long-term deformation. In: Wallner, M., Lux, K.-H., Minkley, W., Reginald Hardy, J. H. (Eds.): *The mechanical behavior of salt, Understanding of THMC processes in salt ; proceedings of the 6th Conference on the Mechanical Behavior of Salt, Saltmech6*, Hannover, Germany, 22 - 25 May 2007. *Conference on the Mechanical Behavior of Salt, Balkema - Proceedings and monographs in engineering, water and earth sciences*, pp. 149–158, ISBN 978-0-415-44398-2, Taylor & Francis / Balkema: London, 2007.

- /URA 08/ Urai, J. L., Schlöder, Z., Spiers, C. J., Kukla, P. A.: Flow and Transport Properties of Salt Rocks. In: Littke, R., Gajewski, D. (Eds.): Dynamics of complex intracontinental basins, The central European basin system. pp. 277–290, ISBN 978-3-540-85084-7, Springer: Berlin, Heidelberg, 2008.
- /WIE 12/ Wieczorek, K., Lerch, C., Müller-Hoeppe, N., Czaikowski, O., Navarro, M.: Zusammenstellung von Stoffparametern für Salzgrus, Technischer Bericht im Vorhaben "Vorläufige Sicherheitsanalyse für den Standort Gorleben". Gesellschaft für Anlagen- und Reaktorsicherheit (GRS) gGmbH: Braunschweig, 2012.
- /WIE 14/ Wieczorek, K., Behlau, J., Heemann, U., Masik, S., Müller, C., Raab, M., Simo, E.: VIRTUS, Virtuelles Untertagelabor im Steinsalz. Gesellschaft für Anlagen- und Reaktorsicherheit (GRS) gGmbH, GRS, vol. 354, 79 p., ISBN 978-3-944161-34-1, Ges. für Anlagen- und Reaktorsicherheit (GRS) gGmbH: Köln, December 2014.
- /ZHA 07/ Zhang, X., Peach, C. J., Grupa, J., Spiers, C. J.: Stress relaxation experiments on compacted granular salt: effects of water. In: Wallner, M., Lux, K.-H., Minkley, W., Reginald Hardy, J. H. (Eds.): The mechanical behavior of salt, Understanding of THMC processes in salt ; proceedings of the 6th Conference on the Mechanical Behavior of Salt, Saltmech6, Hannover, Germany, 22 - 25 May 2007. Conference on the Mechanical Behavior of Salt, Balkema - Proceedings and monographs in engineering, water and earth sciences, pp. 159–165, ISBN 978-0-415-44398-2, Taylor & Francis / Balkema: London, 2007.

List of Figures

Fig. 2.1	Extended systematic laboratory program as developed in the KOMPASS-I project.....	4
Fig. 2.2	Main aspects of a long-term strategy for investigations to ensure reliable statements in the prognostic analysis of the compaction behavior of crushed salt as a backfilling and sealing material in repositories in rock salt	6
Fig. 2.3	Long-term strategy for investigations – itemization of aims and milestones	7
Fig. 2.4	Long-term strategy for experimental investigations - work packages and project partners involved.....	9
Fig. 2.5	Long-term strategy for investigations – details of the work packages and achieved milestones for experimental investigations for lifetime of the forerunner project KOMPASS-I.....	10
Fig. 2.6	Long-term strategy for investigations – details of work packages and achieved milestones for experimental investigations for lifetime of the current project KOMPASS-II.....	10
Fig. 2.7	Long-term strategy for investigations – details of work packages and milestones to be reached for experimental investigations for lifetime of the follow-up project.....	11
Fig. 2.8	Long-term strategy for investigations – details of objectives & achieved milestones for constitutive modeling and numerical simulations for the lifetime of the forerunner project KOMPASS-I	11
Fig. 2.9	Long-term strategy for investigations – details of objectives & achieved milestones for constitutive modeling and numerical simulations for the lifetime of the current project KOMPASS-II.....	12
Fig. 2.10	Long-term strategy for investigations – details of objectives & milestones to be reached for constitutive modeling and numerical simulations for the lifetime of the planned follow-up project	12
Fig. 2.11	Sketch of the combined backfill body in the KOMPASS drift /SCH 23/.....	13
Fig. 2.12	Test site setup for the KOMPASS backfill body /SCH 23/	13
Fig. 2.13	Construction process of the KOMPASS backfill body. a) Wetting of the KOMPASS material. b) Emplacement of the dry crushed salt backfill. c) KOMPASS backfill body before densification. d) Densification process of the KOMPASS backfill body /SCH 23/	14

Fig. 2.14	Measurements for the settlement and pressure development of the KOMPASS backfill body and the matrix-stabilized backfill body (GESAV) /SCH 23/	15
Fig. 2.15	Measurement of gap between the KOMPASS backfill body and the roof of the drift /SCH 23/	15
Fig. 3.1	Lab tests TUC-V2 (750 d) and TUC-V4 (190 d) performed in the framework of the current project KOMPASS-II.....	17
Fig. 3.2	Lab tests TUC-V5 to TUC-V8 (each in duration of 200 – 240 d) planned to perform in the framework of the follow-up project	18
Fig. 3.3	Test procedure for pre-compaction at dry material. Procedure 1: VK-20 – controlled by different customized compaction speed, sample reversed; procedure 2: VK-32 – controlled by different compaction speed; procedure 3: VK-46 and VK-48 – constant loading rate of 6 kN/d and individual creep phase	22
Fig. 3.4	Creep-test for pre-compaction at dry and wet crushed salt from Sondershausen	23
Fig. 3.5	Creep-test for pre-compaction at dry (0.1 wt.-%, magenta and red) and wet (0.35 wt.-%, blue and green) crushed salt. Dotted lines show the logarithmic trend (extrapolated) for porosity	24
Fig. 3.6	Creep-tests at dry (0.1 wt.-%, magenta and red) and wet (0.35 wt.-%, blue and green) crushed salt. The extrapolated trend of the strain rate is marked in the dotted lines	24
Fig. 3.7	Creep-tests at dry (0.1 wt.-%, magenta and red) and wet (0.35 wt.-%, blue and green) crushed salt. Strain rate vs. porosity – the extrapolated trend is marked by the dotted lines	25
Fig. 3.8	Pre-compaction experiment with distance pieces. Crushed salt was filled in five equal layers with defined material weights, lightly compacted to get a flat surface	26
Fig. 3.9	Pre-compaction – dry/wet crushed salt. +D experiments with distance pieces. -D experiments with a color marker spray between the layers	27
Fig. 3.10	Pre-compaction - dry/wet crushed salt. Porosity distribution for plugs. +D experiments with distance pieces. -D experiments with a color marker spray between the layers	27

Fig. 3.11	Pre-compaction - wet crushed salt with distance pieces. Porosity distribution for plugs (porosity calculated from mass, volume and grain density, calculated from ultrasonic velocity and by measurements with He-pycnometer)	28
Fig. 3.12	Schematic drawing of the large oedometric cell test setup including three strain gauges (“DMS” for German: “Dehnungsmessstreifen”). With increasing compaction, the first and second strain gauges will be passed by the piston and stop delivering measurements	30
Fig. 3.13	KOMPASS-II crushed salt for laboratory tests: a) Specification of the optimized crushed salt from the ELSA II project. b) Crushed salt in Big-Bag as delivered by GSES Sondershausen	30
Fig. 3.14	Preparation of the „large IfG oedometer cell“: Salzgrus (initial state as delivered, pre-treatment (homogenization) and stepwise filling and weight control of the cell	31
Fig. 3.15	Example of examination of homogeneity during filling: a) Infill parameters per layer until maximum height of ca. 80.07 cm. b) Density of each layer alongside cumulative density for the entire specimen (aim was to reach 1.40 g/cm ³ – final measured density was 1.405 g/cm ³). This scheme is presented for all KOMPASS-II experiments of IfG	32
Fig. 3.16	Examination of the porosity distribution in the center and outer sides of the large sample from Experiment GV 4 (wet 3) – initial height approximately 56 cm: (a) The sample was segmented using a chainsaw, first into two halves and then into quarter sections (b) Localization of the samples with respect to the application of force and the cell. (c) Nominal porosity along the sample height (calculated based on grain density; the red curve represents the average porosity profile in the center, serving as a reference).....	33
Fig. 3.17	Crushed salt as a complex multi-phase system with rock salt grains (S), air/gas phase (G), and fluid phase (F).....	34
Fig. 3.18	Diagram of layer and cumulative density distribution in experiment GV3 (wet 2)	37
Fig. 3.19	Porosity (top), compaction rate, i.e., porosity reduction rate (middle), and axial stress (bottom) of experiment GV3 (wet 2)	37
Fig. 3.20	Diagram of layer and cumulative density distribution in experiment GV4 (wet 3)	39

Fig. 3.21	Porosity (top), Compaction rate, i.e., porosity reduction rate (middle), and axial stress (bottom) of experiment GV4 (wet 3)	40
Fig. 3.22	Compaction creep of crushed salt experiment GV 4 (wet 3): (a) Creep phases with porosity reduction vs. creep time per load stage (calculated mean load = average of p_{Ax} , middle and lower strain gauges); (b) Fit and extrapolation of creep curves using a power law ($bx^c + a$), indicating short expected times to full compaction	41
Fig. 3.23	Stress evolution for experiment GV4 (wet 3). Mean stress is calculated as the arithmetic average of axial stress, two times lower strain gauge.....	41
Fig. 3.24	The compacted body was pressed out from the cell after finishing the test. From this large-scale sample several smaller sized cylindrical samples ($l = 80\text{mm}$, $d = 40\text{mm}$) were prepared by sawing small segments and machining with a lathe	42
Fig. 3.25	Diagram of layer and cumulative density distribution in experiment GV5 (wet 4)	43
Fig. 3.26	Two hydraulic pressure cushions were installed in the lower third of the filled cell while filling it with the crushed salt material. One records the horizontal, the other records the vertical acting pressure.....	44
Fig. 3.27	Porosity (top), Compaction rate, i.e., porosity reduction rate (middle, moving 12 h average added as grey line), and axial stress (bottom) of experiment GV5 (wet 4)	46
Fig. 3.28	Fluid volume squeezed out from the crushed salt test GV (wet 4) vs. calculated porosity	47
Fig. 3.29	Stress evolution for experiment GV5 (wet 4). Mean stress is calculated as the arithmetic average of axial stress, two times lower strain gauge. The naming of the pressure cushions corresponds to the measured stress (pressure cushion hor = horizontal stress measured, pressure cushion vert = vertical stress measured)	48
Fig. 3.30	Different processes of progressing crushed salt compaction, edited from /SPA 98/. With decreasing porosity, the dominant processes shift from stress-dependent grain rearrangement and breaking to time-dependent creep deformation	50

Fig. 3.31	Co-plot of mean backfill stress and compaction rate vs. porosity for experiments (a) GV5 (wet 4), (b) GV4 (wet 3) and (c) GV1 (dry), which all have the same load history. Load ramps are shown with gray background. Thin dotted lines indicate the mean backfill stress level (average of axial stress and lower strain gauge) at the beginning of each creep phase	52
Fig. 3.32	Challenges in the framework of the plain-strain pre-compaction	53
Fig. 3.33	Sample quality without sieving in the lab compared to the sample quality by sieving in the laboratory	55
Fig. 3.34	Measurement of the bulging of sample after pre-compression to the required height before performing the pre-compaction test.....	56
Fig. 3.35	Verification of homogeneity of pre-compacted dry sample ($w = 0.1\%$)	58
Fig. 3.36	Verification of homogeneity of pre-compacted wet sample ($w = 1\%$)	59
Fig. 3.37	Results of test series considering (a) a variation of pre-compaction duration and (b) a variation of water content of samples (porosity difference means $\varphi_{\text{start}} - \varphi_{\text{end}}$). The dashed line indicated the trend	59
Fig. 3.38	Creation of four samples pre-compacted under plain-strain conditions considering target porosity and sample size for further compaction tests by GRS	60
Fig. 3.39	Measurements of ultrasonic wave velocity belonging to pre-compacted samples from the projects KOMPASS-I, KOMPASS-II as well as the sample, which has been compacted in the long-term test TUC-V4	61
Fig. 3.40	M5 - Load frame with cell and principal sketch (with $F_2 =$ friction force and $F_1 =$ axial force) and M4 – smaller oedometric cell (200 mm diameter)	64
Fig. 3.41	Displacement controlled oedometric tests – test parameter: run time, moisture content, temperature, starting porosity and material	65
Fig. 3.42	Comparison of strain-controlled oedometer tests – evolution of a) backfill resistance; b) porosity; c) evolution of backfill resistance for the short tests; d) relation porosity ~ backfill resistance for all tests	70
Fig. 3.43	Backfill resistance ~ Porosity for different strain rates: a) 0.36 mm/h = $6.7E^{-7}$ 1/s; b) 0.036 mm/h = $6.7E^{-8}$ 1/s; c) 0.0036 mm/h = $6.7E^{-9}$ 1/s; d) 0.00036 mm/h = $6.67E^{-10}$ 1/s	71

Fig. 3.44	Decay of backfill resistance ~ reference time of relaxation phase for different compaction levels, note different time scales	72
Fig. 3.45	Oedometric multistage creep test – Estimation of deformation rate after 20 MPa a) Deformation rate for 2 nd load stage to reference time for the 20 MPa stage b) Deformation rate to logarithmic time axis, yellow time range for calculating the potential trend function and the value calculated from it for day 7	73
Fig. 3.46	Oedometric multistage creep test - small cell Ø 200 mm - different moisture: a) porosity, b) deformation rate, c) stress regime, d) deformation rate vs. porosity.....	74
Fig. 3.47	Oedometric multistage creep test – scaling effects for dry and wet crushed salt with different cell diameter Ø 300, 200, 100 mm: a) porosity; b) deformation rate; c) stress regime; d) deformation rate vs. porosity	75
Fig. 3.48	Oedometric multistage creep test – moisture and scaling effects for different cell diameter Ø 300, 200, 100 mm: a) porosity end and after 20 MPa; b) deformation rate for 20 MPa after 7 days – end of second loading step	76
Fig. 3.49	Triaxial testing system with load frame, sketch of the pressure cell and the burette system	77
Fig. 3.50	Pre-compaction triaxial test – axial stress and porosity.....	80
Fig. 3.51	Test parameters of BGR triaxial test including run time, initial moisture content, temperature, starting porosity and max. average stress. The final porosity is given in the legend.....	81
Fig. 3.52	Example for determination of end values for the axial deformation rate: thin line data, thick line used data area for trend.....	82
Fig. 3.53	Axial deformation rates last loading step 20 MPa for TK-037, TK-041, TK-045 & old TK-031, TK-033. a) in relation to the reciprocal reference time from start 20 MPa step; b) in relation to the porosity; c) axial deformation rate for 5 % porosity from trend in b)	88
Fig. 3.54	Cross section of BGR (left), IfG (middle) and TUC sample (right) with CT before triaxial compression test.....	90
Fig. 3.55	Configuration of the triaxial cell at GRS	91
Fig. 3.56	Distribution of stress for the isotropic approach	92
Fig. 3.57	Development of axial, radial and volumetric strain in BGR sample	95

Fig. 3.58	Development of axial, radial and volumetric strain in IfG sample.	96
Fig. 3.59	Development of axial, radial and volumetric strain in TUC sample.....	97
Fig. 3.60	Axial strain rate [1/s] versus axial strain [%] of the BGR, IfG and TUC samples in the triaxial compression test at GRS	98
Fig. 3.61	Radial strain rate [1/s] versus radial strain [%] of the BGR, IfG and TUC samples in the triaxial compression test at GRS.....	99
Fig. 3.62	Setup „New IfG crushed salt compaction cell“	101
Fig. 3.63	Isotropic creep tests were conducted to demonstrate the influence of moisture.....	102
Fig. 3.64	Test experiment for crushed salt compaction in the “new IfG compaction cell”. (a) Compaction curve (system stiffness compensated) with the various load stages and the calculated porosity evolution. (b) Relative change of ultrasonic travel times, normalized to the initial value (note: S-wave was likely detected with some delay)	103
Fig. 3.65	Test bench at TUC employed to perform long-term compaction tests and the EMC system for volume change measurement	105
Fig. 3.66	Test TUC-V2 – boundary conditions and investigated ranges for influencing factors in relation to in situ relevant ranges (sig_z – axial stress, sig_x – confining stress, sig_m – mean stress, sig_v – deviatoric stress).....	106
Fig. 3.67	Test TUC-V4 – boundary conditions and intervals for investigated influencing factors in relation to in situ relevant ranges	107
Fig. 3.68	Test TUC-V2 – measurements of vertical strain, volumetric strain and porosity (derived from the volumetric strain)	109
Fig. 3.69	Test TUC-V2 – measurements of vertical and volumetric strain rates	110
Fig. 3.70	Test TUC-V2 – bandwidth of measurements of vertical strain, volumetric strain and horizontal strain, including measurement and calibration uncertainties as well as the influence of temperature fluctuation	110
Fig. 3.71	Test TUC-V4 – measurements of vertical strain, volumetric strain and porosity (derived from volumetric strain)	111
Fig. 3.72	Test TUC-V4 – measurements of vertical and volumetric strain rates	112

Fig. 3.73	Initial comparison of test results TUC-V2 and TUC-V4 – measurements of volumetric strain rates and ultrasonic wave velocities (normalized to the assumed rock salt value of 4500 m/s)	113
Fig. 3.74	Loading history for the multi-stage long-term test TUC-V2 (phase I – 150 d)	114
Fig. 3.75	Comparison of the test results for TUC-V2 - phase I and TK-044 – volumetric and vertical strains.....	115
Fig. 3.76	Comparison of the test results for TUC-V2 – phase I and TK-044 – volumetric and vertical strain rates.....	116
Fig. 3.77	Comparison of the test results for TUC-V2 - phase I, TK-044 and TK-045 – volumetric and vertical strains.....	117
Fig. 3.78	Representative examples of permeability measurement results obtained for samples TK-031 and TK-033 in regard to the influence of confining pressure, gas pressure difference and gas flow time	120
Fig. 3.79	Comparison of permeability results of KOMPASS-II and REPOPERM II /KRÖ 17/.....	120
Fig. 4.1	Sum-curves for the different starting GSD	125
Fig. 4.2	Sketches of the sampled locations for the sections used. Samples S2 (BGR VK-043), S3 and (TUC-14) were prepared from cylinder halves; (a) Sample S4 (IfG-684) was prepared from a more cubic shaped sample; (b) The dotted lines in the sketches and the images exemplary show the size of the prepared thick section. Scale bars are 3 cm. White arrow in c S4 point to lenses of fine-grained material ...	126
Fig. 4.3	The AOI (red boundary) in sample S1 (loose crushed salt). 1547 grains (marked in green) were segmented. Scale bar is 3.2 mm and image width is 24.5 mm	128
Fig. 4.4	Overview of the AOI (red boundary) in sample S2 (BGR VK-043). 2677 grains (marked in green) were segmented. Scale bar is 2.4 mm and image width is 27 mm	128
Fig. 4.5	Overview of the AOI (red boundary) in sample S3 (TUC-14). 5491 grains (marked in green) were segmented. Scale bar is 2.3 mm and image width is 30 mm	129

Fig. 4.6	Sections of polished thick sections, made of the Samples S1 (a: originating from the starting material), S2 (b: originating from test BGR VK-043), S3 (c: originating from test TUC-14) and S4 (d: originating from test IfG-684). White arrows mark porosity and scale bars in each micrograph are 1 mm	131
Fig. 4.7	Micrograph and zoom-in on a lens of fine grained material in S4. White arrows mark tight, indenting grain boundaries (c) and orange arrows mark bent grains	132
Fig. 4.8	Grain with intragranular (green arrows) fractures in sample S1. Note also the fully shattered grain, partly offset along its fractures (red arrow). Scale bar is 1 mm	134
Fig. 4.9	Grain with lines of fluid inclusions (light blue arrow) in the sample S1. Scale bar is 500 μm	135
Fig. 4.10	Grain with subgrains (thin black lines) in the sample S1. Scale bar is 500 μm and image width is 1.5 mm	137
Fig. 4.11	Contact area between grains showing dense deformation/slip bands (red arrows) – sample S2. Recrystallized grains are also visible at the contact. Scale bar is 200 μm and image width is 1 mm.....	138
Fig. 4.12	Contact area between grains with dense slip bands (red arrow) in the larger, upper grain – sample S3. Scale bar is 200 μm and image width is 1 mm.....	138
Fig. 4.13	Contact area between grains showing dense slip bands (red arrows) in the upper and central grains in the image – sample S4. Scale bar is 200 μm and image width is 1 mm.....	139
Fig. 4.14	Bent grain (orange arrow) from sample S2. Scale bar is 200 μm and image width is 1.4 mm	139
Fig. 4.15	Bent grains (orange arrows) in sample S3. Scale bar is 300 μm and image width is 1.7 mm	140
Fig. 4.16	Bent and fractured grain locked (orange arrow) between two others in sample S4 (IfG-684). Scale bar is 200 μm and image width is 1.4 mm	140
Fig. 4.17	Tight, indenting/truncated grain boundary (magenta arrow) in sample S2. Scale bar is 200 μm and image width is 0.8 mm.....	142
Fig. 4.18	Tight, indenting/truncated grain boundary (magenta arrow) in sample S3. Scale bar is 300 μm and image width is 1.3 mm.....	142

Fig. 4.19	Tight, indenting/truncated grain boundary with small, recrystallized grains (magenta arrow) in the sample S4. Scale bar is 200 μm and image width is 1 mm	143
Fig. 4.20	Contact area between two large grains with recrystallized, microstructure-free grains (white arrows) in sample S2. Image width is 1.3 mm	144
Fig. 4.21	Contact area between two large grains with recrystallized, microstructure-free grains (white arrows) in sample S3. Image width is 0.7 mm	144
Fig. 4.22	Truncated contact area between two large grains with recrystallized, microstructure-free grains (white arrows) in sample S4. Image width is 0.8 mm	145
Fig. 4.23	Results of semi-quantitative (subjective) evaluation of microstructural indicators for deformation mechanisms. The term “tight grain boundaries” refers to tight, indenting, truncating or interpenetrating grain boundaries /SVE 22/	146
Fig. 4.24	The slopes of the regression lines (S1: $D = -1.56$; S2: $D = -1.73$; S3: $D = -1.55$) illustrate the differences in self-similarity of the samples' grain sizes	147
Fig. 4.25	Cumulative GSD of the three investigated AOIs.....	148
Fig. 4.26	Grain size parameters (GSP) axial ratio (ARNorm) and circularity calculated and plotted for the samples S1 (a), S2 (b) and S3 (c). Darker color illustrates higher quantity of grains. Shape examples (d) GSPs' ratio of some generic shapes (for illustration).....	149
Fig. 4.27	Pre-compacted and compacted granular salt samples from oedometric tests at IfG (a through g) and triaxial tests at TUC (h through k)	156
Fig. 4.28	Photomicrographs from “Big Cell” pre-compacted samples under “dry” (a, c, e, g,) and “wet” (b, d, f, h) conditions. Arrows: fractures (red), fluid inclusions (blue), TITIGB (green), deformation bands (yellow), recrystallization (white)	160
Fig. 4.29	Photomicrographs from IfG long-term compacted samples at 10MPa under dry (a, c, e, g) and wet (b, d, f, h) conditions. Arrows: fractures (red), fluid inclusions (blue), TITIGB (green), deformation bands (yellow), recrystallization (white)	163
Fig. 4.30	Photomicrographs from IfG long-term compacted samples at 20MPa under “dry” (a, c, e, g) and “wet” (b, d, f, h) conditions	166

Fig. 4.31	Photomicrographs from IfG long-term compacted sample at 30 MPa under dry conditions. Arrows: fluid inclusions (blue), TITIGB (green), deformation bands (yellow), recrystallization (white)	167
Fig. 4.32	Photomicrographs from TUC pre-compacted samples under dry (a, c, e) and wet (b, d, f) conditions. Arrows: fractures (red), fluid inclusions (blue), TITIGB (green), deformation bands (yellow), recrystallization (white)	170
Fig. 4.33	Overview of grain size mixtures used in this study for (a) a single grain size fraction of 137 μm , (b) a 50 – 50 % mixture of 137 and 450 μm grains (Mixture 1), (c) a 75 – 25 vol-% mixture of 137 and 450 μm grains (Mixture 2), and (d) a log-normal volume distribution with a mean of 225 μm , a mode of 183 μm and a standard deviation of 0.45. For Mixture 3, a mixture was constructed using the available sieves that approached the same distribution as the continuous distribution shown in d (solid line). Note that the y-axis indicates the volume probability, for which the scales in a, b, c and d are different.....	174
Fig. 4.34	Strain rate versus stress data obtained from relaxation steps on a brine-saturated sample with a mean grain size of 137 μm	175
Fig. 4.35	Strain rate versus stress data obtained during brine-saturated experiments on aggregates with grain sizes between 115 and 450 μm at a porosity of 10 % (solid lines).	176
Fig. 4.36	Strain rate versus stress for the experiments on (a) Mixture 1 and (b) Mixture 2 and single grain size aggregates (137 and 450 μm) at 5 % porosity (solid lines)	177
Fig. 4.37	(a) Volumetric strain (/day) versus backfill porosity (%) for a backfilled repository in rock salt grain size of 0.3, 1.0 and 3.0 mm, using an analytical solution for coupled-convergence. b) Backfill porosity (%) versus time (years) until a porosity of 1 % is reached. c) Predicted mean stress evolution versus backfill porosity and (d) Mean stress versus backfill porosity in-situ (model) and during typical long-term experiments /KOM 20/ and stress relaxation experiments (example of experiment on sample with 137 μm)	179
Fig. 5.1	Classification schemes of deformation behavior in salt - Assignment in mechanics and microstructure analysis (according to /ELL 04/)	186
Fig. 5.2	Idealized model of a unit crystal with peak-to-peak contact to six adjoining crystals	191
Fig. 5.3	Flow potential at two different relative densities	198

Fig. 5.4	Test TK-031 from BGR – measurements for compaction rate and porosity, boundary conditions and investigated ranges of the influencing factors in comparison to the in situ relevant ranges.....	208
Fig. 5.5	Tests GRS-dry/GRS-0.1%/GRS-wet from GRS – measurements for porosity, boundary conditions and investigated ranges of the influencing factors in comparison to the in situ relevant ranges.....	209
Fig. 5.6	Database preparation for the five chosen tests and comparison of measurements with analytical curves for the dependency of compaction from porosity in the newly developed constitutive model EXPO-COM.....	213
Fig. 5.7	Structure of the new constitutive model EXPO-COM for the material behavior of crushed salt.....	214
Fig. 5.8	Back-analysis of selected tests used to develop the new constitutive model EXPO-COM from TUC.....	220
Fig. 5.9	Variants of the porosity function of elasticity.....	224
Fig. 5.10	Variants of the Functions <i>h1</i> and <i>h2</i> of Grain Deformation; <i>hHK</i> , <i>hmK</i> and <i>hm2K</i> with <i>c</i> = 0.7 and if required <i>r</i> = 1.2	228
Fig. 5.11	Increase of the models' validation status by the usage of the measurement database from test TUC-V2 (KOMPASS reference material).....	234
Fig. 5.12	Discretization of the TUC-V2 laboratory test and validation of the boundary conditions.....	235
Fig. 5.13	Comparison of simulation and laboratory measurements for different strains.....	237
Fig. 5.14	Simulated void ratio against measurement (left) and decomposition of the creep strain (right).....	237
Fig. 5.15	Calibration of the flow potential parameters against the radial-to-axial strain rate ratio. The experimental strain rate ratio is smoothed using a LOWESS algorithm with a smoothing window of 15 days (shorter windows only affect the magnitude and fluctuations around the large peaks where $\mathcal{R} > 1$, which does not affect the calibration).....	244
Fig. 5.16	Calibrated response of the Callahan model to TUC-V2.....	247
Fig. 5.17	Simulation of the pre-compaction test with the calibrated model.....	248
Fig. 5.18	CODE_BRIGHT model with mesh of the TUC-V2 test.....	250

Fig. 5.19	Auxiliary functions <i>gDCve</i> and <i>gDCde</i> as implemented in CODE_BRIGHT (modified after /OLI 02/) and the function <i>gDCv</i> as derived from the experimental data of the TUC-V2 test /FRI 23/.....	251
Fig. 5.20	Function <i>gDCve</i> . Blue: as implemented in CODE_BRIGHT, yellow: as derived from the experimental data of TUC-V2, red: as derived from the modification using an equivalent void ratio.....	252
Fig. 5.21	Porosity for the TUC-V2 test. Black: measurement, blue: simulation with initial data set /KOM 20/ and red: simulation with equivalent void ratio	253
Fig. 5.22	Volumetric strain rate for the TUC-V2 test. Black: measurement data, blue: simulation with the initial dataset, red: simulation using the equivalent void ratio, grey: mean stress and deviatoric stress.....	253
Fig. 5.23	Overview of all individual functional relations and influencing factors with the corresponding phases of test TUC-V2	254
Fig. 5.24	Influence of porosity on the compaction rate: measured values (normalized), theoretical curve from EXPO-COM with a tripartite approach and with the corresponding material parameters for the functional relations.....	255
Fig. 5.25	Influence of mean stress on the compaction: measured values, theoretical curve from EXPO-COM and corresponding material parameters	256
Fig. 5.26	Influence of temperature on the compaction: measured values and theoretical curve from EXPO-COM in comparison to the model approaches Arrhenius and C-WIPP (no dependency from temperature).....	257
Fig. 5.27	Diagram for the temperature dependence of the compaction behavior: measured points and theoretical curves from EXPO-COM compared to the model approaches Arrhenius and C-WIPP (no dependency from temperature).....	257
Fig. 5.28	Influence of porosity on the shear creep rate: measured values and theoretical curves from EXPO-COM ('EXPO-COM st' in the modLubby2 part of the model and 'EXPO-COM_eff' for the total effective strain rates from the both model parts producing volume true	258
Fig. 5.29	Back-analysis results for the volumetric strains with two different parameter sets for EXPO-COM: UB (upper-bound) and LB (lower-bound)	259

Fig. 5.30	Scattering of the parameter set UB and LB produced in regard to the influencing factor porosity due to different extrapolations of the theoretical curve in the not investigated ar-ea of porosity (high to middle range).....	260
Fig. 5.31	Comparison of the back-analysis results from EXPO-COM performed on a single element model as well as for a cylinder-segment model	260
Fig. 5.32	Relationship between the logarithmic values of the material parameters a and c of the constitutive model to the solution.....	264
Fig. 5.33	Mean stress vs. change in deformation within the stage of isotropic load increase $\Delta\sigma_0$ (2) to $\Delta\sigma_0$ (6) – a.) Measured axial and volumetric strain increment; b.) Calculated radial expansion increment.....	265
Fig. 5.34	Stress deformation behavior of the deviatoric load cycles $\Delta S\sigma 01$ to $\Delta S\sigma 05$ during the phase of isotropic load increase – a.) Measured axial stress vs. measured axial and volumetric strain increment; b.) Measured radial stress vs. calculated radial stress	266
Fig. 5.35	Stress deformation behavior of the deviatoric load cycles $\Delta S201$ to $\Delta S207$ during the phase of constant isotropic load – a.) Measured axial stress vs. measured axial and volumetric strain increment; b.) Measured radial stress vs. calculated radial stress	266
Fig. 5.36	Measured and calculated deformation behavior in axial direction – a.) Increment of axial stress in the deviatoric load cycles $\Delta S\sigma 01$ to $\Delta S\sigma 05$; b.) Increment of axial stress in the deviatoric load cycles $\Delta S201$ to $\Delta S207$; c.) Increment of the mean stress during the phase of isotropic load increase $\Delta\sigma 02$ to $\Delta\sigma 06$	268
Fig. 5.37	Measured deformation behavior in the thermal load cycles $\Delta T(1)$ to $\Delta T(3)$ as a function of temperature – a.) Axial strain increment; b.) Volumetric strain increment	269
Fig. 5.38	Comparison of measured and calculated thermal deformation in the thermal load cycles $\Delta T(1)$ to $\Delta T(3)$ depending on temperature – a.) Axial strain increment; b.) Volumetric strain increment.....	270
Fig. 5.39	Comparison of measured and calculated deformation behavior – a.) Deformation behavior over time; b.) Rate of pore ratio over pore ratio based on calculation; c.) Axial stress over axial strain increment during deviatoric load cycles $\Delta S\sigma 01$ to $\Delta S\sigma 05$; d.) Axial strain increment over temperature change in the thermal load cycles $\Delta T1$ to $\Delta T3$	271

Fig. 5.40	Illustration of analytical procedure for parameter determination for IfG CWIPP. (a) Data and model fit for porosity-time curves for each isotropic load stage (data: blue, model: black). Cyan curves show intermittent deviatoric load phases. These phases are compensated for by an offset. (b) Analytical fit term containing C_0 and C_1	273
Fig. 5.41	Arrhenius plot of temperature dependent volumetric strain rates and analytical fit.....	274
Fig. 5.42	Porosity evolution over time for the Benchmark calculation of the TUC-V2 experiment with numerical result in blue and laboratory measurements in black. The grey curves show load phases and durations.....	276
Fig. 5.43	Deviatoric strain evolution over time for the Benchmark calculation of the TUC-V2 experiment with numerical result in blue and laboratory measurements in black. The grey curves show load phases and durations.....	276
Fig. 5.44	Volumetric strain rate evolution over time for the Benchmark calculation of the TUC-V2 experiment with numerical result in blue and laboratory measurements in black. The grey curves show load phases and durations	277
Fig. 5.45	Benchmark results: volumetric strain and porosity	278
Fig. 5.46	Benchmark results: vertical and horizontal strain	278
Fig. 5.47	Benchmark results: volumetric strain rates for phase I of the test	280
Fig. 5.48	Benchmark results: effective strain rates for phases I and II of the test	281
Fig. 5.49	Benchmark results: effective strain rates for phase V of the test.....	282
Fig. 5.50	Benchmark results: volumetric strains for phases IV and V of the test in regard to the temperature impact	283
Fig. 5.51	Benchmark results: volumetric strain rates for phases IV and V of the test in regard to temperature impact	283
Fig. 5.52	Benchmark results: volumetric strain rates for different microstructural mechanisms from the model BGR_CRUSHED SALT3	284
Fig. 5.53	Role of the virtual demonstrator in the constitutive development process.....	285

Fig. 5.54	Geological reference sections from /BOL 18/ for a salt-hosted repository in bedded salt. The encircled red rectangle represents a repository at 800 m depth, which would correspond to the boundary conditions chosen for the virtual demonstrator	286
Fig. 5.55	Geometry and boundary conditions of the virtual demonstrator model. (a) Full scale view of the 2D model, (b) simplified technical drawing of a drift from the generic KOSINA repository design (/BOL 18/), (c) close-up view of the implemented drift in the virtual demonstrator	287
Fig. 5.56	Stationary creep data and curve chosen for the virtual demonstrator (blue curve), representing an additive two-component power law with a linear creep branch for pressure solution creep (dotted black line) and a $n=5$ power law for dislocation creep (\approx BGRa creep law)	289
Fig. 5.57	Discretization of the virtual demonstrator with JIFE 6.3.....	290
Fig. 5.58	Discretization of the virtual demonstrator in CODE_BRIGHT	291
Fig. 5.59	Mesh used in demonstrator simulation. a) Close-up view of backfill and host rock salt mesh and b) view of full model domain	293
Fig. 5.60	Results from the open drift benchmark calculation. (a) Close-up view of the converging drift showing z-displacement after 10 years and points to document convergence and stresses. (b-d) x/z-displacement, and mean stress curves, respectively, for all partners. Note that GRS and BGR curves lie on top of each other, the same applies to IfG, TUC, BGE-TEC and Sandia.....	294
Fig. 5.61	Averaged porosity vs. time curves for demonstrator runs of all partners using the parameter sets derived from the TK-031 compaction experiment. Results for a host with (a) two-component creep, and (b) a single component (BGRa) creep	296
Fig. 5.62	Results for drift-averaged volumetric strain rates (a, b) and mean stress (c, d) vs. porosity for host with two component (left column) and single-component (BGRa) creep (right column) for the TK-031 reference demonstrator simulation.....	298
Fig. 5.63	Averaged porosity vs. time curves for demonstrator runs of all partners using the parameter sets derived from the TUC-V2 compaction experiment.....	300
Fig. 5.64	Results of demonstrator runs of all partners using the parameter sets derived from the TUC-V2 compaction experiment. Drift-averaged volumetric strain rate (a) and mean stress (b) vs. porosity	302

Fig. 5.65	Results of demonstrator runs using TUC-V2 derived parameters. Volumetric strain rate vs. porosity at two locations within the backfill body, (a) centrally above floor (b) centrally below roof	303
Fig. 5.66	Results of the demonstrator runs using TUC-V2 derived parameters, but without additional gravity (stress boundary conditions remain) to isolate gravitational effects. Note that GRS and BGR could not provide such tests due to their numerical implementation in in-house software. Volumetric strain rate vs. porosity at two locations within the backfill body, (a) centrally above floor (b) centrally below roof	305
Fig. 5.67	Results of demonstrator runs using TUC-V2 derived parameters. Evolution of mean stress and von-Mises stress (“effective stress”) at the roof, center and wall of the backfill body. Each im-age represents a different partner (constitutive model): (a) IfG (IfG-CWIPP), (b) BGE-Tec (Hein-Korthaus), (c) Sandia (Callahan), (d) TUC (EXPO-COM), (e) GRS (Olivella-Gens). (f) Indications history locations for numerical time series	307
Fig. A.1	OE 117 a) Evolution of load resistance, friction and porosity b) Load resistance versus porosity, colors represent the differing compaction speeds.....	351
Fig. A.2	OE 118 a) Evolution of load resistance, friction and porosity b) Load resistance versus porosity, colors represent the differing compaction speeds.....	353
Fig. A.3	OE 119 a) Evolution of load resistance, friction and porosity b) Load resistance versus porosity, colors represent the differing compaction speeds.....	355
Fig. A.4	OE 120 a) Evolution of load resistance, friction and porosity b) Load resistance versus porosity, colors represent the differing compaction speeds.....	357
Fig. A.5	OE 122 a) Evolution of load resistance, friction and porosity b) Load resistance versus porosity, colors represent the differing compaction speeds.....	359
Fig. A.6	OE 123 a) Evolution of load resistance, friction and porosity b) Load resistance versus porosity, colors represent the differing compaction speeds.....	361
Fig. A.7	TK-037 a) stress regime and sample temperature b) volume change and sample high c) strain and strain rates d) experimental data e) axial strain ~ strain rate.....	363

Fig. A.8	TK-38 a) stress regime and sample temperature; b) volume change and sample high; c) strain and strain rates; d) experimental data; e) axial strain ~ strain rate.....	366
Fig. A.9	TK-041 a) stress regime and sample temperature; b) volume change and sample high; c) strain and strain rates; d) experimental data; e) axial strain ~ strain rate.....	368
Fig. A.10	TK-42 a) stress regime and sample temperature; b) volume change and sample high; c) strain and strain rates; d) experimental data; e) axial strain ~ strain rate.....	370
Fig. A.11	TK-044 a) stress regime and sample temperature; b) volume change and sample high; c) strain and strain rates; d) experimental data e) axial strain ~ strain rate.....	372
Fig. A.12	TK-045 a) stress regime and sample temperature; b) volume change and sample high; c) strain and strain rates; d) experimental data; e) axial strain ~ strain rate.....	375
Fig. A.13	TK-045 long creep phase 20 MPa: porosity and axial strain rate ~ reciproke time with trends	377

List of Tables

Tab. 3.1	Evolution of test procedure	20
Tab. 3.2	Test parameters for all pre-compaction tests	21
Tab. 3.3	Experimental data of samples in the initial and final compaction state, respectively.....	35
Tab. 3.4	Layer and bulk sample preparation parameters for of experiment GV3	36
Tab. 3.5	Layer and bulk sample preparation parameters for of experiment GV4 (wet 3)	38
Tab. 3.6	Layer and bulk sample preparation parameters for of experiment GV5 (wet 4)	43
Tab. 3.7	Overview of pre-compaction tests and prepared samples performed by TUC (colored by aims)	57
Tab. 3.8	Displacement controlled oedometric tests – parameter and end porosity	67
Tab. 3.9	Multistage oedometric test – parameter, porosity, deformation rate after 20 MPa	73
Tab. 3.10	Test parameter for the triaxial compaction tests by BGR	78
Tab. 3.11	Test parameter and end porosity	83
Tab. 3.12	Results – deformation and deformation rate at the end of every creep phase.....	86
Tab. 3.13	Overview about crushed salt samples for compaction tests at GRS.....	89
Tab. 3.14	Sample properties before testing	89
Tab. 3.15	Stress states of triaxial compaction tests in GRS lab	92
Tab. 3.16	Parameters after 200 days compaction.....	99
Tab. 3.17	Overview of the permeability test results.....	119
Tab. 4.1	Overview of microstructurally investigated samples by BGR.....	125
Tab. 4.2	List of distinguished microstructural indicators and corresponding deformation mechanisms, after /BLE 02/	133

Tab. 4.3	Spot checked subgrain extent with size of the spot-checked region (number of subgrains), minimum and maximum ECAD (Equ. 4-5) and calculated differential stress (according to Equ. 4-4). Calculated differential stress shows the lowest value, than the arithmetic average, than the highest value. Note: outliers are included	136
Tab. 4.4	Summary of samples and associated experimental test conditions.....	155
Tab. 5.1	Functional dependencies between mean coordination number and porosity /HEI 91/	190
Tab. 5.2	Material parameters for TUC-V2 simulation in the BGR-CRUSHED SALT3 framework.....	236
Tab. 5.3	Model parameters for intact Sondershausen salt /DEV 11/	239
Tab. 5.4	Loading history for TUC-V2. The stress is linearly interpolated between the given times	242
Tab. 5.5	Temperature history for TUC-V2. The temperature is linearly interpolated between the given times.....	242
Tab. 5.6	Calibrated flow potential parameters for TUC-V2.....	243
Tab. 5.7	Calibrated creep consolidation parameters for TUC-V2	245
Tab. 5.8	Parameter sets for EXPO-COM model determined from the test TUC-V2	261
Tab. 5.9	Material parameters for the TUC-V2 simulation with the material model Hein-Korthaus	263
Tab. 5.10	IfG-CWIPP parameters relevant for compaction creep based on TUC-V2.	275
Tab. A.1	OE 117 - Experiment phases and respective key values	352
Tab. A.2	OE 117 - results.....	352
Tab. A.3	OE 118 - Experiment phases and respective key values	354
Tab. A.4	OE 118 - results.....	354
Tab. A.5	OE 119 - Experiment phases and respective key values	356
Tab. A.6	OE 119 - results.....	356
Tab. A.7	OE 120 - Experiment phases and respective key values	358
Tab. A.8	OE 120 - results.....	358

Tab. A.9	OE 122 - Experiment phases and respective key values	360
Tab. A.10	OE 122 - results.....	360
Tab. A.11	OE 123 - Experiment phases and respective key values	362
Tab. A.12	OE 123 - results.....	362
Tab. A.13	TK-037 experimental data.....	364
Tab. A.14	TK-037 results – deformation, deformation rates at the end of pressure steps	365
Tab. A.15	TK-38 experimental data.....	367
Tab. A.16	TK-38 results – deformation, deformation rates at the end of pressure steps	367
Tab. A.17	TK-041 experimental data.....	369
Tab. A.18	TK-041 results – deformation, deformation rates at the end of pressure steps	369
Tab. A.19	TK-42 experimental data.....	371
Tab. A.20	TK-42 results – deformation, deformation rates at the end of pressure steps	371
Tab. A.21	TK-044 experimental data.....	373
Tab. A.22	TK-044 results – deformation, deformation rates at the end of pressure steps	374
Tab. A.23	TK-045 experimental data.....	376
Tab. A.24	TK-045 results – deformation, deformation rates at the end of pressure steps	377

A Compaction test executed by BGR

A.1 Oedometer

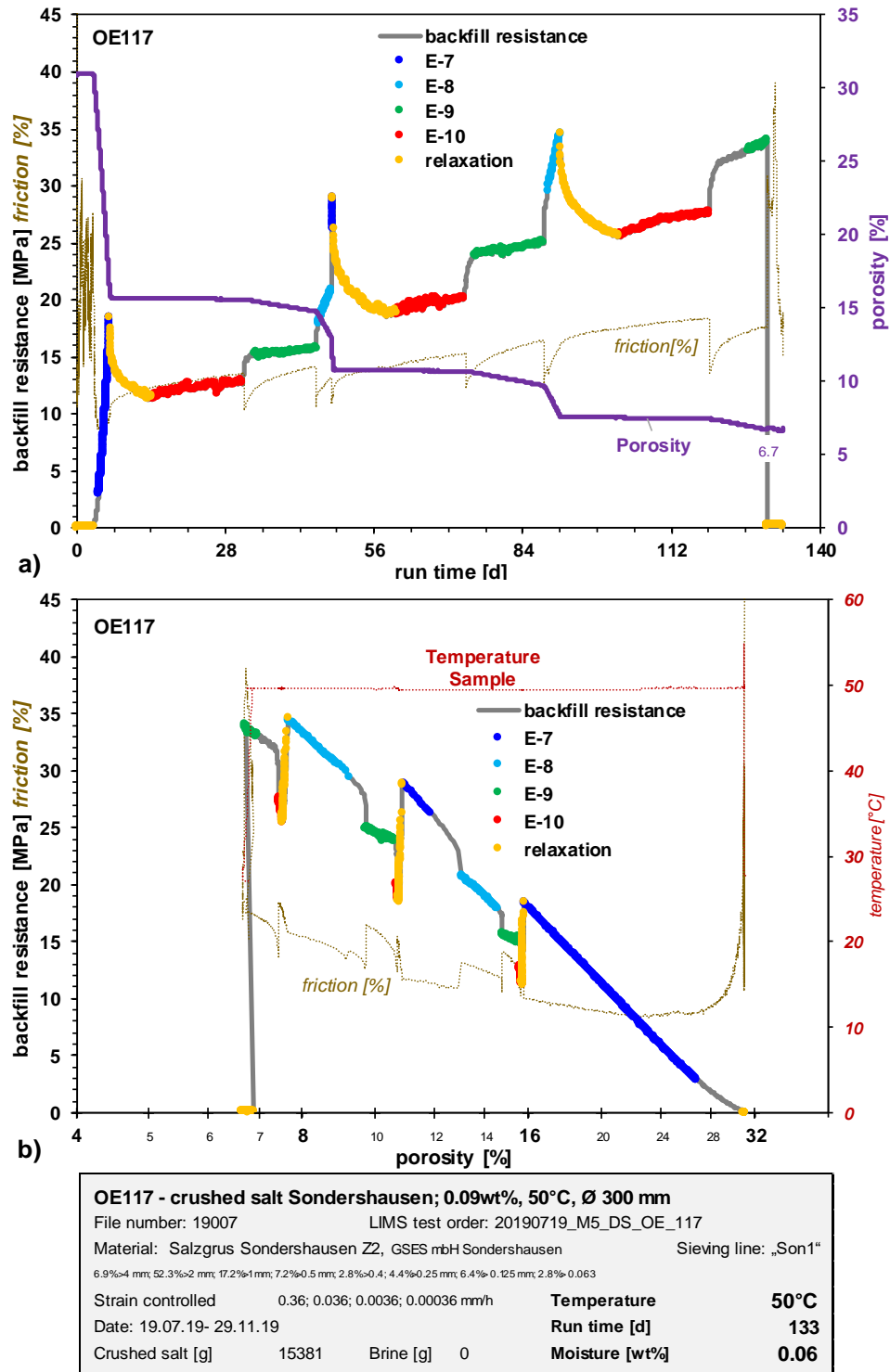


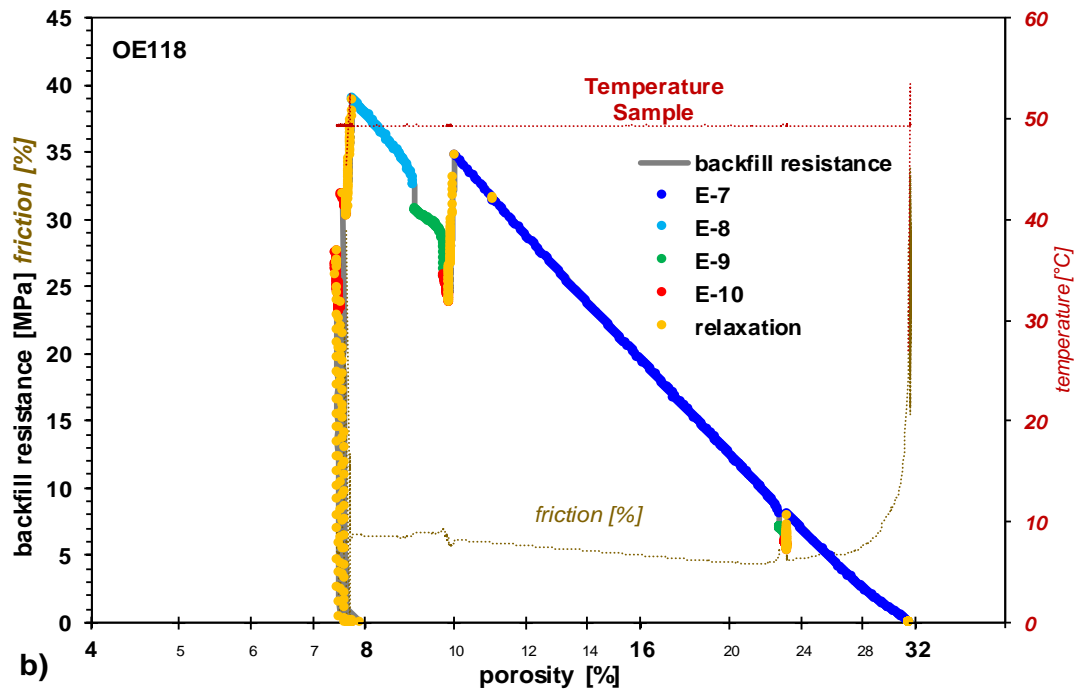
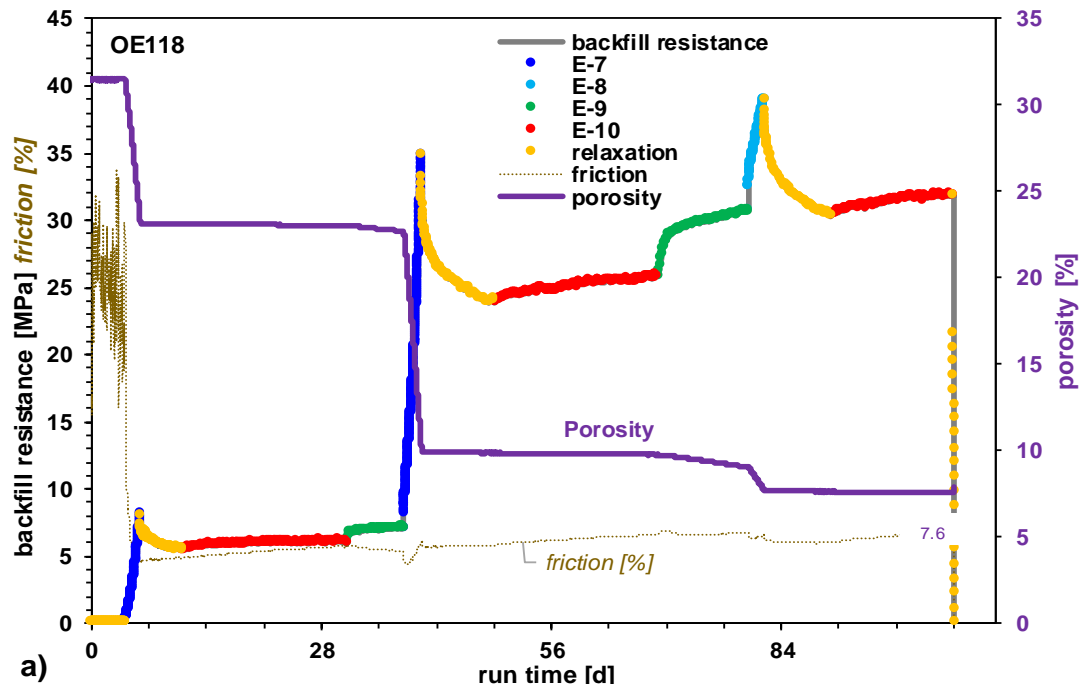
Fig. A.1 OE 117 a) Evolution of load resistance, friction and porosity b) Load resistance versus porosity, colors represent the differing compaction speeds

Tab. A.1 OE 117 - Experiment phases and respective key values

Action	Run time [d]	Duration [d]	Backfill resistance [MPa]	Friction [%]	Porosity [%]
heating	0.0		0.1		30.91
E-7	3.1	3.1	0.1	23.4	30.99
relaxation	6.2	7.8	18.5	10.0	15.77
E-10	14.0	17.1	11.5	12.3	15.68
E-9	31.1	14.0	12.6	13.5	15.60
E-8	45.1	2.8	15.7	14.1	14.76
E-7	47.9	0.3	23.0	11.0	12.90
relaxation	48.3	11.8	28.9	11.7	10.87
E-10	60.1	12.8	18.7	14.2	10.75
E-9	73.0	15.0	20.2	15.3	10.69
E-8	88.0	3.0	25.0	16.5	9.71
relaxation	91.0	11.1	34.6	15.8	7.65
E-10	102.1	16.9	25.6	17.5	7.53
E-9	119.0	11.0	27.6	18.4	7.43
Failure / power crash	130.0		0.1	24.6	6.89
cooling	131.1		0.2		6.85
end of test	133.0		0.0	15.1	6.79

Tab. A.2 OE 117 - results

OE 117 - crushed salt Sondershausen; 0.09wt%, 50°C, Ø 300 mm					
File number: 19007			LIMS test order: 20190719_M5_DS_OE_117		
Material: Salzgrus Sondershausen Z2, GSES mbH Sondershausen				Sieving line: „Son1“	
6.9% >4 mm; 52.3% >2 mm; 17.2% >1 mm; 7.2% >0.5 mm; 2.8% >0.4; 4.4% >0.25 mm; 6.4% > 0.125 mm; 2.8% > 0.063					
Strain controlled	0.36; 0.036; 0.0036; 0.00036 mm/h			Temperature	50°C
Date: 19.07.19- 29.11.19				Run time [d]	133
Crushed salt [g]	15381	+ Brine [g]	0	Moisture [wt%]	0.06
Density _{dry} [g/cm ³]	2.174	Density _{wet} [g/cm ³]			2.176
High [mm]	145.13	-			107.51
Mass [g]	15381	-			15371
Volume [cm ³]	10248	-			7579
Pore number [-]	0.45	-			0.07
Porosity [%]	31.0	-			6.79
				friction@ Sig max [%]	15.8



OE118 - crushed salt Sondershausen; 0.09wt%, 50°C, Ø 300 mm			
File number: 19058	LIMS test order: 20191206_MS_DS_OE_118		
Material: Salzgrus Sondershausen ZZ, GSES mbH Sondershausen	Sieving line: „Son1“		
6.9%>4 mm; 52.3%>2 mm; 17.2%>1 mm; 7.2%>0.5 mm; 2.8%>0.4; 4.4%>0.25 mm; 6.4%>0.125 mm; 2.8%>0.063			
Strain controlled	0.36; 0.036; 0.0036; 0.00036 mm/h	Temperature	50°C
Date: 06.12.19- 20.03.20 (+ 20.5.-10.6)		Run time [d]	105 (187)
Crushed salt [g]	15381	Brine [g]	0
		Moisture [wt%]	0.06

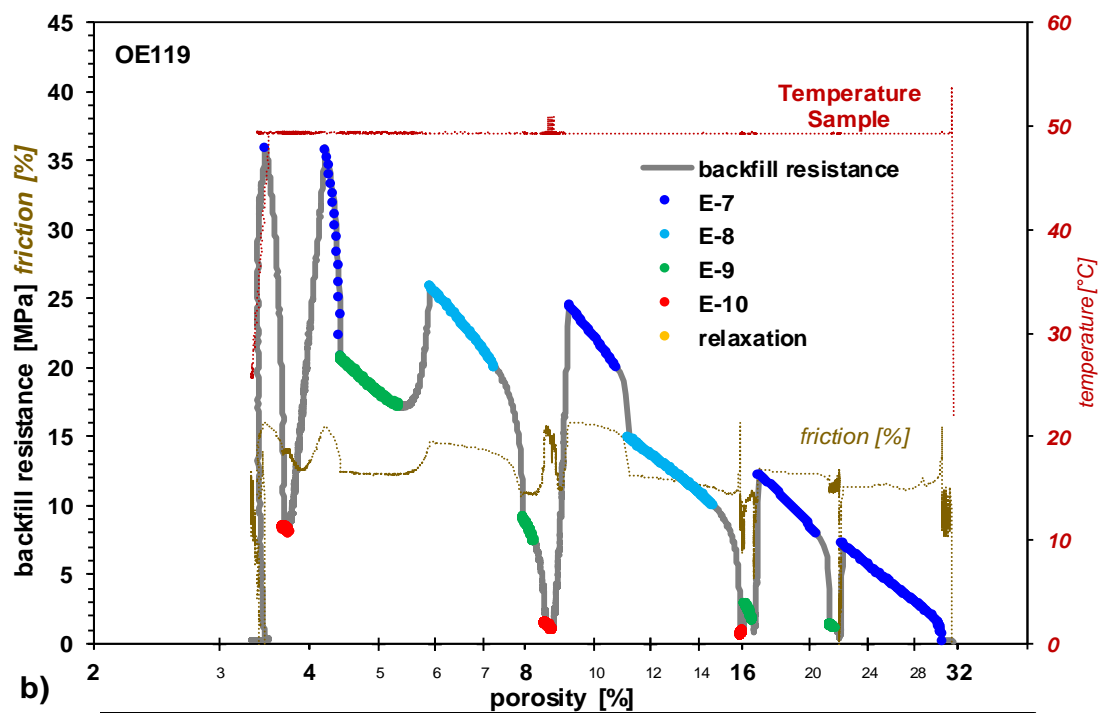
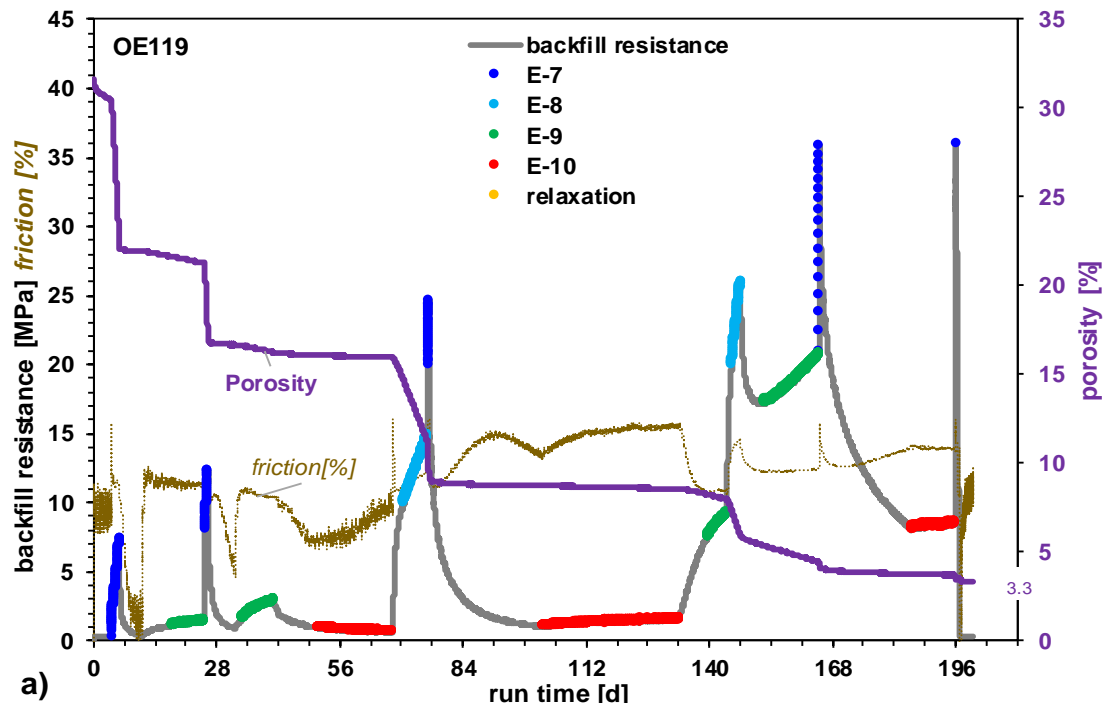
Fig. A.2 OE 118 a) Evolution of load resistance, friction and porosity b) Load resistance versus porosity, colors represent the differing compaction speeds

Tab. A.3 OE 118 - Experiment phases and respective key values

Action	Run time [d]	Duration [d]	Backfill resistance [MPa]	Friction [%]	Porosity [%]
heating	0.0		0.1		31.5
E-7	4.1	1.9	0	29.87	31.5
relaxation	6.0	5.1	8	4.63	23.2
E-10	11.1	20.0	5.4	4.83	23.1
E-9	31.1	6.9	6	5.68	23
E-7	38.0	2.2	7.1	5.37	22.7
relaxation	40.2	8.7	34.9	6.14	10
E-10	40.2	8.7	34.9	6.14	10
E-9	68.9	11.0	25.9	6.64	9.8
E-8	79.9	1.9	30.8	6.69	9
relaxation	81.9	8.1	38.9	6.55	7.7
E-10	90.0	14.9	30.3	6	7.6
Corona-shutdown	105.0		21.6		7.6
restart / heating	139.9		0		7.5
E-10	143.1	17.7	23.9	5.83	7.5
relaxation	161.1	2.9	0.1		7.7
restart	164.9		0.2		7.7
E10 - 0.00036 mm/h	165.1	13.9	26.7	5.22	7.4
loading to 2420kN +15kN/min	178.9		30.2		7.4
E-10	178.9	7.9	32.1		7.4
end	187.0		31.8		7.3

Tab. A.4 OE 118 - results

OE 118 - crushed salt Sondershausen; 0.09wt%, 50°C, Ø 300 mm					
File number: 19058			LIMS test order: 20191206_MS_DS_OE_118		
Material: Salzgrus Sondershausen Z2, GSES mbH Sondershausen				Sieving line: „Son1“	
6.9% >4 mm; 52.3% >2 mm; 17.2% >1 mm; 7.2% >0.5 mm; 2.8% >0.4; 4.4% >0.25 mm; 6.4% > 0.125 mm; 2.8% > 0.063					
Strain controlled	0.36; 0.036; 0.0036; 0.00036 mm/h			Temperature	50°C
Date: 19.07.19- 29.11.19				Run time [d]	105 (187)
Crushed salt [g]	15381	+ Brine [g]	0	Moisture [wt%]	0.06
Density _{dry} [g/cm ³]	2.174	Density _{wet} [g/cm ³]		2.176	
High [mm]	145.8	-		107.9	
Mass [g]	15381	-		15375	
Volume [cm ³]	10307	-		7606	
Pore number [-]	0.46	-		0.08	
Porosity [%]	31.42	-		7.32	
				friction@ Sig max [%]	6.54



OE119 - crushed salt Sondershausen; 0.35wt%, 50°C, Ø 300 mm			
File number: 20010		LIMS test order: 20200630_M5_KZ_OE_119	
Material: Salzgrus Sondershausen Z2, GSES mbH Sondershausen		Sieving line: „Son1“	
6.9%>4 mm; 52.3%>2 mm; 17.2%>1 mm; 7.2%>0.5 mm; 2.8%>0.4; 4.4%>0.25 mm; 6.4%>0.125 mm; 2.8%>0.063			
Strain controlled	0.36; 0.036; 0.0036; 0.00036 mm/h	Temperature	50°C
Date:	02.7.20 -18.01.21	Run time [d]	200
Crushed salt [g]	15456	Brine [g]	56
		Moisture [wt%]	0.35

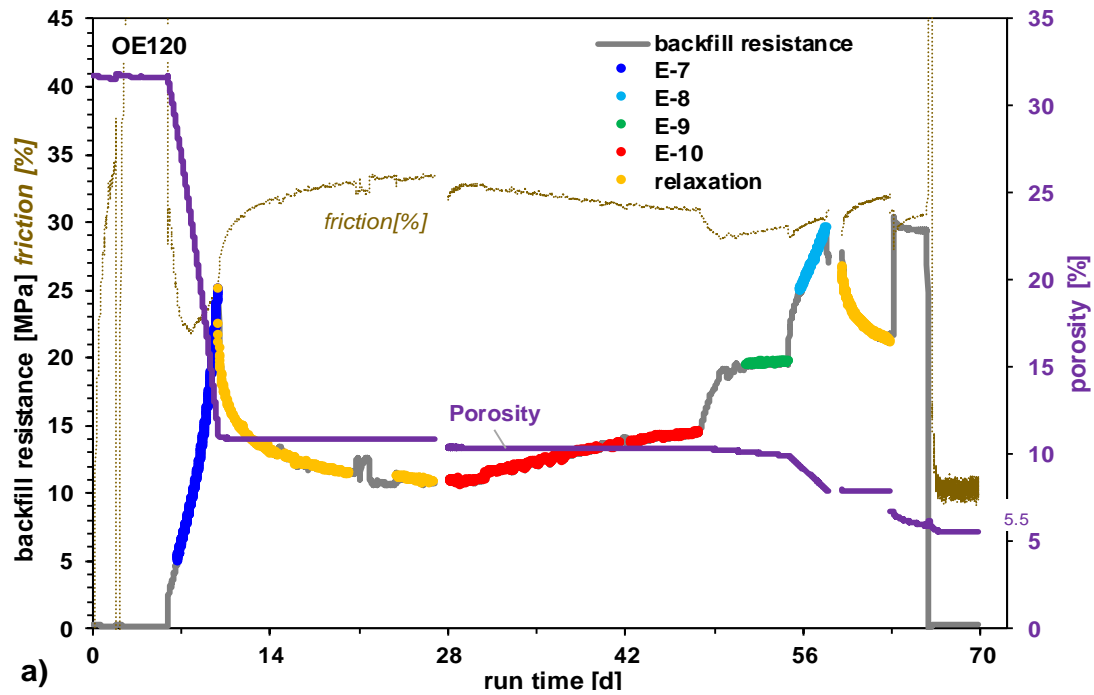
Fig. A.3 OE 119 a) Evolution of load resistance, friction and porosity b) Load resistance versus porosity, colors represent the differing compaction speeds

Tab. A.5 OE 119 - Experiment phases and respective key values

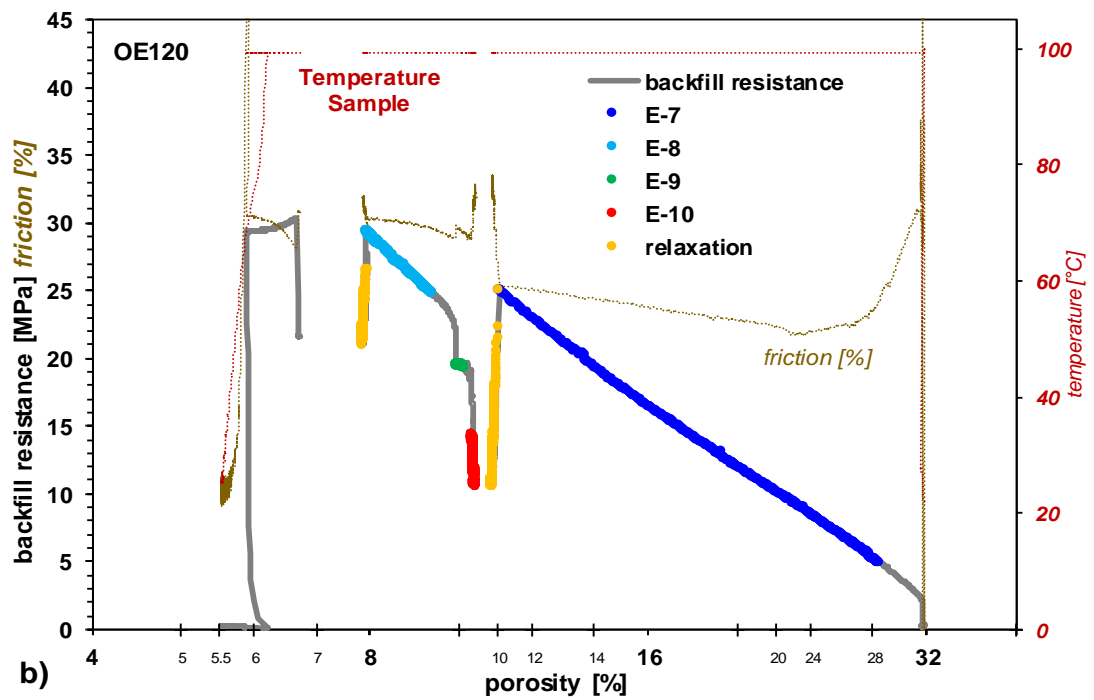
Action	Run time [d]	Duration [d]	Backfill resistance [MPa]	Friction [%]	Porosity [%]
heating	0.0		0.3		31.4
E-7	4.0	1.8	0.2	9.5	30.5
relaxation	5.9	5.1	7.3	11.3	22.2
E-9	11.0	14.2	0.3	0.5	21.9
E-7	25.2	0.8	3.9	12.2	21.2
relaxation	26.0	6.1	12.4	12.6	16.9
E-9	32.1	8.9	0.8	5.1	16.7
E-10	41.0	26.9	2.8	10.4	16.2
E-8	67.9	8.0	0.6	9.8	16
E-7	76.0	0.3	18	13.9	11.1
relaxation	76.2	25.9	24.6	16	9.2
E-10	102.2	30.9	1	13.6	8.7
E-9	133.1	10.9	1.5	15.7	8.5
E-8	144.0	3.1	9.2	10.9	7.9
E-9	147.1	17.9	25.9	14.6	5.9
E-7	165.0	0.1	20.8	12.5	4.4
E-10	186.0	10.0	8.2	13.9	3.8
E-7	195.9	0.1	8.7	13.8	3.7
relaxation	196.0	0.1	35.9	16	3.5
unloading	196.2	0.8	31.1	14.9	3.4
cooling	197.0		0.3		3.5
end	200.0		0.3	11.5	3.3

Tab. A.6 OE 119 - results

OE 119 - crushed salt Sondershausen; 0.35wt%, 50°C, Ø 300 mm					
File number: 20010			LIMS test order: 20200630_M5_KZ_OE_119		
Material: Salzgrus Sondershausen Z2, GSES mbH Sondershausen				Sieving line: „Son1“	
6.9% >4 mm; 52.3% >2 mm; 17.2% >1 mm; 7.2% >0.5 mm; 2.8% >0.4; 4.4% >0.25 mm; 6.4% > 0.125 mm; 2.8% > 0.063					
Strain controlled	0.36; 0.036; 0.0036; 0.00036 mm/h			Temperature	50°C
Date: 19.07.19- 29.11.19				Run time [d]	200
Crushed salt [g]	15381	+ Brine [g]	0	Moisture [wt%]	0.35
Density _{dry} [g/cm ³]	2.174	Density _{wet} [g/cm ³]			2.182
High [mm]	146.5	-			103.61
Mass [g]	15456	-			15408
Volume [cm ³]	10356	-			7323.6
Pore number [-]	0.46	-			0.03
Porosity [%]	31.6	-			3.32
				friction@ Sig max [%]	15.98



a)



b)

OE120 - crushed salt Sondershausen; 0.35wt%, 100°C, Ø 300 mm			
File number: 21003		LIMS test order: 20210118_M5_KZ_OE-120	
Material: Salzgrus Sondershausen Z2, GSES mbH Sondershausen		Sieving line: „Son1“	
6.9%>4 mm; 52.3%>2 mm; 17.2%>1 mm; 7.2%>0.5 mm; 2.8%>0.4; 4.4%>0.25 mm; 6.4%>0.125 mm; 2.8%>0.063			
Strain controlled	0.36; 0.036; 0.0036; 0.00036 mm/h	Temperature	100°C
Date: 19.01.21- 30.03.21		Run time [d]	70
Crushed salt [g]	15456	Brine [g]	56
		Moisture [wt%]	0.35

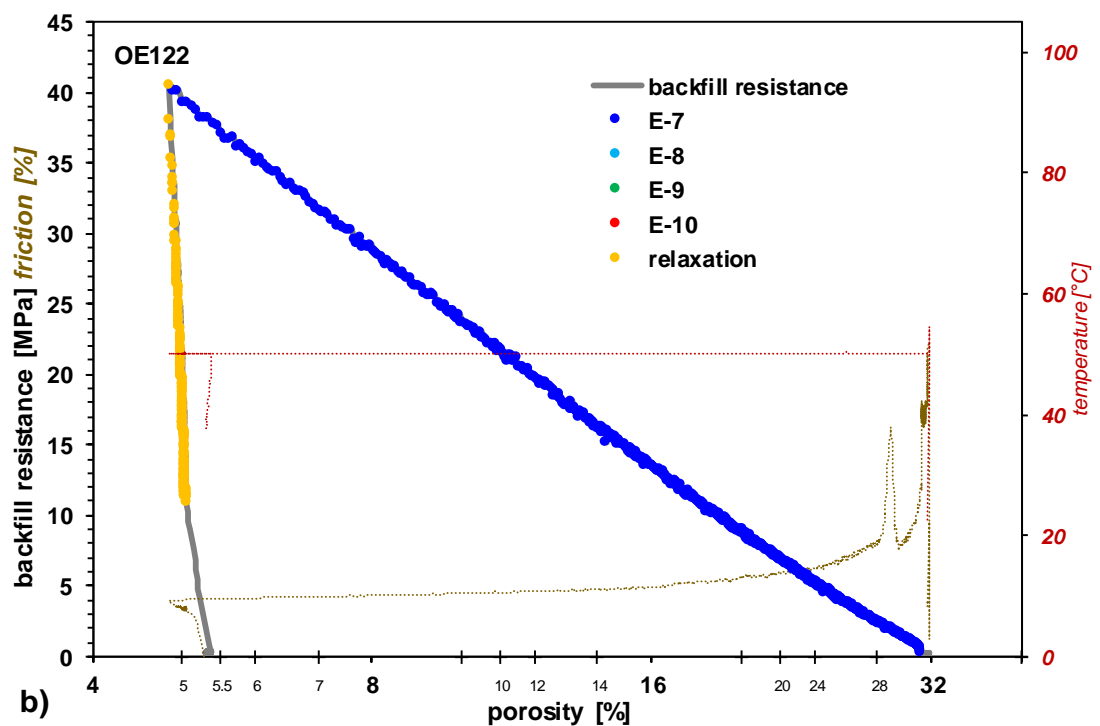
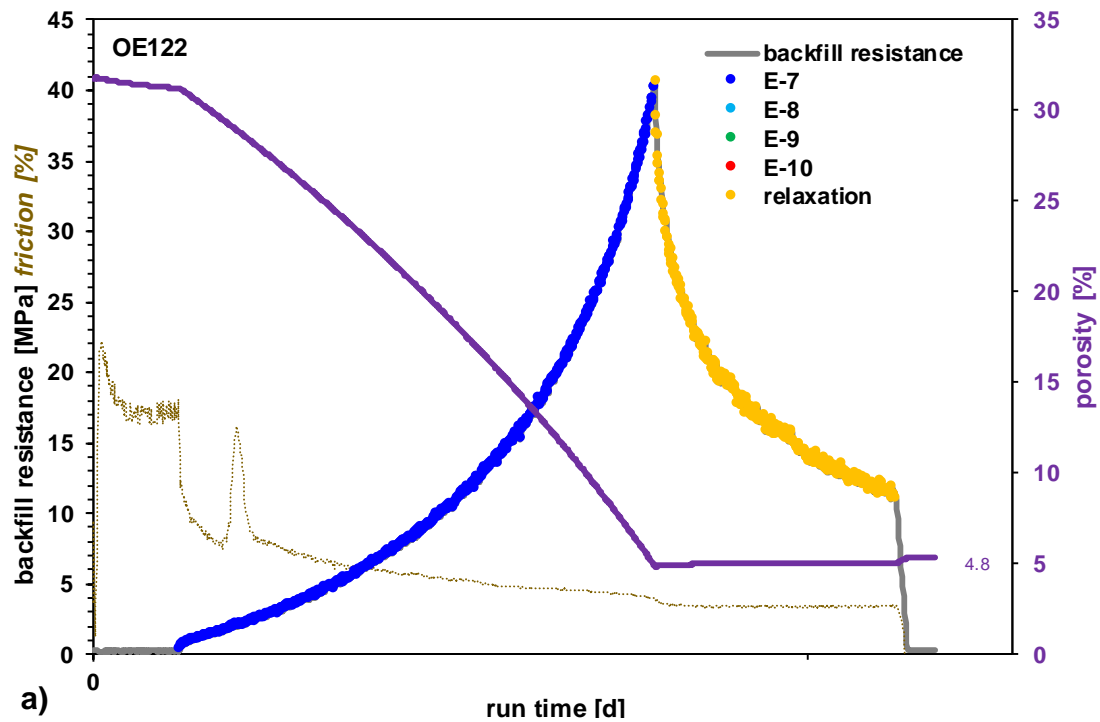
Fig. A.4 OE 120 a) Evolution of load resistance, friction and porosity b) Load resistance versus porosity, colors represent the differing compaction speeds

Tab. A.7 OE 120 - Experiment phases and respective key values

Action	Run time [d]	Duration [d]	Backfill resistance [MPa]	Friction [%]	Porosity [%]
heating	1.9	4.0	0.3		31.9
E-7	5.9	4.0	0.2	43.8	31.7
relaxation	9.9	16.9	25.1	25.3	11.0
E-10	26.9		10.7	33.5	10.8
failure hydraulic	27.8		0.0	0.0	10.5
loading 15kN/min	27.9		0.0	0.0	10.5
E-10	28.0	19.8	11.1	31.6	10.4
E-9	47.8	7.0	14.5	30.8	10.3
E-8	54.8	3.0	19.6	29.7	9.9
relaxation	57.8	5.0	29.4	30.3	7.9
failure unloaded	58.0		27.0	31.1	7.9
loading	59.1		27.8	29.1	8.0
@ 3000kN	63.1	2.7	30.4	28.0	6.6
unloading	65.8		29.1	30.7	5.9
cooling	65.9		0.1	77.3	6.2
end	69.8		0.3	9.9	5.5

Tab. A.8 OE 120 - results

OE 120 - crushed salt Sondershausen; 0.35wt%, 100°C, Ø 300 mm					
File number: 21003			LIMS test order: 20210118_M5_KZ_OE-120		
Material: Salzgrus Sondershausen Z2, GSES mbH Sondershausen				Sieving line: „Son1“	
6.9% >4 mm; 52.3% >2 mm; 17.2% >1 mm; 7.2% >0.5 mm; 2.8% >0.4; 4.4% >0.25 mm; 6.4% > 0.125 mm; 2.8% > 0.063					
Strain controlled	0.36; 0.036; 0.0036; 0.00036 mm/h		Temperature	100°C	
Date: 19.01.21- 30.03.21			Run time [d]	70	
Crushed salt [g]	15381	+ Brine [g]	0	Moisture [wt%]	0.35
Density _{dry} [g/cm ³]	2.174	Density _{wet} [g/cm ³]		2.182	
High [mm]	146.5	-		106.1	
Mass [g]	15456	-		15402	
Volume [cm ³]	10384	-		7498	
Pore number [-]	0.47	-		0.06	
Porosity [%]	31.8	-		5.52	
			friction @ Sig max [%]	30.26	



OE122 - crushed salt Sondershausen; 0.45wt%, 50°C, Ø 300 mm; PTFE					
File number: 21036		LIMS test order: 20210628_M5_KZ_OE_122			
Material: Salzgrus Sondershausen Z2, GSES mbH Sondershausen			Sieving line: „Son1“		
6.9%>4 mm; 52.3%>2 mm; 17.2%>1 mm; 7.2%>0.5 mm; 2.8%>0.4; 4.4%>0.25 mm; 6.4%> 0.125 mm; 2.8%> 0.063					
Strain controlled	0.36;	Temperature	50°C		
Date:	28.06.2021 - 07.07.2021	Run time [d]	9		
Crushed salt [g]	15456	Brine [g]	56	Moisture [wt%]	0.45

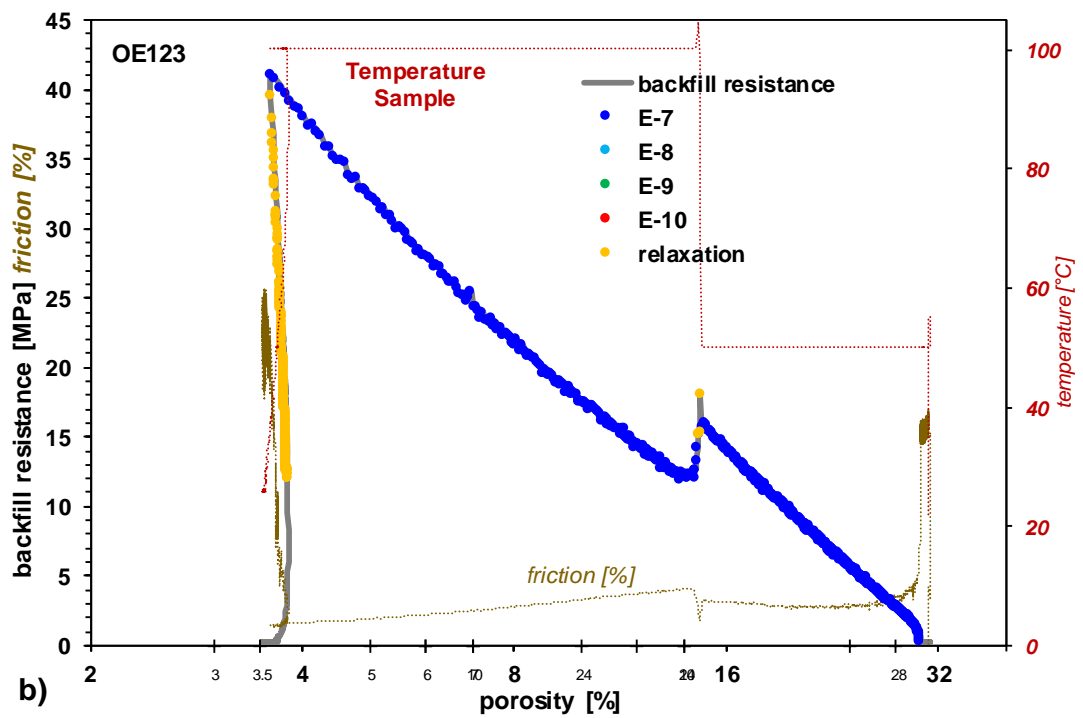
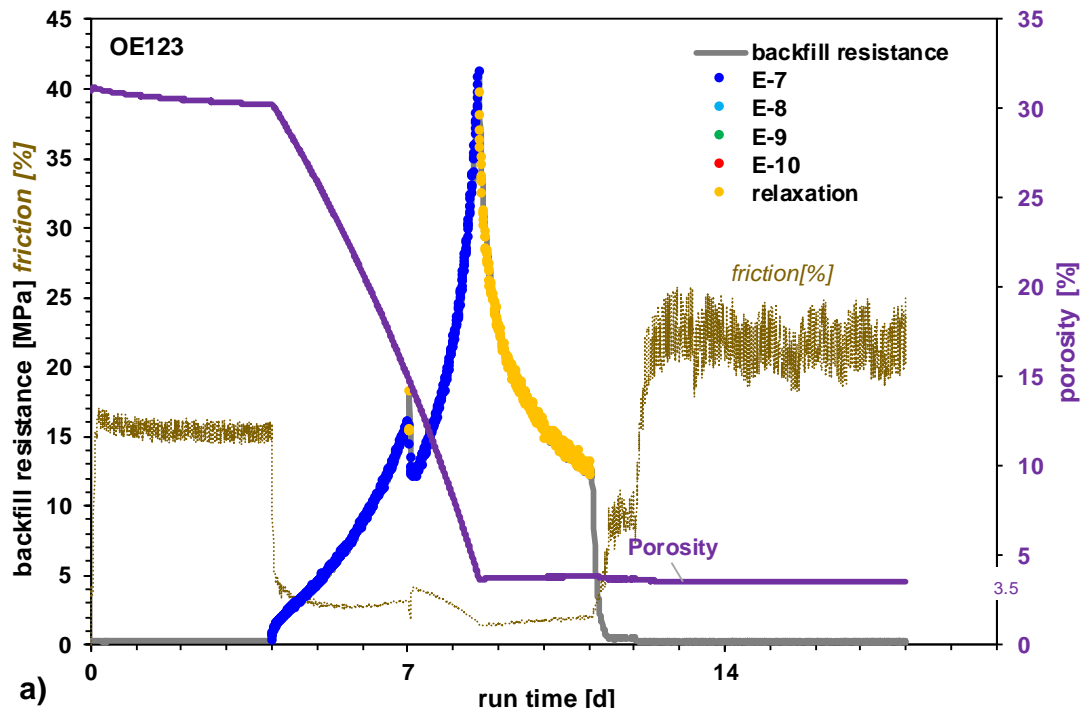
Fig. A.5 OE 122 a) Evolution of load resistance, friction and porosity b) Load resistance versus porosity, colors represent the differing compaction speeds

Tab. A.9 OE 122 - Experiment phases and respective key values

Action	Run time [d]	Duration [d]	Backfill resistance [MPa]	Friction [%]	Porosity [%]
heating	0.0		0.3		31.7
E-7	0.8	4.7	0.3	14.0	31.2
relaxation	5.5	2.3	40.6	4.0	4.8
cooling	7.9	0.1	11.5	3.5	5.0
end	8.0		0.3		5.4

Tab. A.10 OE 122 - results

OE 122 - crushed salt Sondershausen; 0.35wt%, 50°C, Ø 300 mm, PTFE					
File number: 21036			LIMS test order: 20210628_M5_KZ_OE_122		
Material: Salzgrus Sondershausen Z2, GSES mbH Sondershausen				Sieving line: „Son1“	
6.9% >4 mm; 52.3% >2 mm; 17.2% >1 mm; 7.2% >0.5 mm; 2.8% >0.4; 4.4% >0.25 mm; 6.4% > 0.125 mm; 2.8% > 0.063					
Strain controlled	0.36 mm/h		Temperature		50°C
Date: 28.06.21 - 07.07.21			Run time [d]		9
Crushed salt [g]	15400	+ Brine [g]	56	Moisture [wt%]	
Density _{dry} [g/cm ³]	2.174	Density _{wet} [g/cm ³]			2.184
High [mm]	146.5	-			105.6
Mass [g]	15456	-			15442
Volume [cm ³]	10355	-			7467
Pore number [-]	0.46	-			0.06
Porosity [%]	31.7	-			5.22
				friction@ Sig max [%]	4.00



OE123 - crushed salt Sondershausen; 0.45wt%, 50 & 100°C, Ø 300 mm; PTFE			
File number: 21039	LIMS test order: 20210728_M5_KZ_OE-123		
Material: Salzgrus Sondershausen ZZ, GSES mbH Sondershausen	Sieving line: „Son1“		
6.9%>4 mm; 52.3%>2 mm; 17.2%>1 mm; 7.2%>0.5 mm; 2.8%>0.4; 4.4%>0.25 mm; 6.4%>0.125 mm; 2.8%>0.063			
Strain controlled	0.36;	Temperature	50°C
Date: 29.07.21 - 16.08.21		Run time [d]	18
Crushed salt [g]	15456	Brine [g]	56
		Moisture [wt%]	0.45

Fig. A.6 OE 123 a) Evolution of load resistance, friction and porosity b) Load resistance versus porosity, colors represent the differing compaction speeds.

Tab. A.11 OE 123 - Experiment phases and respective key values

Action	Run time [d]	Duration [d]	Backfill resistance [MPa]	Friction [%]	Porosity [%]
heating 50°C	0.0		0.3		31.1
E-7	0.0		0.3		31.1
heating 100°C	4.0	3.0	0.3	14.8	30.2
E-7	7.0		15.4		14.8
relaxation	7.1	1.5	15.3	2.4	14.6
cooling 50°C	8.6	2.5	41.2	1.5	3.6
relaxation	11.1		12.7		3.8
cooling	11.1	0.9	12.7	2.1	3.8
end	12.0		0.5		3.7

Tab. A.12 OE 123 - results

OE 123 - crushed salt Sondershausen; 0.45wt%, 50° & 100°C, Ø 300 mm, PTFE					
File number: 21039			LIMS test order: 20210728_M5_KZ_OE-123		
Material: Salzgrus Sondershausen Z2, GSES mbH Sondershausen				Sieving line: „Son1“	
6.9% >4 mm; 52.3% >2 mm; 17.2%>1 mm; 7.2%>0.5 mm; 2.8% >0.4; 4.4%>0.25 mm; 6.4%> 0.125 mm; 2.8%> 0.063					
Strain controlled	0.36 mm/h		Temperature		50° / 100 °C
Date: 29.07.21 - 16.08.21			Run time [d]		18
Crushed salt [g]	15400	+ Brine [g]	56	Moisture [wt%]	
Density _{dry} [g/cm ³]	2.174	Density _{wet} [g/cm ³]			2.184
High [mm]	145	-			103.5
Mass [g]	15456	-			15439
Volume [cm ³]	10249.4	-			7317
Pore number [-]	0.45	-			0.03
Porosity [%]	31.0	-			3.33
				friction@ Sig _{max} [%]	1.5

A.2 Triaxial tests

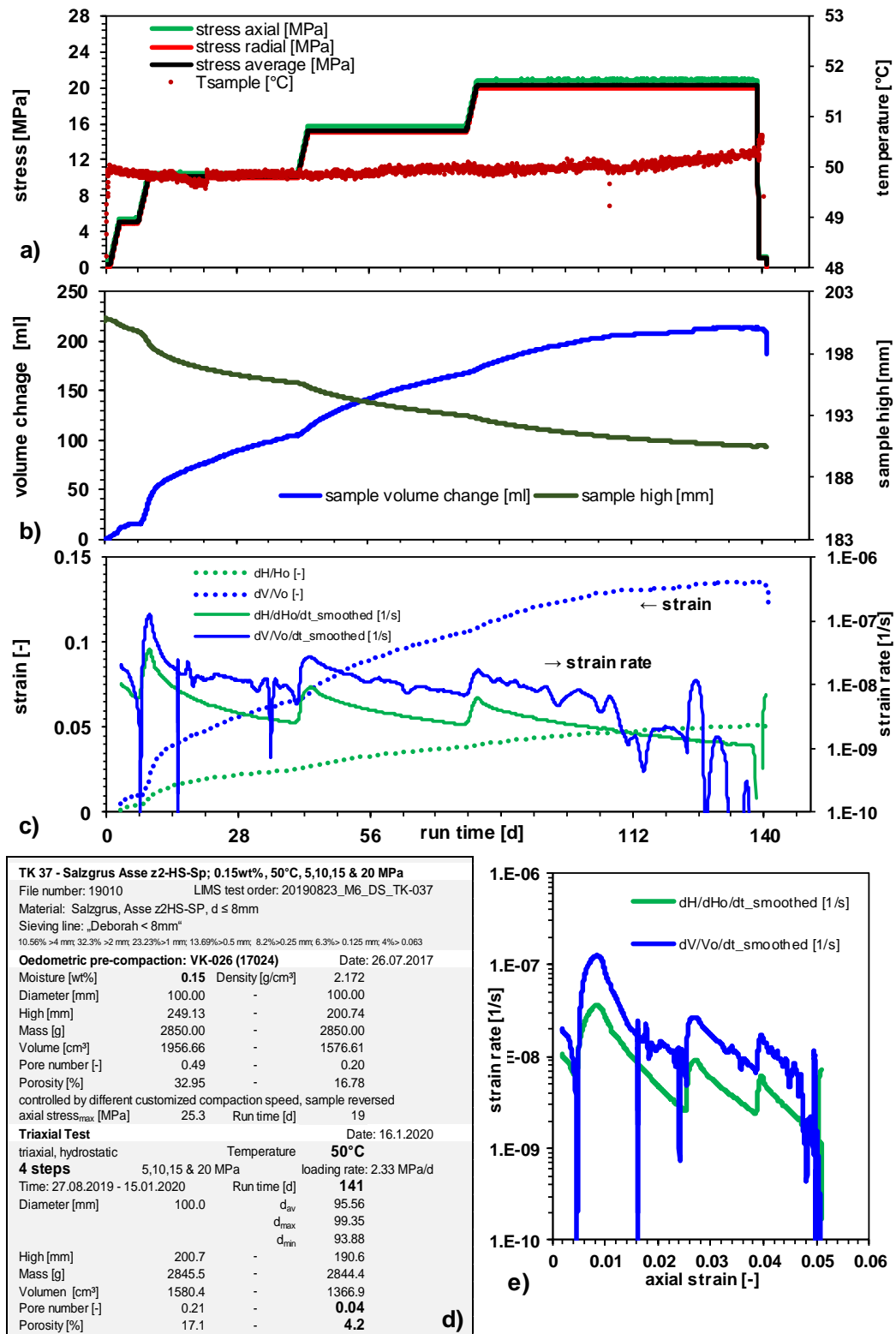


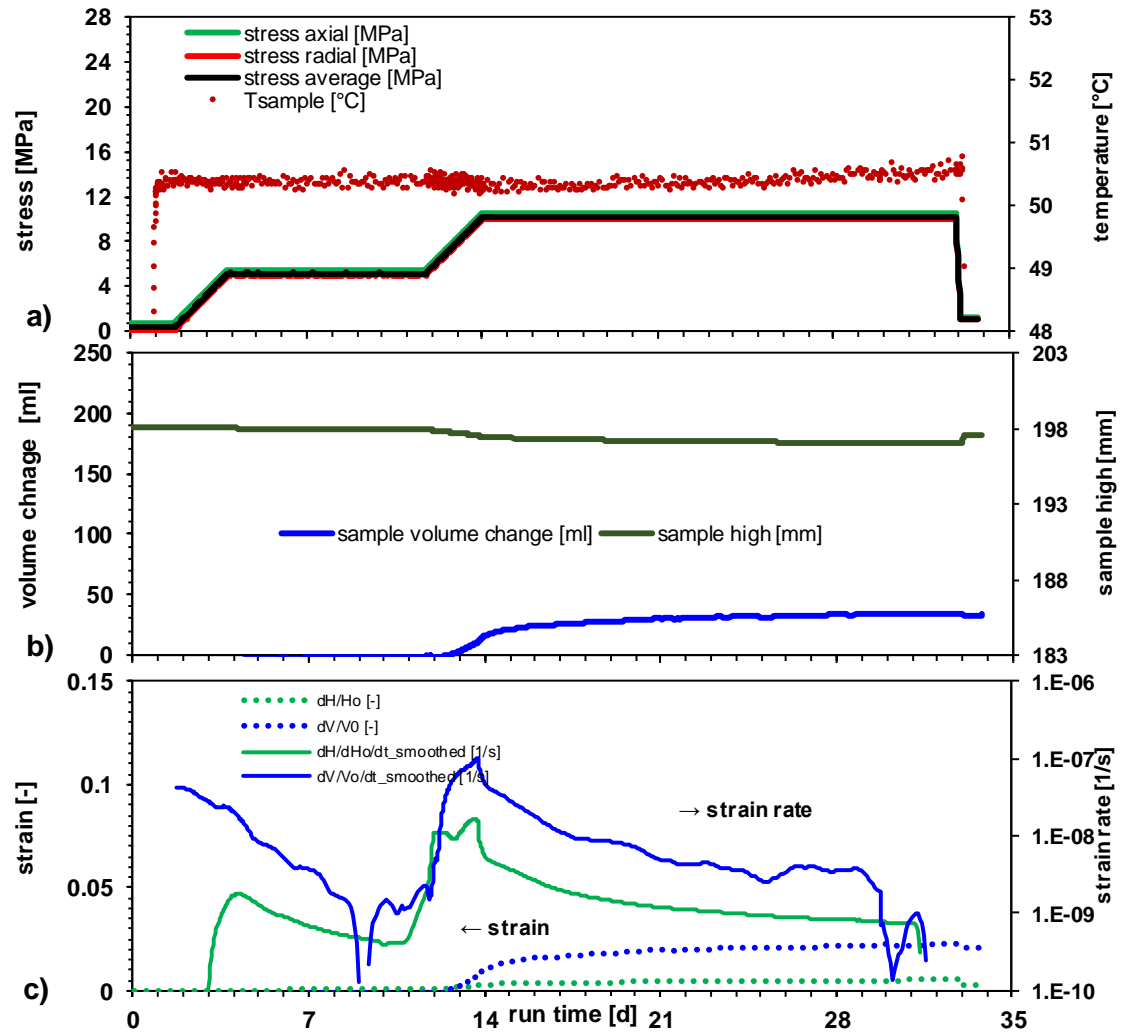
Fig. A.7 TK-037 a) stress regime and sample temperature b) volume change and sample high c) strain and strain rates d) experimental data e) axial strain ~ strain rate

Tab. A.13 TK-037 experimental data

TK-037 Action	Time [d]	Duration [d]	Porosity [%]	High [mm]	Sig_m [MPa]	Temperature [°C]
start / heating	0		0	200.7	0.3	27.1
venting	0.23		0.00	200.8	0.3	49.9
	2.28	MPa/d	loading rate			
start loading 5 MPa	0.92	2	0.00	200.8	0.3	49.9
creep @ 5 MPa	3.04	4	16.61	200.4	5.2	49.9
end creep	6.9		16.27	199.8	5.2	49.9
	2.23	MPa/d	loading rate			
start loading 10 MPa	6.96	2	16.27	199.8	5.2	49.9
creep @ 10 MPa	9.21	32	15.18	198.9	10.2	49.8
venting	10.1		14.64	198.5	10.2	49.8
refill	31.0					
venting	36.0					
end creep	41.0		11.20	195.6	10.2	49.9
	2.30	MPa/d	loading rate			
start loading 15 MPa	41.00	2	11.20	195.6	10.2	49.8
creep @ 15 MPa	43.21	34	10.78	195.3	15.3	49.9
venting	58.0					
refill	63.1					
end creep	76.9		7.27	193.0	15.3	50.0
	2.3	MPa/d	loading rate			
start loading 20 MPa	76.96	2	7.26	193.0	15.3	50.0
creep @ 20 MPa	79.17	60	7.00	192.8	20.3	50.0
venting	87.0					
refill	91.0					
refill	132.1					
end creep	138.8		4.18	190.5	20.3	50.3
	-66	MPa/d	loading rate			
start unloading	138.92	0.3	4.18	190.5	20.3	50.3
@ 1 MPa	139.21		4.21	190.6	1.1	50.4
cooling	139.9		4.22	190.6	1.1	50.5
end	140.9					27.6

Tab. A.14 TK-037 results – deformation, deformation rates at the end of pressure steps

TK-037	Main pressure	Creep time [d]	Achieved porosity [%]	Calculated regression for day x in reziproke time area				
				Deformation [-]		Deformation rate [1/s]		Day x
				volumetric	axial	volumetric	axial	
5.2	4	16.27	0.014	0.006	2.3E-09	3.7E-09	10	
10.2	32	11.20	0.062	0.024	1.0E-08	2.6E-09	30	
15.3	34	7.27	0.101	0.037	8.1E-09	2.7E-09	30	
20.3	60	4.18	0.129	0.047	5.5E-09	2.1E-09	60	



TK 38 - crushed salt Sondershausen; 0.1wt%, 50°C; 5 & 10 MPa
 File number: 20003 LIMS test order: 20200211_M6_KS_TK-038
 Material: Salzgrus, Sondershausen Z2, GSES mbH Sondershausen
 Sieving line: „Som1“
 6.9% >4 mm; 52.3% >2 mm; 17.2% >1 mm; 7.2% >0.5 mm; 2.8% >0.4; 4.4% >0.25 mm; 6.4% > 0.125 mm; 2.8% > 0.063

Oedometer pre-compaction: VK-028 (19057) Date: 18.11.2019

Moisture [wt%]	0.10	Density [g/cm³]	2.177
Diameter [mm]	100.0	-	100.0
High [mm]	237.1	-	197.9
Mass [g]	2800.9	-	2799.4
Volume [cm³]	1861.8	-	1554.4
Pore number [-]	0.45	-	0.21
Porosity [%]	30.9	-	17.2

controlled by different customized compaction speed, sample reversed
 axial stress_{max} [MPa] 24.7 Run time [d] 18

Triaxial Test Date: 18.03.2020

triaxial, hydrostatic	Temperature	50°C
2 steps	5 & 10 MPa	loading rate: 2 MPa/d
Run time: 12.02.2020 - 17.03.2020	Run time [d]	34
Diameter [mm]	100.00	d _{av} 98.67
		d _{max} 100.05
		d _{min} 97.26
High [mm]	198.1	-
Mass [g]	2787.8	-
Volume [cm³]	1538.3	-
Pore number [-]	0.20	-
Porosity [%]	16.7	-

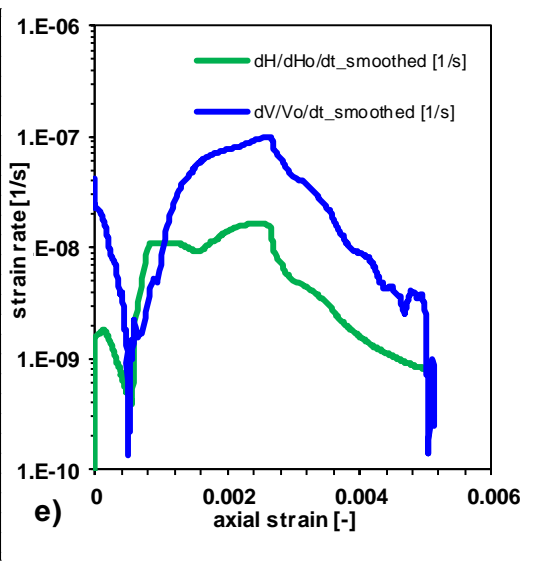


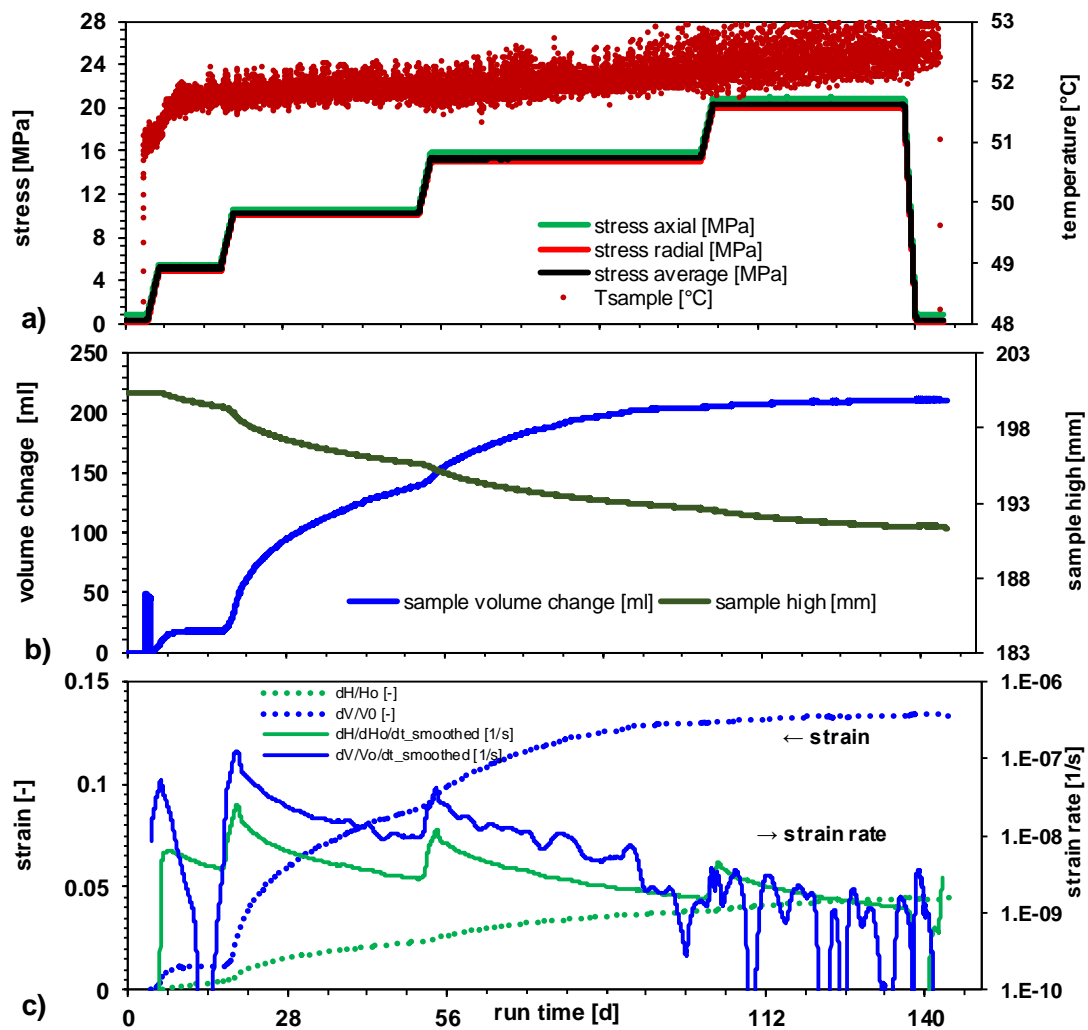
Fig. A.8 TK-38 a) stress regime and sample temperature; b) volume change and sample high; c) strain and strain rates; d) experimental data; e) axial strain ~ strain rate

Tab. A.15 TK-38 experimental data

TK-038 Action	Time [d]	Duration [d]	Porosity [%]	High [mm]	Sig _m [MPa]	Temperature [°C]
start	0		17.74	198.1	0.3	20.8
heating	0.74		17.74	198.1	0.3	25.5
venting	1.03		17.74	198.1	0.3	50.3
	2	MPa/d	loading rate			
start loading 5 MPa	1.7	2.1	17.56	198.1	0.3	50.4
creep @ 5 MPa	3.9	7.8	17.05	198.1	5.2	50.4
end creep	11.7		16.77	197.9	5.2	50.4
	2	MPa/d	loading rate			
start loading 10 MPa	11.74	2.00	16.77	197.9	5.2	50.5
creep @ 10 MPa	13.74	19.08	16.11	197.5	9.6	50.3
venting	13.74	-13.74	16.11	197.5	9.6	50.4
end creep	32.82		14.79	197.0	10.2	50.5
	-55	MPa/d	loading rate			
start unloading	32.89	0.17	14.79	197.0	10.2	50.7
@ 1 MPa	33.05	0.73	14.90	197.6	1.1	50.6
cooling	33.07		14.92	197.6	1.1	50.8
End	33.78		14.85	197.6	1.1	29.7

Tab. A.16 TK-38 results – deformation, deformation rates at the end of pressure steps

TK-038	Main pressure	Creep time [d]	Achieved porosity [%]	Calculated regression for day x in reziproke time area				Day x
				Deformation [-]		Deformation rate [1/s]		
				volumetric	axial	volumetric	axial	
	5.2	8	16.77					10
	10.2	19	14.79	0.023	0.005	1.63E-09	7.03E-10	20



TK 41- crushed salt Sondershausen; 0.35wt%, 50°C, 5,10,15 & 20 MPa
 File number: 20012 LIMS test order: 20200717_M6_KZ_TK-041
 Material: Salzgrus, Sondershausen Zz, GSES mbH Sondershausen
 Sieving line: „Son1“
 6.9% >4 mm; 52.3% >2 mm; 17.2% >1 mm; 7.2% >0.5 mm; 2.8% >0.4; 4.4% >0.25 mm; 6.4% >0.125 mm; 2.8% > 0.063

Oedometric pre-compaction: VK-032 (20008) Date: 08.06.2020
 Moisture [wt%] **0.35** Density [g/cm³] 2.182
 Diameter [mm] 100.0 - 100.0
 High [mm] 250.6 - 200.4
 Mass [g] 2850.0 - 2848.4
 Volume [cm³] 1968.0 - 1573.9
 Pore number [-] 0.51 - 0.21
 Porosity [%] 33.62 - 17.04

controlled by different customized compaction speed
 axial stress_{max} [MPa] 13 Run time [d] 21

Triaxial Test Date: 26.01.2021
 triaxial, hydrostatic Temperature **50°C**
4 steps 5,10,15 & 20 MPa loading rate: 2.33 MPa/d
 Time: 17.07.2020 - 26.01.2021 Run time [d] **145**
 Diameter [mm] 100.0 d_{av} 95.35
 d_{max} 98.21
 d_{min} 94.12
 High [mm] 200.3 - 191.4
 Mass [g] 2845.9 - 2837.8
 Volume [cm³] 1578.8 - 1367.0
 Pore number [-] 0.21 - **0.05**
 Porosity [%] 17.4 - **4.8**

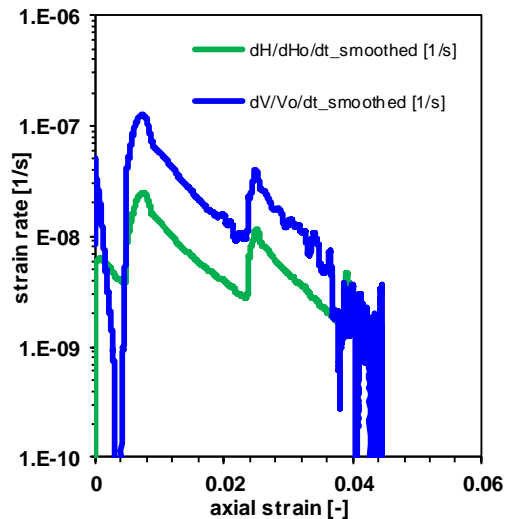


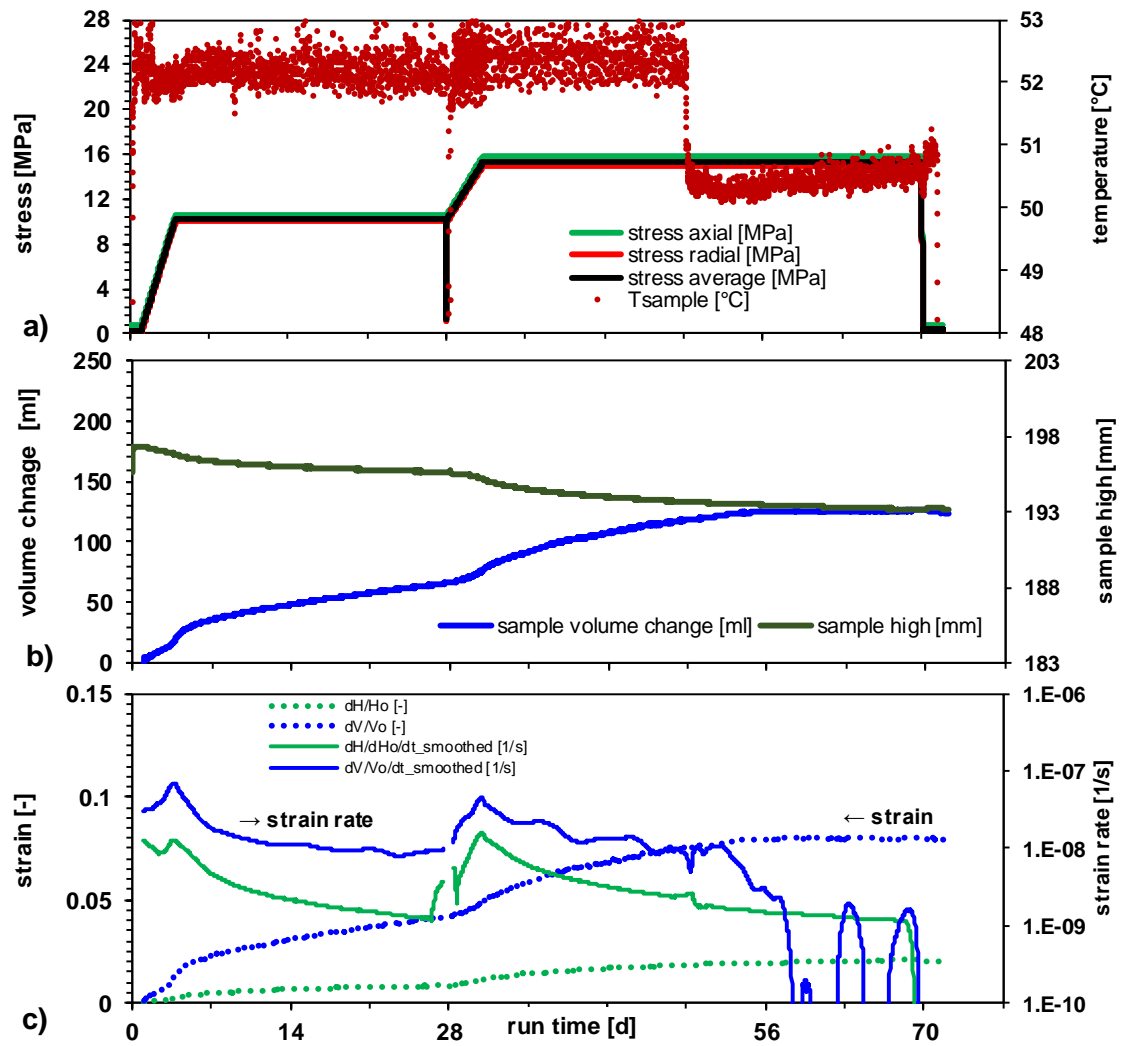
Fig. A.9 TK-041 a) stress regime and sample temperature; b) volume change and sample high; c) strain and strain rates; d) experimental data; e) axial strain ~ strain rate

Tab. A.17 TK-041 experimental data

TK-041 Action	Time [d]	Duration [d]	Porosity [%]	High [mm]	Sig _m [MPa]	Temperature [°C]
start	0		17.37	200.3		24.4
heating	2.91		17.37	200.3	0.3	25.0
venting	3.91		15.10	200.3	0.3	51.1
	2.3	MPa/d	loading rate			
start loading 5 MPa	3.91	2	17.38	200.3	0.3	51.1
creep @ 5 MPa	6.04	11	16.85	200.3	5.2	51.4
venting	16.9					
end creep	16.9		16.42	199.4	5.2	51.7
	2.23	MPa/d	loading rate			
start loading 10 MPa	16.91	2	16.42	199.4	5.2	51.7
creep @ 10 MPa	19.16	33	15.13	198.8	10.2	51.7
venting/refill	21.1					
venting/refill	34.9					
venting/refill	51.9					
end creep	51.9		9.33	195.6	10.2	51.9
	2.3	MPa/d	loading rate			
start loading 15 MPa	51.95	2	9.32	195.6	10.2	52.0
creep @ 15 MPa	54.16	48	8.79	195.3	15.3	51.9
venting	69.9					
refill	101.9					
end creep	101.9		5.06	192.6	15.3	52.2
	2.3	MPa/d	loading rate			
start loading 20 MPa	101.95	2	5.06	192.6	15.3	52.4
creep @ 20 MPa	104.16	34	5.00	192.5	20.3	52.0
venting	63.0					
end creep	138.0		4.66	191.4	20.3	52.3
	-9.58	MPa/d	loading rate			
start unloading	138.00	2	4.66	191.4	20.3	53.0
@ 1 MPa	140.08		4.61	191.5	0.3	52.5
cooling	143.9		4.63	191.4	0.3	52.6
end	144.9		4.71	191.3	0.3	27.6

Tab. A.18 TK-041 results – deformation, deformation rates at the end of pressure steps

TK-041 Main pressure	Creep time [d]	Achieved porosity [%]	Calculated regression for day x in reziproke time area				
			Deformation [-]		Deformation rate [1/s]		Day x
			volumetric	axial	volumetric	axial	
5.2	11	16.42	0.012	0.004		4.23E-09	10
10.2	33	9.33	0.096	0.025	6.91E-09	2.19E-09	30
15.3	48	5.06	0.131	0.037	4.45E-09	1.74E-09	30
20.3	34	4.66	0.134	0.045		1.02E-09	30



TK 44 - crushed salt Sondershausen; 0.5wt%, 33°C; 4, 8, 12, 16 & 20 MPa
 File number: 21035 LIMS test order: 20210624_M6_KZ_TK-044
 Material: Salzgrus, Sondershausen Z2, GSES mbH Sondershausen
 Sieving line: „Son1“
 6.9% >4 mm; 52.3% >2 mm; 17.2% >1 mm; 7.2% >0.5 mm; 2.8% >0.4; 4.4% >0.25 mm; 6.4% > 0.125 mm; 2.8% > 0.063

Oedometric pre-compaction: VK-045 (21035) Date: 14.06.2021
 Moisture [wt%] **0.5** Density [g/cm³] 2.186
 Diameter [mm] 100.0 - 100.0
 High [mm] 256.5 - 202.2
 Mass [g] 2860.0 - 2858.0
 Volume [cm³] 2014.9 - 1587.8
 Pore number [-] 0.54 - 0.22
 Porosity [%] 35.1 - 17.7

constant loading rate of 6 kN/d
 axial stress_{max} [MPa] 13.8 Run time [d] 19

Triaxial Test Date: 19.11.2021
 triaxial, hydrostatic & deviatoric pha Temperature **33°C**
5 steps 4,8,12,16 & 20 MPa loading rate: 4 MPa/d
 Date: 28.06.2021 - 19.11.2021 Run time [d] **144**
 Diameter [mm] 100.0 d_{av} 96.83
 d_{max} 98.89
 d_{min} 95.56
 High [mm] 202.2 - 185.5
 Mass [g] 2858.0 - 2841.3
 Volume [cm³] 1587.8 - 1366.1
 Pore number [-] 0.22 - **0.05**
 Porosity [%] 17.7 - **4.6**
 v_p [m/s] 3904

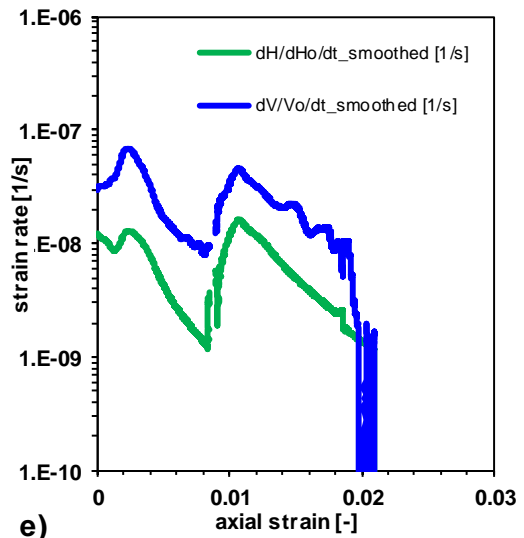


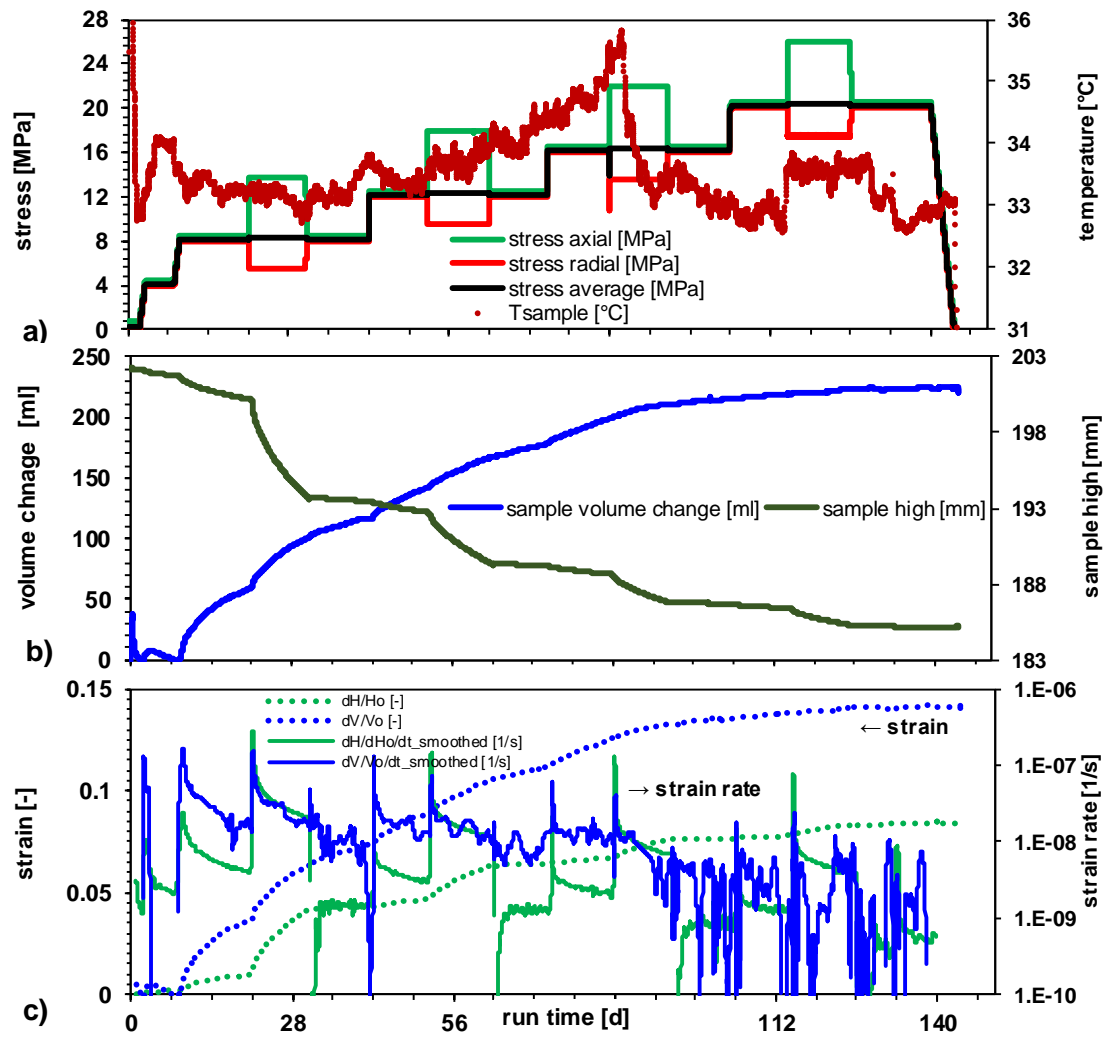
Fig. A.10 TK-42 a) stress regime and sample temperature; b) volume change and sample high; c) strain and strain rates; d) experimental data; e) axial strain ~ strain rate

Tab. A.19 TK-42 experimental data

TK-42	Time	Duration	Porosity	High	Sig _m	Temperature
Action	[d]	[d]	[%]	[mm]	[MPa]	[°C]
start			17.39	197.3		
heating	0.02		17.39	197.3	0.3	26.6
venting	0.98		17.32	197.3	0.3	52.4
	3.3	MPa/d	loading rate			
start loading 10 MPa	1.02	3	17.26	197.3	0.3	52.1
creep @ 10 MPa	4.02	21	16.14	196.8	10.2	52.3
venting	4.1		16.09	196.7		52.2
T Room defect	9.0		15.16	196.2		52.0
refill	22.1					52.4
venting	25.0					52.6
end creep	22.1		14.07	195.8	10.2	52.4
	1.6	MPa/d	loading rate			
start loading 15 MPa	28.08	3	13.66	195.6	10.2	51.6
creep @ 15 MPa	31.24	21	12.94	195.1	15.3	52.4
failure central hydraulic	28.06		13.66	195.7	1.2	51.3
temperature regulation ?	28.11		13.66	195.6	10.2	50.8
venting	34.98					52.9
refilling	45.07					52.6
temperature regulation ok	49.04					52.3
change pump capacity	49.06					52.1
venting	52.07					50.3
end creep	69.96		10.10	193.2	15.3	50.4
	-59.71	MPa/d	loading rate			
start unloading	69.98	0.25	10.12	193.2	15.2	50.5
@ 1 MPa	70.23		10.13	193.3	0.3	50.6
venting	71.0					50.8
cooling	71.2					50.9
end	71.98		10.27	193.2	0.3	29.2

Tab. A.20 TK-42 results – deformation, deformation rates at the end of pressure steps

TK-42			Calculated regression for day x in reziproke time area				
Main pressure	Creep time [d]	Achieved porosity [%]	Deformation [-]		Deformation rate [1/s]		Day x
			volumetric	axial	volumetric	axial	
10.2	14.07	0.039	0.008	8.24E-09	1.26E-09	24	14.07
15.3	10.10	0.077	0.019	8.67E-09	1.84E-09	24	10.10



TK 44 - crushed salt Sondershausen; 0.5wt%, 33°C; 4, 8, 12, 16 & 20 MPa
 File number: 21035 LMS test order: 20210624_M6_KZ_TK-044
 Material: Salzgrus, Sondershausen Z2, GSES mbH Sondershausen
 Sieving line: „Son1“
 6.9% >4 mm; 52.3% >2 mm; 17.2% >1 mm; 7.2% >0.5 mm; 2.8% >0.4; 4.4% >0.25 mm; 6.4% > 0.125 mm; 2.8% > 0.063

Oedometric pre-compaction: VK-045 (21035) Date: 14.06.2021

Moisture [wt%]	0.5	Density [g/cm³]	2.186
Diameter [mm]	100.0		100.0
High [mm]	256.5		202.2
Mass [g]	2860.0		2858.0
Volume [cm³]	2014.9		1587.8
Pore number [-]	0.54		0.22
Porosity [%]	35.1		17.7

constant loading rate of 6 kN/d
 axial stress_{max} [MPa] 13.8 Run time [d] 19

Triaxial Test Date: 19.11.2021
 triaxial, hydrostatic & deviatoric pha Temperature **33°C**
 5 steps 4,8,12,16 & 20 MPa loading rate: 4 MPa/d
 Date: 28.06.2021 - 19.11.2021 Run time [d] **144**

Diameter [mm]	100.0	d _{av}	96.83
		d _{max}	98.89
		d _{min}	95.56
High [mm]	202.2		185.5
Mass [g]	2858.0		2841.3
Volume [cm³]	1587.8		1366.1
Pore number [-]	0.22		0.05
Porosity [%]	17.7		4.6

v_p [m/s] 3904

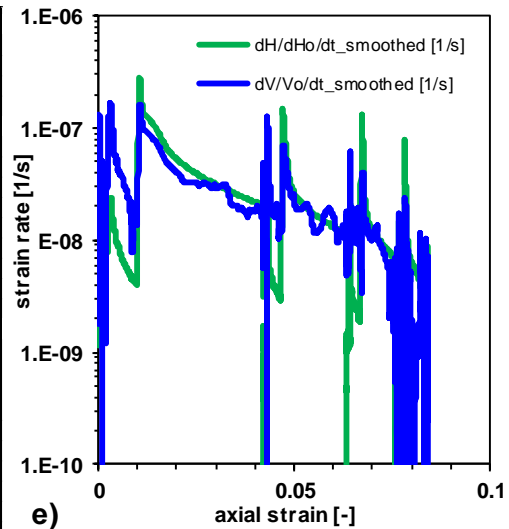


Fig. A.11 TK-044 a) stress regime and sample temperature; b) volume change and sample high; c) strain and strain rates; d) experimental data e) axial strain ~ strain rate

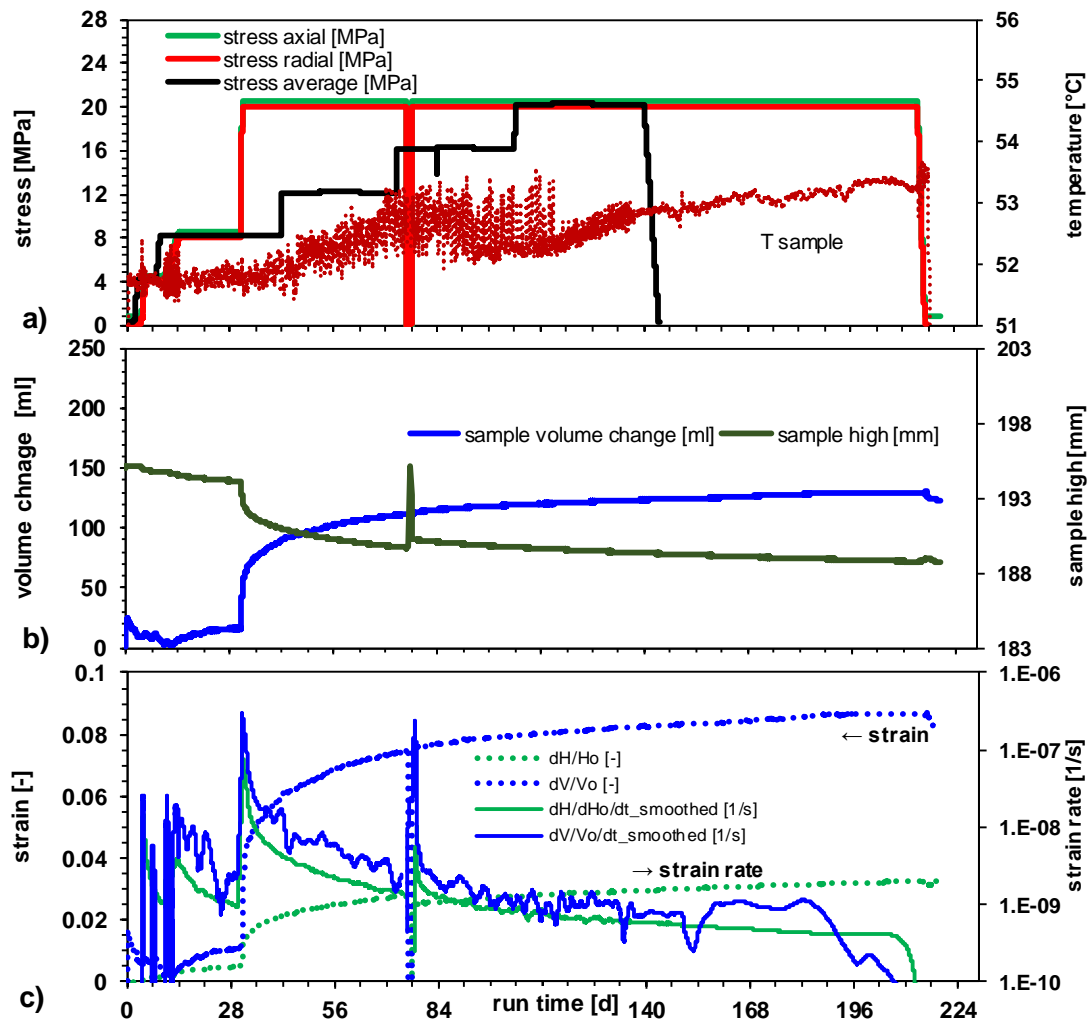
Tab. A.21 TK-044 experimental data

TK-044 Action	Time [d]	Duration [d]	Porosity [%]	High [mm]	Sig _{ax} [MPa]	Sig _{rad} [MPa]	Temperature [°C]
start	0.0		17.70	202.2	0.8	0.1	25.7
heating 50 °C	0.0		17.70	202.2	0.8	0.1	25.7
heating 30 °C	0.1		17.70	202.2	0.8	0.1	49.6
venting	1.0		17.70	202.2	0.8	0.1	33.6
start loading 4 MPa	2.0		17.70	202.1	0.8	0.1	32.8
creep @ 4 MPa	3.0		17.70	202.0	4.5	4.0	33.2
end creep	8.0	5	17.70	201.7	4.5	4.0	33.6
start loading 8 MPa	8.0		17.74	201.7	4.5	4.0	33.5
creep @ 8 MPa	9.0		17.10	201.5	8.5	8.0	33.5
venting	16.3		15.01	200.5	8.5	8.0	33.1
end creep	21.0	13	14.43	200.2	8.5	8.0	33.3
start loading dev stress	21.0		14.43	200.2	8.5	8.0	33.3
creep	21.1		14.36	199.8	13.8	5.5	33.2
venting	25.0		13.09	196.2	13.7	5.5	33.2
end creep	31.0	10	12.06	193.6	13.7	5.5	32.8
start unloading dev stress	31.0		12.06	193.6	13.7	5.5	32.8
creep @ 8 MPa	31.1		12.03	193.7	8.5	8.0	32.9
refill	38.0		11.34	193.5	8.5	8.0	33.1
end creep	42.0	11	11.12	193.4	8.5	8.0	33.7
start loading 12 MPa	42.0		11.12	193.4	8.5	8.0	33.7
creep @ 12 MPa	42.1		11.05	193.4	12.5	11.9	33.8
venting	45.0		10.44	193.1	12.5	12.0	33.5
end creep	52.0	10	9.53	192.7	12.5	12.0	33.5
start loading dev stress	52.0		9.53	192.7	12.5	12.0	33.5
creep	52.1		9.50	192.5	17.9	9.5	33.5
venting	59.0		8.39	190.2	17.9	9.5	33.4
end creep	63.0	11	7.96	189.3	17.9	9.5	33.9
start unloading dev stress	63.0		7.96	189.3	17.9	9.5	33.9
creep @ 12 MPa	63.1		7.95	189.4	12.5	12.0	34.0
end creep	73.0	10	7.16	189.2	12.5	12.1	34.3
start loading 16 MPa	73.0		7.16	189.2	12.5	12.1	34.3
creep @ 16 MPa	73.1		7.12	189.1	16.5	16.0	34.5
venting	80.0		6.26	188.8	16.5	16.0	34.6
end creep	84.0	11	5.81	188.6	16.5	16.0	35.4
start loading dev stress	84.0		5.81	188.6	16.5	16.0	35.4
creep	84.1		5.79	188.5	22.0	13.5	35.5
refill	87.0		5.46	187.8	22.0	13.5	34.2
end creep	94.0	10	5.06	186.8	22.0	13.5	33.3
start unloading dev stress	94.0		5.06	186.8	22.0	13.5	33.3
creep @ 16 MPa	94.1		5.06	186.8	16.5	16.0	33.4
refill			4.83	186.7	16.5	16.0	33.1

end creep	105.0	11	4.77	186.7	16.5	16.0	33.0
start loading 20 MPa	105.0		4.76	186.7	16.5	16.0	33.0
creep @ 20 MPa	105.1		4.75	186.6	20.5	20.0	33.2
end creep	115.0	10	4.48	186.4	20.5	20.0	33.6
start loading dev stress	115.0		4.48	186.4	20.5	20.0	33.6
creep	115.1		4.47	186.3	26.0	17.5	33.6
venting	122.0		4.33	185.5	26.0	17.5	33.3
end creep	126.0	11	4.14	185.3	26.0	17.5	33.5
start unloading dev stress	126.0		4.13	185.3	26.0	17.5	33.5
creep @ 20 MPa	126.1		4.14	185.3	20.5	20.0	33.6
refill	129.0		4.12	185.3	20.5	20.0	33.7
failure central hydraulic			4.14	185.2	20.5	20.0	33.5
end creep	140.0	14	4.14	185.1	20.5	20.0	33.0
start unloading	140.0		4.13	185.1	20.5	20.0	33.0
@ 1 MPa	144.0		4.42	185.2	0.8	0.1	33.0
end	144.2	144	4.06	185.2	0.806344	0.09	31.1

Tab. A.22 TK-044 results – deformation, deformation rates at the end of pressure steps

TK-044				Calculated regression for day 10 in reziproke time area			
Sig _{ax} [MPa]	Sig _{rad} [MPa]	Creep time [d]	Achieved porosity [%]	Deformation [-]		Deformation rate [1/s]	
				volumetric	axial	volumetric	axial
4.5	4.0	5	17.70	-0.003	0.002		2.0E-09
8.5	8.0	13	14.43	0.034	0.009	1.89E-07	2.14E-08
13.7	5.5	10	12.06	0.063	0.042	8.68E-08	8.81E-08
8.5	8.0	11	11.12	0.073	0.043	1.08E-08	1.28E-09
12.5	12.0	10	9.53	0.089	0.047	3.13E-08	6.71E-09
17.9	9.5	11	7.96	0.104	0.062	2.86E-08	3.45E-08
12.5	12.1	10	7.16	0.112	0.064	1.03E-08	1.06E-09
16.5	16.0	11	5.81	0.124	0.067	1.35E-08	3.94E-09
22.0	13.5	10	5.06	0.133	0.076	1.05E-07	2.08E-08
16.5	16.0	11	4.77	0.135	0.077		6.63E-10
20.5	20.0	10	4.48	0.138	0.078		1.90E-09
26.0	17.5	11	4.14	0.140	0.083		9.78E-09
20.5	20.0	14	4.14	0.141	0.084		



TK 45 - crushed salt Sondershausen; 0.5wt%, 50°C; 8 & 20 MPa
 Filenummer: 22002 LIMS test order: 20220202_M6_KZ_TK-045
 Material: Salzgrus, Sondershausen Z2, GSES mbH Sondershausen
 Sieving line: „Son1“
 6.9% >4 mm; 52.3% >2 mm; 17.2% >1 mm; 7.2% >0.5 mm; 2.8% >0.4; 4.4% >0.25 mm; 6.4% > 0.125 mm; 2.8% > 0.063

Oedometric pre-compaction: VK-047 (21046) Date: 14.06.2021

Ausgangsgrößen

Moisture [wt%]	0.48	Density [g/cm³]	2.185
Diameter [mm]	100.0	-	100.0
High [mm]	252.8	-	195.0
Mass [g]	2854	-	2853
Volume [cm³]	1985	-	1531
Pore number [-]	0.52	-	0.17
Porosity [%]	34.2	-	14.7

constant loading rate of 6 kN/d
 axial stress_{max} [MPa] 14.7 Run time [d] 22

Triaxial Test Date: 12.09.2022

triaxial, hydrostatic, one long phase	Temperature	50°C	
2 steps	8 & 20 MPa	loading rate: 2 MPa/d	
Date: 04.02.2022 - 12.09.2022	Run time [d]	220	
Diameter [mm]	d _{av}	96.23	
Moisture [wt%]	0.44	d _{max}	98.84
		d _{min}	94.92
High [mm]	195.1	-	188.9
Mass [g]	2836.6	-	2836.5
Volume [cm³]	1497	-	1373
Pore number [-]	0.15	-	0.06
Porosity [%]	13.2	-	5.4
v _p [m/s]	3488	-	4337

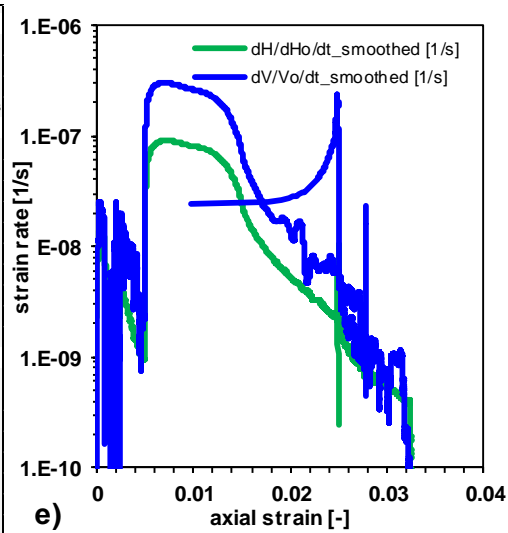


Fig. A.12 TK-045 a) stress regime and sample temperature; b) volume change and sample high; c) strain and strain rates; d) experimental data; e) axial strain ~ strain rate

Tab. A.23 TK-045 experimental data

TK-045 Action	Time [d]	Run time [d]	Porosity [%]	High [mm]	Sig _m [MPa]	Temperature [°C]
start	0.0		13.2	195.1	0.3	26.3
heating	0.0		13.2	195.1	0.3	26.3
@ 50°	0.1		11.9	195.2	0.3	50.3
venting	3.0		12.64	195.1	0.3	52.3
	3.8	MPa/d	loading rate			
start loading 4 MPa	4.0	1.00	12.71	195.1	0.3	51.8
creep @ 4 MPa	5.0	5.16	12.56	194.9	4.2	51.9
end creep	10.2		13.03	194.7	4.2	51.5
	1	MPa/d	loading rate			
start loading 8 MPa	10.2	4.00	13.03	194.7	4.2	51.6
creep @ 8 MPa	14.2	16.83	12.87	194.6	8.2	51.5
end creep	31.0		12.27	194.1	8.2	51.6
	2	MPa/d	loading rate			
start loading 20 MPa	31.0	0.25	12.27	194.1	8.2	51.7
creep @ 20 MPa	31.3	44.47	10.78	193.2	20.2	52.3
venting	31.3		10.61	193.1	20.2	52.1
venting	33.3		8.99	192.0	20.2	51.7
venting	52.3		7.06	190.4	20.2	51.7
refill	60.0		6.68	190.1	20.2	51.7
technical defect	75.7		0.00	189.7	-0.1	51.2
refill	80.0		6.09	190.2	20.2	52.3
	10.1	MPa/h	loading rate			
restart	77.0	0.08	0.00	193.2	0.0	52.8
venting	77.0		6.48	190.8	4.0	52.8
creep @ 20 MPa	77.1	40.9	6.25	190.4	20.2	52.8
refill	118.0		5.58	189.6	20.2	53.0
refill	150.0		5.35	189.2	20.2	52.7
failure airpressure data	169.6		5.21	189.1	20.2	53.6
refill	173.0		5.15	189.0	20.2	52.9
venting	175.0		5.14	189.0	20.2	53.0
airpressure ok	178.2		5.13	189.0	20.2	52.9
refill	189.0		5.03	188.9	20.2	53.2
end creep	214.0		5.00	188.8	20.2	53.3
	-0.4	MPa/h	loading rate			
unloading	214.0	2.08	4.99	188.8	20.1	53.4
@ 0.1 MPa	216.1		5.19	188.9	0.3	52.6
cooling	217.0		5.30	188.9	0.3	53.7
end	220.0		5.46	188.8	0.3	25.9

Tab. A.24 TK-045 results – deformation, deformation rates at the end of pressure steps

TK-045	Main pressure	Creep time [d]	Achieved porosity [%]	Calculated regression for day x in reciproke time area				Day x
				Deformation [-]		Deformation rate [1/s]		
				volumetric	axial	volumetric	axial	
	8.2	17	12.27	0.011	0.005	1.73E-07	8.96E-10	10
	20.3	44	6.68	0.073	0.027	2.96E-09	1.50E-09	40
	20.3	183	5.23	0.088	0.033	3.68E-10	3.20E-10	200

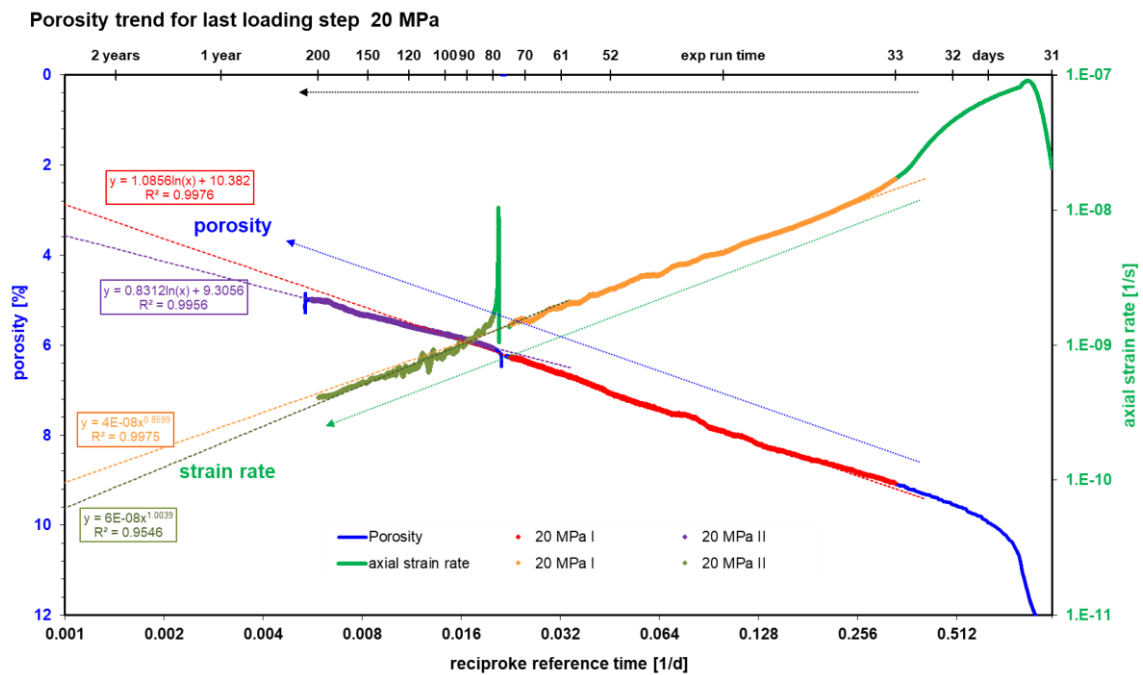


Fig. A.13 TK-045 long creep phase 20 MPa: porosity and axial strain rate ~ reciproke time with trends

B CT Scans of pre-compacted samples

B.1 BGR

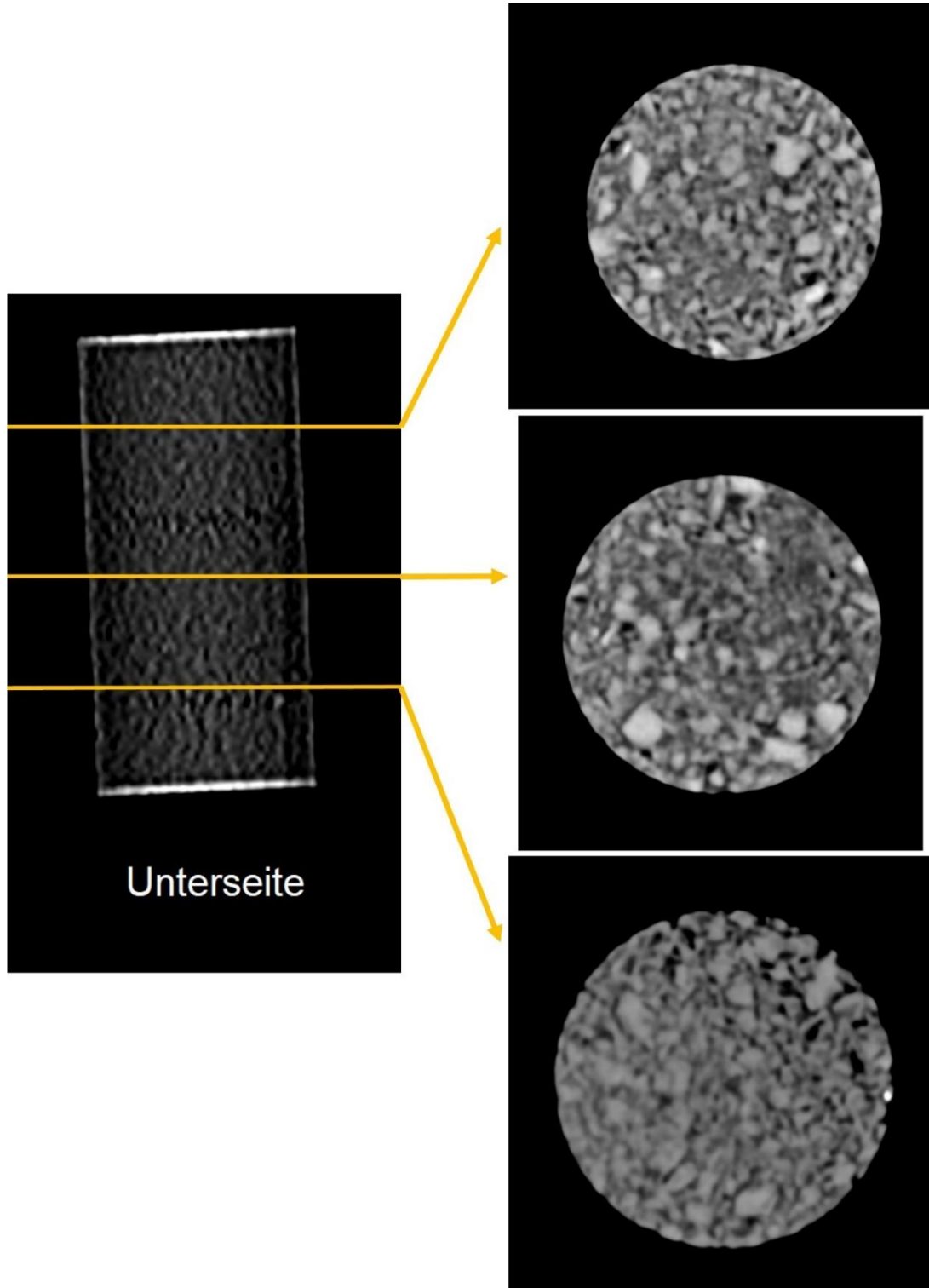


Fig. B.1 CT-Scan of the BGR sample used in the triaxial compaction test at GRS

B.2 IfG

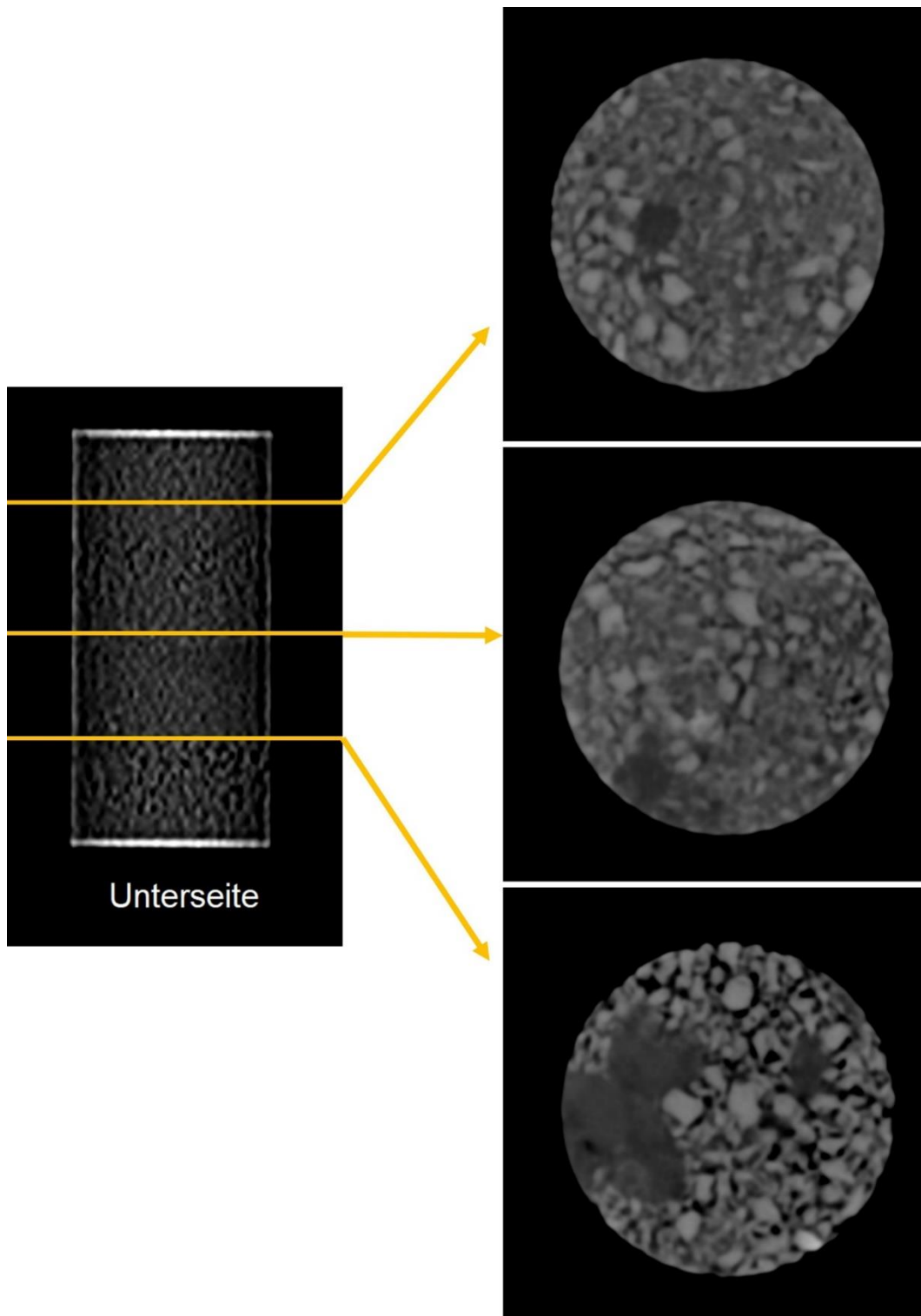


Fig. B.2 CT-Scan of the IfG sample used in the triaxial compaction test at GRS

B.3 TUC

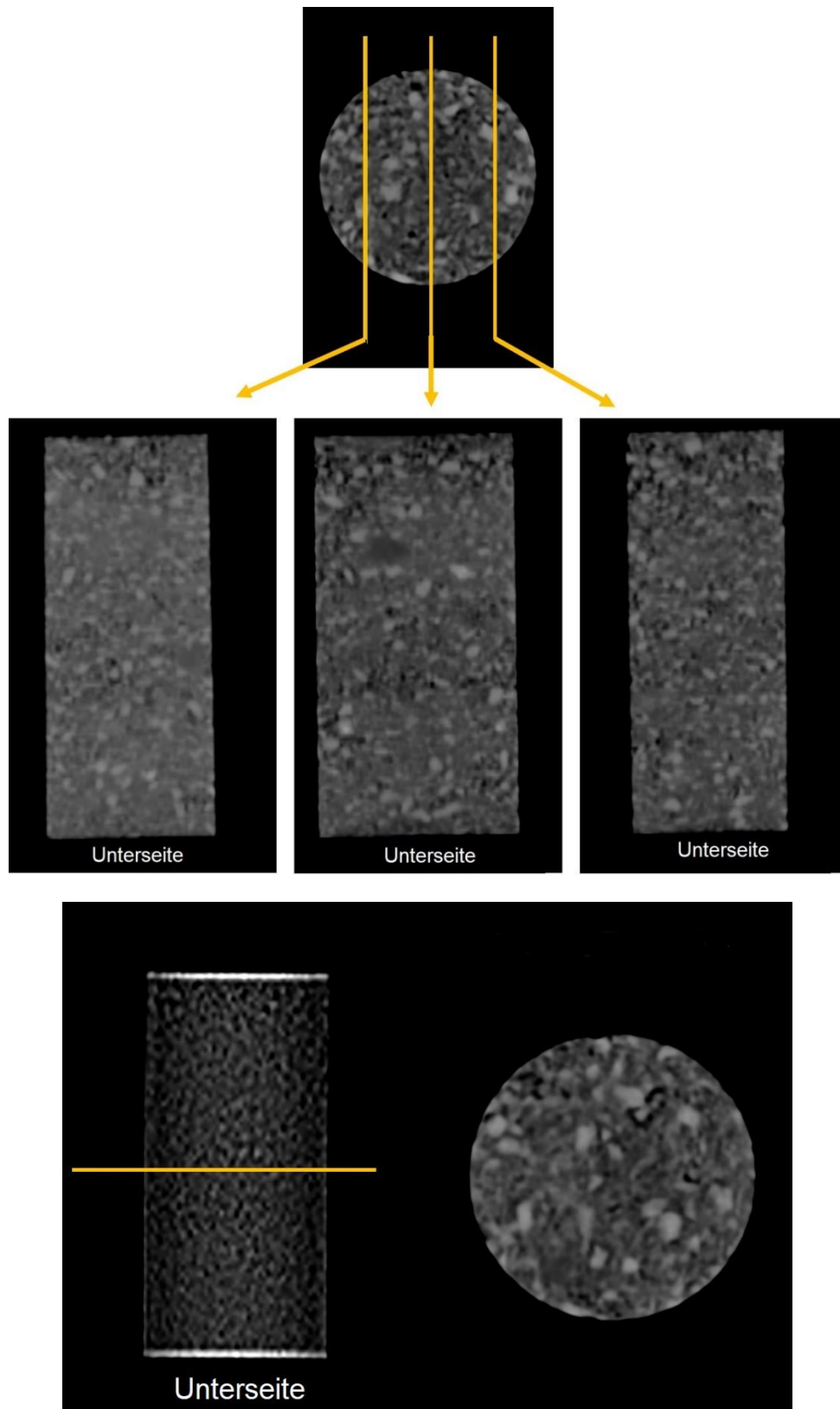


Fig. B.3 CT-Scan of the TUC sample used in the triaxial compaction test at GRS

**Gesellschaft für Anlagen-
und Reaktorsicherheit
(GRS) gGmbH**

Schwertnergasse 1
50667 Köln

Telefon +49 221 2068-0

Telefax +49 221 2068-888

Boltzmannstraße 14

85748 Garching b. München

Telefon +49 89 32004-0

Telefax +49 89 32004-300

Kurfürstendamm 200

10719 Berlin

Telefon +49 30 88589-0

Telefax +49 30 88589-111

Theodor-Heuss-Straße 4

38122 Braunschweig

Telefon +49 531 8012-0

Telefax +49 531 8012-200

www.grs.de